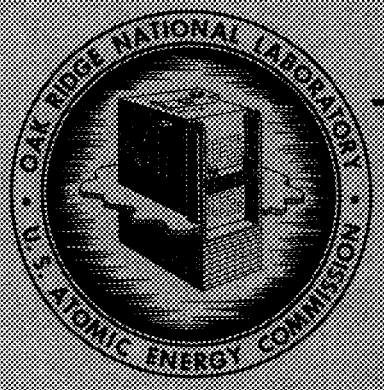
ORNL
MASTER COPY

ORNL-3049
UC-80 - Reactor Technology

GAS-COOLED REACTOR PROJECT

QUARTERLY PROGRESS REPORT

FOR PERIOD ENDING DECEMBER 31, 1960



OAK RIDGE NATIONAL LABORATORY
operated by
UNION CARBIDE CORPORATION
for the
U.S. ATOMIC ENERGY COMMISSION

Printed in USA. Price $4.50, Available from the
Office of Technical Services
Department of Commerce
Washington 25, D.C.

LEGAL NOTICE

This report was prepared as an account of Government sponsored work. Neither the United States, nor the Commission, nor any person acting on behalf of the Commission:

A. Makes any warranty or representation, expressed or implied, with respect to the accuracy, completeness, or usefulness of the information contained in this report, or that the use of any information, apparatus, method, or process disclosed in this report may not infringe privately owned rights; or

B. Assumes any liabilities with respect to the use of, or for damages resulting from the use of any information, apparatus, method, or process disclosed in this report.

As used in the above, "person acting on behalf of the Commission" includes any employee or contractor of the Commission, or employee of such contractor, to the extent that such employee or contractor of the Commission, or employee of such contractor prepares, disseminates, or provides access to, any information pursuant to his employment or contract with the Commission, or his employment with such contractor.

ORNL-3049

Reactor Technology
TID-4500 (16th ed.)

Contract No. W-7405-eng-26

GAS-COOLED REACTOR PROJECT

QUARTERLY PROGRESS REPORT

For Period Ending December 31, 1960

Staff

Oak Ridge National Laboratory

DATE ISSUED

MAR - 2 1961

OAK RIDGE NATIONAL LABORATORY
Oak Ridge, Tennessee
operated by
UNION CARBIDE CORPORATION
for the
U. S. ATOMIC ENERGY COMMISSION

CONTENTS

SUMMARY vii

PART 1. DESIGN INVESTIGATIONS

1. PEBBLE-BED REACTOR STUDIES 3
The Pebble-Bed Reactor Experiment 3
Design Precepts 3
Reactor Core Geometry Considerations 5
Proposed Reactor Design 6
Proposed Plant 8
Reactor Physics Considerations 11
Steam Generator Design 17
Ball-Handling System 18
Helium Cleanup and Equipment Decontamination 19
Hazards Evaluation 24
Research and Development Program 25
The Full-Scale Pebble-Bed Reactor Power Plant 28
Parametric Analysis of Design Requirements 28
Reactor Design 51
2. REACTOR PHYSICS 81
Zone Loading of EGCR Core 81
Reactivity Effects Associated with Operation of the EGCR 84
Neutron Source Required for the EGCR 85
EGCR Shielding 86
Heat Deposition in the EGCR 88
3. REACTOR DESIGN STUDIES 92
Thermal Behavior of EGCR Fuel Assemblies 92
Effect of Control Rod Programing and Mode of Operation 92
Fuel Temperature Variations During Transients 101
Alternate Fuel Assemblies 112
Mass and Heat Transfer Correlation Studies 114
EGCR Control Rods 118
Decontamination of EGCR Components 122
Helium Purification System Studies 123

EGCR Hazards Evaluation 127
Graphite Oxidation 127
Identification of Maximum Credible Loss of Pressure Accident for EGCR 133
Empirical Representation of Neutron Exposure of Moderator Columns in EGCR 134
Estimate of Irradiation-Induced Bowing of Graphite Columns ... 137
Structural Investigations of EGCR Through Tubes 144
Model Tests 145
Prototype Tests 146
Experimental Stress Analysis of a Spherical Shell with an Attached Nozzle 154
Stress Analysis of Compressor for GCR-ORR Loop No. 2 161
4. EXPERIMENTAL INVESTIGATIONS OF HEAT TRANSFER AND FLUID FLOW 169
Resistance-Heated-Tube Heat-Transfer Experiment 169
Mass-Transfer Measurements 173
Velocity Distribution Studies 174
Gas-Mixing Experiments 177

PART 2. MATERIALS RESEARCH AND TESTING

5. MATERIALS DEVELOPMENT 189
Fabrication and Physical Properties of UO_2 189
Powder Processing and Fabrication of UO_2 189
Thermal-Conductivity Studies 190
Thermal Expansion of Dished Pellets 190
Bulk-Density Measurements on Small Irregular Particles 191
Fission-Gas-Release Studies 192
Advanced Fuel Materials Development 196
Fabrication of Fueled BeO Bodies 196
Fabrication of Fueled Graphite 202
Fission-Gas-Release Studies 204
Arc Casting of Uranium Carbide Shapes 205
Volatility of UC at Elevated Temperatures 206
Structural Materials Evaluation 208
Coating for EGCR Graphite Support Sleeves 208

Evaluation of Commercial High-Density Graphite 212
Tube-Burst Testing of Stainless Steel 212
Dimensional Studies of Simulated EGCR Fuel Elements at Elevated Temperatures 213
Reactions of Type 304 Stainless Steel with $CO-CO_2$ Mixtures 216
Manufacturing and Inspection Methods Development 220
Fabrication of Instrumented Fuel Elements and Irradiation Test Capsules 220
Welding of Dissimilar Metals 224
Nondestructive Inspection of EGCR Loop Through Tube Welds 226
Beryllium Investigations 228
Compatibility of Beryllium with Coolant Impurities 228
Beryllium Tubing Evaluation 230
Beryllium Joining 231
Stress-Rupture Properties of Beryllium Tubing 234
6. IN-PILE TESTING OF COMPONENTS AND MATERIALS 238
Fuel Element Irradiation Program 238
Full-Diameter Prototype EGCR Fuel Capsules 238
Beryllium-Cladding and UO_2-Grain-Size Studies 238
Miniature-Capsule Fission-Gas-Release Experiments 244
Advanced Fuel Element Testing 246
Examination of Irradiated Capsules 247
LITR-Irradiated Miniature Capsules 247
ORR-Irradiated Prototype Capsules 250
Instantaneous Fission-Gas-Release Experiment 261
Examination of Thin-Plate UO_2 Sample 261
Tests of a Graphite-Clad UO_2 Sample 261
Oxygen-to-Uranium Ratio Determinations 263
ORR Closed-Cycle-Loop Experiments 265
Graphite-Canned UO_2 265
Graphite-Canned UC_2 Dispersed in Graphite 265
Facility Modifications 265
Radiation Effects on Structural Metals 266

Pressure Vessel Steels 266
Beryllium 266
Type 304 Stainless Steel 269
Inconel 270
7. OUT-OF-PILE TESTING OF MATERIALS AND COMPONENTS 273
Compatibility Tests of Graphite, Structural Materials, and Helium 273
Tests of Prototype EGCR Purification System 276
Evolution of Gas from Graphite 287
Transport of Gases Through Graphite 297
Investigation of Adsorbers for Removing Fission-Product Gases from Coolants 302
Measurement of High Temperatures 308
Thermocouples in Stagnant Helium 308
Thermocouples Inserted in Graphite in a Helium Atmosphere 312
8. DEVELOPMENT OF TEST LOOPS AND COMPONENTS 313
EGCR In-Pile Loops 313
Through-Tube Design 314
Loop Component Designs 317
Hazards Evaluations 321
Stress Analyses 322
Revised Pressure Drop Estimate for Small Loops 322
GCR-ORR Loop No. 2 323
Component Tests 327
Heater and Microswitch Electrical Breakdown Tests 327
EGCR Valve Tests 333
GCR-ORR Loop No. 2 Components 335
Mechanical Joint Service Testing 337
Special Compressors 338
Regenerative Compressors 338
Compressors with Gas-Lubricated Bearings 339
High-Temperature Gas Bearing Compressor Test System 340
Study of Back Diffusion Through Labyrinth Seals 340

SUMMARY

Part 1. Design Investigations

1. Pebble-Bed Reactor Studies

Two design studies have been carried out of the pebble-bed reactor which Sanderson & Porter studies have indicated to be potentially capable of producing low-cost power. First, a preliminary design was prepared for a 10-Mw experimental reactor with which to obtain sufficient data for the design of a full-scale pebble-bed power reactor.

The core of the experimental reactor is 8.1 ft long and 18 in. in diameter and is surrounded on all sides by a 3-ft-thick graphite reflector. The fuel consists of 1 1/2-in.-diam balls composed of 90.0 wt % graphite, 5.49 wt % UO_2, and 4.51 wt % ThO_2. The uranium is fully enriched. The core has 39% of its volume as space for the coolant gas (helium). It is intended that the fuel residence time be 246 days, which will give a uranium burnup of 10%. These conditions will subject a fuel ball to the same temperature, power density, and burnup as would be experienced in a full-scale power reactor. An unusual feature of the reactor design is the use of control blades placed circumferentially in the reflector. Since the reactor is mainly reflector-moderated, this location provides effective control without interference with the fuel balls in the core.

The gas-cooling system is designed to supply helium at a pressure of 1000 psi with a core inlet temperature of 550°F and a core outlet temperature of 1250°F. The gas system configuration was chosen to assure removal of afterheat by thermal convection. A steam generator designed to deliver steam at 1000°F and 1000 psi is provided to remove heat during normal operation.

The second study produced a design of a 330-Mw (electrical) pebble-bed reactor power plant based on a parametric analysis of the design requirements. In this design the reactor thermal output (800 Mw) is removed by helium entering at 550°F and leaving at 1350°F under a pressure of 700 psia. Three concepts of gas flow through the core were analyzed: axial

downflow, radial outflow, and axial upflow; the last was chosen for the design study.

The cylindrical core is 20.7 ft in diameter and 12.4 ft high. It is surrounded by a 3-ft-thick graphite reflector. The core and the reflector are contained in a 31.4-ft-i.d. spherical pressure vessel of 4-in.-thick carbon steel.

The fuel consists of 2.5-in.-diam graphite balls containing 0.44 wt % U^{235} and 8.45 wt % Th. The core power density is 6.6 w/cm^3 and is limited by the levitation of the fuel. Larger fuel balls, which could withstand higher gas flows without levitation, appeared to be limited to lower power densities because of thermal stresses. The conversion ratio, which is initially 0.75, will eventually rise to about 0.8. The fuel residence time in the core is 700 days.

The two steam generators are once-through boilers containing economizer, boiler, reheat, and superheat sections. Feed water enters at 400°F and leaves as steam at 2480 psia and 1055°F. Reheat steam enters at 470 psia and 623°F and leaves at 460 psia and 1005°F. The turbine-generator, a tandem-compound type, is rated at 345 Mw and is designed for indoor installation.

2. Reactor Physics

A zone-loading pattern for the EGCR has been designed that is a satisfactory compromise between the requirements for power flattening and the desire for high loop power. Since installation of the loops is to be deferred, this fuel loading will not be required for the initial core.

Reactivity effects associated with operation of the EGCR were studied to obtain data needed for determining the control actions that must be available. Also, calculations were made of the neutron source required for the EGCR. A point source and a shell source were considered, and it was found that the flux in the fission chambers depended significantly on the shutdown reactivity and on the source position.

Studies of the flux levels at EGCR shield penetrations and the dose rates around the charge and service machines were made. The dose rates at points where men will be working are not expected to exceed 17 mr/hr.

Further calculations of the heat deposition in the EGCR core have included the additional heating by gamma rays originating in a loop experiment and the heating effect of fast neutrons. The core heat deposition by fast neutrons was found to be 1.97 Mw, and the reflector heat deposition was 0.19 Mw.

3. Reactor Design Studies

The thermal behavior of the EGCR fuel assemblies has been analyzed in terms of the effect of control programing and mode of operation. Three different control rod positions were evaluated with respect to (1) operation with all orifices set so that the exit gas temperature from each fuel channel would be the same and (2) operation with the orifices set to maintain a uniform maximum fuel element surface temperature in each channel. The analyses indicated that the difficulties associated with setting the orifices to maintain a uniform maximum fuel element surface temperature are not warranted.

The ORNL analog computer was used to analyze EGCR fuel temperatures during the following transients: (1) the extremes of the normal conditions, (2) variations caused by loss of gas flow, (3) variations caused by reactivity increases, and (4) variations caused by loss of power. The results are pertinent to design evaluations.

Preliminary designs have been prepared for four types of beryllium-clad fuel elements to be used in alternate fuel assemblies for the EGCR core. Clusters of 7, 12, and 19 rods are being considered.

Correlation studies were made of mass transfer data and heat transfer data applicable to EGCR fuel assemblies. The agreement between heat transfer data for a seven-rod bundle and mass transfer data for a simulated EGCR fuel element was within 7% and with 10% (with the exception of the first half of the center tube, which was within 20%) of data from heat transfer experiments on round tubes.

The design of the EGCR control rod has been modified, and a full-scale mockup is being assembled to establish fabricating techniques. Limited tests will be made on the mockup to confirm design assumptions.

A method for decontaminating EGCR components has been developed. An oxalate-peroxide solution of controlled pH is used that simultaneously dissolves UO_2 and decontaminates steel surfaces.

A kinetics study of the oxidation of H_2, CO, and CH_4 in a flowing stream of helium in a fixed bed of Girdler G-43 platinum catalyst has been completed. The experimental data have been correlated empirically. Apparent reaction rates and design equations for determining the necessary bed volumes for a helium purification system were determined.

In EGCR hazards evaluations, the possibility of ignition of the graphite if air entered the system because of a rupture was considered. Since there are areas in the EGCR where unprotected graphite surfaces are at temperatures in excess of 1100°F, means must be provided to control or eliminate graphite oxidation. Experimental studies of this problem are under way. It appears that coating the fuel element sleeves will be effective in inhibiting graphite oxidation in the EGCR.

A review of the maximum credible accident postulated for the EGCR has been made by an AEC-appointed task force. As a result of the review, a single-ended pipe failure was defined as the maximum credible failure based on (1) physically restricting the piping system in key locations so that double-ended failure is not possible and (2) providing for inspections and tests to preclude the possibility of a nonductile failure for the portion of the piping external to the biological shield.

An empirical representation of the neutron exposure of the moderator columns in the EGCR has been developed for use in evaluating the induced stresses. A detailed comparison with numerical data showed that the empirical representation gives a good approximation for those columns that contain four fuel channels and is sufficiently accurate for those which contain less than four channels.

Fast-neutron exposure will lead to bowing of the EGCR graphite columns, and therefore an evaluation of the deflection of each column is required as a basis for designing the supports. The maximum unrestrained bowing potential was found to be 3.61 in. along both the x and y axes.

Instantaneous collapse and creep buckling tests of type 304 stainless steel cylindrical shells are being conducted in order to obtain data

applicable to the experimental tubes in the EGCR. In model tests, the critical buckling pressure is being correlated with time, and geometrical variables are being studied. In prototype tests, 8- and 4-in.-o.d. tubes are being tested at service temperatures. Some correlation of collapse geometry with original variations in the tubing have been noted.

An experimental stress analysis was made of a spherical shell with an attached nozzle in order to check the hypothesis that the total stresses resulting from combined loadings may be obtained by linearly adding the stresses corresponding to each component separately applied, so long as the elastic limit is not exceeded. Excellent agreement was found.

An analysis was made of means for reducing thermal stress in the region of the junction of the pressure-vessel body and the flange that forms a part of the volute of the compressor for GCR-ORR loop No. 2. Design criteria were established.

4. Experimental Investigations of Heat Transfer and Fluid Flow

Analytical studies of previously reported heat-transfer data obtained with a 2:1 ligament-ratio spacing and inlet screens are continuing based on complete transverse mixing of the gas stream. The results indicate that a flow asymmetry exists that arises in the entrance to the cluster. In the upstream portion of the cluster, diminished flow in the inner region of the channel exists, which is followed by flow redistribution between the inner and outer regions. Both of these effects are largely wiped out by the mid-cluster spacer. A comparison was made of these data with data from experiments using a 4:1 ligament-ratio spacing and experiments using a 2:1 ligament-ratio spacing without screens. The results indicate that for the $\gamma = 2$ arrangements, the mid-cluster spacer effectively eliminates flow vagaries introduced at the channel inlet. Heat-transfer coefficients of the $\gamma = 4$ arrangement are, in general, lower than those of the $\gamma = 2$ arrangements.

Recent mass-transfer experiments indicated that the mass-transfer factors approached a higher asymptotic value in the downstream section of the tube cluster than in the upstream region. In order to investigate this further, a run was made with naphthalene covering the entire rod so

that mass removal would be effected simultaneously on both halves of the rod. The results of this double run agree quite closely with the earlier data, negating the possibility of geometrical or operational variations during the previous runs. The study of this phenomenon is being continued.

The accumulation of data for delineating the velocity field in the downstream element of two EGCR clusters has been continued using three similar experimental assemblies. Comparable data from the different systems agree, in general, as to the profile shape, with slight deviations in magnitude that probably result from the slight geometrical differences. Flow variations introduced by the spiders are clearly discernable; in contrast, the spacers appear to have much less influence on the gross flow. Experiments to provide similar characterization of the flow at positions far removed from the spiders and spacers are in progress.

An experimental program has been initiated in an effort to establish the magnitude of intra- and intercluster mixing. The experimental technique consists of injecting a small amount of a tracer gas at a given point in the flow channel and measuring concentrations of this tracer gas at various sampling points downstream. Using air as the flowing gas and helium as the tracer gas, preliminary data show a prevalence of radial mixing with very little circumferential mixing. These preliminary data do not indicate any gross mixing due to spiders or spacers. Experimentation is continuing using improved equipment to obtain more detailed traverses.

Part 2. Materials Research and Testing

5. Materials Development

The conditions for fabrication of UO_2 specimens with controlled grain sizes for use in various experiments are being established. Grain growth of UO_2 is inhibited by sintering in argon. The final grain size is only one fifth as large as that obtained during sintering in hydrogen.

Several modifications were made to the apparatus being developed for measuring the thermal conductivity of UO_2. The coefficient of thermal conductivity of INOR-8 alloy was then measured at temperatures up to 700°C

with a precision of ±1%. The measurement of bulk density of fragments and particles of UO_2 by an embedment technique using Castoglas resin shows promise of assisting in the evaluation of broken pellets from irradiated capsules.

A comparison of data from Chalk River on fission-gas release from UO_2 with ORNL data on duplicate specimens shows poor correlation, except for specimens with high BET surface areas. Data obtained at ORNL were for larger samples and, in general, agreed with the theoretical data for release by diffusion. It appears that the BET surface area is indicative of the fission-gas-retention properties of UO_2 up to temperatures at which structural changes occur.

Rates of fission-gas release from a fine-grained dispersion of UO_2 in BeO were measured at temperatures of 1200 to 1800°C. Up to temperatures of 1400°C, the calculated D′ values compare favorably with those of high-density UO_2. The release-rate parameters were also determined for a fueled-graphite body prepared by the National Carbon Company, designated as TS-160 mix, that consisted of UC_2 dispersed in graphite.

Fine-grained dispersions of UO_2 plus ThO_2 in BeO were fabricated for use in high-temperature irradiation experiments. Three phases — BeO, a ThO_2-UO_2 solid solution, and a small amount of free UO_2 — were identified in the structure of the as-fabricated material. In addition, techniques were developed for the fabrication of large-particle dispersions of UO_2 in BeO by matching the shrinkage of the two starting materials.

Several commercial binder materials considered for use in graphite fabrication were found to have adverse reactions with UC. Other specimens were prepared by wet mixing with a solution of uranyl nitrate, which, when fired, developed good physical properties. The fabrication of graphite fueled with coated and uncoated particles of UC_2 was also studied. Fuel particles consisting of UC_2 coated with pyrolytic graphite showed very promising results.

The cause of cracking in arc-cast UC cylinders has been determined to be the result of rapid cooling. Modifications in melting practice designed to reduce the cooling rate have eliminated internal cracking in all but the larger diameter cylinders. Large cylinders of UC cast in graphite

molds exhibited evidence of considerably slower cooling rates than similar cylinders cast in copper molds and showed only slight internal cracking.

The loss of material from UC during high-temperature sintering was studied by means of a mass spectrometer. Ion species identified included only U^+, UO^+, and UO_2^+, indicating that oxide phases present as impurities may be responsible for loss of material.

The oxidation resistance of uncoated and siliconized SiC-coated graphite samples was determined. The coating is completely protective on type 901S graphite, a relatively isotropic grade. However, on type 580 graphite the coating cracks badly as a result of anisotropic contraction and is only partially protective. The thickness of SiC coating on EGCR support sleeves was measured by an eddy-current technique to be 0.030 to 0.060 in. The mechanical properties of several commercial high-density grades of graphite were determined as part of an evaluation program.

The grain growth of type 304 stainless steel tubing during brazing of spacers at 2150°F was previously shown to promote premature failure in tube-burst tests. The substitution of copper, which is brazed at 2020°F, has resulted in much less grain growth. The effects of the copper braze on the stress-rupture properties of the tubing are being studied.

Thermal cycling of simulated EGCR fuel elements was found to cause axial elongation of the cladding in those elements having no diametral gap between the cladding and fuel pellets. This elongation is affected by the external pressure and the temperature and frequency of the cycles. A mathematical relationship between the axial strain and the cladding temperature was developed.

The oxidation of type 304 stainless steel in low concentrations of CO-CO_2 mixtures in helium has been found to be insignificant below 1200°F, while above this temperature the oxidation rates are dependent on temperature but independent of the total content or the ratios of CO and CO_2. Activation energies were calculated to be 32 200 cal/mole for temperatures up to 1525°F and 6400 cal/mole above this temperature. The change in the reactivity can be correlated with the formation of different reaction products.

Carburization of type 304 stainless steel was found to depend upon the temperature, the CO_2/CO ratio, and the reaction time. Nonequilibrium carbon contents were evident in 0.002-in. foils after exposures of 200 hr and in 0.020-in.-thick sheet after 800-hr exposures. Carburization did not occur at temperatures below 1200°F.

Improved methods are being developed for fabricating in-pile capsules and instrumented fuel assemblies containing thermocouple wells and tungsten-rhenium thermocouples. The use of stranded tungsten wire is being studied as a means of improving the integrity of such thermocouples. Techniques for attaching sheathed Chromel-Alumel thermocouples to stainless steel tubing also are being investigated.

High-temperature mechanical properties of ferritic steel-to-stainless steel welds were determined. All specimens failed in the base material. Thermal-cycling studies of these welds are being conducted.

Defects as small as 1/8 in. in diameter in V-groove welds on EGCR loop through tubes can be detected by a through-transmission ultrasonic technique. Lack-of-fusion areas that were undetected by visual and radiographic inspection have been found by this technique and confirmed by metallographic examination.

The oxidation rates of extruded or hot-pressed beryllium in CO_2 have been found to compare favorably with previous data on beryllium powder. The "break-away" phenomenon reported between beryllium and wet CO_2 was not observed in the presence of water vapor alone. The experimental results indicate that the presence of Be_2C is a requirement for the accelerated oxidation of beryllium.

Metallographic examination of surface cracks and internal pits detected in beryllium tubing from Pechiney showed the cracks to be as much as 0.003 in. deep and the pits to be 0.003 to 0.004 in. deep.

Welding and brazing studies on beryllium have been continued with emphasis on end closures of tubes. The influences of the welding process and type of material on the final grain size have been studied, and methods that yield a small grain size have been developed.

Approximately 150 tube-burst specimens of beryllium have been successfully fabricated, with a rejection rate of about 10%. These specimens

are being used to determine the mechanical properties of tubing from various commercial sources. Preliminary stress-rupture data show that tubing machined from hot-pressed block has the highest strength and lowest ductility of the eight different types tested.

6. In-Pile Testing of Components and Materials

Irradiation of 14 prototype EGCR fuel capsules in the ETR and the eight group III capsules in the ORR has continued. The series of irradiations in the LITR of UO_2 specimens for fission-gas-release experiments was completed. Irradiations of small specimens of BeO-ThO_2-UO_2 and UC were initiated. Irradiation of the second graphite-encapsulated test element fueled with a UC_2-graphite matrix was completed.

Postirradiation examinations of LITR-irradiated specimens have continued. Information on the effect of irradiation on density and grain growth is being collected.

The nondestructive examinations of the ORR-irradiated group II capsules were completed. Gamma scans and cladding profile measurements were made. The activity plots showed quite uniform burnup along the length of the capsules. The diameters decreased, but the change was less than 1%. The cladding collapsed around the pellets in most of the capsules. Variations from straightness were a minimum for the capsules with hollow pellets tested at 1300°F and increased with temperature.

The thin-plate UO_2 sample that had been used as the source for instantaneous fission-gas-release experiments was examined. This plate had been oxidized during irradiation by trace quantities of oxygen in the sweep gas and then reduced by adding hydrogen. When the capsule was opened, the UO_2 was found to be in granules 0.050 in. in diameter or smaller. Such fragmentation is not characteristic of irradiated UO_2 and can probably be attributed to the reduction reaction.

A sample of high-density UO_2 clad in low-permeability graphite coated with pyrolytic carbon was irradiated to evaluate the effectiveness of the carbon coated graphite in retaining fission gases. Since the release of fission gases was about the same as for unclad UO_2, it was concluded that the cladding was probably broken. The sample has been removed for examination.

Since the properties of UO_2 fuel elements are sensitive to the oxygen-to-uranium ratio, techniques for determining the ratio in irradiated material are being developed. Thermogravimetric and polarographic methods are being studied.

A capsule containing two Si-SiC coated graphite-canned UO_2 cyclinders has been removed from the ORR closed-cycle loop for examination. There was evidence of fission-gas release during the last thermal cycle. Two UO_2 samples canned in uncoated low-permeability graphite that had been irradiated for 1000 hr at 1800°F were also withdrawn. Out-of-pile tests of enriched UC_2 dispersed in graphite and canned in Si-SiC coated graphite have shown no weight or density changes.

Equipment for irradiating pressure vessel steels in the ORR has been completed.

The second high-temperature experiment for studying the irradiation-induced swelling of beryllium was completed. Specimens were irradiated at 500, 600, and 700°C to a neutron dose of 1.4×10^{20} neutrons/cm^2. The extent of swelling was smaller than the experimental error in the measurement. Postirradiation bend tests indicated that the mechanical properties were unaffected. Bend tests on samples from an irradiated specimen exposed at 120°F to a dose of 6×10^{20} neutrons/cm^2 indicated that extensive embrittlement occurred. Hot-extruded specimens showed the most severe effect. A third experiment is under way.

In-pile tube-burst-type stress-rupture tests of type 304 stainless steel have shown that at 1500°F neutron bombardment reduces the rupture strength by about 1500 psi in the stress range studied, i.e., 3000 to 6300 psi.

7. Out-of-Pile Testing of Materials and Components

A fourth test of graphite and structural materials in flowing helium containing controlled amounts of CO_2 and CO was completed. The maximum temperature of the loop was 1100°F, and the cooled section was at 500°F. The steel specimens that contained less than 7% chromium gained appreciable weight and had relatively heavy, poorly adherent oxide films. In contrast, the steel specimens that contained 7% or more chromium had relatively

thin, extremely adherent oxide films and showed minor increases in weight. A type 304 stainless steel tube that was suspended in the loop and was independently heated to 1500°F had a somewhat heavier but equally protective oxide film.

Tests are being carried out on a small-scale model of the EGCR purification system for determining the effectiveness of the system in removing gaseous impurities from circulating helium. Preliminary results indicate that hydrogen, carbon monoxide, and the methane can be satisfactorily removed by oxidation in a catalytic converter. The gaseous oxygen added upstream of the converter is essentially completely removed by passage over the platinum catalyst bed. Removal of CO_2 and H_2O by use of molecular-sieve and silica-gel adsorber beds, respectively, has also been successfully demonstrated.

Experimental studies of the degassing behavior of selected grades of graphite have been continued. Results of tests of a series of graphite samples prepared from needle coke by the Speer Carbon Co. have indicated that variations in the particle-size distribution in the coke mix do not have a significant effect on the gas content of the graphite. Other variables of the manufacturing process appear to be more important. Plots of the volume of gas evolved versus the log of time have shown that at 600°C the relationship is linear, but at 1000°C the slopes of essentially linear portions of the curves differ. The data suggest that different processes of gas evolution exist during the early and latter parts of the degassing period. The composition of the evolved gas changes in that the relative concentration of hydrogen increases and the $CO + CO_2$ concentration decreases.

A series of room-temperature permeability determinations were made on a typical EGCR-moderator graphite block. The data obtained showed considerable variation even in the same block of graphite. Apparatus for obtaining permeability data for graphite having permeabilities in the range 10^{-4} to 10^{-6} cm^2/sec has been constructed.

Means for the removal of radioactive iodine vapor from high-temperature helium streams are being studied. Initial results on the use of Pittsburgh BPL activated charcoal or silver-plated copper ribbon for iodine-vapor

removal indicate that the silver-bearing material is the more promising for use at high temperatures under EGCR conditions.

Investigations of adsorbers for radioactive krypton and xenon were continued. Effective diffusion coefficients were evaluated for krypton in PCB charcoal at 0, 25, and 60°C. Static adsorption coefficients were compared with dynamic coefficients, and good agreement was noted. The heating that occurs upon pressurization of adsorbers and krypton holdup by Linde molecular sieves partially saturated with water or carbon dioxide were also studied.

Further study of the negative emf drifts experienced with Chromel-P in stagnant helium at 1000°C has indicated that the principal mechanism involved is the selective oxidation of chromium in the thermal-gradient region (800–900°C). Also traces of carbon oxides may be partly responsible for the emf drifts. Metallographic studies of sections of wire from the thermal-gradient region showed gradual increases in depth of intergranular oxidation of chromium with increases in time at temperature. Portions of the wires outside the thermal gradient experienced only nonselective surface oxidation.

Theoretical calculations from thermodynamic data indicate that it should be possible to selectively oxidize chromium in Chromel-P with a mixture of water vapor in hydrogen. Attempts are being made to correlate thermal emf drift data with controlled selective oxidation.

Preliminary experiments over a seven-week period indicated that Chromel-P-Alumel thermocouples sheathed in type 304 stainless steel were showing a negative emf drift while exposed to a graphite-helium atmosphere at 870°C. Thermocouples sheathed with type 310 stainless steel did not show a negative drift. It seems possible that the atmosphere was responsible for the drift, since controls of both types showed only slight positive drifts when exposed to the same thermal history but open to air. Further experiments are necessary before understanding the cause of the emf drifts.

8. Development of Test Loops and Components

Work continued on the design of the EGCR in-pile loops. The Title I design is to be completed and the preliminary hazards report is to be

prepared, although completion of loop installation is to be deferred until at least July 1, 1965. Title II design of the upper and lower nozzle tee sections, the upper and lower horizontal piping chases, and the necessary chases for cooling ducts will be completed in order to make the required minimum provisions in the present EGCR construction.

Construction work continued on GCR-ORR loop No. 2. The evaporator, condenser, and heater components of the heat transfer system were subjected to performance tests. Criteria were prepared for the design of a gas-sampling station.

Electrical breakdown tests were made of heaters and a microswitch proposed for use in EGCR loops and ORR loop No. 2 in order to establish operating characteristics. A ball valve with a Limitorque operator for use in the EGCR was tested in a furnace at approximately 1000°F. During these tests in which performance of the valve was unsatisfactory, the volume between the valve stem packing and the bellows seal was at the same pressure as that in the valve. It was learned later that the valve was designed to operate with 1000-psig internal pressure and no bellows backup pressure. The valve has been returned to the manufacturer for repair.

Three 5-in.-IPS, double-seal, gas-buffered Conoseal joints and two 6-in.-IPS, double-seal, gas-buffered Grayloc joints were tested during the quarter. Efforts are being made to improve the performance of these units.

The two regenerative compressors that were installed in the twin-turbine vessel of ORR loop No. 1 have operated satisfactorily for approximately 1000 hr. Further difficulties with bearing whirl have occurred at the Bristol Siddeley plant where compressors with gas-lubricated bearings are being fabricated. The application of hydrodynamic bearing theory to these problems was studied further.

The study of back diffusion through labyrinth-type seals was completed. The numerous tests failed to show any evidence of water-vapor back diffusion into the gas chamber.

Part 1. Design Investigations

1. PEBBLE-BED REACTOR STUDIES

(A. P. Fraas, R. S. Carlsmith, J. M. Corum,
J. Foster, B. L. Greenstreet, W. O. Harms,
T. Hikido, R. B. Korsmeyer, J. W. Michel,
S. E. Moore, M. L. Myers, M. N. Ozisik,
A. M. Perry, M. W. Rosenthal, J. C. Suddath,
M. M. Yarosh)

Sanderson & Porter have carried out a series of studies over the past four years which indicate that a pebble-bed reactor could be developed to produce low-cost power.[1,2] At the request of the AEC, two design studies have been carried out at ORNL. The first was a preliminary design of a pebble-bed reactor experiment (PBRE) for the purpose of establishing design objectives that would most effectively demonstrate the feasibility of this reactor system and of estimating the research and development required in support of the experiment.[3] The second was a design study of a large-scale plant (PBR) following the general approach in the Ten-Year Program studies.[4] The highlights of these two studies are presented here.

The Pebble-Bed Reactor Experiment

Design Precepts

The following set of precepts was established as a basis for evolving the design:

1. The major objectives of the 10-Mw PBRE should be to study the structural stability and fission-product retention characteristics of fueled-graphite spheres, to study the deposition of fission-product

---

[1] "Design and Feasibility Study of a Pebble Bed Reactor-Steam Power Plant," S&P-1963, May 1, 1958.

[2] "Pebble-Bed Reactor Program Progress Report, NYO-2373, June 1959.

[3] "Preliminary Design of a 10-Mw(t) Pebble-Bed Reactor Experiment," ORNL CF-60-10-63, November 1, 1960.

[4] A. P. Fraas et al., "Design Study of a Pebble-Bed Reactor Power Plant," ORNL CF-60-12-5, December 15, 1960.

activity throughout the system, to develop means of dealing with problems posed by this activity (e.g., gas leaks, equipment decontamination for maintenance, etc.), and to develop a suitable fuel-handling system.

2. The design should not be compromised by requirements for tests not concerned with the pebble-bed concept.

3. The size of the fuel spheres, the core power density, the operating temperatures, the temperature distribution, and the pebble bed height should be the same as for a full-scale core.

4. In order to simplify the system and cut costs, the PBRE should not include a thorium blanket.

5. The fuel-handling system requirements should be studied and selected to provide for one of the following: charging at full power, charging at zero power but full pressure and temperature, or charging at zero power, atmospheric pressure, and the temperatures characteristic of full-power operation.

6. A fast gas-system pumpdown (not more than 1 hr) should be possible to reduce hazards in the event a small leak developed suddenly.

7. The fuel elements should be of a type shown by in-pile testing to give a fission-product release rate of less than 10^{-4} times the rate of fission-product generation at full power.

8. Provisions for coping with the fission products released should include means for handling the isotopes characteristically released from UO_2 and those to be expected from UC and UC_2 fuels.

9. The gas system configuration should give satisfactory removal of afterheat by thermal convection if practicable.

10. The means for coping with differential thermal expansion in the system configuration should be consistent with means that would be suitable for a full-scale plant.

11. The moving parts of the blowers should be replaceable.

12. Provisions should be made to permit decontamination of the blowers and the fuel-handling system before the initiation of maintenance work. These should include means for hydraulically isolating the component affected to permit spraying or flooding it with a cleaning solution.

13. Provisions for maintenance of the main heat exchanger need to include only access to tube headers outside the shield to permit plugging of a leaky tube and an access opening in the pressure vessel for inspection with a periscope or TV camera and removal of samples.

14. The fuel-handling system should be designed to permit clearing a region of jammed balls.

15. The graphite core structure should be accessible for inspection and maintenance. If possible, parts in the high fast-neutron flux region should be replaceable, preferably through an access opening about 2 ft in diameter.

16. The temperature of the structural envelope should not exceed 650°F.

17. Full pressure containment should be provided.

Reactor Core Geometry Considerations

Two types of reactor core were considered: a short, squat, cylinder 30 in. in diameter and 30 in. high and a tall, thin, cylinder 18 in. in diameter and 8 ft high. Both cores would require a 3-ft-thick graphite reflector.

The most important design requirements were that the core should give a power density and a temperature distribution similar to those of a full-scale reactor. The gas inlet temperature should be roughly 550°F to give as high a gas temperature as is compatible with type SA-212, grade B, pressure vessel steel, and the reactor gas outlet temperature should be at least 1250°F to give significant improvement over the outlet temperature obtainable with stainless steel-clad UO_2 fuel elements. The required gas temperature rise would be associated with peak fuel surface and internal temperatures of approximately 1800 and 2200°F, respectively, for the tall, thin core, as compared with corresponding values of 2600 and 3000°F for the short, squat core. In view of the likelihood that the fuel spheres would be damaged by temperatures above 2200°F, it appeared that the short, squat core was less desirable than the tall, thin core. This and other considerations led to the choice of the tall, thin core for the design of the experiment.

Sanderson & Porter have considered both upflow and downflow cores. Downflow cores have the advantage of not requiring a structure over the top of the bed to hold the balls in place at the gas flow rates required for power densities above 15 w/cm^3. However, the problems of material strength under heavy loads and the difference in thermal expansion between graphite and steel in a core support structure subjected to the reactor exit gas temperature render the design difficult. An upflow core was therefore chosen with the realization that the experiment would have to be limited to low-power-density operation if a suitable core top restraint could not be designed. The upflow core has the advantage that it provides for the removal of afterheat by natural thermal convection in the event of blower failure.

Proposed Reactor Design

The design of the proposed reactor experiment is shown in Fig. 1.1. The control rods are curved Inconel plates that slide in an annulus between the intermediate and outer graphite portions of the reflector. The blades are so effective in poisoning the reactor that a thickness of only 0.062 in. will suffice. For strength, however, thicker, perforated blades surrounded by a tubular frame are used. The rods operate through an annulus provided between the shield plug and the top reactor access tube. A small pressure vessel attached to the top flange of this access tube houses each control rod drive assembly.

The reactor pressure vessel is cylindrical, with hemispherical heads, and is made of type SA-212, grade B, carbon steel. There is a 28-in.-i.d. vertical access tube in the center of each head. The steam generator is attached to the side of the pressure vessel in such a way that its base also serves as a major mounting foot for the support of the reactor-steam generator assembly. The reactor, steam generator, and blower assembly are supported on a 3-point suspension. In addition to the fixed foot under the steam generator, a foot is located under each of the two blowers. Thus the ducts to the blowers also serve as elements of the reactor vessel support structure. To increase their stiffness they are larger in diameter than is required by fluid pressure drop considerations,

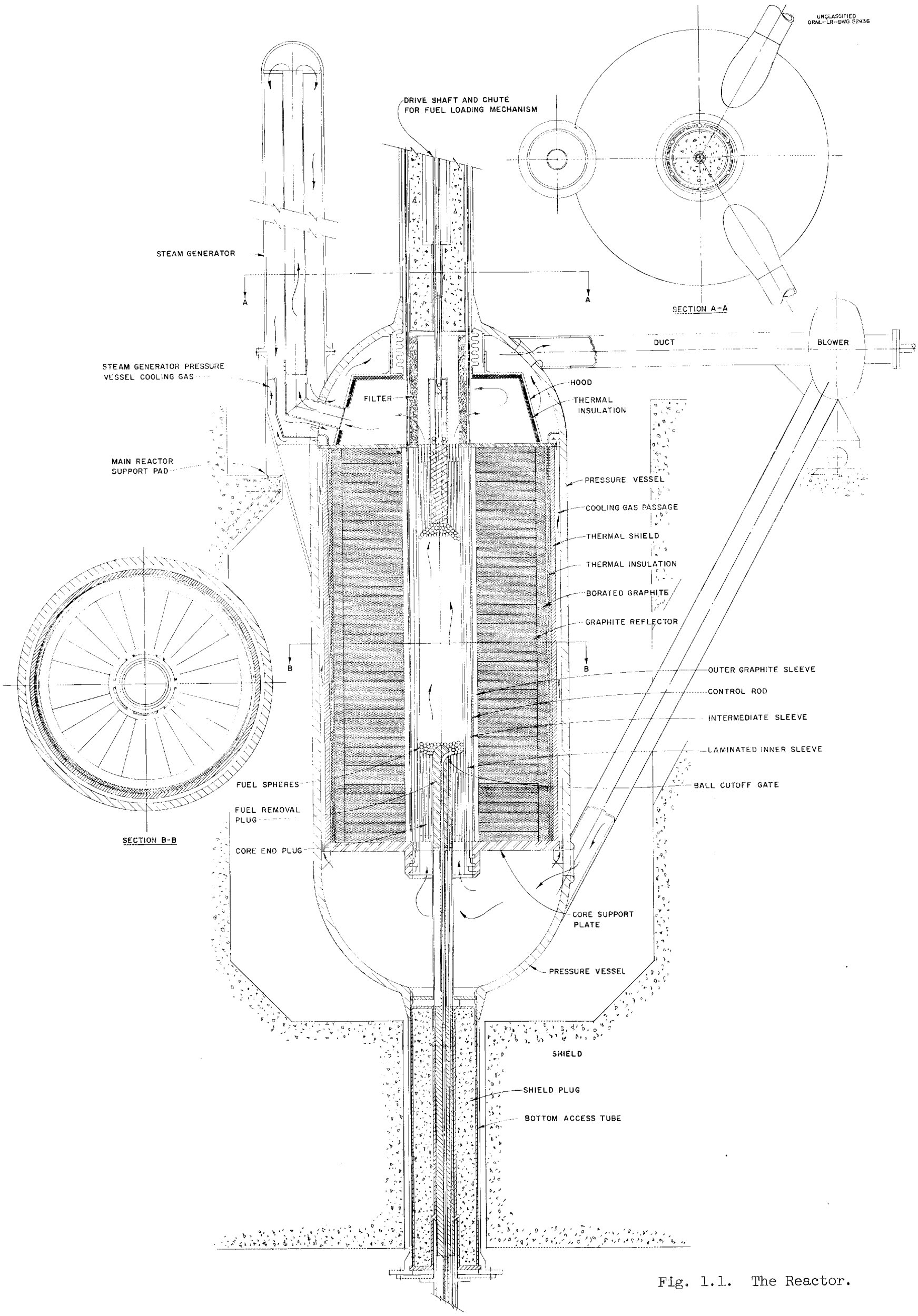


Fig. 1.1. The Reactor.

and their wall thickness is double that required to withstand the internal pressure. Vertical splitter webs have been provided through the ducts at the blowers to transmit the load in shear from the horizontal to the diagonal duct. The blowers are mounted on rollers to accommodate thermal expansion.

The unfavorable surface-to-volume ratio in a small power reactor makes pressure-vessel cooling somewhat more of a problem than it would be in a full-scale plant. About 10% of the blower output bypasses the core to cool the pressure vessel, thermal shield, and steam-generator pressure vessel. The bypass stream provides forced flow of cooling gas around these pressure vessels at essentially reactor inlet temperature.

Proposed Plant

The reactor was designed to produce a gross thermal output of 10 Mw. Although the addition of a turbine-generator to produce a gross electrical output of about 3 Mw was considered, the cost of the addition appeared to be prohibitive, since the plant is primarily an experiment. The basic design data of the plant follow:

Over-all Power Generation Data

Reactor thermal output, Btu/hr	34.1×10^6
Reactor thermal output, Mw	10
Gross electrical output, Mw	3

Fuel Element Characteristics

Sphere outside diameter, in.	1.5
Sphere thermal stress (for ideal rigid body), psi	2500
Sphere surface, ft^2/ft^3 of fuel	48
Sphere surface, ft^2/reactor (39% voidage assumed)	418
Sphere average surface temperature, °F	~1200
Sphere maximum allowable internal temperature (including hot spots), °F	2200

Number of spheres per reactor (39% voidage assumed)	8500
Average power density in core, w/cm^3	25
Average surface heat flux, $Btu/hr \cdot ft^2$	81 500

Reactor Core Material and Dimensions

Material	Graphite
Core height, ft	8.1
Core diameter, ft	1.5
Core face area, ft^2	1.77
Height of core plus reflector, ft	14
Diameter of core plus reflector, ft	7.5
Machined weight of graphite, tons	32
Core density, g/cm^3	1
Total graphite volume, ft^3	600
Number of fuel channels	1
Number of fuel charge tubes	1

Pressure Vessel Dimensions

Shape	Cylinder
Outside diameter, ft	9.25
Material	Type SA-212, grade B, steel
Vessel height, ft	25
Thickness, in.	3.25
Working pressure, psig	1000
Design stress, psi	15 000
Maximum temperature, °F	600
Volume, ft^3	1300
Gross vessel weight (including vessel and core supports, thermal barriers, nozzles, steam generator, and insulation), lb	~200 000

Coolant Characteristics

Gas	Helium
Working pressure, psia	1000
Total flow (normal), lb/sec	12.0
Reactor inlet temperature, °F	550
Reactor outlet temperature, °F	1250
Number of inlet pipes	2
Number of outlet pipes	1
Inside diameter of pipe, ft	1
Mean coolant velocity in cool pipe, ft/sec	20.7
Mean coolant velocity in hot pipe, ft/sec	71
Total volume occupied by coolant, ft^3	950
Circuit pressure drop, psi	30
Specific heat capacity of coolant, Btu/lb·°F	1.24

Coolant Blowers

Type	Centrifugal
Number per reactor	2
Adiabatic efficiency, %	70
Compressor power, Bhp	127
Power, kw (at 90% motor efficiency and 70% adiabatic efficiency)	150 each
Blower drive motor power, Bhp	182 each

Steam Generator

Type of generator	Natural recirculation
Number per reactor	1
Number of steam generator sections	2
Shell height between heads, ft	43
Shell height including heads, ft	45
Shell inside diameter, ft	2

Shell thickness, in.	1
Gas inlet inside diameter, ft	0.75

A plan view of the plant is shown in Fig. 1.2, and an elevation through the containment vessel and building is shown in Fig. 1.3. The reactor area is enclosed in a hermetically sealed containment shell that is approximately 80 ft in diameter and 200 ft high, the bottom of which is located 104 ft below ground, bringing the top of the reactor pressure vessel about 10 ft below ground level. The cooling gas, helium, circulates in two parallel loops placed 120 deg apart from the heat exchanger. Above each of the blowers there is a removable floor panel for maintenance access. A small covered shaft is located between the blower panels to provide access for raising spent fuel, suitably contained in shielded caskets, to the ground floor for transportation to reprocessing facilities. In the service canyon directly under the reactor there is a ram and drive assembly that is capable of reaching up to remove the shield plug, elements of the fuel-handling mechanism, the graphite sleeve assemblies surrounding the core, and other components. On the west side of the service canyon is a room for storing and cooling spent fuel as it comes out of the fuel-unloading tube. After appropriate cooling the fuel is loaded by remote means into shielded casks and withdrawn for transportation to reprocessing facilities.

Since the helium circulation system is designed to operate at pressures as high as 1000 psi and is subject to fission-product contamination, its leaktightness is essential. All connections in the high-temperature region are welded, and mechanical closures are provided in regions of low enough temperature to permit the use of elastomeric gaskets, since this type of seal is the only one known to be both reliable and relatively easily made leaktight. The blower shaft seals, which are similar to those for the EGCR, are a combination labyrinth and oil pressure-buffered sleeve seal.

Reactor Physics Considerations

In the full-scale power reactor described by Sanderson & Porter,[1] the fuel balls consist of 90.0 wt % graphite, 9.17 wt % ThO_2, and

0.83 wt % UO_2. The average core power density is 23.7 w/cm^3, and the specific power is 3900 kw/kg of uranium. The core burnup is 0.021% of total atoms.

A 10-Mw reactor experiment cannot, of course, have the same values for all these parameters as a 350-Mw power reactor. In order to provide the most meaningful experiment, values were chosen so that the experiment would be the same as the power reactor in core height, core power density, weight percentage of oxides in the fuel balls, and fraction of total atoms burned in the fuel. By keeping the power density and core height the same as for the reference case, the gas flow rate and temperature distribution approximate those to be found in the full-scale reactor, and the fuel balls are subjected to the same internal temperature gradients and thermal stresses. The total oxide content of the fuel balls is the primary factor in determining their physical properties, and the fractional burnup determines the radiation damage and the fission-product release.

The critical concentrations of U^{235}-Th mixtures are shown in Fig. 1.4 for various core diameters and values of thorium-to-uranium atom ratios. The uranium was assumed to be 93% U^{235} and 7% U^{238}. Equilibrium quantities of xenon and samarium were assumed, together with fission products equivalent to 5% U^{235} burnup. The point in Fig. 1.4 corresponding to a fuel element containing slightly less thorium than uranium was taken as the design value. The fuel element parameters of interest are the following:

Composition, weight fraction	
Graphite	0.9000
$U^{235}O_2$	0.0513
$U^{238}O_2$	0.0036
ThO_2	0.0451
U^{235} burnup, %	10
Average fuel residence in core, days	246
Conversion ratio	0.084

As a consequence of the low total power output and small core diameter, the PBRE has a much higher ratio of uranium to thorium, a much lower specific power, and a much lower conversion ratio than the reference

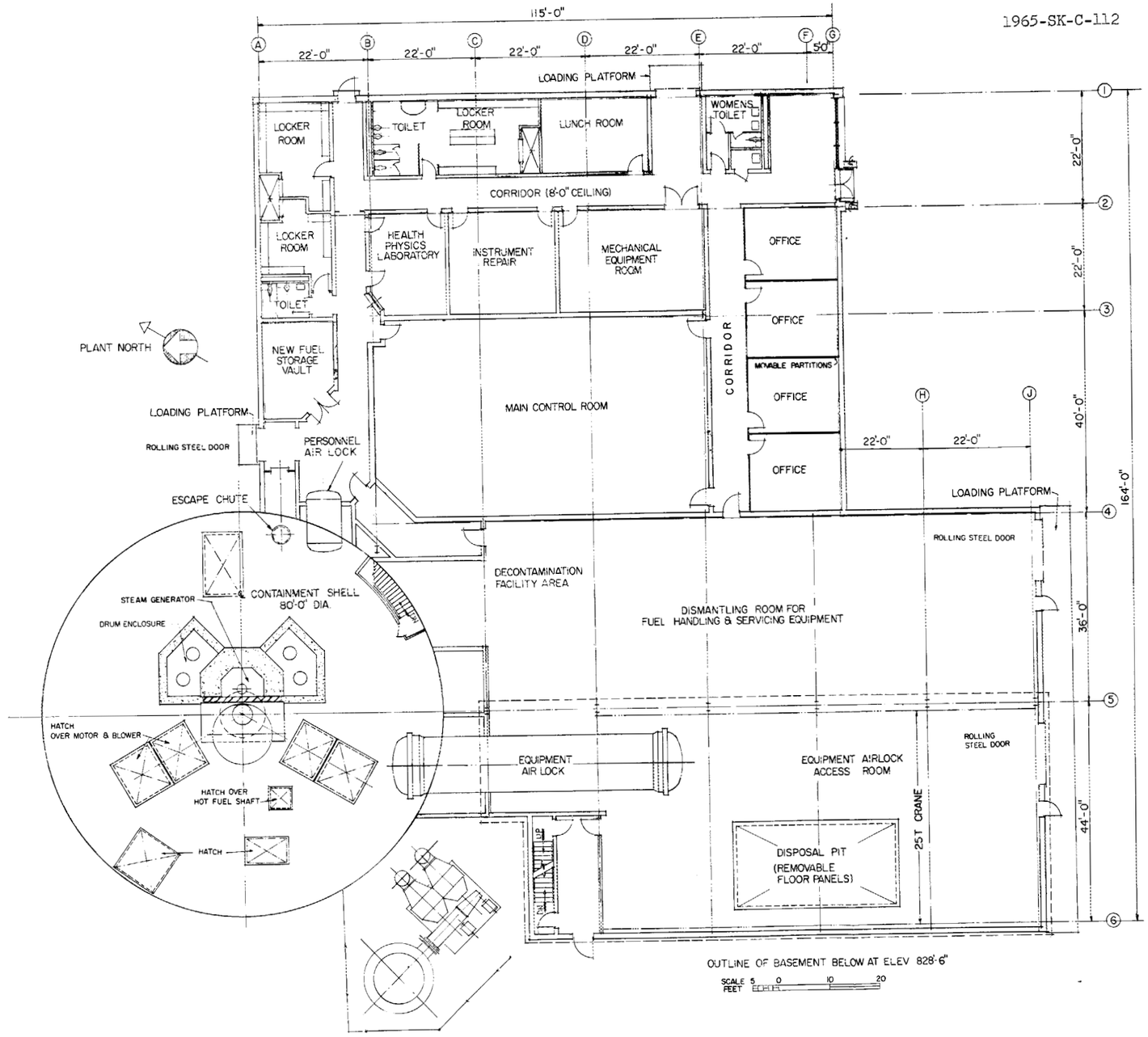


Fig. 1.2. Ground Floor Plan of Building and Containment Vessel.

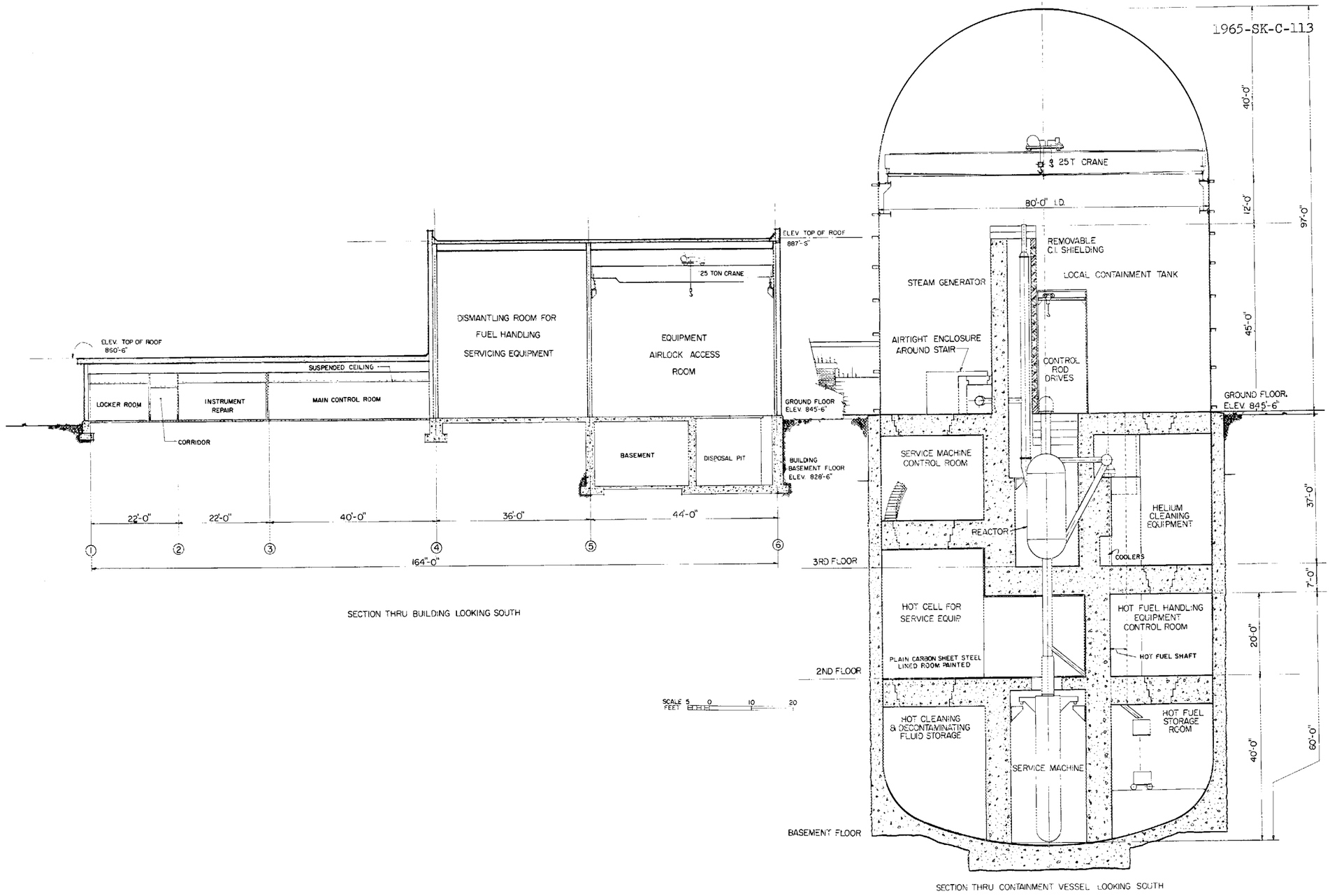


Fig. 1.3. Section Through Containment Vessel and Building.

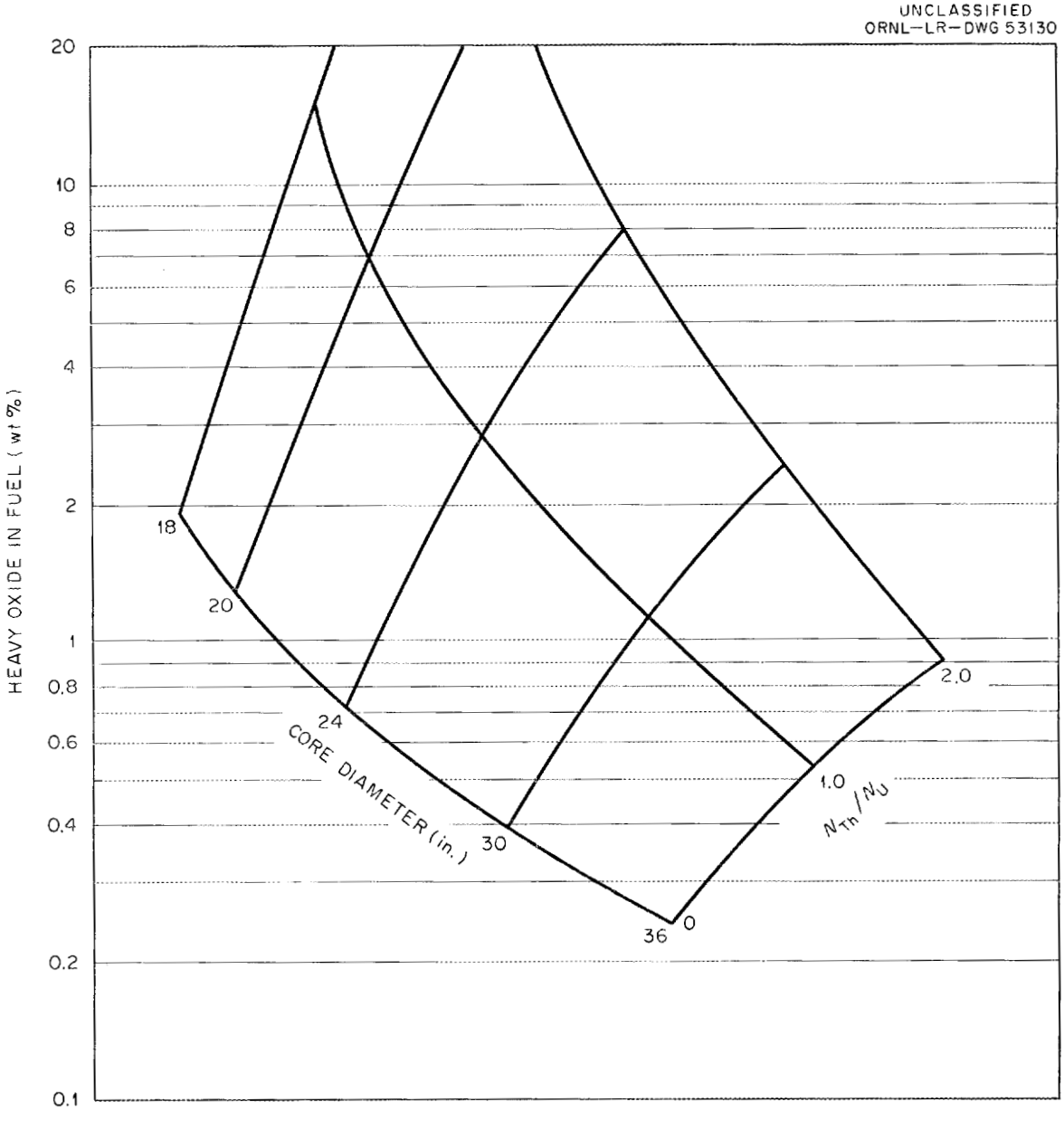


Fig. 1.4. Critical Concentrations of U^{235}-Th Mixture as a Function of Core Diameter and Total Oxide Content of the Fuel in the PBRE.

case. For a total burnup in the fuel of 0.10 fission/initial fissile atom, the reactivity change is 1.17%. The reactivity loss due to equilibrium xenon poisoning at full power is 2.71% and can rise to a maximum of 3.60% if the reactor is shut down and then brought to power when the xenon concentration reaches maximum. Thus the reactivity control needed for xenon override is 0.89%. The reactivity loss due to equilibrium

samarium poisoning is 1.16%. Since over 90% of the thermal neutrons absorbed in the core attain thermal energies in the reflector, the moderator temperature coefficient depends mainly on reflector conditions. The overall temperature coefficient is

$$\frac{1}{k}\frac{dk}{dT} = -0.4 \times 10^{-5}/°F \quad .$$

Since the dominant contributor to the negative temperature coefficient is the thorium resonance integral, it follows that the presence of the thorium in the core is important in providing a stable reactor, as well as in providing a fuel ball of the desired physical properties.

Control rods in the form of blades which surround the core in a nearly continuous ring were chosen in preference to conventional rods in order to avoid scalloping effects on the circumferential power distribution when the rods are partially inserted. The various items affecting reactivity are indicated below:

	$\Delta k/k$
Uranium burnup	0.0058
Equilibrium xenon	0.0271
Xenon override	0.0089
Samarium	0.0116
Temperature defect	0.0052
Total	0.0586

A strong reactivity effect is noted with comparatively thin layers of absorber because of the high importance of the reflector region. A thickness equivalent to 1/16 in. of Inconel was chosen, giving a total reactivity control of 0.140 $\Delta k/k$ from full insertion to full withdrawal. The maximum control needed in changing from a cold, clean core to a hot, equilibrium core and maximum xenon is 0.0586, so 0.0814 $\Delta k/k$ is available for shutdown margin. When the xenon poisoning is reduced to the equilibrium value, the control blades are inserted 0.7 ft into the core (equilibrium burnup distribution), and the blades are inserted to a depth of 2.6 ft for a hot, clean core. The position of the blades when the reactor

first attains criticality (cold, clean core) is insertion to a depth of 4.4 ft.

The power distribution depends on the position of the control blades. Two cases are shown in Figs. 1.5 and 1.6. The peak power density with the blades withdrawn is 2.08 times the average; it is 2.38 times the average for 2.7-ft insertion, and the peak occurs 1 ft below the center of the core rather than at the center. Flux traverses in the radial direction at the mid-plane are shown in Fig. 1.7. The prominent peak of the thermal flux in the reflector may be seen, as well as the relatively high ratio of epithermal to thermal flux in the core, indicating an "under-moderated" reactor. Only 56% of the fissions occur at thermal energies.

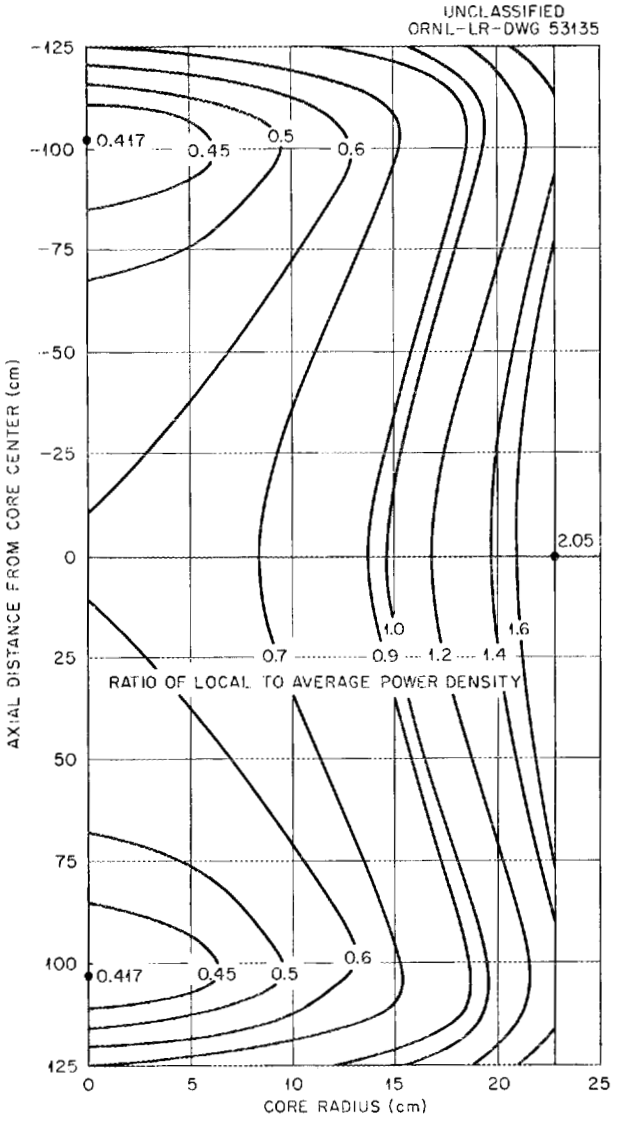


Fig. 1.5. Power Distribution with Control Blades Withdrawn.

Steam Generator Design

Two basic types of steam generator were examined: a once-through unit and a natural recirculation boiler and superheater section. The natural circulation boiler was chosen principally because of the greater latitude in the selection of steam flow rates to give good flow stability in the economizer and boiler regions at design and off-design conditions. A schematic diagram of the generator is shown in Fig. 1.8. Hot helium is directed up a central 6-in. stainless steel pipe to the top where guide vanes direct it downward across the tube matrix. Gas for cooling the

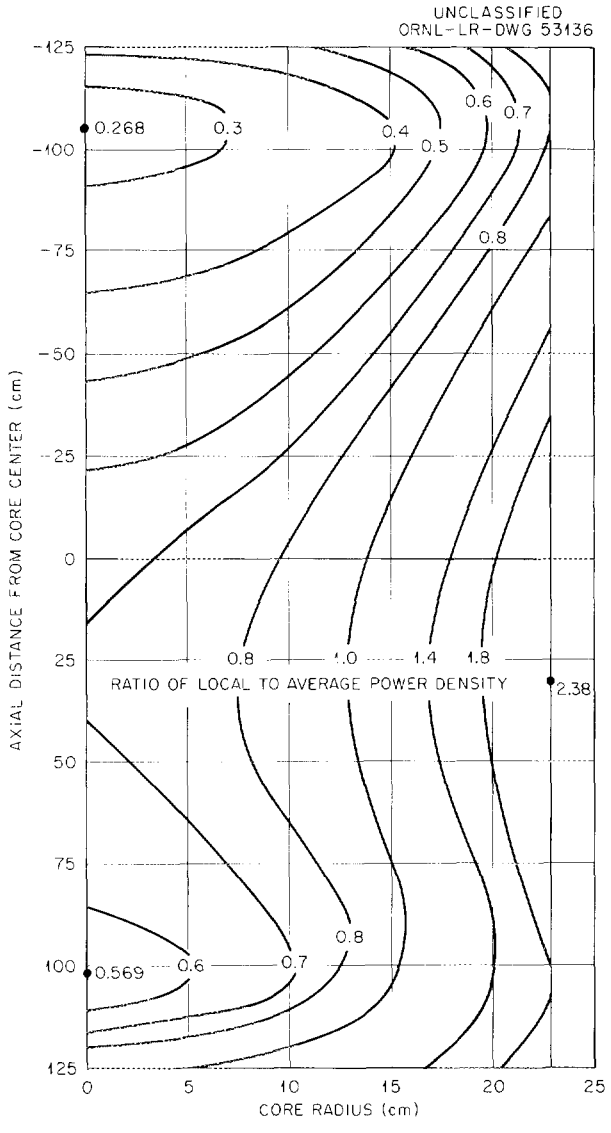


Fig. 1.6. Power Distribution with Control Blades Inserted 2.7 ft.

pressure vessel is directed up the outer annulus and joins the hot gas stream at the top. A number of tube diameter and spacing arrangements were examined, and the data finally selected are shown in Table 1.1. The helium and steam characteristics of the steam generator are indicated in Fig. 1.9.

In order to permit the plugging off of defective tubes without entering the main shielding, all header drums are fitted with flanged openings and are outside the primary shielding but within shielded cubicles.

Ball-Handling System

Every ball-removal system proposed to date appears to require some mechanical motion at the point of ball exit from the reactor. The arrangement developed in this study, and shown in Fig. 1.10, provides a round ball drain duct from the bottom center of the core. This duct has a diameter slightly greater than five ball diameters and is fitted with a round graphite fuel-removal plug equal in height to the core and reflector support structures. Removal of fuel is accomplished by retraction of a ball cutoff gate just inside the ball port and by rotation of the removal plug. Balls entering the plug are ducted down the center of the vertical drive shaft which supports and drives the plug. The drive mechanism is located outside of the shield where it is accessible for maintenance.

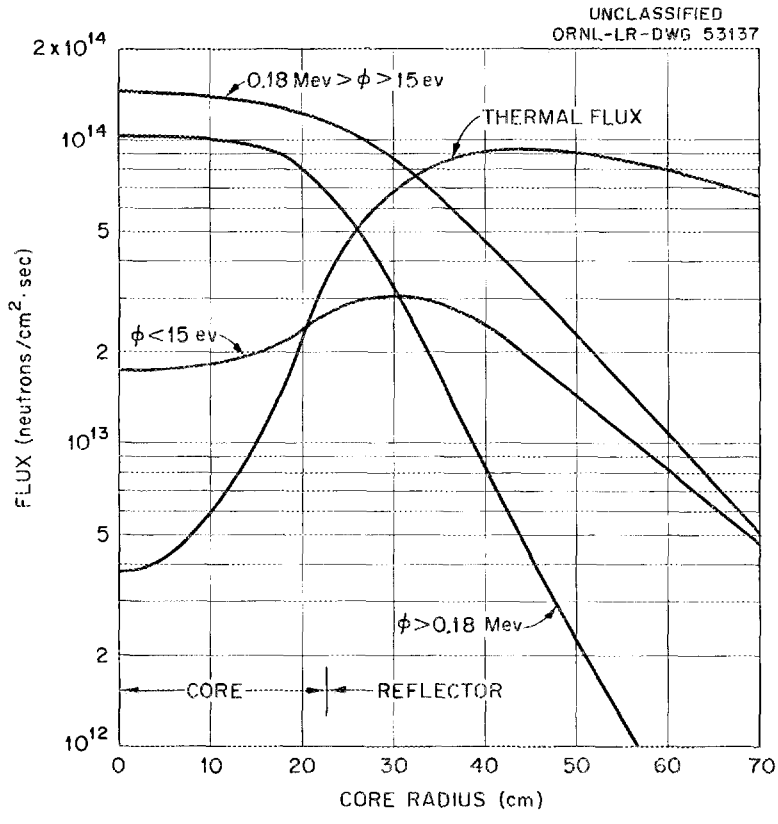


Fig. 1.7. Radial Flux Traverse at the Reactor Mid-Plane.

The balls removed from the core are guided through the drive shaft and dropped on a spring-mounted graphite anvil, from which they enter an inclined tube and flow past a ball-counting and cutoff device. From the cutoff device the balls enter a gas lock for depressurizing to atmospheric pressure and discharge to the storage and removal facilities.

The fresh-fuel-loading device, like the fuel-discharge facility, will require experimental development. The loading device at the top of the reactor includes a single duct extending from the top of the core upward through the upper plenum, shield plug, and top nozzle closure to a magazine and drive system. Space allocations between the fuel feed system and the control rod drives will require careful attention.

Helium Cleanup and Equipment Decontamination

The amount of particulate activity to be expected in an all-ceramic gas-cooled reactor presents one of the greatest uncertainties in the design.

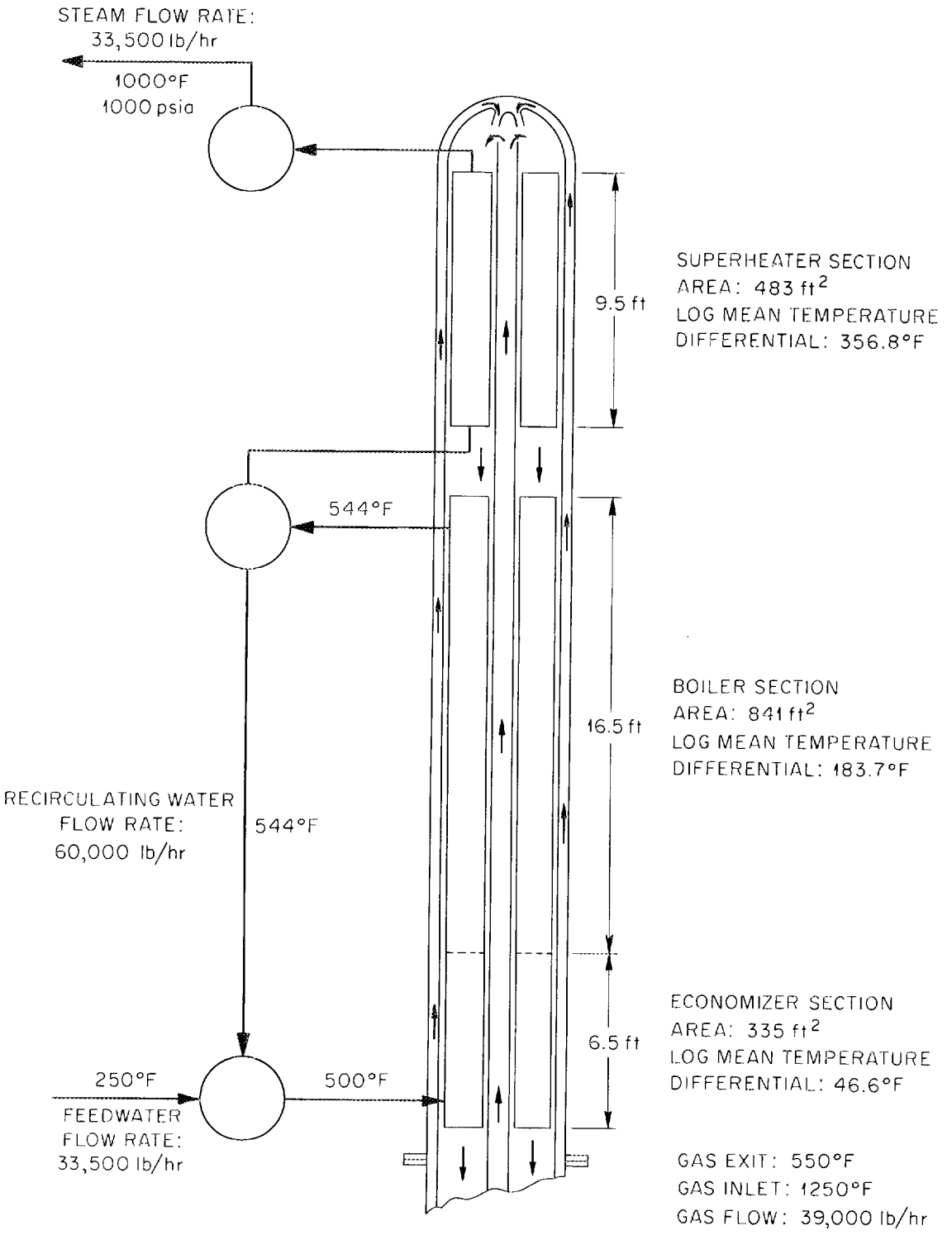


Fig. 1.8. Schematic Diagram of Steam Generator.

In the system proposed, 1% of the gas flow is bypassed through a cleanup system which should remove most of the reactive volatile and particulate matter and much of the rare gas from the bypass stream. This, coupled with the full-flow filter at the top of the reactor, which should remove

Table 1.1. Steam Generator Design Data

	Economizer	Boiler	Superheater	Total
Flow scheme	Axial counterflow gas outside tubes			
Tube outside diameter, in.	1.0	1.0	1.0	
Tube inside diameter, in.	0.875	0.875	0.875	
Number of tubes				195
Tube arrangement and spacing	Equilateral spacing on 1.375-in. centers			
Shell side area, ft^2	335	841	483	1660
Straight height of section, ft	6.5	16.5	9.5	
Over-all estimated exchanger height, ft				45
Gas mass velocity, $lb/ft^2 \cdot sec$				9.44
Gas pressure drop, psi				3
Gas pressure (design), psia				1000
Gas flow, lb/hr				39 000
Water inlet temperature, °F	500			
Steam exit temperature, °F			1000	
Net steam flow, lb/hr				33 500
Steam exit pressure, psia				1000
Log mean temperature differential, °F	46.6	183.7	356.8	
Heat load, Btu/hr	1.84×10^6	21.77×10^6	10.49×10^6	34.1×10^6
Percentage of total heat load	5.4	63.8	30.8	
Gas-side heat transfer coefficient, $Btu/hr \cdot ft^2 \cdot °F$				150
Tube-side heat transfer coefficient, $Btu/hr \cdot ft^2 \cdot °F$	700	5000 (assumed)	160 (average)	
Heat flux, $Btu/hr \cdot ft^2$ (outside area)	5500	25 900	21 700	
Over-all heat transfer coefficient, $Btu/hr \cdot ft^2 \cdot °F$	118	141	71	

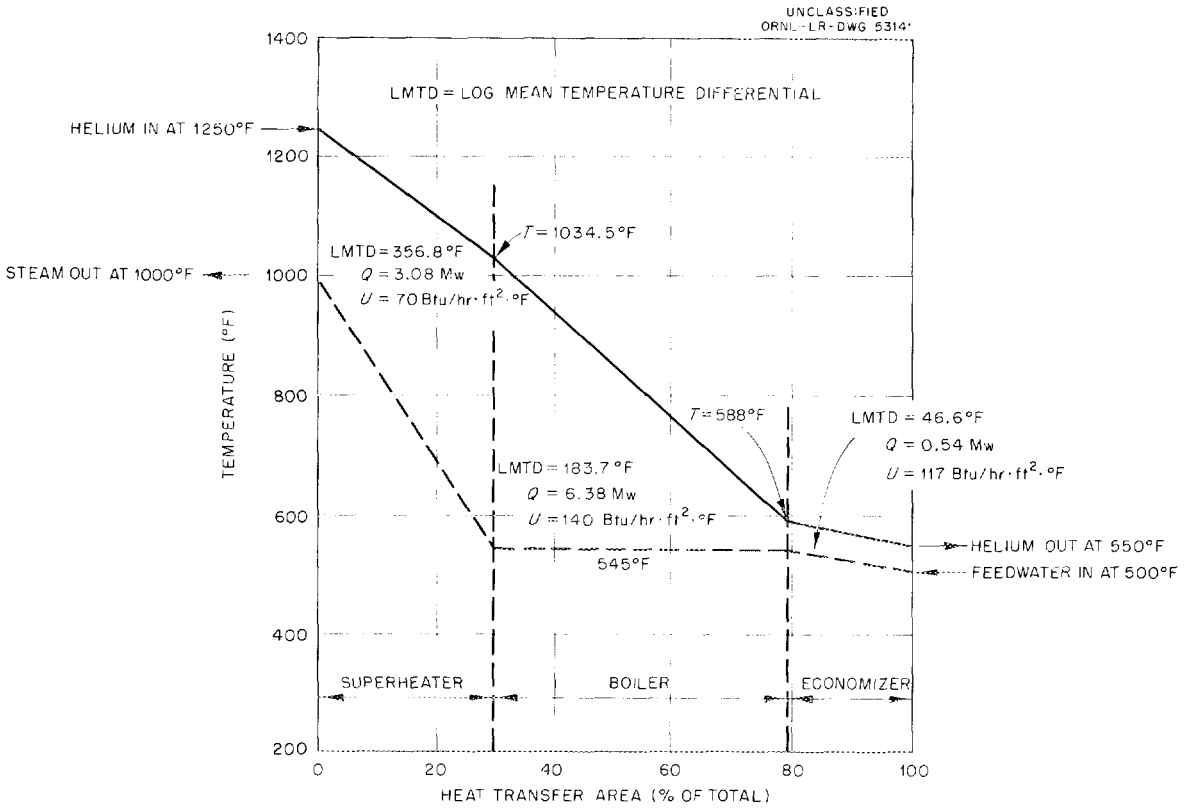


Fig. 1.9. Helium and Steam Characteristics of PBRE Steam Generator.

particulate matter down to 0.3 μ, should keep the level of particulate activity throughout the system at as low a value as it is practical to obtain with any given fuel element design.

The helium bypass stream is split, with the greater part cooled to 85°F prior to admission to a charcoal fission-product delay trap. The other part of the stream is heated to 750°F and passed over copper oxide to convert hydrocarbons, CO, and hydrogen to CO_2 and water vapor. The gas is then cooled and passed through a molecular sieve absorber where the water vapor and CO_2 are removed. The clean helium streams from the molecular sieve and the charcoal trap are combined and returned to the reactor.

The fission products that will contaminate metal surfaces exposed to the circulating helium include volatile elements, such as iodine, tellurium, cesium, cerium, and ruthenium, and minor amounts of less volatile elements, such as barium, strontium, zirconium, and niobium,

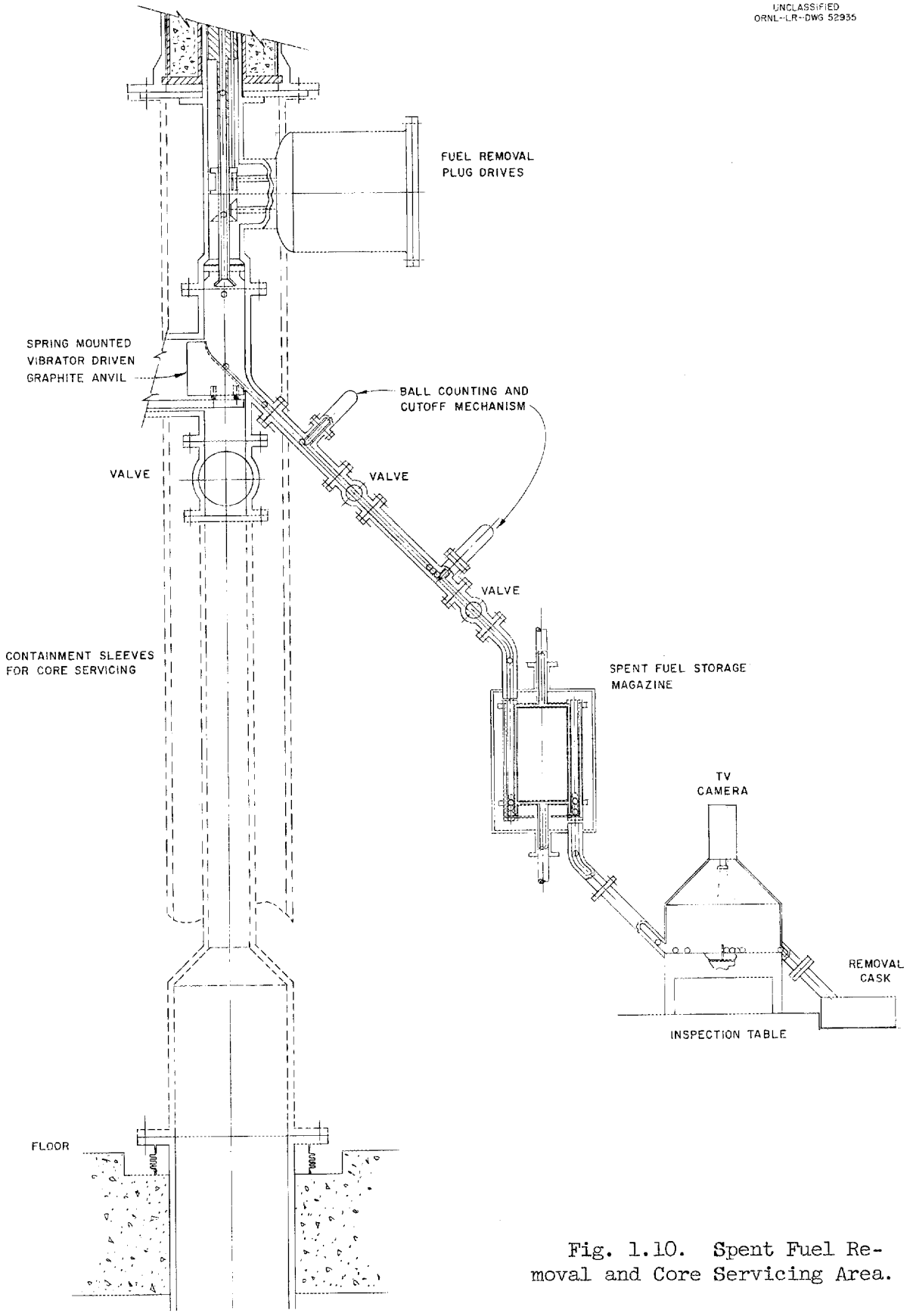


Fig. 1.10. Spent Fuel Removal and Core Servicing Area.

together with their daughters. There will also be daughters of the rare gases xenon and krypton. Badly contaminated graphite dust may also be present. The reagent that has been found to be most effective in removing these fission products and is at the same time noncorrosive to stainless or plain carbon steel consists of an aqueous solution of 4% sodium oxalate with 3% hydrogen peroxide and 0.7% oxalic acid at a pH of 5.0. The pH tends to rise with time, however, and within 1 hr or less at 95°C in a steel vessel, rapid decomposition of the peroxide may result. The pH must therefore be monitored at least every half-hour and adjusted to 4.5 to 5.0 by the addition of oxalic acid.

The component to be decontaminated (such as a blower) will be isolated hydraulically from the rest of the system, such as by insertion of inflatable rubber bladders in the connecting piping, and the contaminated surfaces will be sprayed or washed with the reagent. When the desired degree of decontamination has been accomplished, the equipment will be flushed with water and then drained and dried. Decontamination by this procedure should reduce the activity by a factor of 50 to 10 000, depending on the initial activity level and the effectiveness with which all the contaminated surfaces are contacted by the cleaning solution.

Hazards Evaluation

The containment vessel design is based on a postulated rupture of the primary coolant system that results in oxidation or melting of the fuel material (maximum credible accident). If allowance is made for reaction of all the oxygen in the container with graphite, the temperature and pressure are 20 psig and 700°F, respectively. Melting or oxidation of the fuel was assumed to release 100% of the noble gases, 50% of the volatile fission products (notably iodine), and 5% of the nonvolatile products. With leakage of 0.4%/day of the container volume at ground level, the resulting exposure 1000 ft downwind for an inversion condition would not exceed 25 rem in an 8-hr period.

About 900 curies of fission-product activity was estimated to be circulating in the primary system at equilibrium conditions, with cleanup of the helium taken into account. Although the estimate involves

considerable uncertainty, the calculated release rate from the primary system at an assumed helium leakage of 0.1% of the system volume per day (and its disposal from the containment shell) is low enough that a hundred-fold increase would be required to exceed the maximum permissible concentration. Natural circulation appears to be adequate for cooling the fuel in the event of simultaneous blower failures, so long as the helium pressure does not fall much below 900 psi.

Research and Development Program

In service, the fuel balls will be subjected to impact loads during charging and unloading operations, compressive loads primarily from thermal expansion between the fuel bed and the core wall, abrasive actions, thermal stresses, oxidation by impurities in the helium, and radiation damage from both neutron and fission-fragment bombardment. Under these conditions the balls must maintain structural integrity, must retain a large portion of the fission products generated, and must not self-weld to adjacent spheres. The data on the ability of the fueled-graphite matrix to withstand the mechanical and thermal stresses are encouraging, although not extensive. Self-welding is a problem only in the case of siliconized silicon carbide-coated spheres, and then only at surface temperatures well above the currently anticipated maximum of 1800°F. Additional tests are required, however, to define more clearly the temperature, time, and contact pressure under which self-welding will occur. The major uncertainty at present is the fission-product release at high temperatures and high burnups. The one in-pile experiment (at Battelle Memorial Institute) completed thus far that has involved high burnup showed progressive fission-product release with exposure and thus indicated failure of the Al_2O_3 particle coatings. The data from this experiment are shown in Fig. 1.11. The rate of fission-gas release as a function of temperature and burnup will need to be determined not only for Al_2O_3-coated UO_2 particles but also for BeO-coated UO_2 and pyrolytic-carbon-coated UC_2, all dispersed in a graphite matrix.

Information is needed with respect to the oxidation of graphite by impurity gases, primarily CO_2 and H_2O, in the coolant stream. The rates of these reactions are complex functions of temperature, pressure, gas

flow rate, gas composition, graphite characteristics, and probably radiation. The need for an oxidation-resistant surface coating must be carefully assessed because the temperatures required to apply Si-SiC, the most promising coating for this purpose, would preclude the use of Al_2O_3- or BeO-coated UO_2 as the fuel particles. At the 3500 to 3600°F

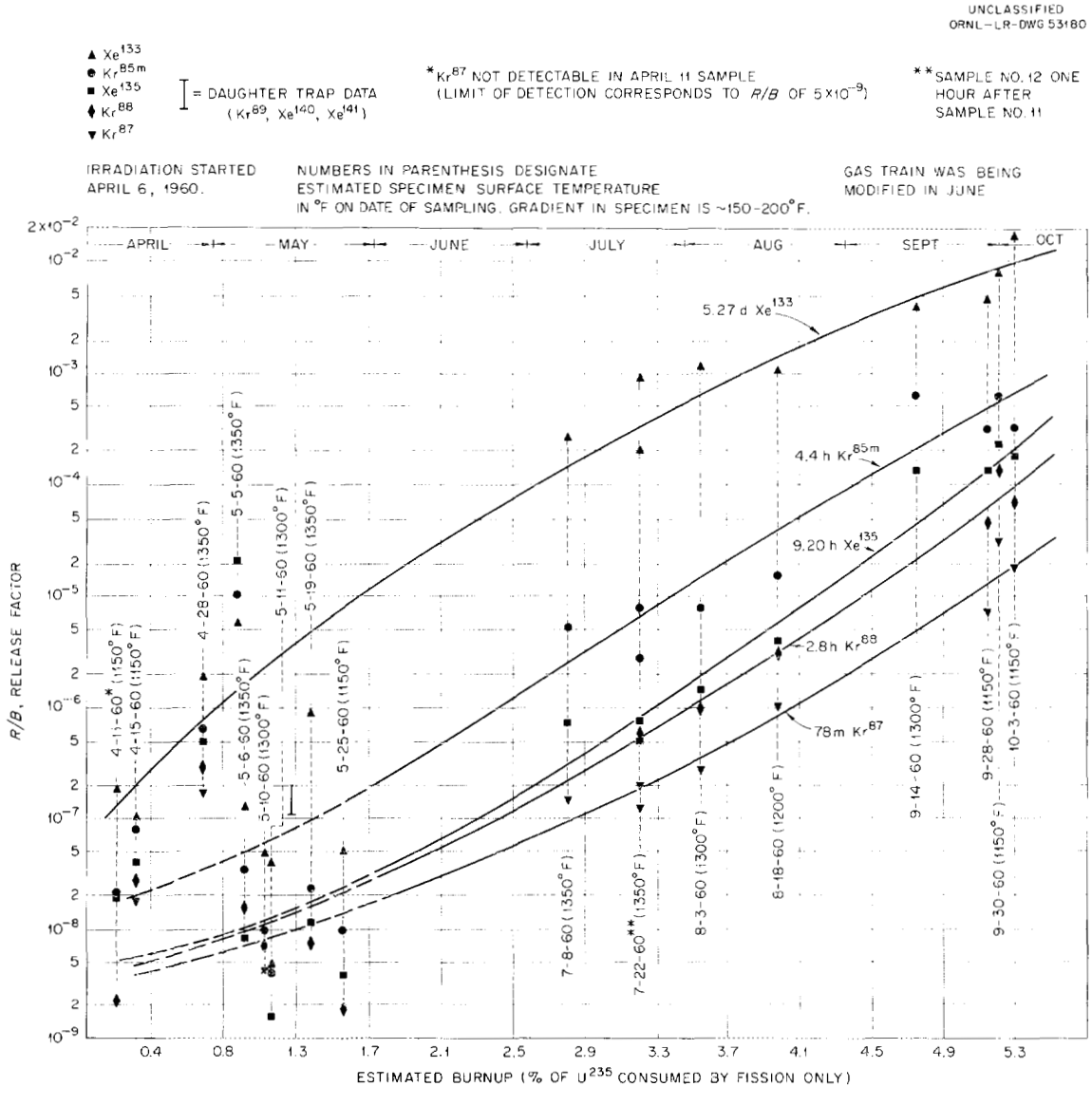


Fig. 1.11. Release Factors Versus Time and Burnup for Specimen FA-22 Irradiated in Sweep Capsule SP-5. Specimen fueled with Al_2O_3-coated UO_2.

coating-application temperature, both of these compounds react excessively with graphite.

Comprehensive evaluation tests of ball fabrication are required to establish the ranges of process variables, since such properties as thermal conductivity, thermal expansion, impact and abrasion resistance, and dimensional stability under irradiation can be expected to vary with type and quantity of filler and binder, baking cycle, and temperature used in fabrication.

Matching the gas flow distribution to the power distribution will probably require both model and full-scale tests. If the radial gas flow distribution can be matched reasonably well to the nuclear power distribution, it is important to get some idea of the extent to which radial mixing of the cooling gas will alleviate an excessive gas temperature rise in a hot-spot region.

Containment of the helium within the high-pressure system is more than a routine design problem because (1) there has been little experience with containment of helium at both high temperature and high pressure, particularly where closures of one sort or another are involved, and (2) much more than conventional leaktightness is required because of the contained radioactivity (including tritium). In order to transport fuel into and out of the reactor, even at reduced pressure, an elaborate system of pressure-buffered locks will be required to keep the external contamination under control. Elastomeric materials cannot be used because of both the high temperature and the high radiation dose rates, and no hard-seated valves are known which can be operated repeatedly and yet give this degree of leaktightness, or anywhere near it, especially with gritty materials passing over the valve seats. The operating sequence of the locks calls for a rather intricate system of mechanical or electrical interlocks as a guarantee against operator error. The operation must be conducted in sealed chambers, and the spent fuel discharging must be done completely remotely behind heavy shielding. Finally, the equipment must be successfully checked for tightness after each operation.

Along with development of a leaktight fuel transport system it will be essential to demonstrate that the ball feed mechanism assures proper

distribution and flow across the core without exceeding the ball jacket impact limits. The ball-removal mechanism below the core must demonstrate positive ball movement, adequate ball cooling, and freedom from jamming.

The direct access to the blowers assumed in this study is based on the fission-product release being very small and the possibility of removing activity that lodges in the blower casing by wet decontamination. It remains to be demonstrated that the scheme presented for hydraulically isolating the casings is feasible and that all trash and decontaminating solution residue can be prevented from leaking into the rest of the system.

The Full-Scale Pebble-Bed Reactor Power Plant

Parametric Analysis of Design Requirements

There are certain design requirements that must be met in the full-scale pebble-bed reactor power plant (PBR) irrespective of the type of core flow chosen. The pressure vessel must be properly protected against excessive temperatures, excessive thermal stresses, and fast neutrons. The latter requirement is best satisfied by employing a reflector having a thickness equivalent to approximately 3 ft of graphite. Vessel temperatures and thermal stresses can be kept to reasonable values by thermally isolating the reflector from the vessel with thermal insulation and providing for gas cooling of the interior surface of the vessel. It is also important to inhibit gamma-ray heating of the pressure vessel by adsorbing the low-energy neutron leakage from the reflector in a layer of material such as steel or borated graphite. The latter appears to be the more promising for this application.

Since irradiation shrinkage cracking will probably limit the life of graphite components exposed to a high fast-neutron flux gradient, graphite so exposed must be designed for replacement. The machined graphite blocks surrounding the vertical sides of the PBR core are therefore protected with a layer of unfueled graphite balls that are fed through the core in much the same way as the fuel. They are smaller than the fuel balls to avoid excessive gas bypass flow through this region. The thickness of the layer of unfueled graphite balls required to protect

the fixed graphite is about 1.0 ft. If the fuel charging is carried out in other than batch operations, unfueled graphite balls should not be used to line the reflector at the top and bottom of the reactor. Thus this graphite is designed to be replaceable with special equipment through suitable access tubes. The supports for the top reflector pass through the vessel liner and over the hot-gas plenum for anchorage to the pressure vessel. The guide tubes for the control rods are also exposed to an intense fast-neutron flux and hence are likewise designed for easy replacement, probably on a preventive-maintenance schedule. Cracking of the control rod guide tubes could not be tolerated because control rod operation would be adversely affected.

Reactor core size and shape are influenced by reactor physics considerations in several respects. Probably the most important of these are the effects of core geometry on conversion ratio and consequently on fuel cycle costs. Typical values illustrating these effects are shown in Fig. 1.12, which presents data[5] for a generalized series of graphite-uranium carbide cores surrounded by graphite-thorium carbide blankets. In preparing Fig. 1.12 it was assumed that the number of fissionable atoms in the fuel should not be allowed to drop to less than 80% of the initial number of fissionable atoms in order to keep the hot-spot problem within reasonable limits. Figure 1.12 implies that, for the 0.39 void fraction characteristic of pebble-bed reactors, the core diameter should be at least 14 ft to give reasonable fuel cycle costs.

The neutron leakage from a core varies with the length-to-diameter ratio for a constant power density. For a bare reactor with a cylindrical core, the minimum neutron leakage loss is obtained with a length-to-diameter ratio of 0.92. The corresponding value for a reflected reactor would be somewhat lower. This is to be compared with a core length-to-diameter ratio of 0.70 for the maximum core volume that can be installed in a given-diameter, spherical, pressure vessel. Thus for both good neutron economy (and low fuel cycle costs) and minimum pressure vessel

---

[5]A. P. Fraas and M. N. Ozisik, "Relative Capital Charges and Fuel Cycle Costs for All-Ceramic Gas-Cooled Reactors," ORNL CF-60-7-41, July 20, 1960.

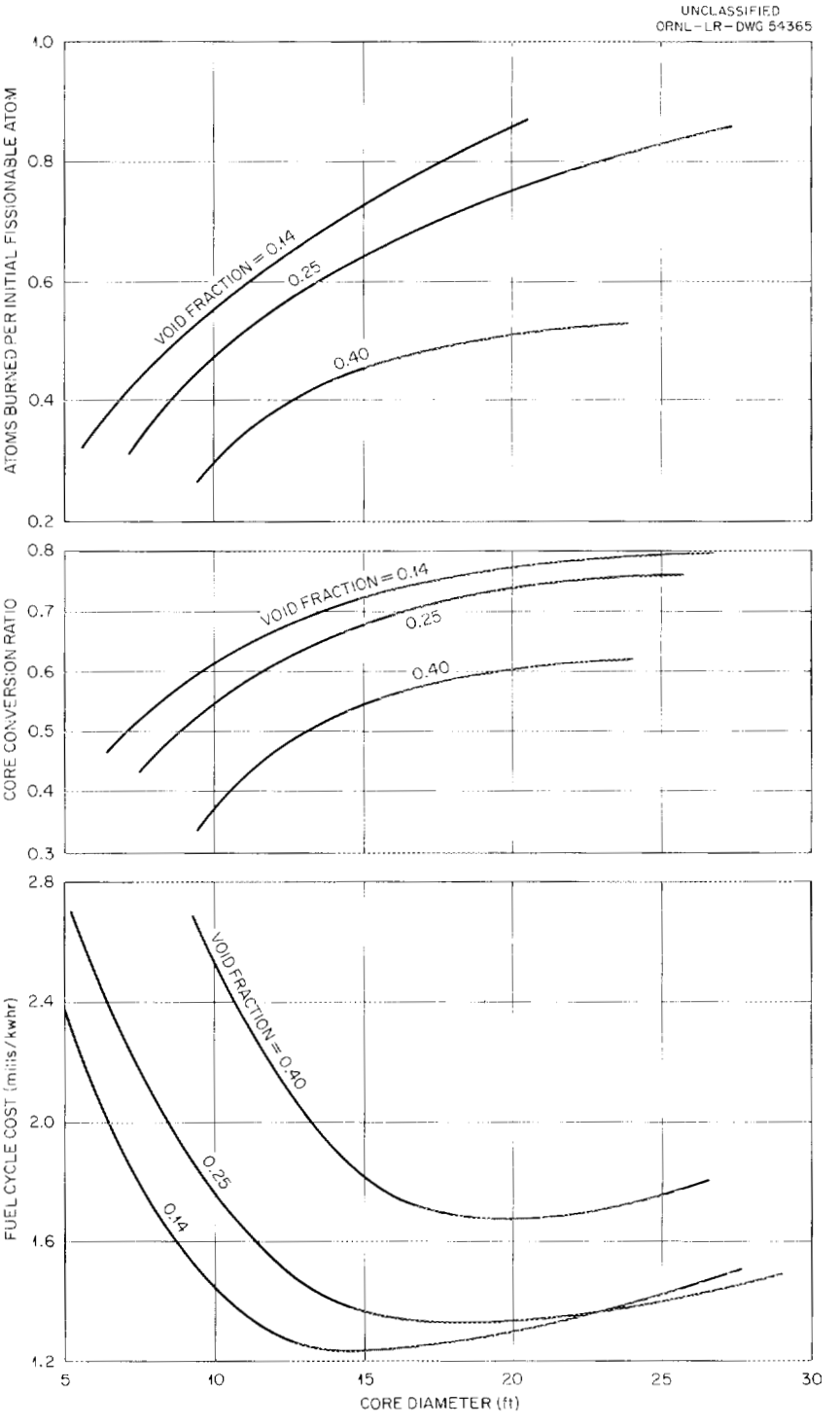


Fig. 1.12. Typical Values for Conversion Ratio, Burnup, and Fuel Cycle Costs as Functions of Core Diameter for 10-ft-Long, Cylindrical, Graphite–Uranium Carbide Pebble-Bed Reactor Cores with Graphite–Thorium Carbide Blankets.

costs, the core length-to-diameter ratio should be kept between 0.70 and 0.92 if a spherical pressure vessel is to be employed and no other considerations interfere.

A second important factor in the choice of core geometry from the reactor physics standpoint is the power distribution through the core. If a well-proportioned design is to be obtained so that all the fuel is employed to good advantage, the power distribution should be well matched to the cooling-gas flow distribution. Since there appears to be no way of controlling the flow distribution across the face of the pebble-bed reactor, it is important that the power distribution be as nearly uniform as possible. If a thorium blanket is employed in an axial-flow core, the power density near the core perimeter is so low that a poor gas temperature distribution at the core outlet is unavoidable. Thus it appears to be better to employ a thick reflector rather than a thorium blanket. This has the advantage that, in addition to flattening the power distribution, it increases the conversion ratio in the core. Even though the over-all conversion ratio suffers somewhat, the increased cost of fissionable material is offset by reduced fuel fabrication and reprocessing costs.

The pressure-vessel diameter and thickness can be related to the core diameter and the system pressure level. Layout studies have shown that at least 7 ft must be added to the core diameter to obtain the inside diameter for a cylindrical pressure vessel, while about 11.5 ft must be added to the core diameter to obtain the inside diameter for a spherical vessel. Actually, the diameter of a spherical pressure vessel varies somewhat with a given core diameter depending on the core length-to-diameter ratio. Using the above values and a gas pressure of either 1000 psi or that given by an allowable stress of 16 600 psi, whichever was the smaller, the vessel diameter, thickness, and gas system pressures for both spherical and cylindrical pressure vessels were plotted as a function of core diameter, as shown in Fig. 1.13. As a matter of interest, the weights and estimated costs of these pressure vessels are also plotted in Fig. 1.13, based on the length of the straight cylindrical portion of the vessel being equal to the diameter. The estimated costs do not include costs for penetrations, internal structure, or support structure.

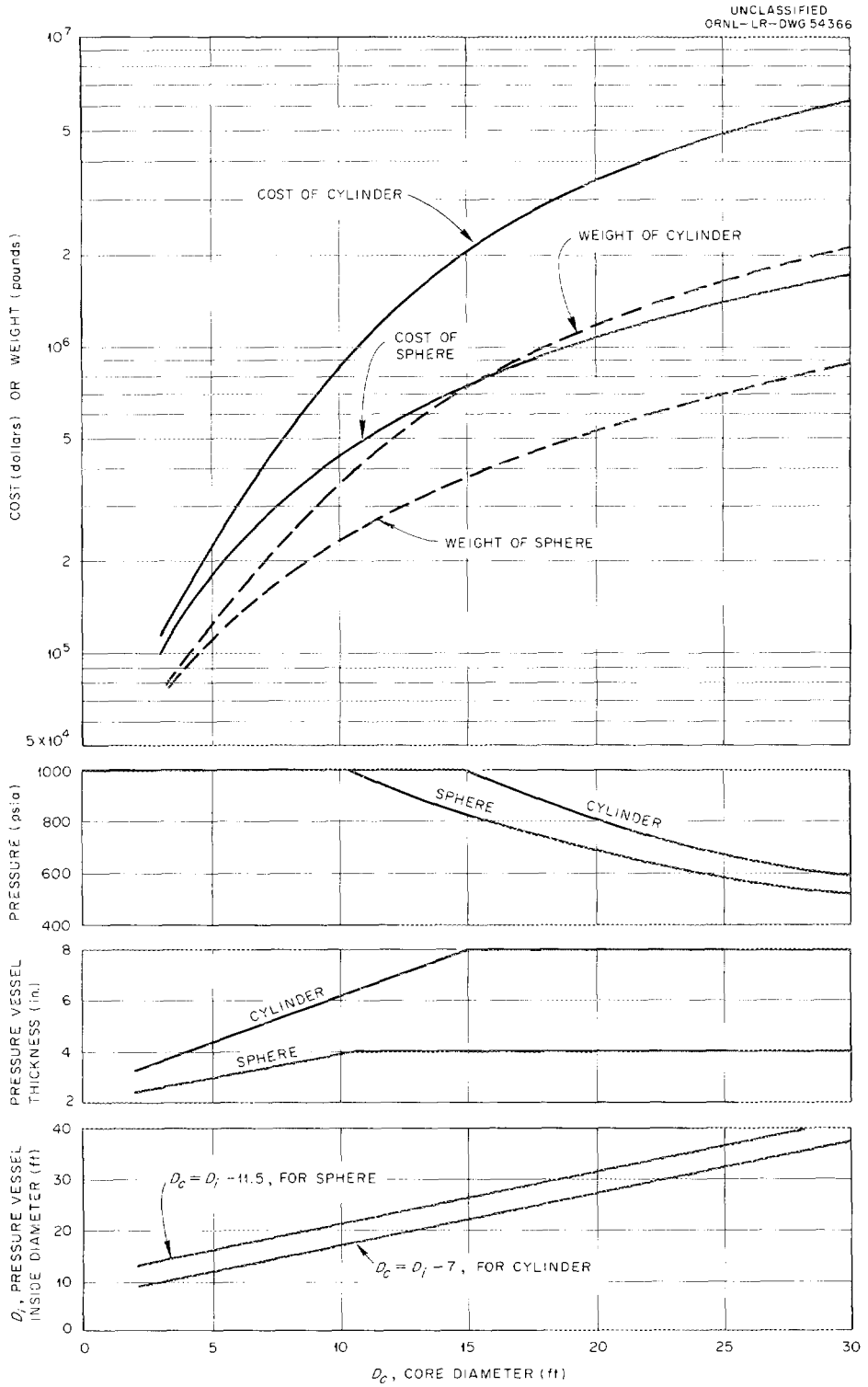


Fig. 1.13. Pressure Vessel Diameter, Allowable System Pressure, and Vessel Cost and Weight Versus Core Diameter for Cylindrical and for Spherical Vessels with a Core Length-to-Diameter Ratio of 0.7.

Fluid Flow and Heat Transfer Relations. Materials considerations limit the mean gas temperature at the core outlet to a value in the neighborhood of 1300°F, while good steam-cycle efficiency demands a core inlet gas temperature of at least 500°F. Previous studies of other types of gas-cooled reactor[6] showed that diversion of more than 8 to 10% of the generated power to gas circulation was uneconomical and that there was often an incentive to make the diversion even less. For thermodynamic efficiencies close to 40%, the ratio of pumping power to total heat generation (W/Q) cannot, therefore, exceed 0.03 to 0.04, and, if the losses in the external system amount to one-half this, the pumping losses in the core alone must not exceed 0.015 to 0.02.

The experimental data available on thermal conductivity, modulus of elasticity, and stress to rupture for irradiated fueled graphite are meager. Figure 1.14 summarizes the estimated power density and fuel-ball internal temperature drop as a function of ball size for a limiting thermal stress of 2000 psi, a thermal conductivity of 8 Btu/hr·ft^2 (°F/ft), a modulus of elasticity of 1.5×10^6 psi, a value for Poisson's ratio of 0.3, and a coefficient of thermal expansion of 3×10^{-6} in./in.·°F. Dashed lines for the limiting power density as defined by this thermal stress have been superimposed on the curves of Fig. 1.15.

The parametric studies of fluid flow and heat transfer were based on expressions developed in the PBRE studies that relate the power density and average film temperature drop to the system pressure, the fuel ball diameter, the temperature rise per unit of core length, and the ratio of pumping power to heat removal. The equations were evaluated for the ranges of variables of interest, and the chart shown in Fig. 1.15 was prepared to facilitate analysis. It may be seen that the temperature rise per unit of core length and the power density define both the core length and the core diameter for any desired reactor power output. The data presented in Fig. 1.15 can be used for other temperatures, void fractions, or gases by multiplying by the appropriate factors given in Fig. 1.16.

---

[6]A. M. Perry, "Economic Effects of Gas-Cooled Reactor Parameters," ORNL CF-59-12-40, December 9, 1959.

Axial Flow in Reactor Core. In choosing a reactor core that would conform to the design limitations outlined above, the first step was to establish the core diameter and length defined by pumping power limitations. For a given system pressure and gas temperature rise through the

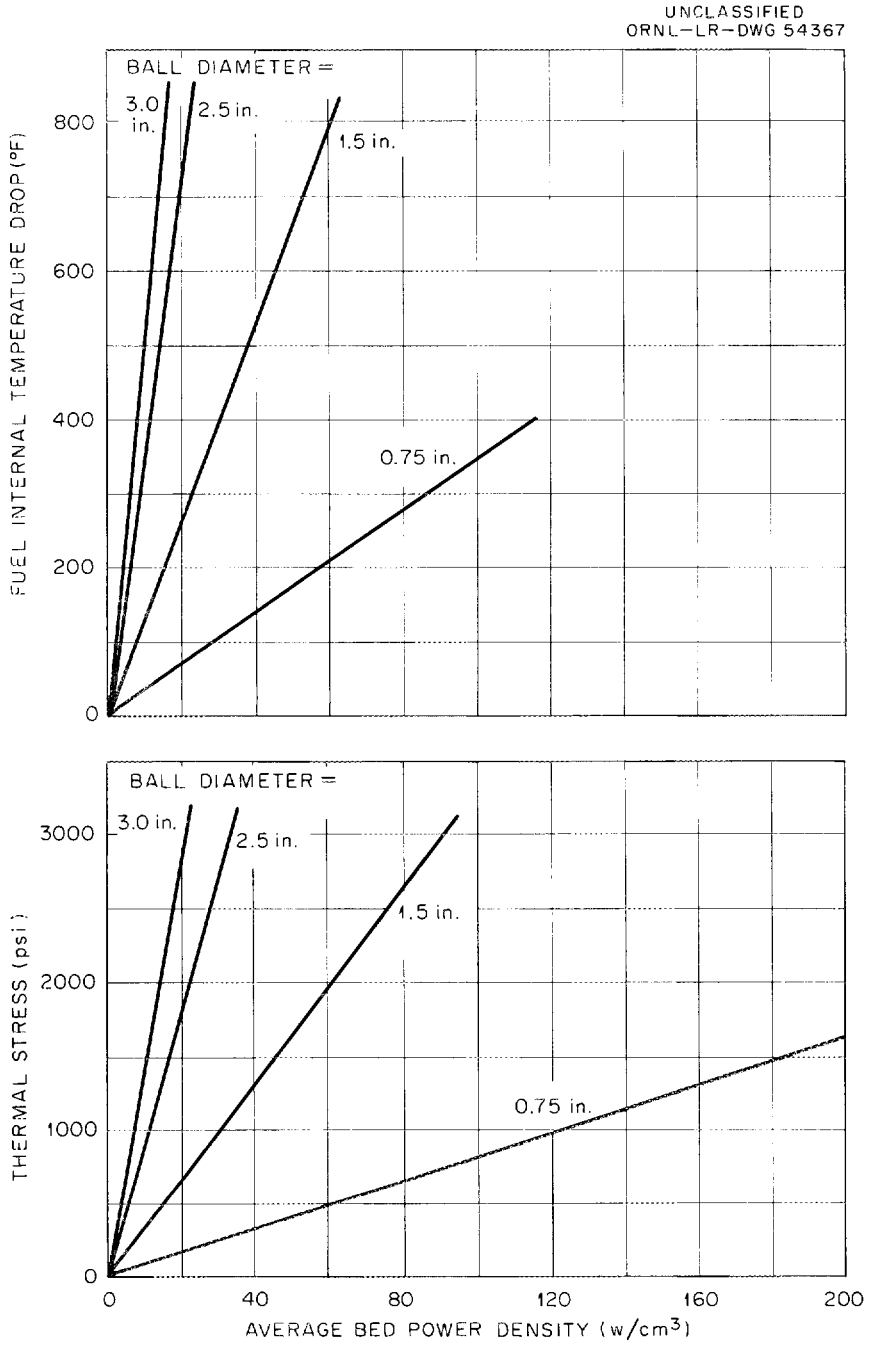


Fig. 1.14. Effects of Power Density and Fuel-Ball Diameter on Thermal Stress and Internal Temperature Drop.

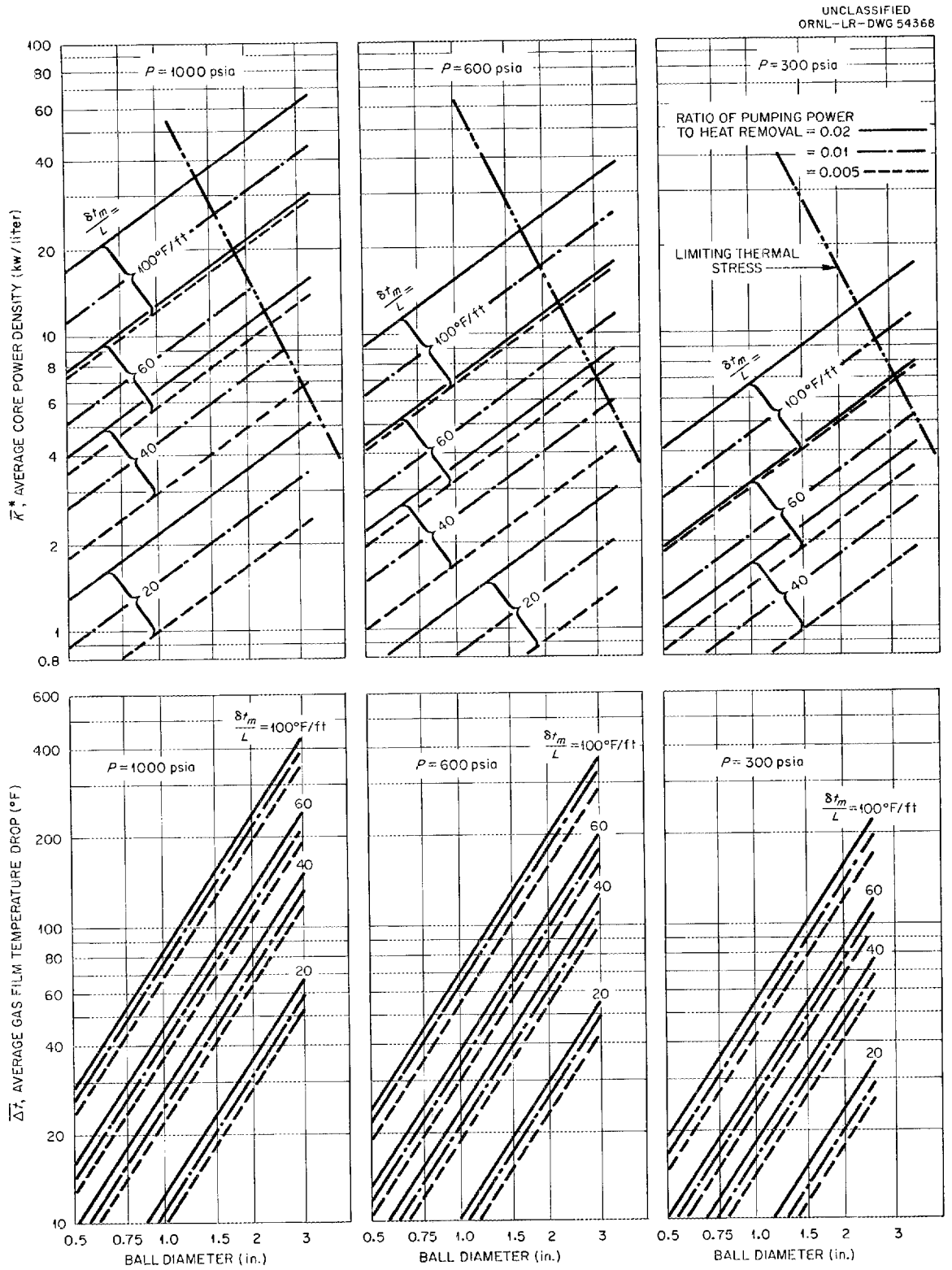


Fig. 1.15. Effects of Fuel-Ball Diameter on Power Density and Film Temperature Drop for Typical Values of System Pressure, Temperature Rise Per Unit Length of Core, and Ratio of Pumping Power to Heat Removal.

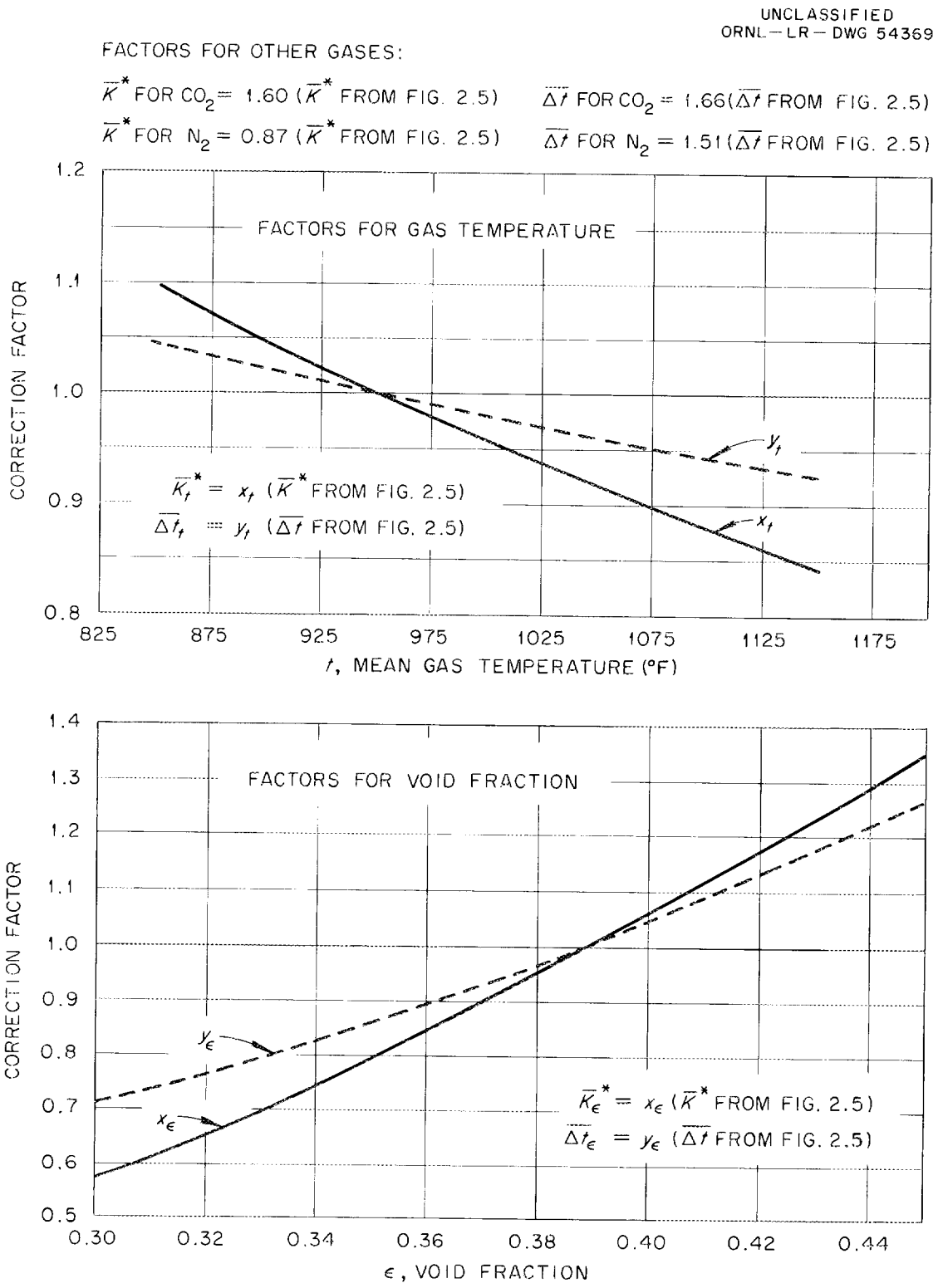


Fig. 1.16. Curves for Correcting Fig. 1.15 for Changes in System Temperature Level, Void Fraction, or Coolant Gas.

core, the maximum core depth in the direction of flow was then determined for a given power density, fuel ball size, and ratio of pumping power to heat removal. Once these conditions were established, the core diameter depended only on the total heat generation.

The relationship between core height, diameter, and power density is shown in Fig. 1.17 for various values of the ratio of pumping power to

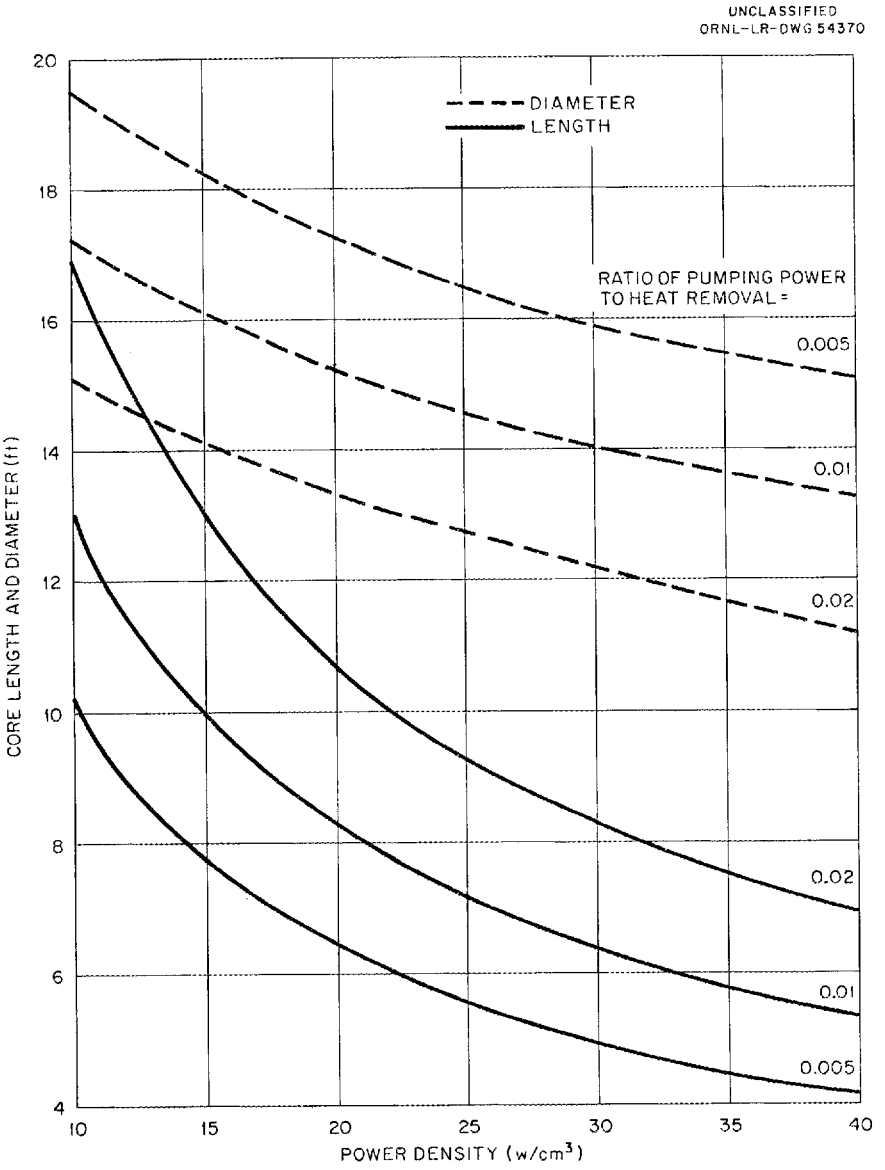


Fig. 1.17. Effects of Power Density and Ratio of Pumping Power to Heat Removal on Diameter and Length of an Axial Flow Core with a Gas Pressure of 1000 psia.

heat removal for a total heat output of 850 Mw, a gas temperature rise of 700°F, and a fuel-ball diameter of 1.5 in. It is evident that increasing power densities lead to low core length-to-diameter ratios, particularly at low values of the ratio of pumping power to heat removal, and that these are undesirable from the standpoint of neutron economy.

Increasing the fuel-ball diameter decreases the pumping power, or permits longer cores for the same power density. Thus the core length-to-diameter ratio can be increased simply by increasing the ball diameter, as shown in Fig. 1.18, without adversely affecting the pumping power. The increase in power density obtainable with large fuel balls at a given pumping power-to-heat removal ratio is limited, however, by the allowable thermal stress in the balls.

The greater voidage at the core walls permits a considerable fraction of the gas flow to bypass the fueled bed. Additional bypassing occurs through the high-voidage regions around the control rod tubes. If a layer of small, unfueled, graphite balls is used to line the reflector, the interface between the fueled and unfueled layers will be free of a high-voidage region and thus should, in part, offset the bypass flow through such a buffer layer provided ball movement and distribution can be satisfactorily controlled. Preliminary estimates indicate that a 1.0-ft-thick layer of 1.25-in.-diam unfueled graphite balls around a 20-ft-diam bed of 2.5-in.-diam fueled balls would permit approximately 14% of the flow to bypass the core. This requires that the mean gas temperature rise through the fueled region be increased to 800°F, and this value was used in most subsequent studies. While this increases the fuel temperature, it reduces the core pumping power requirements and eases the fuel bed levitation problem for upflow cores.

The curves of Fig. 1.12 indicate that, from the fuel-cycle-cost standpoint, the core diameter should be at least 14 ft, while an examination of fluid flow problems indicates that there is an incentive to increase it to about 20 ft. Figure 1.17 shows that these 14-ft- and 20-ft-diam cores would have lengths of about 12.6 and 10 ft, respectively, and would entail ratios of pumping power to heat removal of about 0.2 and 0.005, respectively. Since these two cores seemed to be representative of those that might be

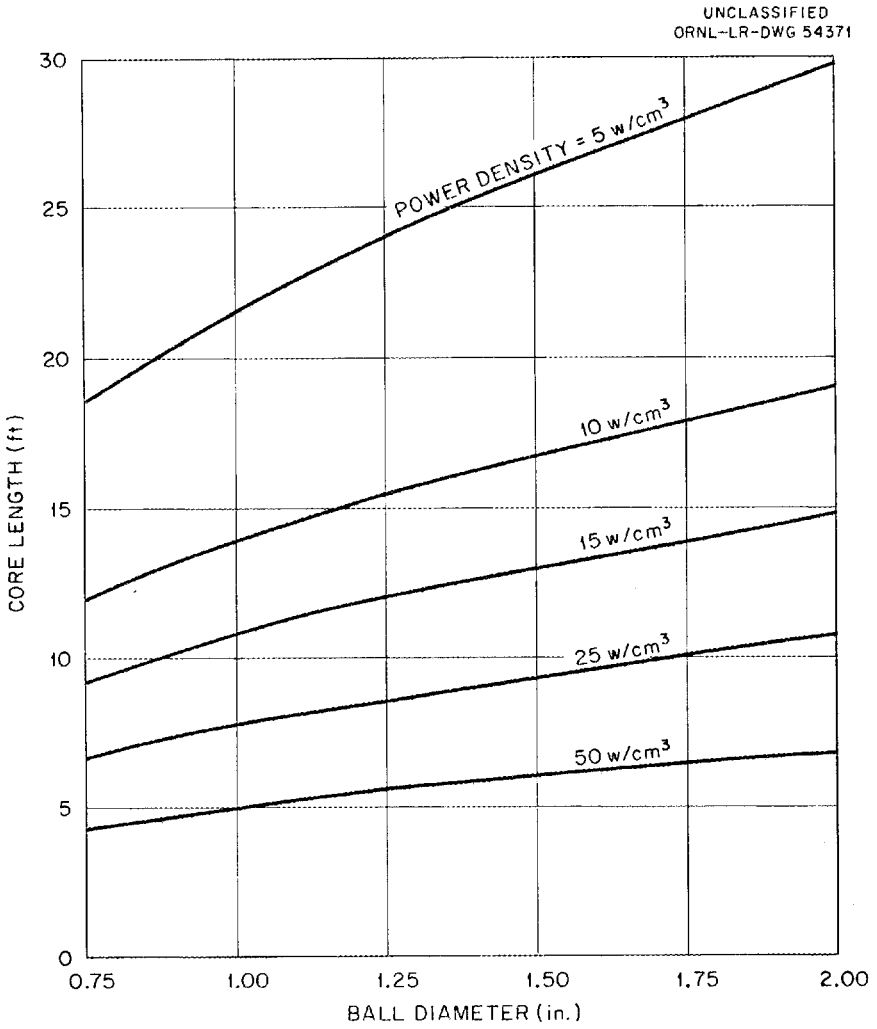


Fig. 1.18. Effects of Fuel-Ball Diameter and Power Density on the Length of an Axial Flow Core for a Pumping Power-to-Heat Removal Ratio of 0.02 and a Gas Pressure of 1000 psia.

used, they were selected for a more detailed study of their characteristics. The 14-ft-diam core requires a gas system pressure of 1000 psi if the ratio of pumping power to heat removal is not to exceed the limit of 0.02.

Cores about 20 ft in diameter can be designed for upflow cooling that will have a pressure drop low enough that bed flotation will not occur. It has been found that the bed will begin to float at a pressure drop per unit of length equivalent to 87% of the bed density and that it would be best to design for a limiting core pressure drop per unit of length of not more than

80% of the bed density.[7] For graphite fuel elements, the bed density is about 70 lb/ft^3, so, for design purposes, the pressure gradient should be limited to about 56 lb/ft^3. Since the pressure gradient depends only on the gas pressure, gas flow, and fuel-ball diameter, the limiting heat output per unit of core inlet face area can be expressed in terms of the fuel-ball diameter and the system pressure for a given gas temperature rise. Figure 1.19 is such a plot prepared from Sanderson & Porter data[7] by adjusting for a gas temperature rise of 800°F (550 to 1350°F) instead of 700°F. As may be seen, the thermal output per unit of core inlet face area can be determined from Fig. 1.19 without stating the core height, since that depends on the gas temperature rise and the film temperature drop at the surface of the balls. The levitation-limited core diameter for a given total thermal output can be easily determined by using Fig. 1.19. In order to facilitate such estimates, the relationship between the fuel-ball diameter, the levitation-limited core diameter, and the helium pressure is shown in Fig. 1.20 for a thermal output of 800 Mw. For a given core diameter, the core length determines the average power density and the core length-to-diameter ratio. These relations are also shown in Fig. 1.20, together with a scale for the diameter of spherical vessels based on the maximum inside diameter for the indicated pressure for a 4-in.-thick shell. The average core power density increases with the fuel-ball diameter because higher gas flows are required to levitate beds of larger balls. The internal temperature drop and the thermal stress in the fuel increases, however, as the square of the ball diameter (see Fig. 1.14), so the power density is limited by one factor or another to a relatively low value if the core is designed for upflow without levitation.

This analysis indicates that the principal limitations to be considered in settling on a specific value for the diameter of an upflow core are those imposed by pressure vessel fabrication considerations, flotation of the bed, and thermal stresses in the fuel. For a given

---

[7] "Progress Report, Pebble Bed Reactor Program, June 1, 1959 to September 30, 1960," NYO-9071.

gas system pressure the fuel-ball diameter required to avoid flotation was calculated as a function of core diameter for an 800°F gas temperature rise to give the constant-pressure lines of Fig. 1.21. The maximum core diameter for a 4-in.-thick spherical pressure vessel and a core length-to-diameter ratio of 0.7 was then determined for each pressure, and the data were plotted as a dotted line of Fig. 1.21 to indicate the region giving pressure vessels less than 4 in. thick. An additional dotted line showing the limiting fuel-ball diameter as a function of core

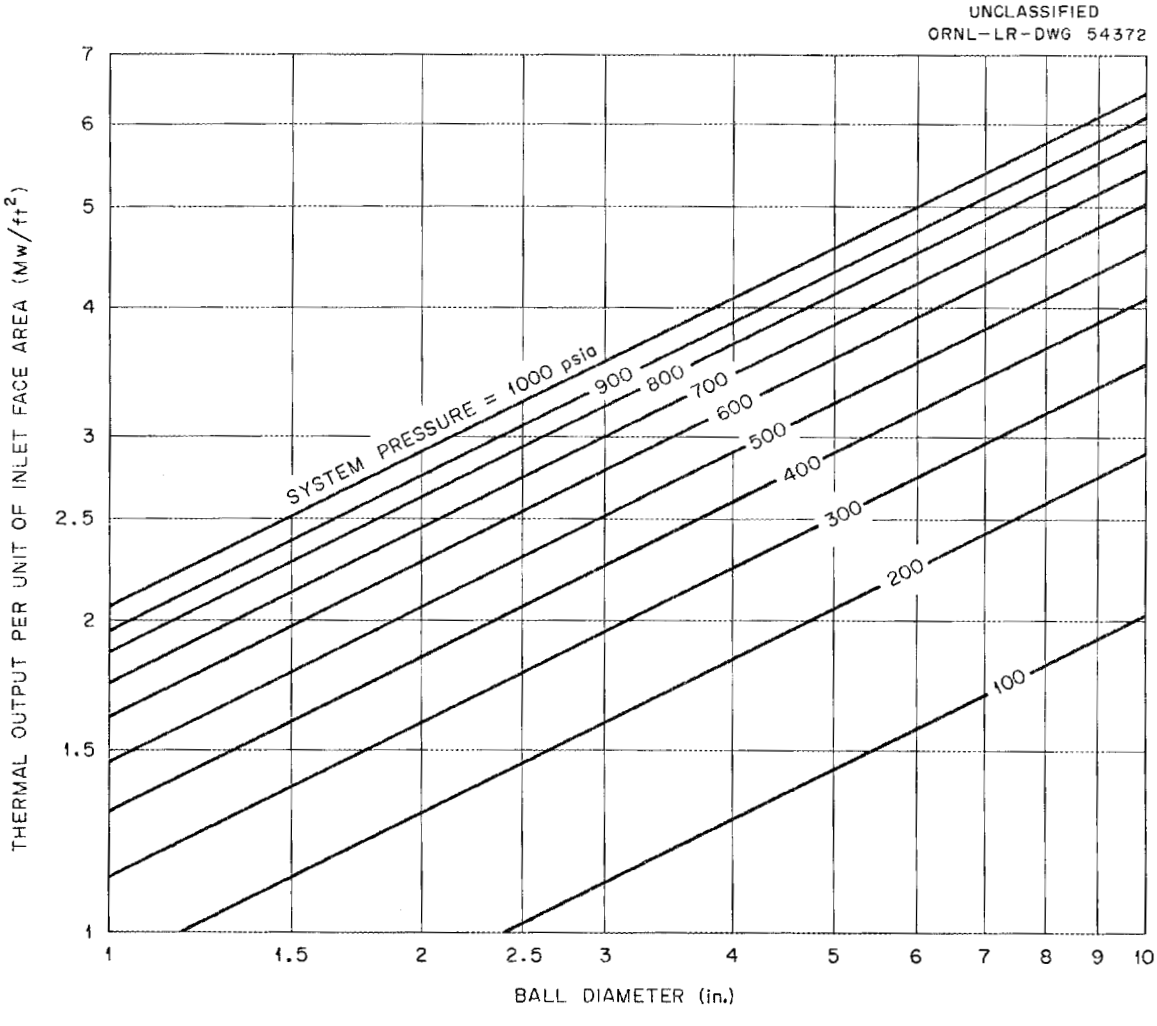


Fig. 1.19. Levitation-Limited Power Output per Unit of Core Inlet Face Area as a Function of Fuel-Ball Diameter and Cooling-Gas Pressure for Axial Upflow Cores. The curves were constructed for a pressure drop equal to 80% of the fuel bed weight per unit of face area and helium inlet and outlet temperatures of 550 and 1350°F, respectively.

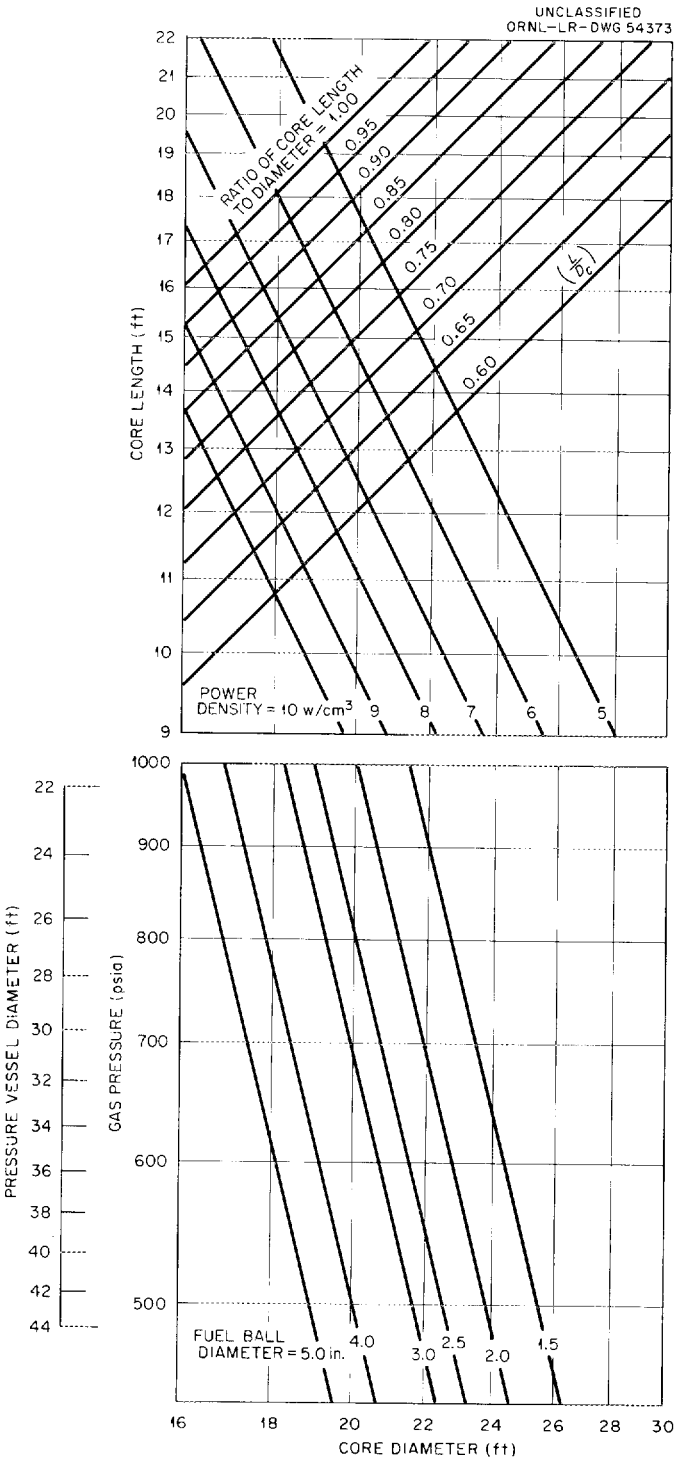


Fig. 1.20. Effects of Fuel-Ball Diameter on Core Diameter and Length, Pressure Vessel Diameter, and Helium Pressure for Levitation-Limited Axial Upflow Cores. The curves were constructed for a pressure drop equal to 80% of the fuel bed weight per unit of face area, 4-in.-thick spherical pressure vessels of maximum inside diameter for the indicated pressure, and helium inlet and outlet temperatures of 550°F and 1350°F.

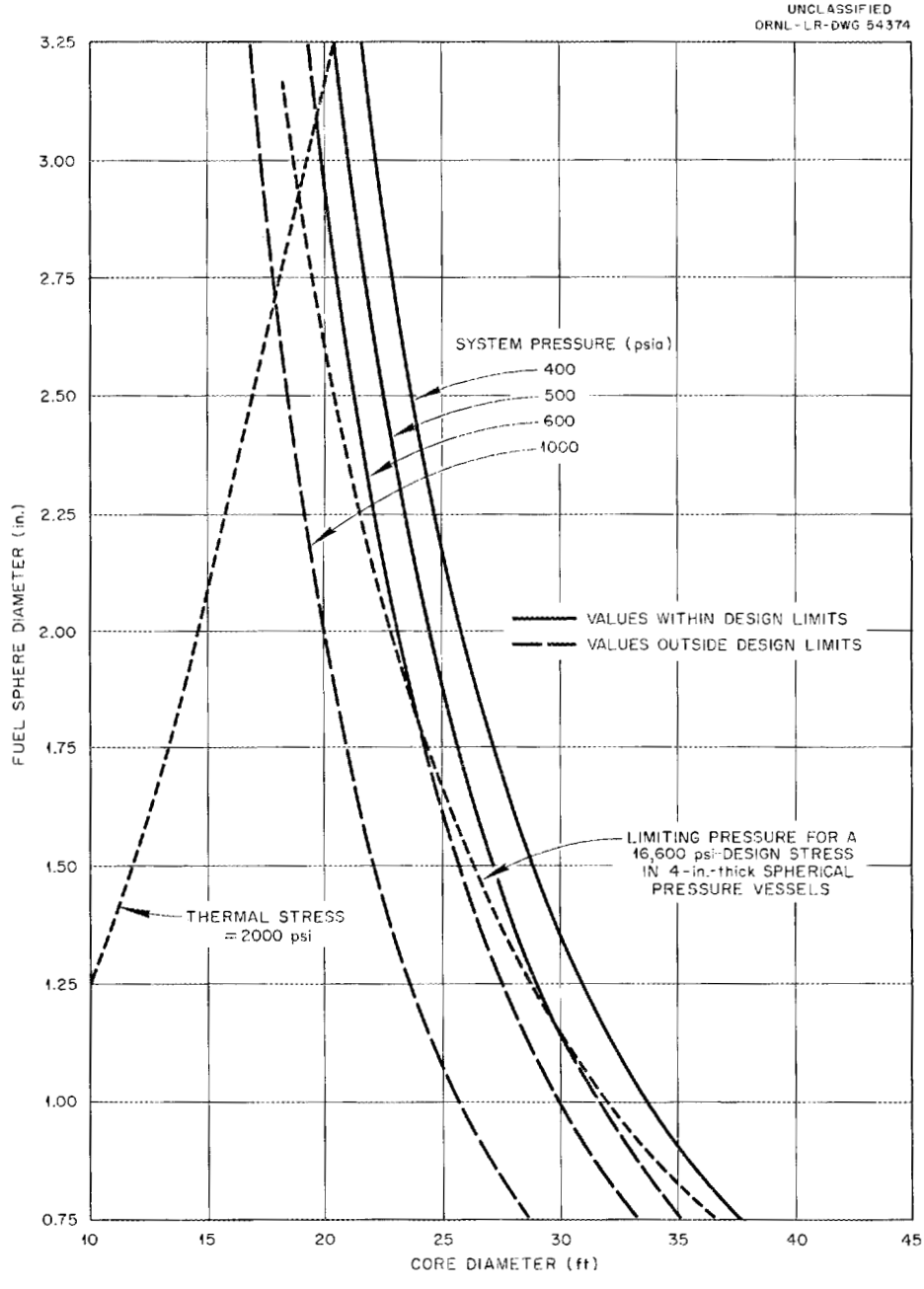


Fig. 1.21. Design Chart for Axial Upflow Cores Showing Combinations of Fuel-Ball Diameter, Core Diameter, and System Pressure Which Give Thermal Stresses in the Fuel of Less than 2000 psi and Spherical Pressure Vessels Having Thicknesses Less than 4 in. for 800 Mw and Helium Inlet and Outlet Temperatures of 550 and 1250°F.

diameter was then plotted based on a peak-to-average power density ratio of 2.0. The constant-pressure curves in the region to the right of both this curve and that for a 4-in.-thick pressure vessel are drawn in solid form to indicate that this region is within the design limits, and the portions of these curves to the left of the limiting lines are dashed to indicate that they fall in a region of questionable feasibility.

After study of Fig. 1.21 and similar charts, a 20.7-ft-diam core 12.6 ft high with 2.5-in.-diam fuel spheres and a 700-psi helium system pressure was chosen as a well-proportioned axial upflow core. The length-to-diameter ratio of this core is somewhat less than that for which Fig. 1.21 was prepared and has the effect of moving the design point to the right and well into the region for good bed stability. Larger fuel balls might also have been used, but this seemed undesirable, since larger balls would increase both the size of the fuel-handling equipment and the peak internal temperature in the fuel.

In reviewing these configurations and summarizing, it appears that a 20.7-ft-diam upflow core with 2.5-in.-diam balls is definitely preferable to a 14-ft-diam downflow core. The fuel cycle and pressure vessel costs are lower; the pressure vessel size falls in the region of demonstrated feasibility; the formidable problems of supporting a downflow core are avoided; hazards problems are reduced by greatly improved thermal convection; and, since the pumping power is much lower, the blowers are smaller, simpler, and more easily maintained.

Radial Flow in Reactor Core. A radial-flow pattern of the type shown in Fig. 1.22 was also considered in selecting the reactor core. Cooling gas enters the core axially through a 4-ft-diam passage at the center of the core. Graphite tubes housing the control rods are placed around the perimeter of this inlet passage. The cooling gas flows radially outward through the 3/4-in.-wide gaps between these 4-in.-diam graphite tubes. The pebble bed lies in an annulus between the control rod tubes and a graphite grid at the outer perimeter. The hot gas leaves the reactor through axial ducts in the outer portion of this grid. This configuration not only increases the flow passage area for the cooling gas, but it also reduces the depth of the bed in the cooling-gas flow direction.

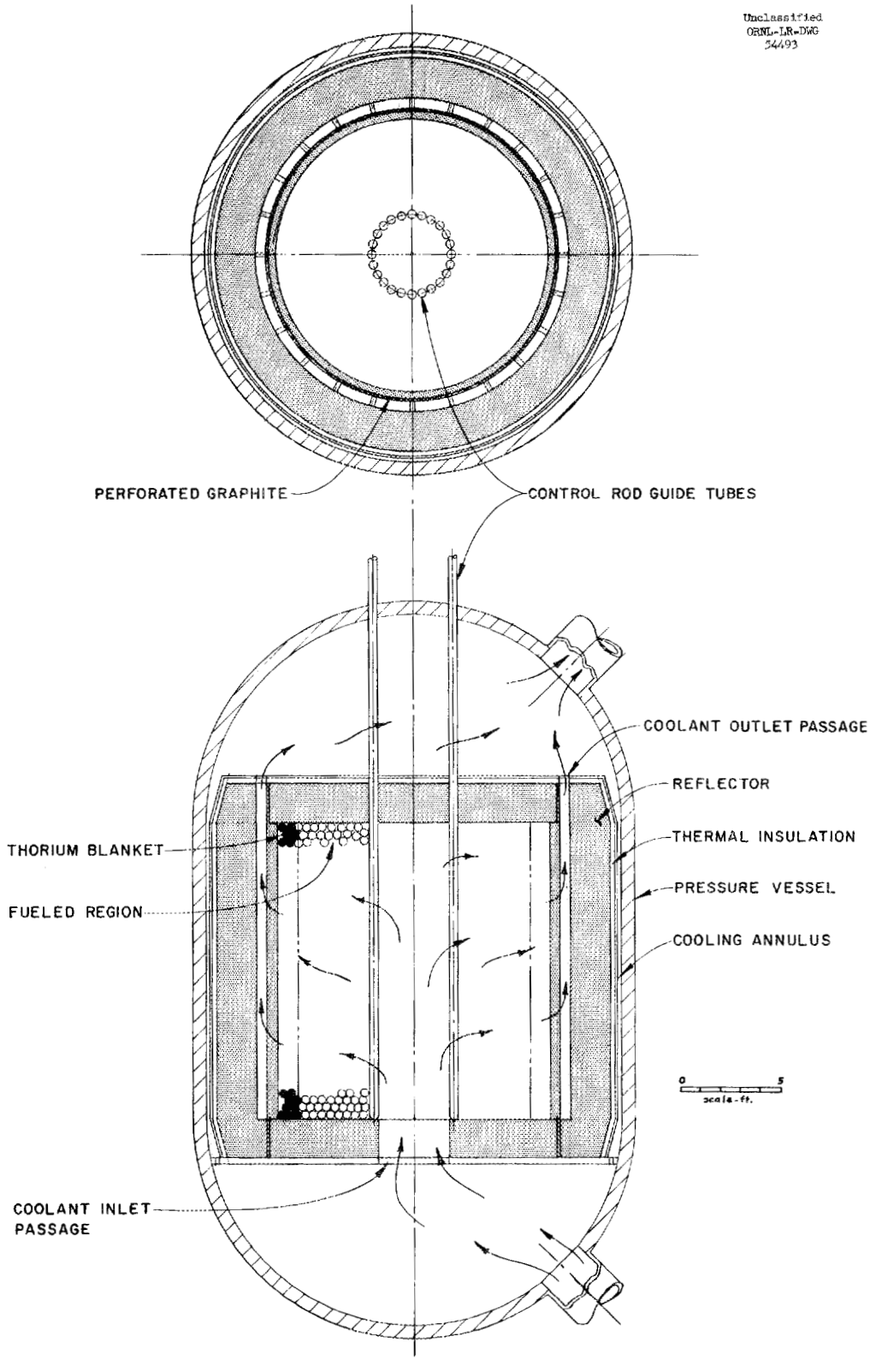


Fig. 1.22. Sections Through an Idealized Radial Outflow Pebble-Bed Reactor Showing the Principal Components.

One of the important factors in the design of such a core is the effectiveness of the control rods. The configuration of Fig. 1.22 gives an adequately effective set of control rods for fuel bed annulus thicknesses of up to about 4 ft.

Preliminary estimates show that the core pressure drop with radial flow is reduced drastically, so the power density is not limited by the economics of pumping. However, if the diameter of the core is not greater than for the axial flow reference case (a necessary condition for inclusion in the same diameter pressure vessel), the power density in the bed itself must be higher, or the height of the core must be greater for the same total heat generation because of the central hole. Therefore, the radial flow concept favors a higher power density and a smaller fuel ball size than is desirable for the axial flow core. The situation is illustrated in Fig. 1.23, which gives the mass flow rate at the core inlet face, the pressure drop through the core (Δp), and the ratio of core pumping power to heat removal (W/Q) vs the core diameter for three different densities for cores with a central opening 4.0 ft in diameter and an output of 850 Mw of heat. As in Fig. 1.17 for axial flow, the gas temperature rise was taken to be 700°F. The solid lines for Δp and W/Q refer to a ball diameter of 1.5 in., and the dotted lines give corresponding values for 0.75-in.-diam fuel balls. These curves indicate that power densities of more than 10 w/cm^3 are required to keep the height to a reasonable value.

The problem of gas bypassing through the high-voidage zones at the core boundaries, discussed in connection with the axial flow concept, is also present with radial flow. Here the problem would be especially bad at the top of the reactor because the balls would not tend to pack tightly against the top reflector.

There are several serious disadvantages inherent in the radial flow concept. The reduction in mass flow per unit of flow passage area as the gas progresses through the bed requires a rather steep radial reduction in power density if excessive fuel temperatures are to be avoided at the core periphery. The power density at the perimeter can be reduced by using a thorium blanket in place of a thick reflector. The power distribution, shown in Fig. 1.24, was calculated for different core sizes, with

the first 1 ft of the reflector loaded with 10 wt % thorium oxide. For the largest core, 14 ft in diameter, the power density at the core periphery is only 0.7 of the average, but, even in this case, the temperature

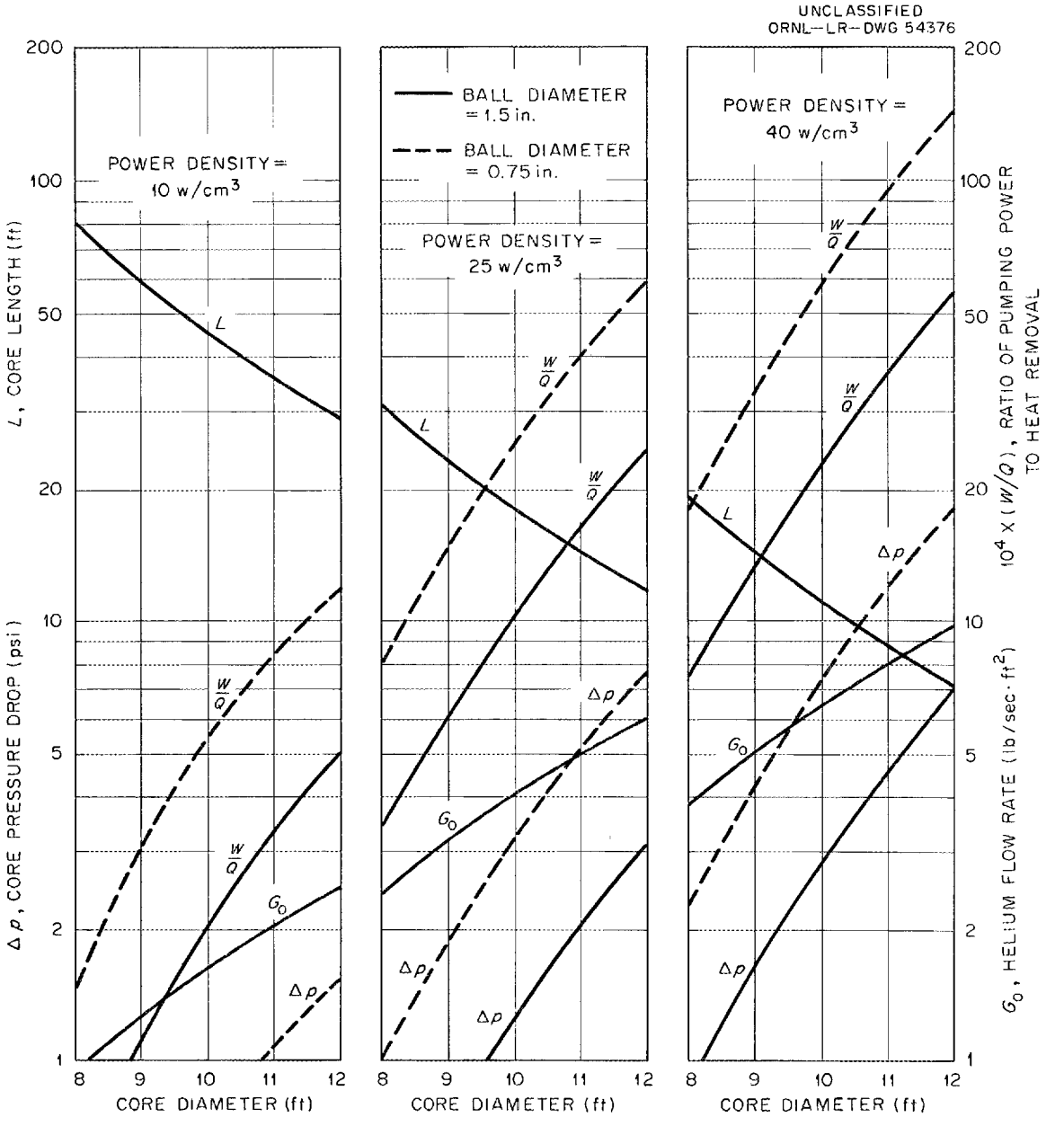


Fig. 1.23. Effects of Power Density, Fuel Sphere Diameter, and Core Outer Diameter on Core Pressure Drop, Core Length, Helium Flow Rate at the Core Inlet Face, and Ratio of Pumping Power to Heat Removal for Radial Outflow Cores Having an Inner Diameter of 4 ft, a Power Output of 850 Mw, and Inlet Temperature Rise of 700°F.

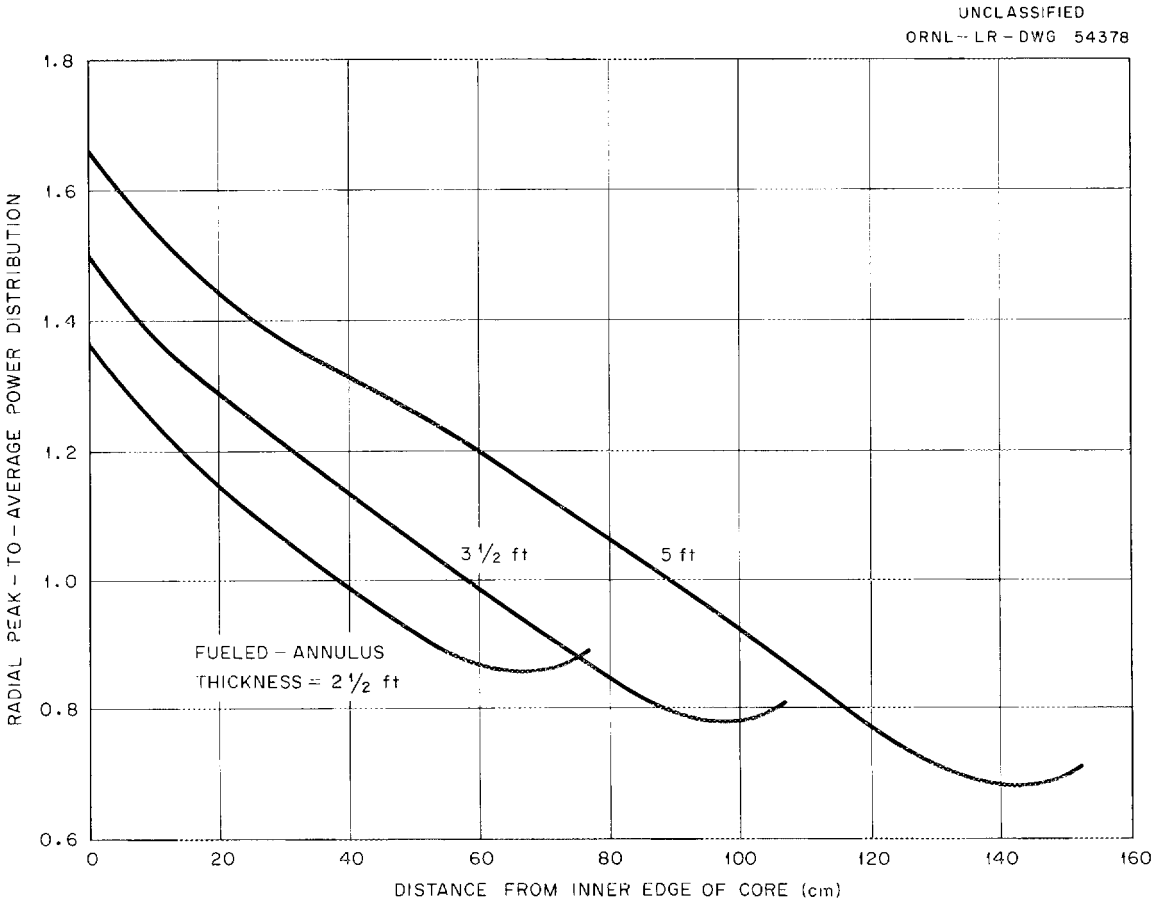


Fig. 1.24. Radial Power Distribution in a Radial Flow Core Having a 4-ft-diam Central Hole, a 1-ft-Thick Blanket Containing 10 wt % ThO_2, and a 2 1/2-ft-Thick Graphite Reflector.

difference between the gas and fuel surface at the periphery was estimated to be 1.5 times the average. Conical ends could be used on the core to increase the radial gas velocity near the perimeter and thus relieve these excessive fuel temperatures somewhat. The effectiveness of changing the core shape in this manner can be estimated only by extensive calculations, but the prospects do not appear to be good, except for a core having a length-to-diameter ratio less than unity, because making the ends conical would have little effect on the flow at the center for the longer cores.

Another disadvantage of the radial flow concept is inherent in the movement of both the control rods and the fuel at right angles to the gas flow. Operation at power with partial control rod insertion depresses

the power density all across the top of the core, with the result that the gas passing through the upper region experiences a smaller temperature rise than the average for the core. In a similar manner, cold gas bypasses through the spent fuel near the bottom. Consequently, the gas in the central region must reach substantially higher temperatures in order to give the desired mixed-mean gas outlet temperature, and excessive gas and fuel temperatures are likely to occur in the central part of the reactor. Thus it appears that the matching of the gas flow to the power distribution is much less favorable than for axial flow cores.

The graphite structure for the radial flow core is complicated by the necessity for gas passages through the inner and outer circumferential boundaries. Probably the best arrangement evolved is that shown in Fig. 1.22, which utilizes the control rod guide tubes as a bar-grid at the core inlet surface. The neutron economy is not sensitive to the material of the outer grid, since it is outside the thorium blanket. In Fig. 1.22 the outer grid is shown as built up of graphite to avoid the use of steel structure in the highest gas temperature zone.

The high axial velocity in the central hole of a radial flow core might lead to poor flow distribution and substantial core inlet pressure losses; time did not permit a careful examination of these problems. An undesirable characteristic of the radial flow core from the physics standpoint is that the large void at the center leads to severe neutron leakage losses. Preliminary estimates indicate that the core conversion ratio would be only about 0.40 for a 14-ft-o.d. core. This corresponds roughly to the 9.7-ft-diam, 40% void fraction core shown in Fig. 1.12, which indicates that the fuel cycle costs would be so large as to make the radial flow core quite unattractive. In review, it appears that poorer neutron economy and higher fuel cycle costs coupled with the more complex fluid flow and construction problems and inherently poor matching of the gas flow to the power distribution make the radial flow core less attractive than the large axial flow core.

Hot-Spot Estimates. The hot-spot problem for the 20.7-ft-diam, axial-flow, 800-Mw reference design reactor was examined for peak-to-

average power density ratios of 1.5 and 2.0. The significant temperatures and temperature differences are shown in Table 1.2.

Comparison of Design Problems of Spherical and Prismatic Fuel Element Reactors. The numerous complex relations discussed above indicate the many limitations imposed on the designer of a pebble-bed reactor. These restraints are more severe than for similar reactors employing tubular or prismatic fuel elements of the same basic material. In such reactors the designer has the option of varying the effective flow passage diameter and the fuel element thickness independently so that the fuel element can be proportioned to give the desired heat transfer characteristics, both internally and externally. Further, tubular or prismatic fuel elements have an aerodynamically cleaner configuration, and hence much lower pumping power losses are incurred for a given core size. As an illustration, a series of tubular fuel element cores was compared with a similar series of pebble-bed reactors for core diameters in the range from 10 to 35 ft. The effects of core diameter on the ratio of pumping

Table 1.2. Factors in a Simplified Hot Spot Temperature Estimate

Core diameter = 20.7 ft
Fuel ball diameter = 2.5 in.
Reactor power = 800 Mw
Helium inlet temperature = 550°F
Helium outlet temperature = 1350°F

	Temperature (°F) Based on Peak-to-Average Power Density of 2.0 in Hot Zone	Temperature (°F) Based on Peak-to-Average Power Density of 1.5 in Hot Zone
Average film temperature drop for entire core	126	126
Average film temperature drop for hot zone	250	190
Film drop in wake of a closely packed cluster in hot zone	550	415
Temperature drop within an average ball uniformly cooled (average power density assumed)	235	235
Same as above except for peak power density in hot zone	470	350
Average gas temperature in hot zone	1100	1100
Peak gas temperature in hot cluster	1400	1400
Hot-ball surface temperature	1950	1815
Hot-ball internal temperature	2420	2165

power to heat removal, the fuel element thermal stress, and the fuel element internal temperature drop are shown in Fig. 1.25. In each case the reactor length was determined first for the pebble-bed reactor, and the tubular fuel element core was made to have the same length. The markedly lower pumping power, thermal stress, and internal temperature for the tubular fuel elements at any given core diameter are indicated.

The prismatic or tubular fuel element core has the advantage that it permits reducing the void fraction to 0.14 or 0.25 from the 0.39 value characteristic of the pebble-bed reactor. Reducing the void fraction improves the conversion ratio and reduces the fuel cycle costs. The savings indicated by Fig. 1.12 are more than enough to justify the capital charges for a quite elaborate fuel-handling machine.

An additional advantage offered by a prismatic or tubular fuel element core is that the flow distribution across the inlet face can be varied by orificing the core inlet or outlet or by varying the diameter of the coolant flow passages through the fuel elements. In either case, better matching of the coolant flow to the power-density distribution can be obtained than would be possible in a pebble-bed core, so the peak fuel element surface temperature should be substantially lower for a given core outlet gas temperature. Further, a thorium blanket could be employed to reduce neutron leakage losses while still maintaining a good match of power density and gas flow.

If, as seems likely from the limited data available, the inner layers of the reflector will have to be replaced from time to time because of graphite shrinkage cracking, a service machine will be required for a pebble-bed reactor. Preliminary studies indicate that such a machine has much in common with a fuel-handling machine suitable for prismatic or tubular fuel elements.

Reactor Design

The PBR is enclosed within a 32-ft-diam, 4-in.-thick, pressure vessel of type SA-212, grade B, carbon steel. Two separate steam generators and two blowers are provided, as indicated in Fig. 1.26. The control rods are uniformly distributed through the core and are actuated by drive units

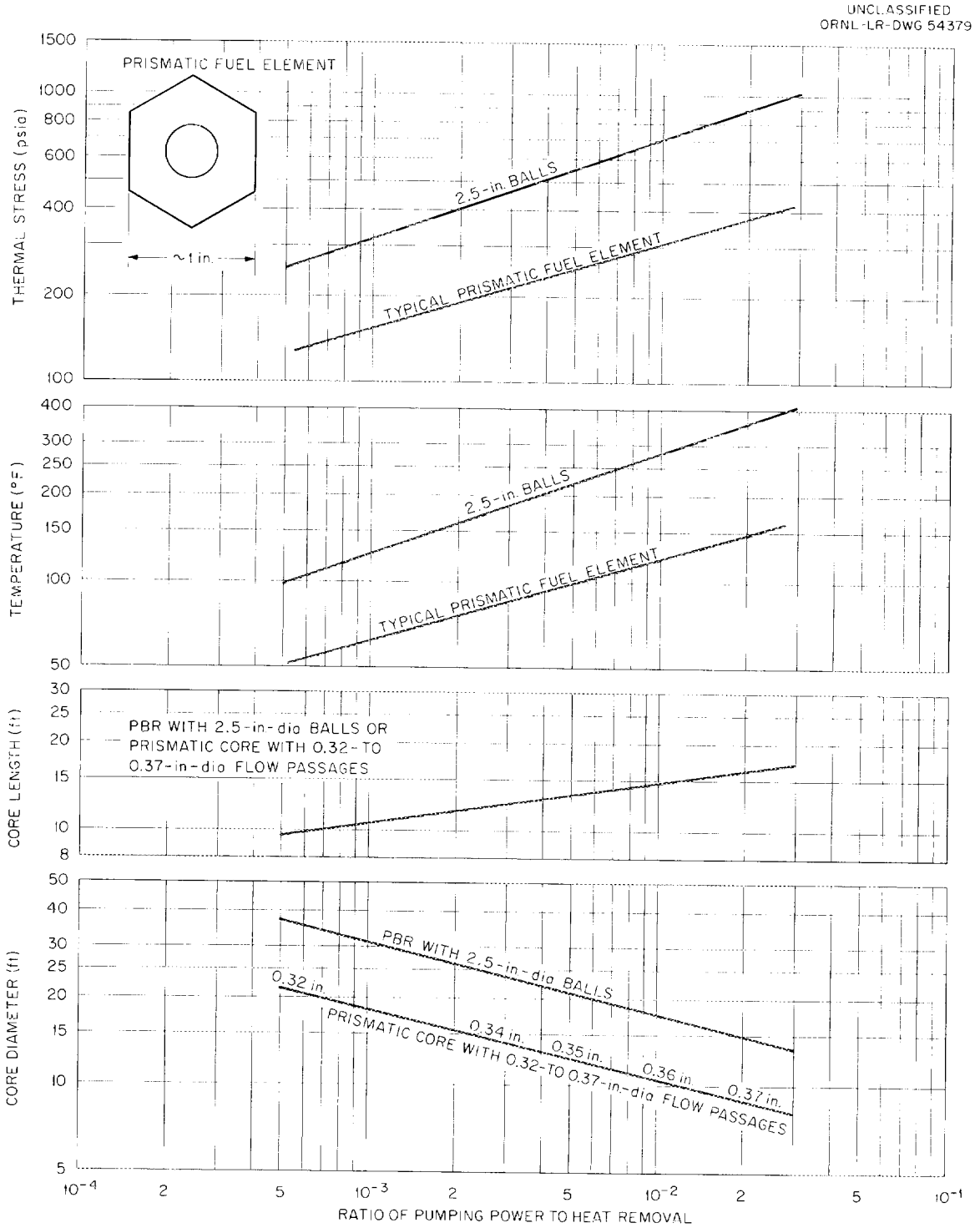


Fig. 1.25. Comparison of Core Diameters, Thermal Stresses, Internal Temperature Drops, and Pumping Power Requirements for Spherical and Tubular Graphite–Uranium Carbide Fuel Elements Using the Void Fraction, Core Length, and Cooling-Gas Temperature Conditions Best Suited to an Axial Upflow Core.

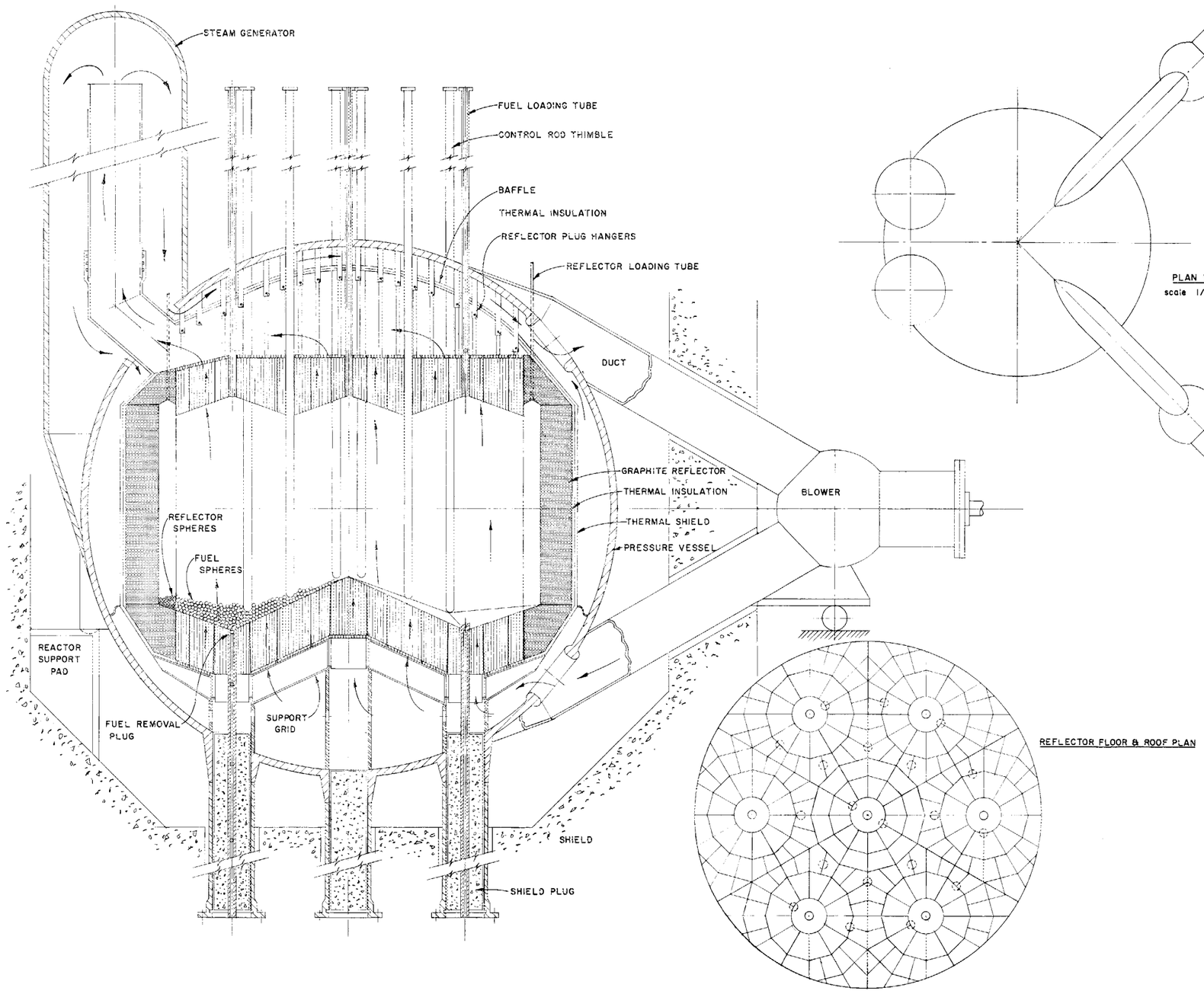


Fig. 1.26. Pebble-Bed Reactor. Scale — 1/2 in. = 1 ft.

at the top. Seven large access tubes at the base are provided for servicing the fuel removal.

The graphite reflector provided over the top and bottom of the core, as well as around the sides, to protect the pressure vessel from fast-neutron damage is 3 ft thick. The outer 2-in. layer of this graphite is borated to inhibit gamma heating in the pressure vessel and to ease the shielding problem, particularly in the vicinity of ducts where thermal-neutron and gamma-ray streaming would present serious problems.

The reactor assembly has been designed to be supported at three points, one between the two steam generators and two under the blowers, all three being in the same horizontal plane. The supports at the blowers will be on rollers to provide for thermal expansion without the use of bellows in the ducts. The blowers are fairly well isolated from the core by shielding. The line-of-sight paths from the core into the blower cell pass through the 3-ft-thick reflector, a 1-in.-thick skirt, and the 4-in.-thick pressure vessel, and the radiation must penetrate the 2-in.-thick ducts twice, both times obliquely. Eight hours after shutdown, this gives a gamma dose from the core of roughly 50 mr/hr at the blowers, which is an acceptable value.

The reactor core support grid is divided into seven segments, each of which is supported independently by one of the access tubes at the base of the reactor. The weight load introduced into the pressure vessel in this fashion is less than 0.5% of the pressure load, so the consequent bending stresses in the pressure vessel should not be serious.

The large-diameter core poses serious design problems in making provisions for fuel handling. In order to obtain a reasonably uniform ball flow distribution across the core, it appears to be necessary to make use of at least six ball inlet and discharge positions, and a substantial slope toward one or another of these positions must be provided over the entire top and bottom faces of the core. If this were not done, there might be local relatively "dead" zones where fuel balls might dwell for excessive periods. Concern for this latter factor led to the use of control rod tubes that do not extend to the face of the bottom reflector,

since otherwise the balls might lodge at the base of one of the tubes instead of flowing as desired.

Twenty-two 8-in.-diam access tubes are provided at the top of the reactor for control rods. Graphite tubes, 6 in. in diameter and 3/4 in. thick, are inserted into the core through these access tubes to provide passages in the pebble bed for the control rods. The control rods consist of stainless steel tubes containing boron carbide and are operated by control rod drives similar to those planned for the EGCR. It is expected that these graphite tubes for the control rods will require replacement every few years because of graphite shrinkage cracking.

The principal performance and dimensional data for the plant are presented below:

Power Generation

Thermal output, Btu/hr	2.73×10^5
Thermal output, Mw	800
Gross electrical output, Mw	347
Net electrical output, Mw	330
Gross thermal efficiency, %	42.7
Net thermal efficiency, %	40.6

Fuel Elements

Sphere diameter, in.	2.5
Maximum thermal stress (for ideal rigid body), psi	1300
Sphere surface, ft^2/ft^3 of fuel	28.7
Sphere surface, ft^2/ft^3 of core (39% voidage)	17.5
Number of spheres per ft^3 of core	129
Average power density in fuel, w/cm^3	10.7
Average surface heat flux, $Btu/hr \cdot ft^2$	35 800
Graphite thermal conductivity, $Btu/hr \cdot ft^2$ (°F/ft)	8
Maximum fuel surface temperature, °F	2000

Maximum fuel internal temperature, °F	2200
Fractional fission-product release rate (R/B)	10^{-4} to 10^{-5}

Reactor

Core	Cylindrical, axial upflow
Core diameter, ft	20.7
Core height, ft	12.4
Core inlet face area, ft^2	336
Core average power density, w/cm^3	6.6
Reflector	1 1/4-in.-diam graphite balls plus fixed graphite
Total reflector thickness, ft	3.0
Core fuel feed positions	One in center, six on 7.3-ft-radius circle
Reflector feed positions	Twelve on 10.8-ft-radius circle
Fuel removal positions	Six on 7.3-ft-radius circle
Diameter of core plus reflector, ft	26.7
Core density, g/cm^3	1.0
Machined weight of fixed graphite, tons	288
Weight of unfueled graphite balls, tons	27
Weight of fueled graphite balls, tons	134

Pressure Vessel

Shape	Sphere
Outside diameter, ft	32.1
Inside diameter, ft	31.4
Thickness, in.	4.0
Material	Type SA-212, grade B, carbon steel

Working pressure, psia	700
Design stress, psi	16 600
Maximum temperature, °F	600
Volume, ft^3	31 000
Gross vessel weight, including core supports, thermal barriers, nozzles, and insulation, lb	~500 000

Coolant System Characteristics

Gas	Helium
Working pressure, psia	700
Flow through core, lb/sec	763
Flow to steam generators, lb/sec	868*
Reactor inlet temperature, °F	550
Reactor outlet temperature above core, °F	1350
Mixed-mean gas temperature to steam generator, °F	1250
Number of inlet pipes	2
Number of outlet pipes	2
Cool pipe inside diameter, ft	3.5
Mean coolant velocity in cool pipe, ft/sec	194
Diameter of ports to blower ducts, ft	3.0
Mean coolant velocity in ports, ft/sec	255
Diameter of hot gas port to steam generator, ft	3.25
Mean coolant velocity in hot gas port, ft/sec	337
Total volume occupied by coolant, ft^3	30 000
Circuit pressure drop, psi	12.0
Pressure drop through core only, psi	3.8
Specific heat of coolant, Btu/lb.°F	1.24

*The bypass flow through the unfueled ball layer lining the reflector is about 14% of the flow through the core.

System pressure losses in terms of ratio of pumping power to heat removal	
Core	0.003
Ducts	0.003
Steam generator	0.004
Total	0.010

Coolant Blowers

Number	2
Type	Single-stage, centrifugal
Blower drives	Steam turbines
Compression power, Bhp	5400
Adiabatic efficiency, %	70
Turbine power, Bhp	7700

Steam Generator

Type of generator	Once-through
Number of generators	2
Shell height between heads, ft	60
Shell height including heads, ft	75
Shell outside diameter, ft	8.5
Shell thickness, in.	~2.25
Gas inlet inside diameter, ft	3
Steam pressure, psi	2450
Steam pressure at throttle, psi	2400
Steam temperature at high-pressure stage, °F	1050
Reheat temperature, °F	1000

The general layout of the plant is shown in Figs. 1.27 and 1.28. The largest and most important element of the system, the reactor building, is located at the center. The other facilities are located for convenience relative to the reactor and to each other.

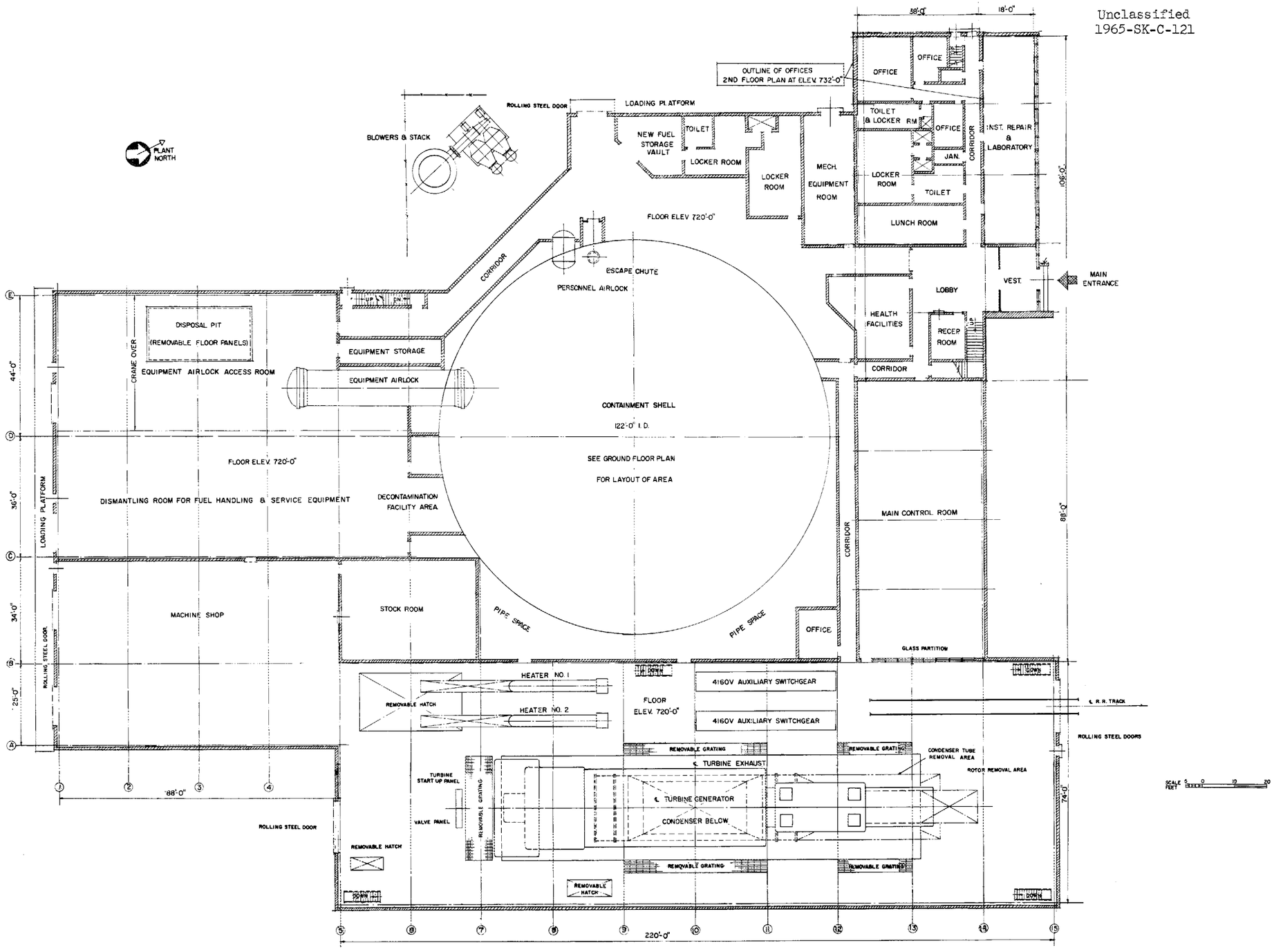


Fig. 1.27. Plan View of Pebble-Bed Reactor Power Station.

Unclassified
1965-SK-C-125

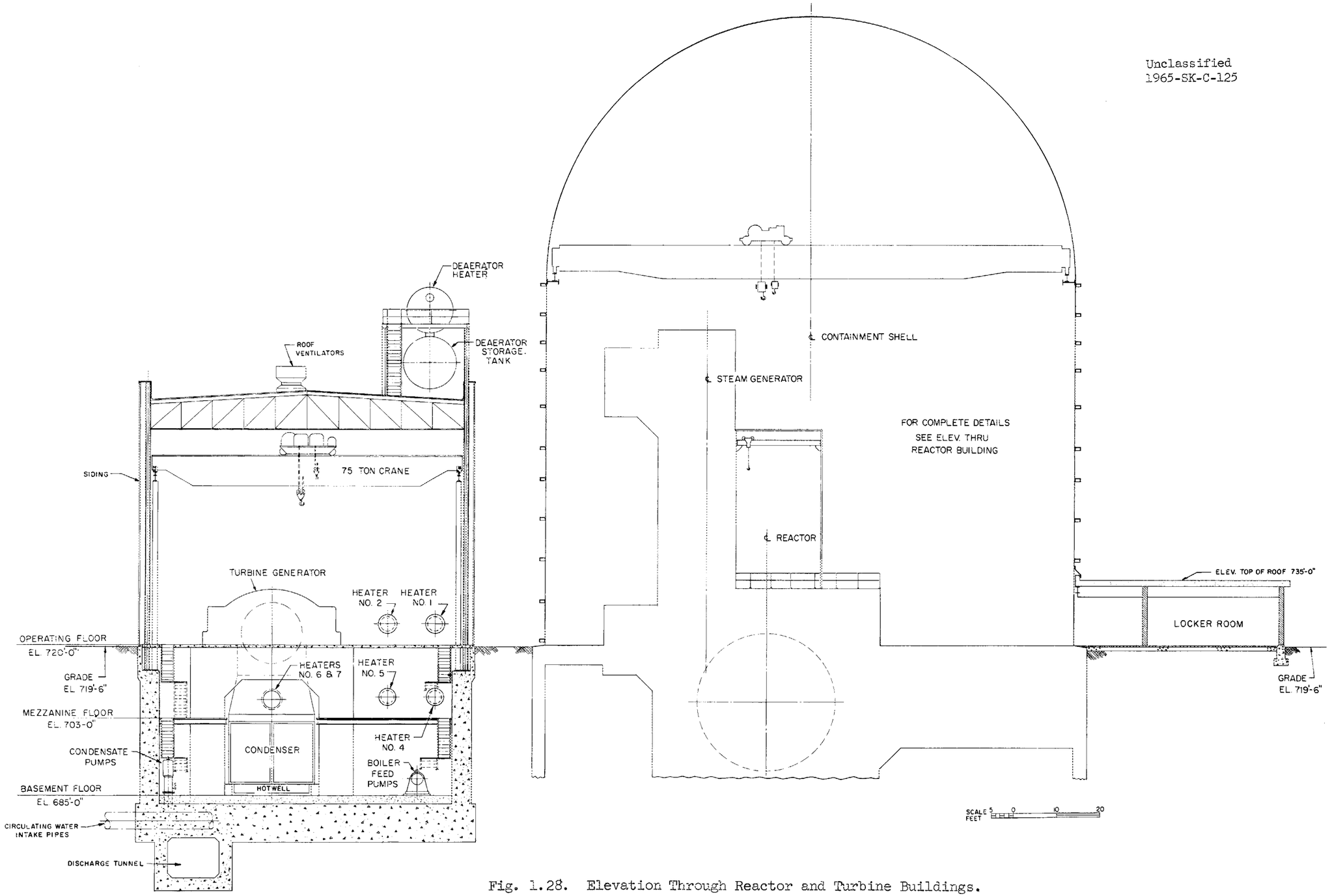


Fig. 1.28. Elevation Through Reactor and Turbine Buildings.

The turbine-generator unit is located immediately adjacent to the reactor building in order to minimize the lengths of steam piping required, particularly for the reheater. The turbine building is located on the river side of the plant to give a good layout for the condenser cooling-water system. The feedwater pumps, feedwater heaters, and other components of the steam system are also located in this bay.

The control room is located at the north end of the plant adjacent to the reactor containment shell and the turbine-generator bay. This arrangement provides a good view of the turbine-generator bay and minimizes the length of instrumentation lines both to the reactor and to the turbine-generator. Offices and other facilities for personnel are located adjacent to the control room or on the floor above it.

The machine shop is located at the south end of the turbine bay. The large equipment lock to the reactor containment shell opens into a reactor service area adjacent to the machine shop. The stack, with its filters and related core equipment, is located to the west of the reactor building.

The reactor and its associated equipment are enclosed in a pressure-tight containment shell 122 ft in diameter and 221 ft high. A vertical section through this building is shown in Fig. 1.29. The layout generally follows that used for the PBRE, with the lower portion modified to reduce the height of the reactor building. To facilitate decontamination, metal-lined rooms enclose all flanged joints for the contaminated-gas system pressure envelope. These rooms are the blower rooms, the service area below the reactor, the hot-fuel storage vaults, and the control-rod drive region on the top of the reactor.

Reactor Physics. As mentioned above, three basic core arrangements were considered: radial flow, axial downflow, and axial upflow. In comparison with the axial flow reactor, the radial flow reactor suffers from the disadvantage of a considerably lower core conversion ratio. This characteristic arises from a combination of the streaming down the central gas passage, the greater outward radial leakage caused by the central gas passage, and the greater outward radial leakage caused by the presence of thorium in the reflector. As a consequence, it is found that the fission cross section decreases more rapidly with burnup and that the axial power

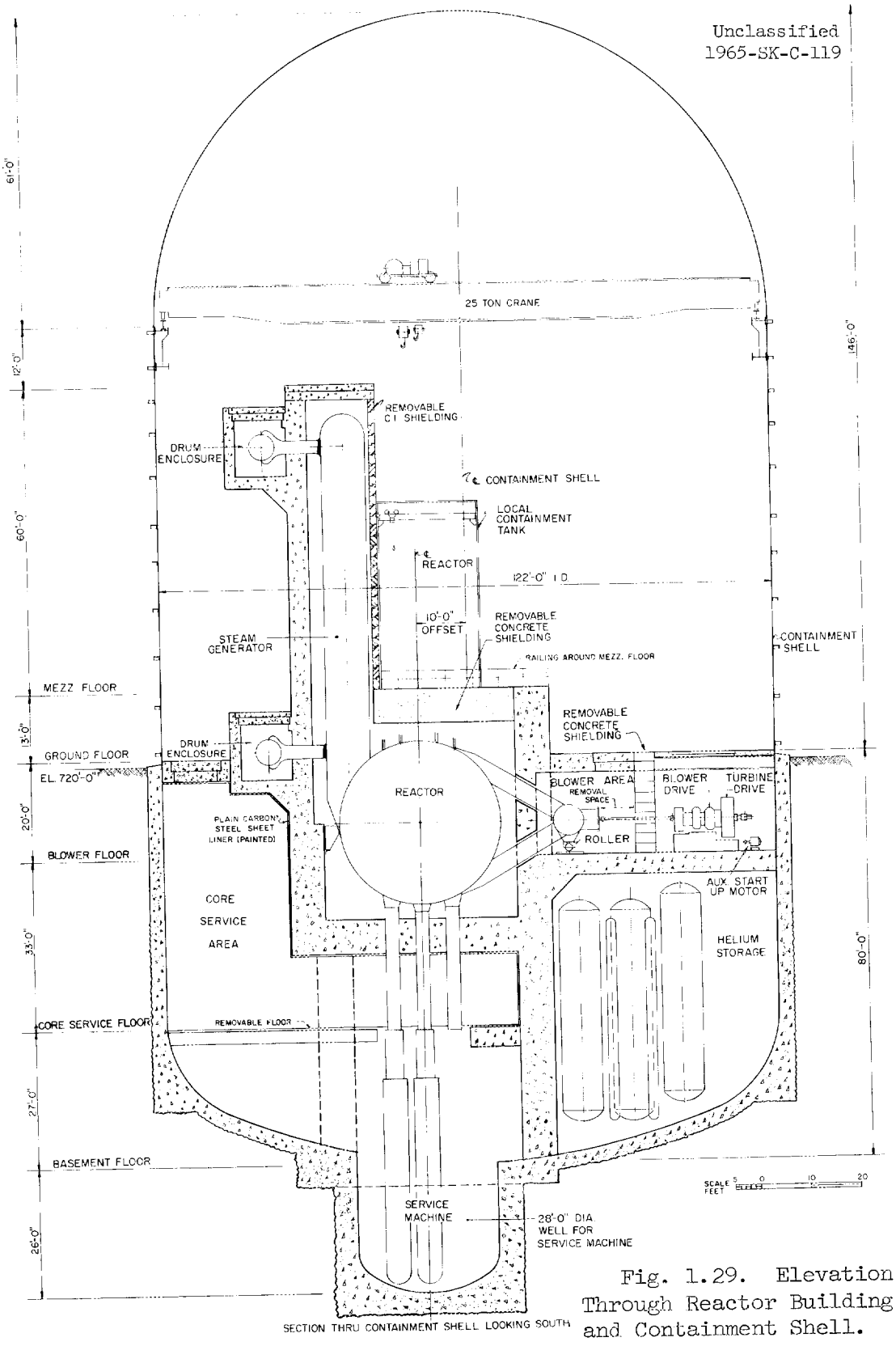


Fig. 1.29. Elevation Through Reactor Building and Containment Shell.

distribution has a greater peak-to-average ratio for a given terminal burnup than is the case in the axial flow reactor. In addition, the available reactivity-limited burnup is reduced. The decrease in conversion in the core is not all lost because some conversion occurs in the thorium of the blanket. It appears likely, however, that the additional complexity of design required to provide for reprocessing a fertile blanket, together with the cost of the blanket reprocessing, would come close to offsetting the value of the U^{233} recovered from the blanket. To the extent that the smaller size of the fuel balls allows a higher peak power density in this core, some of the disadvantages of the power distributions mentioned above might be minimized.

The power distribution for a reactor with axial downflow (average power density of 25 w/cm^3) appears to match the gas flow distribution reasonably well, although it would be necessary to analyze more carefully the discontinuous nature of the details of the power distribution next to the core wall. The core conversion ratio is higher than with the radial flow core, since there is no central gas passage and no thorium in the reflector. However, the conversion ratio is less than with the larger core to be discussed below.

The third type of reactor has axial upflow of the coolant gas. A core diameter of 20.7 ft is required to assure that the gas flow at the design pressure does not cause levitation of the bed of fuel balls. A core height of 12.4 ft is required to obtain a thermal output of 800 Mw at an average core power density of 6.6 w/cm^3.

An initial carbon-to-U^{235} ratio of 4000 was chosen, corresponding to an initial specific power of 1280 kw/kg. This value has not been optimized, although it is believed that the optimum is not far from the value chosen.

Criticality calculations were made (with a 27-group one-dimensional diffusion code) to determine the thorium concentration in the core. Doppler-broadened effective thorium resonance integrals were computed for this purpose from the resonance parameters. The calculations give an initial thorium-to-U^{235} ratio of 18.1.

A neutron balance is given below for the hot, fresh core, with equilibrium xenon and samarium poisoning, but no other fission products, and no buildup of heavy isotopes.

	Neutron Absorptions per Source Neutron
Core	
Graphite	0.0130
U^{235}	0.5094 ($\bar{\eta}$ = 1.96)
Th^{232}	0.3845
Xe	0.0212
Sm	0.0067
Reflector graphite	0.0148
Escapes	
Radial	0.0138
Axial	0.0212
Shim control rod	0.0154
Total	1.0000

It may be seen from these numbers that the initial conversion ratio is 0.75. The poisoning effect of low-cross section fission products and the loss in reactivity from burnup of U^{235} will be offset initially by the higher fission cross section and higher $\bar{\eta}$ of the U^{233}. It is to be expected that the high conversion ratio of the system will allow burnups of from 1.0 to 2.0 fissions per initial fissionable atom before the reactivity finally decreases to an objectionable level.

The moderator temperature coefficient, resulting almost entirely from the change in the ratios of the effective cross sections, was computed by the multigroup method for the initial loading of U^{235}. A value of $-2.4 \times 10^{-5}/°F$ was obtained. The fuel temperature coefficient was obtained by comparing the effective thorium resonance integrals obtained from the resonance parameters and taking into account the Doppler-broadened self-shielding at two different temperatures. A value of $-1.4 \times 10^{-5}/°F$ was obtained. Adding these two contributions, the over-all initial temperature coefficient is -3.8×10^{-5} $(\delta k/k)/°F$.

Requirements for reactivity control during operations will come from the temperature coefficient, the fission-product accumulation, and the fuel burnup. The poisoning from low-cross section fission products, heavy isotope buildup, and fuel depletion depend upon the fuel lifetime selected. The other requirements are summarized below:

	$\delta k/k$
Moderator temperature coefficient	0.0238
Fuel temperature coefficient	0.0179
Equilibrium xenon	0.0315
Equilibrium samarium	0.0106
Total	0.0838

The control system consists of 20 B_4C poison rods, each 4 in. in diameter. The rods travel vertically through the length of the core. Two central rods are located 1 ft from the center of the core, have a combined worth of 0.013 $\delta k/k$, and are to be used for regulating and for shim control of fuel burnup. A circle of eight equally spaced rods is placed 4 ft from the center of the reactor, and 10 rods are 7 ft from the reactor center. These 18 rods have a combined worth of 0.098 $\delta k/k$ and would serve to overcome the temperature defect and the equilibrium xenon poisoning and to provide a shutdown margin of safety of 0.025 $\delta k/k$. Each of the control rods travels through a 5-in.-i.d., 6.5-in.-o.d. graphite sleeve. When the core has reached an equilibrium fuel distribution, compensation for fuel burnup would be by periodic partial refueling (insertion of fresh fuel balls at the top of the core and removal of spent fuel balls from the bottom), with the two central shim rods serving to provide control between refuelings.

During initial operations, prior to the establishment of an equilibrium fuel distribution, there will be somewhat larger changes in reactivity resulting from the accumulation of samarium, other stable fission products, and heavy isotopes. It is anticipated that these would be compensated for by appropriate periodic changes in the height of the fuel bed, combined

if necessary with the use of a burnable poison. The amount of reactivity control available by changing the bed height is given in Fig. 1.30. The use of a decreased bed height to control reactivity is particularly appropriate to the first few months of operation, since it is likely that the reactor would operate for a period of time at reducing power levels while the operating characteristics of the system were being studied. The value of the reactivity control needed to balance the moderator temperature coefficient (0.0213) was computed for the initial conditions of pure U^{235} fuel. As the U^{233} builds up, the moderator temperature coefficient will decrease because of the difference in energy dependence between the U^{235} and U^{233} cross sections. A core in which the U^{235} had all been replaced by U^{233} would have a k_{eff} at room temperature only 0.0039 greater than at operating temperature.

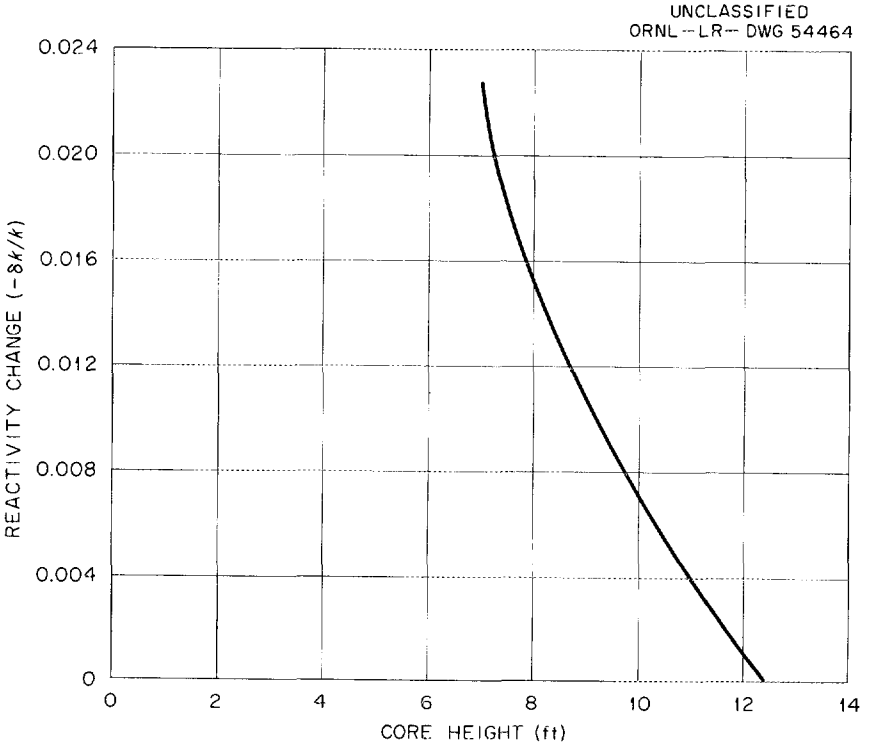


Fig. 1.30. Change in Reactivity with Core Height Based on a Height of 12.4 ft.

No provision has been made in the control system for overriding the peak xenon poisoning, which will occur several hours after a shutdown. It was assumed that scheduled shutdowns and shutdowns from equipment failure would normally be of such duration that the xenon concentration would fall below its equilibrium value before startup was attempted and that the control instrumentation could be made sufficiently reliable so that instrument shutdowns would be infrequent. If it should be necessary to override the peak xenon poisoning, an additional 0.043 $\delta k/k$ would have to be provided in the form of control rods which would remain inserted during normal operations. There would be a corresponding decrease of 0.056 in the conversion ratio and a probable decrease in the fuel lifetime.

The heating rates in the inner portions of the reflector are shown in Fig. 1.31. The neutron heating was computed from the fluxes of the one-dimensional multigroup calculation and the scattering cross sections. The gamma heating was computed by summation of contributions from a six-group space-dependent source distribution. The points of discontinuity occur at the interface between the movable reflector and the fixed reflector because of the higher density of the fixed reflector.

A two-dimensional horizontal cross section of the power distribution in the core is given in Fig. 1.32. The plot is calculated for a normal operating condition of complete insertion of the two central control rods and complete withdrawal of the remaining control rods. The power distribution is normalized to an average value of 1.0.

The mean generation time for prompt neutrons was computed by perturbation theory. The fluxes and adjoint fluxes were determined by a one-dimensional four-group calculation. A value of 0.3×10^{-3} sec was found.

Steam Generators. The reactor system incorporates two steam generators, each 8.5 ft in outside shell diameter and approximately 70 ft high. The units are located as shown in Figs. 1.26 and 1.29. The use of two units eases the problems of leak detection and makes possible the isolation of a unit in the event of a tube failure.

A once-through steam generator was selected to minimize the number of tube penetrations through the heat exchanger shell. In addition, a

once-through design permits a higher boiling point in the steam generator than is possible with a recirculating unit, and this, in turn, is reflected in a higher plant thermal efficiency. A limitation, perhaps not generally recognized, on gas-cooled reactor power plants involves the requirement for reducing return gas temperatures to values normally below the optimum feedwater temperatures for the most modern steam power plants. In the present design the feedwater temperature to the steam generator is 400°F, whereas

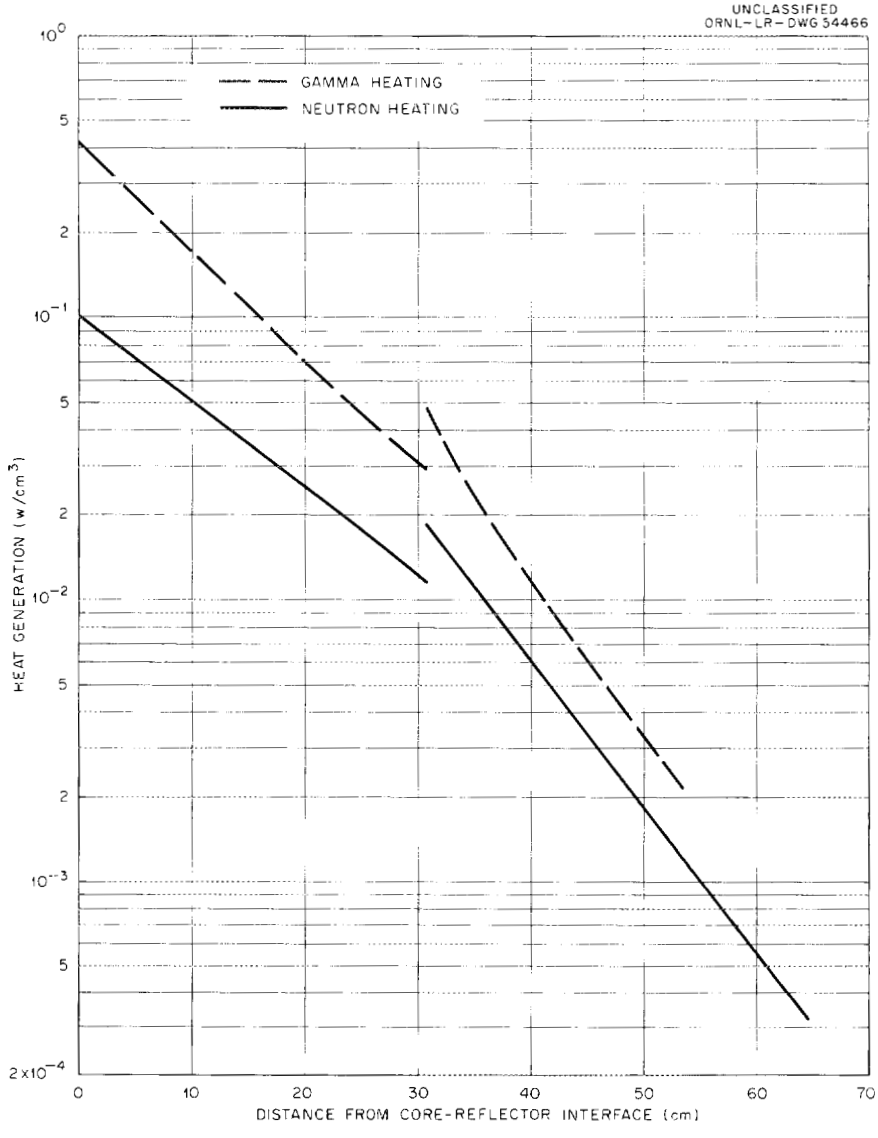


Fig. 1.31. Heating in Inner Portions of Reflector of Axial Upflow Core.

UNCLASSIFIED
ORNL-LR-DWG 54467

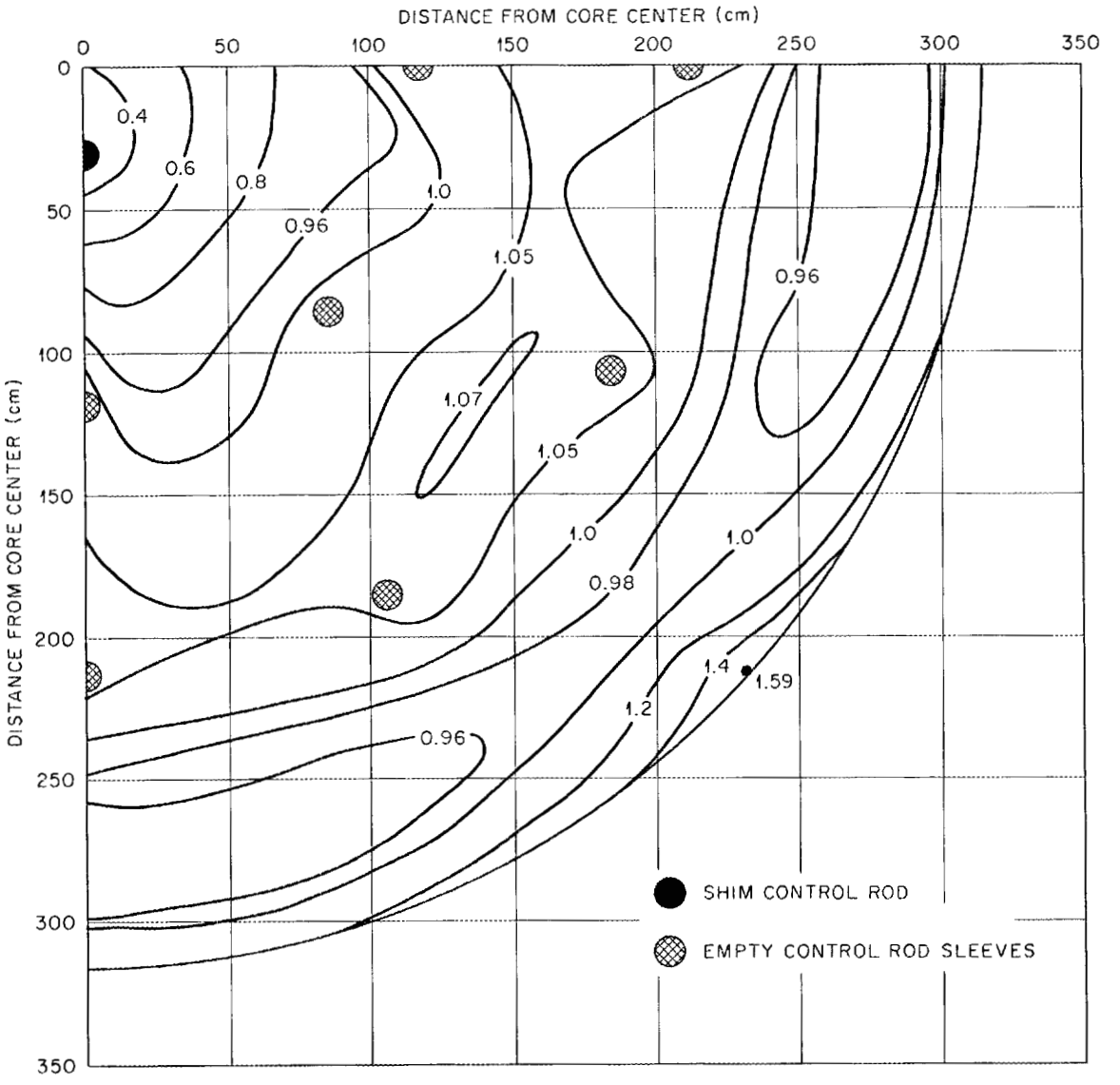


Fig. 1.32. Core Power Distribution Relative to an Average Power of 1.0.

a comparable conventional plant operating at similar conditions would employ additional feedwater heaters and might operate with feedwater temperatures well in excess of 500°F. This limitation on maximum feedwater temperature, because of minimum gas temperature requirements, results in a lower thermal efficiency for recirculating boilers unless preceded by a feedwater heater that utilizes the exit helium from the boiler before

it is returned to the reactor. The once-through generator combines these two functions in a single unit.

The design selected is shown schematically in Fig. 1.33. Gas from the reactor core is directed through an entrance nozzle to the central circular upflow pipe of the steam generator. At approximately two-thirds of the vessel height, the gas passes through a transition piece to a square section containing the reheater of the generator unit. At the top of the vessel, turning vanes reverse the gas flow downward around the outside of the reheater shroud and into the main tube annulus. The gas is directed parallel to the superheater, boiler, and economizer tubes and countercurrent to the tube-side flow. Cool gas from the core inlet is directed up the cooling annulus between the shell and a layer of thermal insulation designed to maintain shell temperatures below 600°F. The annulus gas discharges into the main helium stream at the top of the steam generator unit.

Table 1.3 and Figs. 1.33 and 1.34 summarize the pressures and temperatures of the fluids entering and leaving the steam generator. The requirement of the added heat from the blowers necessitates a gas temperature of 535°F leaving the steam generator to achieve a 550°F core inlet

Table 1.3. Gas and Steam Conditions in Steam Generator

Helium	
Flow per generator, lb/hr	1.56×10^6
Inlet temperature, °F	1250
Outlet temperature, °F	535
Pressure drop, psi	9
Steam	
Flow per generator, lb/hr	1.05×10^6
Feedwater inlet temperature, °F	400
Feedwater inlet pressure, psia	2550
Superheated steam outlet temperature, °F	1055
Superheated steam outlet pressure, psia	2480
Reheater inlet temperature, °F	623
Reheater outlet temperature, °F	1005
Reheater inlet pressure, psia	470
Reheater outlet pressure, psia	460

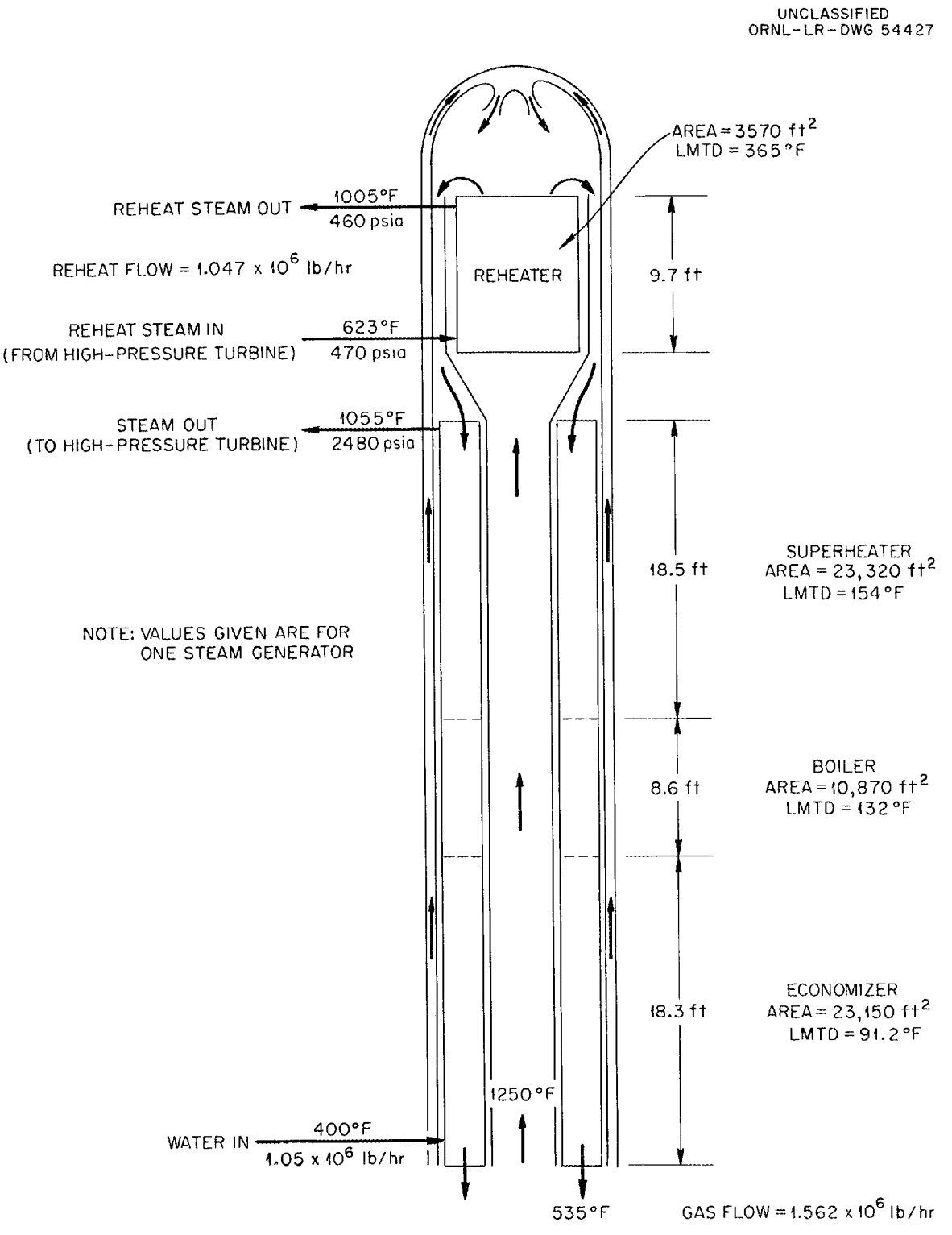


Fig. 1.33. Schematic Diagram of Steam Generator.

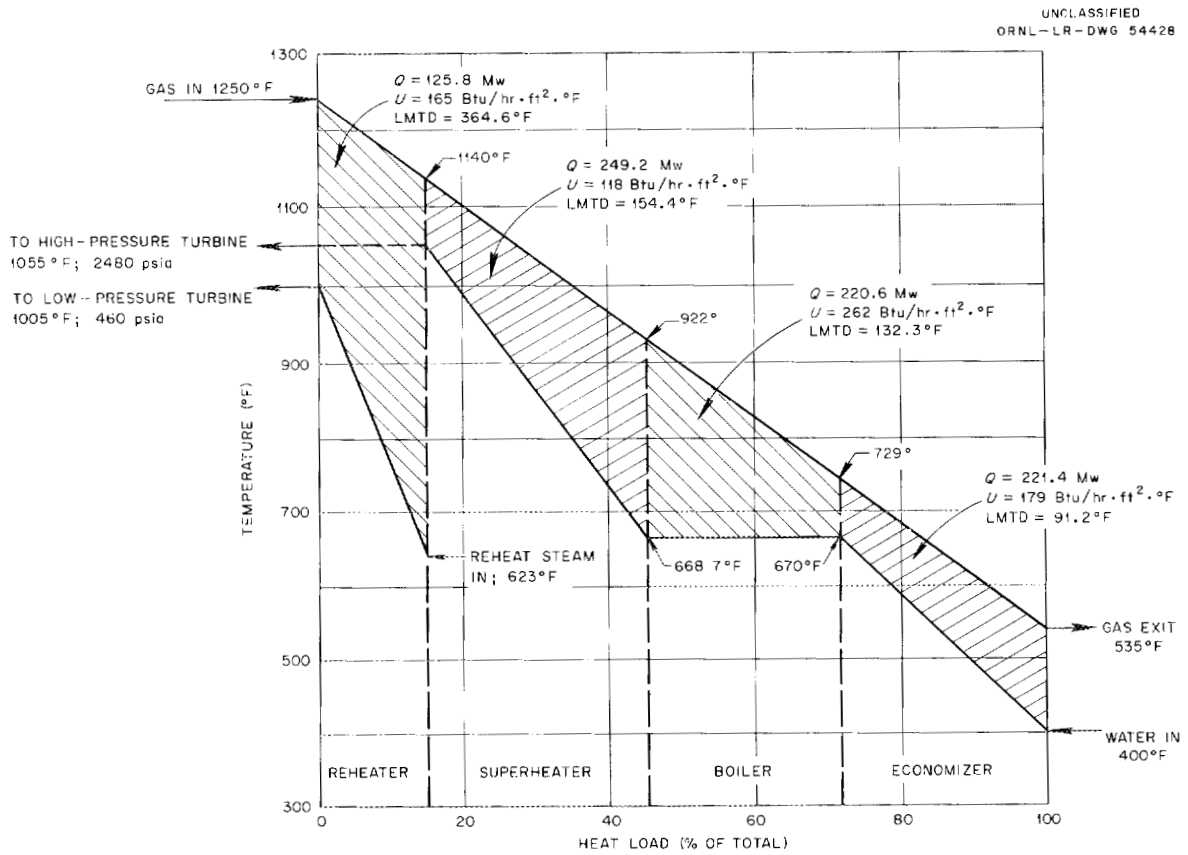


Fig. 1.34. Helium-Steam Temperature Diagram for PBR Steam Generators.

temperature. The two turbine drives for the blowers utilize approximately 300 000 lb/hr of steam between the superheat and reheat steam pressures. The discharge steam from the drive turbine mixes with the high-pressure turbine-generator discharge steam and returns to the reheat section of the steam generator.

Specific design parameters for the steam generator are given in Table 1.4. Water enters the feedwater drum at 400°F and passes into the shell through 1 3/4-in.-diam feeder lines. These feeder lines terminate in 6-in. spherical headers serving 61 tubes 5/8 in. in diameter arranged in a hexagonal tube bundle, as indicated in Fig. 1.35. Time has not permitted the development of a suitable layout, and therefore the tubes are vertical within the heat exchanger. They terminate at the top in spherical steam headers identical to the lower feedwater headers. The superheated steam passes from the spherical steam headers through collector

tubes to the superheater drum. The proposed design utilizes approximately 7700 tubes 5/8 in. in diameter. Approximately 125 header and shell-wall penetrations are required at the entrance to the economizer section and a like number at the superheater exit. Tubes near the inner and outer

Table 1.4. Design Data for One Once-Through Steam Generator

	Economizer, Boiler, and Superheater Section	Reheater Section
Flow scheme	Axial counterflow of gas outside tubes	Cross flow
Tube outside diameter, in.	0.625	1.75
Tube inside diameter, in.	0.400	1.62
Tube material	Carbon steel in economizer, low-alloy Cr-Mo steel in boiler, high-alloy stainless steel in superheater	High-alloy stainless steel
Number of tubes	7700	200
Tube spacing and arrangement	Equilateral pitch, 0.875 in. on centers	Transverse spacing, 2.5 in.; longitudinal spacing, 1.875 in. (staggered)
Upflow pipe diameter, ft	3.25	
Dimensions of tube sections, ft	3.25, i.d.; 7.58, o.d.	5.25 square
Tube length, ft	45.5	50
Straight height of each section, ft	18.3, economizer; 8.6, boiler; 18.5, superheater	9.7
Estimated over-all shell height, ft	70-75	
Gas mass velocity, lb/sec·ft^2	22.8	50.1
Shell-side area (total, 61 000), ft^2	23 200, economizer; 10 900, boiler; 23 300, superheater	3580
Water-side mass velocity, lb/sec·ft^2	43.4	98.7
Log mean temperature difference, °F	91.2, economizer; 132, boiler; 154.4, superheater	~365
Heat load (total = 1.39×10^9), Btu/hr	3.78×10^8, economizer; 3.76×10^8, boiler; 4.25×10^8, superheater	2.15×10^8
Heat load as percentage of total load, %	27.1, economizer; 27.0, boiler; 30.5, superheater	15.4
Gas-side heat transfer coefficient, Btu/hr·ft^2·°F	330	652
Tube-side heat transfer coefficient, Btu/hr·ft^2·°F	708, economizer; 5000, boiler; 334, superheater	293
Heat flux (outside area), Btu/hr·ft^2	16 300, economizer; 34 500, boiler; 18 200, superheater	60 000
Over-all heat transfer coefficient, Btu/hr·ft^2·°F	179, economizer; 262, boiler; 118, superheater	165

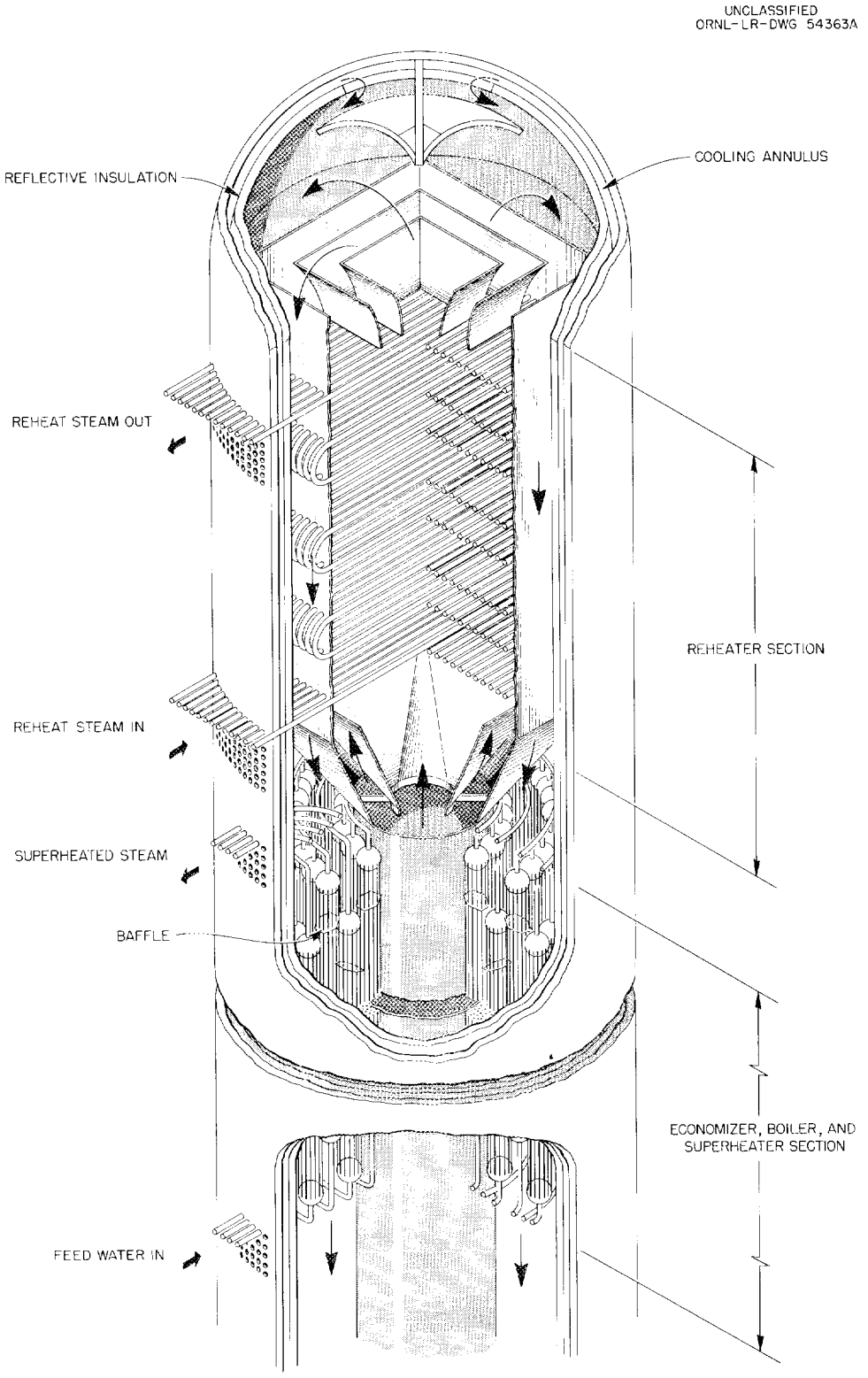


Fig. 1.35. Sketch of PBR Steam Generator.

peripheries that cannot be accommodated in the hexagonal tube bundles are fed by special headers.

Thermal expansion loops on the feedwater line and superheater tubes are provided in the primary section of the steam generator. The tube bundles are hung from support cradles on the expansion loops in the superheater section. The support cradles are, in turn, tied to the vessel wall. Thus the individual tube bundles are free to move independently in a vertical direction and are permitted limited relative lateral motion before contacting adjacent bundle spacers. The tube bundle spacers are tied to apex points of the hexagonal bundle.

In order to avoid the complication of an additional header system or an excessive number of shell penetrations, the reheater section is designed as a serpentine coil, as shown in Fig. 1.35. The reheater section is housed in a 5.3-ft-square shroud with the serpentine tubes of the reheater section supported from the hemispherical dome. Reheat steam from the high-pressure turbine enters the reheat section through a bank of eight rows of tubes having 25 tubes per row. Thus 200 tube wall penetrations are required at each end of the reheat section. Gas from the upflow pipe passes through the transition piece to the reheat section. Guide vanes are required in the transition piece to prevent localized high-impingement gas velocities and poor gas flow distribution across the reheater tubes.

It is estimated that approximately 4 ft of shell height will be required for accommodating thermal expansion loops and interior headers on each end of the primary section. Approximately 2 to 3 ft will be required for the upflow transition piece. The over-all steam generator shell height is estimated to be 70 to 75 ft.

Ball-Handling System. The fuel-loading arrangement shown in Fig. 1.26 consists of two sets of ball ducts leading to the top of the reflector from the floor above the reactor. Twelve equally spaced feeders for 1 1/4-in.-diam unfueled balls are located on a circle at the core perimeter. The 2 1/2-in.-diam fueled balls are added at seven locations; one feeder is at the center of the core, and six are spaced equally on a circle over the fuel bed. Individual ball-loading devices are provided at these 19 positions.

It is not clear how the top of the core should be shaped to give both good filling and good flow distribution for both the fueled and unfueled balls. The problems introduced by the use of two ball sizes and regions appear to be much greater than was anticipated when the layout of Fig. 1.26 was initiated. Not only does it appear to be difficult to maintain a uniform thickness of the unfueled ball layer, both circumferentially and axially, but there may be difficulties with the fueled balls mixing with unfueled reflector balls and vice versa. Both types of intermixing are to be avoided, since large fueled balls in the reflector region would not be sufficiently cooled, and small unfueled balls in the fuel bed would obstruct the coolant flow.

Since balls cannot be used for the inner layers of the top and bottom reflector regions in continuously fueled cores, these will require replacement by some sort of servicing machine during extended shutdowns for such operations. This being the case, it appears that it would be better to design for replacement of the inner layer of the side reflector at the same time with the same machine rather than to attempt to line the reflector with unfueled balls. Such a provision would greatly simplify the design of the ball-handling system and would remove the basic uncertainties introduced by an uncontrolled interface between two ball regions.

The zoning of the round core support grid to accommodate six ball drain ports creates noncircular "funnel zones." There are few experimental data to demonstrate the extent or type of ball flow control which can be induced by contouring these funnels in various ways, but it appears that the bottom of the core should slope toward the exit port at an angle of at least 15 deg relative to the horizontal.

The general arrangement contemplated for the design of Fig. 1.26 employs six ball drain ducts. By arranging the drain ducts into two groups of three to route the balls outward to opposite sides of the reactor vessel, as shown in Fig. 1.36, the central area under the reactor is kept clear for the service machine, and accessibility to each of the six drainage systems should be good. However, an investigation of this problem represents a major test and development item, even for a core containing only uniformly sized fuel balls, and an indeterminately greater effort for a

core with two ball sizes in separate zones. The problem of ball flow through the core can be approached effectively only by experimentation.

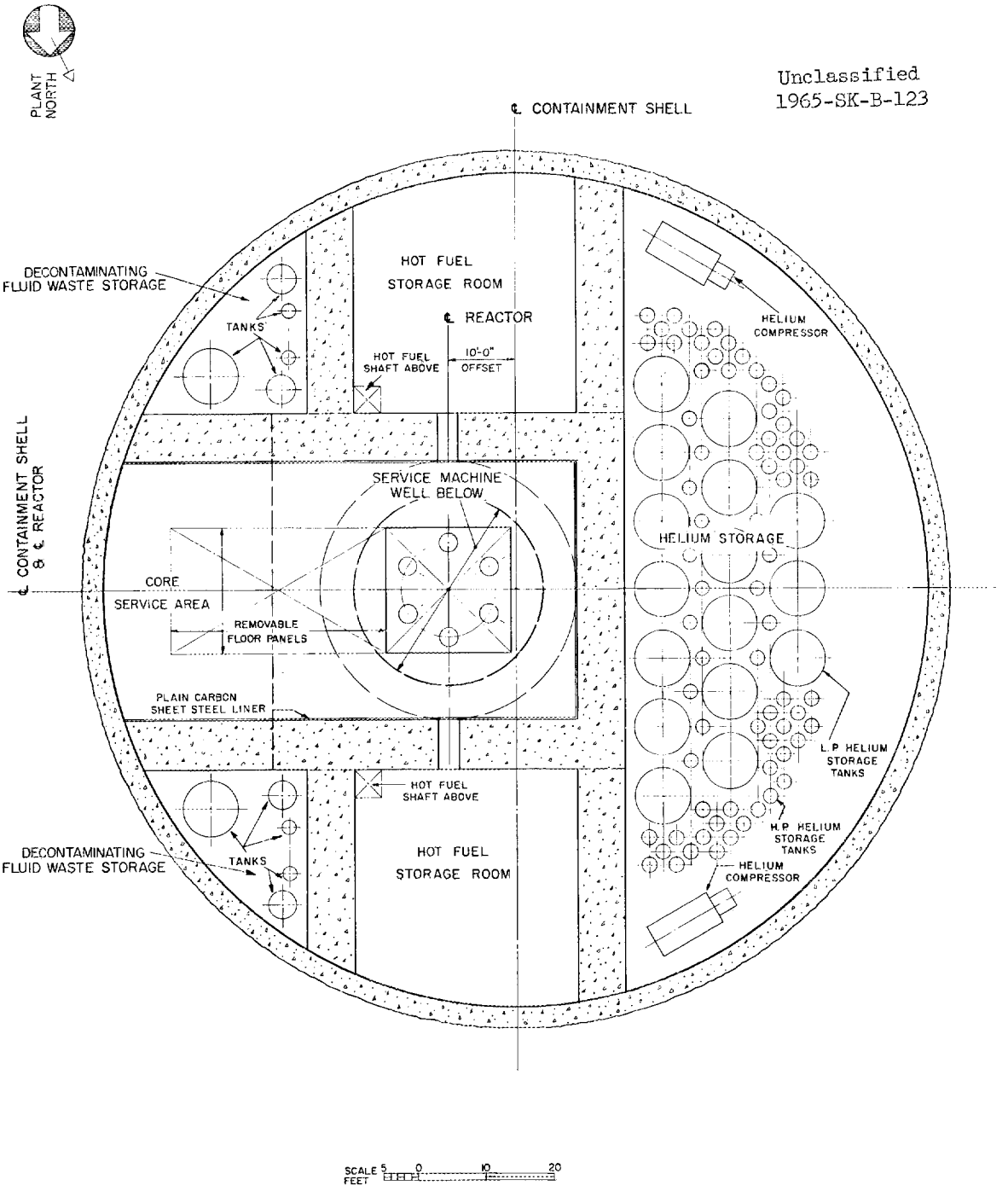


Fig. 1.36. Plan View of Core Service Area.

Power Plant. In order to expedite the design study of the power plant, the design of a coal-fired plant scheduled for completion of construction in 1964 was chosen as a reference design.[8] Some modifications were required, including a reduction in the feedwater temperature to give a well-proportioned steam generator with the 550°F reactor helium inlet temperature used, and allowances were made for the steam required for the blower drive turbines.

A 350-Mw, tandem, compound, turbine-generator unit for indoor service was chosen for the plant, partly because of its cost advantage and partly because it gave a favorable layout for the steam piping. The steam conditions chosen are 2400 psig, 1050°F, with a single reheat to 1000°F. The turbine exhausts at 1.5 in. Hg absolute. The generator is rated at 345 000 kva for a 0.85 power factor and a short-circuit ratio of 0.64 and is cooled with hydrogen at 30 psig. The unit, complete with accessories, includes a directly connected exciter, a lube oil system, and a gland-sealing system.

A regenerative cycle is employed to heat the feedwater to 400°F. Further heating would increase both steam-generator capital charges and blower pumping power requirements. This system includes six feedwater heaters, with the deaerator preceding the highest pressure heater. Electric motors are used for the boiler feed pump drives. The exhaust steam from the blower drive turbines is passed through the reheater and fed to the intermediate turbine.

A flow sheet for the steam plant is presented in Fig. 1.37 that indicates the principal features of the plant. The main condenser is a twin-shell, 150 000-ft^2 unit employing a two-pass, divided-water-box design. Cooling water, lube oil, and gland-sealing systems are provided. The condenser cooling-water system includes trash racks, traveling screens with wash equipment, and algae control equipment. Accessory equipment includes isolated phase-generation leads, exciter connections, transformer and cables, control wiring, storage batteries with a charger and an

[8] "Study of a Typical 306 Mw Net Coal-Fired Installation," Contract AT (10-1)-1010 Between the Division of Reactor Development, USAEC, and Ebasco Services Inc., April 1959.

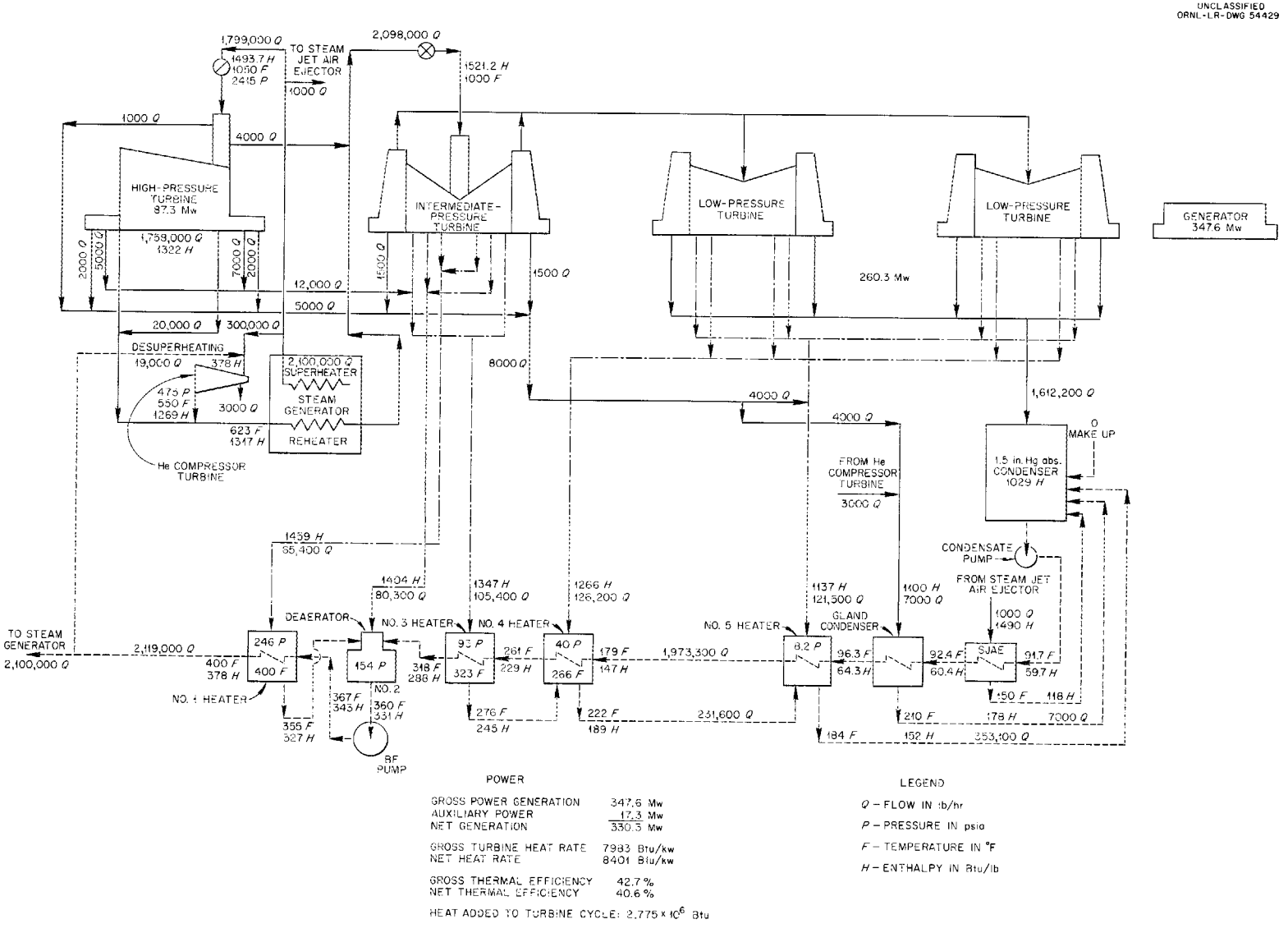


Fig. 1.37. Diagram of Steam and Electrical Plant.

emergency generator set, and station-grounding protection. Miscellaneous plant equipment includes cranes, cleaning equipment, fire-fighting gear, air-gas-oil facilities, office and laboratory services, tools, and communication provisions. The outdoor switch yard includes an oil circuit breaker, disconnect switches, and relaying devices. A single 230-kv transmission-line takeoff is provided.

2. REACTOR PHYSICS

Zone Loading of EGCR Core

(C. A. Preskitt)

Studies of the EGCR power distribution have been extended to include radial zone loading of the core with elements of either two or three initial enrichments. As anticipated, considerable power flattening results when the core is properly zone loaded, and thus a fuel loading procedure is available which supplements the control rod program described previously.[1] The additional power flattening produced by zone loading the core overcomes the severe hot-channel problem associated with loading fresh fuel elements of a high feed enrichment during the initial refueling operations.

Four zone-loading cases have been examined and are compared with the reference case of uniform loading in Tables 2.1 through 2.6. In this comparison the three zones are numbered from the center of the core outward and contain, respectively, one-fourth, one-fourth, and one-half the fuel elements. The central control rod is fully inserted in all cases and the four central loops are loaded with the reference homogeneous graphite-uranium experiments with C/U = 200 (0.33 kg of U^{235} per foot of length).

[1] "GCR Quar. Prog. Rep. Sept. 30, 1960," ORNL-3015, pp. 3–11.

Table 2.1. Comparison of the Power Distribution of Several Zone-Loaded Cores with that of a Uniformly Loaded Core

Zone Enrichment (%)			Radial Peak-to-Average Power Ratio	Loop Power (Mw)
I	II	III		
2.2	2.2	2.2	1.352	1.07
2.2	2.2	2.4	1.242	0.99
2.2	2.2	2.8	1.186	0.90
2.2	2.4	2.4	1.267	0.99
2.2	2.4	2.8	1.155	0.91

Table 2.2. Radial Power Distribution in EGCR Core with Uniform Radial Loading[a]

y	Radial Power Distribution in Indicated Channel (x,y)[b]								
	x = 4	x = 12	x = 20	x = 28	x = 36	x = 44	x = 52	x = 60	x = 68
4	0.885	1.170	1.342	1.349	1.274	1.150	0.999	0.837	0.735
12	1.170		1.320	1.327	1.240	1.111	0.961	0.816	0.745
20	1.342	1.320	1.335	1.277	1.168	1.031	0.884	0.786	
28	1.349	1.327	1.277	1.185	1.056	0.907	0.763	0.681	
36	1.274	1.240	1.168	1.056	0.909	0.753	0.616	0.553	
44	1.150	1.111	1.031	0.907	0.753				
52	0.999	0.961	0.884	0.763	0.616				
60	0.837	0.816	0.786	0.681	0.553				
68	0.735	0.745							

[a]Normalized to average channel power of unity.

[b]x and y are coordinates of channel in inches from center of reactor.

Table 2.3. Radial Power Distribution in EGCR Core Zone Loaded to an Enrichment of 2.2% in Zone I, 2.2% in Zone II, and 2.4% in Zone III

y	Radial Power Distribution in Indicated Channel (x,y)[a] and Zone								
	x = 4	x = 12	x = 20	x = 28	x = 36	x = 44	x = 52	x = 60	x = 68
	Zone I, 2.2%				Zone II, 2.2%		Zone III, 2.4%		
4	0.779	1.050	1.210	1.242	1.198	1.114	1.076	0.917	0.825
12	1.050		1.189	1.226	1.172	1.075	1.040	0.898	0.845
20	1.210	1.189	1.221	1.191	1.113	1.004	0.963	0.874	
28	1.242	1.226	1.191	1.121	1.016	0.956	0.839	0.771	
36	1.198	1.172	1.113	1.016	0.960	0.812	0.693	0.649	
44	1.114	1.075	1.004	0.956	0.812				
52	1.076	1.040	0.963	0.839	0.693				
60	0.917	0.898	0.874	0.771	0.649				
68	0.825	0.845							

[a]x and y are coordinates of channel in inches from center of reactor.

Table 2.4. Radial Power Distribution in EGCR Core Zone Loaded to an Enrichment of 2.2% in Zone I, 2.2% in Zone II, and 2.8% in Zone III

y	Radial Power Distribution in Indicated Channel (x,y)[a] and Zone								
	x = 4	x = 12	x = 20	x = 28	x = 36	x = 44	x = 52	x = 60	x = 68
	Zone I, 2.2%				Zone II, 2.2%		Zone III, 2.8%		
4	0.664	0.899	1.049	1.098	1.091	1.042	1.186	1.042	0.964
12	0.899		1.036	1.090	1.071	1.015	1.148	1.022	0.991
20	1.049	1.036	1.076	1.070	1.028	0.951	1.068	1.002	
28	1.098	1.090	1.070	1.025	0.946	1.034	0.935	0.888	
36	1.091	1.071	1.028	0.946	1.038	0.895	0.783	0.755	
44	1.042	1.015	0.951	1.034	0.895				
52	1.186	1.148	1.068	0.935	0.783				
60	1.042	1.022	1.002	0.888	0.755				
68	0.964	0.991							

[a] x and y are coordinates of channel in inches from center of reactor.

Table 2.5. Radial Power Distribution in EGCR Core Zone Loaded to an Enrichment of 2.2% in Zone I, 2.4% in Zone II, and 2.4% in Zone III

y	Radial Power Distribution in Indicated Channel (x,y)[a] and Zone								
	x = 4	x = 12	x = 20	x = 28	x = 36	x = 44	x = 52	x = 60	x = 68
	Zone I, 2.2%				Zone II, 2.4%		Zone III, 2.4%		
4	0.756	1.021	1.183	1.218	1.267	1.172	1.055	0.895	0.801
12	1.021		1.163	1.204	1.238	1.136	1.018	0.876	0.820
20	1.183	1.163	1.198	1.168	1.176	1.060	0.942	0.853	
28	1.218	1.204	1.168	1.186	1.074	0.942	0.821	0.750	
36	1.267	1.238	1.176	1.074	0.942	0.796	0.677	0.631	
44	1.172	1.136	1.060	0.942	0.796				
52	1.055	1.018	0.942	0.821	0.677				
60	0.895	0.876	0.853	0.750	0.631				
68	0.801	0.820							

[a] x and y are coordinates of channel in inches from center of reactor.

Table 2.6. Radial Power Distribution in EGCR Core Zone Loaded to an Enrichment of 2.2% in Zone I, 2.4% in Zone II, and 2.8% in Zone III

y	Radial Power Distribution in Indicated Channel (x,y)[a] and Zone								
	x = 4	x = 12	x = 20	x = 28	x = 36	x = 44	x = 52	x = 60	x = 68
	Zone I, 2.2%				Zone II, 2.4%		Zone III, 2.8%		
4	0.645	0.875	1.028	1.080	1.155	1.103	1.163	1.017	0.936
12	0.875		1.017	1.074	1.135	1.072	1.125	0.998	0.962
20	1.028	1.017	1.060	1.053	1.088	1.006	1.047	0.978	
28	1.080	1.074	1.053	1.087	1.002	1.020	0.916	0.865	
36	1.155	1.135	1.088	1.002	1.020	0.879	0.765	0.734	
44	1.103	1.072	1.006	1.020	0.879				
52	1.163	1.125	1.047	0.916	0.765				
60	1.017	0.998	0.978	0.865	0.734				
68	0.936	0.962							

[a] x and y are coordinates of channel in inches from center of reactor.

It may be seen from Table 2.1 that an undesirable effect of zone loading is a reduction of loop power, but it must be emphasized that this reduction is not due directly to zone loading, but, rather, results from flattening of the power distribution and will occur when the flattening is achieved by any means. It has been observed that the ratio of peak channel power to loop power is essentially constant for a wide range of core operating conditions. The configuration described by the second line of Table 2.1 (equal numbers of 2.2 and 2.4% enriched fuel elements) has been judged to be a satisfactory compromise between the requirements for power flattening and the desire for a high loop power and has been considered for the initial loading of the EGCR core if the four central loops are installed at that time. Since it now appears that the installation of all loops will be deferred to a later date, the fuel loading described above will not be required for the initial core.

Reactivity Effects Associated with Operation of the EGCR

(C. A. Preskitt, D. R. Gilfillan)

Some of the reactivity effects which might be encountered during operation of the EGCR, both in normal operation and as a result of an accident,

have been calculated to assist in determining the control actions that need to be available. It has been found that if an experimental fuel assembly were dropped into the core it could, almost instantaneously, increase the reactivity by as much as +1%. The unloading of a fuel channel could produce an increase in reactivity that could be as large as +0.1%. The increase would result mainly from a local increase in the resonance escape probability in adjacent channels. If steam entered the core, the resulting excess k, which would be essentially linear with steam pressure, would be $\sim 5 \times 10^{-4}$ (0.05%) per 100 psi. Complete flooding of the core with water would increase k by about +0.06 (6%).

Neutron Source Required for the EGCR

(A. M. Perry, T. H. Row)

The neutron source in the EGCR must be large enough to yield, when the reactor is shut down, a thermal neutron flux of at least 14 neutrons/cm^2·sec in the startup fission chambers. The flux in the fission chambers is a function of source strength (neutrons/sec), source location, and the subcritical multiplication factor of the reactor. Early estimates of the required source strength were based on a shutdown k of 0.97, but considerations of variable reactivity conditions resulting from different loop experiments have made it clear that a k as low as 0.85 will occur at times.

The neutron flux produced by a unit source of fast neutrons has therefore been estimated for k = 0.97 and k = 0.85 and for two different source configurations, the first a point source at the center of the reactor and the other a spherical shell source 150 cm in diameter. The calculations were carried out with four-group diffusion theory, and a properly-normalized source was added to the fission neutrons at each iteration of the multigroup calculation. Three quantities of interest obtained in the calculations are compared in Table 2.7. Table 2.7 gives the quantity $(1 - k)^{-1}$, which is a familiar approximation for the source multiplication; the calculated source multiplication, defined as (source neutrons plus fission neutrons) divided by source neutrons; and the ratio, (ϕ/ϕ_0), of the flux at

Table 2.7. Source Strength Required for the EGCR

	k_{eff}	$(1 - k_{eff})^{-1}$	M[a]	ϕ/ϕ_0	$(\phi/\phi_0)(1 - k)$	S, Source Strength[b] (neutrons/sec)
						$\times 10^9$
Point source	0.97	33.3	28.4	22.8	0.68	0.56
	0.85	6.67	4.61	1.45	0.22	8.8
Shell source	0.97	33.3	35.5	29.9	0.90	0.41
	0.85	6.67	7.48	3.66	0.55	3.3

[a]Source multiplication as defined in text.

[b]Source strength required to yield 2 × 14 neutrons/cm^2·sec at instrument position; factor of 2 allows for 60-day decay.

the instrument position per source neutron to the flux at the instrument position per fission neutron for a normal-mode fission distribution in the core.

The fission distributions for the four cases listed in Table 2.7 are shown in Fig. 2.1. From Table 2.7 it can be seen that the flux per source plus fission neutron depends significantly on k and on the source position. The reason for this is clear from Fig. 2.1, which shows the greater flux peaking near the center of the reactor for the central point source and for the lower value of k.

EGCR Shielding

(J. G. Delene)

The flux levels in the vicinity of the penetrations through the top and bottom shields of the EGCR have been investigated. Fast-neutron streaming up the annuli around the shield plugs was found to be the major flux contributor for the control-rod, special, and fuel-charge nozzles. The expected fast flux levels are ~5 neutrons/cm^2·sec over the control-rod and special nozzles and ~8 neutrons/cm^2·sec under the fuel-charge nozzles.

The dose rate around the service machine, with shielding as shown on Allis-Chalmers drawings MS-126 and MS-221, with ordinary spent fuel and a

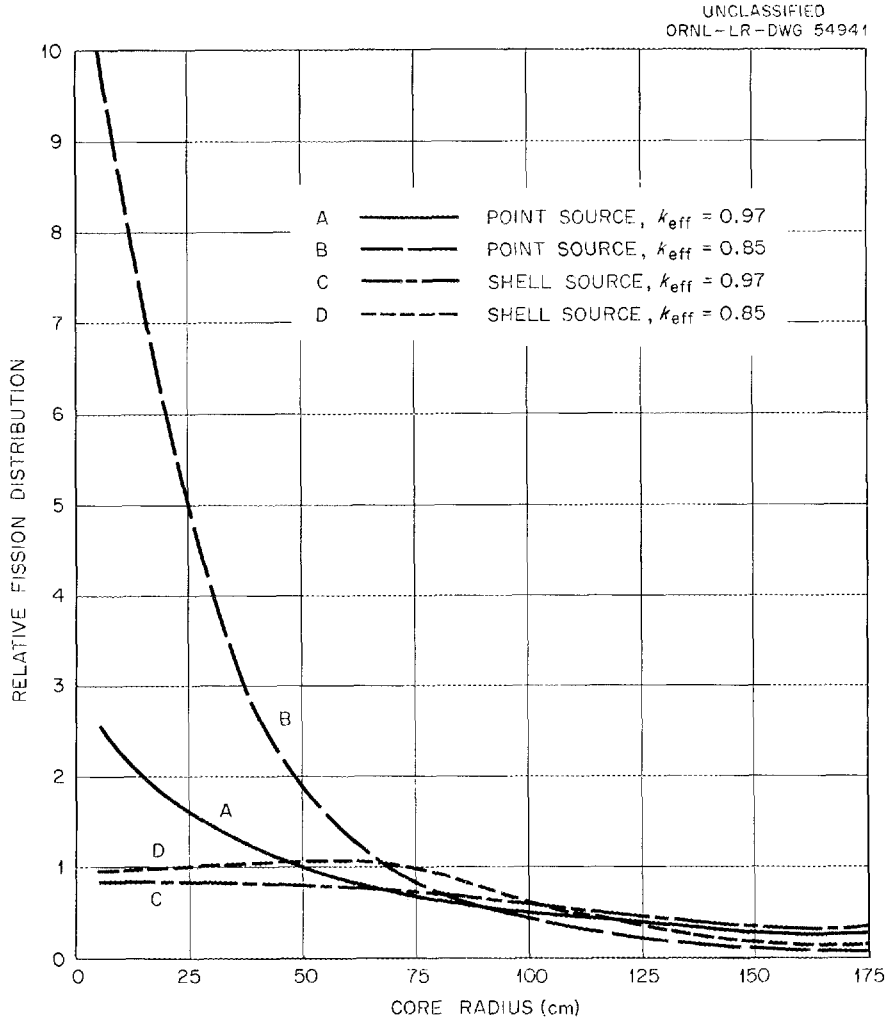


Fig. 2.1. Fission Distribution Normalized to a Unit Fission Plus Fixed Source.

spent control rod stored in their appropriate lead casks, was calculated to be 7.5 mr/hr on the bottom surface and 1 mr/hr on the side surface. Modifications now being made to the shielding will result in a dose rate on the side surface of ~7.5 mr/hr with EGCR fuel or 25 mr/hr with a 1.5-Mw experiment (3 hr after removal from the neutron flux). Along the surface of the charge machine, dose rates of up to 66 mr/hr are expected with 12 fuel assemblies stored in their appropriate storage positions. However, the dose rates at points where men will be working are not expected to exceed 17 mr/hr. The various shield penetrations, both on the charge and service machine, appear to be adequately shielded.

Heat Deposition in the EGCR

(E. A. Nephew)

Heat deposition in the EGCR by core gamma rays has been calculated and was discussed previously.[2] The additional heating by gamma rays originating in a loop experiment can be estimated from Figs. 2.2 and 2.3. Here the gamma heat deposition rate for a typical loop experiment is given as a function of the distance from the loop tube.

The total heat deposition in the EGCR core must also include the heating effect due to fast neutrons. The heat deposition rate due to the moderation of fast neutrons is assumed to be directly proportional to the fast flux distribution in the EGCR core. Figures 2.4 and 2.5 show the manner in which this heat is distributed in a reactor core quadrant. This distribution was calculated by means of the two-dimensional PDQ program for the case of a uniform core loading in which the central control rod is fully inserted and the remaining control rods are inserted to a depth of 62 in. as a bank. The four central loops were considered to contain a homogeneous graphite-uranium experiment, C/U = 200, operating at a power of 1.07 Mw. Based on an average fission spectrum energy of 1.98 Mev and an average $\overline{\nu}$ of 2.53, which includes the effect of plutonium buildup, the total energy deposited in the core by fast neutrons is 5.01 Mev/fission or 2.16 Mw. From the PDQ fast flux calculations it was found that 91% of the total fast neutron energy is deposited in the core. This gives a core heat deposition of 1.97 Mw and a reflector heat deposition of 0.19 Mw by fast neutrons.

---

[2]"GCR Quar. Prog. Rep. Sept. 30, 1960," ORNL-3015, pp. 14–20.

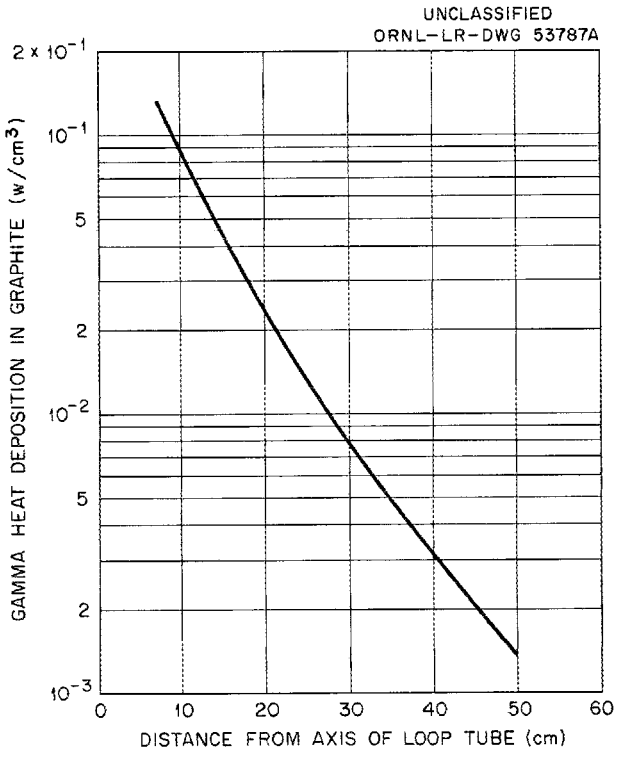


Fig. 2.2. Gamma Heat Deposition Rate in EGCR Graphite as a Function of Distance from the Axis of a Small Loop Tube Operating with a 1-Mw EGCR-Cluster Experiment.

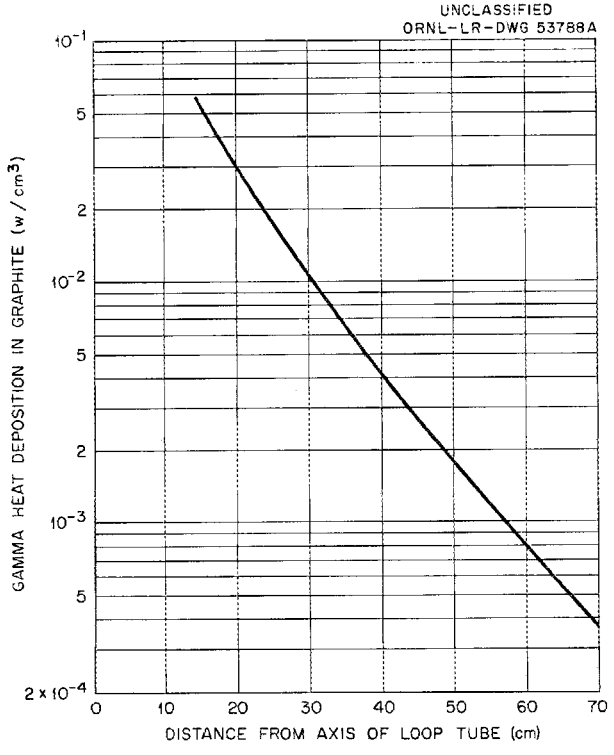


Fig. 2.3. Gamma Heat Deposition Rate in EGCR Graphite as a Function of Distance from the Axis of a Large Loop Tube Operating with a 1-Mw EGCR-Cluster Experiment.

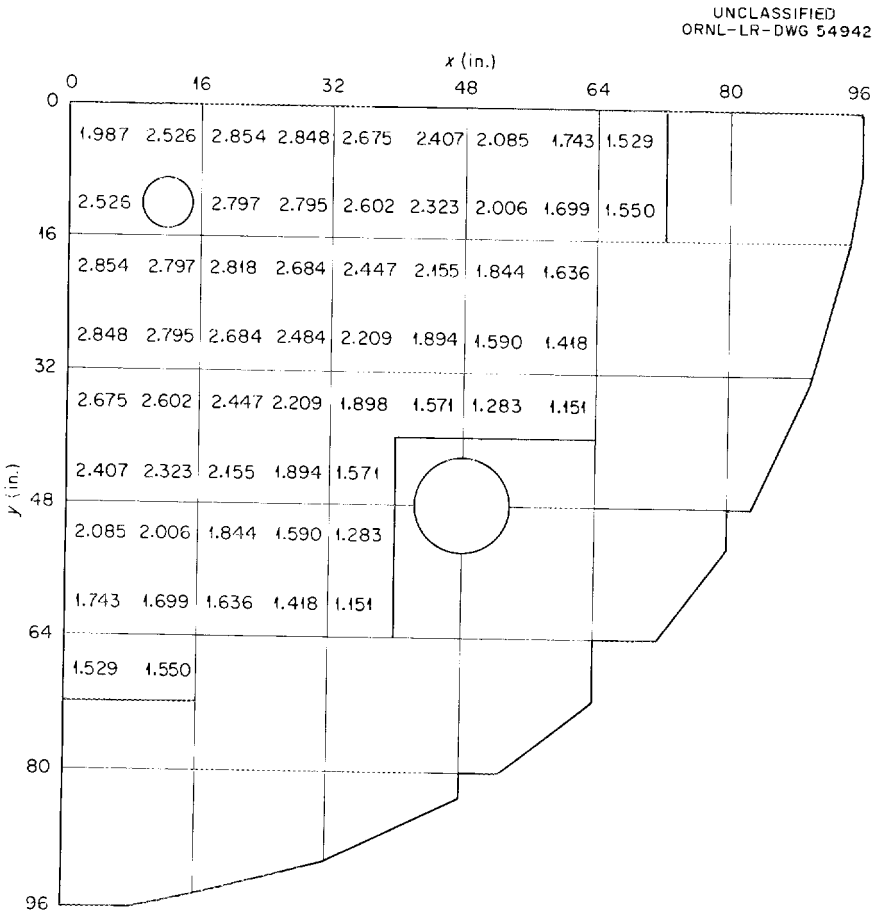


Fig. 2.4. Fast-Neutron Heat Deposition (kw) in Graphite Fuel Assembly Sleeves.

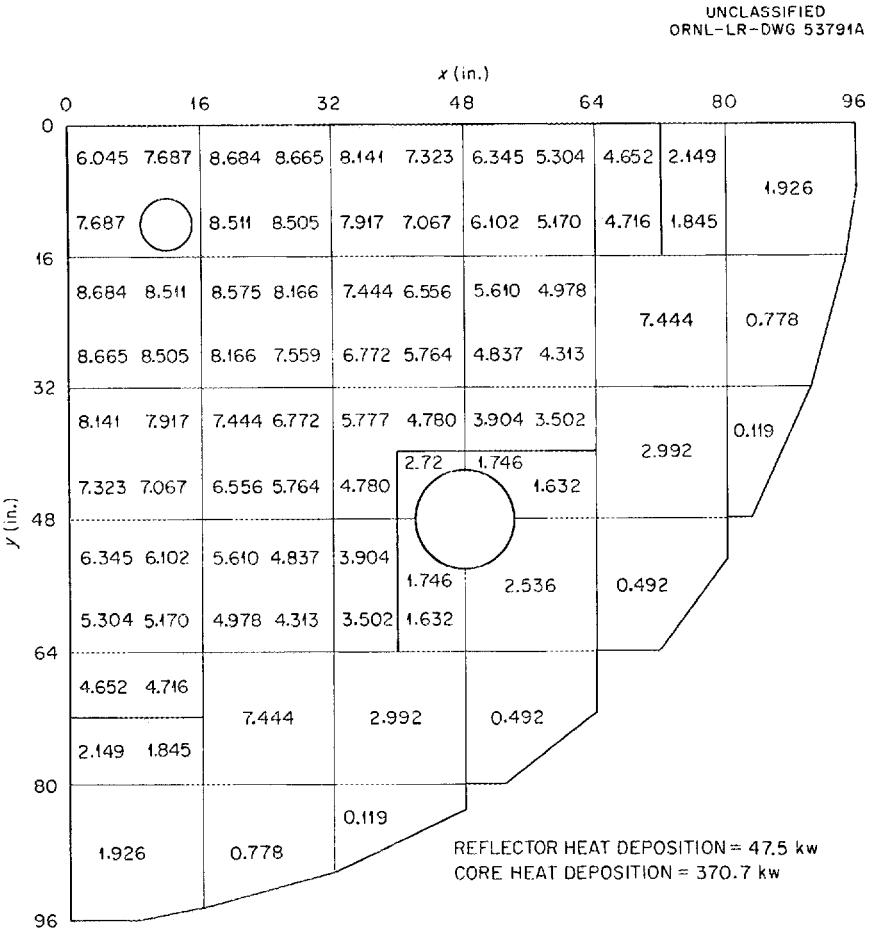


Fig. 2.5. Fast-Neutron Heat Deposition (kw) in 16 × 16-in.-Square EGCR Graphite Columns.

3. REACTOR DESIGN STUDIES

Thermal Behavior of EGCR Fuel Assemblies

Effect of Control Rod Programing and Mode of Operation (G. Samuels, M. E. Lackey, R. S. Holcomb)

A thermal analysis of the EGCR fuel assemblies has been made based on the design shown in Fig. 3.1. In computing the surface temperature for the EGCR fuel elements, it was necessary to make a number of assumptions concerning the gas temperature and flow and the heat deposition in the core. The major assumptions were the following:

1. The temperature of the gas leaving the reactor vessel is 1043°F.
2. The mixed-mean gas temperature exiting from the core is 1050°F.
3. The inlet gas temperature to the core is 510°F.
4. The total flow through the core is 427 000 lb/hr.
5. Of the 427 000 lb/hr core flow, 387 000 lb/hr flows through the fuel assembly and 40 000 through the annuli and core structure.
6. Of the total heat generation rate of 84.3 Mw, 80 Mw is removed by the fuel assembly flow and 4.3 Mw is removed by the bypass flow.
7. All 80 Mw of heat removed from the fuel assemblies is removed from the elements and none from the sleeve.
8. Thermal radiation from the elements to the sleeve is neglected.
9. The core is loaded uniformly.

The possible error introduced by these assumptions is, in general, small. The most questionable assumption is the bypass flow rate of 40 000 lb/hr, which will be reduced by using top cooling for the control rods. This reduction could be more than offset by the additional cooling required by the flux scanner and additional annulus flow. The difficulty in maintaining the proper annulus flow results from the possible wide variations in radial power distribution as the control rod pattern is shifted to maintain a maximum radial peak-to-average power ratio of 1.35. In order to match the annulus flow rate to the heat generation rate in the graphite, it would be necessary when the control rod pattern is shifted to disassemble and replace the annulus orifices in the bottom dummy, and this is not feasible. The only choice is to establish the annulus flow to adequately cool

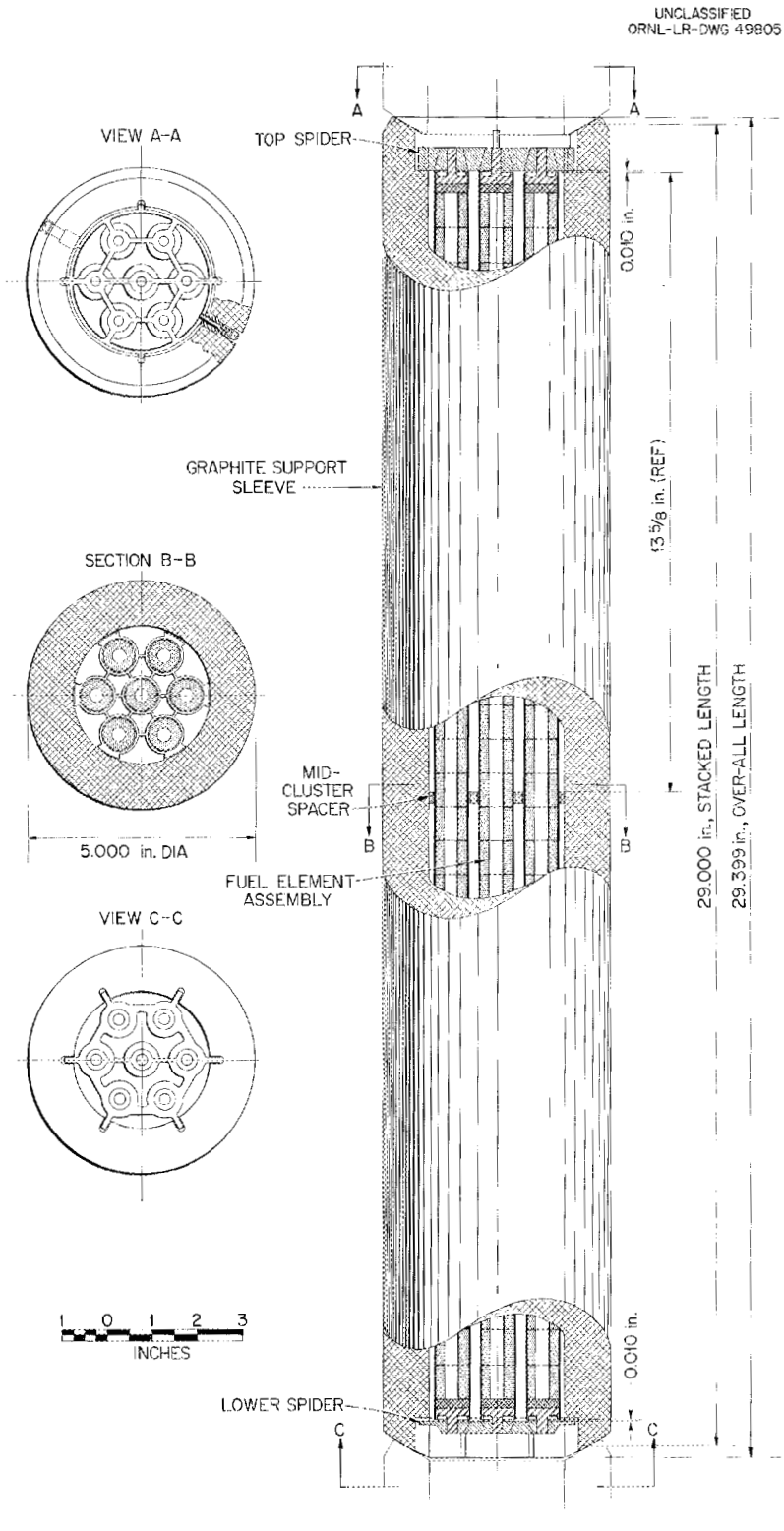


Fig. 3.1. EGCR Title-II Fuel Element Assembly.

the core for any rod pattern, and this results in excess flow to a large percentage of the channels in all cases considered.

The latest physics calculations indicate that 7% (5.9 Mw) of the heat generated by the elements is deposited elsewhere. Based on previous calculations, about 30 to 35% of this will be deposited in the sleeves and the remainder in the core blocks. The division of the heat in the sleeves is not known at this time and, in any case, will vary depending on the radial flux distribution in the core and the final maximum allowable graphite temperature, which is yet to be determined. Assumptions 6 and 8 are conservative and will overestimate the surface temperature of the fuel elements by about 10°F.

The thermal radiation between the elements and the sleeve will amount to about 3% of the heat generation at the maximum nominal surface temperature. This effect, which has been neglected, would reduce the peak surface temperature by about 15 or 20°F. Although the radiative heat transfer is not very effective in reducing the nominal temperature, it will be important in analyzing the magnitude of the hot streak that is expected to exist on the outer surface of the outer six elements because of self-shielding of the cluster. Approximately 90% of the radiative heat transfer is from these surfaces and will reduce their temperatures by about 30°F.

The calculations were based on uniform core loading; that is, the fuel in each channel was assumed to have the same fission cross section. For the equilibrium core, the rundown of the fuel is expected to be a maximum of 10%. This means the radial flux distribution of the average or uniform core loading will have ±5% perturbations imposed on it. If the blower head is sufficient to take care of the additional 5% flow requirement (or 10% in channel pressure drop), there will be about a 5°F increase in the surface temperature of the new fuel. If the blower head is limited to that required to supply a channel with a peak-to-average radial flux distribution of 1.35, the additional 5% in power will result in a 50°F increase in the maximum nominal surface temperature.

For the three cases analyzed it was considered that the central control rod was fully inserted and the remaining rods were operated as a bank. The worth of the bank for the three cases was 2.5, 1.6, and 0.9%. The

maximum nominal surface temperatures of the elements for two different operating conditions as functions of the mixed-mean exit gas temperature from the fuel channels for these cases are shown in Figs. 3.2, 3.3, and 3.4. The two conditions involve (1) operation with all orifices set so that the exit gas temperature from each fuel channel is the same and (2) operation with the orifices set to maintain a uniform maximum fuel element surface temperature in each channel. As may be seen from Figs. 3.2, 3.3, and 3.4, the reduction in surface temperature by orificing for a uniform maximum surface temperature is about 40°F. This latter method of operation is somewhat more difficult than maintenance of a uniform exit gas temperature, since it requires not only a knowledge of the radial peak-to-average flux ratio but also the distribution of the radial and axial flux.

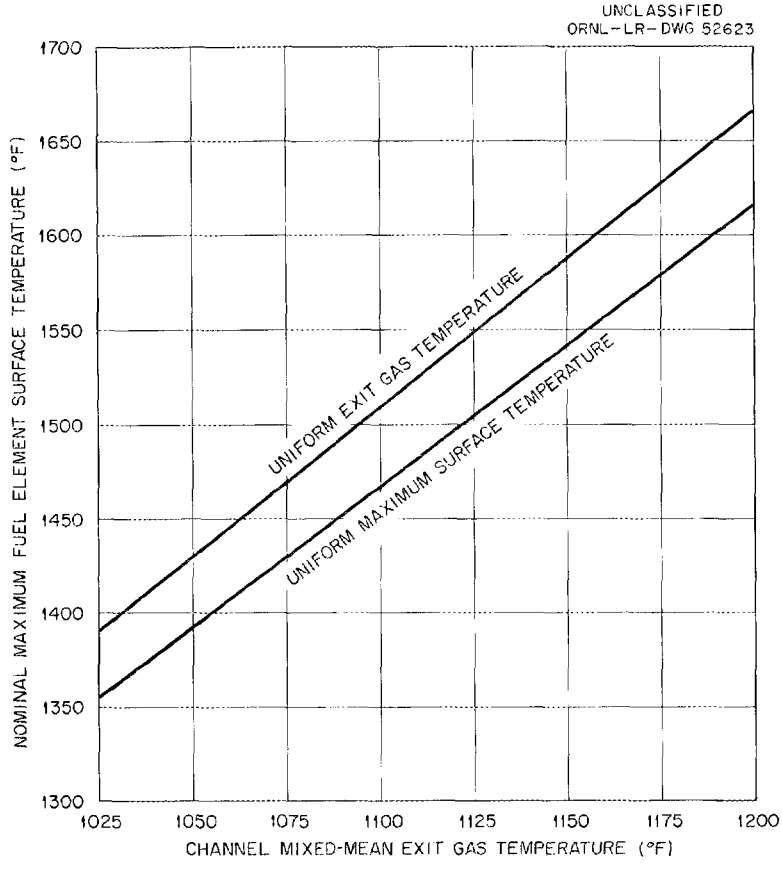


Fig. 3.2. Maximum Fuel Element Surface Temperature Versus Mixed-Mean Exit Gas Temperature for Central Control Rod Fully Inserted and Bank Insertion of Remaining Rods to a Depth of 62 in.

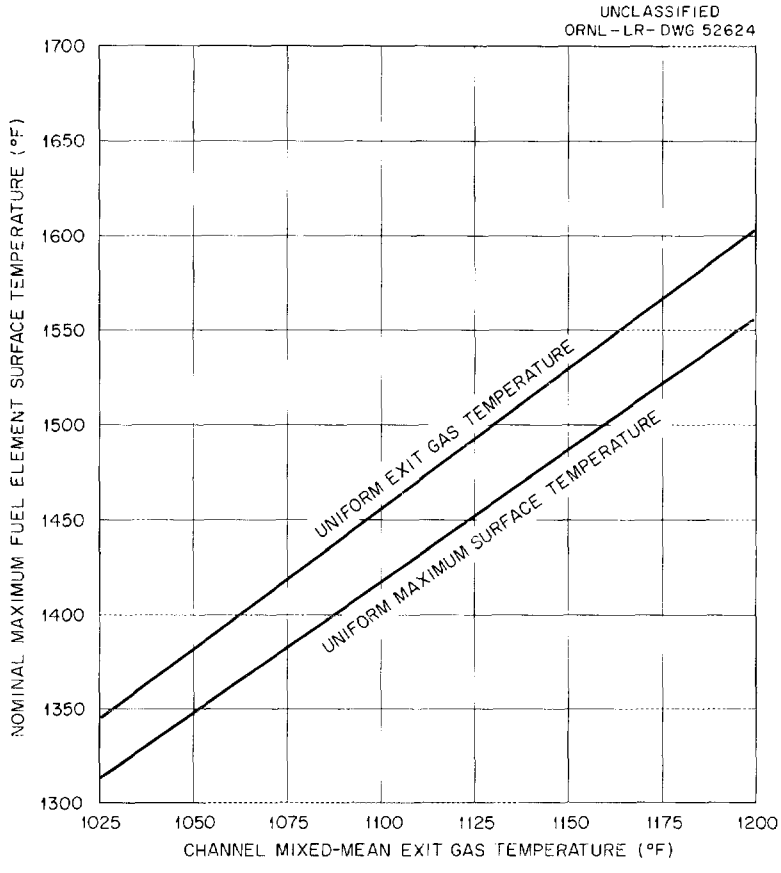


Fig. 3.3. Maximum Fuel Element Surface Temperature Versus Mixed-Mean Exit Gas Temperature for Central Control Rod Fully Inserted and Bank Insertion of Remaining Rods to a Depth of 47 in.

Whether the relatively small gain is worth the additional analytical work required for such operation is questionable. There are other types of control-rod programing in which it is most advantageous to orifice for maximum surface temperature.[1]

The required mixed-mean exit gas temperature from the fuel channels can be calculated from assumptions 2, 5, and 6. With 4.3 Mw of heat deposited in the core and a core flow of 40 000 lb/hr, a mixed-mean exit gas temperature of 1075°F is required from the 232 fuel channels to give a gas temperature of 1050°F from the core.

Plots of both gas and fuel element surface temperatures along the high power channel for a mixed-mean exit gas temperature from the channels of

[1]"GCR Quar. Prog. Rep. June 30, 1960," ORNL-2964, p. 21.

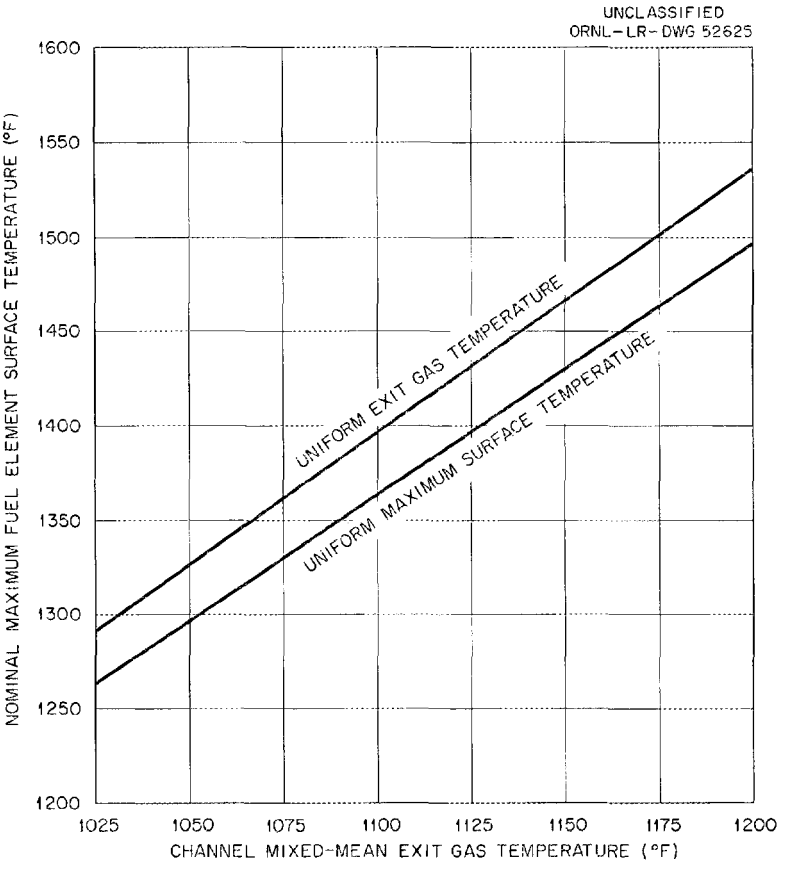


Fig. 3.4. Maximum Fuel Element Surface Temperature Versus Mixed-Mean Exit Gas Temperature for Central Control Rod Fully Inserted and Bank Insertion of Remaining Rods to a Depth of 31.5 in.

1075°F are shown in Figs. 3.5 through 3.8. Figures 3.5 and 3.6 are for bank insertion of control rods to a depth of 62 in. for a control rod worth of 2.5%, and Figs. 3.7 and 3.8 are for bank insertion of control rods to a depth of 47 in. for a control rod worth of 1.6%. Figures 3.5 and 3.7 are based on orifice control to maintain a uniform maximum surface temperature in each channel, whereas Figs. 3.6 and 3.8 are for the case in which the exit gas temperature from all the channels is 1075°F. The fuel element surface temperatures and/or exit gas temperatures for each channel for these cases are given in Table 3.1. The channels are identified by their x and y coordinates measured in inches. The data are reported for only one octant of the core but are applicable to the other seven, since the fuel loading, experiments, and control-rod pattern are assumed to be symmetrical.

Table 3.1. Gas Flow Rates, Exit Gas Temperatures, and Maximum Surface Temperatures for All Channels for Bank Insertion of Control Rods to a Depth of 47 in. or 62 in. and for a Channel Mixed-Mean Exit Gas Temperature of 1075°F

Channel Group x and y Dimensions (in.)	Uniform Exit Gas Temperature			Uniform Maximum Surface Temperature	
	Flow Rate (lb/hr)	Maximum Surface Temperature (°F)		Flow Rate (lb/hr)	Exit Gas Temperature (°F)
		62-in. Insertion of Control Rod Bank	47-in. Insertion of Control Rod Bank		
4-4	1589	1366	1376	1448	1130
12	2021	1416	1402	1996	1082
20	2283	1470	1419	2379	1052
28	2278	1468	1417	2375	1052
36	2140	1466	1415	2218	1055
44	1925	1454	1400	1964	1064
52	1669	1423	1380	1663	1077
60	1395	1404	1361	1354	1092
68	1223	1383	1348	1171	1100
12-20	2237	1470	1418	2331	1052
28	2236	1467	1416	2322	1054
36	2082	1461	1409	2146	1058
44	1859	1447	1392	1882	1068
52	1605	1420	1378	1593	1079
60	1359	1401	1359	1317	1093
68	1240	1381	1347	1184	1102
20-20	2255	1469	1417	2346	1053
28	2147	1467	1416	2229	1054
36	1957	1454	1404	2003	1062
44	1723	1426	1384	1726	1074
52	1474	1410	1367	1446	1086
60	1309	1398	1356	1262	1096
28-28	1988	1456	1406	2038	1061
36	1768	1431	1388	1777	1072
44	1515	1414	1371	1491	1084
52	1271	1385	1352	1219	1099
60	1134	1373	1339	1072	1108
36-36	1519	1416	1375	1500	1082
44	1257	1384	1348	1203	1100
52	1026	1367	1334	961	1113
60	921	1352	1320	846	1125

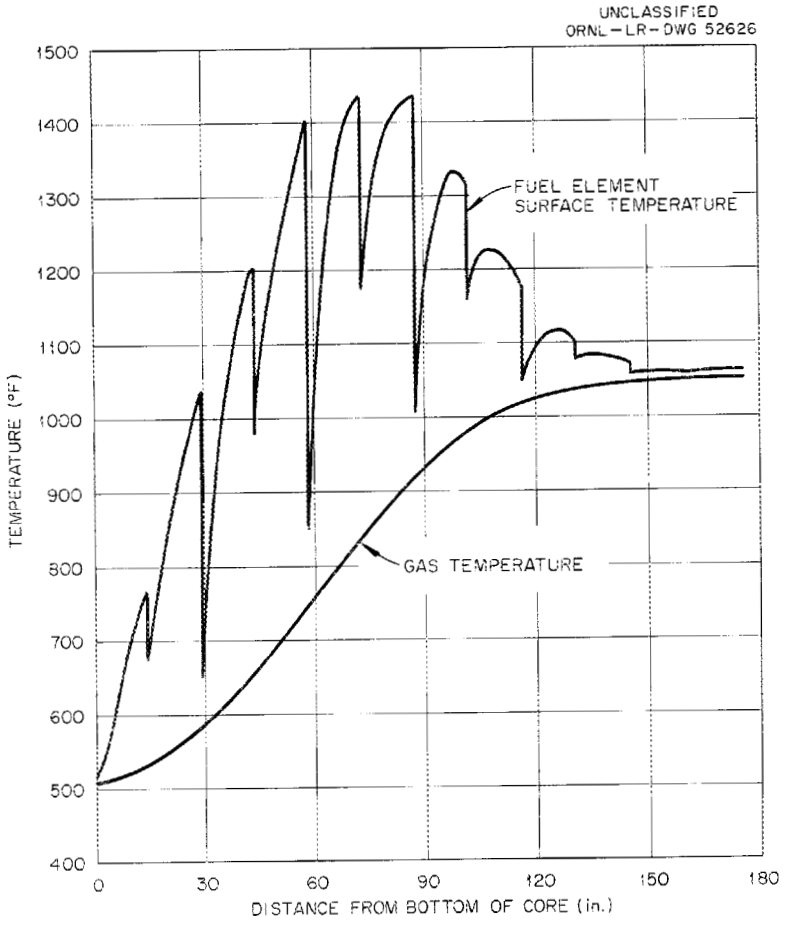


Fig. 3.5. Axial Temperature of Channel 4-20 for a Mixed-Mean Exit Gas Temperature of 1075°F, a Uniform Maximum Element Surface Temperature, and Bank Insertion of Control Rods to a Depth of 62 in.

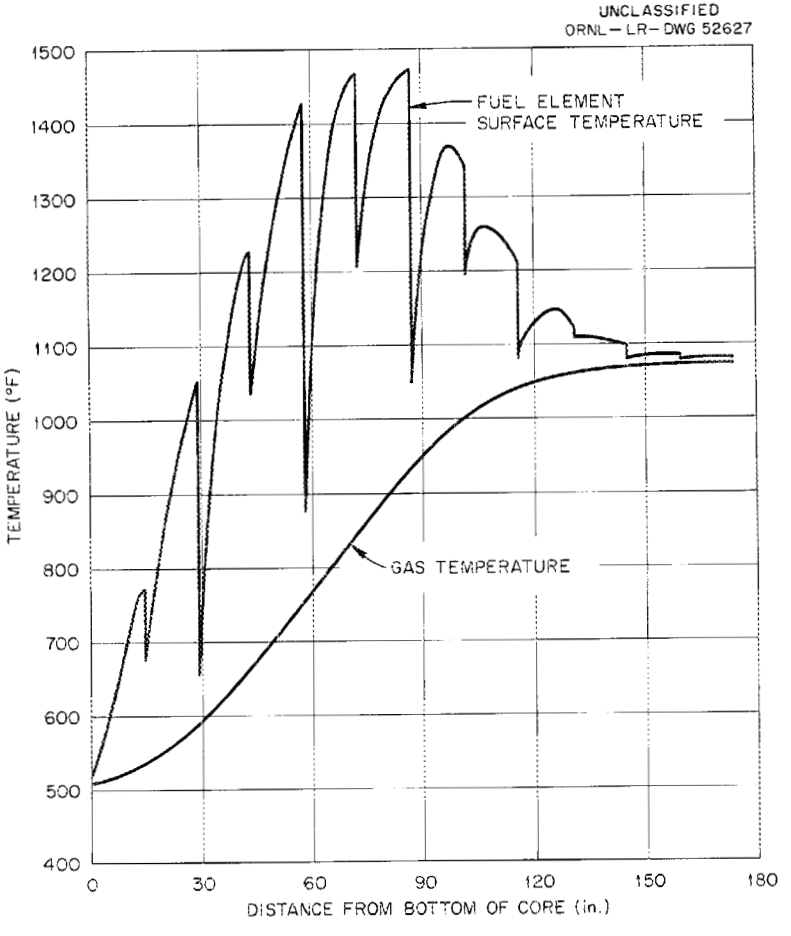


Fig. 3.6. Axial Temperature of Channel 4-20 for a Uniform Exit Gas Temperature and Bank Insertion of Control Rods to a Depth of 62 in.

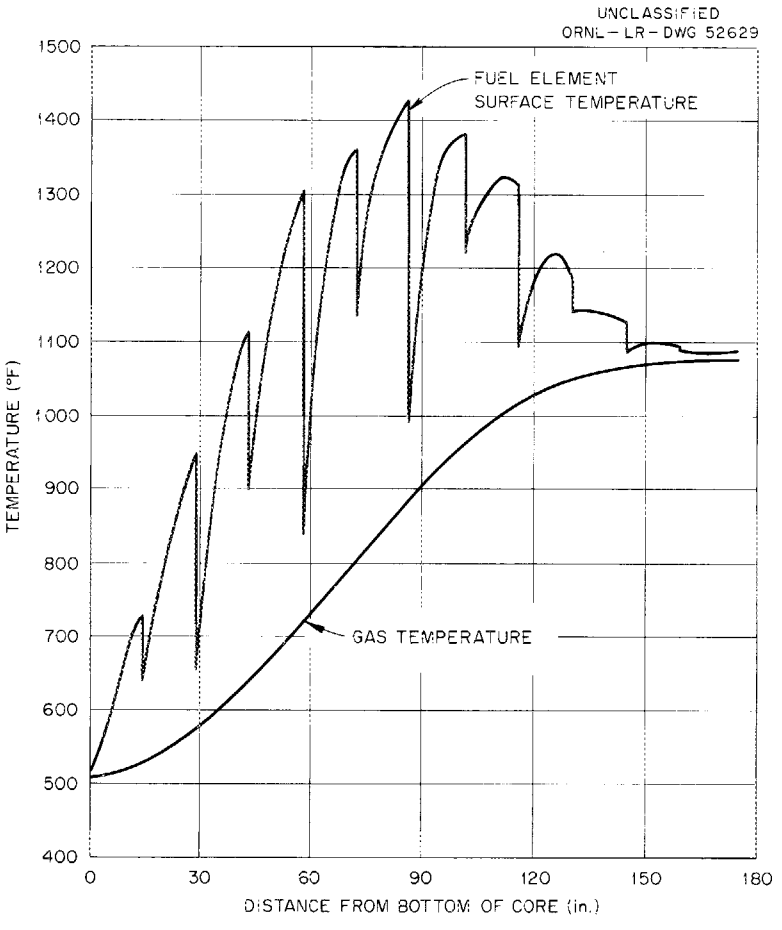


Fig. 3.7. Axial Temperature Plot of Channel 4-20 for a Mixed-Mean Exit Gas Temperature of 1075°F, a Uniform Maximum Fuel Element Surface Temperature, and Bank Insertion of Control Rods to a Depth of 47 in.

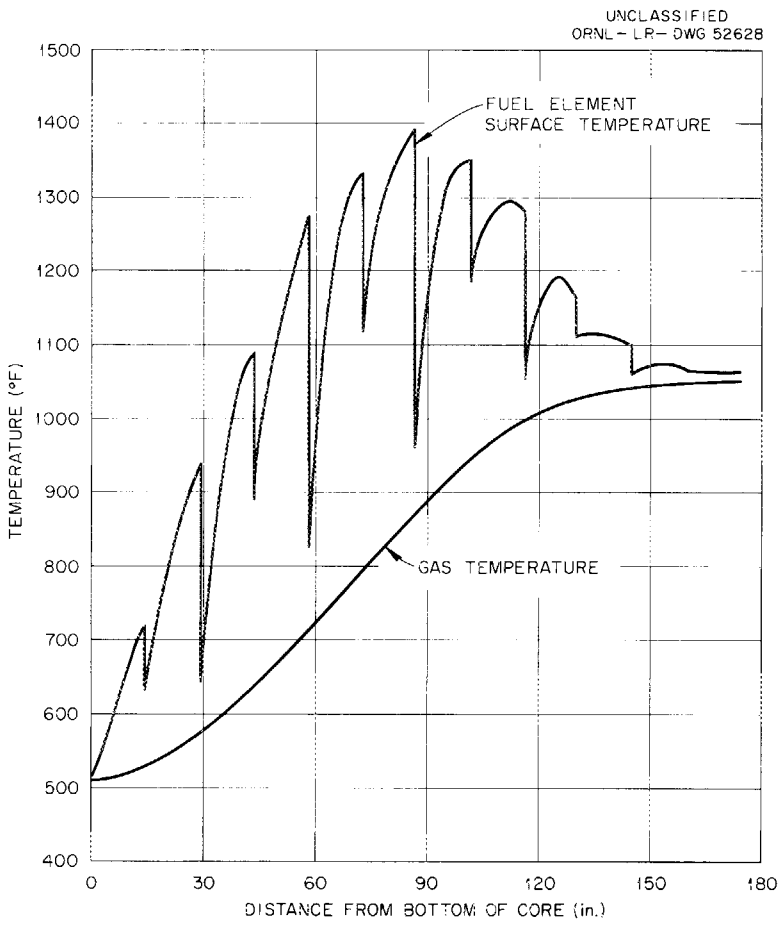


Fig. 3.8. Axial Temperature of Channel 4-20 for Uniform Exit Gas Temperature and Bank Insertion of Control Rods to a Depth of 47 in.

It should be emphasized that the values of Table 3.1 are for the nominal temperature, which is defined as the average temperature of the seven elements of the cluster for normal operating conditions with an equilibrium core. No allowance has been made for temperature asymmetries within the cluster, hot-channel factors, or the effect of adjacent empty fuel channels.

When fuel is removed from one of the channels, the heat generation rate in the adjacent channels increases by 8%. If the flow in these channels is increased by 8% to match the increased heat rate, the surface temperature of the elements will increase by only 10°F. If the orifices are not opened to increase the flow, the temperature will increase by 75°F. Considering the time involved to change the orifices of these channels both before and after a fuel change, the operator will prefer to leave the orifice settings constant and take the increased surface temperature for the period required to reload a channel. Unless subsequent analyses indicate that this increased surface temperature of 75°F cannot be tolerated, this mode of operation is recommended.

The magnitudes of the temperature asymmetries within the clusters are not known at this time, and their determination must await the results of the velocity profile and mixing experiments. A series of calculations in which an attempt was made to bracket the temperature variation within the cluster indicated that the maximum temperature will not exceed the average by more than 75°F.

Fuel Temperature Variations During Transients

Variations During Extreme Normal Conditions. (O. W. Burke, E. R. Mann, R. M. Pierce, C. S. Walker) The ORNL analog computer was used to examine the thermal behavior of the EGCR fuel under certain idealized conditions.[2] The purposes of this investigation were to determine the magnitude of the thermal "time constant" of the fuel and to evaluate the temperature variations in terms of EGCR design considerations.

---

[2]R. M. Pierce, "Preliminary Analysis of the Thermal Behavior of the EGCR Type Fuel Element," ORNL CF-60-10-107 (Oct. 27, 1960).

The fuel thermal time constant is a measure of the time interval required for the fuel temperatures to change in response to sudden changes in reactor power levels. It is a limiting factor that concerns any change in the rate of heat flow from the fuel to the gas stream. Certain fuel temperature transients will take place during normal operation. For example, each time a scram action occurs when the EGCR is operating normally, the fuel will undergo a very rapid temperature change. Also, there will be temperature variations of lesser magnitude each time the reactor power is increased during startup and each time the reactor gas inlet temperature varies. These transients are not necessarily the result of any sort of accident nor do they produce abnormally high fuel temperatures.

The calculations were idealized to the extent that the thermal power could be varied according to any desired function of time, rather than by adjustment of the multiplication of a nuclear reactor. An examination was made of the thermal behavior of the fuel rather than of the kinetic behavior of a complete reactor. The computer model utilized the central channel, which was broken into three axial sections. Each section was assumed to be composed of a single stainless-steel-clad UO_2 fuel rod surrounded by an annulus that provided a passage for the gas. The gas annulus was enclosed by a hollow graphite cylinder which represented the moderator. The UO_2 in the fuel rod of each section was subdivided into three cylindrical regions to simulate heat conduction as well as heat storage. The entire volume of each small section was assumed to be at the mean temperature of that particular section. The investigation was carried out both for no gap and for a 6-mil gap between the UO_2 and stainless steel cladding.

One of the fastest transients encountered is described by the curves shown in Fig. 3.9. These curves represent the variations of the mean temperatures of the hottest axial section of the central fuel element upon the instantaneous reduction of nuclear power from design conditions to zero at 30 sec on the time scale. The gas flow was 100%, and the temperature of the gas returning to the reactor from the heat sink was held constant at 510°F. For this particular transient, there was a 6-mil gap between the UO_2 and cladding. The initial rate of decrease of the average temperature of the UO_2 was approximately 60°F/sec, whereas the initial rate of decrease

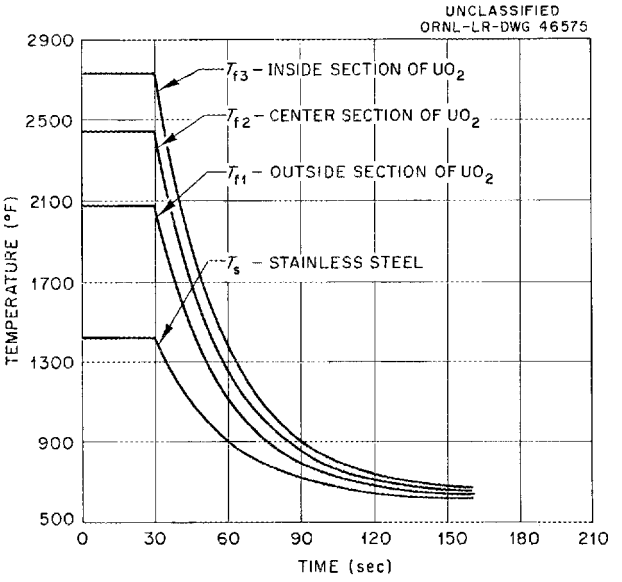


Fig. 3.9. Temperature of UO_2 and Stainless Steel Cladding of Hottest EGCR Fuel Element Upon Instantaneous Loss of Nuclear Power.

of the temperature of the stainless steel cladding was approximately 30°F/sec. The temperature variations were almost completed at the end of 2 min. Each curve very closely approximates those representing first-order differential equations in which the change in temperature can be represented by functions of the type $1 - e^{t/\tau}$, where t is time and τ is the thermal time constant of the fuel. Under the conditions for which these curves were obtained, with 100% gas flow, the thermal time constant is slightly larger than 30 sec for the UO_2 as well as for the stainless steel cladding. The thermal time constant was found to increase with a decrease in gas flow, being of the order of 60 sec at 20% gas flow.

Variations Caused by Loss of Gas Flow. (F. P. Green, R. M. Pierce, C. S. Walker) There are three basic means by which the gas flow through the reactor can be reduced: (1) a normal reduction in blower speed through the action of the speed-control mechanism, (2) coastdown of the blower upon the loss of driving torque, and (3) action of any quick-operating valve. These three variations were examined in order to determine the design requirements for safe operation. A reduction in blower speed by means of the speed control actuator was simulated as a ramp decrease in flow. The blower coastdown curves were calculated[3] and incorporated into the analog computer for the condition in which the blower is completely declutched from the drive motor, as well as for the condition in which the motor is turned off and coastdown occurs with the blower and motor fully clutched.

[3]Personal communication from E. R. Taylor, ORNL.

Step reductions in gas flow from 100% design conditions were simulated to represent the action of quick-operating valves.[4]

The thermal model for this computer work was similar to that described above for normal conditions, except that the temperature profiles used were those computed[5] for fuel channel 4-20, and the heat transfer variations from the fuel to the gas due to changes in gas flow were included. The nuclear portion of the reactor was also included in the simulation, with six delayed-neutron groups, as well as a fuel temperature coefficient of -1.1×10^{-5} $\delta k/°F$.[6] Scram safety actions were initiated by a set point of 1075°F on the outlet gas temperature, or a flux-minus-flow deviation of +10%, whichever occurred first. A scram was assumed to cause a rod acceleration of 20 ft/sec^2. The δk reduction by rod insertion was then obtained from a function generator which related rod position and rod worth.[7] A maximum of 5.2% negative δk was inserted in 1.205 sec. A 2-sec first-order-sensor delay was included in the flow signal. Another function generator was employed to incorporate the effect of afterheat. The gas returning to the reactor was assumed to remain at a constant temperature of 510°F.

The examination of ramp reductions in gas flow revealed that decreases equal to less than 0.4%/sec would not produce rates of temperature rise of the fuel cladding exceeding 2.5°F/sec. Scram action was initiated by a high reactor gas outlet temperature. It should be possible for the design of the actuator on the blower speed control mechanism to provide for an inherent limitation of the rate of decrease of the blower speed to a value in the order of 0.4%/sec.

The blower coastdown curves and the temperature transients of the fuel are shown in Figs. 3.10 and 3.11, respectively. The rise in fuel cladding temperature after an elapsed time of 200 sec is caused by the afterheat. The transients shown are those for the declutched coastdown of the blowers

---

[4]R. M. Pierce and F. P. Green, "Thermal Behavior of the EGCR Upon Loss of Gas Flow," ORNL CF-60-10-127 (October 31, 1960).

[5]Personal communication from G. Samuels, ORNL.

[6]Personal communication from A. M. Perry, ORNL.

[7]Personal communication from C. A. Preskitt, ORNL.

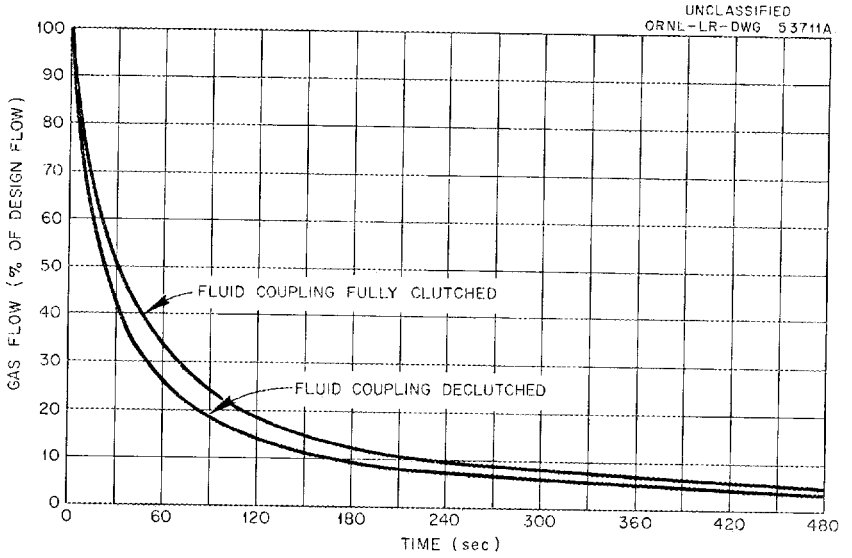


Fig. 3.10. Effect of EGCR Main Blower Coastdown on Gas Flow Rate.

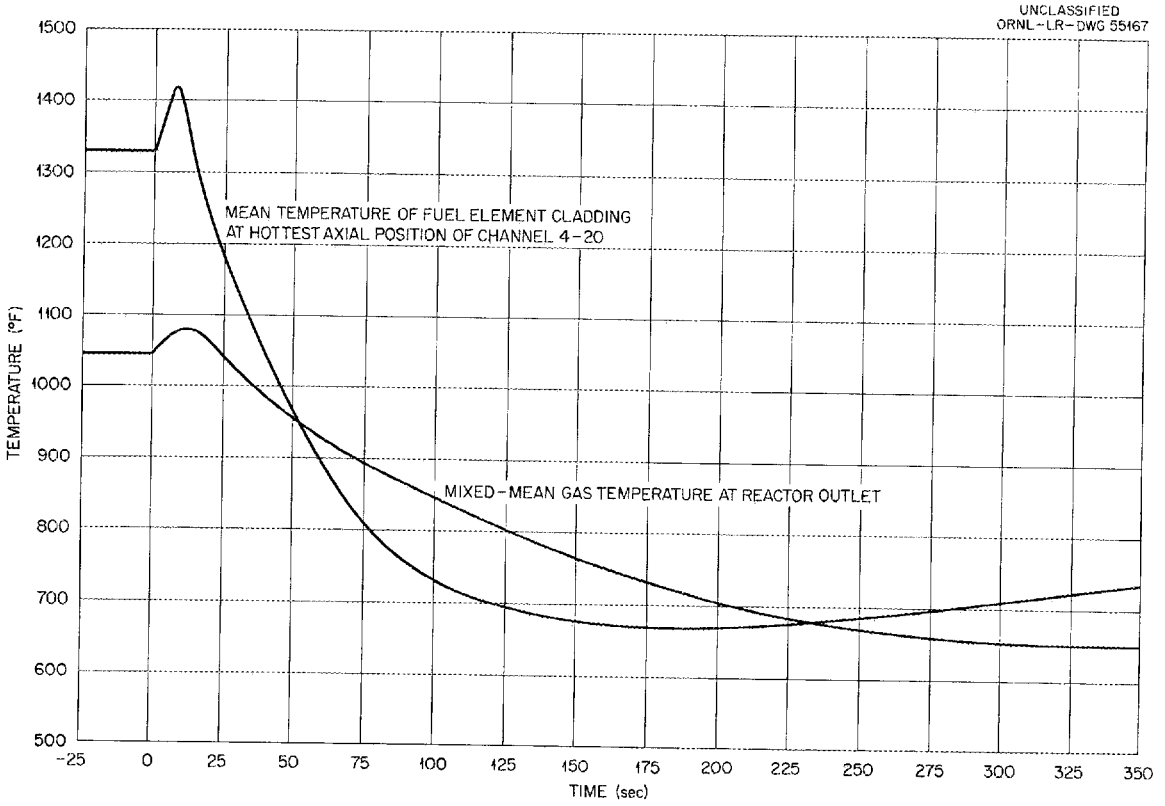


Fig. 3.11. Temperature Transients for a Fully Declutched Blower Coastdown.

and are more severe than for the fully clutched case. The reactor scram was initiated by a flux-minus-flow signal approximately 4 sec after the start of the blower coastdown.

A summary of the effect of step reduction in gas flow from 100% design conditions is shown in Fig. 3.12. Rather severe temperature transients having large maximum values, as well as high rates of increase, were produced by large step decreases. There was no reactor scram for a 5% reduction in flow, the temperature being limited by the negative temperature coefficient of the fuel. The scram was caused by high outlet gas temperature in the range from 10% to 15% step reductions. The flux-minus-flow signal initiated the scram for reductions of 30% and larger.

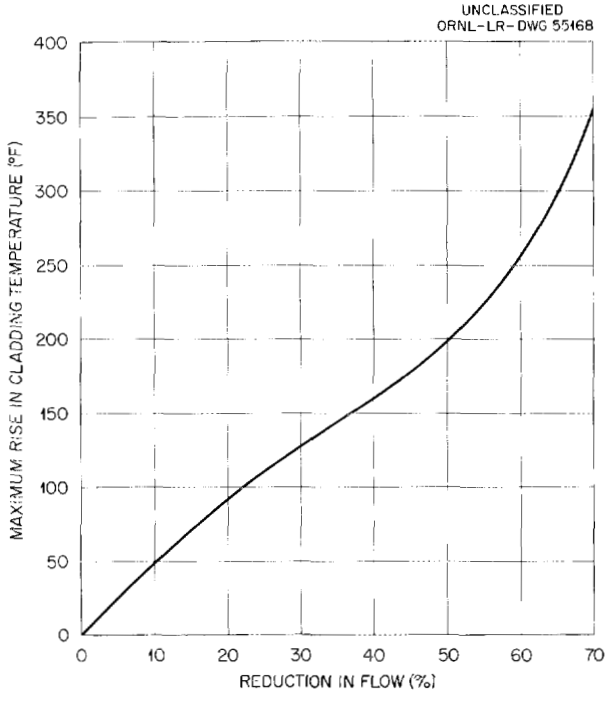


Fig. 3.12. Maximum Rise in Mean Temperature of Fuel Element Cladding at Hottest Axial Position of Channel 4-20 Following Step Reductions in Gas Flow.

Variations Caused by Reactivity Increases. (F. P. Green, R. M. Pierce, C. S. Walker) The effect of reactivity increases was analyzed to determine whether a step-value or ramp-insertion rate existed that would cause the metallurgical limit of the fuel element cladding to be exceeded before one of the safety devices would trip and scram the reactor.[8] It was assumed that a reactor scram would be caused by an outlet gas temperature in excess of 1075°F or by a flux-minus-flow signal of +10%, whichever occurred first. The computer model was identical to that employed in the examination of the loss of gas flow accidents.

[8]R. M. Pierce, "Analog Computer Analysis of the Thermal Behavior of the EGCR Due to Reactivity Accidents," ORNL CF-60-12-49 (in press).

Step insertions of reactivity can occur when the charge and service machine are operating or during the changing of an experiment. It has not been determined at what power level and coolant flow rate these operations will occur; therefore, the investigation was carried out for various power levels, flow rates, and step insertions of reactivity. The maximum fuel element cladding temperature that was reached was approximately 20°F above the operating value at full-load conditions with a step increase in δk of 0.25%. Large step increases in reactivity were not simulated because of limitations in the equipment.

In order to examine the effect of a failure in the safety instrumentation, it was postulated that only one of the safety devices, either flux-minus-flow or outlet gas temperature, was operable for various ramp insertions of δk while the reactor was operating at 100% power and 100% flow. Ramp insertion rates from 1×10^{-5} δk/sec to 2.5×10^{-4} δk/sec were used. The maximum temperature rise of the fuel element cladding above design point is shown in Fig. 3.13. The flux-minus-flow scram limited the temperature rise to less than 64°F for all insertion rates investigated. The reactor outlet gas temperature scram limited the temperature rise to less than 126°F. If both scram actions are available, the maximum rise of the cladding temperature is 56°F at a reactivity insertion rate of 1.22×10^{-5} δk/sec.

Variations During Loss of Power. (G. Samuels) The temperature of the gas leaving the core is of concern because of its effect on the low-temperature piping between the attemperator and the steam generator. The maximum normal operating temperature for this piping has been specified as 1080°F, and no difficulty is expected with short-time transients up to 50°F above this value.

The two time periods of most interest are the first minute after loss of power and about 23 min later when the natural-convection gas flow is equal to the afterheat rate. In determining the temperatures to be expected following a loss of power, the coastdown time of the blower becomes of prime importance. The coastdown curves for both the clutched and declutched case are presented in Fig. 3.10. The times required for the flow to reach 5% are 7.9 and 5.7 min, respectively, for the two cases, and after

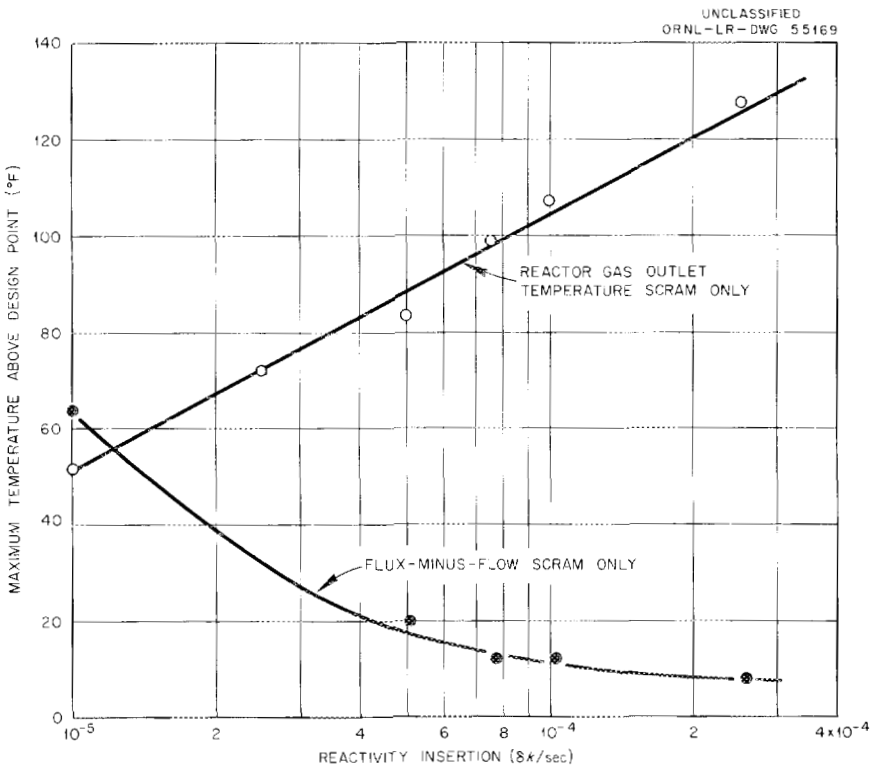


Fig. 3.13. Maximum Rise Above Design Point of Mean Temperature of Fuel Element Cladding for Ramp Increases in Reactivity with Reactor Operating at 100% Power and 100% Flow.

8 min the flow is estimated to be 4.75% and 3.5%, respectively, for the two cases. In the following analysis it was assumed that the blower was declutched and that after 5.7 min, when the flow had dropped to 5%, the blower abruptly stopped.

The analog computer studies gave the exit gas temperature, the cladding temperature, and the UO_2 temperature during the coastdown, but they did not include the effect of the sleeves and moderator blocks during the coastdown. The effects of the sleeves and moderator blocks are such that the temperatures found in the computer studies are too high for the first 10 to 20 sec and too low thereafter. The exit gas temperature and the maximum cladding temperature overshoot their normal values by 35 and 90°F, respectively. After the 5.7-min coastdown of the blowers, the following temperatures were found:

Exit gas temperature	650°F
Maximum cladding temperature	720°F
Maximum UO_2 temperature	750°F

The gas temperature overshoot for the short period after loss of power results in a 1080°F gas temperature in the hot-leg piping, which should present no difficulties. The 90°F overshoot in the temperature of the fuel element cladding does not lead to a temperature in excess of the 1800°F maximum allowable temperature.[9] Physics studies have shown that if a fuel channel is empty, the adjacent channels will show an 8% increase in heat generation. If it is assumed that one of the channels in the highest power region of the core is empty at the time of the loss of power, some small probability exists that the temperature of the elements adjacent to the empty channel may exceed 1800°F. For this case the nominal surface temperature of the elements is 1545°F. Adding 75°F for temperature asymmetries and 90°F for the overshoot, the temperature becomes 1710°F. At these high temperatures the radiation between the elements and the sleeve becomes appreciable and must be considered. For a fuel element cluster temperature of 1800°F the radiation between the elements and the sleeve is 7% of the normal maximum power rate in the reactor. Applying this 7% to the normal maximum heat transfer film drop leads to a predicted reduction in the temperature of 42°F. Deducting this from 1710°F leaves 1668°F or 132°F less than the 1800°F maximum allowable temperature. The probability of the temperature of any single element exceeding its calculated mean value by 132°F is 0.01. Considering that there are only four channels which may be subjected to the 8% additional heat input and that within each channel there are at most 14 elements that can reach these high temperatures, it would not be expected that there would be any significant number of failures and certaintly there would be no hazardous conditions. The length of time the elements would be exposed to this overshoot would be about 10 sec.

---

[9] "GCR Quar. Prog. Rep. Sept. 30, 1960," ORNL-3015, p. 25.

In examining the transient behavior of the fuel element, sleeve, and coolant temperatures after the blower stops, the fuel element temperature was assumed to be 800°F along the entire channel and the sleeve temperature was assumed to be equal to the coolant temperature along the channel at the instant the power failed. These values are conservative in that both temperatures will actually be slightly less. Assuming that none of the afterheat is given to the coolant gas, that is, there is only thermal radiation between the elements and sleeve, then the fuel element surface temperature and the sleeve temperature at the end of 5.7 and 23 min will be as shown in Fig. 3.14. At the end of 23 min the heat generation rate and the natural-convection flow rate will both be about 1.2% of normal.

Rather than speculate about the laminar flow heat transfer coefficient within the element, a different and conservative approach was used. An examination of the configuration of the fuel assembly, Fig. 3.1, shows that the distance from the fuel elements to the center of one of the flow areas in the cluster is about 1/4 in. Assuming conduction through a 1/4-in. stagnant helium film to the flow in the center of the passages gives an effective coefficient of 7 Btu/hr·ft^2·°F at 1.2% of full power. The maximum heat flux in the reactor will be 2100 Btu/hr·ft^2, and the maximum temperature difference between the fuel elements and the coolant will be 300°F. The coolant temperature profile at this time will be very close to that existing at the time of the power failure. Thus, the maximum fuel element temperature that can exist will be about 1200°F.

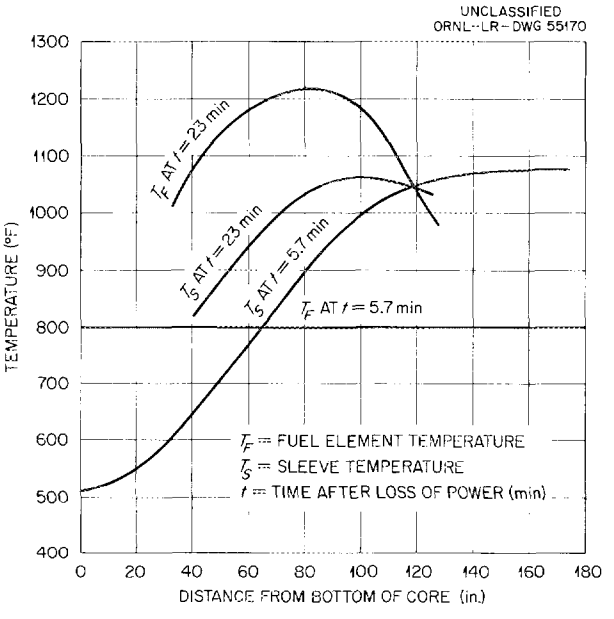


Fig. 3.14. Fuel Element and Sleeve Temperatures at Times of 5.7 and 23 min After Loss of Power for Case of No Afterheat Removed by Convection.

In order to place a limit on the maximum coolant exit temperature, the curves of Fig. 3.15 were calculated. The coolant temperature curves were determined by

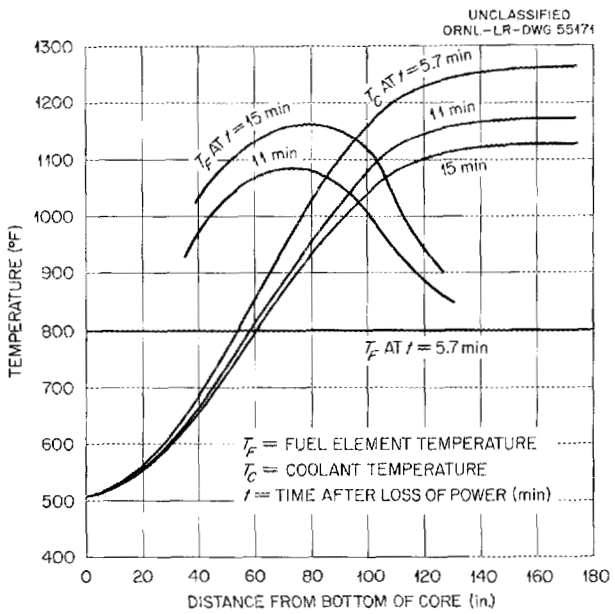


Fig. 3.15. Fuel Element Temperature Based on No Afterheat Transfer to Coolant and Coolant Temperature Based on Transfer of All Afterheat to Coolant.

assuming that all the afterheat was removed by the coolant, and the fuel element temperatures were determined by assuming that no heat was removed by the coolant. At 5.7 min after loss of power the coolant temperature will exceed 1250°F based on these assumptions, but this is impossible because the fuel element temperature is 800°F and the maximum sleeve temperature is 1075°F. The same argument applies to the 11-min case because there is no temperature available to raise the temperature of the gas above about 1075°F. After 15 min, the fuel element temperature would be 1160°F if no heat were transferred by convection, but the maximum temperature that could be reached by the gas, assuming all heat transferred by convection, would be 1070°F, the point of intersection of the two curves. Thus, the fuel elements will not be the controlling factor in determining the coolant exit temperature from the core. The exit temperature will follow very closely the graphite temperature at the top of the core. It should be noted that these curves are for the highest power channel in the core and that the temperatures in the other channels will be less.

The results of preliminary calculations to determine the sleeve and moderator temperatures show their average temperature at the top of the reactor to be less than 1000°F. For these calculations it was assumed that the annulus flow was set so that the maximum moderator temperature would be 1100°F, and, further, the flow was set so that this temperature would not be exceeded even for large variations in the radial flux in the reactor. This means that most of the channels would be over-cooled for any one flux profile. The total annulus flow for this case was about

32 000 lb/hr, which would result in a total core bypass of about 37 000 to 38 000 lb/hr. For this type of core flow control the maximum exit coolant temperatures from the reactor will not exceed the 1080°F specified for the exit piping.

Alternate Fuel Assemblies

(G. Samuels, M. E. Lackey, R. S. Holcomb)

Since the EGCR is to serve as a "test bed" for fuel elements, alternate fuel elements are being developed. Some elements will be identical in design to the EGCR fuel elements but will consist of different materials; other elements will be of configurations different from that of the EGCR reference elements and of various materials.

The preliminary designs of four types of beryllium-clad fuel elements have been completed. Three of these are shown in Figs. 3.16, 3.17, and 3.18; the fourth is essentially the same as the reference stainless steel-clad element of the EGCR. The design dimensions and operating conditions are summarized in Table 3.2 for elements operating at an exit gas temperature of 1050°F. The basic design considerations were an exit gas temperature from the fuel channel of 1050°F with a maximum surface temperature of 1300°F for the maximum available pressure drop across the fuel column. The design nominal surface temperature was 1150 to 1200°F to allow for temperature asymmetries of 100 to 150°F. The design was restricted to clusters of 7, 12, and 19 rods. The longitudinal fins on the 7-rod cluster eliminate the need for a

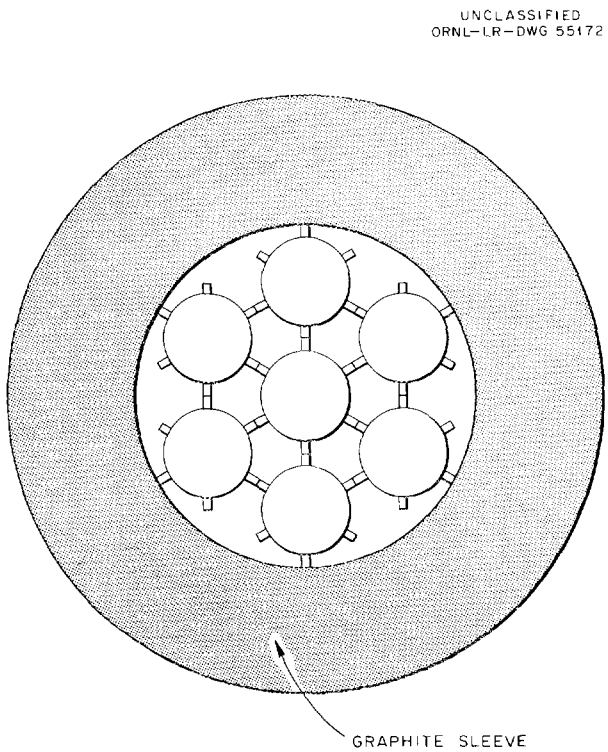


Fig. 3.16. EGCR Beryllium-Clad Fuel Elements in Finned Seven-Rod Cluster.

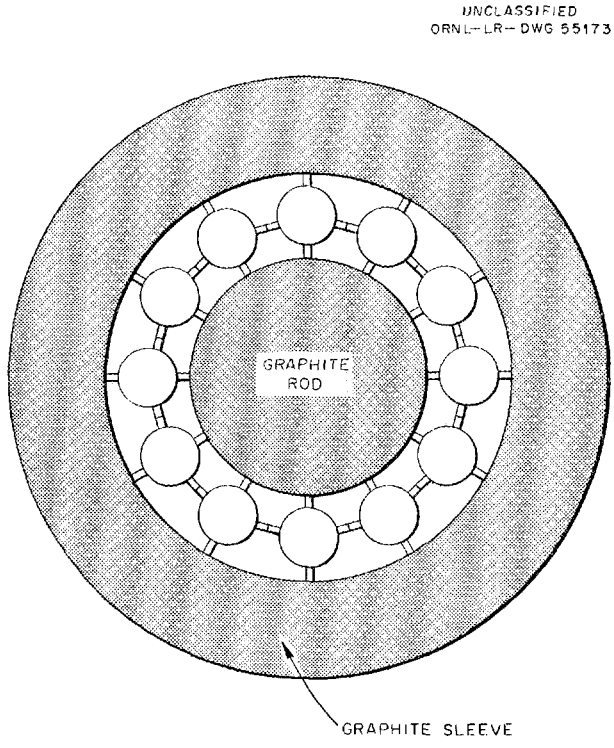


Fig. 3.17. EGCR Beryllium-Clad Fuel Elements in Finned 12-Rod Cluster.

mid-spacer, in addition to providing more surface area.

The 12-rod cluster is arranged on a circular pitch about a 1.83-in.-diam central graphite rod. The 19-rod cluster is arranged on an equilateral triangular pitch in a hexagonal hole with rounded corners in the graphite sleeve. The radial peak-to-average power ratio listed in Table 3.2 indicates at what radial position in the core the fuel element could operate with the reactor at full power with the same fuel enrichment as the rest of the core. This ratio may be varied by changing either the enrichment or the flow area in the cluster.

The reason for the 12-rod circular pattern rather than a 13-rod hexagonal design is that the random angular rotation of the stacked assemblies in a channel could result in severe flow maldistribution at the inlet to an assembly. Even for aligned assemblies, the flow distribution in a 13-rod hexagonal array is very poor. The 19-rod design is also subject to these difficulties, but to a lesser degree.

Table 3.2. Design Data for EGCR Beryllium-Clad Fuel Elements

Number of Rods Per Assembly	Outside Diameter of Beryllium Tube (in.)	Number of Fins Per Rod	Clearance Between Rods (in.)	Inside Diameter of Graphite Sleeve (in.)	Radial Peak-to-Average Power Ratio	Nominal Maximum Surface Temperature (°F)
7	0.75	0	0.150	2.70	0.706	1179
7	0.75	6[a]	0.200	2.85	0.761	1166
12	0.50	0	0.150	3.13	0.835	1148
19	0.50	0	0.200	3.61	1.345	1183

[a]Fins 0.040 in. thick and 0.100 in. wide.

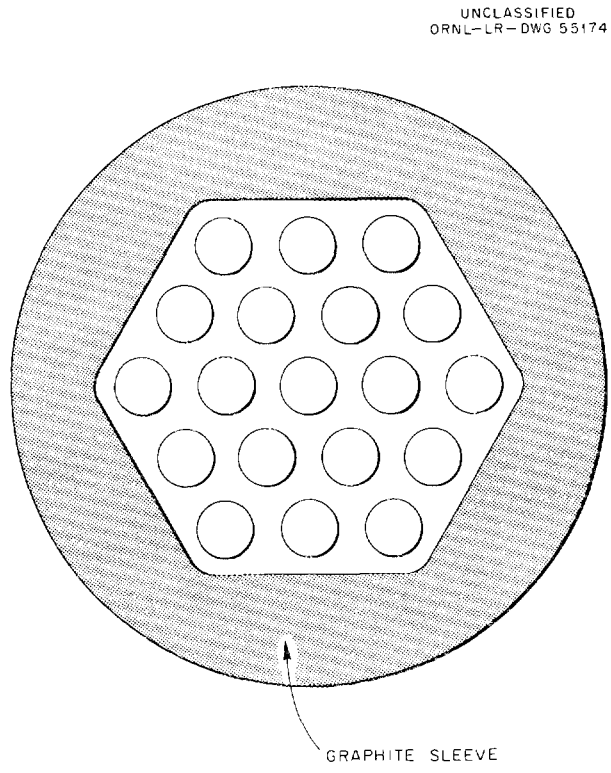


Fig. 3.18. EGCR Beryllium-Clad Fuel Elements in 19-Rod Cluster.

Mass and Heat Transfer Correlation Studies

(M. E. Lackey, R. S Holcomb)

The local velocity data for tubes 1, 2, 3, and 7 obtained from a mock-up of the EGCR fuel channel[10] at L/d_e = 3.9 and 0-deg orientation have been reduced to lines of constant velocity. These lines are shown in Fig. 3.19. The velocity distribution was determined by graphical integration of the velocity profile. The ratio of the flow in the outer channel to the flow in the inner channel[11] at the bundle entrance is determined by the ratio of the flow area in the outer channel of the spider to the flow area in the inner channel of the spider. Values of this flow ratio are given in

[10]"GCR Quar. Prog. Rep. June 30, 1960," ORNL-2964, pp. 67–80.

[11]The arbitrary dividing line is chosen to be the hexagon formed by connecting the centers of the six peripheral tubes.

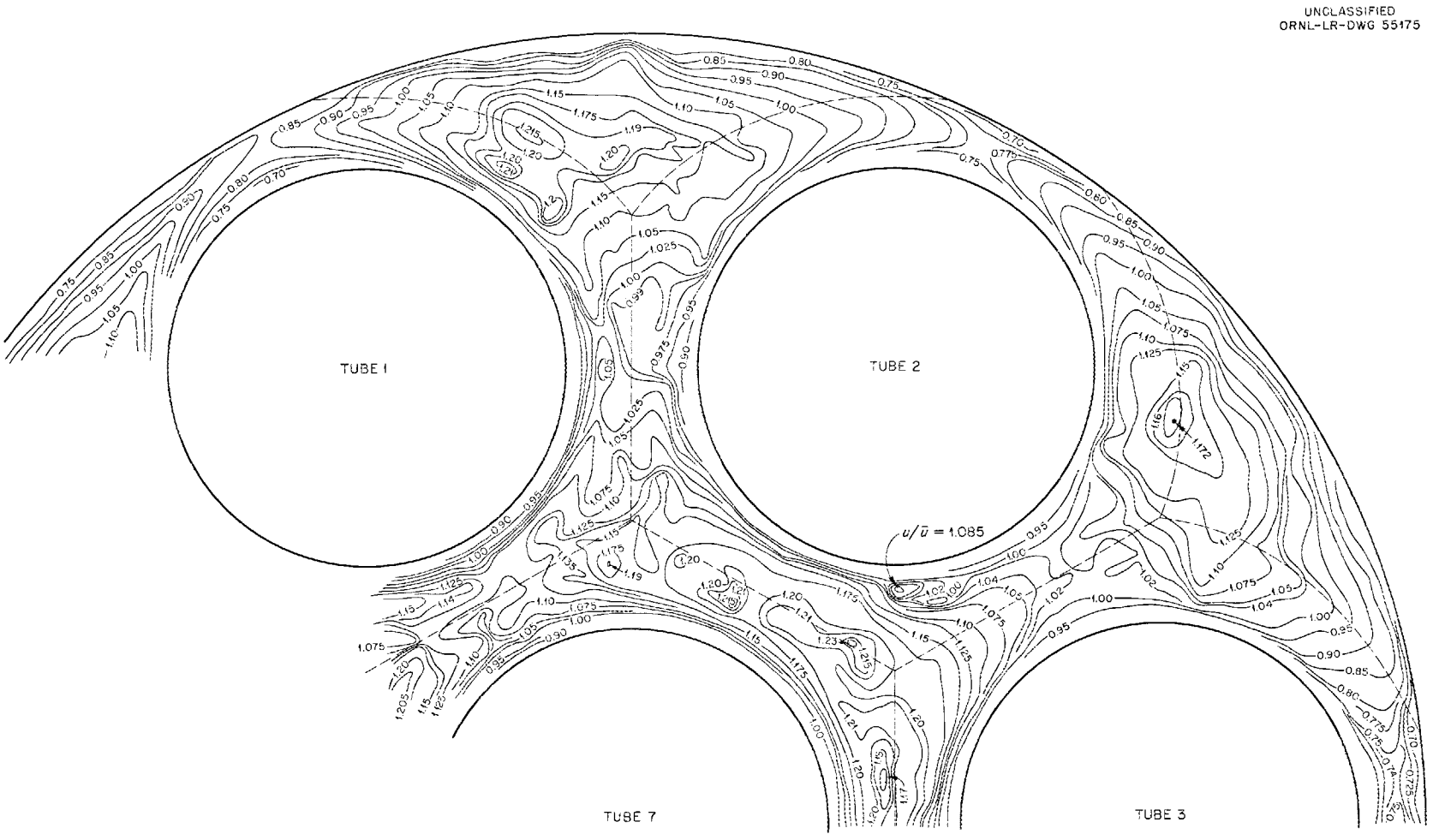


Fig. 3.19. Isothermal Velocity Profile for Seven-Rod EGCR Fuel Cluster with 2:1 Tube Spacing and 0-deg Orientation at an L/d_e of 3.9.

Table 3.3 as applied to the channel at $L/d_e = 3.9$. A comparison of the values in Table 3.3 indicates that the flow ratio has been shifted from the value that existed at the entrance of the first bundle, which would be the "equal velocity value" of 2.125, past the "equilibrium value" of 2.002 toward the "calculated bundle entrance value" of 1.688. Some flow redistribution has occurred between $L/d_e = 0.0$ and $L/d_e = 3.9$ toward establishing the equilibrium value of 2.002.

Table 3.3. Ratio of the Flow in the Outer Channel to the Flow in the Inner Channel

Calculated bundle entrance ratio, $L/d_e = 0.0$	1.688
Experimental ratio at $L/d_e = 3.9$	1.884
Equilibrium ratio	2.002
Ratio for equal velocity in the inner and outer channels	2.125

A comparison of the heat transfer coefficients obtained from an Allis-Chalmers heat transfer experiment[12] performed on a seven-rod bundle with 60-deg mid-cluster spacers and from heat transfer experiments performed on round tubes at NACA[13] and at Stanford University[14] with the mass transfer coefficients obtained from a completely simulated EGCR fuel element[15] has been completed for the center rod and an outside rod of the seven-rod cluster. For the purpose of this analysis the outer tube was divided into two segments. The inner segment consisted of the 120-deg arc that falls within the inner channel, and the outer segment consisted of the remaining

[12]Allis-Chalmers, Run 212-C, unpublished data.

[13]L. V. Humble, W. H. Lowdermilk, and L. G. Desmon, "Measurements of Average Heat Transfer and Friction Coefficients for Subsonic Flow of Air in Smooth Tubes at High Surface and Fluid Temperatures," NACA Report 1020 (1951).

[14]M. E. Davenport and P. M. Magee, "Heat Transfer to a Gas at High Temperature," Technical Report No. 247-1 (May 1960), Nuclear Technology Laboratory, Stanford University.

[15]"GCR Quar. Prog. Rep. Sept. 30, 1960," ORNL-3015, pp. 53–63.

240-deg arc. It was assumed that the flow which effected the heat and mass transfer was contained within the boundaries formed by the locus of the intersections of the perpendiculars erected on the tubes and the adjacent associated walls. The influence boundaries are shown as dotted lines in Fig. 3.19. It was further assumed that the flow obtained from the analysis of the velocity profile at $L/d_e = 3.9$ for the aligned case was the flow that existed in the heat and mass transfer experiments at $L/d_e = 0$ and that the flow ratio shifted to the equilibrium flow ratio just upstream of the mid-cluster spacer. It was assumed that at the mid-cluster spacer the flow shifted to a ratio value of 2.086, as determined by the mid-cluster spacer geometry, and that just upstream of the bundle exit spider it shifted back to the equilibrium value.

The data were correlated by using a modified Colburn equation of the form

$$Nu_s = j_{HB} Re_s Pr_s^{0.4} \quad , \tag{1}$$

which refers all physical properties of the gas to the surface conditions. Rewriting Eq. (1) in the form of a Dittus-Boelter equation and referring the Reynolds moduli to the average bundle flow gives

$$Nu_s = j_{HB} \left(Re_a \frac{D_B}{D_a} \frac{G_B}{G_a} \right)^{0.2} \left(Re_a \frac{D_B}{D_a} \frac{G_B}{G_a} \right)^{0.8} \frac{T_a}{T_s} \frac{\mu_a}{\mu_s} Pr_s^{0.4} \quad . \tag{2}$$

If

$$C_{HB} = j_{HB} \left(Re_a \frac{D_B}{D_a} \frac{G_B}{G_a} \right)^{0.2} \quad ,$$

Eq. (2) becomes

$$Nu_s = C_{HB} \left(Re_a \frac{D_B}{D_a} \frac{G_B}{G_a} \right)^{0.8} \frac{T_a}{T_s} \frac{\mu_a}{\mu_s} Pr_s^{0.4} \quad . \tag{3}$$

The mass transfer factor j_M is corrected from the average bundle velocity to the local velocity and used in the mass transfer–heat transfer–friction analog to determine the corresponding mass coefficient C_M:

$$\frac{G_a}{G_B} j_{MB_{experimental}} = j_{MB_{corrected}} ,$$

$$j_{MB_{corrected}} \left(Re_{aM} \frac{D_B}{D_a} \frac{G_B}{G_a} \right)^{0.2} = C_{MB} . \qquad (4)$$

In these equations the subscript s refers to the surface in question, H refers to heat transfer, M refers to mass transfer, a refers to average bundle conditions, and B refers to the sector in question.

The heat transfer and mass transfer coefficients C_{HB} and C_{MB} were determined for the center rod, the inner and outer sectors of an outside rod, and the cluster average of the bundle heat and mass transfer experiments, respectively. These values are shown in Figs. 3.20 through 3.23, in addition to the C_{HB} values determined from the NACA and Stanford round-tube data. In general the agreement between the bundle heat and mass transfer coefficients is within 7% and within 10% (with the exception of the first half of the center tube, which is within 20%) of the NACA and Stanford data.

EGCR Control Rods

(J. W. Michel)

The design of the EGCR control rod has been modified from that previously described[16,17] and is shown in Fig. 3.24. The rod is composed of four 5-ft-long segments supported on an inner stainless-steel rod. The three lower segments contain annular rings of B_4C as the nuclear poison.

[16] "GCR Quar. Prog. Rep. June 30, 1960," ORNL-2964, pp. 35–37.

[17] "GCR Quar. Prog. Rep. Sept. 30, 1960," ORNL-3015, pp. 32–34.

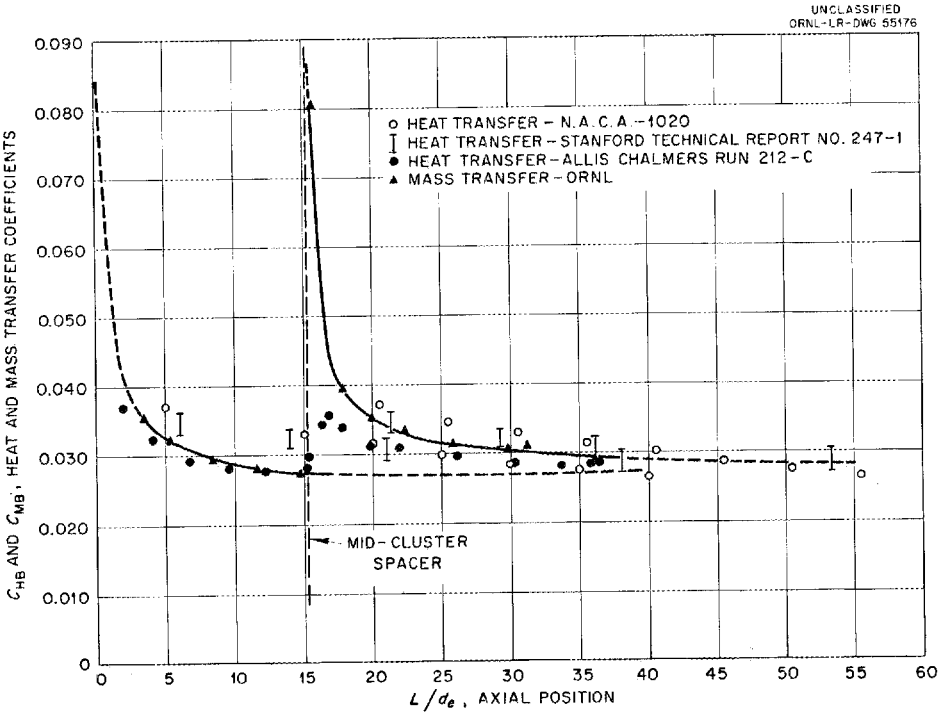


Fig. 3.20. Transfer Coefficients for the Center Tube of a Seven-Rod Cluster.

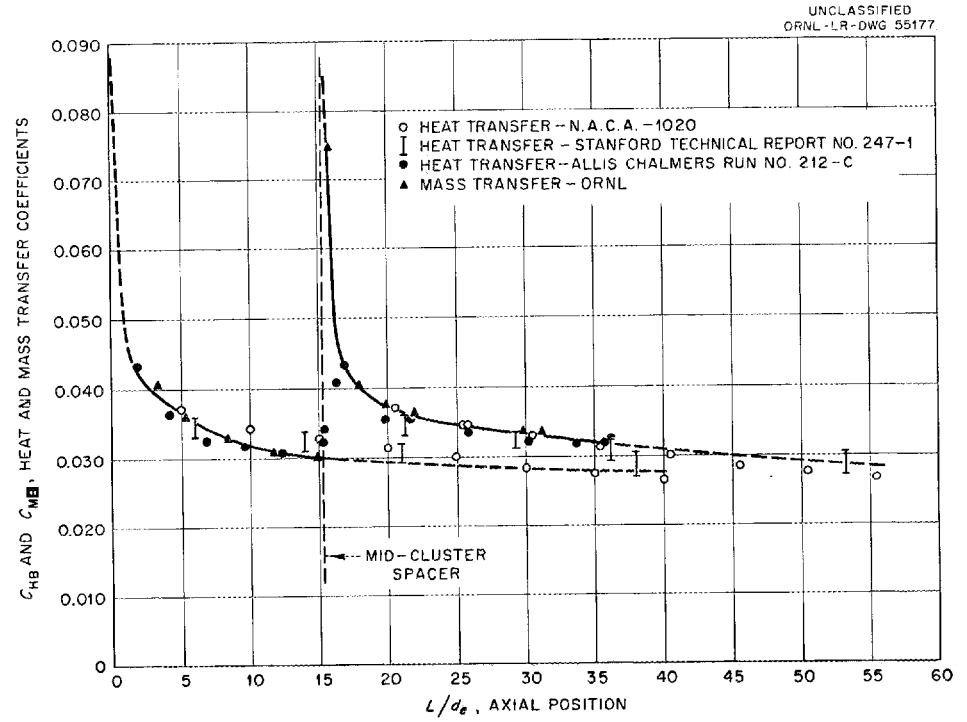


Fig. 3.21. Transfer Coefficients for the Inside 120-deg of an Outside Tube of a Seven-Rod Cluster.

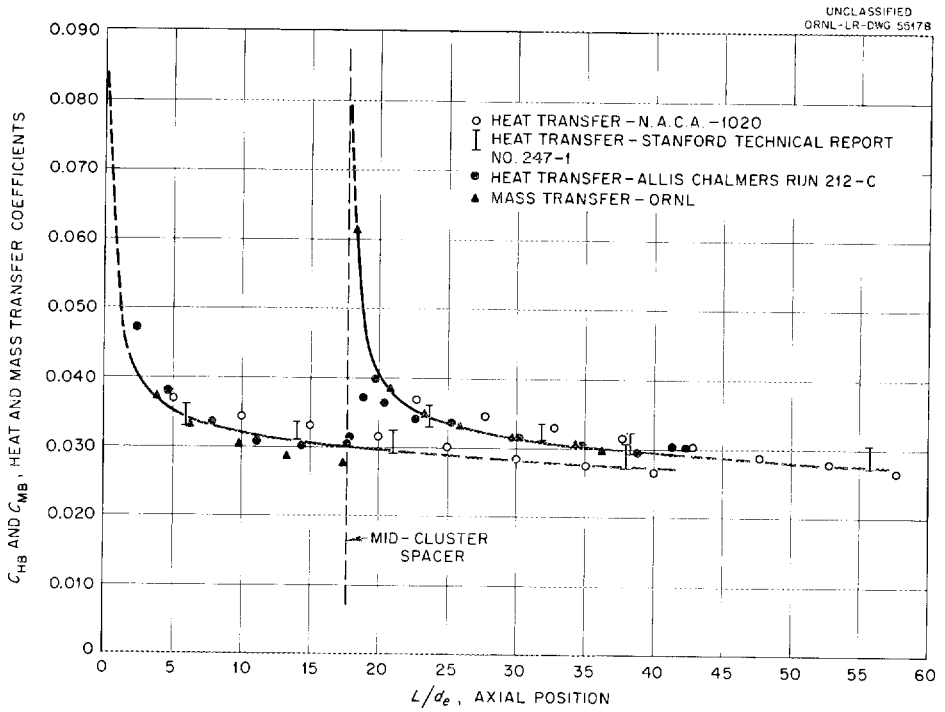


Fig. 3.22. Transfer Coefficients for the Outside 240-deg of an Outside Tube of a Seven-Rod Cluster.

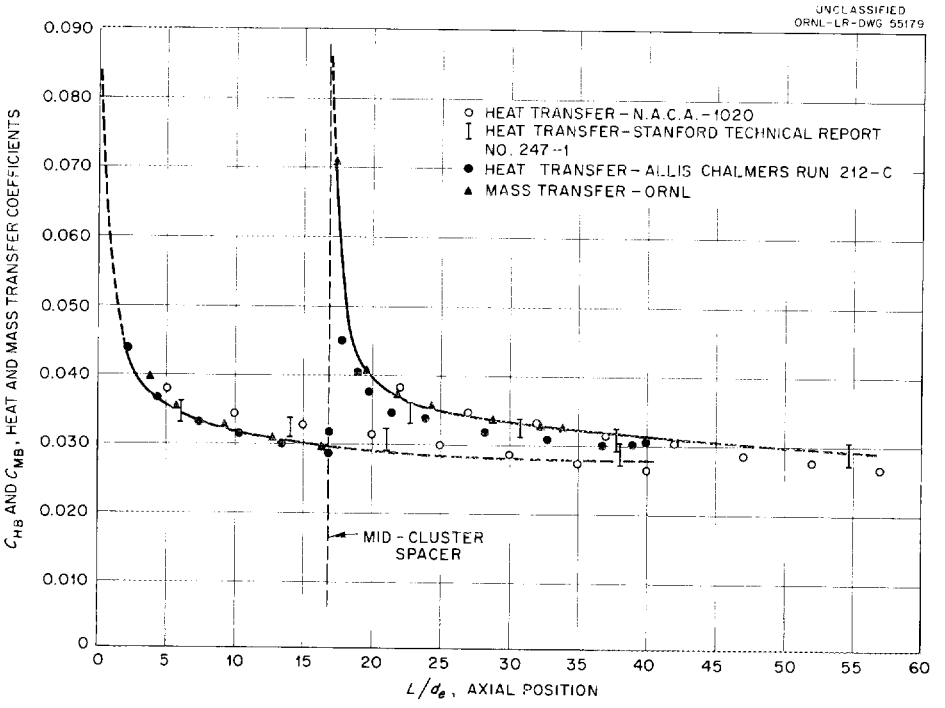


Fig. 3.23. Average Transfer Coefficients for a Seven-Rod Cluster.

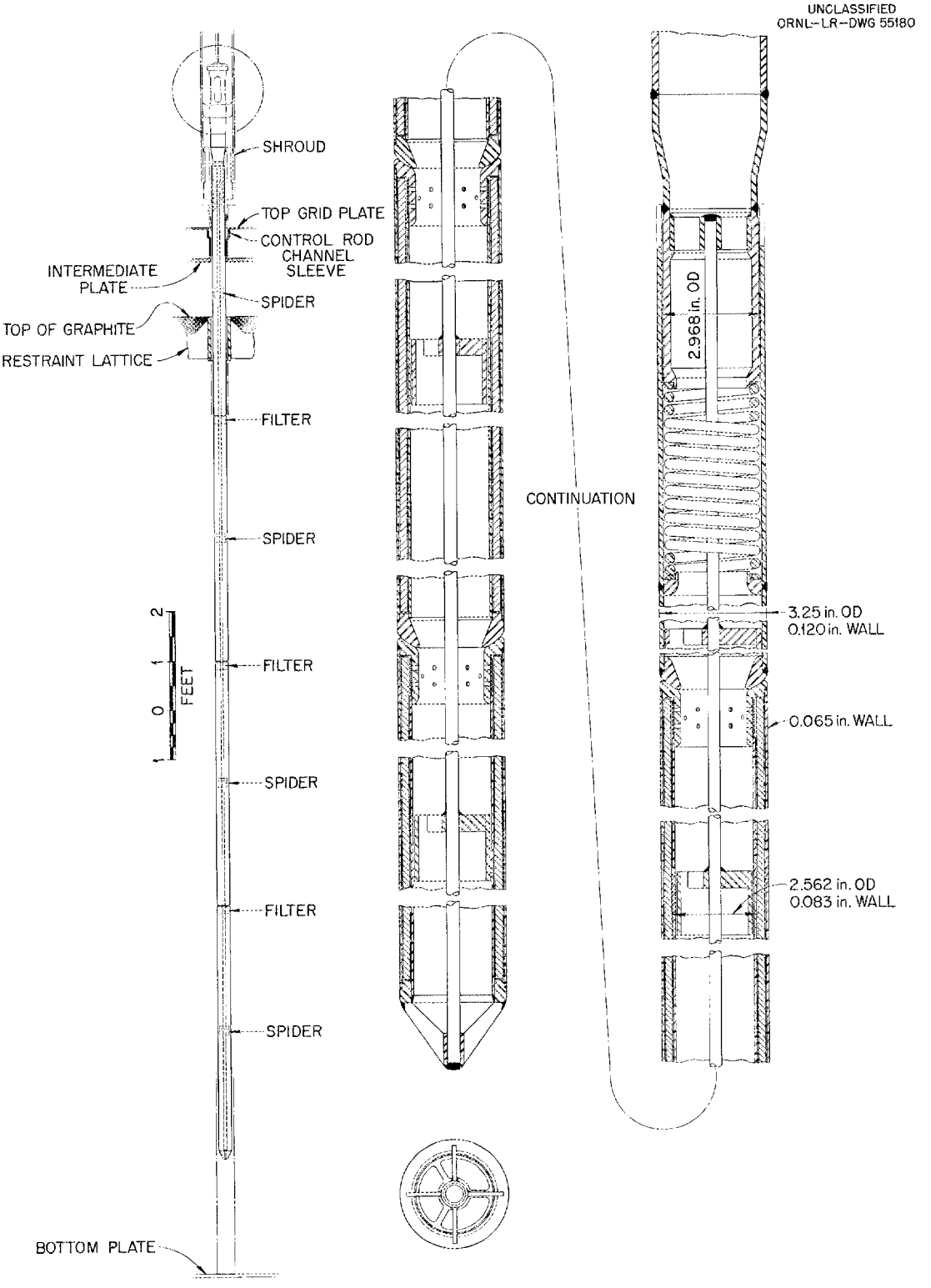


Fig. 3.24. EGCR Control Rod.

A metallic filter is installed in these segments to vent the B_4C section to the reactor without loss of B_4C. Cooling is achieved by downflow of cool helium from the top control rod nozzle and depends on achieving a partial seal between the outside of the control rod and the shroud. The four segments are compressively loaded by the top spring to maintain a seal in the ball-and-socket joints between segments.

A full-scale mockup of this rod design is being assembled to establish fabricating techniques and to indicate possibilities for reducing the cost of the rods; for example, one segment is to be assembled by press-fitting and tack-welding the parts together. A limited test program is to be performed on this rod primarily to confirm cooling and flexibility design assumptions.

Decontamination of EGCR Components

(A. B. Meservey, J. M. Chilton)

A method for decontaminating the EGCR charge and service machines using a carbonate-peroxide reagent to dissolve finely divided UO_2 and a proprietary oxalic acid mixture for fission-product removal was described previously.[18] It has since been found that oxalate-peroxide solutions of controlled pH are superior UO_2 solvents and decontaminating agents and that they are only slightly corrosive to mild steel. With the oxalate-peroxide solutions it is feasible to simultaneously dissolve UO_2 and decontaminate the surfaces in one operation. A detailed description of the proposed decontamination procedure using oxalate-peroxide has been published.[19]

In summary, the reagent is 0.4 M sodium or ammonium oxalate with 1 M H_2O_2, adjusted to pH 4.5 with oxalic acid; it is used at 95°C. The pH must be controlled by periodic additions of oxalic acid, since it tends to rise spontaneously. Above pH 6, which may be reached in 1/2 to 1 hr if the

---

[18]"GCR Quar. Prog. Rep. June 30, 1960, ORNL-2964, pp. 51–54.

[19]A. B. Meservey, J. M. Chilton, and D. E. Ferguson, "Decontamination of EGCR Charge and Service Machines," ORNL CF-60-10-46 (Oct. 13, 1960).

pH is not controlled, the peroxide decomposes rapidly to O_2 and H_2O. At a pH of 4.5 and a temperature of 95°C, whole sintered UO_2 slugs of the EGCR type can be dissolved in 2 to 3 hr, with a corrosion rate on mild steel of about 0.007 mil/hr. At a lower pH, the corrosion rate is higher, and the oxalate ion reacts at increased rates with the peroxide to produce CO_2 and water. Fission product decontamination is better with this reagent than with any other low-corrosion reagent tested. Ammonium oxalate is preferable to sodium oxalate because it is cheaper, more effective, more soluble, and easier to dispose of than sodium oxalate.

Recent comparisons between peroxide-oxalate mixtures and other reagents have shown that these mixtures also rank high in decontaminating type 347 stainless steel.[20] The corrosion rate of 1% H_2SO_4 on type 347 stainless steel at 95°C was reduced from 0.016 mil/hr to 0.001 mil/hr by making it 1 M in H_2O_2. Peroxide also reduced the corrosion rate of sulfuric-fluoride mixtures.

Helium Purification System Studies

(J. C. Suddath, C. D. Scott)

Experimental data pertinent to the design of coolant purification systems for high-temperature gas-cooled reactors and in-pile loops are being obtained. The coolants under consideration are helium and carbon dioxide with both radioactive and nonradioactive contaminants.

A kinetics study of the oxidation of H_2, CO, and CH_4 in a flowing stream of helium by O_2 in a fixed bed of Girdler G-43 platinum catalyst has been completed.[21] The experimental tests were carried out in the 2-in.-diam oxidizer of the helium purification test facility described previously.[22] Twenty-five tests were made to study the catalytic oxidation

---

[20]A. B. Meservey, "Decontamination of EGCR Components," ORNL CF-60-12-37 (December 1960).

[21]C. D. Scott, "Kinetics of the Catalyzed Oxidation of H_2, CO, and CH_4 by Oxygen in a Flowing Stream of Helium," ORNL-3043 (in press).

[22]"GCR Quar. Prog. Rep. March 31, 1960," ORNL-2929, pp. 54–56.

of H_2 at 500°C ± 20°C and 300 psia with catalyst bed depths of 6 and 12 in. Two gas flow rates, approximately 28.4 and 93.0 std. liters/min, were used for each bed size, and the hydrogen concentrations were varied from 0.35 to 2.00 vol %. The data obtained in these tests are presented in Table 3.4.

Fifteen similar experimental tests were made in the study of the oxidation of CO. In these tests the bed temperature was 500°C ± 25°C, the pressure was 300 psia, and the catalyst bed depths were 3 and 6 in. Three different gas flow rates, approximately 28.6, 49.3, and 92.4 std.

Table 3.4. Experimental Data from the Kinetic Study of the Oxidation of H_2 with O_2 in a Fixed Bed of Girdler G-43 Catalyst

Run No.	Bed Height (in.)	Average Bed Temperature (°C)	Total Gas Feed Rate (g·mole/min)	Initial Concentration		Final Concentration	
				H_2 (vol %)	O_2 (vol %)	H_2 (vol %)	O_2 (vol %)
4B	6	510	1.28	2.000	0.956	0.142	0.027
4C	6	490	1.28	2.000	0.900	0.204	0.011
4D	6	500	1.28	2.000	0.887	0.238	0.006
4E	6	515	1.28	2.000	0.774	0.460	0.004
4F	6	490	1.28	2.000	0.691	0.500	0.002
5C	6	490	1.27	1.000	0.499	0.013	0.006
5D	6	490	1.27	1.000	0.503	0.012	0.009
5E	6	490	1.27	1.000	0.517	0.003	0.018
6B	6	510	1.26	0.400	0.260	0.002	0.061
6C	6	490	1.26	0.400	0.246	0.003	0.048
7A	12	490	1.27	0.830	0.413	0.007	0.001
7B	12	490	1.27	0.830	0.415	0.004	0.002
7D	12	500	1.27	0.830	0.411	0.009	0.001
7E	12	490	1.27	0.830	0.409	0.014	<0.001
8B	12	505	1.26	0.350	0.175	0.002	0.001
9A	12	495	4.15	1.010	0.481	0.052	0.002
9C	12	520	4.15	1.010	0.445	0.123	0.001
9D	12	500	4.15	1.010	0.399	0.214	0.001
10B	12	515	4.13	0.430	0.213	0.006	0.001
11A	6	490	4.15	1.050	0.418	0.217	0.002
11B	6	500	4.15	1.050	0.447	0.173	0.002
11C	6	510	4.15	1.050	0.474	0.124	0.002
11D	6	505	4.15	1.050	0.309	0.434	0.001
11E	6	500	4.15	1.050	0.240	0.570	<0.001
12A	6	510	4.13	0.540	0.221	0.100	0.001

liters/min, and CO concentrations from 0.425 to 1.94 vol % were used. The data from these tests are presented in Table 3.5.

Seventeen experimental tests were made in the study of the oxidation of CH_4. The test conditions were the same as those used in the tests with CO. The gas flow rates were approximately 28.4, 49.2, and 93.0 std. liters/min, and the CH_4 concentrations varied from 0.219 to 0.627 vol %. The data obtained in these tests are listed in Table 3.6.

The experimental data have been correlated empirically in a manner similar to that outlined by Weller.[23] Apparent reaction rates and design equations for determining the necessary bed volumes were determined.

---

[23]S. Weller, "Analysis of Kinetic Data for Heterogeneous Reactions," AIChE Journal, Vol. 2, No. 1, p. 39 (1956).

Table 3.5. Experimental Data from the Kinetic Study of the Oxidation of CO with O_2 in a Fixed Bed of Girdler G-43 Catalyst

Run No.	Bed Height (in.)	Average Bed Temperature (°C)	Total Gas Flow Rate (g·mole/min)	Initial Concentration		Final Concentration	
				CO (vol %)	O_2 (vol %)	CO (vol %)	O_2 (vol %)
5A	6	510	4.14	0.95	0.3767	0.1969	0.0003
6A	6	495	1.30	1.94	0.9613	0.0240	0.0033
7A	3	480	1.28	1.06	0.0307	0.9988	0.0001
7B	3	485	1.28	1.06	0.4192	0.2252	0.0018
8A	3	520	4.14	1.09	0.3142	0.4624	0.0004
8B	3	515	4.14	1.09	0.3948	0.3060	0.0028
8C	3	520	4.14	1.09	0.4648	0.1710	0.0003
9B	3	510	1.27	0.463	0.0071	0.4498	0.0005
9C	3	490	1.27	0.463	0.0261	0.4112	0.0002
9F	3	510	1.27	0.463	0.2331	0.0316	0.0074
10A	3	480	4.10	0.425	0.1613	0.1096	0.0036
10B	3	500	4.10	0.425	0.2105	0.0213	0.0086
10C	3	505	4.10	0.425	0.1956	0.0478	0.0070
11A	3	520	2.20	1.08	0.3372	0.4072	0.0008
11B	3	510	2.20	1.08	0.4234	0.2376	0.0022

Table 3.6. Experimental Data from the Kinetic Study of the Oxidation of CH_4 with O_2 in a Fixed Bed of Girdler G-43 Catalyst

Run No.	Bed Height (in.)	Average Bed Temperature (°C)	Total Gas Flow Rate (g·mole/min)	Initial Concentration		Final Concentration	
				CH_4 (vol %)	O_2 (vol %)	CH_4 (vol %)	O_2 (vol %)
1B	6	490	1.277	0.4760	0.7149	0.1210	0.0049
1C	6	500	1.277	0.4760	0.5800	0.1906	0.0092
2A	6	560	1.280	0.5400	0.5092	0.2860	0.0002
2B	6	545	1.277	0.5400	0.3081	0.3860	0.0001
3A	6	480	1.263	0.2190	0.0101	0.2140	0.0001
3C	6	490	1.272	0.2190	0.4746	0.0307	0.0982
5A	6	505	4.14	0.3520	0.5725	0.1034	0.0533
7A	6	540	4.14	0.4450	0.8708	0.0606	0.1020
7B	6	530	4.14	0.4450	0.6500	0.1242	0.0094
8A	6	530	4.12	0.3780	0.4770	0.1426	0.0062
9A	3	515	2.18	0.3660	0.0122	0.3600	0.0002
9B	3	490	2.18	0.3660	0.3666	0.1980	0.0306
9C	3	500	2.18	0.3660	0.5325	0.1325	0.0655
10A	3	480	1.272	0.3920	0.5351	0.1415	0.0341
10B	3	530	1.272	0.3920	0.3639	0.2155	0.0109
11A	3	530	2.20	0.6270	0.7552	0.2550	0.0012
11B	3	510	2.21	0.6270	0.7668	0.1488	0.0104

For hydrogen,

$$V = \frac{248F}{\pi G^{0.65}} \ln \frac{\left(2y_{O_0} y_{H_0}\right)^{1/2} + y_{H_0} + \dfrac{2y_{O_0} - y_{H_0}}{2}}{\left[\left(2y_{O_0} - y_{H_0}\right) y_{H_f} + \left(y_{H_f}\right)^2\right]^{1/2} + y_{H_f} + \dfrac{2y_{O_0} - y_{H_0}}{2}} ;$$

for carbon monoxide with less than stoichiometric oxygen,

$$V = \frac{1.05F}{\pi^{1.5} G^{0.982} \left(y_{C_0} - 2y_{O_0}\right)^{1/2}} \times$$

$$\times \ln \frac{\left[\left(y_{C_0}\right)^{1/2} - \left(y_{C_0} - 2y_{O_0}\right)^{1/2}\right] \left[\left(y_{C_f}\right)^{1/2} + \left(y_{C_0} - 2y_{O_0}\right)^{1/2}\right]}{\left[\left(y_{C_0}\right)^{1/2} + \left(y_{C_0} - 2y_{O_0}\right)^{1/2}\right] \left[\left(y_{C_f}\right)^{1/2} - \left(y_{C_0} - 2y_{O_0}\right)^{1/2}\right]} ;$$

for carbon monoxide with greater than stoichiometric oxygen,

$$V = \frac{2.11F}{\pi^{1.5}G^{0.982}\left(2y_{O_0} - y_{C_0}\right)^{1/2}} \left\{ \tan^{-1}\left[\frac{y_{C_0}}{\left(2y_{O_0} - y_{C_0}\right)}\right]^{1/2} - \tan^{-1}\left[\frac{y_{C_f}}{\left(2y_{O_0} - y_{C_0}\right)}\right]^{1/2} \right\} ;$$

for methane,

$$V = \frac{2.21F}{\pi^{2}G^{0.772}\left(2y_{CH_0} - y_{O_0}\right)} \ln\left(\frac{y_{CH_f} y_{O_0}}{y_{CH_0} y_{O_f}}\right) .$$

In these expressions

V = volume of catalytic bed required, cm^3,

F = gas flow rate, g·mole/min,

$y_{H_0}, y_{C_0}, y_{CH_0}, y_{O_0}$ = initial mole fractions of H_2, CO, CH_4, and O_2,

$y_{H_f}, y_{C_f}, y_{CH_f}, y_{O_f}$ = final mole fractions of H_2, CO, CH_4, and O_2,

π = total pressure, atm,

G = mass flow rate, g·mole/cm^2·min.

EGCR Hazards Evaluation

Graphite Oxidation (M. H. Fontana)

In the event the main coolant envelope of the EGCR ruptures, air is likely to enter the system. There are areas in the EGCR where unprotected graphite surfaces are at temperatures exceeding 1100°F, and ignition might occur at these surfaces. The containment vessel is not designed to withstand either the pressures and temperatures generated by combustion of a significant fraction of the graphite or the increase in fission-product

release which would accompany the oxidation excursion. Therefore, some means is required to control or to eliminate graphite oxidation.

A two-phase experimental program is under way at Hanford[24] to investigate the EGCR graphite oxidation problem. The basic experimental study will provide information on the effects of factors such as density, purity, coke and pitch source, temperature, coolant flow rate, gamma-ray field intensity, irradiation damage, surface area-to-volume ratio, oxygen partial pressure in the coolant, prior oxidation, and water vapor in the coolant. Laboratory-scale experiments are planned to test the validity of theoretical models in the prediction of ignition conditions.

Along with the laboratory-scale studies, experiments are being conducted with a simulated EGCR fuel-channel and annulus assembly. This prototype is full scale in the radial direction and is 6 ft long, whereas the EGCR channel is 19.5 ft long. Preliminary tests were run on the annulus region of the fuel channel, and it was shown that run-away combustion could be expected in the annulus at graphite temperatures of about 1100°F and annulus flow rates equivalent to 6.5% of 40 000 lb/hr of air. The assembly is being modified for tests of the effects of flow through the central channel with a simulated radiant heat load from the fuel element to the inner surface of the sleeve.

Since it is probable that the sleeves will be subject to catastrophic oxidation in the event of a rupture of the main coolant system if steps are not taken to protect them, the following proposed schemes for protecting the system have been studied:

1. Valve off the ruptured coolant system and allow the air that has entered the system to burn while continuing to cool the reactor with the remaining coolant system.

2. Valve off the ruptured system and, while cooling the reactor with the remaining system, provide a purge gas to reduce the oxygen concentration in the core or to prevent entry of oxygen to the core. The gases that may be used are helium, nitrogen, and carbon dioxide.

---

[24]M. H. Fontana and F. L. Carlsen, Jr., "Report on Trip to Hanford, June 28–29, 1960, Concerning the Graphite Research Program Pertinent to the EGCR," ORNL CF-60-7-78 (July 20, 1960).

3. Completely isolate the reactor and remove the heat by external cooling of the reactor pressure vessel.

4. Maintain the reactor blanketed with nitrogen.

5. Inject a chemical inhibitor such as chlorine gas, freon, or carbon tetrachloride.

6. Use a solid-phase inhibitor in the graphite.

7. Cool the core by means of a water or fog spray.

8. Coat the sleeves with a nonreactive material and allow the moderator to burn. The low air supply in the annulus might reduce the heat from combustion enough so that conduction of heat through the sleeve to the main gas stream could remove both the chemical and decay heat.

It is believed that the instrumentation and control needed to determine which system ruptured would be of sufficient complexity to rule out methods 1 and 2. In addition, the volumes of gas required for method 2 would be quite large. Method 3 is considered to be feasible, although some fuel element melting might occur in the center of the reactor. Shell cooling could be obtained either by eliminating the thermal insulation or by installing cooling coils under the insulation. Method 4 would complicate operation of the reactor and would require excessive design changes for providing a localized inert gas blanket around all primary system components and piping.

Method 5 appears to be feasible inasmuch as chlorine gas has been shown to be quite effective in inhibiting graphite oxidation,[25] but the consequences of inadvertent operation of the chlorine-injection system and the precautions necessary to prevent it are considered to be too drastic for this application. Method 6 would be the most desirable, but no inhibitor is known at this time that possesses radiation stability. Method 7 is feasible, but it suffers from instrumentation and control problems. The consequences of accidental operation of a water spray system would not be as severe as the consequences of chlorine injection, but it would be necessary for the system to operate quickly when required. Further, the system would have to be of sufficient reliability that testing would not be required

---

[25]R. E. Dahl, "Preliminary Evaluation of Chlorine for Use as a Gas-Cooled Reactor Safeguard," USAEC, HW-63902 (February 1960).

during the lifetime of the reactor. This last requirement is a major drawback.

Method 8 is considered to be the most promising of the possible means of controlling the oxidation. Siliconized silicon-carbide coatings are available, and preliminary tests have shown them to be stable in a radiation environment. It is not practical to coat the inner surface of the moderator because of its large size and the precise temperature and timing control required to apply the coating. Furthermore, the integrity of this coating over the lifetime of the moderator could not be assured. The sleeves can, however, be coated to the degree necessary to provide oxidation protection. This scheme does not require operation of any mechanism or instrumentation, but it does require continued operation of one blower after the accident. There is no reason at this time to expect both main blowers to fail concurrently with release of the main coolant.

Analytical and experimental evaluation of this scheme is now under way. A digital computer program has been set up by Allis-Chalmers in which the temperature transient from both decay heat and chemical oxidation heat can be determined. Preliminary calculations have been made to determine the steady-state temperatures required to remove the decay and chemical heat based on the chemical reaction in the annulus being limited by the supply of air in the annulus. It was found that an exit gas temperature of around 1200°F would result.

The computer study will provide a means for determining the effect of stored heat in the graphite on the transient temperatures and reaction rates as a function of time. By varying the percentage of the sleeve that is subject to oxidation, the required effectiveness of the sleeve coating can be found. Also, the time after the accident at which blower operation can be stopped and cooling instituted by the vessel cooling compressor will be found.

The preliminary rate equation to be used was determined by a least-squares fit of results of six different investigators who have reported data on oxidation of high-purity, reactor-grade graphite.[26] The data were

[26]J. W. Prados, "Estimation of Reactions and Heat Release Rates for Graphite Oxidation," ORNL CF-60-10-131 (October 19, 1960)

found to lie within a factor of 6 spread when correlated in terms of oxygen partial pressure and active mass of graphite. First-order dependency on oxygen partial pressure was assumed, and the active mass of graphite was found by means of the depth-of-oxidation concept.

As the temperature of the oxidation reaction is increased, solid-phase diffusion of the reactants to the oxidation sites in the graphite and diffusion of the products out to the gas stream become the limiting factors in the over-all chemical reaction rate. If it is assumed that the reaction rate at any point within the graphite body is dependent on the concentration of oxygen at that point, a profile of rate versus depth from the surface can be found analytically. The depth-of-oxidation concept consists of defining a pseudo depth of oxidation in which the rate is the same as that in the surface of the specimen so that the total weight-loss rate is equal to the integrated rate given by the analtyical solution. It was found that this procedure was effective in reducing the spread of the reported rates. Since graphite oxidation rates are quite sensitive to factors such as coke and pitch source, impurities, etc., a factor of 6 spread was considered to be satisfactory. The least-squares fit of the chemical reaction rates was found to be

$$k = 7.24 \times 10^{9}\ e^{-22\ 100/T} \quad , \tag{1}$$

where k is the weight fraction oxidized per hour and T is in degrees Kelvin.

In calculating the heat released by oxidation, this rate must be applied to the active mass of graphite to find the total weight loss per unit surface area. The equation of heat release per unit surface area and unit time is then

$$\frac{Q}{S} = \Delta H \rho L k \quad , \tag{2}$$

where Q/S is the heat release per unit surface area per unit time, ΔH is the chemical heat release per unit of mass burned, ρ is the density of the graphite, L is the depth of oxidation, and k is the reaction rate defined

above. The depth of oxidation, L, is given by the expression

$$L = \left(\frac{MD_p}{k\rho RT} \right)^{1/2} , \qquad (3)$$

where M is the molecular weight of carbon (12.01), k is the reaction rate defined above, R is the gas constant, T is the absolute temperature, and D_p is the effective diffusivity for oxygen in graphite pores. The value of D_p (in ft^2/hr) can be found from the relation

$$D_p = \frac{0.233\ \epsilon^2}{P} \left(\frac{T}{273} \right)^{1.5} , \qquad (4)$$

where ϵ is porosity (pore volume divided by total sample volume) and P is the absolute pressure in atmospheres.

By combining Eqs. (1), (2), (3), and (4), and substituting numbers, the following equation for heat release was obtained:

$$\frac{Q}{S} = 7.53 \times 10^7 \left(\frac{T}{1660} \right)^{0.25} e^{-19\ 900/T} , \qquad (5)$$

where, in this case, Q is in Btu/hr, S is in ft^2, and T is in °R. Equations (1) and (5) were intended to be preliminary and subject to revision as actual data on EGCR graphite became available from the Hanford tests. Preliminary results show that the oxygen dependency is not first order, being approximately 0.62 order at 500°C and 0.79 order at 600°C. The actual EGCR graphite-air reaction data can therefore be fitted by the equation

$$k_{EGCR,\ air} = 8.13 \times 10^9\ e^{-23\ 600/T} . \qquad (6)$$

This equation is remarkably close to the least-squares equations found by Prados[26] over the temperature range of interest.

At the present time it appears that coating of the sleeves will be effective in inhibiting graphite oxidation in the EGCR. Experimental and analytical work is under way to verify this, and work will continue in evaluating some of the other possible schemes.

Identification of Maximum Credible Loss of Pressure Accident for EGCR (H. N. Culver)

The loss of pressure accident that was described in the preliminary hazards report for the EGCR[27] was postulated to result from the double-ended failure of the coolant-system piping. The double-ended failure was assumed, initially, not because such a failure was believed to be credible, but because the consequences of any other failure whose credibility was unevaluated would not exceed the consequences of the double-ended failure. Such an assumption was justified because information was not available at the time the preliminary report was written for evaluating all possible modes of failure.

Since the design is nearing completion, the AEC appointed a task force, consisting of representatives from Kaiser Engineers, Allis-Chalmers, Oak Ridge National Laboratory, and the Tennessee Valley Authority, for the specific task of establishing the largest or most serious loss of pressure accident that can be considered as credible in the EGCR as it is being designed and constructed. The task force completed their assignment in December 1960 with a report[28] that discusses the modes of failure which are possible in high-temperature, high-pressure piping systems and then reviews the failure experience that exists in systems under somewhat comparable conditions. This background information is then used in evaluating the probability of failure of various parts of the EGCR coolant system.

The task force concludes in the report that the maximum credible loss-of-pressure accident in the EGCR will not expose an area of the pressurized helium system any greater than the cross sectional area of the largest pipe if a number of recommendations are followed. Included in the recommendations

---

[27]"Experimental Gas-Cooled Reactor Preliminary Hazards Summary Report," ORO-196, with Supplement, May 1959.

[28]Unpublished report dated December 1960.

are (1) measures to physically restrict the displacement of piping in some key locations, in the unlikely event of a circumferential failure, and (2) statements which emphasize the importance of rigid control of specifications, inspection, fabrication, choice of materials, and testing. The study points out the difficulty of defining "maximum credible" in realistic terms. The credibility of a failure must necessarily be related to a finite probability, but the determination of the probability cannot be based on technical considerations alone. Although it may be possible to eliminate many types of failure by proper design, there always exists a small probability that human error has been introduced into design, fabrication, inspection, or operation. Therefore although recommendations were established to reduce the incidence of failure, it was not possible to eliminate the credibility of failure. Likewise, in determining the maximum size opening, the human error must be considered. Although the general approach to the problem is to use ductile materials so that if a failure occurs it will result in small cracks or longitudinal breaks, the human error which may be introduced into the materials during fabrication makes it possible that the ductility of the material may be reduced during its lifetime. Thus, although recommendations are made to reduce the probability of such human errors, the possibility of a failure being larger than expected in ductile material cannot be eliminated completely. A single-ended failure is therefore defined as the maximum credible failure based on (1) physically restricting the piping system in key locations so that double-ended failure is not possible and (2) providing for inspections and tests to preclude the possibility of a nonductile failure for the portion of the piping external to the biological shield.

Empirical Representation of Neutron Exposure of Moderator Columns in EGCR

(F. J. Stanek)

It is known that nuclear irradiation of graphite bodies causes dimensional changes, which, in turn, may induce severe internal stresses. A study of such stresses and the strains is analogous to a study of the

stresses and strains caused by temperature variations within the body. The irradiation effect is primarily the result of fast-neutron exposure, and the mathematical expression for the exposure replaces the temperature function in the theory of thermoelasticity.

Theoretical values for the fast-neutron flux distribution over the mid-plane of the core region in the EGCR have been obtained numerically,[29] but an analytical expression for the exposure is needed in evaluating the induced stresses. Therefore an attempt was made to derive an empirical formula that would give a good approximation of the numerical results. A formula for each column that could be solved by simple analytical means from a relatively small set of tabulated values was sought. The results of this study[30] are summarized here.

The general form of the empirical formula consists of 49 terms that reduce to seven terms when one of the coordinates is held constant. The formula is written in the following matrix form:

$$D(x,y) = [-1 \quad y/16 \quad \cos\beta y \quad \cos 2\beta y \quad \cos 4\beta y \quad \sin\beta y \quad \sin 2\beta y]\, A \begin{bmatrix} -1 \\ x/16 \\ \cos\beta x \\ \cos 2\beta x \\ \cos 4\beta x \\ \sin\beta x \\ \sin 2\beta x \end{bmatrix}$$

where

$D(x,y)$ = exposure distribution over an individual 16-in. by 16-in. graphite block in megawatt days per adjacent ton for a 20-yr period times 10^{-4},

x,y = rectangular coordinates for a single block,

$\beta = \pi/8$, a proportionality factor for converting linear coordinates to angular coordinates,

A = 7 by 7 coefficient matrix.

---

[29] "GCR Quar. Prog. Rep. Sept. 30, 1959," ORNL-2835, pp. 3–4.

[30] F. J. Stanek, "Empirical Representation of the Neutron Exposure of the Moderator Blocks in the EGCR," ORNL CF-60-9-4 (Nov. 11, 1960).

The values of the 49 constant coefficients (the elements of matrix A) of the general empirical formula were calculated from an original set of 81 values corresponding to points uniformly distributed over the cross section of the column. The detailed development of the empirical formula and the method for calculating the values of the 49 coefficients are given in a report[30] that also includes the values of these coefficients for each column in one octant of the core (10 columns), which is sufficient because of the core symmetry.

A detailed graphical comparison of the empirical results with the original numerical data for column No. 82 is given in Figs. 3.25 through 3.29, where the variation along one coordinate, y, is shown for the designated values of the other, x. The plot of the numerical data is shown as a smooth curve and the values from the empirical formula are shown as small circles. The cross section and the relative position of column No. 82 are shown in Fig. 3.30. The accuracy of the empirical representation for

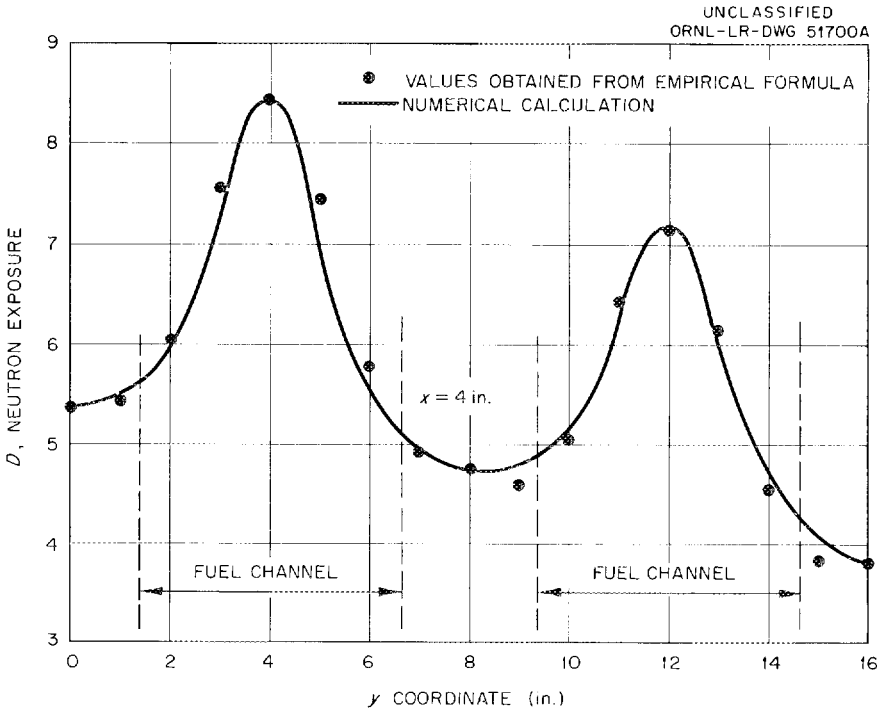


Fig. 3.25. Comparison of Exposure Distribution Obtained from the Empirical Representation with that Calculated Numerically for Column No. 82 at x = 4 in.

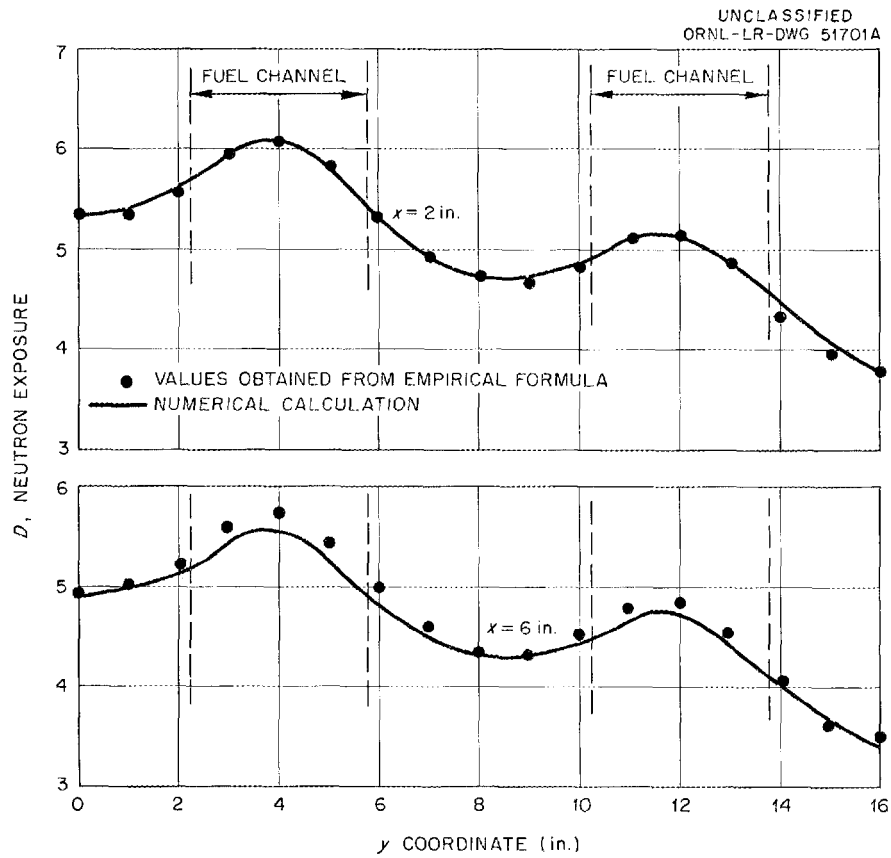


Fig. 3.26. Comparison of Exposure Distribution Obtained from the Empirical Representation with that Calculated Numerically for Column No. 82 at x = 2 and 6 in.

each of the other columns that contain four fuel channels is of the same order of magnitude as that shown for column No. 82.

The empirical representation gives a very good approximation for those columns which contain four fuel channels and is considered sufficiently accurate, for most practical purposes, for those which contain less than this number. There are three columns (in the set of ten) which do not contain four channels, and the graphical comparison for each is also shown in the report.[30]

Estimate of Irradiation-Induced Bowing of Graphite Columns

(S. E. Moore, W. A. Shaw)

Fast-neutron exposure will lead to lateral deflection or bowing in each graphite column because the shrinkage in these members will not be

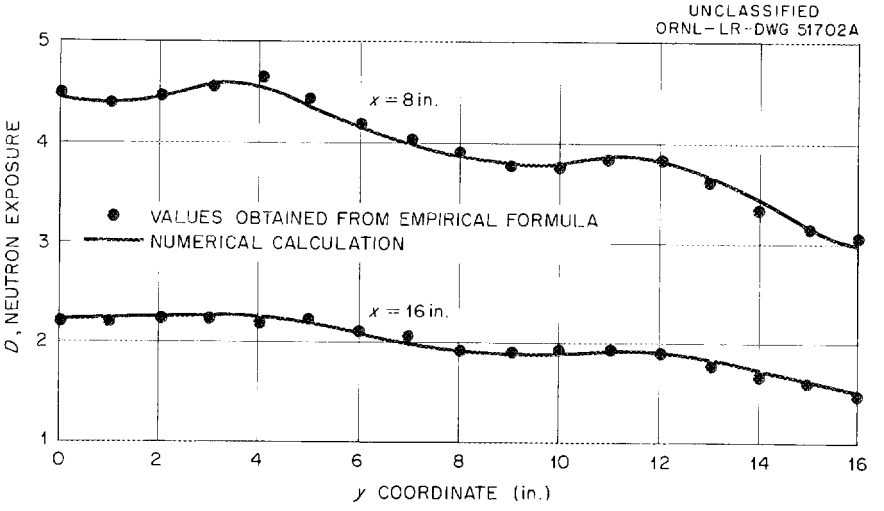


Fig. 3.27. Comparison of Exposure Distribution Obtained from the Empirical Representation with that Calculated Numerically for Column No. 82 at x = 8 and 16 in.

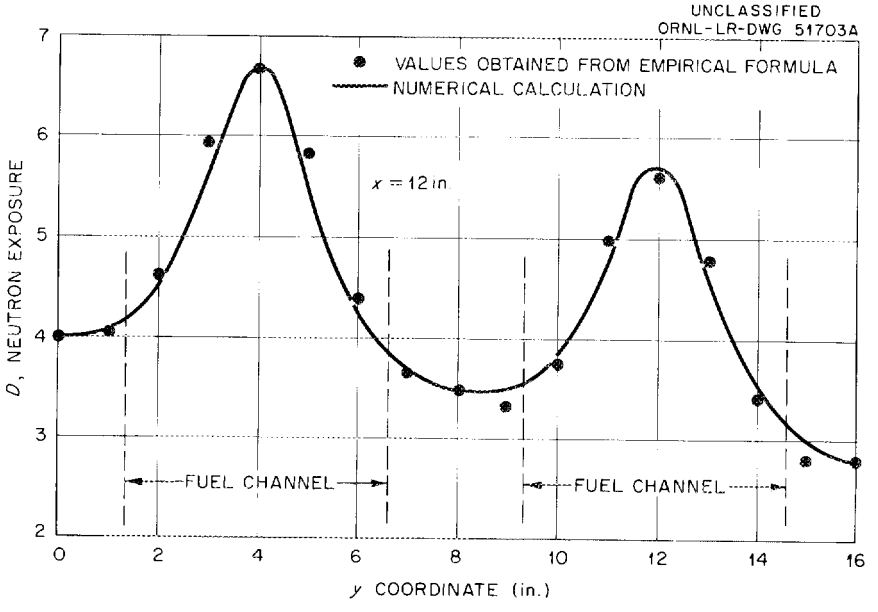


Fig. 3.28. Comparison of Exposure Distribution Obtained from the Empirical Representation with that Calculated Numerically for Column No. 82 at x = 12 in.

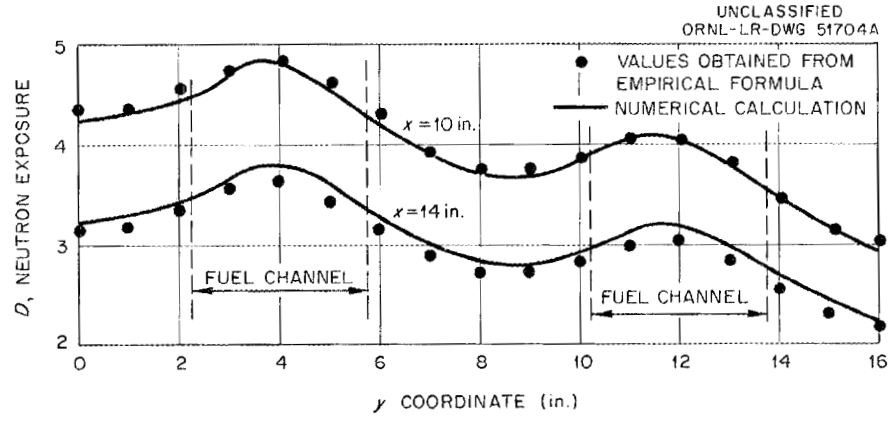


Fig. 3.29. Comparison of Exposure Distribution Obtained from the Empirical Representation with that Calculated Numerically for Column No. 82 at x = 10 and 14 in.

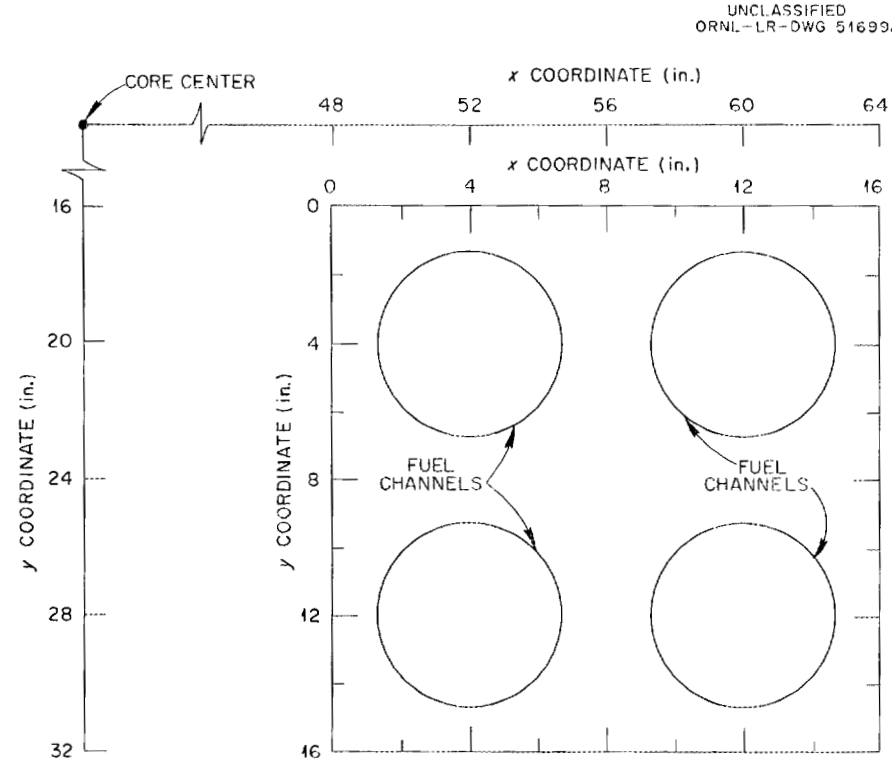


Fig. 3.30. Cross Section and Relative Position of Graphite Column No. 82.

axi-symmetrical. The amount of unrestrained movement will be limited, however, by steel bands around the periphery of the EGCR core. Therefore, stresses will be induced in the columns from this source and lateral forces will be exerted upon the structural members at the top and bottom of the core. Hence, an evaluation of the free lateral deflection for each column is required as a basis for determining the stresses in the graphite and for designing the support structures.

The exposure for a column can be described in the axial direction by a cosine function, as shown in Fig. 3.31, but normal to the axis it is considerably more irregular, as shown in Figs. 3.25 through 3.29. Lines of equal exposure for a column cross section at the mid-plane are shown in Fig. 3.32. The complicated nature of the flux distribution prohibits an exact analysis of the bowing. An estimate can be made, however, by assuming that the strain in the axial direction is unaffected by the transverse stresses, or

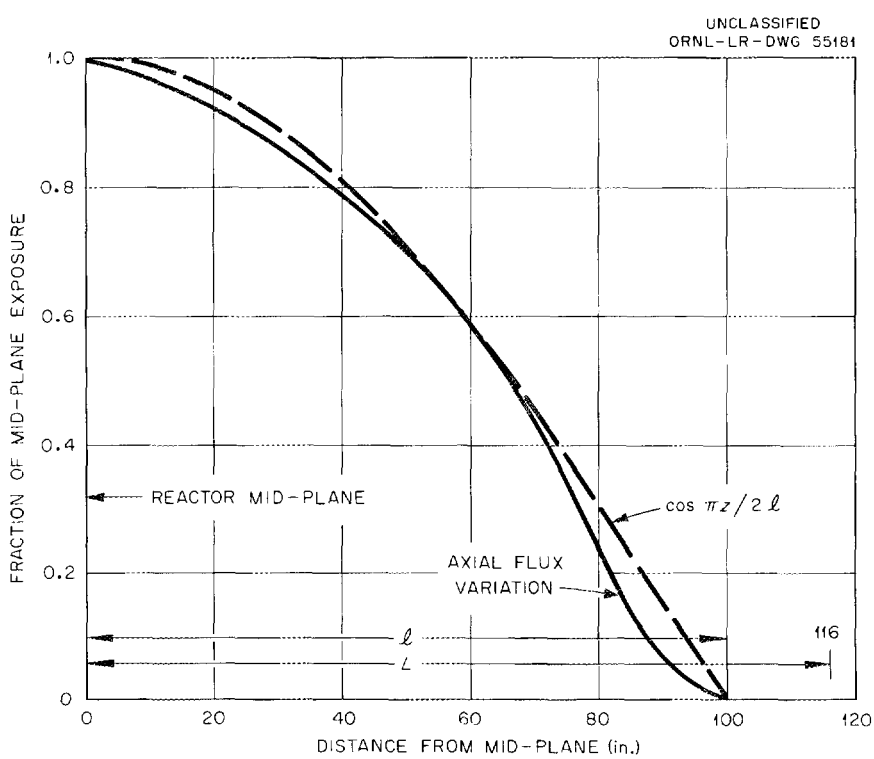


Fig. 3.31. Fast-Neutron Exposure Distribution in EGCR Graphite Column in Axial Direction.

$$\epsilon_z = \gamma D + c \quad ,$$

where ϵ_z is the normal strain component in the axial direction, γ is the coefficient of irradiation growth or shrinkage, D is the neutron exposure, and c is a constant (different for each fiber) such that plane cross sections remain plane.

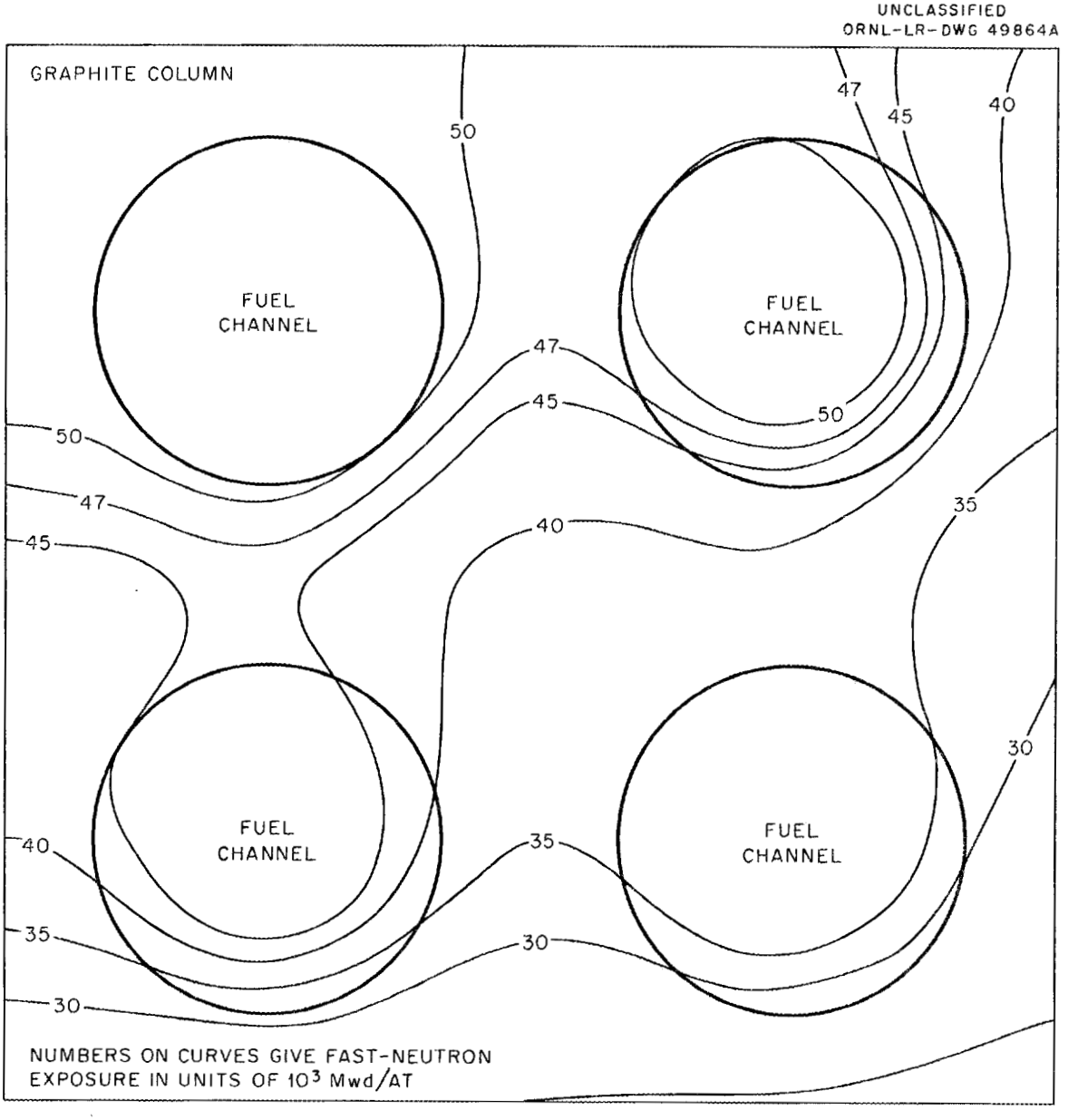


Fig. 3.32. Lines of Equal Fast-Neutron Exposure in Graphite Column No. 103.

If a generic slice with length Δz is taken from a column, as in Fig. 3.33, according to the assumptions, each unrestrained fiber (i.e., $C = 0$) will elongate a length

$$\epsilon_z \Delta_z = \gamma D \Delta z \quad .$$

If the base plane of the slice is taken as a reference, then the top plane will become a warped irregular surface corresponding to the irregularity of the flux. The assumption that plane sections remain plane requires that the warped surface be approximated by a plane. The new configuration of the slice is equivalent to a uniform extension plus a rotation of the top plane relative to the base plane. Only the latter contributes to the bowing of the column.

The neutron exposure of each graphite column is a function of time, t, as well as the space coordinates. This function is approximately of the form

$$D(x,y,z,t) = \psi(x,y,t) \cos \frac{\pi z}{2l} \quad , \qquad 0 \leq z \leq l$$

$$D(x,y,z) = 0 \quad , \qquad l < z \leq L$$

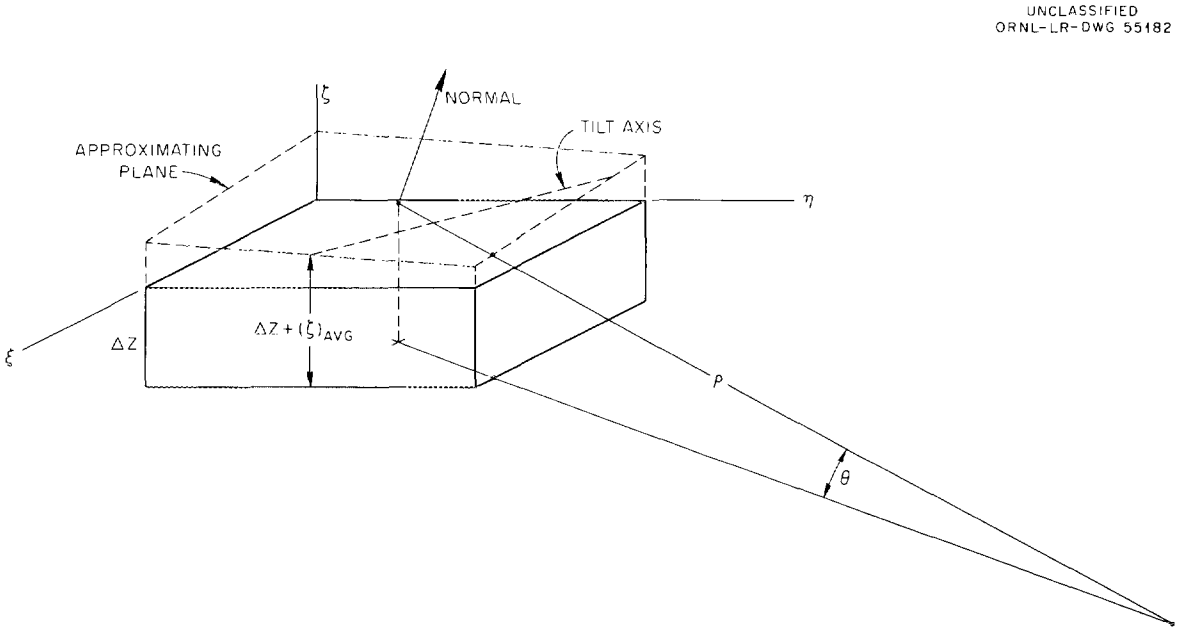


Fig. 3.33. Geometry for Study of Irradiation-Induced Bowing.

where l is the length corresponding to the intersection of the cosine curve and the horizontal axis in Fig. 3.31, and L is one-half the column length (116 in.). The length l was taken as 100 in. in all cases, even though it varies slightly from column to column. The function $\psi(x,y,t)$, which is the exposure at the reactor mid-plane may be obtained from the tabulated values for the neutron flux.

The unrestrained elongation of a longitudinal fiber of a slice Δz in length is

$$\delta = \epsilon_z \Delta z \quad ,$$

and the new position of each cross point relative to its original position is given by

$$\zeta_{ij} = \left(\gamma \psi_{ij} \cos \frac{\pi z}{2l}\right) \Delta z \quad , \qquad 0 \leq z \leq l$$

where ψ_{ij} is the tabulated exposure value for $x = i$ and $y = j$.

The equation of the approximating plane may be obtained relative to the axes at the original position of the top surface (see Fig. 3.33). Using the axes shown and dropping the subscripts, the equation may be written in the general form

$$\zeta = A\xi + B\eta + C \quad .$$

The coefficients may be determined by using the computed data points ζ_{ij} for any values of z and Δz. For convenience, let

$$\overline{\zeta}_{ij} = \frac{\zeta_{ij}}{\gamma \Delta z \cos \frac{\pi z}{2l}} \quad (=\psi_{ij}) \quad .$$

Then,

$$\overline{\zeta}_{ij} = \overline{A}\xi + \overline{B}\eta + \overline{C} \quad ,$$

so the flux data may be used directly in the calculations.

The coefficients $\overline{A}$, $\overline{B}$, and $\overline{C}$ have been computed by the method of least squares for the numbered columns in Fig. 3.34. Using these data, the radii of curvature (the radius is designated by ρ in Fig. 3.33) and, hence, the deflection components in the x and y directions were calculated. The results are given in Table 3.7 for a 20-yr exposure time. From this table it may be seen that column 93 has a bowing potential of 3.61 in. along both axes.

Table 3.7. Unrestrained Bowing of EGCR Graphite Columns

Column No.	Deflection in x Direction (in.)	Deflection in y Direction (in.)
67	1.65	1.65
79	0.50	−0.95
80	0.32	0.32
91	0.46	1.42
92	1.46	1.73
93	3.61	3.61
102	0.44	3.46
103	1.37	3.03
104	3.45	1.56
105	0.67	0.67
111	0.10	2.17
112	0.26	1.80
113	0.58	0.77
114	0.09	0.11
118	0.003	0.074
119	0.018	0.063
120	0.021	0.053

Structural Investigations of EGCR Through Tubes

Instantaneous collapse and creep buckling tests of type 304 stainless steel cylindrical shells are being conducted in order to obtain data applicable to the experimental tubes in the EGCR. The major portion of the work consists of model tests, but specimens near the sizes of the tubing for the reactor are also being used.

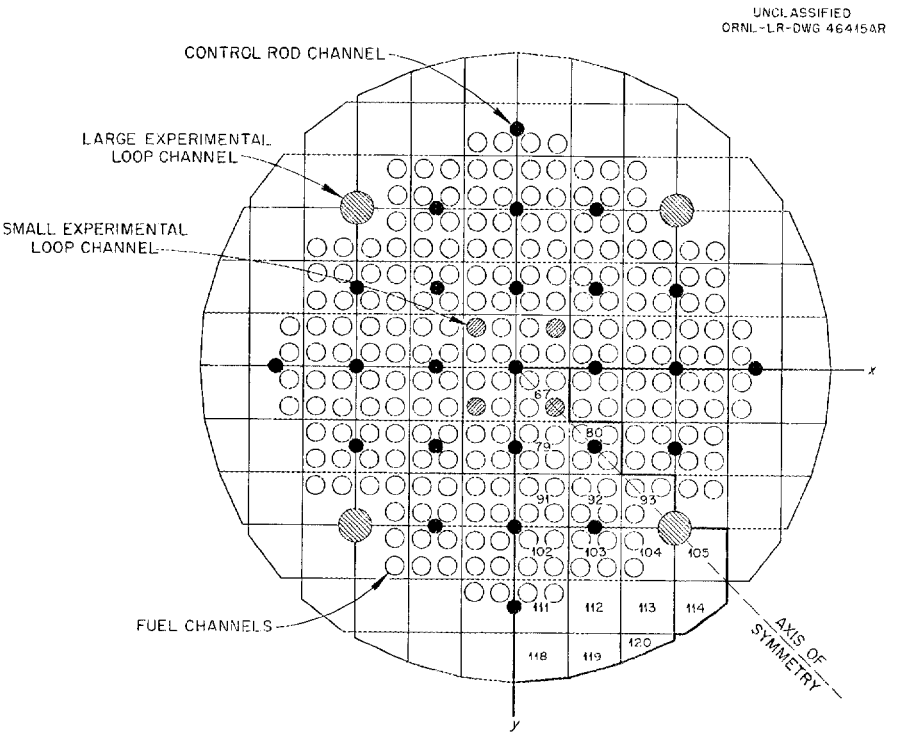


Fig. 3.34. Plan View EGCR Core Showing Numbered Columns for Which Coefficients $\overline{A}$, $\overline{B}$, and $\overline{C}$ Have Been Computed.

Model Tests (J. T. Venard)

The primary objective of the creep buckling work is to obtain a critical pressure versus time correlation for specially machined round tubes with a common mean radius-to-thickness ratio. In preliminary tests with tubes nominally 0.750 in. in outside diameter and 0.025 in. in wall thickness, one tube collapsed in 26 hr with an external pressure of 750 psi and another collapsed in approximately 2800 hr with an external pressure of 600 psi.

The geometrical variables are also being studied in tests of 0.75-in.-o.d. specimens with 0.015-, 0.020-, 0.025-, and 0.030-in. wall thicknesses and 1.00-in.-o.d. specimens with a 0.033-in. wall. The data for 0.75-in.-o.d., 0.025-in.-wall shells will be used for the basic correlation.

Tests have been performed to determine the instantaneous collapse pressure, P_c, as a function of the ratio of the mean radius, r, to the wall thickness, t, as well as the effects of the ovality ratio, k, which is defined as the ratio of the minimum diameter to the maximum diameter,

and wall thickness variations, V, which are defined by the expression

$$V = 100 \frac{t_{avg} - t_{min}}{t_{avg}} .$$

All experiments have been performed at 1200°F on specimens of type 304 stainless steel seamless tubing of essentially infinite length in diameters of 0.75 and 1.00 in. The experimentally determined curve of P_c vs r/t for values of r/t ranging from 10 to 25 is shown in Fig. 3.35. The effects of tube ovality and wall-thickness variations, respectively, are shown in Figs. 3.36 and 3.37.

Prototype Tests (J. C. Amos, J. M. Corum, R. L. Maxwell)

Two sets of large-diameter test units made from commercial tubing are being used in the prototype tests. For one set, 8.0-in.-o.d., 0.25-in.-wall tubes are used, and, for the other set, 4.0-in.-o.d., 0.12-in.-wall

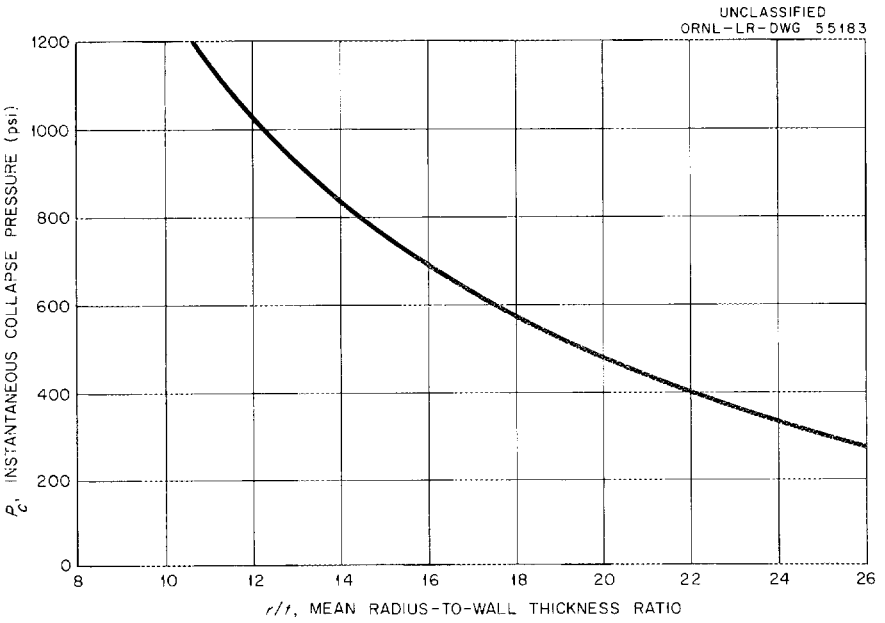


Fig. 3.35. Instantaneous Collapse Pressure Versus Mean Radius-to-Wall Thickness Ratio for Type 304 Stainless Steel Tubes Tested at 1200°F.

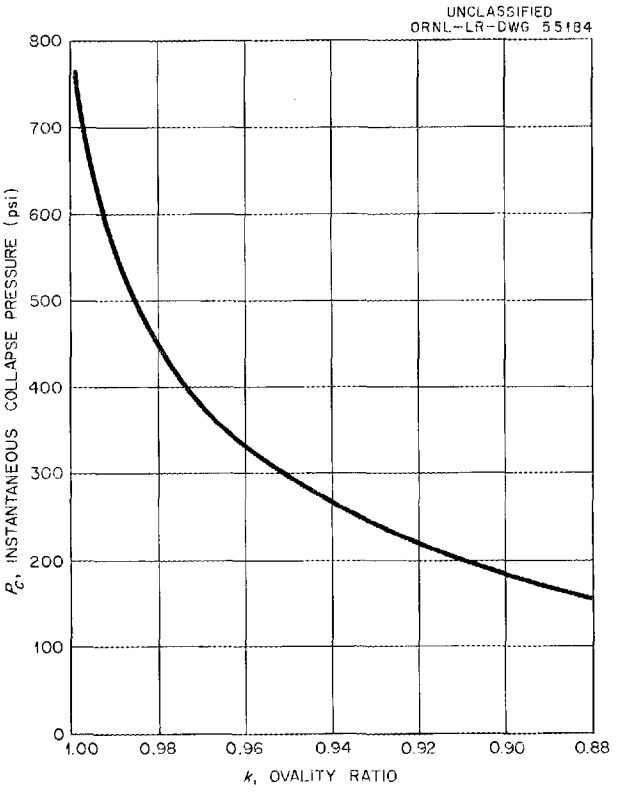


Fig. 3.36. Instantaneous Collapse Pressure Versus Ovality Ratio for Nominal 0.750-in.-o.d., 0.25-in.-Wall Type 304 Stainless Steel Tubes Tested at 1200°F.

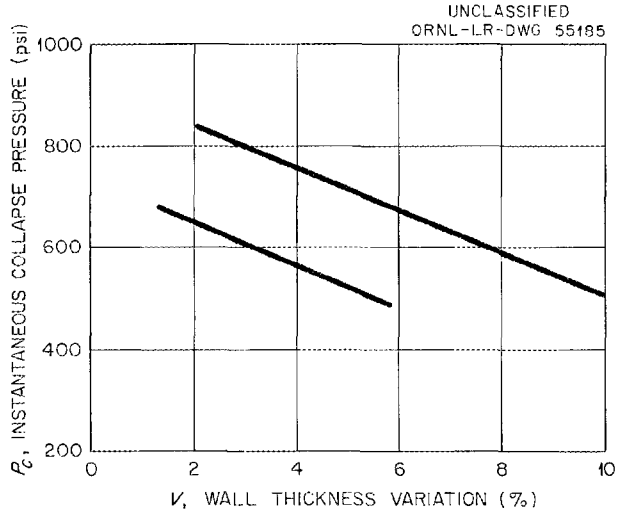


Fig. 3.37. Instantaneous Collapse Pressure Versus Wall-Thickness Variation of 0.750-in.-o.d. Type 304 Stainless Steel Tubes Tested at 1200°F.

tubes are used. The material for the larger specimens is type 304 stainless steel, but the smaller ones are made of both types 304 and 347 stainless steel so that the behavior of the two materials can be compared.

The first of a series of four 8.0-in.-o.d. tubes was tested to determine the instantaneous collapse pressure. The specimens were approximately 9 ft long and were purchased in accordance with ASTM A-213 TP-304 specifications. The average measured mean radius-to-thickness ratio was 15.00 and the ovality ratio was 0.9947. The tube failed under a pressure of approximately 805 psi, which agreed closely with the results obtained in the model tests despite the fact that a portion of the tube was at a temperature considerably below the maximum of 1200°F.

The test facility is an electrically heated autoclave designed to impose a 600-psi external pressure on a test specimen at 1400°F. A 6 1/2-in.-o.d. insert is used inside the test specimen to prevent jamming inside the autoclave as a result of excessive deformation. Two

separate alarm systems indicate collapse. The first utilizes an electrical circuit which rings an alarm bell when the specimen makes contact with the steel insert. The second is activated by the pressure increase due to a volume change in the annulus between the specimen and the insert.

In collapsing the first specimen, the system was pressurized to 50 psi with helium, and the autoclave was then brought up to temperature. After the temperature was stabilized, the pressure was gradually increased until the specimen collapsed. Because of limitations on heater control imposed by the furnace design, large temperature gradients existed along the length of the specimen. The average temperature along the unit immediately prior to collapse is shown in Fig. 3.38; the positions at which the diameter and wall thickness were measured before collapse are also shown.

The collapsed specimen is shown in Fig. 3.39. It collapsed into an elliptical shape with two bulges extending outward beyond the original circular form and two extending inward to form two lobes. An examination showed that the most pronounced change in shape occurred in the region

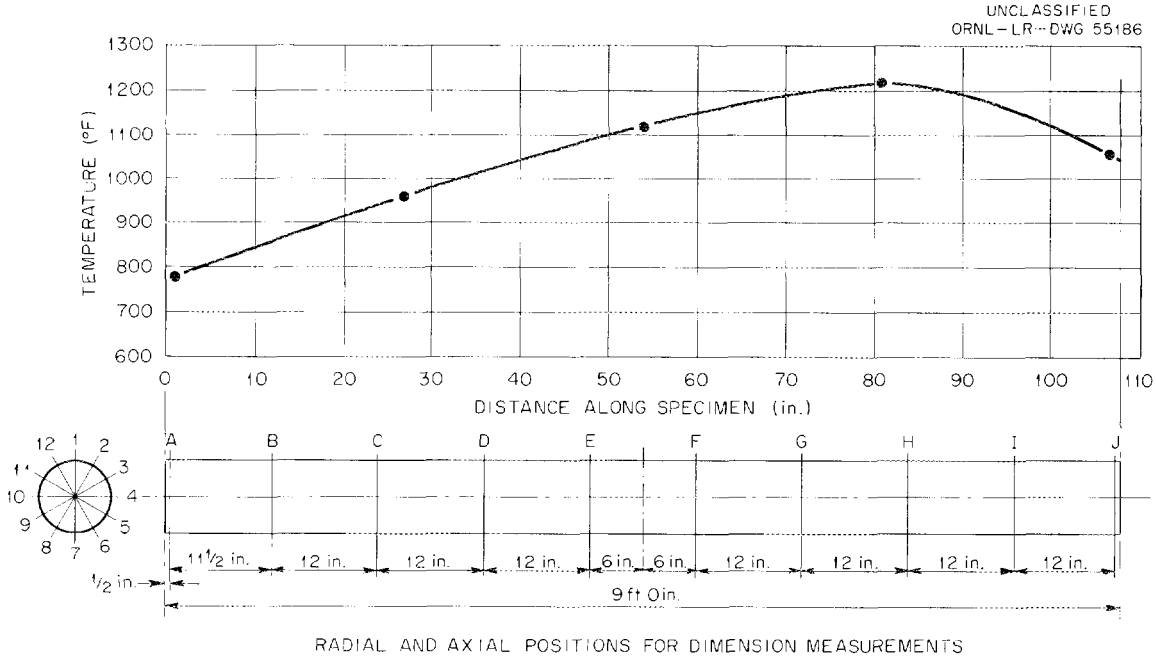


Fig. 3.38. Axial Temperature Distribution Along 8-in.-o.d. Tube at Time of Collapse and Diagram of Positions at Which Diameter and Wall Thickness Were Measured Before Collapse.

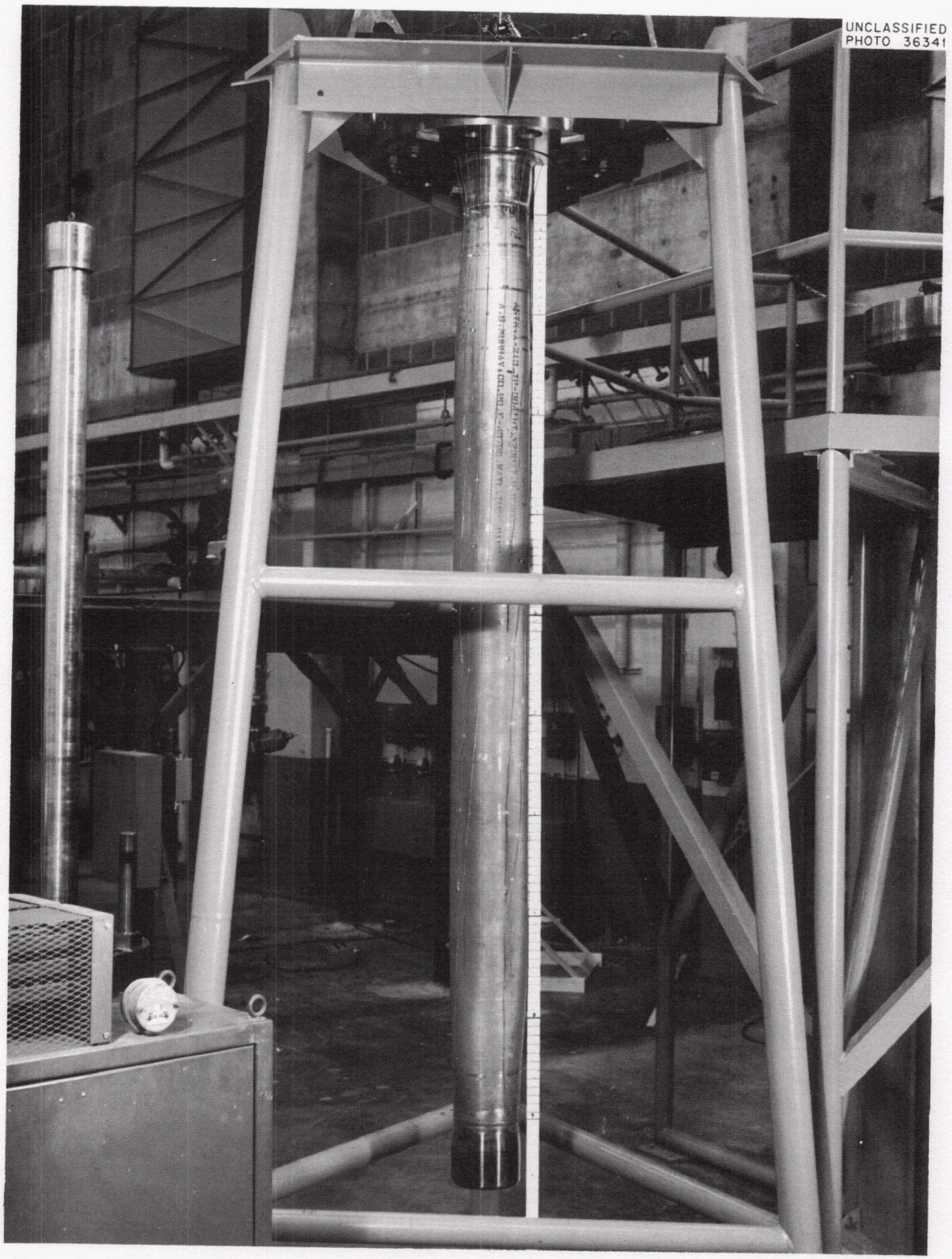


Fig. 3.39. Collapsed 8-in.-o.d., 0.25-in.-Wall Type 304 Stainless Steel Tube.

that was at a temperature of 1200°F. This portion of the collapsed tube is shown in Fig. 3.40. The original variation in outside diameter and wall thickness around the tube at plane H (indicated in Fig. 3.38) is shown graphically in Fig. 3.41. A circle was chosen to represent the nominal 8.0-in. outside diameter. The actual outside diameter was drawn by greatly magnifying the deviations from the nominal diameter. The wall thickness variation was plotted in a similar manner. As an example of the exaggeration, the actual diametral deviation at the 5-11 diameter was +0.0187 in., and the wall thickness deviation at point 5 was +0.0119 in. Figure 3.41 is actually representative of each cross section along the tube, that is, the maximum diameter occurred along diameters 4-10 and 5-11 in every case. In addition, the wall was thinner at points 9 through 12 at most cross sections. Thus, by observing from Fig. 3.40 that the maximum diameter after collapse was at the 4-10 diameter, it may be concluded that the tube collapsed into the same shape as the original variations. Also, it may be seen from Fig. 3.40 that the thinner wall near point 11 deformed concavely outward while the thicker wall at points 2 and 3 remained concave inward. Thus, the tube behaved as would be predicted from the original dimensional variations.

Because of variations in material properties with temperature, the axial temperature gradient probably had some effect on the specimen that would be similar to the end effects for a short tube. Therefore additional heaters with separate controls are being installed in the autoclave before the second specimen is tested. With these heaters and additional insulation at the top of the autoclave, a much more uniform temperature can be obtained.

One 4.0-in.-o.d., type 304 stainless steel tube and one 4.0-in.-o.d., type 347 stainless steel tube have also been tested. Both specimens were approximately 5 ft long and were purchased in accordance with ASTM A312-58T specifications. The type 304 stainless steel tube collapsed under an external pressure of 590 psi while at a uniform temperature of 1200°F. The critical pressure for this tube also agreed with the results obtained from the model tests. The type 347 stainless steel tube failed under an external pressure of 990 psi, but the effective temperature was approximately 900°F.

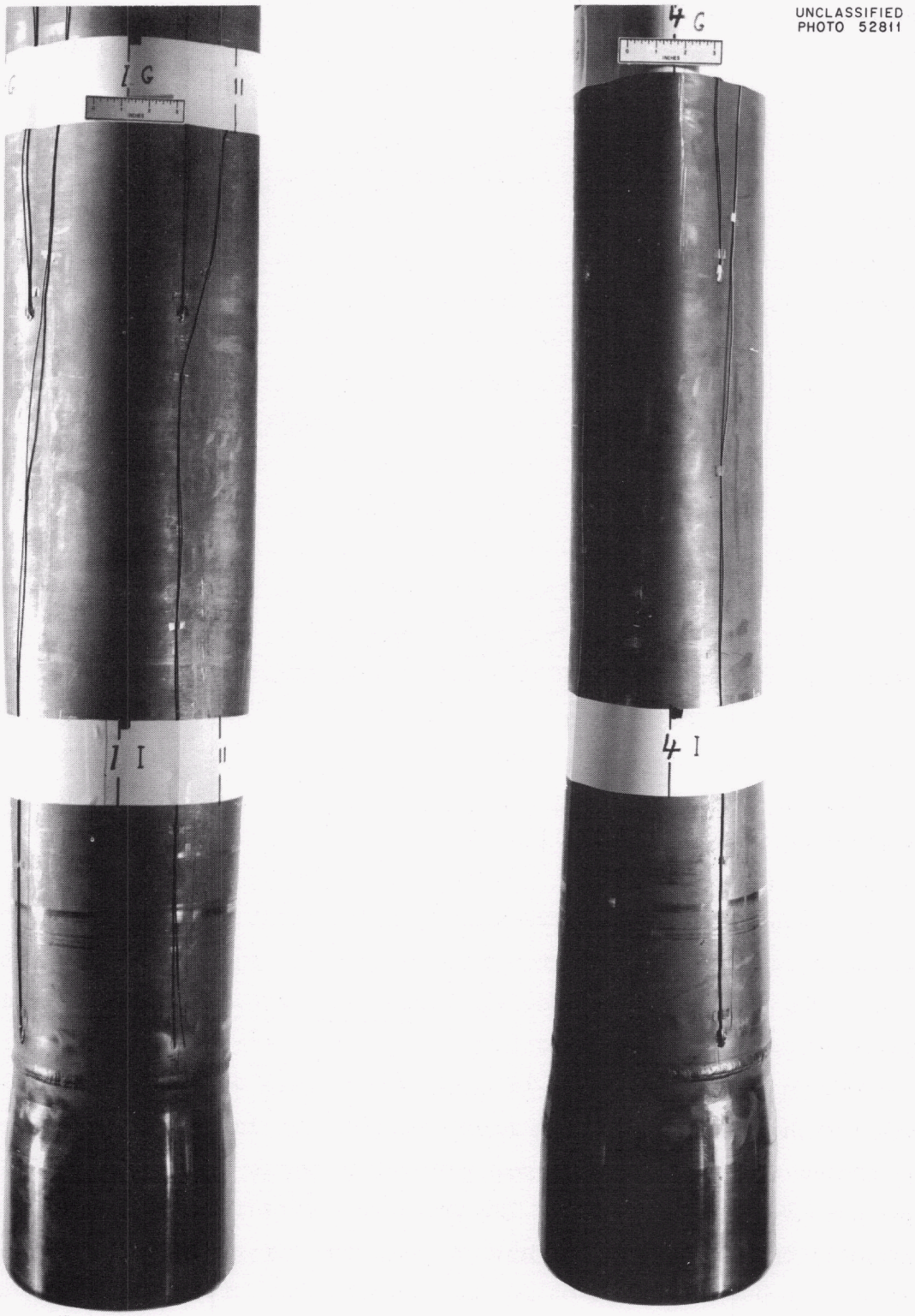


Fig. 3.40. Portion of Collapsed 8-in.-o.d. Tube That Was Subjected to the Highest Temperature.

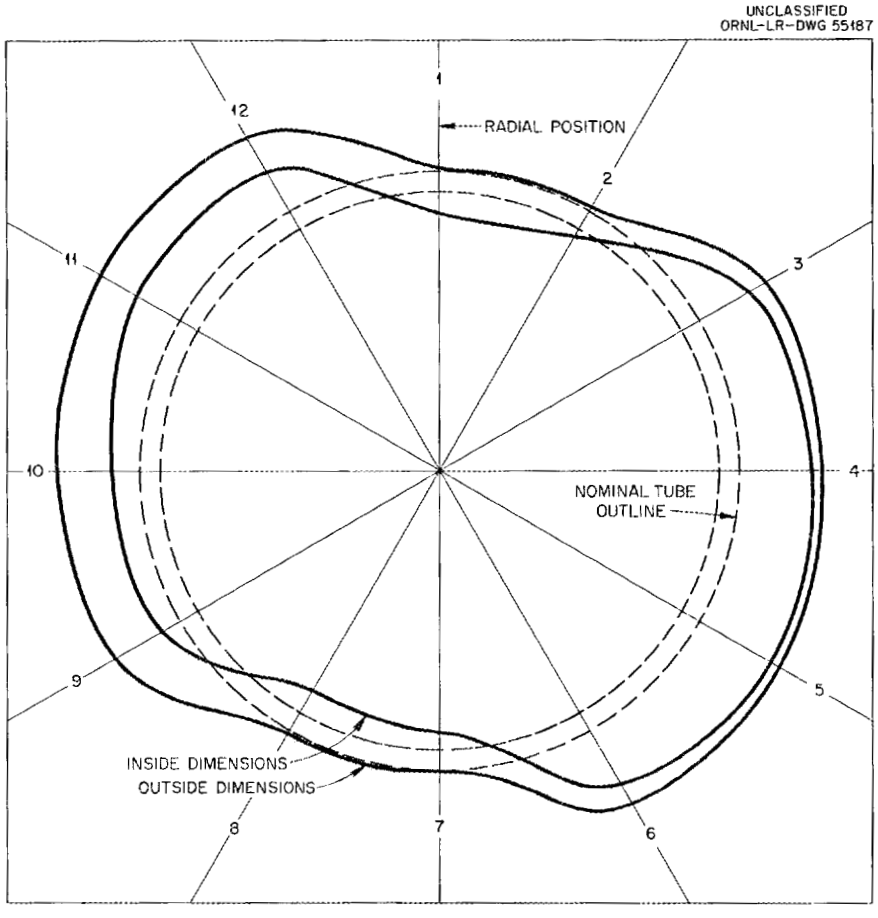


Fig. 3.41. Exaggerated Dimensional Variations at Plane H Prior to Collapse of 8-in.-o.d. Tube.

The tubes were mounted vertically in the test furnace with the type 304 stainless steel tube on top and the type 347 stainless steel tube underneath. The alarm systems used for these tests are the same as those used in the 8-in. tube testing facility. The tubes were evacuated and filled with helium to a pressure of 15 psi. The furnace was then evacuated and filled with helium to a pressure of 100 psi. Following this the furnace was heated slowly to the desired temperature while simultaneously bleeding the tube pressure to 10 psi. The pressure in the furnace was then gradually increased by the addition of helium until the top tube collapsed at a differential pressure of 590 psi. The pressure was further increased until the type 347 stainless steel tube collapsed at a differential pressure of 990 psi. The pressure required for collapse was affected by the fact that

portions of the lower half of the furnace were as much as 300°F below the desired 1200°F temperature. This situation resulted from the addition of cold helium.

The dimensional variations for both the type 304 and type 347 stainless steel specimens are listed in Tables 3.8 through 3.11. Measurements were made at seven planes along the length of each specimen. Points 1 through 6 in Table 3.8 were at 60-deg intervals around the specimens at each plane.

The two collapsed specimens are shown in Fig. 3.42. Both tubes exhibited two-lobe collapse. For the type 304 stainless steel specimen the pronounced bulge occurred between points 1 and 2 along the upper end of

Table 3.8. Wall Thickness Variations of 4.0-in.-o.d. Type 304 Stainless Steel Tube Collapse Specimen

Radial Point of Measurement at 60-deg Intervals	Wall Thickness Variation from 0.120 in. in Thousandths of an Inch						
	Distance of Plane of Measurement from Top of Tube						
	1 ft	1.5 ft	2 ft	2.5 ft	3 ft	3.5 ft	4 ft
1	−6	−9	−14	−14	−13	−11	−8
2	−7.5	−10	−12	−12	−11	−8	−3.5
3	−8	−8	−8	−10	−9	−5	−2.5
4	0	+1	+2	−2	−2	0	0
5	+3	+3.5	+2	−2.5	−3	−2.5	−2
6	+1.5	−1.5	−5	−8	−8	−6.5	−6

Table 3.9. Diameter Variations of 4.0-in.-o.d. Type 304 Stainless Steel Tube Collapse Specimen

Diameter Measured	Diameter Variation from 4 in. in Inches				
	Distance of Plane of Measurement from Top of Tube				
	1 ft	2 ft	2.5 ft	3 ft	4 ft
1-4	0.0149	0.0146	0.0148	0.0155	0.0156
2-5	0.0118	0.0121	0.0135	0.0145	0.0141
3-6	0.0141	0.0154	0.0198	0.0190	0.0162

Table 3.10. Wall Thickness Variations of 4.0-in.-o.d. Type 347 Stainless Steel Tube Collapse Specimen

Radial Point of Measurement at 60-deg Intervals	Wall Thickness Variation from 0.120 in. in Thousandths of an Inch						
	Distance of Plane of Measurement from Top of Tube						
	1 ft	1.5 ft	2 ft	2.5 ft	3 ft	3.5 ft	4 ft
1	−5	−8.5	−10	−14.5	−11.5	−9	−7.5
2	−10	−12	−11.5	−10.5	−6	−2	+1
3	−7.5	−7	−2.5	−1	+1.5	+5	+7
4	+1	0	+4	+3.5	+5	+6	+5.5
5	+5.5	+3	+5.5	+1	+0.5	0	−2
6	+1.5	−2	−3.5	−8.5	−8.5	−8.5	−9.5

Table 3.11. Diameter Variations of 4.0-in.-o.d. Type 347 Stainless Steel Tube Collapse Specimen

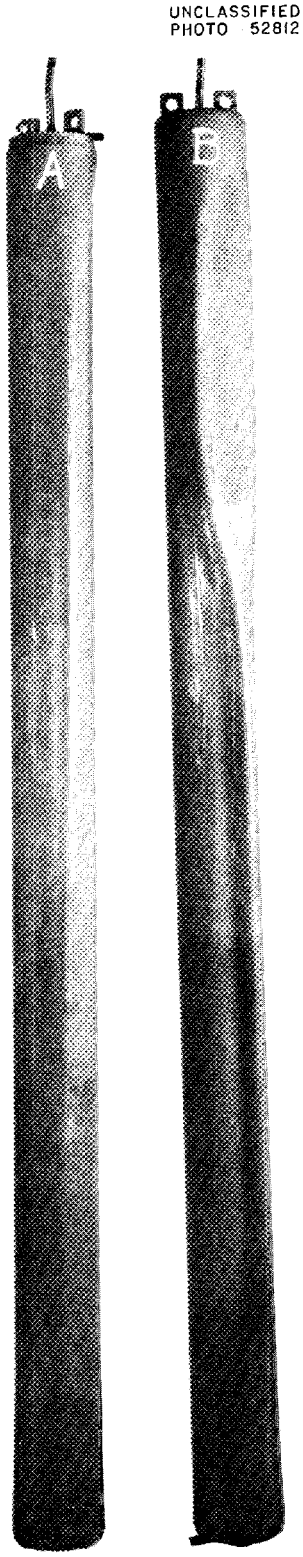
Diameter Measured	Diameter Variation from 4 in. in Inches				
	Distance of Plane of Measurement from Top of Tube				
	1 ft	2 ft	2.5 ft	3 ft	4 ft
1-4	0.0167	0.0110	0.0110	0.0109	0.0155
2-5	0.0078	0.0107	0.0100	0.0106	0.0100
3-6	0.0076	0.0068	0.0105	0.0082	0.0048

the tube and between points 3 and 4 for the remaining portion. The pronounced bulge occurred between points 1 and 2 along the entire length of the type 347 stainless steel tube. An examination of the dimensional deviations and the collapsed tubes reveals some correlation between the collapsed geometry and the original variations. However, the correlation is not nearly as apparent as for the 8.0-in.-o.d. specimen.

Experimental Stress Analysis of a Spherical Shell with an Attached Nozzle

(R. L. Maxwell, J. E. Smith)

When a structure is subjected to external loads which do not produce large deflections relative to the dimensions of the member so that the



loading is not affected by the deformation, and which do not induce stresses beyond the limit of elastic behavior for the material, the stresses are directly proportional to the applied loads. Thus the total stresses resulting from combined loadings may be obtained by linearly adding the stresses corresponding to each component separately applied, so long as the elastic limit is not exceeded. However, it was requested that this hypothesis be checked experimentally for the case of a single nozzle to shell attachment[31] because of the complex nature of the stress distribution in the vicinity of the juncture. The results of this investigation are described here to demonstrate the validity of superposition for elastic stress calculations.

A spherical segment with a single nozzle radially attached at the apex[32] was used, since this test model was available from previous investigations.[33] The model was instrumented with strain gages on both the inside and outside surfaces, and strains were measured in the tangential and meridional directions for the following loads: (1) 30-psi internal pressure, (2) 2000-lb axial load downward on nozzle, (3) 2000-lb axial load upward on

---

[31]Private communication from Kaiser Engineers, Oakland, California.

[32]"GCR Quar. Prog. Rep. Sept. 30, 1960," ORNL-3015, Fig. 2.7, p. 43.

[33]R. L. Maxwell and R. W. Holland, "Experimental Determination of Stresses in a Spherical Shell with Attached Pipe," The University of Tennessee Engineering Experiment Station (April 1959).

Fig. 3.42. Collapsed 4-in.-o.d. Specimens. Specimen A is a type 347 stainless steel tube and specimen B is a type 304 stainless steel tube.

nozzle, (4) combined 30-psi internal pressure load and 2000-lb axial load downward, and (5) combined 30-psi internal pressure load and 2000-lb axial load upward.

The total tangential stresses at the inside surface are given in Table 3.12 for loadings 1, 2, and 4. The gage numbers correspond to the similarly numbered radial lines in Fig. 3.43, since the gages are located at the intersections of these lines and the surfaces of the shell. The total tangential stresses at the outside surface for loadings 1, 2, and 4 are given in Table 3.13. Those at the inside and outside surfaces for loadings 3 and 5 are given in Tables 3.14 and 3.15, respectively. The values from loading 1 are also included for convenience in making comparisons.

The tangential stresses at the inside surface along the profile of the shell are given in Figs. 3.43 through 3.47. Those obtained by adding

Table 3.12. Total Tangential Stresses at Inside Surface for Loadings 1, 2, and 4

Gage No.	Tangential Stress (psi)			
	Loading 1, 30-psi Internal Pressure	Loading 2, 2000-lb Axial Load Downward	Loading 1 Plus Loading 2	Loading 4
1	427	1493	1920	1921
2	374	903	1277	1262
3	399	396	795	766
4	387	252	639	620
5	362	308	670	635
6	389	257	646	
7	375	256	631	631
8	386	225	611	618
9	390	204	594	601
10	374	208	582	533
11				
12	388	129	517	456
13	349	116	465	436
14				
15	218	159	377	281
16	137	104	241	223
17	67	104	171	135
18	−182	57	−125	−89

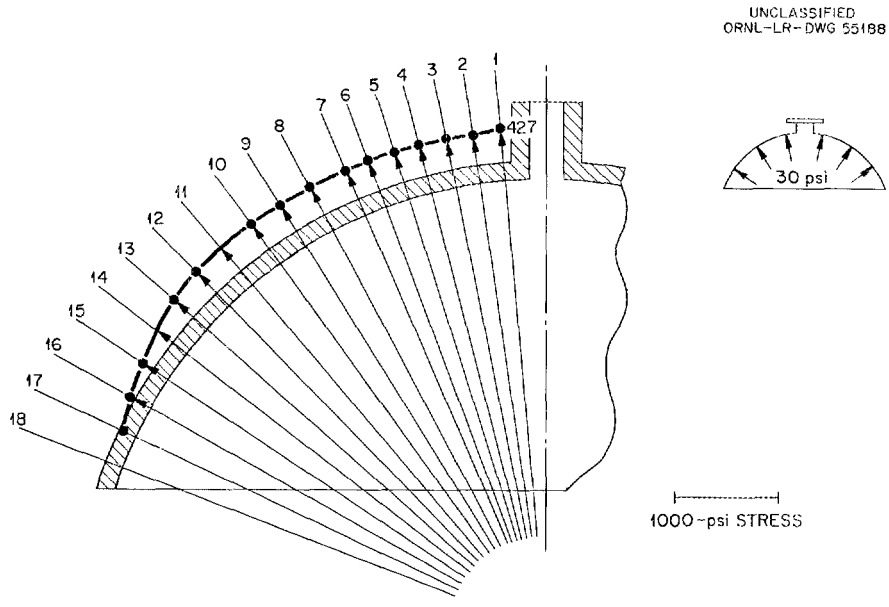


Fig. 3.43. Total Tangential Stresses at the Inside Surface Along the Profile of a Spherical Shell with an Attached Nozzle as a Result of 30-psi Internal Pressure Loading.

Table 3.13. Total Tangential Stresses at Outside Surface for Loadings 1, 2, and 4

Gage No.	Tangential Stress (psi)			
	Loading 1, 30-psi Internal Pressure	Loading 2, 2000-lb Axial Load Downward	Loading 1 Plus Loading 2	Loading 4
1	414	−2693	−2279	−2255
2	376	−1616	−1240	−1165
3	379	−699	−320	−318
4	373	−176	197	237
5	343	145	488	531
6	343	256	599	
7	314	303	617	602
8	333	258	591	615
9	497	241	738	675
10	347	174	521	547
11				
12	370	125	495	477
13	365	88	453	456
14				
15	275	69	344	376
16	144	90	234	253
17	−24	79	55	57
18	−182	57	−125	−89

Table 3.14. Total Tangential Stresses at Inside Surface for Loadings 1, 3, and 5

Gage No.	Tangential Stress (psi)			
	Loading 1, 30-psi Internal Pressure	Loading 3, 2000-lb Axial Load Upward	Loading 1 Plus Loading 3	Loading 5
1	427	-1518	-1091	-1054
2	374	-845	-471	-495
3	399	-408	-9	-23
4	387	-229	158	159
5	362	-298	64	100
6	389	-233	156	149
7	375	-235	140	73
8	386	-321	65	170
9	390	-187	203	213
10	374	-147	227	212
11		-93		242
12	388	-67	321	266
13	349	-52	297	247
14		-51		189
15	218	-52	166	145
16	137	-58	79	65
17	67	-62	5	-26
18	-182	-62	-244	-323

Table 3.15. Total Tangential Stresses at Outside Surface for Loadings 1, 3, and 5

Gage No.	Tangential Stress (psi)			
	Loading 1, 30-psi Internal Pressure	Loading 3, 2000-lb Axial Load Upward	Loading 1 Plus Loading 3	Loading 5
1	414	2716	3130	3155
2	376	1549	1925	2019
3	379	737	1116	1092
4	373	216	589	559
5	343	-115	228	220
6	343	-246	97	38
7	314	-300	14	36
8	333	-244	89	59
9	497	-252	245	143
10	347	-145	202	156
11		-123		242
12	370	-100	270	267
13	365	-70	295	288
14		-77		265
15	275	-77	198	177
16	144	-73	71	104
17	-24	-98	-122	-119
18	-182	-62	-244	-323

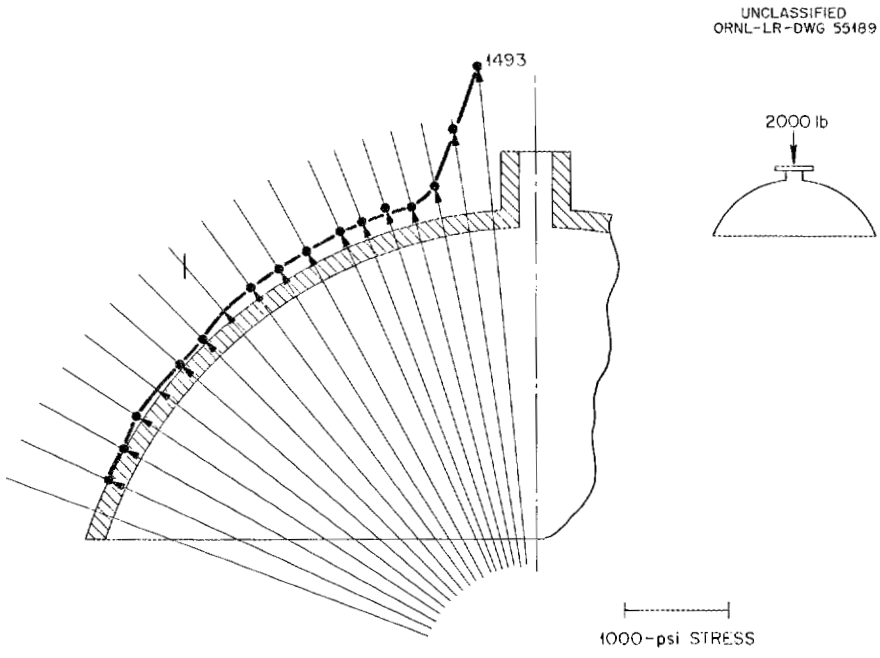


Fig. 3.44. Total Tangential Stresses at the Inside Surface Along the Profile of a Spherical Shell with an Attached Nozzle as a Result of a 2000-lb Axial Load Downward.

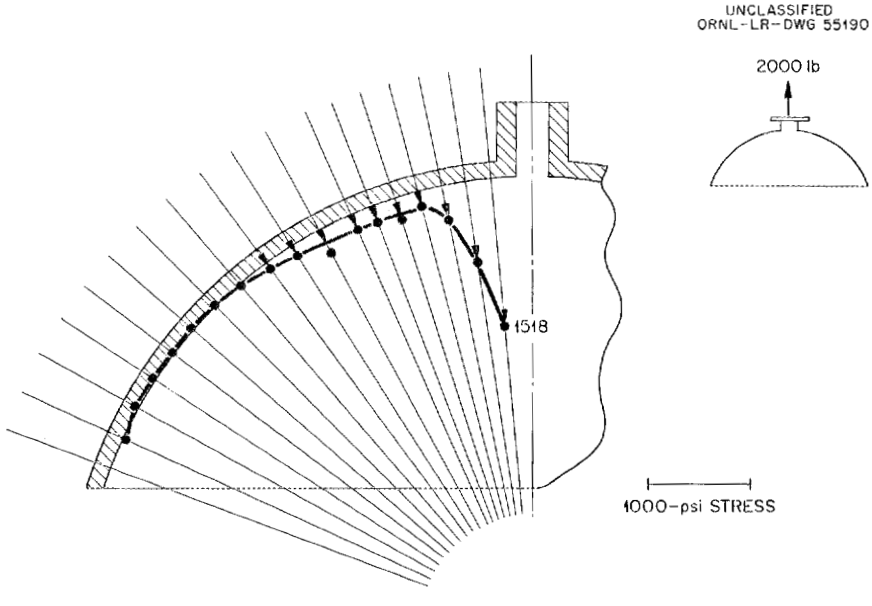


Fig. 3.45. Total Tangential Stresses at the Inside Surface Along the Profile of a Spherical Shell with an Attached Nozzle as a Result of a 2000-lb Axial Load Upward.

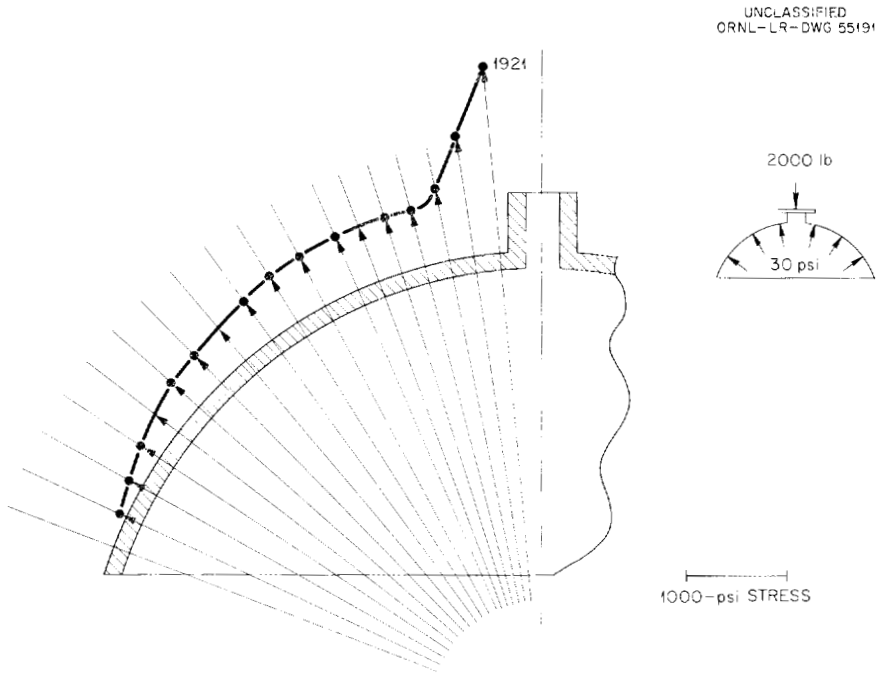


Fig. 3.46. Total Tangential Stresses at the Inside Surface Along the Profile of a Spherical Shell with an Attached Nozzle as a Result of a Combined 30-psi Internal Pressure Load and a 2000-lb Axial Load Downward.

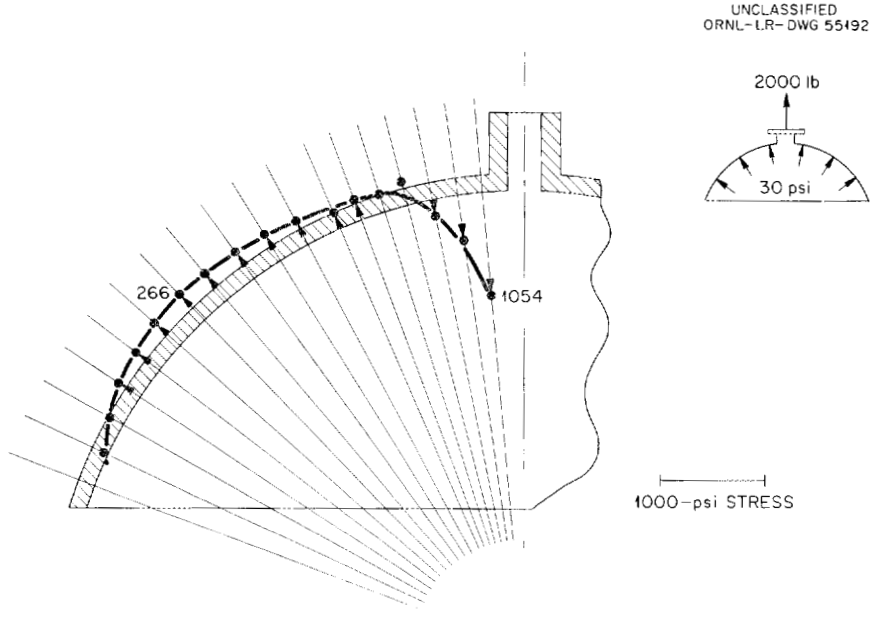


Fig. 3.47. Total Tangential Stresses at the Inside Surface Along the Profile of a Spherical Shell with an Attached Nozzle as a Result of a Combined 30-psi Internal Pressure and a 2000-lb Axial Load Upward.

the stresses from loads separately applied are given in Figs. 3.48 and 3.49. Comparisons of the stresses obtained from linear superposition of axial and pressure loadings with those for the combined loadings show that excellent agreement exists. Any differences are attributable to experimental error. In addition, the fact that reversing the direction of the axial load corresponds to changing the signs of the stress values is clearly demonstrated. The observations made here in regard to the tangential stresses are also true for those in the meridional direction.

Stress Analysis of Compressor for GCR-ORR Loop No. 2

(F. J. Stanek)

The compressors for GCR-ORR in-pile loop No. 2 have water-cooled pressure-vessel bodies. The cooling water flows in a passage formed by the outer surface of the shell and a thin metal jacket. At one end the shell attaches to a massive flange that forms a part of the volute, and the jacket terminates within approximately 5/8 in. of this flange. The

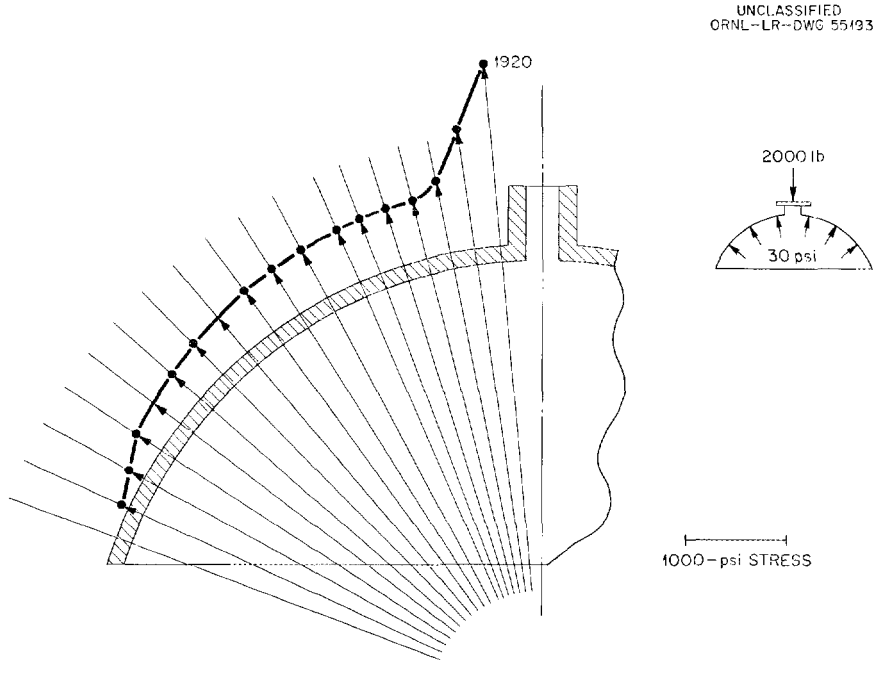


Fig. 3.48. Total Tangential Stresses at the Inside Surface Along the Profile of a Spherical Shell with an Attached Nozzle as a Result of a 30-psi Internal Pressure and a 2000-lb Axial Load Downward Applied Separately.

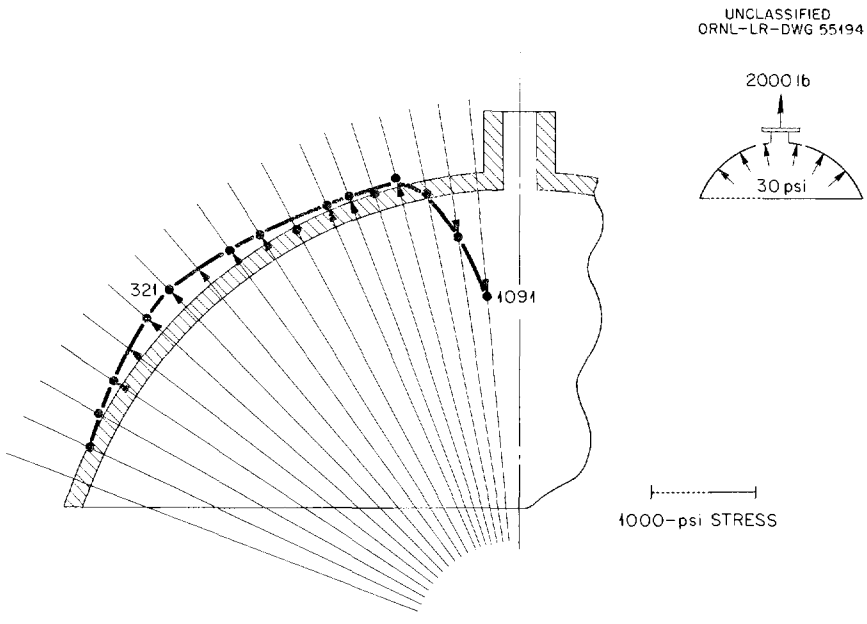


Fig. 3.49. Total Tangential Stresses at the Inside Surface Along the Profile of a Spherical Shell with an Attached Nozzle as a Result of a 30-psi Internal Pressure and a 2000-lb Axial Load Upward Applied Separately.

temperature of the gas in the volute will range from 600 to 700°F, while the maximum water temperature will be approximately 100°F. As a result, high thermal stresses will occur in the region of the junction of the pressure-vessel body and the flange.

The thermal stresses may be reduced if the portion of the cyclinder adjacent to the flange is held at or near the flange temperature. Increasing the distance over which the temperature change occurs will also reduce these stresses. Therefore a study was made to evaluate the effects of these factors and to provide data for guidance in making design changes.

The pressure-vessel body behaves as an infinitely long, thin-walled cylindrical shell with one edge fixed against rotation, as illustrated in Fig. 3.50. Since a temperature change that is linear with length occurs in the flange region, an axisymmetrical temperature distribution with an axial profile, as shown in Fig. 3.51, was used in the analysis. The two length parameters discussed above are designated c and b and a third variable, the total temperature drop, is shown as T_0. The basic equations employed are available from work done to provide solutions for a specific

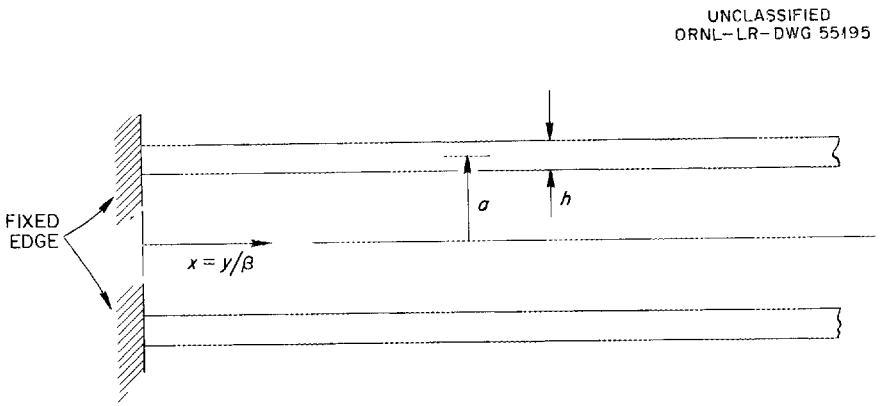


Fig. 3.50. Cylindrical Shell Model Used for the Stress Analysis.

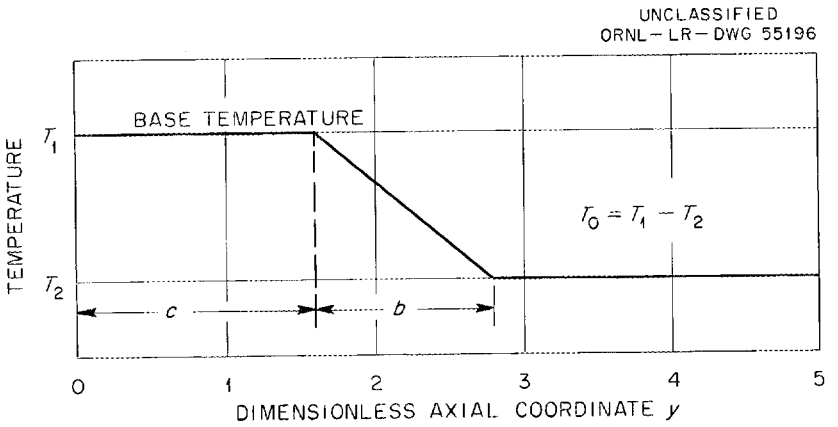


Fig. 3.51. The Temperature Function Used for the Stress Analysis.

application,[34,35] but the results are applicable to any shell of the above description.

The theoretical results are given in two parts. In the first part, c is equal to zero and b is equal to 0.6, 1.8, and 3.0, while in part 2, c is 1.6 and b has the values 0.6, 1.2, and 2.4. The values for the length parameters are given in terms of the dimensionless axial coordinate, y, for the shell. This coordinate is given by

$$y = \beta x \quad ,$$

---

[34]F. J. Stanek, "Stress Analysis of Cylindrical Shells," ORNL CF-58-9-2, (July 22, 1959).

[35]F. J. Witt, "Thermal Stress Analysis of Cylindrical Shells," ORNL CF-59-1-33 (March 26, 1959).

where x is the axial coordinate and β is a shell parameter, which depends upon Poisson's ratio for the material, the radius of the shell, a, and the thickness, h. When Poisson's ratio is taken equal to 0.3, as was done in this study,

$$\beta^2 = \frac{1.6523}{ah} \quad .$$

The dimensionless axial bending stresses at the outer surface, $(\sigma_x)_B/E\alpha T$, are given as a function of the axial coordinate in Figs. 3.52 and 3.53. The dimensionless circumferential membrane stresses, $(\sigma_\theta)_m/E\alpha T_0$, are given in Figs. 3.54 and 3.55 and the dimensionless inward displacements, $w/a\alpha T_0$, are given in Figs. 3.56 and 3.57. Here the symbols have the following meanings:

σ = normal tensile stress, psi,
w = radial displacement, in.,
E = modulus of elasticity, psi,
α = coefficient of thermal expansion, in./in.·°F,
$T_0 = T_1 - T_2$, from Fig. 3.51, °F.

The numerical values listed below were assumed to apply to the compressor:

h = 0.5 in.,
a = 4.0 in.,
$E = 26 \times 10^6$ psi,
$\alpha = 9 \times 10^{-6}$ in./in.·°F,
$T_0 = 600°F$.

Using these values,

$$E\alpha T_0 = 140\ 400 \text{ psi},$$

$$a\alpha T_0 = 2.16 \times 10^{-2} \text{ in.},$$

$$\beta = 0.9089 \text{ in.}^{-1}.$$

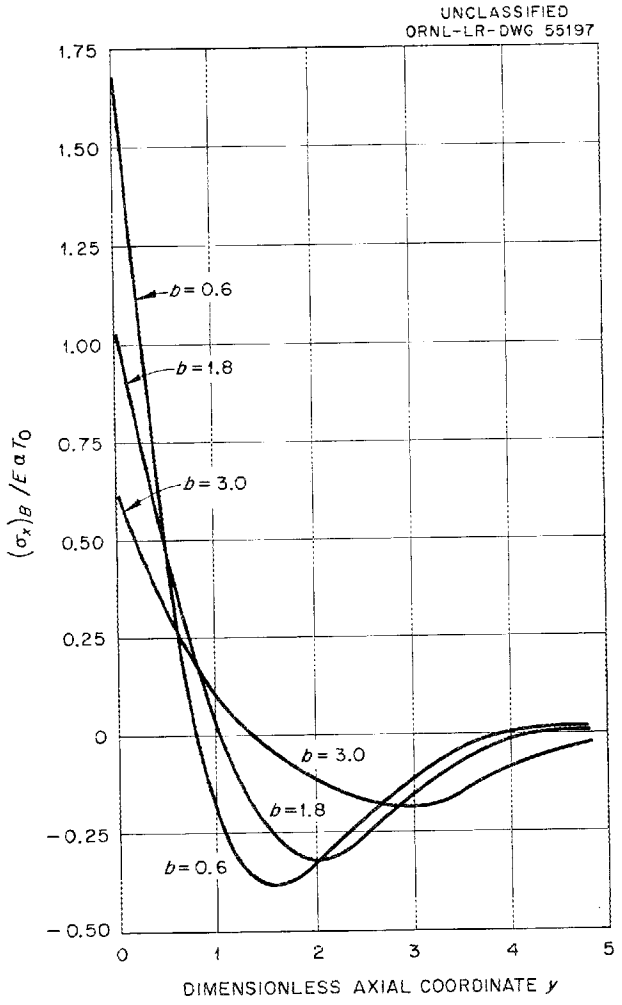


Fig. 3.52. The Axial Bending Stress when c = 0.

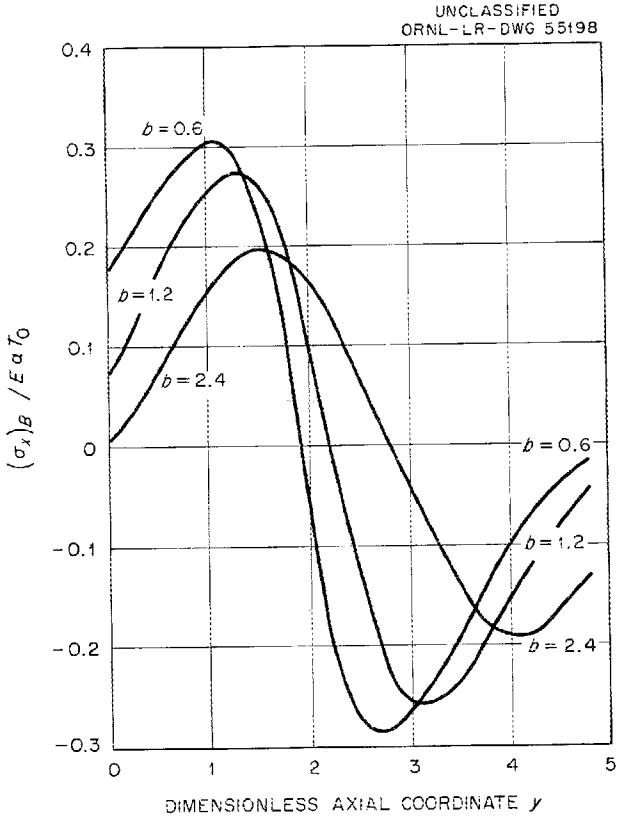


Fig. 3.53. The Axial Bending Stress when c = 1.6.

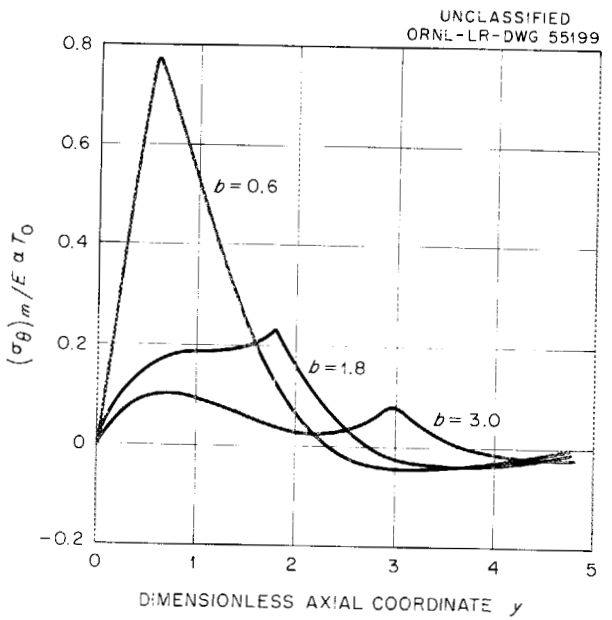


Fig. 3.54. The Circumferential Membrane Stress when c = 0.

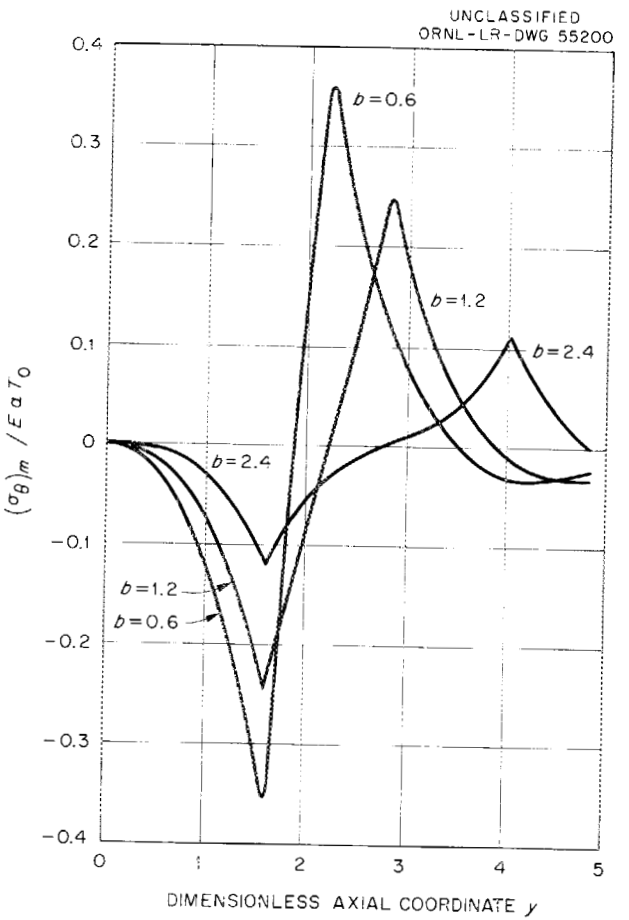


Fig. 3.55. The Circumferential Membrane Stress when c = 1.6.

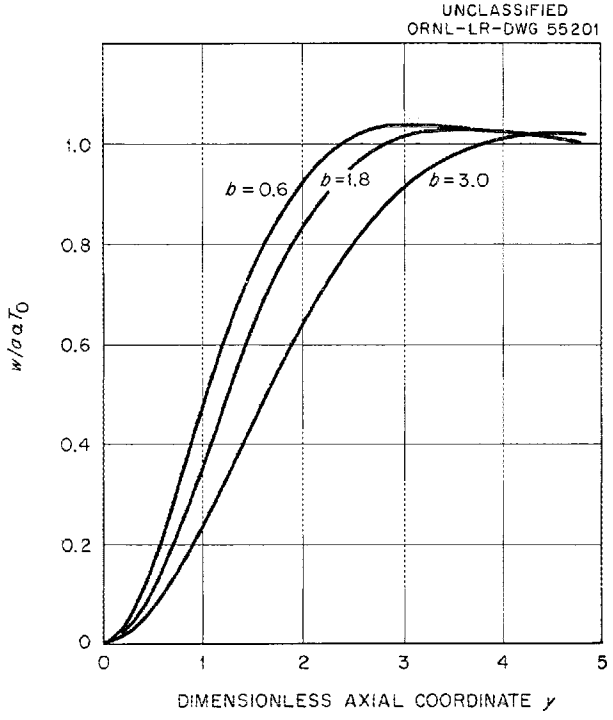


Fig. 3.56. The Radial Displacement when c = 0.

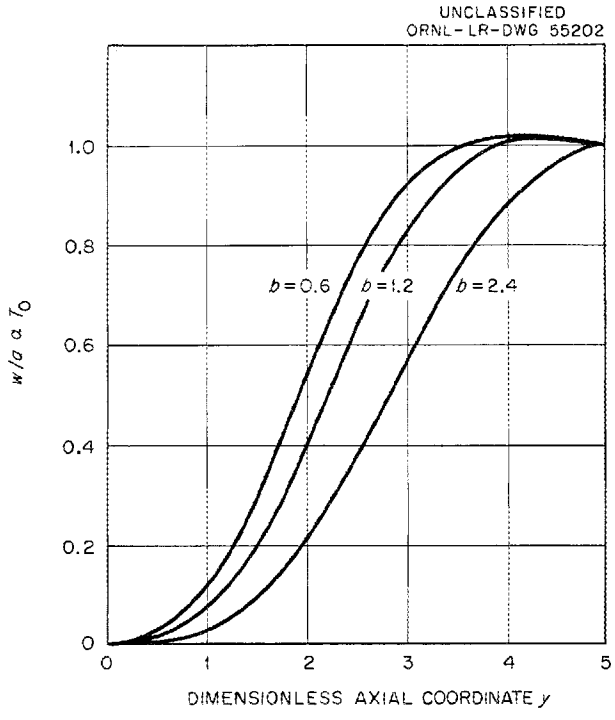


Fig. 3.57. The Radial Displacement when c = 1.6.

If permanent deformation of the pressure vessel body is a limiting factor, the maximum stress should not exceed approximately 30 000 psi. With this criterion, the required values of b and c become 2.6 and 1.2 in., respectively.

4. EXPERIMENTAL INVESTIGATIONS OF HEAT TRANSFER AND FLUID FLOW

(H. W. Hoffman)

Resistance-Heated-Tube Heat-Transfer Experiment

(W. J. Stelzman)

Analytical studies were continued based on the previously reported[1] data for experimental series 4-B (a septafoil cluster at a 2:1 ligament-ratio spacing with a 60-deg-pad mid-cluster spacer[2] and an inlet modified by the addition of several screens[1]). Mean axial heat-transfer coefficients, h, were calculated for each tube from the measured tube-surface temperatures[3] assuming complete transverse mixing of the gas stream; the results are given in Table 4.1. A study of these data shows that (1) the variation of the individual mean coefficients from the average for the six peripheral tubes at any axial level was significantly greater in the section of the cluster upstream of the mid-cluster spacer (±7.5%) than in the downstream portion (±2.0%), (2) the coefficients for tubes 1, 2, and 3 were, on the average, greater than those for tubes 4, 5, and 6, and (3) the mean heat-transfer coefficients for the central tube were markedly below the values for the peripheral tubes, with the deficiency being as high as −40% in the upstream section of the cluster.

The combination of the first two observations indicates that a flow asymmetry existed in the experimental channel which started either in the entrance plenum or in the screens at the channel entrance and was largely wiped out by the mid-cluster spacer. Subsequent repetition of a number of the series 4-B runs with altered inlet screen arrangements showed reasonable agreement between the sets of data; this suggests that

---

[1] "GCR Quar. Prog. Rep. Sept. 30, 1960," ORNL-3015, pp. 48–53.

[2] "GCR Quar. Prog. Rep. Dec. 31, 1959," ORNL-2888, pp. 27–28.

[3] The mean temperature listed in Table 3.2 of reference 1 for peripheral tube 1 at $L/d_e = 5$ should be corrected to ready 408°F.

Table 4.1. Axial Variation in Mean Heat-Transfer Coefficient for Tubes of Experiment 4-B

Axial Position, L/d_e	Mean Heat-Transfer Coefficient (Btu/hr·ft^2·°F)						
	Peripheral Tube No.						Central Tube, No. 7
	1	2	3	4	5	6	
0	43.5	43.7	44.5	42.8	44.5	43.7	39.3
4	25.3	23.7	26.3	22.0	24.9	23.9	16.2
8	25.1	24.0	26.2	22.7	24.9	24.4	15.1
12	25.2	24.2	26.6	23.6	24.7	24.4	15.1
16	25.3	24.4	25.9	23.7	24.2	24.4	18.8
18	25.3	24.7	25.8	23.9	23.9	24.7	20.3
20	47.8	48.8	49.2	47.3	46.6	47.1	41.8
24	31.6	32.1	31.8	30.8	31.2	30.9	25.6
28	26.5	27.0	27.1	26.3	26.7	26.2	23.6
32	24.5	24.8	24.7	24.1	24.3	24.2	22.9
36	23.9	23.9	23.9	23.5	23.7	23.8	23.0
38	24.2	24.3	24.1	23.4	23.7	23.9	23.3

the skewed flow develops either in the upper plenum or in the transition piece joining the gas supply to the plenum.[4]

The axial variation in the average value of the heat-transfer coefficient for the six peripheral tubes is contrasted in Fig. 4.1 with that for the central tube. It may be seen that upstream of the mid-cluster spacer the central-tube coefficient is as much as 40% below the average peripheral tube coefficient. This may be ascribed to diminished flow in the inner region of the channel because of the restriction of the flow in this area by the tube electrodes passing through the plenum chamber. The gradual increase in h for the central tube beyond the x = 0.3 level signifies a process of flow redistribution between the inner and outer regions of the channel. The effect of the mid-cluster spacer in "smoothing" the flow is again shown by the nearly equal values for h for both the central and peripheral tubes.

[4]"GCR Semiann. Prog. Rep. June 30, 1959," ORNL-2767, pp. 76, 78.

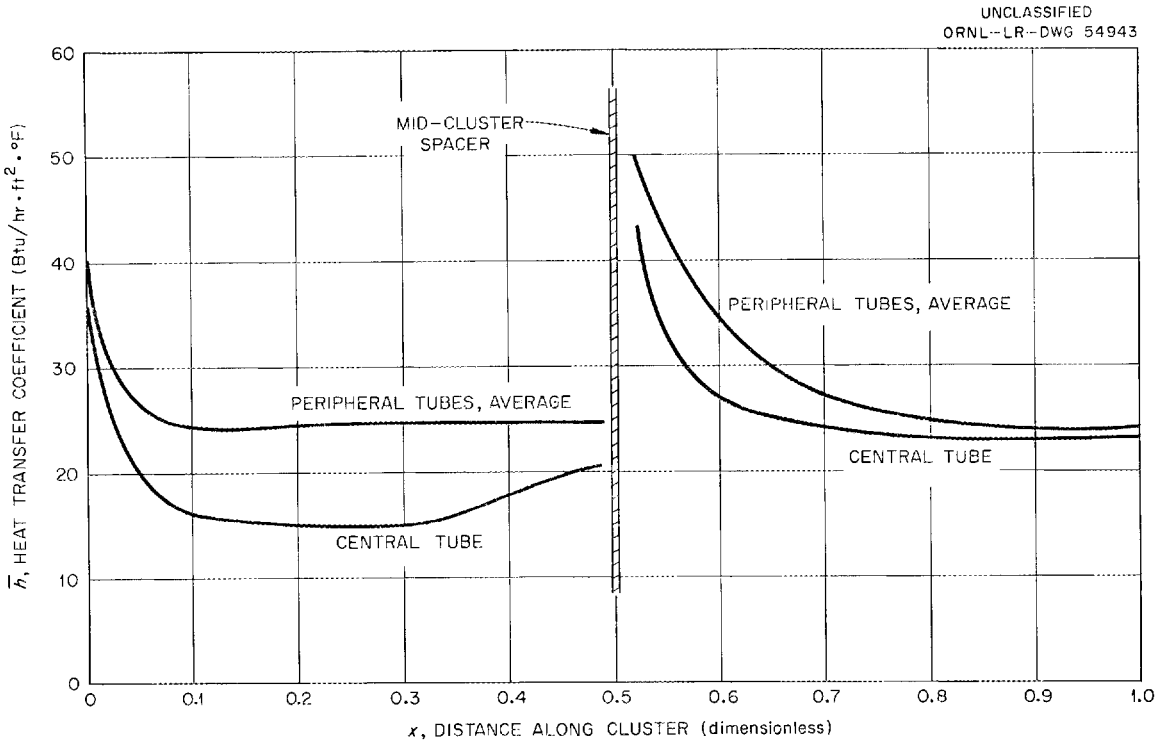


Fig. 4.1. Axial Variation of Average Heat Transfer Coefficient for Experimental Series 4-B; $\gamma = 2$, $N_{Re} = 50\ 500$.

A comparison of these data (peripheral tubes) with the results of the series 2 experiment[5] (tubes 2, 4, and 6 with a 4:1 ligament-ratio spacing and the experimental mid-cluster spacer[4]) and the results of the series 4-A experiment[6] (tubes 4 and 6 only without inlet screens) is given in Fig. 4.2. The data have been adjusted to a common base of $N_{Re} = 50\ 500$, assuming that $h \sim N_{Re}^{0.8}$. While a complete interpretation of these curves with respect to both similarities and dissimilarities is complicated by differences in geometry (e.g., the presence or absence of specific screens in the plenum or channel entrance and the form of the mid-cluster spacer), a number of general conclusions may be stated. The close agreement in the downstream data for the $\gamma = 2$ agreements (with and without screens), as opposed to the differences observed between the two curves in the upstream region, demonstrates the effectiveness of the

[5]"GCR Quar. Prog. Rep. March 31, 1960," ORNL-2929, p. 72.

[6]"GCR Quar. Prog. Rep. June 30, 1960," ORNL-2964, pp. 55–59.

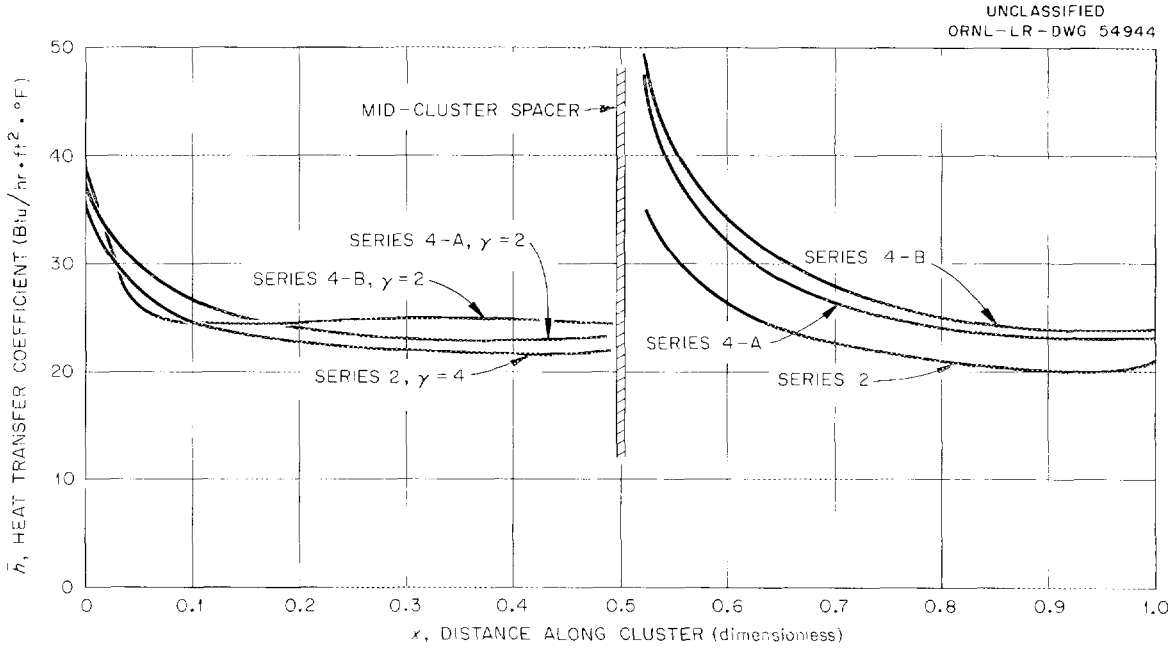


Fig. 4.2. Comparison of Average Heat-Transfer Coefficients for Experimental Series 2, 4-A, and 4-B at N_{Re} = 50 500.

mid-cluster spacer in eliminating flow vagaries introduced at the channel inlet. The existence of the minimum in the upstream portion of the experiment 4-B curve for the peripheral tubes (at x = 0.125) is somewhat uncertain in that the over-all variation in h (~0.5 Btu/hr·ft^2·°F) is of the same order of magnitude as the experimental error associated with these measurements. Check runs have shown that this result is reproducible, and it is planned to continue the investigation of this feature of the axial variation in h at a future time. The difference between the curves for the two spacing ratios (the heat-transfer coefficients for γ = 4 being approximately 15% below those for γ = 2) results from the severe reduction in the flow along the outer side of the peripheral tubes at the 4:1 spacing because of the nearness of the channel wall; this flow deficiency appears to outweigh the effect of the correspondingly greater flow in the inner region. For the central tube, however, the consequence of the wider tube spacing in the series 2 experiment is an increase in the mean heat-transfer coefficient to a value slightly (5%) in excess of that for the peripheral tubes.

Fabrication of the components for the model 4 apparatus[1] has been initiated. Sufficient power has been provided to achieve a surface heat flux of 18 000 Btu/hr·ft^2, which will allow measurements to be made at conditions equivalent to those projected for the hottest region of the reactor. The thermocouple probes are being redesigned for operation at higher ambient temperatures.

Mass-Transfer Measurements

(J. L. Wantland)

Recent mass-transfer experiments[7] conducted with a model of the EGCR Title-II cluster have indicated that the mass-transfer factors (j_M) approach a higher asymptotic value in the downstream section of the tube bundle than in the upstream region. The data yielding this result were obtained with rods on which the naphthalene coating extended over only one-half the rod length. Two runs were necessary to obtain the variation in j_M over the complete length of the rod. Since this procedure introduced the possibility of significant differences in operating conditions (such as changes in the geometry, the gas velocity, and the gas temperature, as well as differences in the crystalline structure of the naphthalene surface), a new rod was constructed that contained an active portion in both the upstream and downstream halves of the rod.

The results of the run made with this "double rod" are compared in Fig. 4.3 with the earlier data. The rod was located in position No. 1, and there was 0-deg relative orientation between clusters. All data have been adjusted to include the effect of the free-stream naphthalene concentration at each axial level; the concentration is assumed to be uniform in the region immediately surrounding the active rod (taken to be 1/6 of the total flow area around the peripheral rods). The two sets of data agree quite closely and thus negate the hypothesis that the higher asymptotic values of j_M previously observed in the downstream cluster section resulted from geometrical or operational variations. A suggested

[7] "GCR Quar. Prog. Rep. Sept. 30, 1960," ORNL-3015, pp. 53–56.

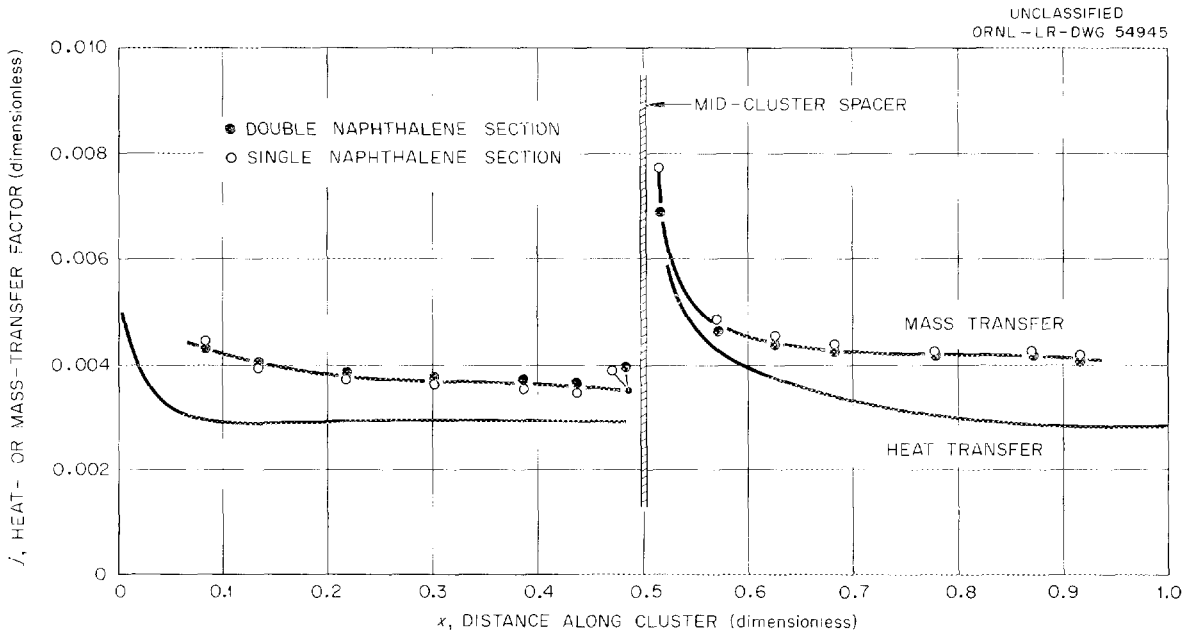


Fig. 4.3. Comparison of j-Factors Obtained in Mass-Transfer and Heat-Transfer Experiments.

explanation for the discrepancy is the possibility of increased turbulence in the downstream region (originating in flow disturbances introduced by the mid-cluster spacer). This seems somewhat questionable in that the heat-transfer results (see Fig. 4.3 and discussion in preceding section on heat transfer) obtained with the same geometry, except the inlet and exit spiders, do not exhibit this same characteristic. The study of this phenomenon is being continued.

An independent analysis[8] of the causes of the deviation between the heat-transfer and mass-transfer results has suggested that the differences arise from the nonisothermal nature of the temperature field, as opposed to the essentially uniform concentration field. The possibility of a definitive experiment is being investigated.

Velocity Distribution Studies

(F. E. Lynch)

The accumulation of data for delineating the velocity field in the downstream element of two EGCR clusters has been continued using the

[8]See section on EGCR Fuel Assemblies in Chap. 3 of this report.

experimental apparatus and procedure previously described.[9] Since making the measurements needed for drawing a detailed velocity contour map at any axial position is time consuming, three different experimental assemblies were used in order to expedite the program. The units have been designated velocity models 3, 4-A, and 4-B and are all basically 4/3-scale representation of the EGCR cluster. Models 4-A and 4-B have a cluster length of 44.8 L/d_e (equivalent to the EGCR); for model 3, the cluster length is 54 L/d_e and the mid-cluster spacers are located off center[10] at 22.4 L/d_e above and below the central pair of spiders. The pitot probe for model 4-B is radially adjustable, in contrast to the fixed probes used in models 3 and 4-A. Despite probe calibration, some differences have been observed in the data obtained in the model 3 and 4-A systems; operation of the model 4-B apparatus has just been initiated. A comparison of typical profiles is given in Fig. 4.4 at $L/d_e = 26.0$; the deviation in magnitude is of the order of 8%, while the profile shape remains essentially unchanged. It is possible that this effect may be related entirely to small differences in configuration of the mid-cluster spacers for the two systems, since the profiles are obtained immediately downstream of the spacer. This problem will be considered further when data are obtained from the model 4-A system at other axial levels.

Velocity measurements for rods 1, 2, 3, and 7 (see Fig. 4.5 for scheme used to designate rod positions and cluster orientations) have been completed at the probe position R = 0.05 in. (measured radially outward from rod surface) at $N_{Re} \sim 50\,000$. The effects of rotational orientation of the two clusters (0, 15, 30, 60, and 90 deg) at four axial levels (L/d_e = 3.9, 20.9, 26.0, and 52.8) were studied. Typical results are shown in

---

[9] "GCR Quar. Prog. Rep. June 30, 1960," ORNL-2964, pp. 67–80.

[10] "GCR Quar. Prog. Rep. Sept. 30, 1960," ORNL-3015, pp. 63–67. A number of errors have been inadvertently included; thus, (1) the profiles (not the captions) of Figs. 3.7 and 3.10 should be interchanged, (2) the abscissas on the velocity profiles of Figs. 3.9, 3.10, and 3.11 should be reversed so as to read from 360 backward to 0 deg, (3) the ordinate for the 90-deg velocity profile (Fig. 3.10 corrected) should be shifted to read from 0.9 to 1.2, and (4) all velocity profiles at $L/d_e = 3.8$ should read $L/d_e = 3.9$.

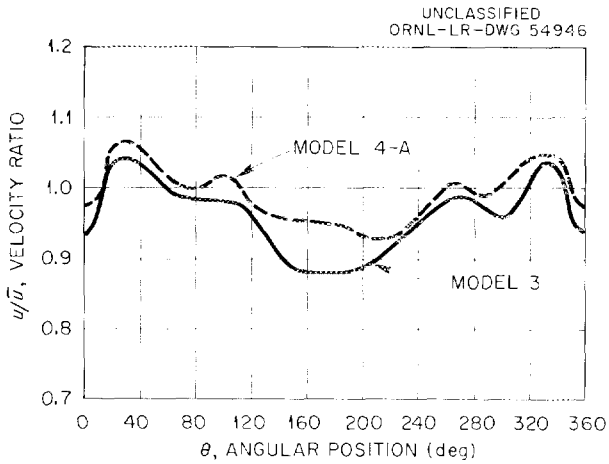


Fig. 4.4. Comparison of Circumferential Velocity Profiles Obtained in Model 3 and Model 4-A Experiments.

Fig. 4.6 for a relative cluster orientation of 90 deg. The major differences in the profiles occur in the vicinity of the flow obstructions created by the structural members of the spiders and spacers; again, the profile shapes are similar. At $L/d_e = 3.9$, rod No. 1 shows a suppression of the flow in the 0-deg region because of the presence in the lower spider of the web supporting the boss for the central tube; for rods 2 and 3, the velocities rise smoothly to a maximum near 0 deg. The effect of the spacer pad in the 180 ± 30-deg region is apparent in the profiles at $L/d_e = 26.0$. As speculated previously, the differences in depth of the minima (~30% over-all) probably reflect small geometrical variations. The agreement in the profiles at $L/d_e = 20.9$ and 52.8 is excellent, indicating that the influence of the spiders and spacers on the profile shape disappears within as short a distance as $L/d_e = 17$ (actual flow length is 14 in.). A comparison between the profiles at these two levels shows, however, that the length of unobstructed bundle required to affect an equilibrium flow pattern is $L/d_e = 27$ or greater.

Contour maps showing the velocity distributions in the 120-deg segment containing rods 1, 2, 3, and 7 are given in Fig. 4.7 ($L/d_e = 3.9$) and Fig. 4.8 ($L/d_e = 26.0$). It should be noted that the angular rotation is opposed to the convention indicated in Fig. 4.5 (i.e., the patterns have been drawn as viewed looking in the direction of flow). The result of a much more detailed evaluation of the data at $L/d_e = 3.9$ (obtained by cross plotting along radial lines emanating from the centers of each rod) is given in Fig. 3.19, Chapter 3, this report. These figures may be compared with those published earlier[11] for a situation in which an effort was made to minimize flow disturbances due to the tube support

[11] "GCR Quar. Prog. Rep. Dec. 31, 1959," ORNL-2888, pp. 60–62.

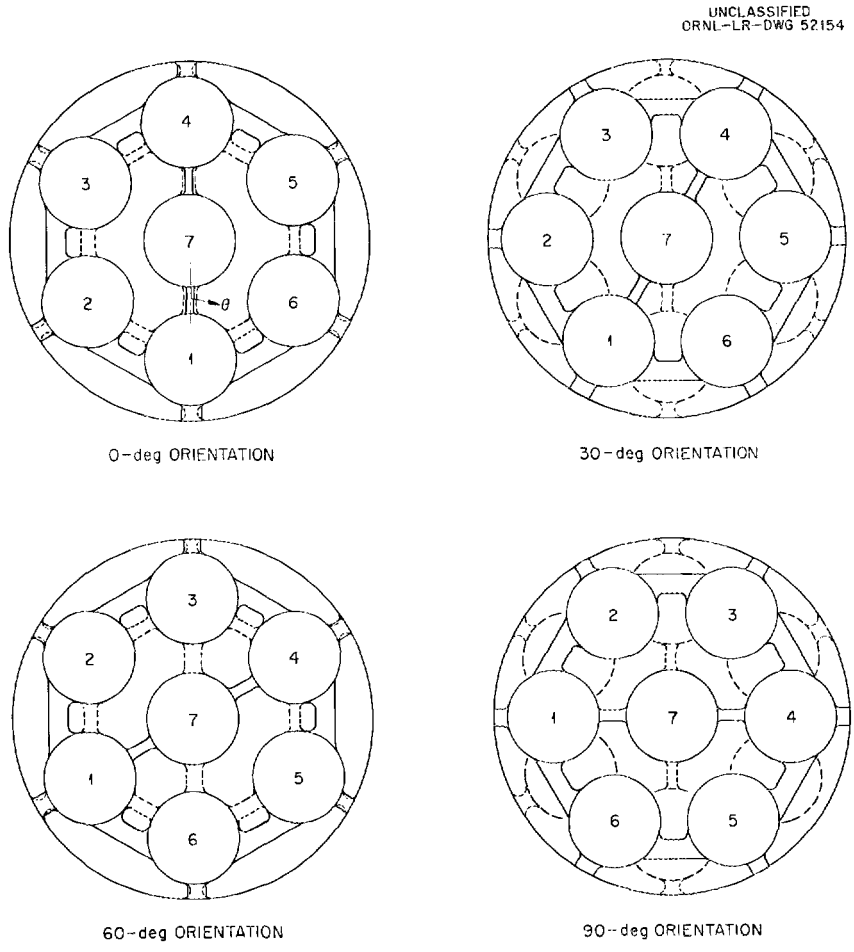


Fig. 4.5. Designation of Rod Positions and Relative Cluster Orientation of Adjacent Title-II Design Spiders as Examined in Experimental Studies with EGCR Rod Clusters.

structures; the result (Fig. 4.9) is repeated here for reference. The additional complications introduced by the spiders are clearly visible; in contrast, the spacers appear to have much less influence on the gross flow. Experiments to provide similar characterization of the flow at positions far removed from the spiders and spacers are in progress.

Gas-Mixing Experiments

(G. J. Kidd)

All studies performed to date in the effort to establish the thermal characteristics of the EGCR fuel-rod cluster have suggested that relatively little mixing occurs between fluid streams moving in the set of

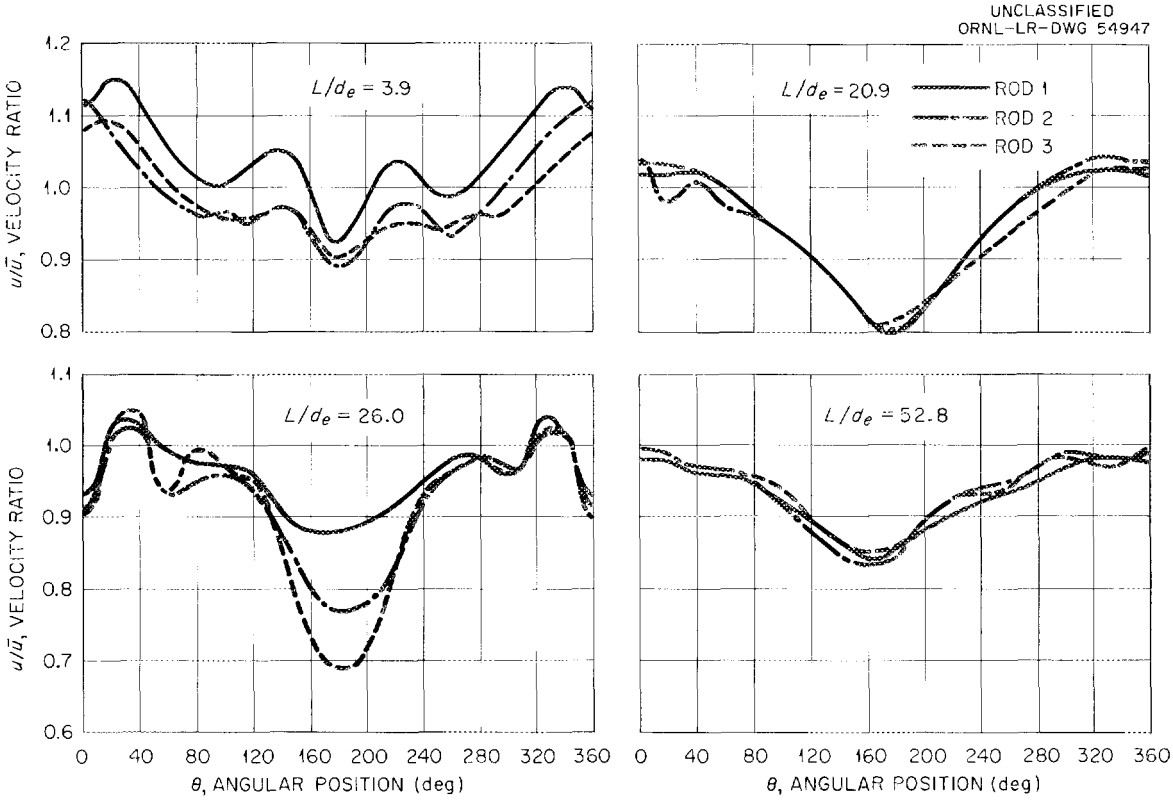


Fig. 4.6. Axial Comparison of Circumferential Velocity Profiles for Rods 1, 2, and 3 at a 90-deg Relative Cluster Orientation; $\gamma = 2$, $N_{Re} = 50\ 000$.

12 interconnecting channels defined by the element geometry. Under such circumstances, a serious possibility exists that there will be "hot-streaking," with its attendant problems. An experimental program has therefore been initiated for determining quantitatively the magnitude of both intra- and intercluster gas mixing and, if necessary, to investigate techniques for increasing such mixing. A byproduct of this study will, of course, be an improved understanding of the results obtained in both the heat-transfer and mass-transfer experiments.

In the experimental technique being utilized, a small amount of tracer gas (which has a thermal conductivity different from that of the main gas stream) is continuously injected into the gas stream at a given point in the flow channel. At one or more stations downstream of this injection point, a sample of the gas mixture is drawn off and passed through a thermal conductivity comparison unit, which compares

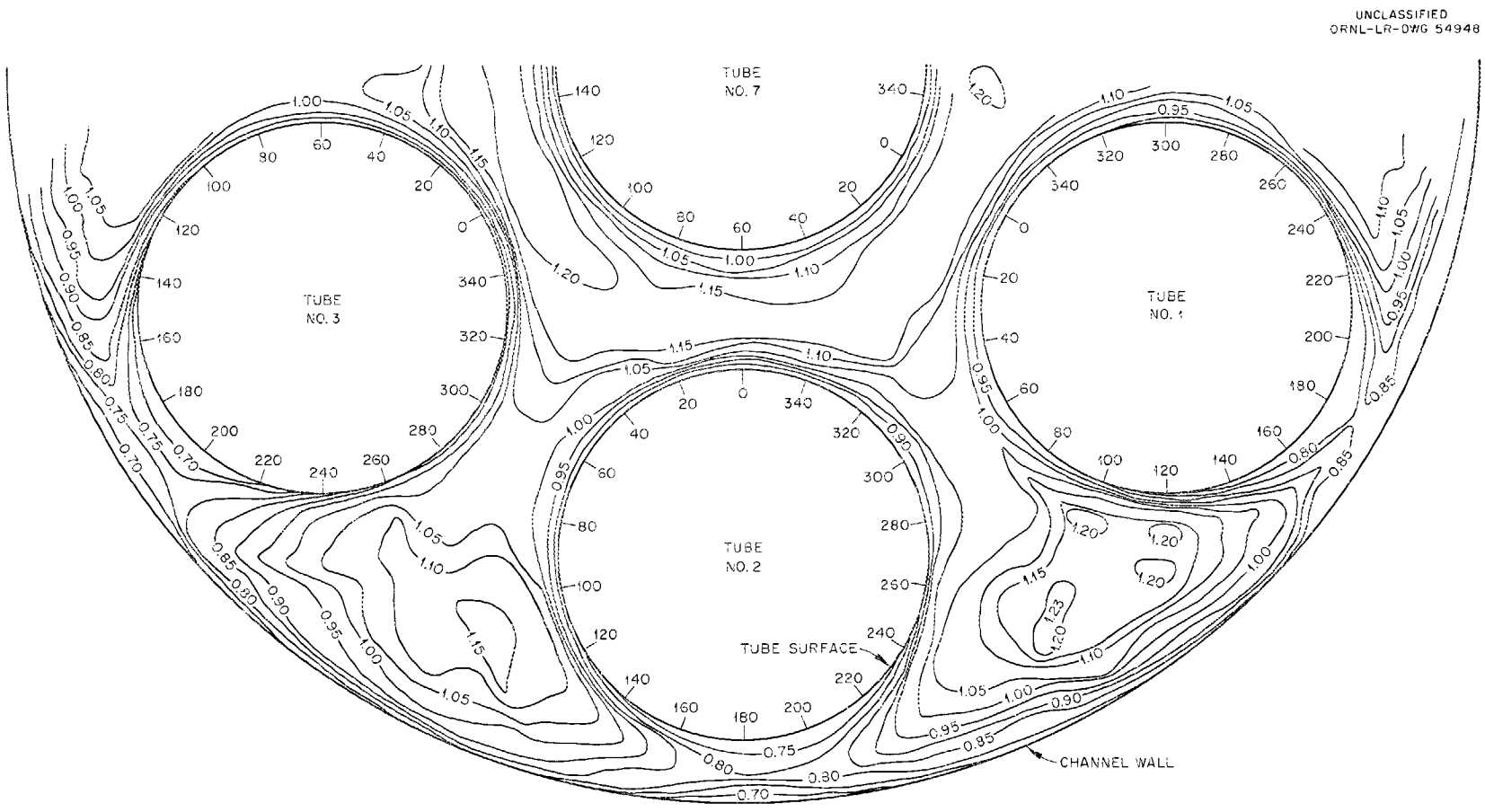


Fig. 4.7. Velocity Contours in an EGCR Channel; L/d_e = 3.9, 0-deg Relative Cluster Orientation, $N_{Re} \sim 50\,000$.

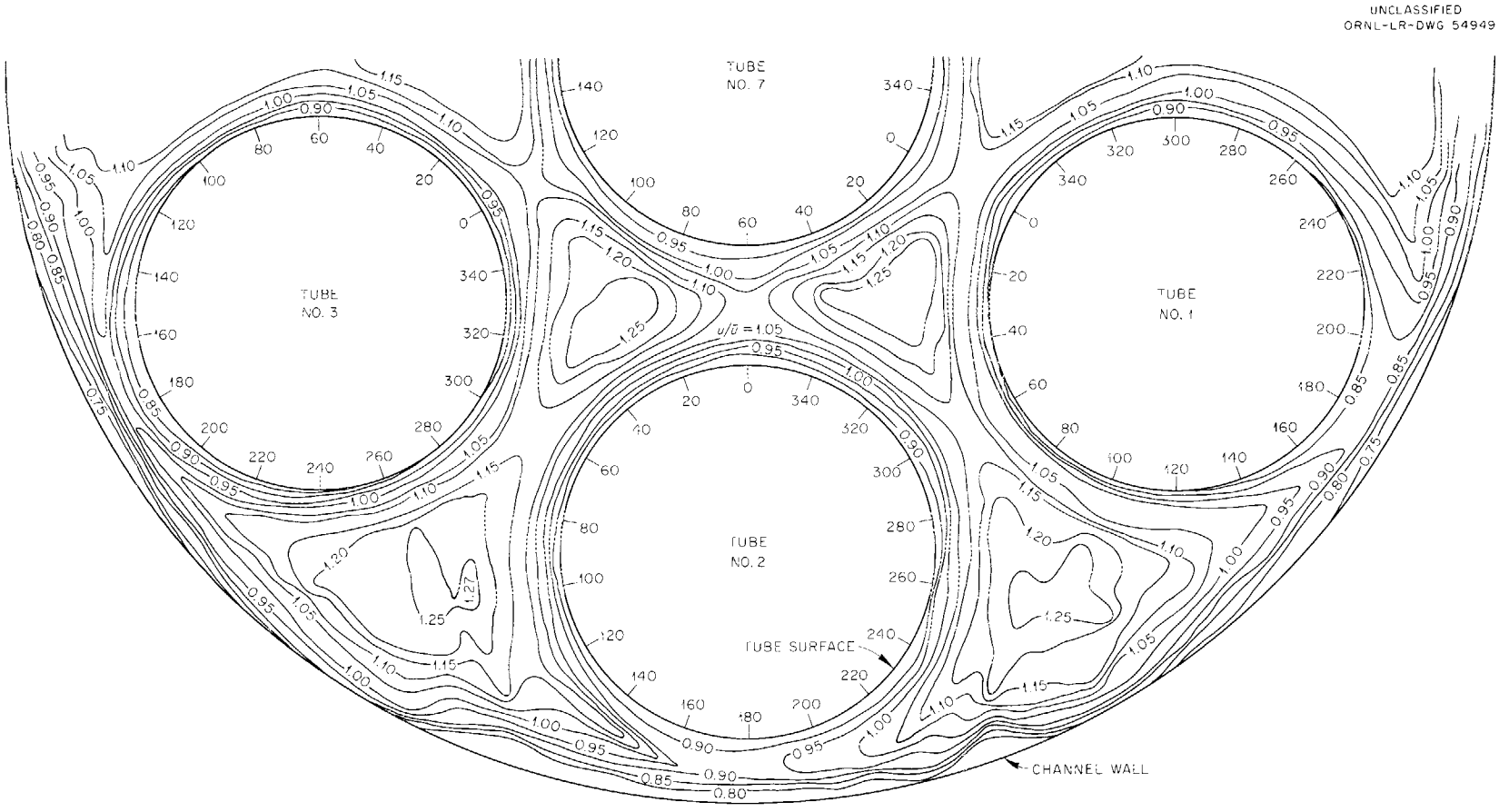


Fig. 4.8. Velocity Contours in an EGCR Channel; L/d_e = 26.0, 0-deg Relative Cluster Orientation, $N_{Re} \sim 50\,000$.

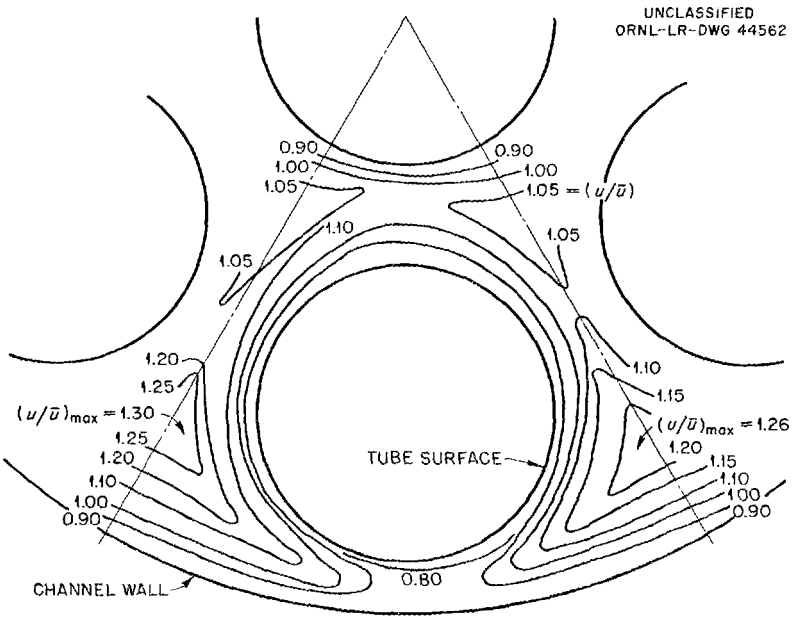


Fig. 4.9. Velocity Contours in a Septafoil Channel with Rod Support Structures Designed to Give Minimum Flow Disturbance; $L/d_e = 23$, $N_{Re} \sim 52\ 000$, $\gamma = 2$.

the thermal conductivity of the gas mixture with that of the main gas stream without tracer gas. This comparison of the thermal conductivities of the two gases is a function of the concentration of the tracer gas in the main gas stream at the point of sampling. The thermal conductivity comparison unit is calibrated by comparing gas mixtures of known concentrations with pure channel gas. For small concentrations of channel gas, this calibration for all practical purposes is linear. By taking samples at several stations in a given radial plane downstream of the injection point, the distribution of the tracer gas and hence the degree of gas mixing can be determined.

The experimental apparatus used in the initial studies is shown in Fig. 4.10. It consists of three full-scale EGCR clusters, each of which can be rotated with respect to the other two. The flowing gas is atmospheric air (at $N_{Re} \sim 50\ 000$); helium is used as the tracer gas because of the large difference in thermal conductivity between air and helium. Injection and sampling is possible at 12 stations at each of three axial planes in each of the three clusters as is shown in Figs. 4.10 and 4.11.

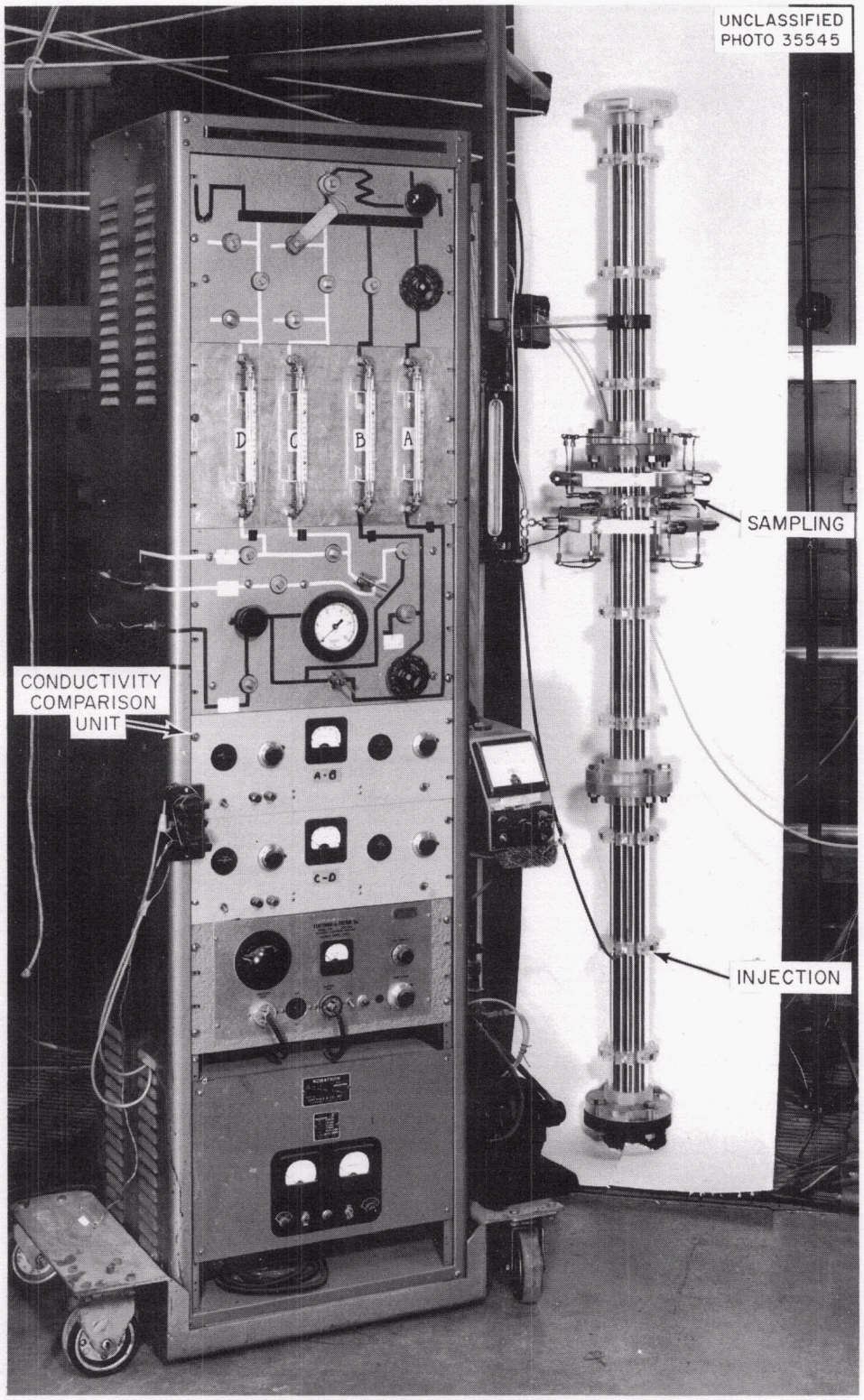


Fig. 4.10. Apparatus for Gas-Mixing Studies.

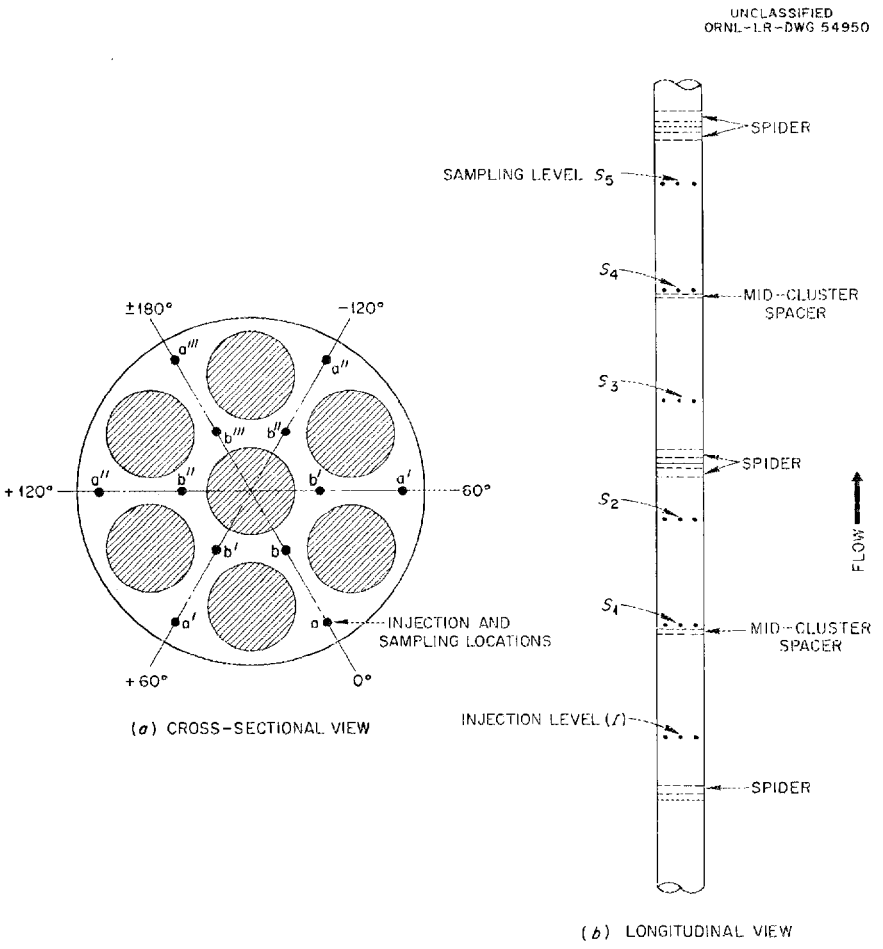


Fig. 4.11. Schematic Diagram of Gas-Mixing Study System Showing Injection and Sampling Stations.

The points a and b in Fig. 4.11a correspond roughly to points of velocity maxima in the six inner and six outer flow regions.

A photograph of a double probe is shown in Fig. 4.12. The two sampling tubes (one coincides with point a and the other with the corresponding point b) are fabricated of stainless steel hypodermic tubing. Six double probes, arranged as shown in Figs. 4.10 and 4.11, are used to conduct a traverse of 12 points at a given axial plane. The individual sampling tubes are alternately connected to the conductivity comparison unit by means of a manifold and a system of valves.

For the first study, all three clusters were directly aligned. Helium was introduced in sequence at the twelve injection stations ("I" of

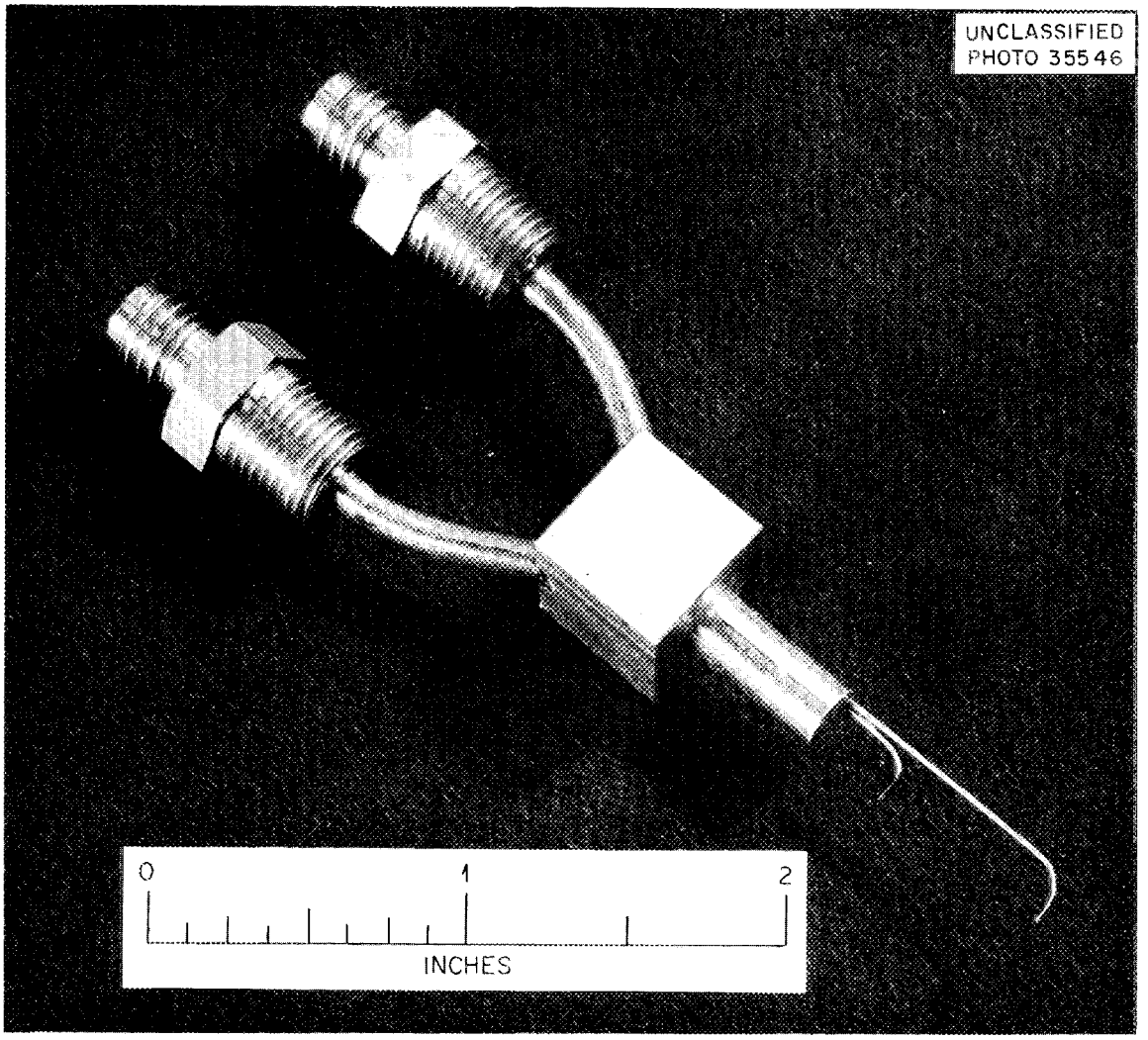


Fig. 4.12. Sampling Probe Used in Gas-Mixing Experiments.

Fig. 4.11) just downstream of the first lower spider. For each injection, concentrations were measured at each of the 12 sampling stations at the axial positions (S_1, S_2, etc.) shown in Fig. 4.11.

The preliminary results of this experiment are shown in Fig. 4.13. These data have been averaged for the six inner injection stations and the six outer injection stations in order that average trends can be observed. The data indicate that radial mixing of the gas stream is more prevalent than is mixing in a circumferential direction. The peaks in the 0-deg curves for interior injection with peripheral sampling, Fig. 4.13b, and for peripheral injection with interior sampling, Fig. 4.13c,

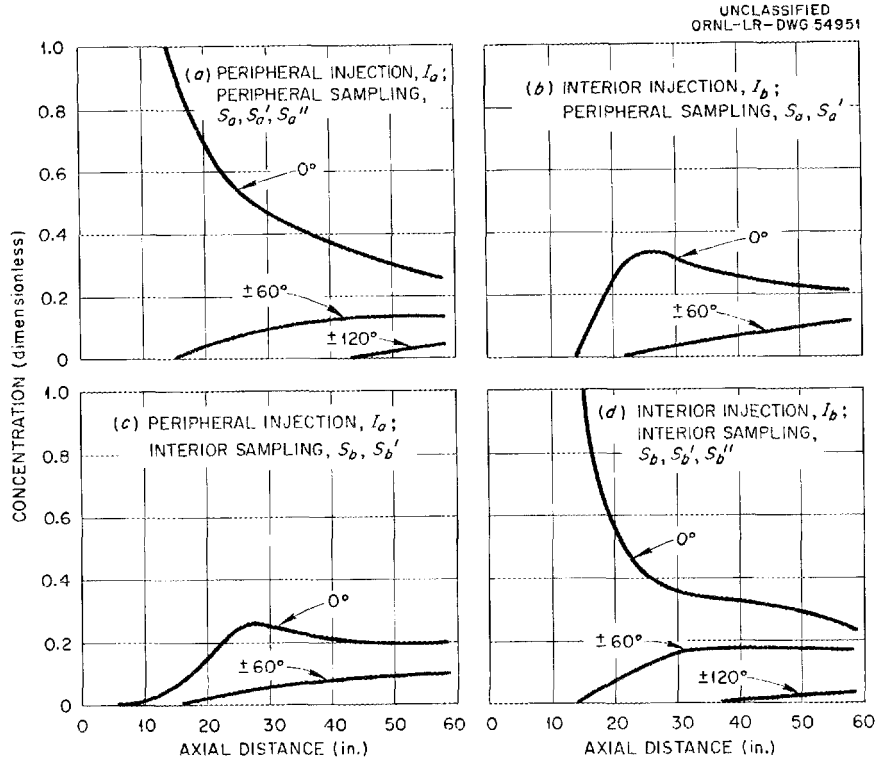


Fig. 4.13. Concentration Profiles in an EGCR Channel; 0-deg Relative Cluster Orientation, N_{Re} = 50 000.

appear to be due to radial mixing of the gas streams accompanied by diffusion of helium into the air. Complete diffusion of helium into the air stream does not occur for several cluster lengths. From these preliminary data, it is difficult to ascertain any definite mixing across the spiders or spacers, and it is evident that more detailed traverses will be needed.

Injection and sampling probes have been developed that will allow complete radial movement of the probe. The central cluster has been modified to contain several more axial probing locations, each consisting of 12 equally spaced radial probing positions (rather than six, as previously used). The probe manifold has been discarded, and only one sampling probe is used at a time.

Experimentation is being continued, and flow across spider pairs and mid-cluster spacers is being studied, as well as the effects of cluster orientation.

Part 2. Materials Research and Testing

5. MATERIALS DEVELOPMENT

(J. H. Coobs)

Fabrication and Physical Properties of UO_2

Powder Processing and Fabrication of UO_2 (A. J. Taylor, J. M. Robbins)

Experimental work has been completed on fabrication techniques for the development of controlled grain sizes in the miniature UO_2-irradiation specimens for the LITR experiments. A series of pellets with two different oxygen-to-uranium ratios was sintered under varying conditions of time and atmosphere. It was determined that grain size in these pellets could be controlled over a range from 10 to 60 μ while sintering the pieces to dimensional tolerances of ±0.001 in. and densities of not less than 10.3 g/cm^3. It was observed that argon has a strongly depressing effect on the grain growth of UO_2. For example, after sintering 5 1/2 hr in hydrogen at 1750°C, a grain size of approximately 60 μ was obtained; whereas under the same conditions of time and temperature in argon, the grain size was only about 15 μ. When sintering is conducted in argon, hydrogen is introduced during the last 30 min to reduce the oxygen-to-uranium ratio to less than 2.01.

Attempts to grind or polish thin plates of UO_2 or ThO_2-UO_2 to a thickness of 0.030 in. for use in instantaneous fission-gas-release experiments in the ORR (see Chap. 6, this report) have been almost completely unsuccessful. Therefore the shape of the plate was changed from rectangular to circular in order to increase the chances of sintering plates directly to the required thickness. A test series of circular plates was made, and thickness and flatness both proved to be controllable to ±0.001 in. These techniques are now being coupled with those developed in the grain-size study in order to produce plates with the required dimensions, density, and grain size.

Fabrication was started on UO_2 disks, 1.6 in. in diameter with a thickness of either 1 or 0.5 in., for use in radial-heat-flow thermal-conductivity studies. The final thickness will depend on the technique that must be used to achieve the required final density. Standard fabrication techniques have not yet yielded the required density without the

formation of laminations, and isostatically pressed pieces have either been distorted by the pressing or have cracked during sintering. Binders are now being blended with the UO_2 powder in order to form these pieces directly to the required size and density.

Thermal-Conductivity Studies (T. G. Godfrey)

The development of the radial-heat-flow apparatus is continuing with the goal of achieving the most reliable and accurate experimental method that is compatible with the existing equipment.[1] Data analysis revealed the need for further equipment changes in order to (1) insure more uniform internal temperatures, (2) permit intercomparisons of thermal emf's, (3) allow the use of automatic temperature controllers, (4) increase the accuracy of the data, and (5) provide for simple equipment assembly. Some of these changes have been made and their effects evaluated by measuring the thermal conductivity of a specimen of INOR-8 alloy that was readily available and applicable as a test specimen. Improvements in the data that are attributable to the changes in the apparatus are reflected in the following thermal-conductivity values for INOR-8 which, when plotted, fall within ±1% of a straight line:

Temperature (°C)	Thermal Conductivity (w/cm·°C)
360	0.1680
455	0.1861
563	0.2052
645	0.2196
703	0.2318

Thermal Expansion of Dished Pellets (W. R. Martin)

The thermal expansion of UO_2 pellets having a 0.003-in. concave dish on one end or both ends has been measured at central pellet temperatures up to 3000°F. Within experimental error, the dimensional behavior of

[1] "GCR Quar. Prog. Rep. March 31, 1960," ORNL-2929, pp. 87–91.

double-dished pellets is equivalent to that of the pellets dished on one end only.

Bulk-Density Measurements on Small Irregular Particles (Mary P. Haydon, A. J. Taylor, J. M. Robbins)

A solid-embedment technique for measuring bulk density is being developed in connection with a study on the characterization of UO_2 particles. The method is applicable also to measurements of the bulk density of irregularly shaped UO_2 fragments taken from irradiation experiments. The technique consists of embedding a known weight sample in an epoxy resin whose density is known, measuring the total volume of sample and resin, and obtaining the sample volume by difference after calculating the volume of the resin from its known weight and density. The features of the technique presently under study are the selection of a resin with the most suitable embedment characteristics, methods of keeping air from being trapped within the mass of the sample or on the surface of the particles, and methods of avoiding penetration of the pores by the resin in its fluid state.

It is necessary to work with particles of known bulk density in order to satisfactorily evaluate the technique. Fused UO_2 was selected as one study material, since the fine, crushed particles should have a bulk density equal to the theoretical density (10.95 g/cm^3) and the densities of even pieces having volumes as large as several cubic centimeters should be very close to theoretical density. A second type of particle of a known low bulk density (5.86 g/cm^3) was made by crushing UO_2 pellets of this density and sizing the particles.

The results presented in Table 5.1 provide a comparison of the densities obtained with the mercury-pycnometer technique and the solid-embedment technique, as well as the results obtained with two different resins. In each case the low results for the crushed, fused UO_2 particles (samples 4, 5, 6, and 7) resulted from the entrapment of air with the sample. This error is aggravated with Castolite resin because of thermal expansion during curing; the inaccurate values obtained with this material indicate that this error is significant. No air was trapped in the embedments

Table 5.1. Solid-Embedment and Mercury-Pycnometer Measurements of Bulk Density of UO_2

Sample Type	Sample No.	Volume of Sample Used (cm^3)	Known Density (g/cm^3)	Measured Bulk Density (g/cm^3)		
				Mercury-Pycnometer	Castolite Embedment	Castoglas Embedment
Single, large pieces of fused UO_2	1	~0.7	10.95[a]		10.52	
	2	~0.7	10.95		10.72	
	3	~0.7	10.95			10.95
Fused UO_2 crushed and sized to						
-70 +100 mesh	4	~1.2	10.95			10.78
-70 +100 mesh	5	~1.2	10.95			10.78
-100 +140 mesh	6	~1.2	10.95	10.36	10.63	
-100 +140 mesh	7	~1.2	10.95	10.36	10.60	
Fabricated pellet, whole	8	4.609	5.78			6.04
-40 +60 mesh particles from crushed, fabricated pellets	9	~1.6	5.86			7.79
	10	~1.6	5.86			7.78

[a]Theoretical value.

containing single, large pieces of fused UO_2 (samples 1, 2, and 3). The low values obtained with Castolite resulted solely from the thermal expansion problem. Very little air was trapped with the particles from the crushed pellets (samples 9 and 10); the high value obtained for bulk density was caused by penetration of resin into the porous material. The depth of penetration was not great for any individual particle, but the increase in the measured density over that of the whole pellet reflects the increased surface-to-volume ratio of these samples.

Fission-Gas-Release Studies (J. L. Scott, D. F. Toner)

When neutron-activation tests on UO_2 pellets for the EGCR were begun at ORNL, it was considered advantageous to obtain independent results on duplicate pellets as a check on the procedure. Since similar tests were being run at Chalk River, a formal agreement between the AEC and AECL was made under which ORNL was to supply UO_2 pellets to Chalk River together with the data required to characterize the material. These pellets were to be tested at AECL while duplicate pellets were being studied at ORNL, and the results of the two series of tests were then to be exchanged.

The results of the tests that have been completed to date are presented in Table 5.2. Two pellets from each lot of UO_2 were supplied to

Table 5.2. Comparison of Values of the Release Rate Parameter (D′) Obtained at Chalk River[a] and the Oak Ridge National Laboratory on Duplicate UO_2 Pellets

UO_2 Sample No.	UO_2 Enrichment (% U^{235})	Manufacturer	Bulk Density (g/cm^3)	BET Surface Area (cm^2/g)	Oxygen-to-Uranium Ratio	D′ Values Obtained at ORNL (sec^{-1})	D′ Values Obtained at Chalk River (sec^{-1})	UO_2 Sample Designation
1	1.803	General Electric	10.27	12.7	2.002	5.92×10^{-11}		GE-5
2	1.803	General Electric	10.27	12.7	2.002			GE-5
3	3.052	ORNL	10.47	89.3	2.006	7.68×10^{-11}	1.17×10^{-11}, 4.28×10^{-11}, 5.43×10^{-11}	1173
4	3.052	ORNL	10.47	89.3	2.003		1.47×10^{-11}, 1.92×10^{-11}	1173
5	0.22	Mallinckrodt	10.23	2.94	2.002	4.72×10^{-14}, 1.15×10^{-13}, 1.1×10^{-13}	1.25×10^{-10}, 1.03×10^{-10}, 6.85×10^{-12}, 5.94×10^{-12}, 2.67×10^{-12}	25-8
6	0.22	Mallinckrodt	10.23	2.94	2.002		1.33×10^{-11}, 1.65×10^{-11}, 2.48×10^{-11}	25-8
7	0.7115	NUMEC	10.39	28.6	2.003	2.51×10^{-13}	6.1×10^{-12}, 1.26×10^{-11}, 4.12×10^{-11}, 5.34×10^{-11}	34-30
8	0.7115	NUMEC	10.39	28.6	2.003		1.28×10^{-11}, 3.55×10^{-12}, 9.35×10^{-12}, 3.91×10^{-12}	34-30
9	0.22	Davison	10.25	34.2	2.011	6.7×10^{-12}, 1.5×10^{-11}	3.47×10^{-10}, 3.63×10^{-10}	33-5

Table 5.2 (continued)

UO_2 Sample No.	UO_2 Enrichment (% U^{235})	Manufacturer	Bulk Density (g/cm^3)	BET Surface Area (cm^2/g)	Oxygen-to-Uranium Ratio	D′ Values Obtained at ORNL (sec^{-1})	D′ Values Obtained at Chalk River (sec^{-1})	UO_2 Sample Designation
10	0.22	Davison	10.25	34.2	2.011		4.61×10^{-10}, 7.49×10^{-11}, 1.97×10^{-11}, 2.3×10^{-11}	33-5
11	4.59	Babcock & Wilcox	10.06	58.0	2.009	2.82×10^{-11}	2.15×10^{-11}, 2.26×10^{-11}, 3.24×10^{-11}	50-6
12	4.59	Babcock & Wilcox	10.06	58.0	2.009		2.75×10^{-11}, 2.83×10^{-11}, 6.39×10^{-11}	50-6
13	4.19	Babcock & Wilcox	10.02	18.9	2.002	6.98×10^{-12}	1.97×10^{-11}, 2.02×10^{-11}, 2.46×10^{-10}	51-5
14	4.19	Babcock & Wilcox	10.02	18.9	2.002		2.15×10^{-11}, 2.20×10^{-11}	51-5
15	4.50	General Electric	10.48	7.7	2.002	3.24×10^{-14}	2.5×10^{-12}, 3.9×10^{-12}	GE-6
16	4.50	General Electric	10.48	7.7	2.002		1.9×10^{-12}, 2.3×10^{-12}	GE-6
17	3.02	ORNL	10.39	11.5	2.003		1.48×10^{-10}, 3.47×10^{-10}, 3.58×10^{-10}	35
18	3.02	ORNL	10.39	11.5	2.003		1.68×10^{-10}, 1.14×10^{-10}	35

[a]Personal communication from W. H. Stevens to J. L. Scott, August 22, 1960.

Chalk River so that the results obtained on a given pair of samples should be identical. The ORNL data were obtained on a third pellet from the same lot of material. In both cases the D′ values were computed from the final slope of the curve of the fraction of Xe^{133} released versus the square root of time; however, the duration of a single test at Chalk River was 3 hr, whereas tests at ORNL were conducted over time periods of 9 to 30 hr. The sample size also differed in that in the tests at Chalk River pieces of UO_2 weighing 50 mg or less were used, whereas the samples used at ORNL weighed 200 to 500 mg.

A comparison of the ORNL and Chalk River data with recent data from Harwell[2] is shown in Fig. 5.1. Data for duplicate pellets tested at ORNL and Chalk River may be compared on the basis of identical BET surface areas. According to the diffusion theory of fission-gas release, a plot of the log of the surface area versus the log of D′ should yield a straight line with a slope of 0.5. The data of ORNL and Harwell are in general agreement with the theory and with one another. The data of Stevens indicate, in Fig. 5.1, that there is no correlation between the BET surface area and D′, but the data are in agreement, for the most part, with the data obtained at Harwell and ORNL for high-surface-area pellets. Values of D′ obtained by Stevens for pellets with low surface areas would be expected to be higher than the true values, because the small sample size results in a relatively high ratio of the geometric surface area to the total surface area.

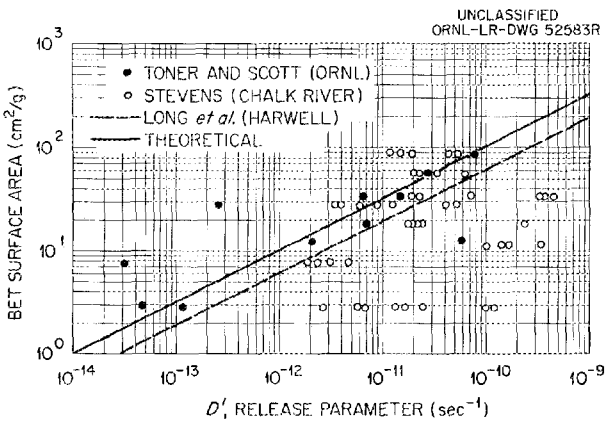


Fig. 5.1. Relation of D′ to BET Surface Area for Duplicate Samples of UO_2 Tested at ORNL and Chalk River.

[2]G. Long, D. Davies, and J. R. Tindley, "Diffusion of Fission Products in Uranium Dioxide and Uranium Monocarbide," Paper presented at the First Conference on Nuclear Reactor Chemistry, Gatlinburg, Tennessee, October 12, 1960.

It is concluded therefore that there is reasonable agreement between the data of the different investigators and that the BET surface area is a useful measure of the fission-gas-retention properties of UO_2 if no structural changes occur during irradiation.

Advanced Fuel Materials Development

Fabrication of Fueled BeO Bodies (R. L. Hamner)

Fine-Grained Fuel Dispersions in BeO. Fueled BeO-UO_2 specimens containing 30 vol % UO_2 enriched 20% in U^{235} for studies of fission-gas-release rates and specimens containing 30 vol % UO_2 enriched 50% in U^{235} for high-temperature irradiation experiments have been fabricated. The fuel was introduced in these specimens as a fine-grained dispersion of submicron-size UO_2 powder, and the specimens were fabricated to close dimensional tolerances in the form of hollow cylinders by cold pressing and sintering. The densities obtained were approximately 95% of theoretical.

In the fabrication of these BeO-UO_2 mixtures, gross cracking occurred during sintering in hydrogen at 1750°C, the same conditions which had been used in the successful fabrication of mixtures of BeO with depleted UO_2. This cracking was attributed to a difference in shrinkage characteristics of the enriched UO_2, which was prepared by a "batch" process, and the depleted UO_2, which was obtained from a "continuous" process.

The shrinkage of the enriched powder was adjusted by maintaining oxygen-to-uranium ratios of approximately 2.17 and 2.4 for the 20 and 50% enriched oxides, respectively, during sintering of the BeO-UO_2 mixtures in an argon atmosphere at 1750°C. The oxygen-to-uranium ratio of the fuel was then reduced to 2.003 ± 0.001 by hydrogen treatment at the sintering temperature.

Fueled BeO specimens containing 17.5 vol % ThO_2 and 12.5 vol % UO_2 fully enriched in U^{235} were also fabricated for high-temperature (~1370°C) irradiation experiments. The fuel was introduced as a mechanical mixture of submicron-size UO_2 and ThO_2 powder. The specimens were cold pressed and sintered in argon at 1750°C. The resulting oxygen-to-uranium ratio in the UO_2 of approximately 2.4 was subsequently reduced to 2.002 ± 0.001

by hydrogen treatment at the sintering temperature. Densities of approximately 94% of theoretical were obtained. The microstructure of a typical $BeO-UO_2-ThO_2$ specimen is shown in Fig. 5.2. The gray phase is BeO; the white phase is a UO_2-ThO_2 solid solution, with some free UO_2, according to petrographic examination of powdered samples and thin sections; and the black areas are voids inherent in the structure or caused by "pull-out" during polishing.

The microstructure of BeO containing 30 vol % UO_2 is shown in Fig. 5.3. With the exception of a few scattered large particles, the microstructures of both the $BeO-UO_2$ and $BeO-UO_2-ThO_2$ specimens show uniform dispersion of the fuel in a fine-grained, dense BeO matrix. Fueled BeO

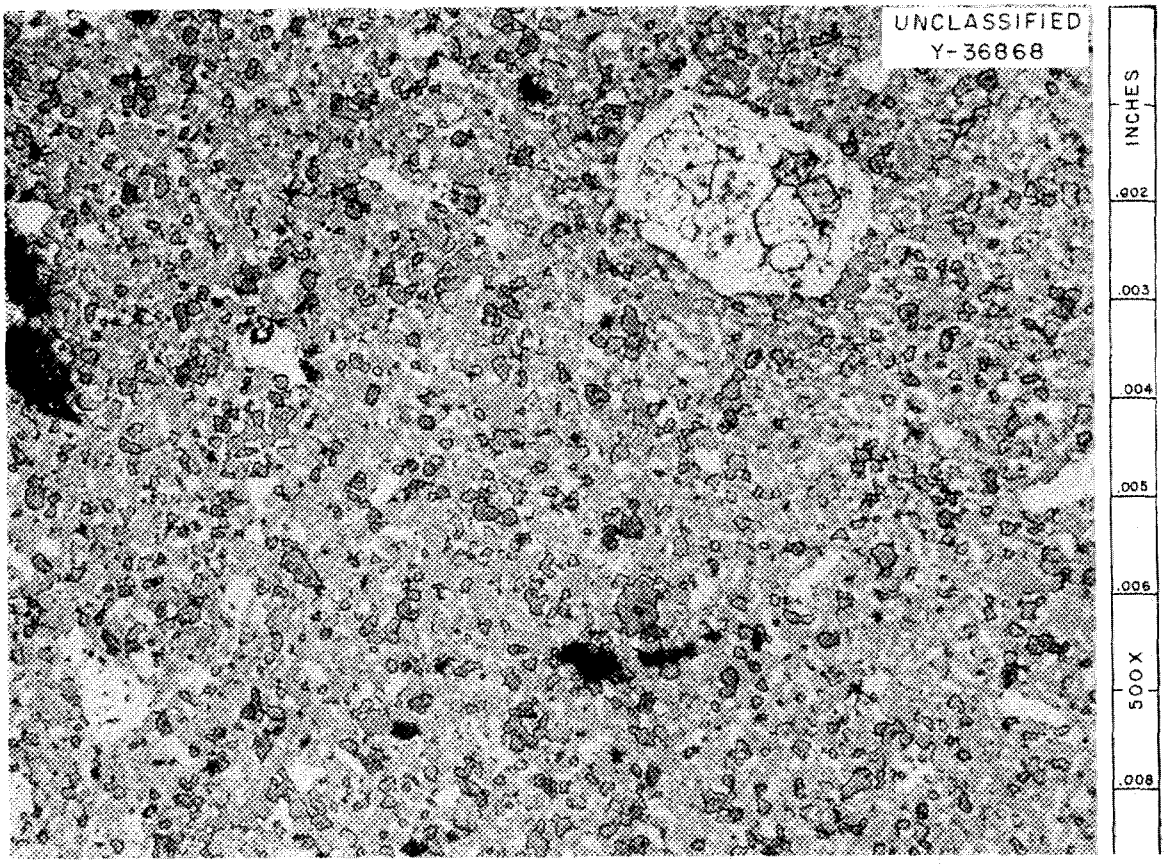


Fig. 5.2. Microstructure of BeO Body Containing 12.5 vol % UO_2 and 17.5 vol % ThO_2. Etchant: 70% H_2O–20% H_2O_2–10% H_2SO_4 + 50% H_2O–50% HF.

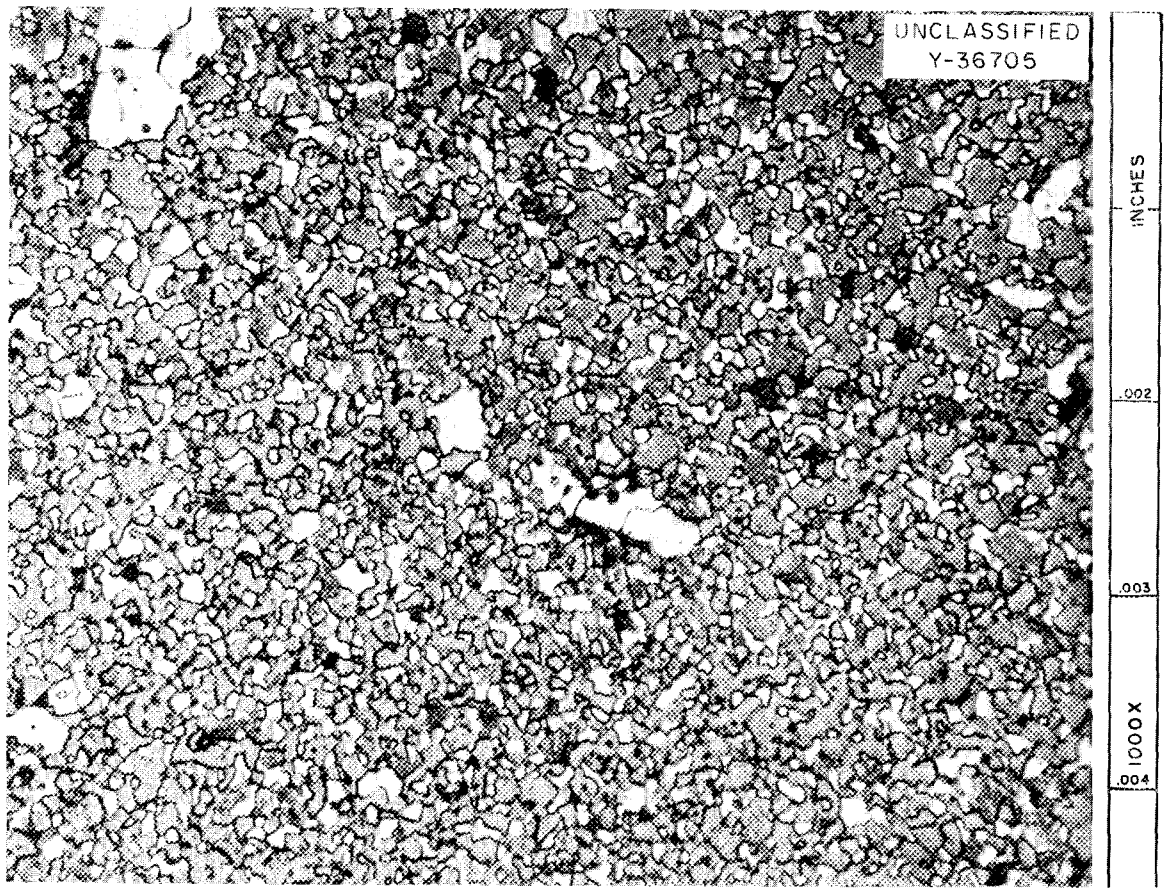


Fig. 5.3. Microstructure of BeO Body Containing 30 vol % UO_2. Etchant: 70% H_2O–20% H_2O_2–10% H_2SO_4 + 50% H_2O–50% HF.

specimens and ThO_2 thermal insulators typical of those fabricated to close dimensional tolerances without machining for the high-temperature irradiation experiments are shown in Fig. 5.4.

Incorporation of UO_2 as Large Particles in BeO. In the use of UO_2 as a fuel dispersed in a BeO matrix, it is desirable from the standpoint of fission-gas retention and radiation damage for the fuel particles to be in the size range 100 to 500 μ. The fabrication of such a composite without the formation of cracks or large voids around the fuel particles requires a knowledge of the shrinkage relationships of both components during sintering.

Linear shrinkage data were obtained on large, single particles of hydrothermally produced $UO_3 \cdot H_2O$ by measuring, microscopically, the change

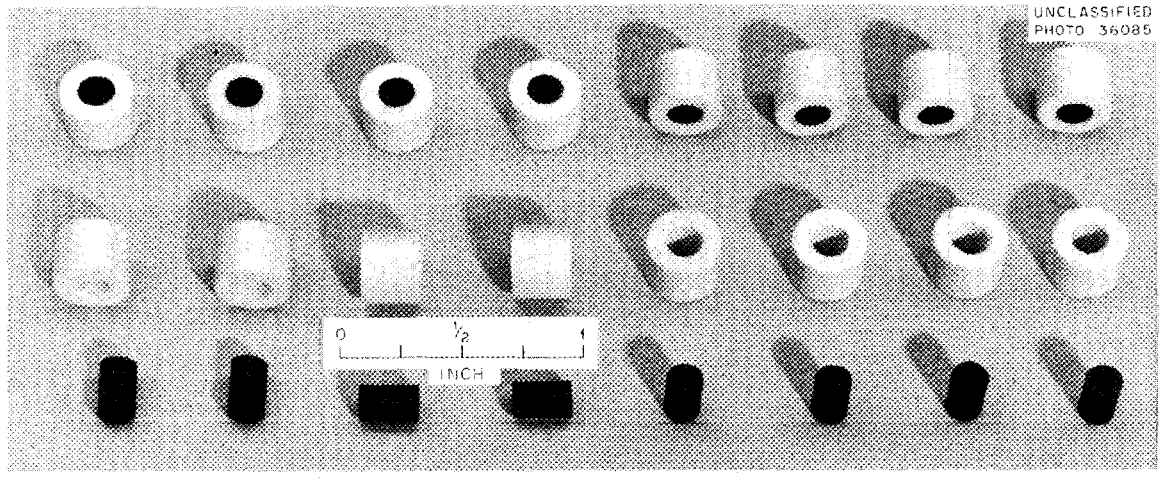


Fig. 5.4. Typical Fueled BeO Specimens and ThO_2 Thermal Insulators Fabricated for Irradiation Experiments.

in dimensions with increasing temperature as the monohydrate crystals were converted to UO_2 by heating in hydrogen. The results were inconclusive because of a significant variation in shrinkage measurements obtained from different particles. The nonuniform shrinkage of these particles is believed to be associated with the orientation of the crystal axes within the particles and the shrinkage along different axes as the crystal structure is changed from orthorhombic to tetragonal and, finally, to cubic during conversion to UO_2. Attempts were then made to prepare the fuel as large granules of polycrystalline UO_2 formed by granulating prepressed, fine-grained powders that should exhibit uniform shrinkage.

Shrinkage characteristics of fuel and matrix were determined by sintering UO_2 and BeO pellets pressed at various green densities. The sintering schedules were designed so that the shrinkage for a given UO_2 or BeO body in an argon or hydrogen atmosphere could be determined at temperatures up to 1750°C. Comparisons of the shrinkage "profiles" obtained, based on selected green densities, are presented in Figs. 5.5 and 5.6. These bodies were compacted to green densities of 40% of theoretical for UO_2 and 54.6% for BeO, in accordance with accepted fabrication procedures. It may be seen that approximately 14 vol % differential shrinkage occurs during the complete sintering cycle. It was calculated that this differential shrinkage could be virtually eliminated by

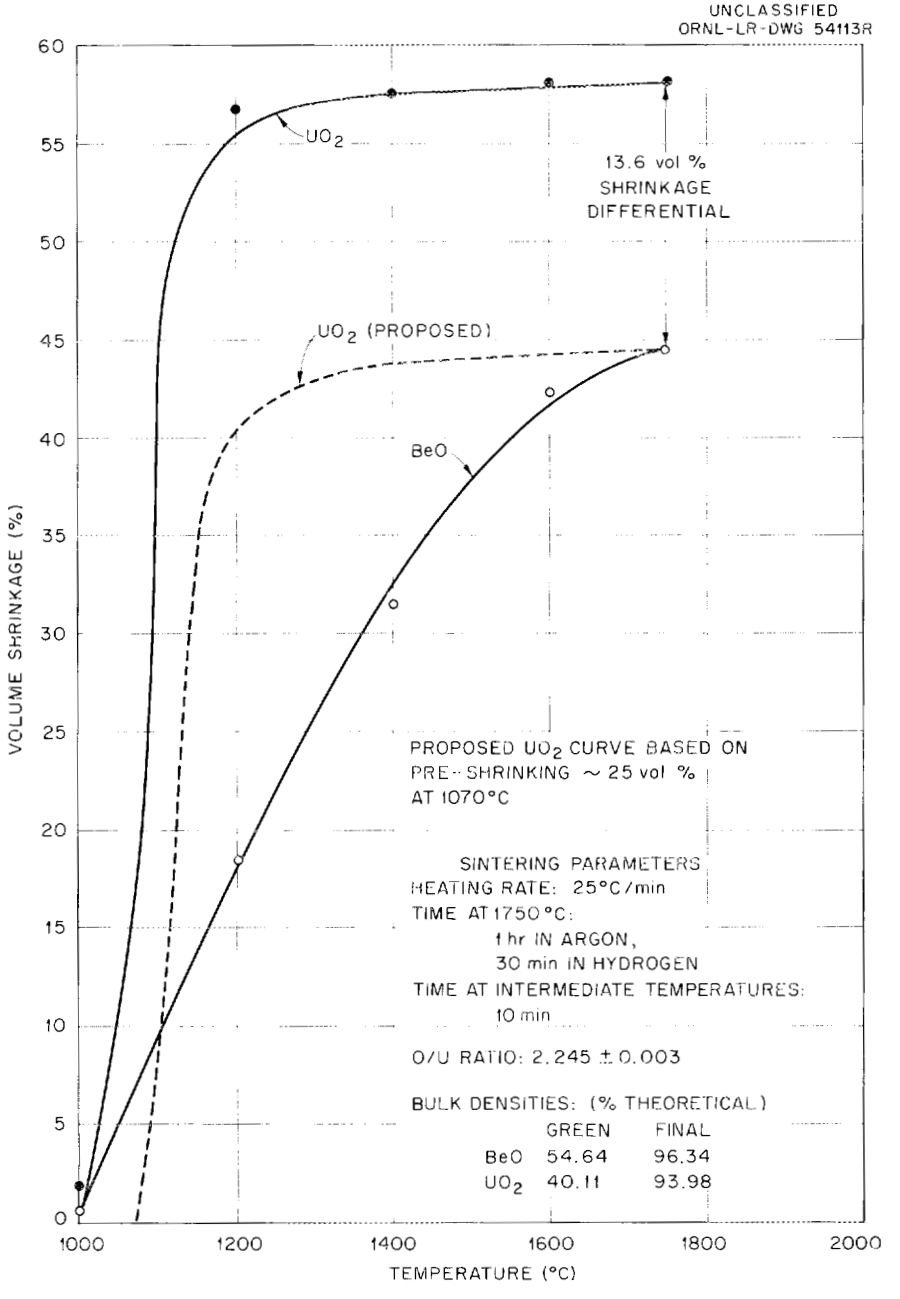


Fig. 5.5. Shrinkage Profiles of BeO and UO_2 Bodies During Sintering in Argon at 1 atm and Subsequent Treatment in Hydrogen at 1750°C.

preshrinking the UO_2 approximately 25% by a prefiring treatment before incorporation in the BeO.

Fueled bodies of BeO containing 30 vol % of UO_2 with a particle size of 150 to 250 μ were fabricated to check these shrinkage relationships.

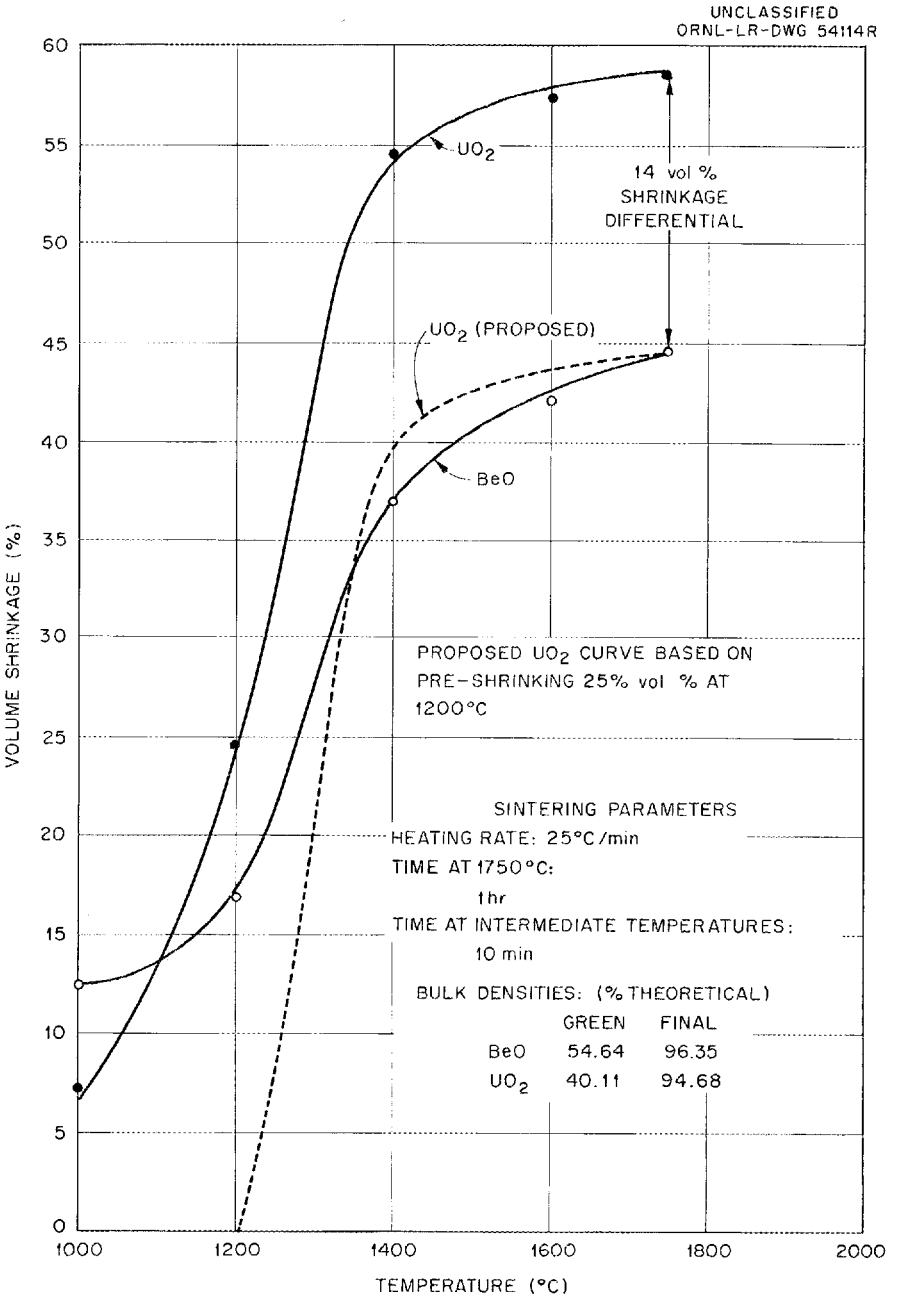


Fig. 5.6. Shrinkage Profiles of BeO and UO_2 Bodies During Sintering in Hydrogen at 1 atm.

The fuel particles were prepared by granulating green and prefired compacts of UO_2. It was assumed that the particles thus obtained would possess the shrinkage and sintering characteristics of the parent compact. In order to promote uniform distribution of the large fuel particles, the mixtures were paste-blended in a water solution of 2 wt % polyvinyl alcohol. The addition of polyvinyl alcohol was necessary only to form a bond between the fuel particles and BeO powder agglomerates. This bonding minimized the segregation of fuel during granulation of the dried mixture prior to compacting. Compacted bodies containing fuel particles prefired to several shrinkage stages were sintered in hydrogen at 1750°C for 1 hr. The results of microscopic surface examination of these specimens are tabulated below:

Fuel Particle Description	Surface Appearance of Sintered Specimens
Unfired (green)	Obvious voids around fuel grains
Preshrunk approximately 14.5 vol %	Relatively smooth surface
Preshrunk approximately 26 vol %	Relatively smooth surface
High-fired, fully shrunk	Very rough-textured surface; fuel grain protrusion prominent

These results are in accordance with the predicted behavior of fueled compacts based on the data of Fig. 5.6.

Fabrication of Fueled Graphite (A. W. Seifert, F. L. Carlsen)

Experiments for determining the reaction of UC with gases evolved at high temperatures from the high-carbon-forming thermosetting binders used in graphite fabrication were extended to include tests with Durite SD-5172, Durez 16470, and pitch. Mixtures consisting of approximately equal volumes of UC and each binder were fired to 1000°C in a hydrogen atmosphere. The relatively large quantity of binder was used so that definite reactions could be easily detected. X-ray diffraction analysis of the heat-treated mixtures showed only UO_2 to be present. It is concluded, therefore, that

these binders, like the ones tested previously,[3] would cause unsatisfactory laminations and surface defects, if used in the preparation of UC-fueled graphite bodies.

In another approach to fueling natural graphite, a 20%-enriched uranyl nitrate solution was wet mixed with natural graphite and a binder, Durite SD-5143. After drying, screening, cold pressing, and firing at 1000°C in hydrogen, the specimens were found to be slightly laminated. These specimens did not, however, have the minute surface defects previously observed with the UC-fueled specimens. An autoradiograph of one of the specimens showed uniform distribution of the fuel.

Fabrication studies were also performed on natural graphite fueled with particles of UO_2 and with uncoated and pyrolytic-carbon-coated UC_2 obtained from the Minnesota Mining and Manufacturing Company. The general fabrication scheme used in all cases involved dry mixing with Durite SD-5143 binder, cold pressing, and firing at a rate of 20°C/hr to 1000°C in argon. The results of these studies are presented in Table 5.3. As may be noted, this fabrication technique produced sound bodies containing UO_2, but problems similar to those reported previously[3] with bodies containing UC were encountered with uncoated UC_2. It is apparent that pyrolytic-carbon-coated particles show promise and that further studies with particles

[3] "GCR Quar. Prog. Rep. Sept. 30, 1960," ORNL-3015, pp. 74–75.

Table 5.3. Properties of Fueled Graphite Bodies

Fuel	Particle Size of Fuel	Distribution of Fuel in Body	Appearance
UO_2	<74 μ (-200 mesh)	Uniform	No visible defects
UO_2	~150–250 μ (-60 +100 mesh)	Sample 1: uniform Sample 2: center only	No visible defects No visible defects
UC_2 spheres[a]	~240 μ	Sample 1: uniform Sample 2: center only	Laminations and surface bumps Laminations
UC_2 spheres coated with pyrolytic carbon[a]	Total: ~760 μ Coating thickness: ~100 μ	Uniform Center only	A few surface bumps No visible defects

[a] Supplied by Minnesota Mining and Manufacturing Company.

of this type are in order. The metallographic and x-ray diffraction analyses completed thus far have shown the "UC_2" in coated particles to consist of approximately 90% UC_2, 10% UC, and a small amount of graphite. A phase tentatively identified as either UO_2 or graphite was found at the interface of the coating and the carbide spheroid. With the exception of the presence of a very small amount of U_2C_3, the uncoated uranium carbide particles appear to have the same composition as the coated "UC_2."

Fission-Gas-Release Studies (D. F. Toner)

The rate of release of Xe^{133} from samples of BeO containing 25 vol % UO_2 as a fine dispersion was measured at a series of temperatures by the neutron-activation technique. The data obtained from these experiments are given in Table 5.4. The release-rate parameter, D′, has not been calculated because no adequate mathematical model for diffusion analysis has been formulated.

Table 5.4. Results of Measurements of the Rate of Release of Xe^{133} from BeO-UO_2

Test Temperature (°C)	Accumulated Time of Test (hr)	Total Fraction Released
1200	2	3.6×10^{-5}
	6	4.6×10^{-5}
	24	7.4×10^{-5}
	32	8.8×10^{-5}
1400	2	8.94×10^{-4}
	5	9.80×10^{-4}
	21	1.23×10^{-3}
	29	1.88×10^{-3}
1600	2	3.76×10^{-2}
	4	4.32×10^{-2}
	21	5.54×10^{-2}
	29	5.83×10^{-2}
1800	2	8.95×10^{-2}
	6	2.09×10^{-1}
	22	8.39×10^{-1}
	30	1.09×10^{0}

Studies are being carried out on the rate of Xe^{133} release from fueled graphite. By using a postirradiation annealing technique for the fission-gas-release measurements, data have been obtained over the temperature range 800 to 1200°C. The fueled graphite was prepared from TS-160 mix obtained from National Carbon Company. High-fired UO_2 particles were blended with the mix, and the samples were fired at 2550°C, at which temperature the UO_2 was converted to UC_2. The fractional release and the release-rate parameter values obtained thus far are listed in Table 5.5.

Table 5.5. Results of Measurements of the Rate of Release of Xe^{133} from Fueled Graphite

Test Temperature (°C)	Accumulated Time of Test (hr)	Total Fraction Released	Calculated Release-Rate Parameter, D' (sec^{-1})
800	1	0.02105	4.82×10^{-12}
	4	0.02153	
	9	0.02199	
	16	0.02223	
1000	1	0.01393	4.55×10^{-11}
	4	0.01536	
	9	0.01706	
	16	0.01784	
1200	1	0.02726	7.44×10^{-10}
	4	0.03551	
	20	0.04973	
	25	0.05197	

Arc Casting of Uranium Carbide Shapes (D. T. Bourgette)

Several UC cylinders, ranging in size from 0.250 in. in diameter and 0.750 in. long to 0.500 in. in diameter and 3.250 in. long, were cast in copper molds and were found to contain severe longitudinal and radial cracks as a result of rapid cooling. It is thought that cracking of this type has been responsible for the difficulty that has been encountered in machining irradiation specimens from such cylinders. Crack-free castings, 0.350 in. in diameter and 1 in. long, of high-purity UC were obtained after changes were made in the melting procedure. The changes included increasing the initial charge weight, decreasing the contact area between

the mold and the water-cooled base plate, using hot water to cool the base plate, melting the charge under low-pressure argon (270 mm Hg), and evacuating the furnace chamber to <1 mm Hg immediately after the charge had been cast. Despite these changes in procedure, larger cylinders still showed internal cracking.

In order to further reduce the cooling rate of cast shapes, several UC cylinders 0.4 in. in diameter and 3.25 in. long were arc cast into graphite mold inserts of the type shown in Fig. 5.7. Metallographic examination of these shapes revealed that the grain size was approximately 30 times larger than that of shapes cast in copper molds. This indicates that the cooling rate in the graphite molds was significantly lower. The grain sizes of these shapes are compared in Fig. 5.8. Radiographs of the shapes cast in graphite molds also showed slight internal cracking.

Volatility of UC at Elevated Temperatures (J. M. Kerr)

In order to investigate the mechanisms leading to the loss of material from UC during vacuum sintering, a mass spectrometer has been used to

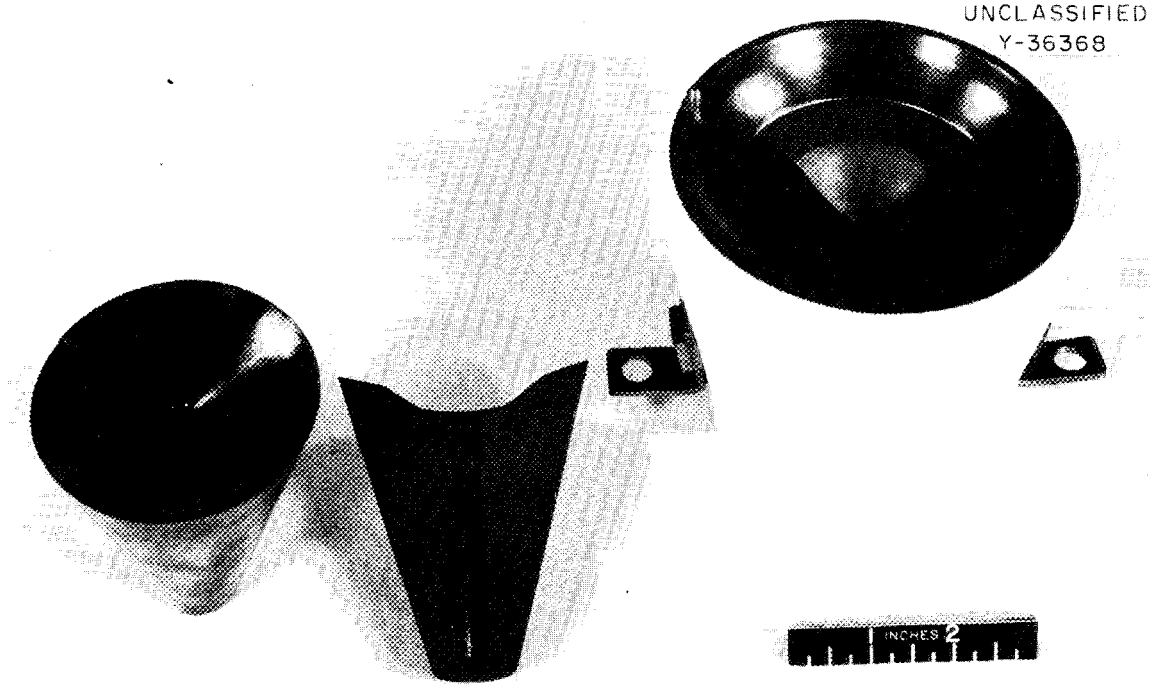


Fig. 5.7. Mold and Mold Insert Arrangements for Both Copper and Graphite Molds.

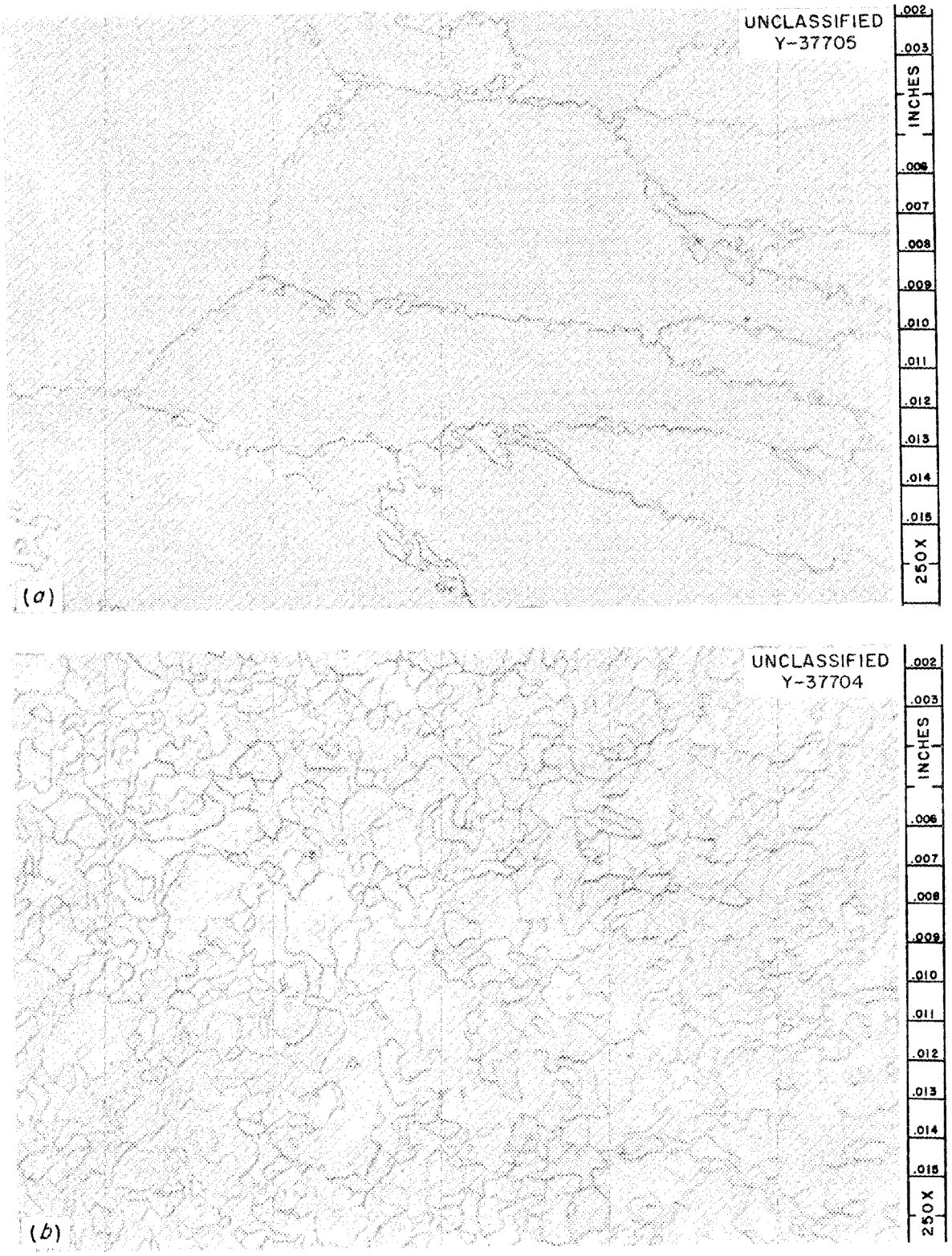


Fig. 5.8. Microstructure of UC Melted and Cast in (a) Graphite and (b) Copper. Note difference in grain size and the free uranium in (b). Etchant: H_2O, HNO_3, and acetic acid.

identify the species emitted and to determine their relative rates of emission from the carbide at temperatures of 1500 to 2150°C and pressures of approximately 2×10^{-6} mm Hg. The mass spectrometric analyses were performed by the Analytical Chemistry Division on a 12-in.-radius, 60-deg-sector, Nier-type instrument developed for the isotopic analysis of solid samples. The starting material for this study was obtained by grinding arc-melted UC castings to −200 +270 mesh powder under argon with a high-alumina mortar and pestle. Chemical analysis indicated 4.77 wt % total carbon, with 0.15% free carbon.

A 200- to 300-μg sample of the UC powder was placed on a tantalum filament in the reaction chamber of the mass spectrometer, and the chamber was evacuated to 2×10^{-6} mm Hg pressure. The sample was then heated to a series of temperatures by passing current through the filament from a precisely controlled source. The temperatures were estimated by using a previously determined current versus temperature graph with a probable accuracy of ±50°C. The power input was held at each setting for 3 min to achieve thermal equilibrium before a scan was made of the ions emitted from the sample. Because the mass spectrometer can detect only charged species, a beam of 75-ev electrons was directed across the opening in the reaction chamber in order to ionize the neutral species and thus permit a more quantitative analysis of the material emanating from the UC sample.

Although the mass spectrometer was adjusted to detect all ions with mass numbers between 200 and 290, only UO_2^+, UO^+, and U^+ ions were observed. No carbide or UO_3^+ ions were detected. The relative rates at which the three ions were emitted from UC as a function of temperature are illustrated in the graphs of Fig. 5.9.

Structural Materials Evaluation

Coating for EGCR Graphite Support Sleeves (F. L. Carlsen, K. V. Cook, R. W. McClung)

The EGCR graphite sleeves will be coated to prevent sustained burning of the graphite in the event air is admitted to the core as a result of a rupture in the coolant system. Since a coating will affect the

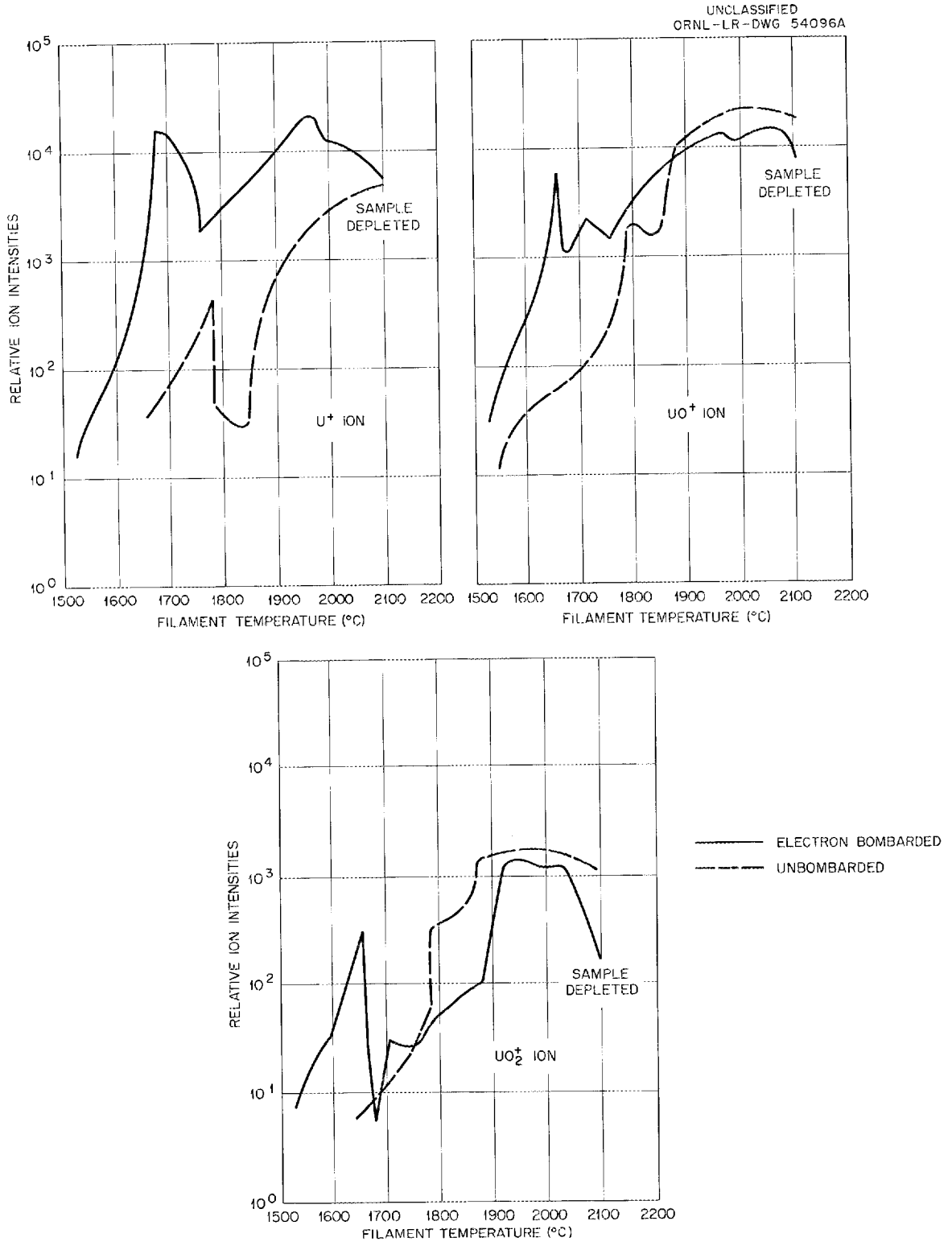


Fig. 5.9. Relative Ion Intensity Versus Filament Temperature for U^+, UO^+, and UO_2^+ Ions.

properties of the support sleeve, a general evaluation of coatings is in progress.

Oxidation Resistance of Coated Graphite. Several small coated and uncoated graphite samples from the Minnesota Mining and Manufacturing Company have been tested for oxidation resistance. The samples were in the form of right circular cylinders, 1 in. in diameter and 2 in. long, weighing approximately 50 g, and they were tested in air at a velocity of approximately 700 ft/hr for 6 to 24 hr at temperatures from 420 to 630°C. The results of these tests are given in Table 5.6.

Table 5.6. Oxidation Resistance of Coated and Uncoated Graphite Samples

Type of Sample	Oxidation Rate (g/g·hr)		
	At 420°C	At 520°C	At 630°C
Uncoated type 580 graphite	0.29×10^{-3}	5.6×10^{-3}	$15.3\text{–}24.8 \times 10^{-3}$
Si-SiC coated type 580 graphite	0.24×10^{-3}	3.7×10^{-3}	$7.9\text{–}8.3 \times 10^{-3}$
Si-SiC coated type 901S graphite	0	0	0
Si-SiC coated type 901S graphite with 5% of the coating removed			$0.36\text{–}1.8 \times 10^{-3}$

The samples were tested in a tube furnace in flowing air. The temperature gradient across the samples was about 30°C, and the temperature of the furnace varied as much as 40°C during a run because of line-voltage fluctuations. The temperatures given in Table 5.6 represent the average temperatures for the tests.

The difference between the type 580 graphite and the type 901S graphite is primarily a matter of anisotropy, with the type 901S graphite being the more isotropic. The Si-SiC coating on the type 580 specimen was observed to contain many cracks prior to testing, whereas that on the type 901S specimen was apparently crack free. Five percent of the area of two type 901S-coated samples was exposed by grinding away the coating on one-half

of one end of each sample. Since the EGCR support sleeves will have approximately 5% of their surface uncoated at the ends in order to maintain tight-fitting joints, the tests of these samples provide a basis for estimating the oxidation rate of the graphite sleeves.

The results of the tests show that the effectiveness of the coating on type 580 graphite increases with increasing temperature. The effectiveness in this case is defined as the reduction in the oxidation rate as compared with that of uncoated graphite. The ratio of the oxidation rate of coated type 580 graphite to that of the uncoated type 580 graphite decreased with temperature from about 1 at approximately 420°C to <0.5 at approximately 630°C. The coating on the type 901S graphite was found to be completely protective under the test conditions and, even with 5% of the coating removed, was shown to be more effective than that on the type 580 specimen. The range of oxidation rates at 630°C reflects the variations in temperature and the differences in samples.

Thickness Measurements on Coated Sleeves. An eddy-current technique is being developed for measuring the thickness of silicon carbide or siliconized silicon carbide coatings on the graphite sleeves. Work thus far has been on a silicon carbide coating applied by the National Carbon Company to representative sleeves from each of three sources.[4] The thickness apparently varies from approximately 0.030 to 0.060 in. It is planned to check the accuracy of these measurements by sectioning the sleeves.

Integrity of Coatings. The feasibility of an electrode oxidation-potential test for detecting defects such as cracks and pinholes in silicon carbide coatings on graphite sleeves has been studied. This system establishes a small galvanic cell through the use of suitable electrodes and a suitable electrolyte. By localizing the contact area of the electrolyte, a difference should be noted in the generated emf when there is a break in the coating that permits the graphite to react in the galvanic cell. However, in the tests completed thus far, no emf difference has been noted between coated and uncoated graphite. This may be due to

[4] "GCR Quar. Prog. Rep. Jan. 30, 1960," ORNL-2964, p. 121.

impurities or voids in the coating or insufficient potential difference between the graphite and the coating using the selected electrodes and electrolyte.

Evaluation of Commercial High-Density Graphite (F. L. Carlsen)

The strength, coefficient of thermal expansion, and ash content of several types of commercial graphite were determined as a part of the general graphite evaluation program. The samples tested were American Metal Products high-density grade 1A, four types of graphite considered for the United Kingdom Dragon program, duPont explosively formed natural graphite, and National Carbon Company type CEY. All samples were received in the form of right circular cylinders and, except for the duPont specimen, were extruded products. The results of the tests are given in Table 5.7.

Tube-Burst Testing of Stainless Steel (J. T. Venard)

Testing of as-received type 304 stainless steel tubing (Superior Tube Co. heat No. 23999X) to provide base-line data for comparison with in-pile tube-burst test data is continuing. Results obtained recently for 2.5-in.-long specimens tested at 1300°F in air are given below:

Tangential Stress (psi)	Time to Rupture (hr)
7 951	1077
8 069	2007
9 710	469
9 821	549
11 403	144
11 593	144

It was observed previously[5] that abnormal grain growth and subsequent premature burst failures occurred in tubing annealed at 2150°F, the brazing temperature used for attaching mid-plane spacers to EGCR fuel elements with GE-81 alloy. Therefore the substitution of copper for GE-81 alloy is being

[5]"GCR Quar. Prog. Rep. March 31, 1960," ORNL-2929, pp. 115–7.

Table 5.7. Properties of Various Types of Graphite

Type	Density (g/cm^3)	Ash Content (wt %)	Coefficient of Thermal Expansion (in./in.·°C)		Room-Temperature Rupture Strength (psi)	
			Parallel[a]	Normal[a]	Tension[b]	Compression[c]
			$\times 10^{-6}$			
AMP-1A	1.97	0.037	2.54		2800	9900
Dragon						
HX10	1.85	0.014	2.87		2300	5400
HX12	1.79	0.025	2.83		1000	7000
EYX60						
Sample 1	1.70	0.021	2.96		2900	8200
Sample 2	1.74	0.024	2.82		3200	
duPont						
Sample 1[d]	2.26	6.1	18.43			
Sample 2	2.25	6.1	12.97			
Sample 3[e]	2.10	6.1		7.85		
NCC CEY	1.92		1.95			

[a]With respect to longitudinal axis of as-received cylindrical sample.

[b]Machined-and-threaded specimens.

[c]Cube specimens, 1/2 in. × 1/2 in. × 1/2 in.

[d]0.7% net expansion observed after cooling to room temperature.

[e]0.3% net expansion observed after cooling to room temperature.

considered as a means of minimizing this grain growth, because copper has a lower brazing temperature (2020°F).

Central spacers were copper brazed to samples of representative EGCR fuel element tubing in the annealed, 1/8-hard, and 1/4-hard conditions. Furnace brazing was carried out without difficulty using copper preplaced either as a powder slurry or as wire. Results indicate a substantial decrease in the grain growth. Tests are in progress to determine the time to rupture of tubing subjected to a typical copper brazing cycle.

Dimensional Studies of Simulated EGCR Fuel Elements at Elevated Temperatures (W. R. Martin)

A further test of a simulated EGCR fuel element was conducted to study the mechanical behavior of fuel pellets and cladding during thermal cycling

under external pressure. Previous tests[6] showed that the expansion of an element after collapse of the tube wall is dependent upon both the inner surface temperature of the pellets and the cladding temperature and that the fracturing of pellets exposed to thermal gradients does not lead to shifting of material within the element. In this experiment the element was subjected to an external pressure of 320 psi during testing, after being held for 32 hr at an average surface temperature of 1420°F and a central UO_2 temperature of 2350°F. Approximately 30 hr at these conditions was required for the cladding to contact the UO_2. The element was then cycled between the central UO_2 temperature limits of 400 and 2350°F for 109 cycles. The heating and cooling rate of the cladding was 150°F/min and the cycle frequency was 20 min.

Analyses of the test data and examination of the element after the test revealed the following:

1. The axial expansion characteristics of the UO_2 column did not change during the 109 cycles.

2. The total axial permanent strain introduced in the cladding was 0.45%.

3. Circumferential ridges were formed in the cladding at the pellet interfaces, but they were not large enough to be measured by a commercial shadowgraph technique.

4. Gaps as large as 0.020 in. were introduced between the UO_2 pellets as a result of thermal cycling.

Following this examination the element was returned to the testing equipment and held at average surface and central UO_2 temperatures of 1475 and 2750°F, respectively. After 65 hr at these conditions, the cladding had collapsed so that it followed very closely the profile of the UO_2 pellets. After a total of 114 hr at the above conditions, the element was cycled between central UO_2 temperatures of 400 and 2750°F for 48 cycles. The test data and the examination made after the test revealed that the dimensional characteristics of the element changed markedly during thermal cycling. The gaps between pellets grew with successive cycling, and

[6] "GCR Quar. Prog. Rep. June 30, 1960," ORNL-2964, pp. 84–90.

openings as large as 0.040 in. were observed. The total permanent axial strain of the cladding was 2.5%.

The element was placed in the test rig a third time to determine whether the cladding would collapse into the gaps between the pellets. No collapse was detectable after 330 hr at average cladding and central UO_2 temperatures of 1550 and 2870°F, respectively.

In two other series of experiments, the thermal cycling behavior was determined with elements that had a 0.007-in. diametral gap between the pellets and the cladding upon assembly and then with elements in which the cladding had been collapsed around the pellets by external pressure. The elements were cycled from cladding temperatures of 1200 to 1500°F to temperatures in the range of 250 to 500°F. The average heating and cooling rates for the cladding were 150°F/min.

The results of these tests indicate that fuel elements having a diametral gap between the cladding and the fuel pellets will respond to thermal cycling in the same manner as the individual components if subjected to the same thermal conditions and tested separately. However, if there is no radial gap between the fuel pellets and the cladding, axial elongation of the cladding occurs during thermal cycling. This elongation is a function of the external pressure, cladding temperature, and cycling conditions. These parameters affect the elongation of the cladding as follows: (1) an increase in external pressure increases the deformation, (2) the plastic strain in the cladding for any given temperature and pressure conditions is a linear function of the number of thermal cycles, (3) the empirical relationship between the permanent axial strain per cycle and the average cladding temperature is of the form

$$\epsilon_p = be^{-\Delta H/RT} ,$$

where ϵ_p is the permanent axial strain per cycle, b, ΔH, and R are constants, and T is the average absolute temperature of the cladding, and (4) an increase in either the heating or cooling rate of the cladding increases the elongation obtained per cycle.

Examinations of the elements after these tests revealed that apparently the frictional force between fuel and cladding is sufficient to prevent relative movement. Therefore, an axial gap is developed between pellets in the fuel column, and the total axial elongation of the cladding approximates the summation of the gaps between pellets. Circumferential ridges form at the pellet interfaces during collapse of the cladding and follow the end of the pellet during the axial elongation of the cladding.

Reactions of Type 304 Stainless Steel with CO-CO_2 Mixtures (H. Inouye)

Studies are being made of the factors that affect the oxidation and carburization of type 304 stainless steel in low concentrations of CO_2 and CO in helium. These studies have included gas concentrations ranging from 1.3×10^{-5} to 6.8×10^{-2} atm (6×10^{-5} to 0.317% based on a helium pressure of 315 psi). The ratios of CO_2 to CO concentration have ranged from ∞ to 0.018.

Oxidation of Type 304 Stainless Steel in CO-CO_2 Mixtures. Representative reaction rates that have been obtained for the oxidation of type 304 stainless steel in CO-CO_2 at 1800°F are shown in Fig. 5.10. These results

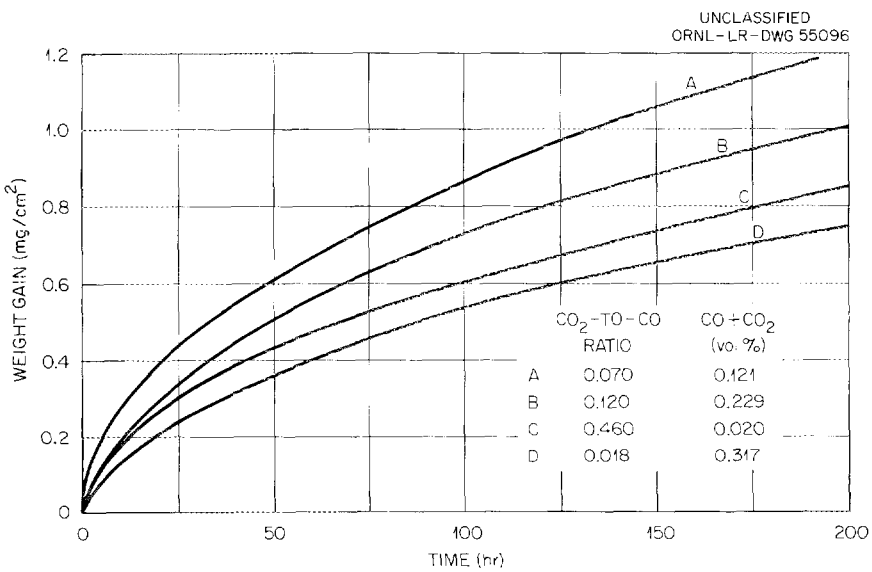


Fig. 5.10. Reaction Rates of Type 304 Stainless Steel with CO-CO_2 Mixtures at 1800°F at Times up to 200 hr.

show that large variations in the concentrations (15:1) and the CO_2-to-CO ratios (25:1) have only a slight effect, if any, on the reaction rate. The slight differences essentially disappear after longer times, as shown in Fig. 5.11. The equations describing the reaction rates are of the form

$$\Delta w = kt^n \quad ,$$

where Δw is the weight increase in mg/cm^2 and t is the time in hours. The constants k and n for the different conditions are listed in Table 5.8.

The effect of temperature on the reaction rates of type 304 stainless steel with a CO-CO_2 mixture (CO + CO_2 = 0.229%; CO_2/CO = 0.12) is shown in Fig. 5.12. The reaction rates were not measureable below 1300°F. Activation energies of 32 000 cal/mole for temperatures between 1300 and 1525°F and 6400 cal/mole for temperatures above 1525°F were calculated.

X-ray diffraction patterns of the oxides present on the specimens after the tests were found to correspond to the spinel-type oxides ($FeO \cdot Cr_2O_3$) at temperatures in excess of 1500°F, whereas, at temperatures below 1500°F, Cr_2O_3 and $3Cr_2O_3 \cdot Fe_2O_3$ predominated. The Arrhenius plot (Fig. 5.12) indicates the formation of a different oxide at the inflection point and supports the x-ray evidence.

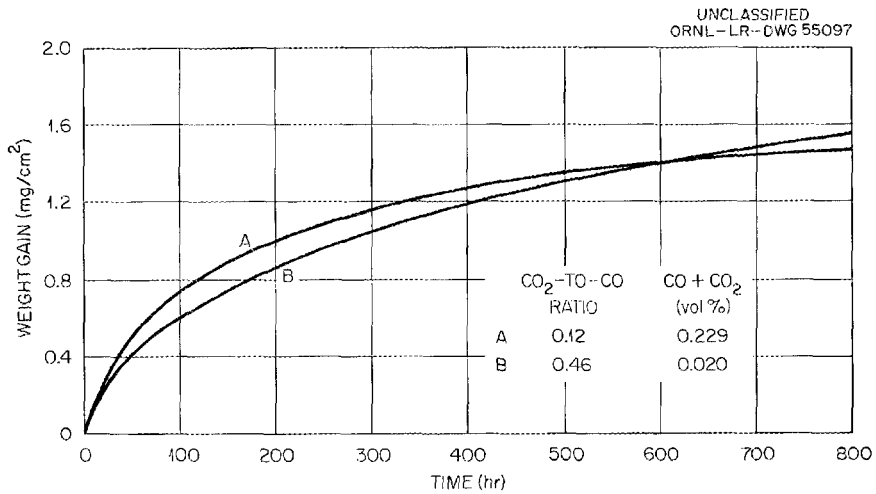


Fig. 5.11. Reaction Rates of Type 304 Stainless Steel with CO-CO_2 Mixtures at 1800°F at Times up to 800 hr.

Table 5.8. Reaction Rate Constants for the Oxidation of Type 304 Stainless Steel in CO-CO_2 Mixtures at 1800°F

Concentration of $CO + CO_2$ (vol %)[a]	CO_2-to-CO Ratio	Rate Constants	
		k	n
0.0201	0.46	0.066	0.481
0.121	0.07	0.086	0.502
0.229	0.12	0.102	0.430
0.317	0.018	0.069	0.567
	Average	0.081	0.495

[a]Based upon helium and impurities at a pressure of 315 psi.

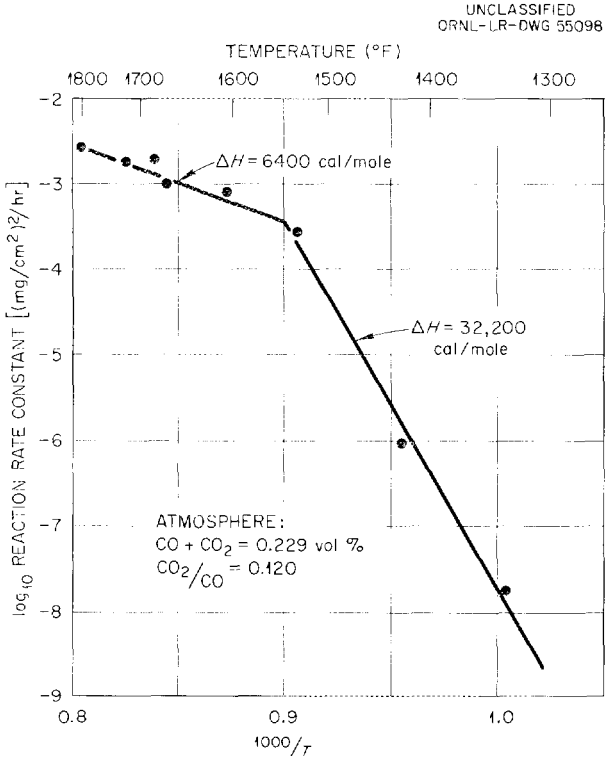


Fig. 5.12. Effect of Temperature on the Reaction Rate of Type 304 Stainless Steel with a CO-CO_2 Mixture.

Carburization of Type 304 Stainless Steel in CO-CO_2 Mixtures. The carburization of type 304 stainless steel in CO-CO_2 mixtures has been found to be dependent on the CO_2-to-CO ratio, temperature, and, when nonequilibrium conditions exist, on the time of exposure to these gases.

The data of Table 5.9 show the variations in the carbon content in 0.002-in. foil specimens after exposure to various CO_2-CO mixtures. The carbon contents of samples tested above 1600°F for 700 and 840 hr are thought to be equilibrium values.

Table 5.9. Carburization of Type 304 Stainless Steel in CO-CO_2 Mixtures

Test Temperature (°F)	Final Carbon Content (wt %)		
	$CO_2/CO = 0.46$, 700-hr Test	$CO_2/CO = 0.12$, 840-hr Test	$CO_2/CO = 0.018$, 200-hr Test
800	0.068	0.070	0.068
1000	0.068	0.078	0.062
1200	0.068	0.078	0.076
1300	0.090	0.081	0.12
1400	0.130	0.163	0.25
1500	0.142	0.305	0.30
1600	0.160	0.309	0.21
1700	0.099	0.528	0.15
1800		0.680	0.15

In the temperature range 1200 to 1600°F, the extent of carburization probably depends on the kinetics of the carburizing reactions (see reactions 1 and 2 below) and would therefore depend on the time. This is apparent from the carbon analyses of the specimens from the 200-hr test. Below 1200°F, carburization does not appear to occur. In 0.020-in.-thick specimens, the carbon content showed a maximum increase of 0.03% when the specimen was exposed for 840 hr to an atmosphere containing CO_2 and CO in the ratio 0.12. It is apparent that nonequilibrium conditions existed in the thicker specimens and that most of the carbon was concentrated at the surface. With extended exposure times, the carbon concentrations of the 0.020-in.-thick specimens are expected to approach the values listed in Table 5.9.

The mechanism by which carburization occurs is not clear at this time. It is thought that the reaction of CO with the alloy that results in the solution of carbon is

$$\text{Stainless steel} + 12CO \rightarrow 6CO_2 + 6C \text{ (in alloy)} \quad . \qquad (1)$$

In stainless steel containing 18% Cr, the carbon taken into solution reacts with the chromium and results in the formation of chromium carbide ($Cr_{23}C_6$) according to the reaction

$$23Cr \text{ (in alloy)} + 6C \text{ (in alloy)} \rightarrow Cr_{23}C_6 \quad . \qquad (2)$$

The net reaction involving only the products and reactants would then be

$$23Cr \text{ (in alloy)} + 12CO \rightarrow Cr_{23}C_6 + 6CO_2 \quad . \qquad (3)$$

The free-energy change involved in reaction 3 increases as the temperature decreases, indicating that the carburizing tendency is greater at the lower temperature. It is not surprising, therefore, to observe a maximum in the carbon content of the stainless steel at some intermediate temperature at which the kinetics of the carburizing reaction is the predominant rate-controlling factor. If the proposed reactions are representative, the maximum in the carbon content would be shifted to lower temperatures with increasing exposure times. Furthermore, the carburization tendencies would also be dependent on the partial pressures of CO and CO_2, since a volume change is involved in the reaction.

Preliminary conclusions are that the principal reaction of type 304 stainless steel with CO and CO_2 is oxidation, which amounts to about 90% of the total reaction at 1800°F, and that carburization comprises only about 10% of the total reaction. Further, the reaction rates for the total reaction are independent of the gas ratios or the gas concentrations. Carburization, on the other hand, appears to depend on these variables. The purification of the helium in the EGCR should take into consideration the futility of removing impurity gases to minimize oxidation. In order to control carburization, however, the data indicate that attention should be directed toward maintaining the proper ratio of CO_2 to CO.

Manufacturing and Inspection Methods Development

Fabrication of Instrumented Fuel Elements and Irradiation Test Capsules (E. A. Franco-Ferreira)

Developmental work is being carried out in an effort to improve the methods of fabricating thermocouples for measuring internal temperatures in irradiation test capsules. This work also is directly applicable to the fabrication of instrumented fuel assemblies for the EGCR.

Thermocouple Wells. The design for the insertion of a tungsten thermocouple well in the end cap of an irradiation-test capsule and a typical completed assembly are shown in Fig. 5.13. In the photograph the tungsten well is at the left and the stainless steel end cap at the right. In this assembly, the well was brazed into the end cap with gold. A typical section of the braze joint, illustrating the good flow attained, is shown in Fig. 5.14. A well of this type was thermal cycled seven times from 1300°F to room temperature, and subsequent metallographic examination showed no evidence of cracking in the braze joint.

Tungsten-Rhenium Thermocouples. The reliability of tungsten-rhenium thermocouples is greatly reduced by the inherent low ductility of tungsten wire and the added embrittlement of the tungsten that results from

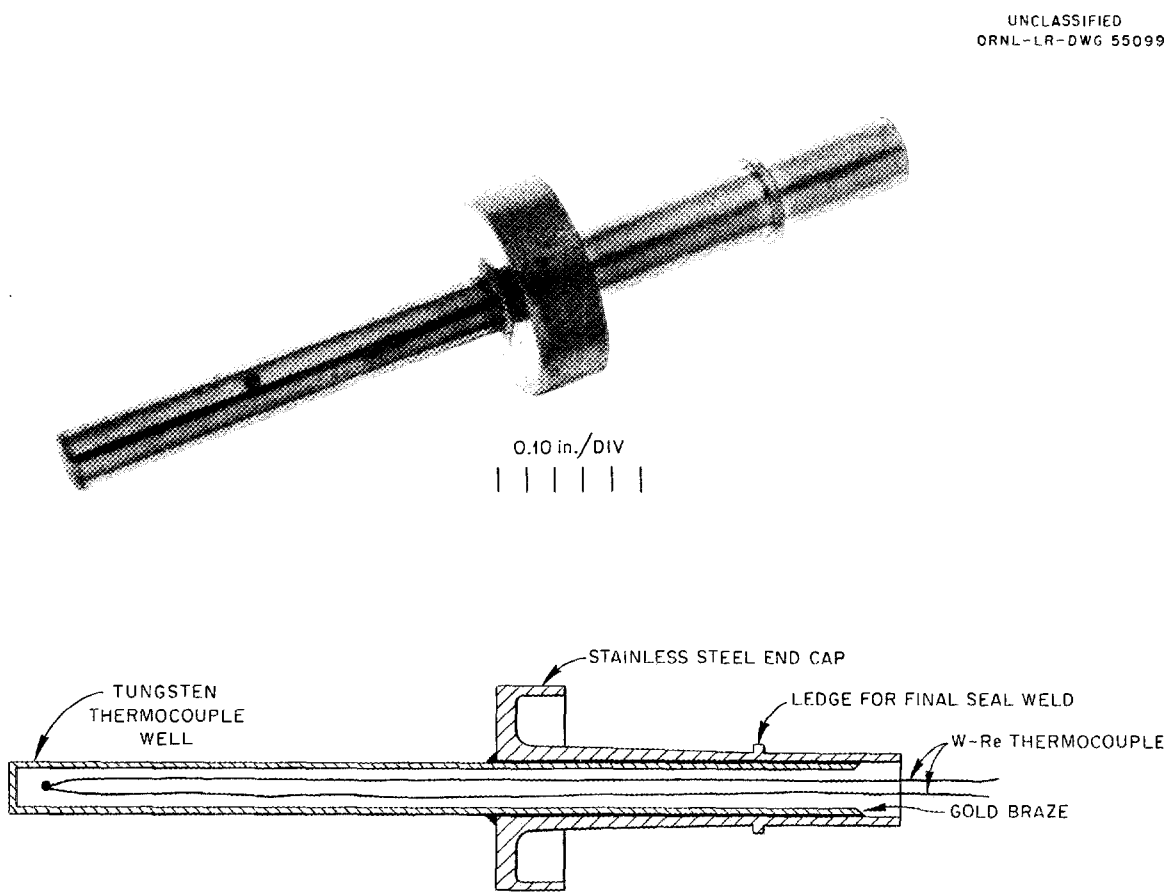


Fig. 5.13. Attachment of Tungsten Thermocouple Well to Stainless Steel End Cap.

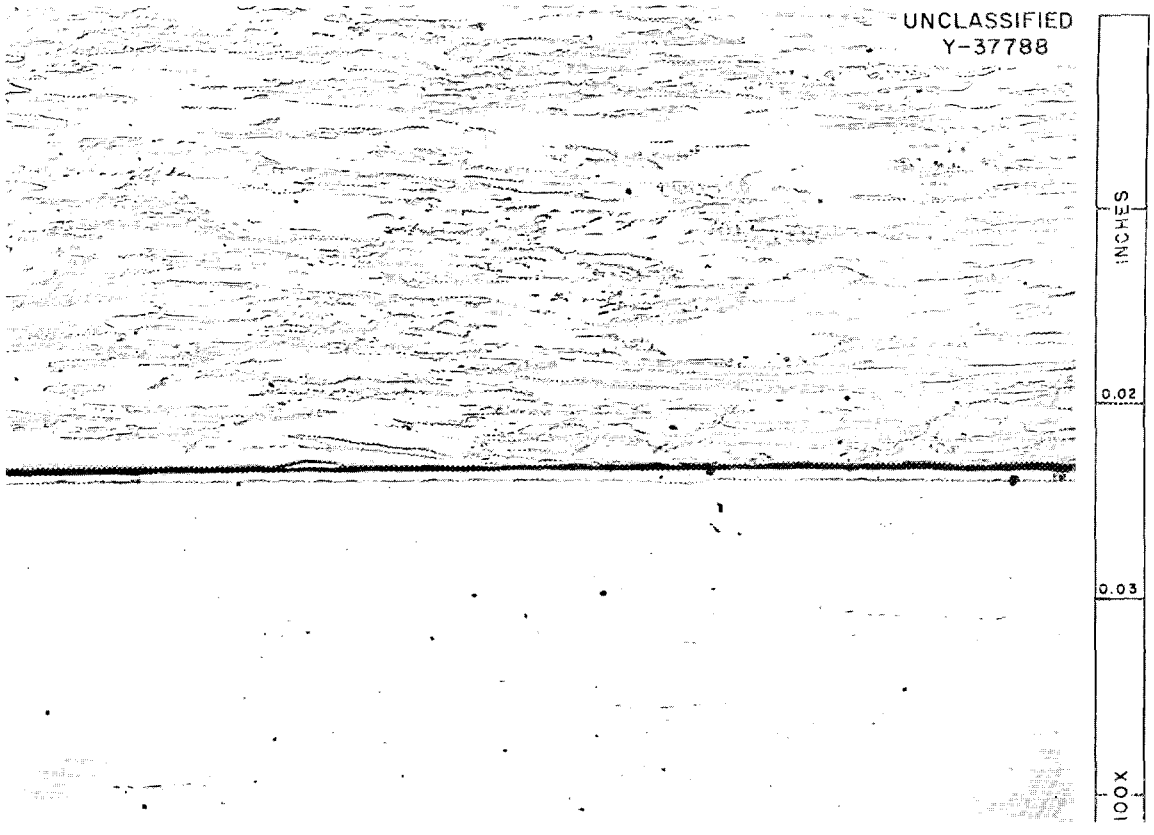


Fig. 5.14. Gold-Brazed Joint Between Tungsten Thermocouple Well and Stainless Steel End Cap. As polished. 100X.

recrystallization during welding. This situation is accentuated by the wide difference between the coefficients of thermal expansion of tungsten and rhenium. Since these physical properties of the thermocouple materials cannot be altered, the thermocouple design must be varied accordingly.

One design approach, which was suggested by investigators at the General Electric Company, is to increase the flexibility of the system through the use of stranded small-diameter tungsten wire. An illustration of the flexibility of such a wire is presented in Fig. 5.15, which shows a knot tied in a stranded wire made up of 40 strands of 0.002-in. wire. A number of tungsten-rhenium thermocouple junctions made with various sizes of wire are shown in Fig. 5.16. The junctions are easily made by standard inert-arc welding procedures, and the finished unit has a high degree of flexibility. It is hoped that this flexibility will relieve thermal

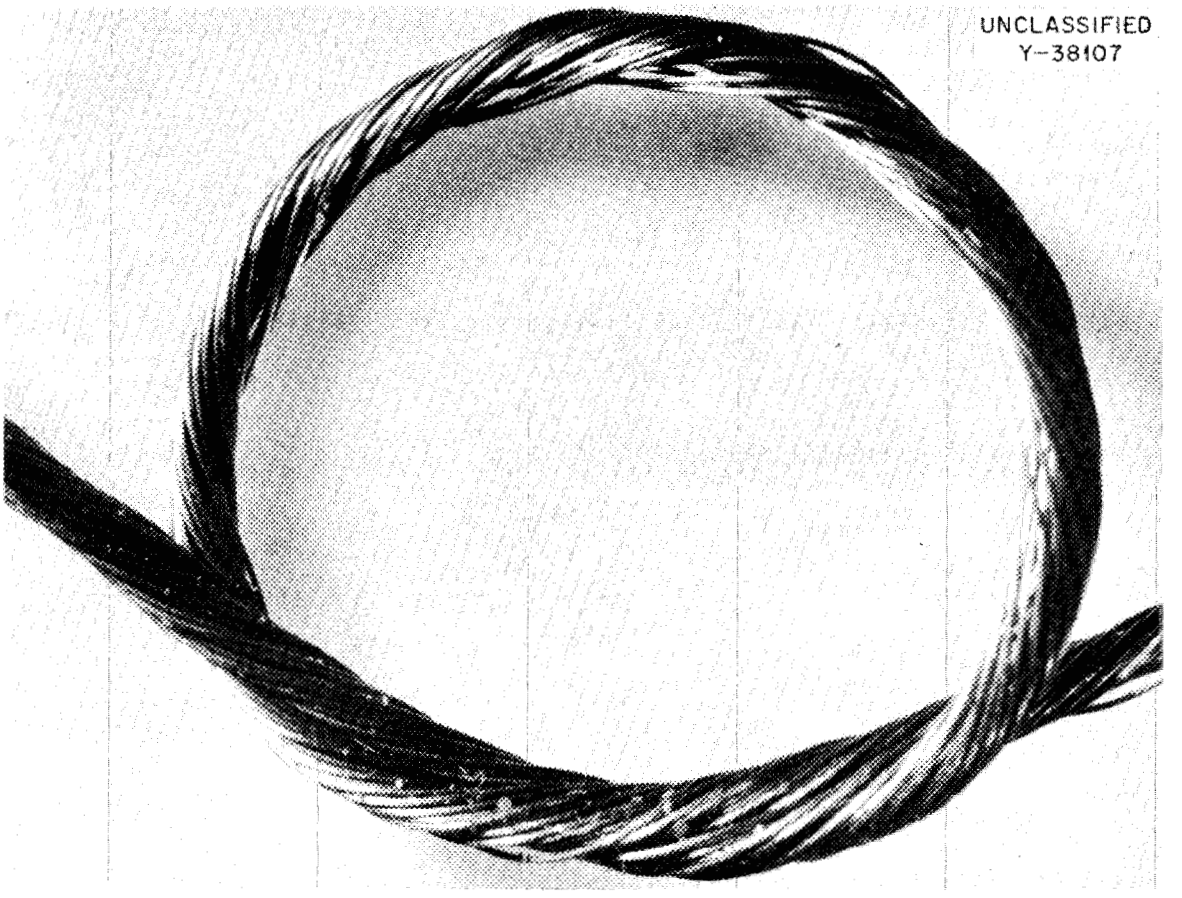


Fig. 5.15. Stranded Tungsten Thermocouple Wire Approximately 0.015 in. in Diameter Tied in a Knot to Demonstrate Flexibility.

stresses on the junction and lengthen the service life of the thermocouple. A number of stranded-wire thermocouples are presently undergoing tests to determine the suitability of their thermoelectric characteristics.

Attachment of Thermocouples to Fuel Elements. Work is also in progress for determining the most suitable way to attach thermocouples to the surface of fuel element tubing for the measurement of surface temperatures. The Chromel-Alumel thermocouples used for this service are clad with 0.040-in.-o.d. stainless steel tubing. Early fuel element designs included the possibility of attaching these thermocouples to the outside of the tube walls, as in Fig. 5.17 which shows grounded and ungrounded junctions brazed to the outside of the tubes. Unfortunately, this method of attachment, while simple, contributes considerable error to the measurement because

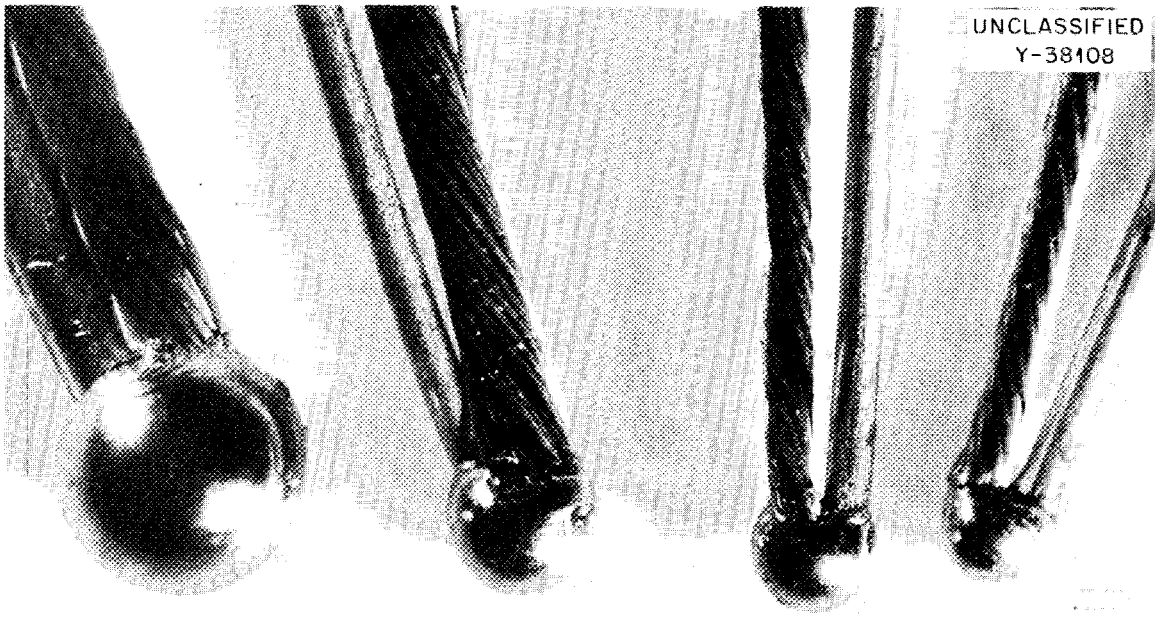
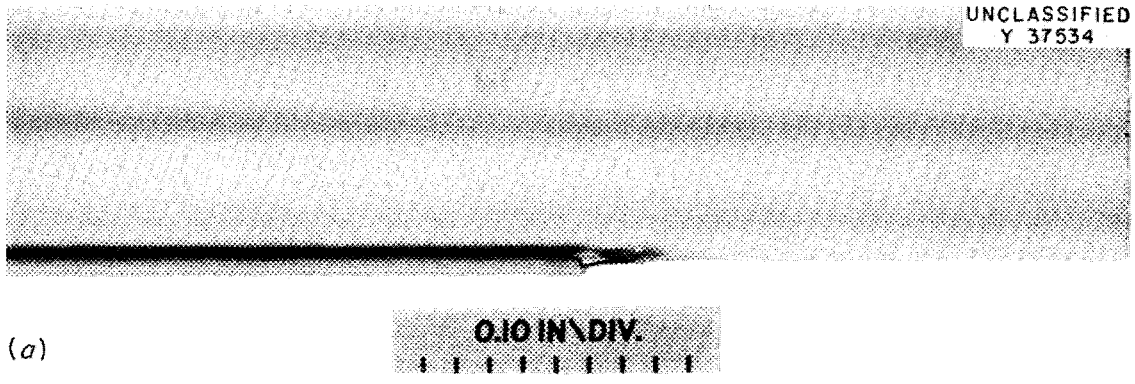


Fig. 5.16. Welded Stranded-Wire Tungsten-to-Rhenium Thermocouple Junctions. Solid wires for the three small junctions are 0.010 in. in diameter and the larger solid wire is 0.025 in. in diameter.

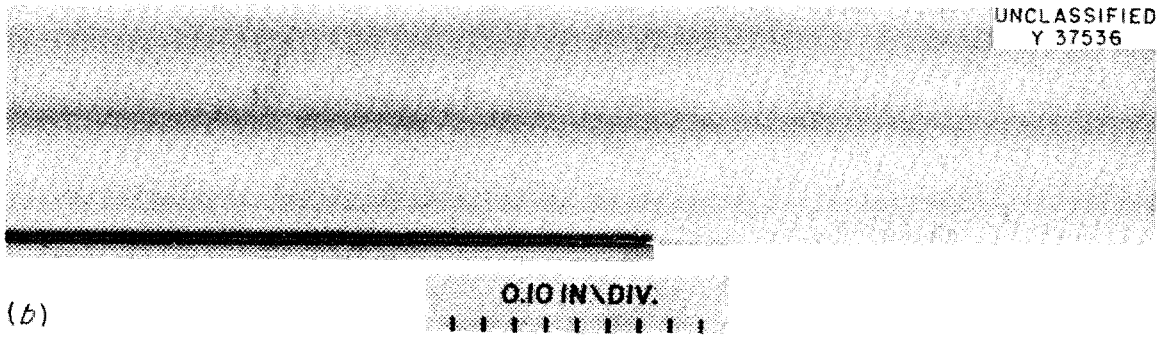
of the cooling effect of the gas stream on the thermocouple. Therefore work is under way on a method for attaching these thermocouples to the inside walls of the fuel tubes and to pass them through slots in the end caps.

Welding of Dissimilar Metals (G. M. Slaughter)

Welding procedures have been completed for the metallic-arc welding of stainless steels to chromium-molybdenum steel plate (ASTM designation: A 387 – 57 T, grade D) and to high-strength carbon-silicon steel plate (ASTM designation: A 212 – 57 T, grade B). In order to provide a further indication of the mechanical properties of these welds, transverse tensile specimens were machined from typical weldments and were tested at room and elevated temperatures. The elevated temperatures selected were those representative of the maximum service temperatures to which each type of joint would be subjected. INCO BP-85 nickel-base alloy electrodes were used for all welds. The tensile strengths of transverse specimens of ASTM A-212, grade B, steel welded to type 304 stainless steel and given a 4-hr



(a)



(b)

Fig. 5.17. (a) Grounded-Junction, Chromel-Alumel Thermocouple Brazed to Fuel Tube. (b) Ungrounded-Junction, Chromel-Alumel Thermocouple Brazed to Fuel Tube.

stress relief at 1150°F and the strengths of similar specimens of ASTM A-387, grade D, steel welded to type 304 stainless steel and given a 1-hr stress relief at 1350°F are listed in Table 5.10.

In every case the specimens failed in the base metal; moreover, the tensile strength at failure was essentially that reported for the base material. Typical as-tested tensile specimens are shown in Fig. 5.18; there is no evidence of cracking in the welds.

The thermal cycling of large (14-in.-diam, 1-in.-wall) welded pipes of these dissimilar metals is under way. The weld metals used were type 347 stainless steel and INCO BP-85. No evidence of cracking was found in the joint welded with stainless steel after 50 cycles between 1050°F and room temperature. Likewise no evidence of cracking was found in the

Table 5.10. Results of Tensile Tests of Dissimilar Metal Welds

Metal Welded to Type 304 Stainless Steel	Test Temperature (°F)	Tensile Strength (psi)	Location of Fracture
ASTM A-212, grade B, steel	Room	73 650	ASTM A-212 base metal
	650	65 700	Stainless steel base metal
ASTM A-387, grade D, steel	Room	72 900	ASTM A-387 base metal
	1050	54 100	ASTM A-387 base metal

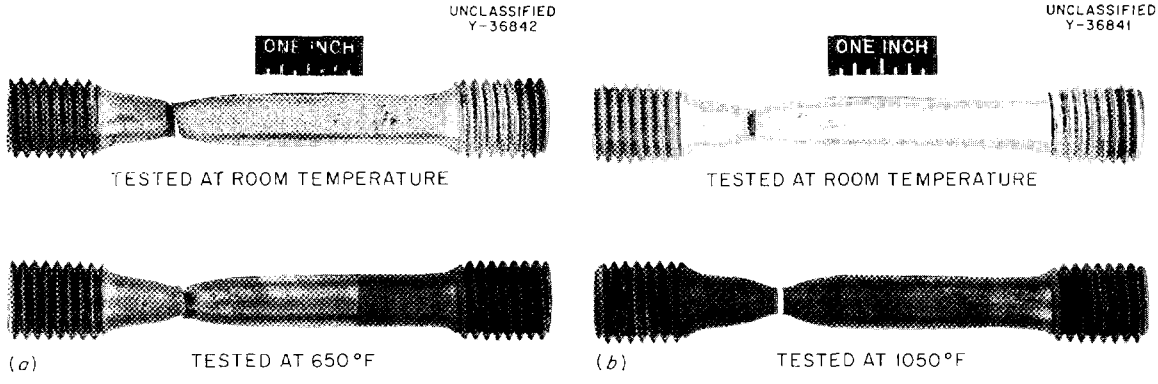


Fig. 5.18. (a) Transverse Tensile Specimens of ASTM A-212, Grade B, Steel Welded to Type 304 Stainless Steel. (b) Transverse Tensile Specimens of ASTM-A-387, Grade B, Steel Welded to Type 304 Stainless Steel.

joint welded with BP-85 after 20 cycles, and the test is continuing. A typical test specimen is shown in Fig. 5.19.

Nondestructive Inspection of EGCR Loop Through Tube Welds (K. V. Cook, R. W. McClung)

Through-transmission dual-crystal ultrasonic techniques have received most of the attention in efforts to develop nondestructive techniques for testing EGCR through tube weldments. The work has been concentrated on the V-notch weld configuration, with the sound being transmitted through the 1/2-in.-thick weld that joins two 1/4-in.-thick parallel sections.

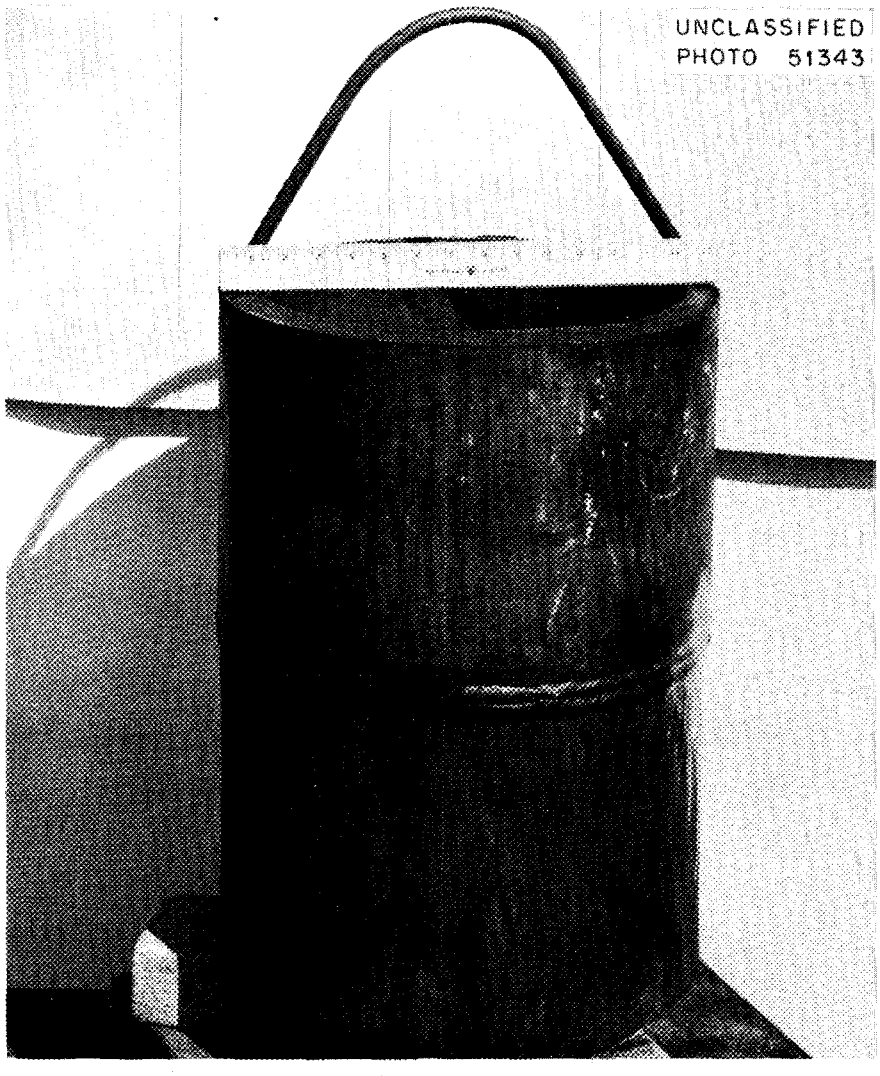


Fig. 5.19. Typical Large-Diameter Welded Specimen for Thermal-Cycling Tests.

The amplitude of the transmitted sound beam provides a direct measurement of deflects in the weldment.

Straight-line welds with the V-groove shape have been examined. The sound beam was restricted with plastic "shoes" to an effective cross section of approximately 1/4 in. in diameter. The tests indicated that a void or lack-of-fusion area equivalent to 1/8 in. in diameter could be readily detected but that the detection of 1/16-in.-diam areas might be questionable. Representative sections of good and bad welds were examined ultrsonically and then sectioned for metallographic examination.

Metallographic data are not complete yet; however, lack-of-fusion areas have been confirmed by sectioning that were undetectable visually or by radiography but which were detectable by ultrasonic inspection.

Beryllium Investigations

Compatibility of Beryllium with Coolant Impurities (W. J. Werner)

Reaction with CO_2. In order to compare the oxidation rate of wrought beryllium with the oxidation rates obtained previously for beryllium powder,[7] specimens from seven different types of beryllium tubing are being prepared for testing. The specimens are from tubing from all the various sources and represent several different fabrication methods. Two sets of specimens have been tested thus far in an atmosphere of dry CO_2 at 700°C for 50 and 500 hr. Two specimens were exposed in each test; one was prepared from tubing machined from hot-pressed block and the other from tubing machined from hot-extruded rod. The weight gains of the samples are comparable with those obtained at 700°C for powder specimens, as shown in Table 5.11.

Reaction with Water Vapor. The compatibility of beryllium with water vapor is being studied at 600°C in flowing helium containing approximately 4% H_2O (v) in an attempt to determine the role of water vapor in the

[7] "GCR Quar. Prog. Rep. Sept. 30, 1960," ORNL-3015, pp. 96–99.

Table 5.11. Comparison of Weight Changes of Different Types of Beryllium in Dry CO_2 at 700°C

Specimen	Weight Change ($\mu g/cm^2$)	
	In 50-hr Test	In 500-hr Test
Hot pressed	24.6	104
Hot extruded	23.5	131
Powders	28	92

"break-away" corrosion that occurs when beryllium is exposed to wet CO_2.[8] Three tests were run; −200 mesh beryllium powder was used in the first test and −200 +230 mesh beryllium powder was used in the last two. The −200 +230 mesh particles comprise approximately 5% of the −200 mesh beryllium powder. A log-log plot of the weight change versus time gave two straight lines intersecting at t ~ 5 hr, as shown in Fig. 5.20. The first part of the curve has a slope of approximately 1, indicating the formation of nonprotective film, whereas the second portion has a slope of 0.5, indicating the formation of a protective film. The important point to be

[8]J. E. Antill, "Oxidation of Beryllium in the Absence of Irradiation," AERE-M-435 (May 1959).

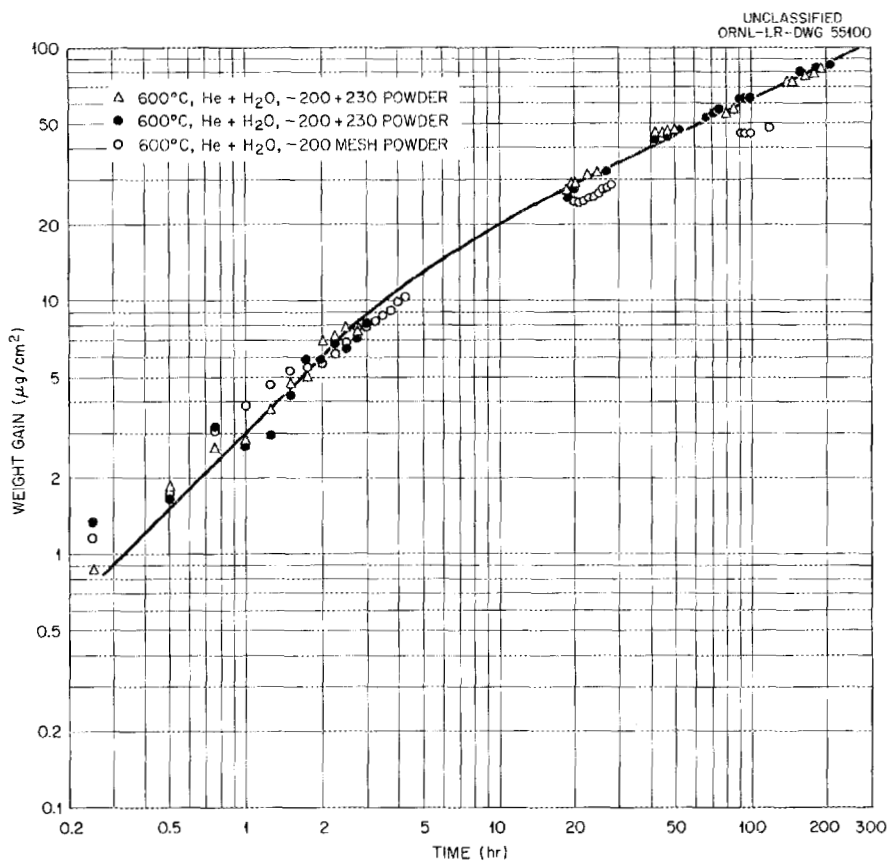


Fig. 5.20. Reaction of Beryllium with Water Vapor (~4%) in Flowing Helium at 600°C.

noted is that although the break-away phenomenon did occur, it terminated after approximately 5 hr.

When the data in Fig. 5.20 were first plotted, the shape of the curve was attributed to a reduction in area of the sample as a result of complete oxidation of the fines in the −200 mesh powder. However, subsequent tests on specimens of −200 +230 mesh powder gave similar data, showing that this was not the case. X-ray analysis of the powder before testing showed Be_2C to be present, but it could not be detected after testing. On the basis of these tests, it appears that the initial slope of the curve is due to the hydrolysis of Be_2C. The point of inflection, then, is the point of complete decarburization of the sample. Taking into account the fact that Be_2C is a product of the reaction of beryllium with CO_2,[9] the indication is that the break-away phenomenon which occurs when beryllium is exposed to wet CO_2 is due to the reaction of the Be_2C with water vapor.

Beryllium Tubing Evaluation (R. W. McClung)

Tubing from Nuclear Metals, Inc. Several lengths of 3/8- and 3/4-in. beryllium tubing fabricated by extrusion of both hot-compacted and cold-pressed billets have been received from Nuclear Metals, Inc., and have been evaluated by nondestructive means. Penetrant and radiographic examinations revealed the presence of pinholes, pits, gouges, and high-density material. The warped condition of the tubing from hot-compacted billets and the rough surface finish of the tubing extruded from cold-pressed billets prevented valid eddy-current or ultrasonic examinations.

Tubing from Pechiney. The circumferential pits on the inner surface and circumferential cracks on the outer surface of tubing from Pechiney have been examined metallographically. These defects were detected by low-voltage radiography and penetrants, respectively, as discussed previously.[10] A cross-sectional view of the deepest cracks, about 0.003 in.,

[9]V. D. Scott, "Formation of Beryllium Carbide During the Corrosion of Beryllium in Carbon Monoxide and in Carbon Dioxide Gas," Nature, 186(4723), 466–7 (1960).

[10]"GCR Quar. Prog. Rep. June 30, 1960," ORNL-2964, p. 137, and Fig. 4.27.

is shown in Fig. 5.21, and typical pits on the inner surface are shown in Fig. 5.22. The polished section shown in Fig. 5.23 indicates that the average depth of the pits is 0.003 to 0.004 in.

Beryllium Joining (R. G. Gilliland)

Investigations are continuing in order to establish procedures for sealing tubular beryllium fuel elements for advanced gas-cooled-reactor applications. The program has included the refinement of fusion-welding techniques, the development of high-temperature brazing alloys, and the fabrication of in- and out-of-pile tube-burst specimens.

Fusion Welding. An investigation is under way of the microstructures of inert-arc and electron-beam welds in beryllium. The grains in inert-arc

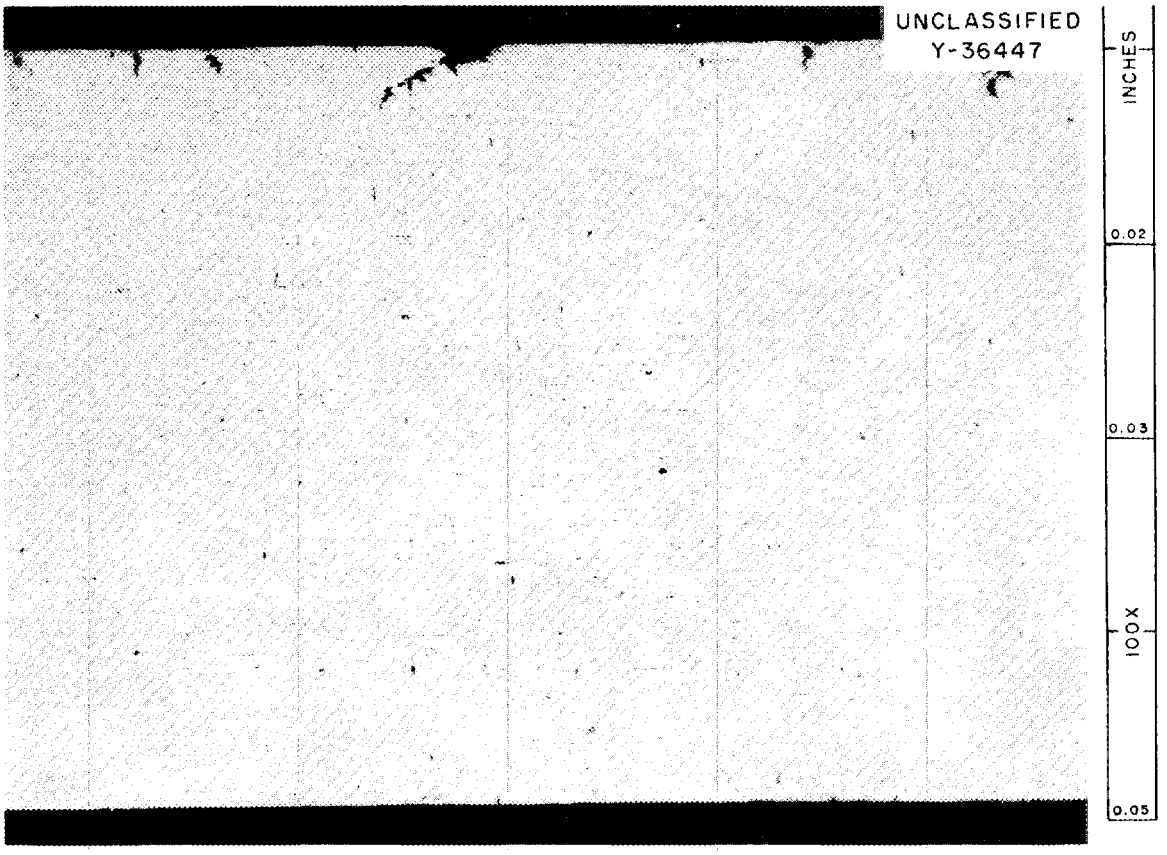


Fig. 5.21. Longitudinal Section Through Cracks in Outer Surface of Beryllium Tubing from Pechiney. As polished.

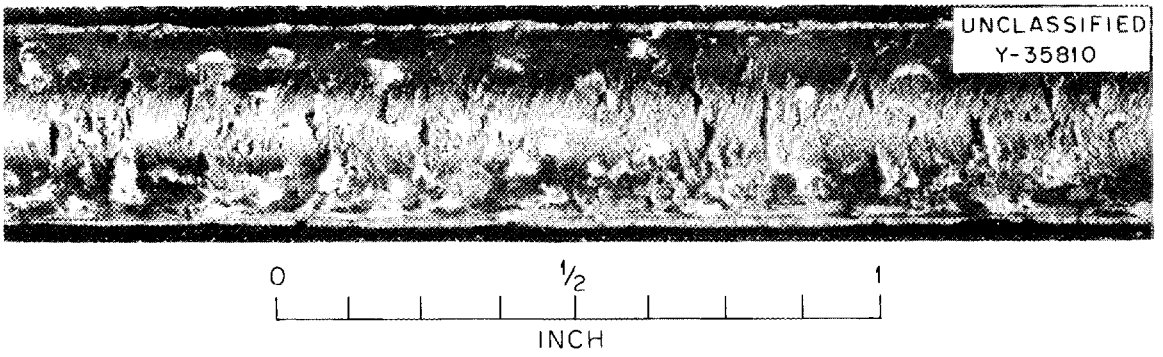


Fig. 5.22. Circumferential Pits on Inner Surface of 0.300-in.-i.d., 0.040-in.-Wall Beryllium Tubing.

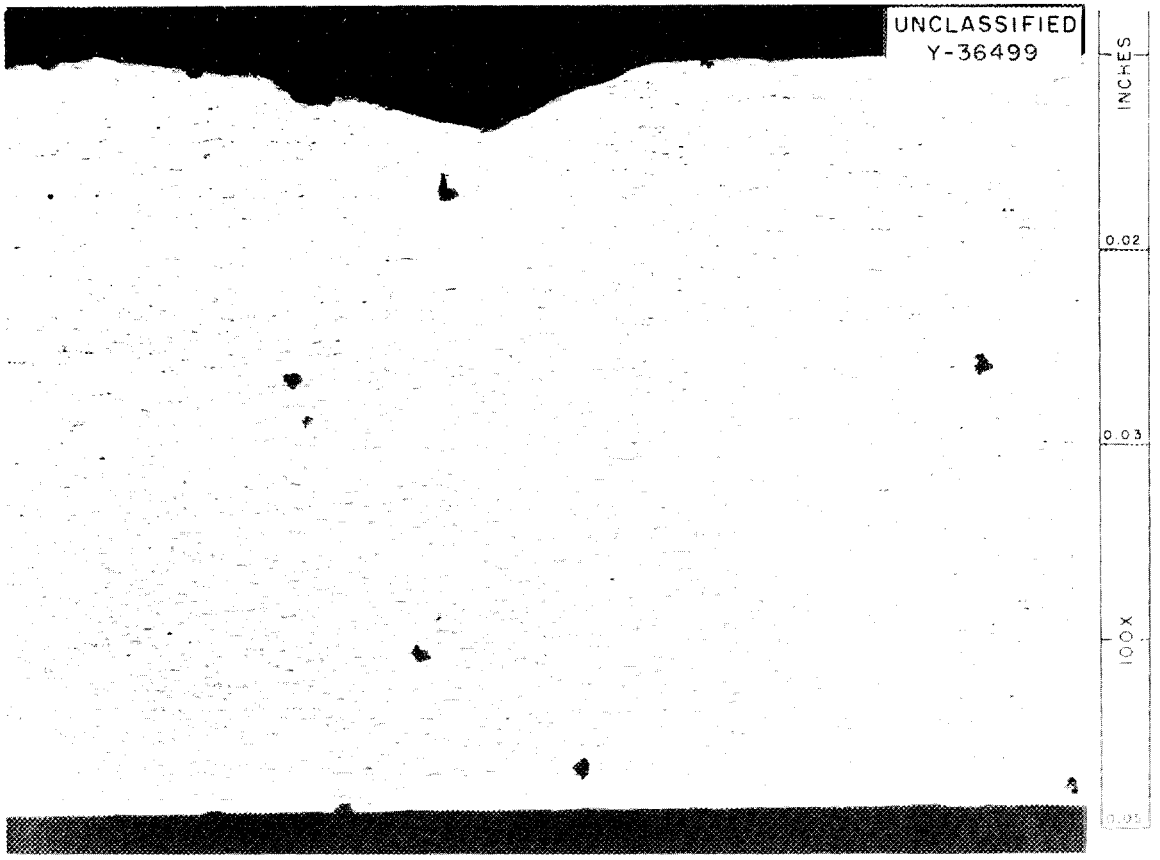


Fig. 5.23. Longitudinal Section Through Surface Pits Shown in Fig. 5.22. As polished.

welds of the type shown in Fig. 5.24 in tubing machined from hot-pressed rod were measured to be 45 to 90 μ in diameter. Such small grains are considered to be beneficial. As was expected, the grain size did not appear to be materially affected by variations in inert-gas-flow rate. Weld microstructures in different types of extruded tubing are currently being investigated.

Tube-Burst Specimen Fabrication. The fabrication of 155 beryllium tube-burst specimens for use in high-temperature in- and out-of-pile testing was completed. The number of specimens fabricated from each of the different types of 0.300-in.-i.d., 0.040-in.-wall beryllium tubing is listed in Table 5.12, and the design of the specimen is illustrated in Fig. 5.25. The end caps and tubing were machined with a slight taper, as described

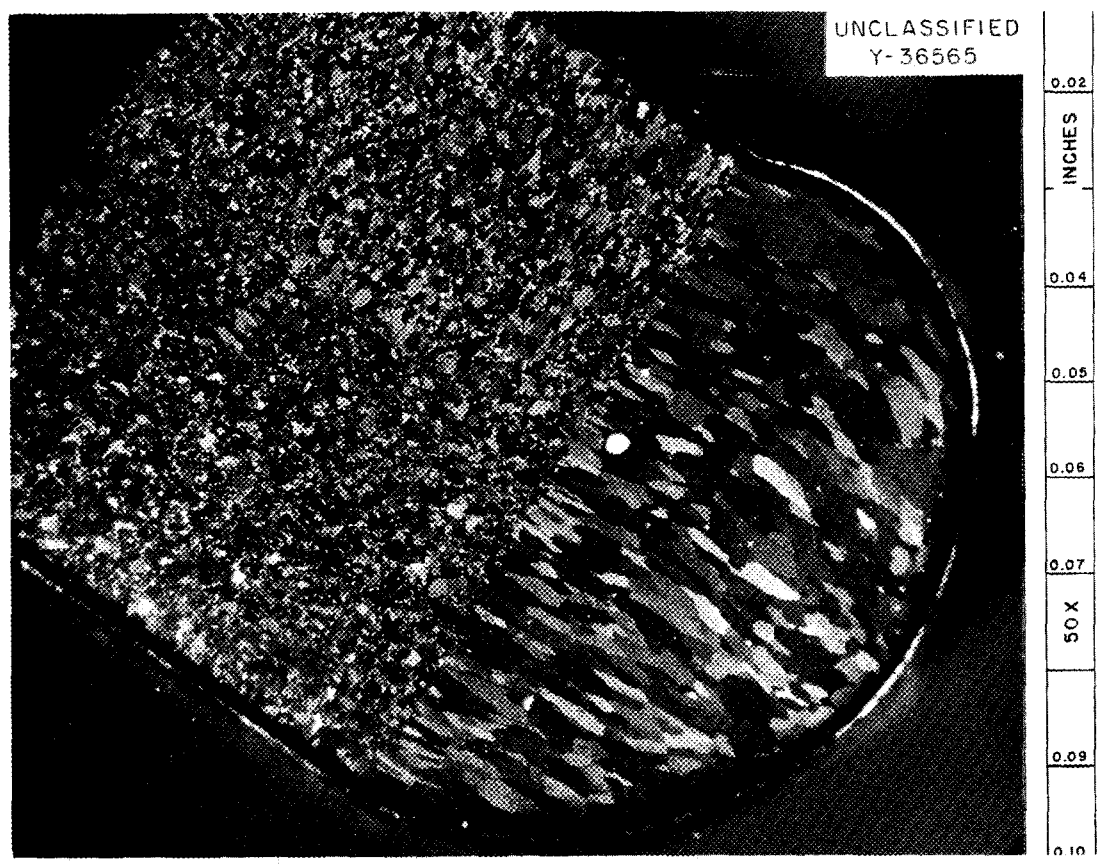


Fig. 5.24. Representative Inert-Arc Weld on Beryllium Tubing Machined from Hot-Pressed Rod. Note the small grain size of the weld. Unetched, polarized light. 50X.

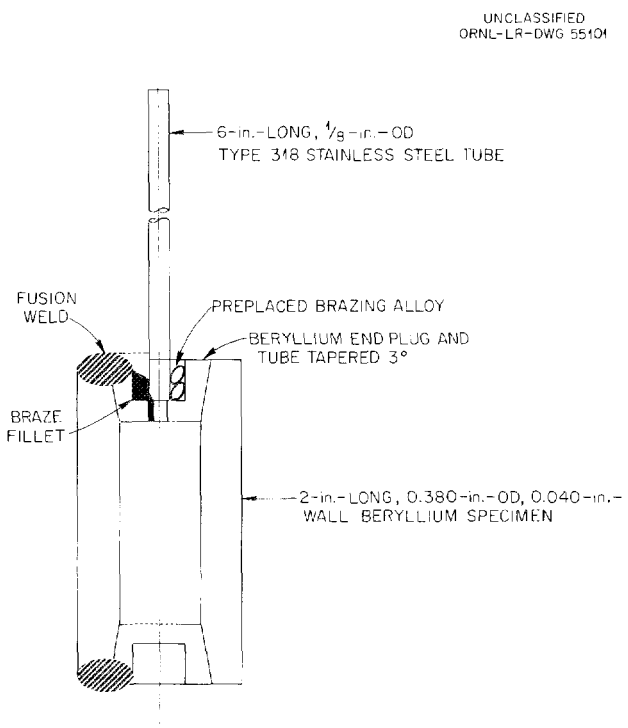


Fig. 5.25. Design of Specimens Fabricated for High-Temperature Tube-Burst Testing of Beryllium.

previously,[11] to permit tight-fitting joints and to minimize assembly difficulties.

The specimens were welded by the inert-arc process. The 0.125-in.-o.d., 6-in.-long, type 318 stainless steel pressurizing tubes were induction-brazed to the beryllium end caps using the experimental brazing alloy, 49 wt % Ti–49 wt % Cu–2 wt % Be. Representative specimens made from the eight different types of beryllium tubing used are shown in Fig. 5.26.

This fabrication program also permitted an evaluation of the weldability of the various types of tubing. Of the total number of specimens, 9.8% were rejected because of leaks in the welded or brazed joints. The number of each type rejected is indicated in Table 5.12. As determined by radiography, 31% of the welds contained pores, the most porous welds being in the Pechiney specimens and the least porous in the specimens made from Brush Beryllium tubing machined from hot-pressed rod or warm extruded to size. All specimens, including those with welds exhibiting porosity, are now being tested. No failures have occurred thus far in the welded or brazed joints.

Stress-Rupture Properties of Beryllium Tubing (J. R. Weir)

It has been known for some time that the mechanical properties of beryllium metal depend strongly on the impurities, the degree of preferred orientation, the grain size, and the annealing treatments. With the

[11] "GCR Quar. Prog. Rep. Sept. 30, 1960," ORNL-3015, pp. 102–6.

Table 5.12. Materials Used for Fabrication of Beryllium Tube-Burst Specimens

Vendor	Fabrication Technique	Specimen Designation	Total Number Fabricated	Number Rejected
Brush Beryllium Company	Machined from hot-pressed rod	Brush A	28	3
Brush Beryllium Company	Machined from hot-extruded rod	Brush B	27	2
Brush Beryllium Company	Machined from warm-extruded rod	Brush C	16	1
Brush Beryllium Company	Warm extruded	Brush D	15	0
Brush Beryllium Company	Machined from hot-pressed rod, 0.15% C	Brush E	16	1
Pechiney	Hot impact extrusion	Pechiney	34	9
Chesterfield Tube Company	Hot extruded	Chesterfield	26	1
Imperial Chemical Industries		I. C. I.	10	0

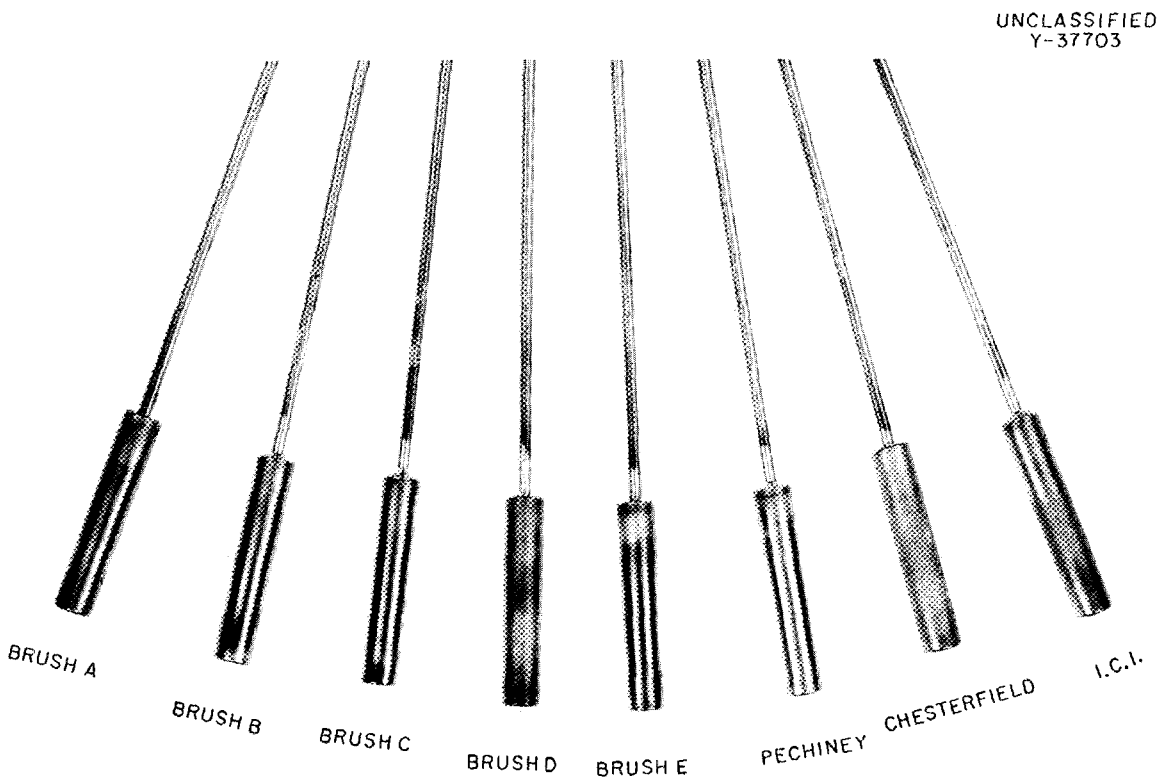


Fig. 5.26. Beryllium Tube-Burst Specimens Representative of the Eight Different Materials Being Used in the Testing Program. Refer to Table 5.12 for designation meanings.

increased interest in beryllium tubing as a fuel-cladding material in gas-cooled reactors, development of fabrication techniques has progressed to the point where sizeable quantities of commercially produced tubing are available. Part of the ORNL program for evaluation of beryllium involves investigating the strength properties of beryllium tubing produced by various commercial fabrication techniques.

Sufficient data have been obtained recently to give the tentative stress-rupture curves shown in Fig. 5.27. It may be seen that the tubing produced by machining from hot-pressed block exhibits the highest stress-rupture strength at 600°C, although the ductility of these tubes is considerably lower than the ductility of tubes manufactured by the Pechiney

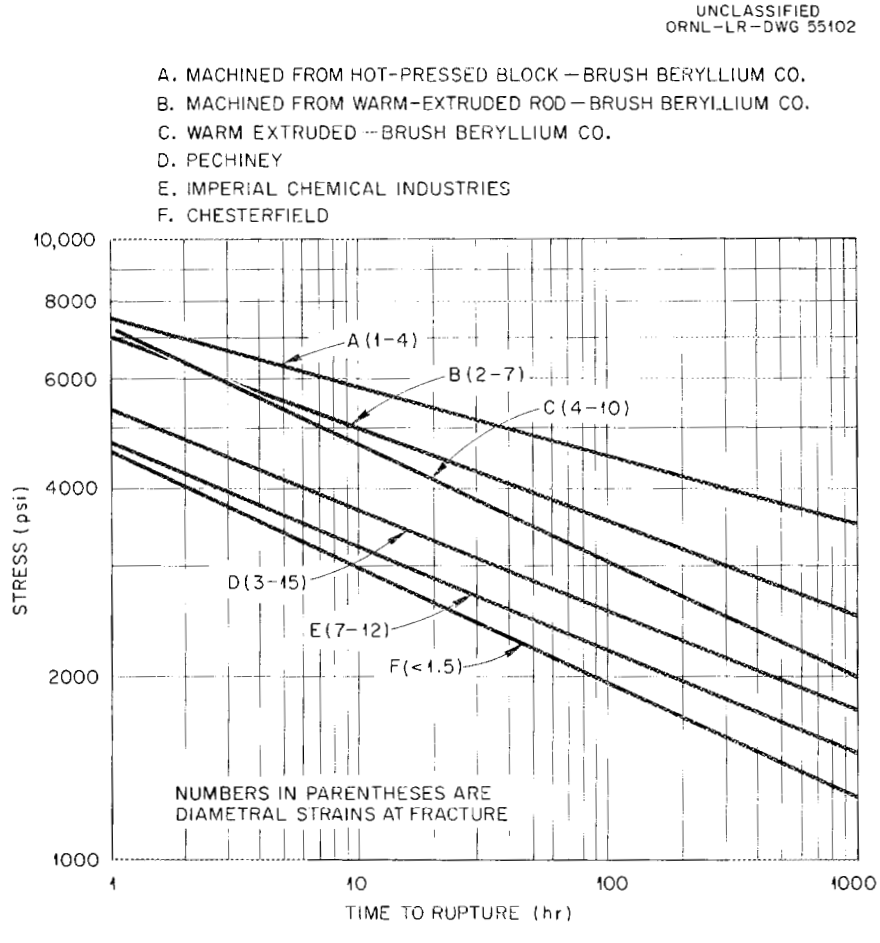


Fig. 5.27. Stress Rupture of Beryllium Tubes at 600°C.

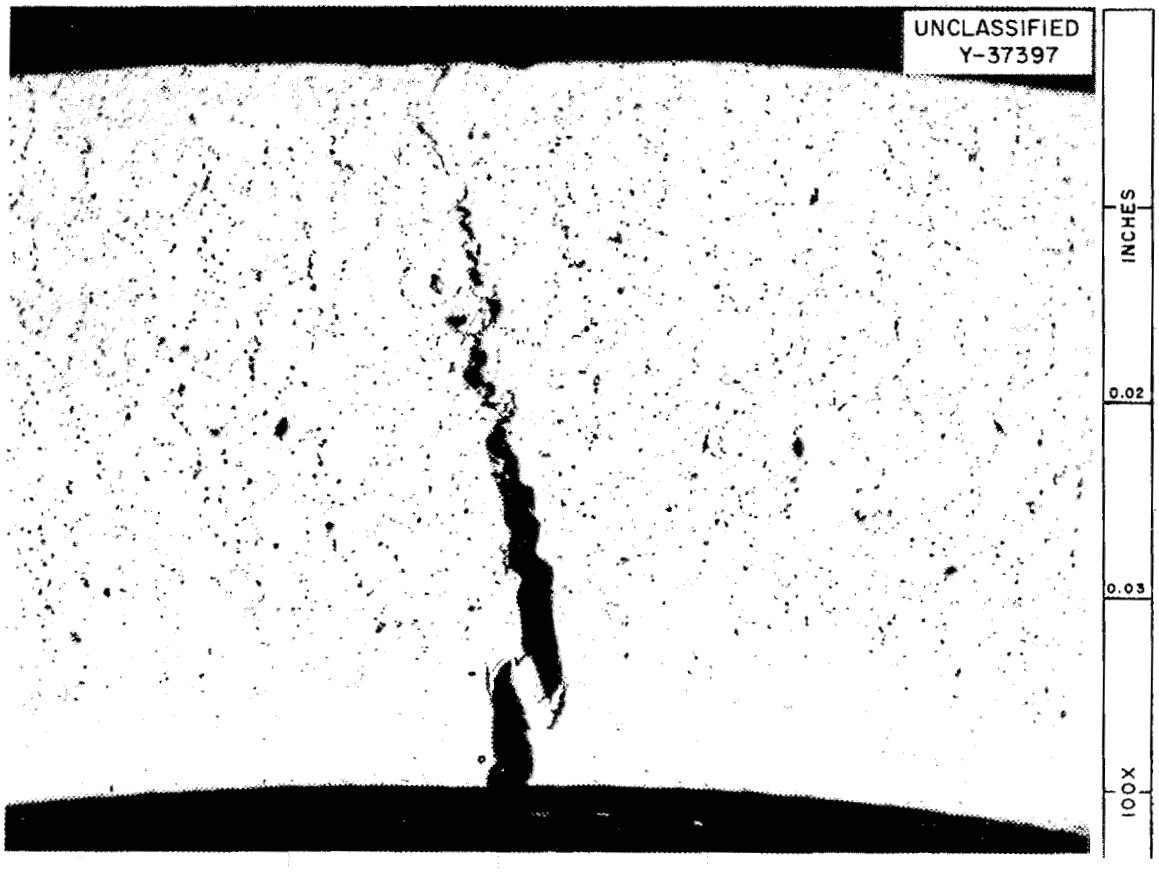


Fig. 5.28. Fracture Initiated on Inner Surface of Beryllium Tube During Tube-Burst Test at 600°C. As polished.

Company, Imperial Chemical Industries, and Brush Beryllium Company (warm extrusion). Examination of the grain size and preferred orientation of these tubes will aid in determining the reasons for the differences in the strength and ductility of the tubing.

An interesting observation is that, from the stress-analysis standpoint, the 0.30-in.-i.d., 0.040-in.-wall tubes are considered as heavy-walled tubing. Thus, under internal pressure, the stress should be significantly higher near the inside surface of the tubes than near the outside. As is shown in Fig. 5.28, the fracture is indeed initiated at the inner surface. This observation strongly implies that defects in the tube wall near the inner surface of the tube are likely to be more detrimental, in so far as mechanical properties are concerned, than defects on or near the outer surface.

6. IN-PILE TESTING OF COMPONENTS AND MATERIALS

Fuel Element Irradiation Program

Full-Diameter Prototype EGCR Fuel Capsules (F. R. McQuilkin)

ORR Experiments (V. A. DeCarlo). Temperature data obtained during irradiation of the group II capsules have been analyzed, and a graph showing the temperature history of the cladding on capsule 05-2, which is typical of this set of capsules, is presented in Fig. 6.1. The temperature readings obtained from six thermocouples during a single daily observation at about midnight are averaged and plotted against time. Also plotted are the high and low individual readings. A similar graph of all readings taken for capsule 05-2 during reactor cycle XXV is shown in Fig. 6.2. Operating data for these capsules were presented previously.[1]

ETR Experiments (F. R. McQuilkin). Irradiation of 14 prototype EGCR fuel capsules designed to obtain various values of UO_2 fuel burnup is continuing in the ETR. Operating temperature data taken recently for this group of capsules are summarized in Table 6.1. Irradiation of capsule E-9 was completed October 31, 1960, after a calculated burnup of 3177 Mwd/MT of UO_2. Capsule E-5R was inserted in the vacated position on November 2 and irradiation commenced November 7, 1960.

Beryllium-Cladding and UO_2-Grain-Size Studies (A. A. Abbatiello, V. A. DeCarlo, R. L. Senn, A. W. Longest)

Irradiation of the eight group III capsules described previously[1] continues in the ORR. Temperatures and pressures recorded on December 5, 1960 are listed in Table 6.2. During the shutdown for reactor cycle XXX, which began on September 25, 1960, capsule 01-3, in which the central thermocouple had failed,[1] was replaced with capsule 01A-3. The new thermocouple and the associated subassembly are shown in Figs. 6.3 and 6.4, respectively. An electrical ground occurred during final welding of the central thermocouple subassembly, and, with a 1 000 000-v x-ray machine

[1] "GCR Quar. Prog. Rep. Sept. 30, 1960," ORNL-3015, p. 107.

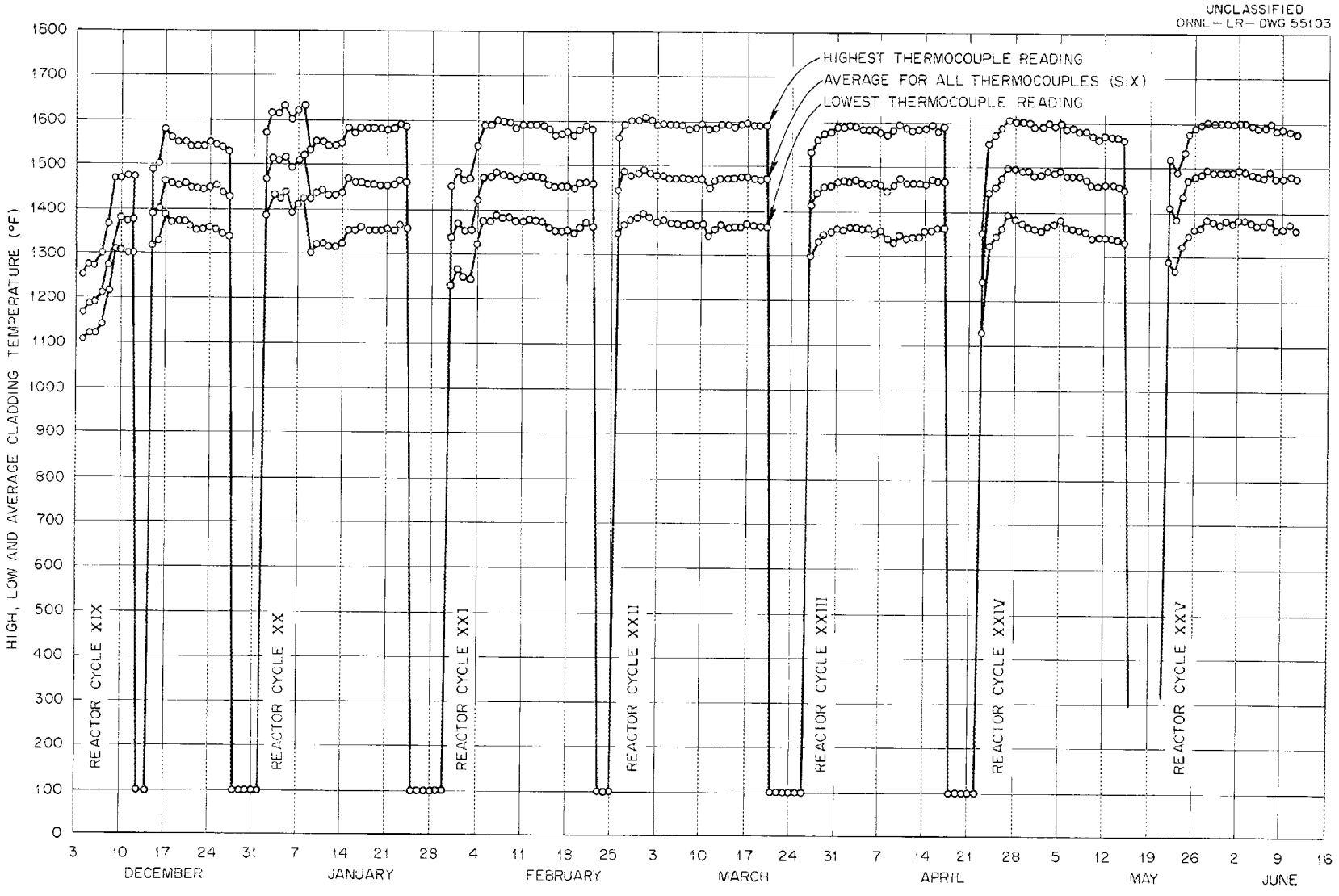


Fig. 6.1. Daily Cladding Temperature History of Capsule 05-2 During Irradiation in ORR.

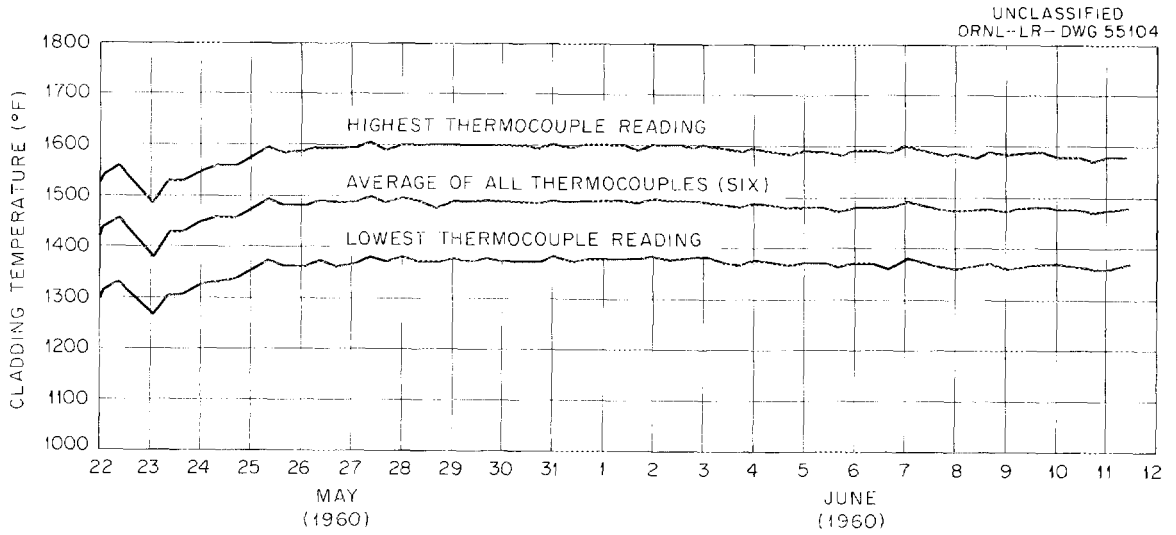


Fig. 6.2. Detailed Cladding Temperature History of Capsule 05-2 During ORR Cycle XXV.

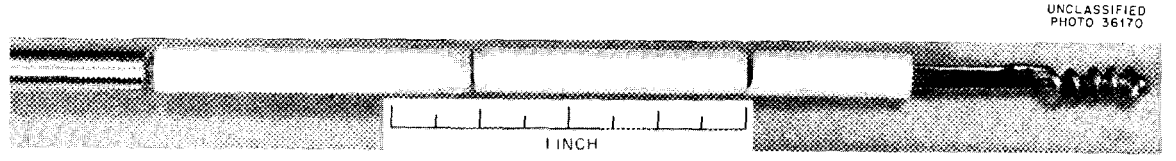


Fig. 6.3. Tungsten-Rhenium Thermocouple for Installation in Center of Capsule 01A-3.

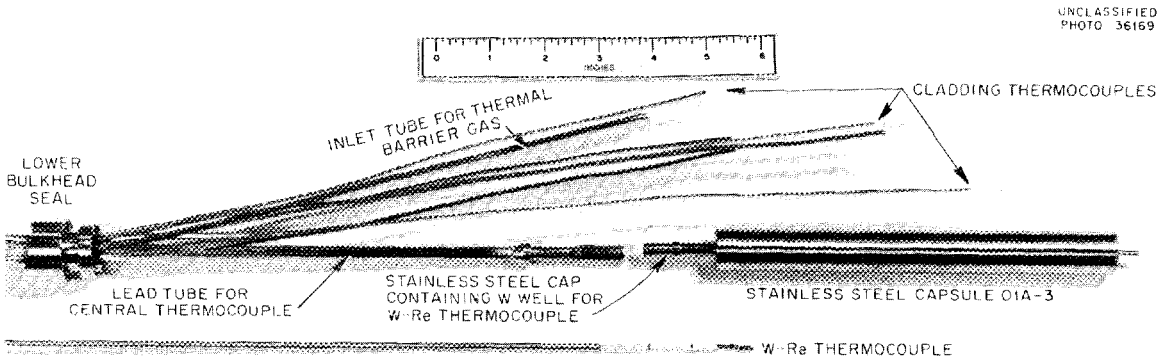


Fig. 6.4. Capsule 01A-3 Showing Central Tungsten-Rhenium Thermocouple Installation Subassemblies and Cladding Thermocouples Prior to Attachment.

penetrating the fuel and tungsten well, as shown in Fig. 6.5, it was observed that the coiled tungsten-rhenium junction was touching the inside wall of the well. The indicated performance of the thermocouple has been satisfactory since irradiation began October 4; a temperature of 2045°F is indicated, and the corresponding cladding temperature is about 1450°F.

Table 6.1. Typical Operating Temperatures for the Full-Diameter Prototype EGCR Fuel Capsules Being Irradiated in the ETR

Capsule No.	Capsule Temperature (°F)				Estimated Total Burnup[a] (Mwd/MT)
	Design	Highest	Lowest	Average	
E-1[b]	1300	1293	1250	1273	1005
E-9[c]	1300	1355	1240	1278	3177
E-1A[d]	1300	1304	1225	1266	2222
E-2	1300	1175	1032	1124	581
E-3	1600	1540	1472	1504	753
E-4	1300	1345	1250	1295	2290
E-5	1300	1145	1118	1131	2013
E-6	1300	1220	1112	1184	2338
E-7	1300	1300	1203	1229	2978
E-8	1600	1520	1323	1414	998
E-10	1600	1425	1276	1342	872
E-11	1300	1140	981	1080	302
E-12	1600	1490	1422	1460	439
E-1R	1600	1655	1505	1592	376
E-4R	1300	1300	1175	1245	247
E-5R	1600	1556	1412	1462	

[a]Estimates of total UO_2 burnup are based on 200 Mev/fission and, except for capsules E-1 and E-9, were calculated as of October 31, 1960.

[b]Irradiation of capsule E-1 was completed October 19, 1959; the temperature readings listed were taken on October 13, 1959, with the reactor operating at 175 Mw; the burnup given is the final calculated value.

[c]Irradiation of capsule E-9 was completed October 31, 1960; the temperature readings listed were taken on July 26, 1960, with the reactor operating at 175 Mw; the burnup given is the final calculated value.

[d]The temperature readings for capsules E-1A through E-5R were taken on November 28, 1960, with the reactor operating at 175 Mw.

Table 6.2. Temperature and Pressure Data for the Group III Capsules Being Irradiated in the ORR

Capsule No.	Cladding Surface Temperature[a] (°F)				Nominal Blanket Pressure (psig)
	Design	Highest	Lowest	Average	
01-3[b]	1600 (max)	1608	1392	1530	300
02-3	1112 (av)	1185	1075	1118	300
03-3	1112 (av)	1150	1090	1120	225
04-3	1112 (av)	1172	1075	1130	300
05-3	1112 (av)	1145	1042	1102	300
06-3	1112 (av)	1158	1095	1117	300
07-3	1112 (av)	1035	1005	1020	300
08-3	1600 (max)	1585	1260	1407	300

[a]Readings taken December 5, 1960.

[b]The temperature indicated by the central thermocouple when these readings were taken was 2050°F.

The calculated central temperature for the estimated operating conditions is 2170°F.

Thermal cycling is being applied to capsules 02-3 through 07-3 by operation of the cadmium shutters. Prior to each scheduled cycle and mid-cycle refueling shutdown, the CEA, France, capsules (03-3 and 04-3) and their ORNL counterpart (02-3) are subjected to 20 low-temperature thermal cycles at hourly intervals. The United Kingdom capsules (05-3 and 06-3) and their ORNL counterpart (07-3) receive one thermal cycle daily. It takes 1 to 2 sec to lower the shutters, which are held down approximately 25 min and then raised at the rate at which they were lowered. The resulting decrease in heat generation is sufficient to drop the cladding surface temperature from 600 to about 250°C.

Capsules 05-3, 06-3, and 07-3 have exhibited rapid temperature fluctuations during irradiation, in contrast to the stable behavior of the capsules irradiated in groups I and II. Although no regular oscillation pattern has prevailed, the temperatures indicated by the recorders for the upper two thermocouples have fluctuated from 30 to 180°F, with a marked tendency at times to vary only in the downward direction from

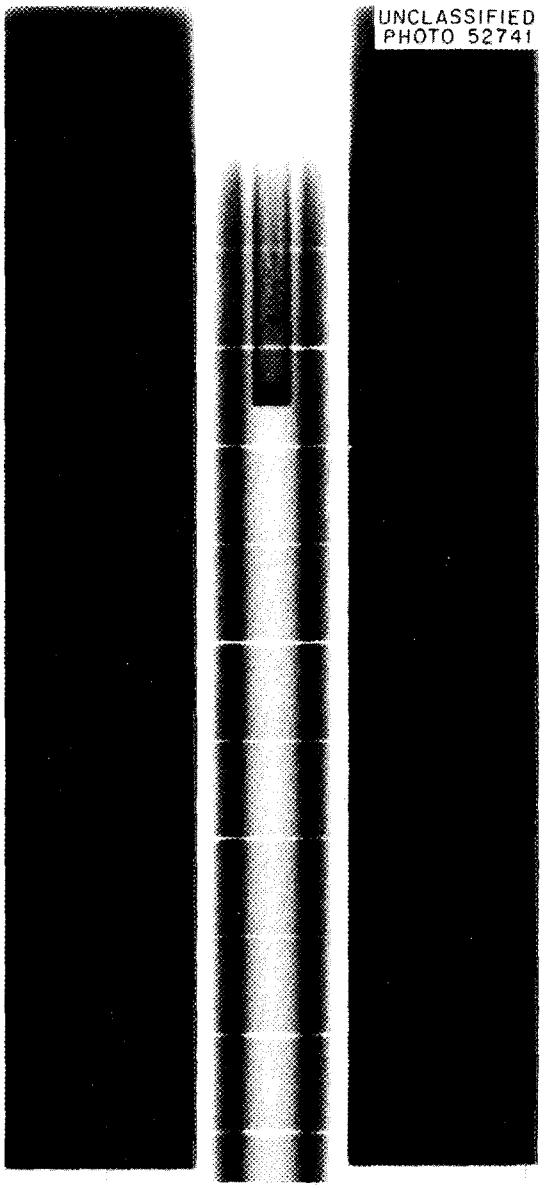


Fig. 6.5. X-Ray Picture Showing the Central Thermocouple in Capsule 01A-3.

normal at frequencies of 4 to 10 cpm. These three capsules have the lowest power generation (9600 Btu/hr·ft, design; ~6600 Btu/hr·ft, developed), smallest diameter (0.039 in. o.d.), and lowest cladding temperature. They have a special mounting arrangement; however, it is the same as for capsules 02-3, 03-3, and 04-3. They also have the largest thermal-barrier-gas gap, 0.020 in. radial, of any capsules of this design. While several possible causes have been postulated for the fluctuations, the strongest indications are that convection disturbances are occurring within the barrier-gas annulus that affect the thermal diffusion separation[2] of the He-N_2 mixture in the thermal barrier and, possibly, within the NaK region.

The magnitude of the oscillations is greatly reduced either by use of 100% helium or by continuous flow of an appropriate mixture of helium and nitrogen. In the latter case, the gas mixture must be depleted in nitrogen to obtain the same temperature as that obtainable after equilibrium with the gas mixture static.

As a result of these findings, small gas circulators have recently been added to establish recirculation flow in the capsules. Initial results indicate that the magnitude of the fluctuations has been reduced but that this is not a complete solution to the problem.

---

[2]"GCR Quar. Prog. Rep. March 31, 1960," ORNL-2929, p. 148.

An unusually high failure rate has been experienced with the stainless-steel-sheathed, grounded-junction, Chromel-Alumel thermocouples. The beryllium-clad capsules 03-3 and 07-3 each has only one of six thermocouples operating, and capsule 05-3 has only two satisfactory thermocouples remaining. A high rejection rate was experienced during inspection of the total lot of thermocouples used for the group III capsules.

Miniature-Capsule Fission-Gas-Release Experiments (F. R. McQuilkin, W. E. Thomas)

The series of UO_2 experiments has been completed, and the last capsules are presently undergoing postirradiation analysis. Operating data for experiments completed or initiated during this reporting period are given in Table 6.3. Experimental assembly L-24 failed on August 23, 1960, apparently during removal from the facility tube. During removal a manifold pressure of approximately 60 psig was applied to the off-gas system, and, as a result, there was simultaneous failure of the five rubber hoses located in the cooling-air system between the facility tubes and the exhaust manifold. None of the hoses in the air-supply system failed. The failed hoses were made from reclaimed rubber and were designed for continuous service with steam at 200 psig and 390°F, conditions well in excess of the maximum experienced during their two years of service. The failures are postulated to have resulted from reaction with ozone in the exit air from the experiment. The rubber hoses have been replaced with flexible stainless steel tubing.

A series of experiments for investigating fission-gas release and fuel stability of small specimens of BeO-ThO_2-UO_2 and UC has been initiated. Four irradiations are currently under way, three for BeO-base materials and one with UC. Fuel mixture LM-1-ab is being irradiated at low temperatures (less than 1800°F) for a postirradiation determination of D′. The specimens are 0.323-in.-o.d., 0.157-in.-i.d., 1/2-in.-long hollow cylinders composed of 70 vol % BeO and 30 vol % UO_2. Fuel mixture LM-2-ab also consists of 70 vol % BeO and 30 vol % UO_2, and each fuel pellet is 0.156 in. o.d., 0.079 in. i.d., and 0.250 in. long. Surrounding each pellet is a 0.157-in.-i.d., 0.323-in.-o.d., 0.250-in.-long insulator fabricated from

Table 6.3. Operating Data for Miniature-Capsule Fission-Gas-Release Experiments

Experimental Assembly No.	Fuel Composition	U^{235} Enrichment (%)	Cladding Temperature (°F)		Central Fuel Temperature (°F)		Date Installed	Date Removed	Estimated Burnup (Mwd/MT)
			Capsule a	Capsule b	Capsule a	Capsule b			
L-22	UO_2	10	1100	1300	1380	1600	11-10-59	11-17-60	13 700
L-24	UO_2	20	1000	1300	2600	3100	12-16-59	8-23-60	28 000
L-27	UO_2	15	1050	1300	2000	2600	3-15-60	9-20-60[a]	15 200
L-28	UO_2	30	1000	1300	2200	3800	4-5-60	9-20-60	14 000
L-32	UO_2	30	1000	1300	3200[b]	3400	6-29-60	9-20-60	7 700
LM-1-ab	$BeO-UO_2$	20	1050	1300	1150	1555	10-20-60		
LM-2-ab	$BeO-UO_2$	50	1100	1300	1990	2490	9-14-60		
LM-3-ab	$BeO-UO_2-ThO_2$	93	1000	1300	1800[b]	2000	11-22-60		
LC-1-ab	UC	10	1050	1300	2150	2300	11-3-60		

[a]The experimental assembly was retracted from the reactor core on August 23, 1960, but it remained in the facility tube until September 20, 1960.

[b]Thermocouple failed on startup; values given are calculated.

thoria. Fuel mixture LM-3-ab is composed of 70 vol % BeO, 17.5 vol % ThO_2, and 12.5 vol % UO_2. Each pellet is 0.177 in. o.d., 0.078 in. i.d., and 0.250 in. long and is surrounded by a thoria bushing 0.323 in. o.d., 0.178 in. i.d., and 0.250 in. long. The UC test pellets, designated LC-1-ab, are 0.262 in. o.d., 0.111 in. i.d., and 1/2 in. long. The desired irradiation temperature is obtained by use of a 0.020-in.-radial helium-gas gap. Central pellet temperatures are measured with tungsten-rhenium thermocouples that are 0.072 in. o.d. and are sheathed with tantalum. The operating conditions for these experiments are given in Table 6.3.

Advanced Fuel Element Testing (J. A. Conlin, C. W. Cunningham)

The second graphite-encapsulated test element fueled with a UC_2-graphite matrix,[3] designated ORNL-MTR-48-2, was inserted in the MTR June 19, 1960 and removed December 5, 1960. The outer surface of the low-permeability (1.5×10^{-8} cm^2/sec) graphite container was purged with helium during irradiation, and the purge effluent was monitored for activity and sampled periodically to determine the concentrations of the various noble-gas fission products. The results of sampling after equilibrium had been approached are summarized below, where the fission-product release rates are given as percentages of the formation rate, with the release rate corrected to the time of emission from the fuel capsule:

Isotope	Measured Release Rate (%)
Kr^{85m}	0.25–0.45
Kr^{88}	0.07–0.18
Xe^{133}	7.0–35
Xe^{135}	0.004–0.03

These measurements are based on a limited number of samples, since difficulty was encountered within the purge system, but they are thought to be representative. This fuel element was tested at a maximum fission heating rate of 140 w/cm^3, and the estimated central fuel temperature was 2500°F.

[3] "GCR Quar. Prog. Rep. June 30, 1960," ORNL-2964, pp. 154–6.

The measured mid-wall graphite container temperature was 1500°F. The element was irradiated during eight MTR cycles for a total U^{235} burnup of 23 and 16 at. %, respectively, in the two sections of the fueled matrix, the higher burnup being in the section nearest the MTR core.

On November 18, a sudden, large increase in activity in the purge effluent lines was observed. It is suspected that a rupture occurred in the encapsulating graphite; however, absolute verification of this cannot be established until the data taken at the time of the incident can be analyzed and the fuel specimen examined.

Examination of Irradiated Capsules

LITR-Irradiated Miniature Capsules (J. G. Morgan, M. T. Morgan, M. F. Osborne, H. E. Robertson)

Postirradiation examinations of seven LITR-irradiated miniature capsules were continued. These seven capsules include L-7x and L-11 of the old design (model 2) and capsules L-23, -24, -25, -27, and -32 (model 3), which contained a depleted-UO_2 sleeve around the hollow-pellet specimens to act as a thermal insulator.

When capsule L-23 was pierced for fission-gas release, leaks were found around the thermocouple seal pins on both ends. The loss of gas from specimen a was apparently due to hot-cell handling; however, the specimen b leak was very small and indicated a possible loss of gas during irradiation. The UO_2 specimens were fused to the insulator sleeves on both the a and b ends of the capsules, as may be seen in Fig. 6.6. Both internal thermocouples had failed early in the irradiation. The central thermocouple in specimen b failed after reaching nearly 3400°F.

The fusion evident in capsule L-23 was not observed in capsule L-25, which was irradiated for a shorter time at lower temperatures. In general, thermocouple failures on capsules that did not have an obvious air leak were accompanied by a reaction of the tantalum sheath, the insulator, and the thermocouple wires themselves with the environment in the capsule. Further metallographic studies have been started in an effort to determine whether this is an oxidation process.

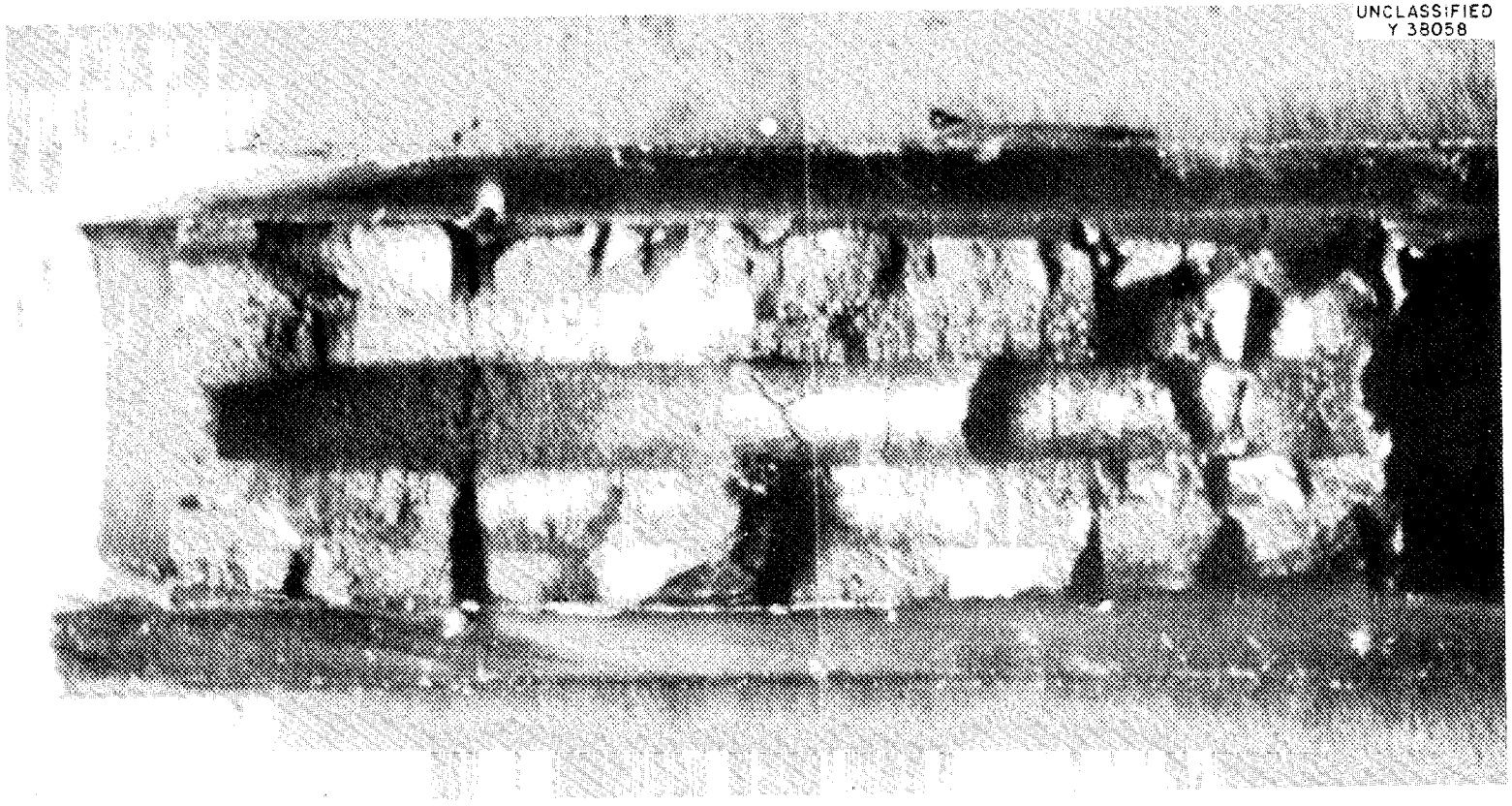


Fig. 6.6. UO_2 Pellets Fused into Depleted UO_2 Insulating Sleeve of Capsule L-23.

Capsule L-7x contained UO_2 of 95% theoretical density and received an estimated burnup of 2900 Mwd/MT. The central thermocouple in specimen a failed at startup, but the central thermocouple in specimen b remained operable throughout the test. The maximum central UO_2 temperature was 2950°F, with an average of 2550°F. A decrease in the immersion density of the pellets irradiated in capsules L-7x, L-10, and L-11 has been found, but the change is within experimental error (see Table 6.4). Burnup figures

Table 6.4. Data Showing Effect of Irradiation on Density of UO_2 Pellets in LITR-Irradiated Capsules

Capsule No.	Burnup Based on Co^{60} Activity (Mwd/MT)	Effective UO_2 Central Temperature (°F)	Pellet Density Before Irradiation			Pellet Immersion Density After Irradiation (g/cm^3)[a]
			Bulk Density (% of theoretical)	Bulk Density (g/cm^3)	Immersion Density (g/cm^3)	
L-7xa	16 000	2200	94.99	10.42	10.51	10.3
L-7xb	16 000	2450	94.85	10.41	10.50	10.3
L-10b	1 600	2800	95.19	10.44	10.48	10.3
L-11a	22 000	2100	85.05	9.33	10.47	10.4

[a]The accuracy of these values is ±0.2.

calculated from radiochemical analyses for Cs^{137} and Ce^{144} are inconsistent. Consequently, mass spectrometric analyses of the fuel will be made to determine the change in the U^{235}-to-U^{236} ratio, which is the basis of the most reliable method for calculating burnup (see Table 6.5).

Table 6.5. Comparison of Burnup Data for UO_2 Pellets in LITR-Irradiated Capsules

Capsule No.	Burnup (Mwd/MT)		
	Estimated from Co^{60} Activity	Based on Ce^{144} Analysis	Based on U^{235}-to-U^{236} Ratio
L-7x	16 000	14 200	14 200
L-11	22 000	19 700	23 600

The UO_2 control sample for both sections of LITR-irradiated capsule L-7x is shown in Fig. 6.7 in both the as-polished and etched conditions. Small light colored phases can be seen evenly dispersed throughout the control in the as-polished condition at 250X. This phase cannot be seen in the etched condition. No chemical analysis is available on the batch of UO_2 pellets from which this capsule was charged; however, the control sample will be submitted for analysis. The grains of the control sample are too small to be clearly resolved at 250X.

Results of metallographic examinations of specimens L-7xa and L-7xb are shown in Figs. 6.8 and 6.9. Grain growth occurred in both L-7xa and L-7xb during irradiation that resulted in a small, equiaxed grain structure. The UO_2 grain size in the irradiated specimens is at least three times larger than the grain size in the control sample. The grains in L-7xb are slightly larger than in L-7xa, which can be explained by the temperature gradient that existed between the upper and lower sections of the capsule during irradiation. In both L-7xa and L-7xb, the grains near the inner surfaces of the pellets are slightly larger than those near the outer surfaces, which can also be explained by the temperature gradient that existed between the inner and outer surfaces of the pellets during irradiation. Several large voids were found in the fuel of capsules L-7xa and L-7xb; however, several large voids were also evident in the control sample. Therefore, the large voids present in the irradiated fuel cannot be definitely attributed to a radiation effect. Small voids were present that were mostly concentrated in the inner two-thirds of the pellet in the L-7xa section that were not present in the control sample. The pellet from the L-7xb section had more voids at the periphery than did the L-7xa pellet. Also, a band of higher density fuel was seen approximately one-third of the way in from the outer edge in the L-7xb pellet. Additional LITR miniature capsules will have to be examined before an attempt can be made to explain the void formation.

ORR-Irradiated Prototype Capsules (J. G. Morgan, M. T. Morgan, M. F. Osborne, H. E. Robertson)

Gamma Scan of Group II Capsules. The nondestructive portions of the postirradiation examinations of group II capsules have been completed. All

UNCLASSIFIED
PHOTO 52801

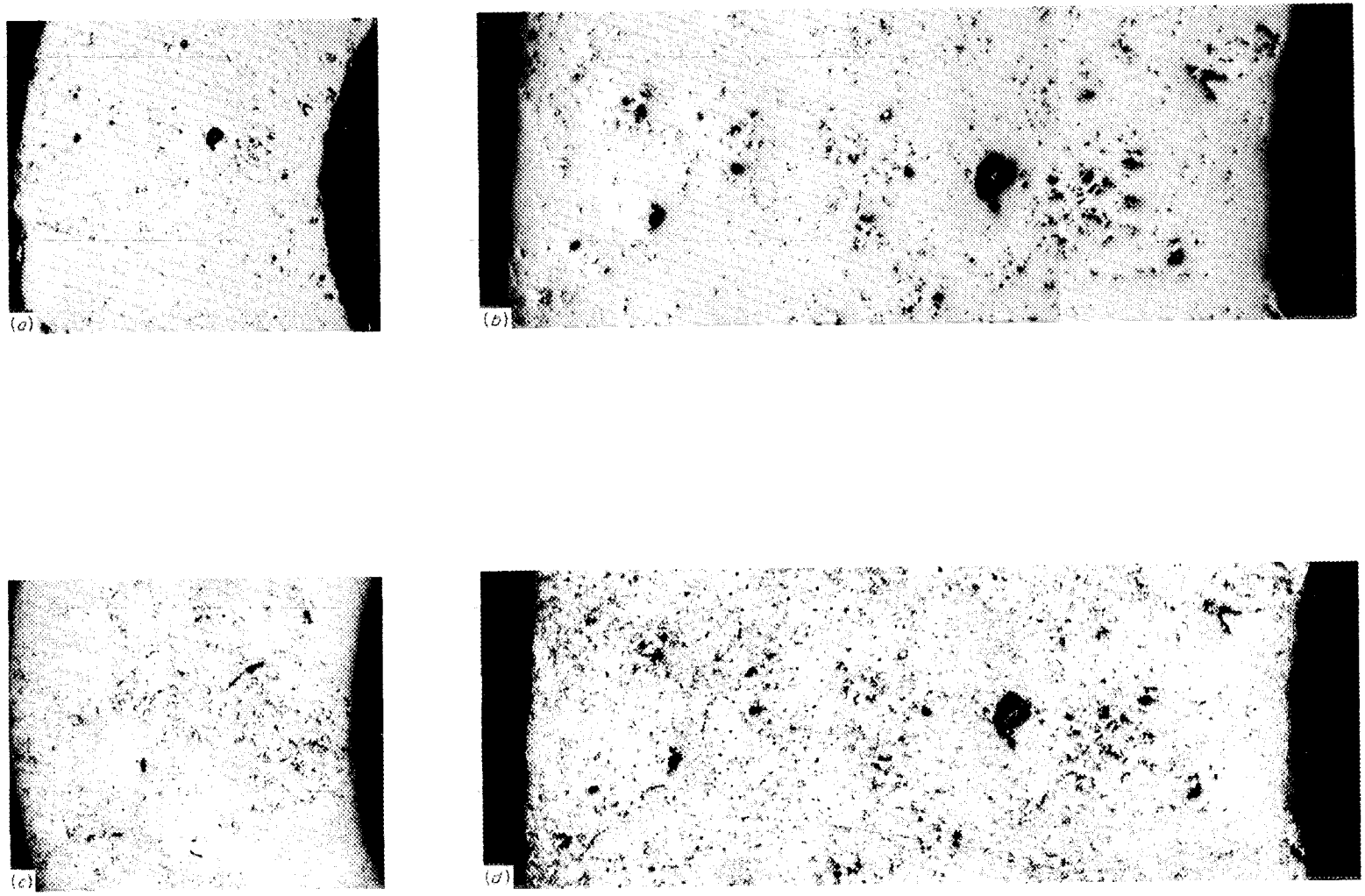


Fig. 6.7. Transverse Section of UO_2 Control Sample for LITR Miniature Capsule L-7x. (a) As polished, 100X. (b) As polished, 250X. (c) Etched, 100X. (d) Etched, 250X. Etchant: 70% H_2O, 10% H_2SO_4, 20% H_2O_2.

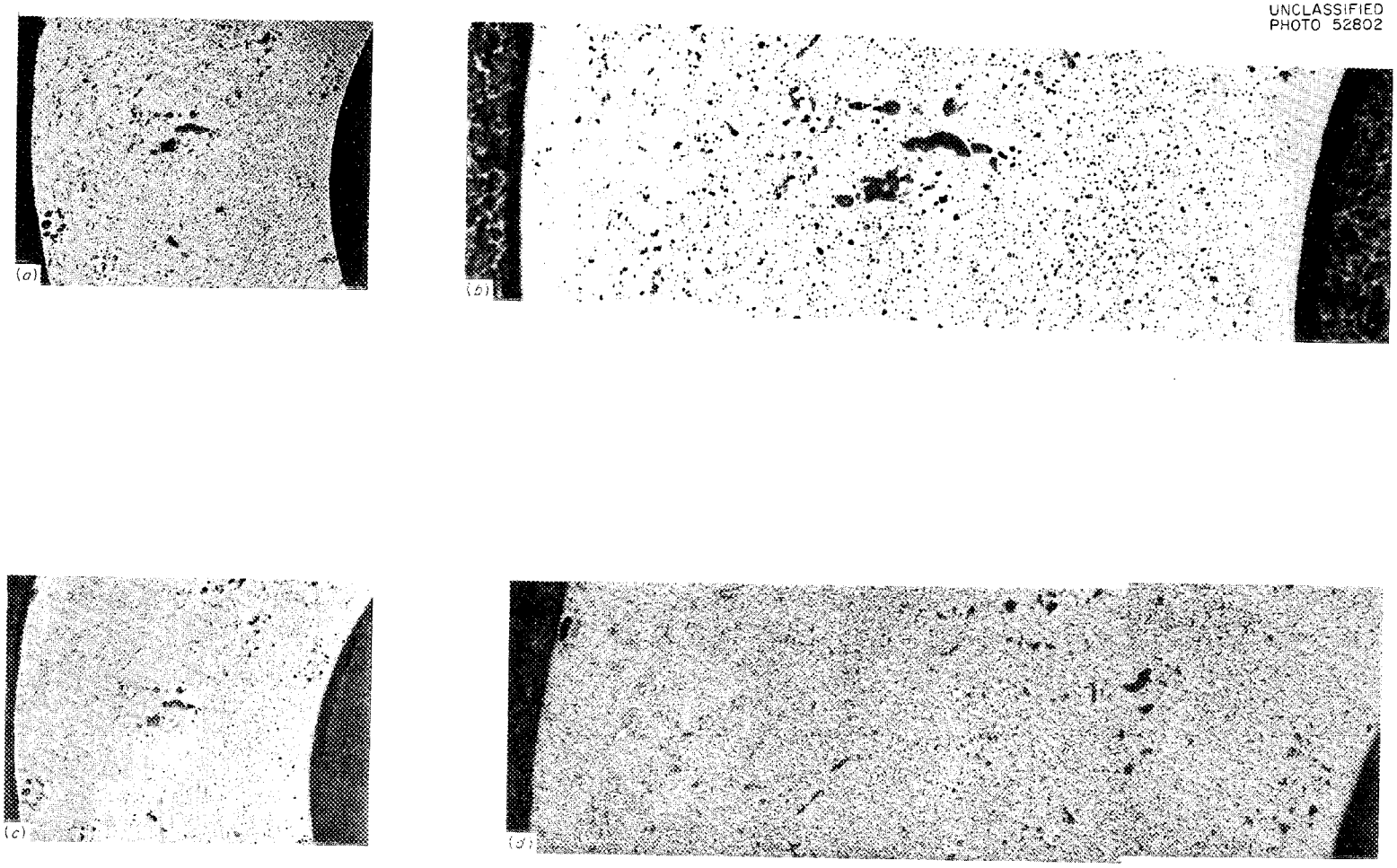


Fig. 6.8. Transverse Section of UO_2 Sample from LITR Miniature Capsule L-7x, Section a. (a) As polished, 100X. (b) As polished, 250X. (c) Etched, 100X. (d) Etched, 250X. Etchant: 70% H_2O, 10% H_2SO_4, 20% H_2O_2.

UNCLASSIFIED
PHOTO 52803

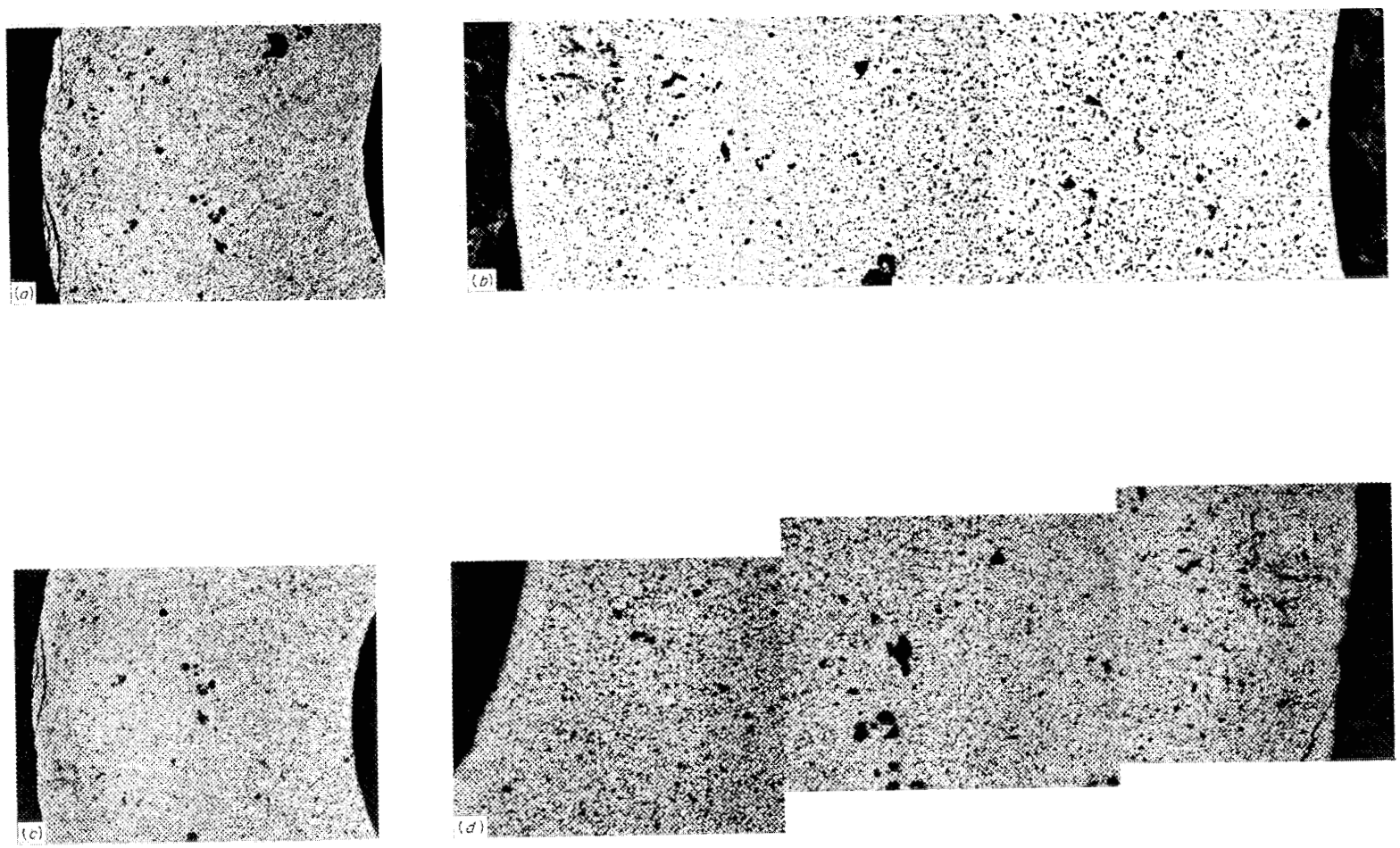


Fig. 6.9. Transverse Section of UO_2 Sample from LITR Miniature Capsule L-7X, Section b. (a) As polished, 100X. (b) As polished, 250X. (c) Etched, 100X. (d) Etched, 250X. Etchant: 70% H_2O, 10% H_2SO_4, 20% H_2O_2.

eight capsules were gamma scanned and cladding profile measurements were taken. Three typical activity scans may be seen in Fig. 6.10. Capsule 02-2 contained hollow pellets, 04-2 solid pellets, and 08-2 hollow pellets, with a BeO center rod. The plots show quite uniform burnup along the length of the capsules.

Dimensional Measurements of Group II Capsules. The outside cladding diameters were measured at 1-in. intervals in at least three positions circumferentially. The reproducibility of the measurements, listed in Table 6.6, is ±0.0005 in. The diameters and changes in diameter listed in Table 6.6 are averages of the circumferential readings before and after irradiation. In general, there was a decrease in diameter of from 0.001 to 0.006 in., i.e., less than 1% change. The diametral clearance between the outer surface of the UO_2 and the inner surface of the cladding was 0.005 ± 0.001 in. before irradiation. The cladding had collapsed around the UO_2 pellets in all but one of the capsules irradiated at 1600°F and one-half of the capsules irradiated at 1300°F.

Circumferential ridges were formed in the cladding at the pellet interfaces on all capsules irradiated at a cladding temperature of 1600°F. These ridges extended about 0.005 in. above the normal cladding surface.

Capsule profiles were charted at 90-deg intervals with a mobile dial indicator. The variation from straightness was a minimum for the capsules containing hollow pellets that were irradiated at 1300°F and increased with irradiation temperature. The capsules with solid pellets or central BeO bushings were not as straight as the capsules with hollow pellets. The maximum and minimum profile variations for the group II capsules are illustrated in Fig. 6.11. Capsule 01-2 contained hollow pellets and was irradiated at a cladding temperature of 1300°F, whereas capsule 06-2 contained hollow pellets with a central BeO bushing and was irradiated at 1600°F. The UO_2 burnup was about 1800 Mwd/MT in both cases.

General Conclusions Regarding Group I Capsules. In contrast to the group I capsules opened previously, much less cracking and breaking up of the pellets has been observed in the capsules that were opened recently. As may be seen in Fig. 6.12, almost all the pellets in capsule 02-1 appeared to be whole, and it was possible to remove some of the pellets from

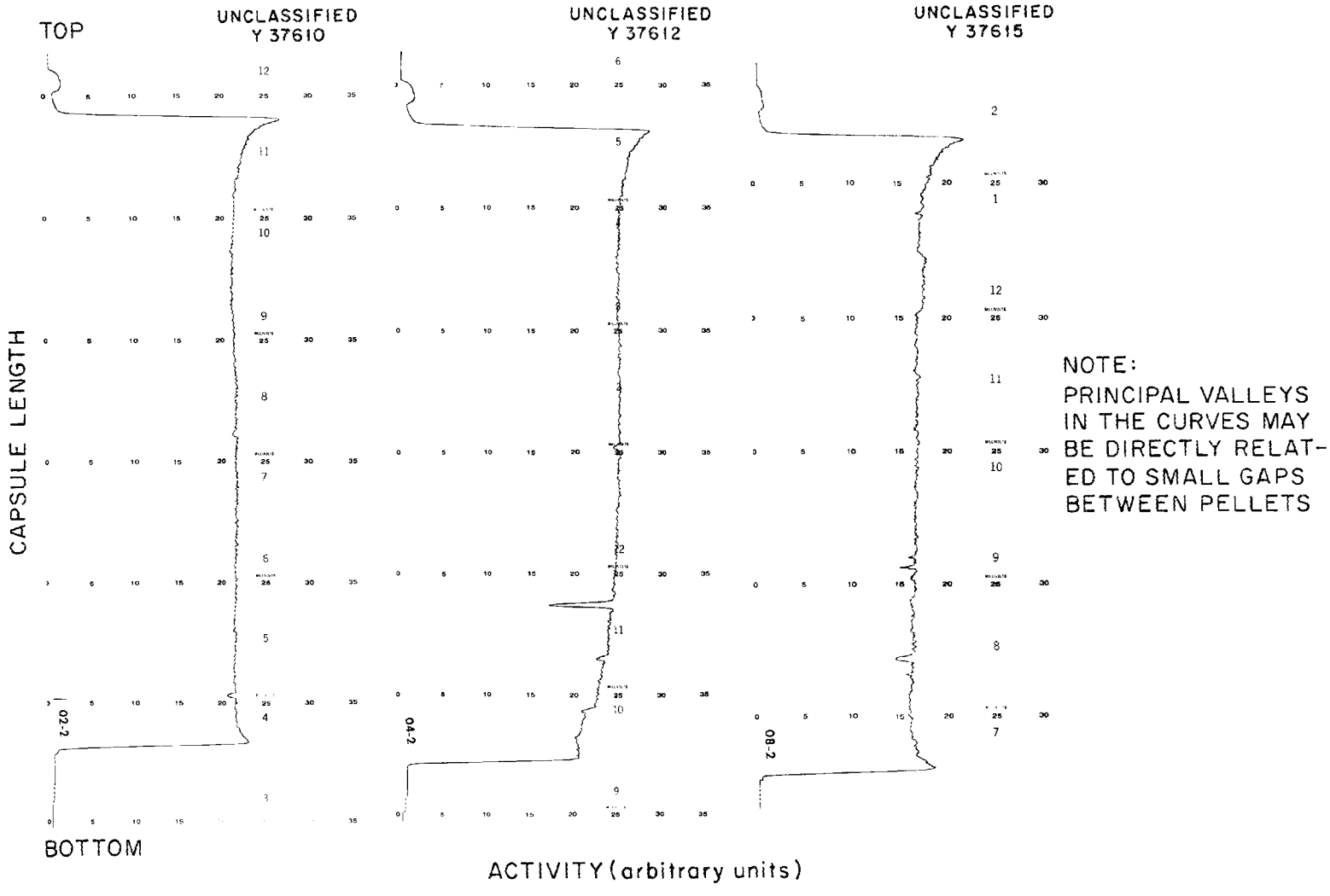


Fig. 6.10. Gamma Scans of ORR Group II Capsules 02-2, 04-2, and 08-2.

Table 6.6. Diameter Measurements of ORR-Irradiated Group II Capsules

Capsule No.	Cladding Temperature During Irradiation (°F)	Measurement Position Along Length (in.)	Average Diameter Before Irradiation (in.)	Change in Diameter After Irradiation (in.)
01-2	1300	1	0.7525	0
		2	0.7524	0
		3	0.7526	-0.001
		4	0.7526	0
		5	0.7527	0
		6	0.7526	0
02-2	1600	1	0.7529	-0.002
		2	0.7529	-0.001
		3	0.7528	-0.003
		4	0.7531	+0.002
		5	0.7531	-0.003
		6	0.7529	-0.003
03-2	1300	1	0.7527	-0.002
		2	0.7525	-0.004
		3	0.7523	-0.004
		4	0.7523	-0.005
		5	0.7523	-0.005
		6	0.7525	0
04-2	1300	1	0.7526	-0.003
		2	0.7526	-0.002
		3	0.7524	-0.002
		4	0.7523	-0.005
		5	0.7522	-0.001
		6	0.7523	0
05-2	1600	1	0.7527	-0.003
		2	0.7524	-0.005
		3	0.7526	-0.006
		4	0.7525	-0.005
		5	0.7524	-0.003
		6	0.7525	-0.002
006-2	1600	1	0.7523	-0.005
		2	0.7520	-0.006
		3	0.7521	-0.008
		4	0.7519	-0.004
		5	0.7519	-0.005
		6	0.7523	-0.003
07-2	1300	1	0.7521	-0.003
		2	0.7520	-0.002
		3	0.7520	-0.004
		4	0.7519	-0.003
		5	0.7520	-0.003
		6	0.7522	+0.001
08-2	1600	1	0.7520	-0.004
		2	0.7519	-0.005
		3	0.7518	-0.004
		4	0.7515	-0.004
		5	0.7519	-0.004
		6	0.7520	-0.002

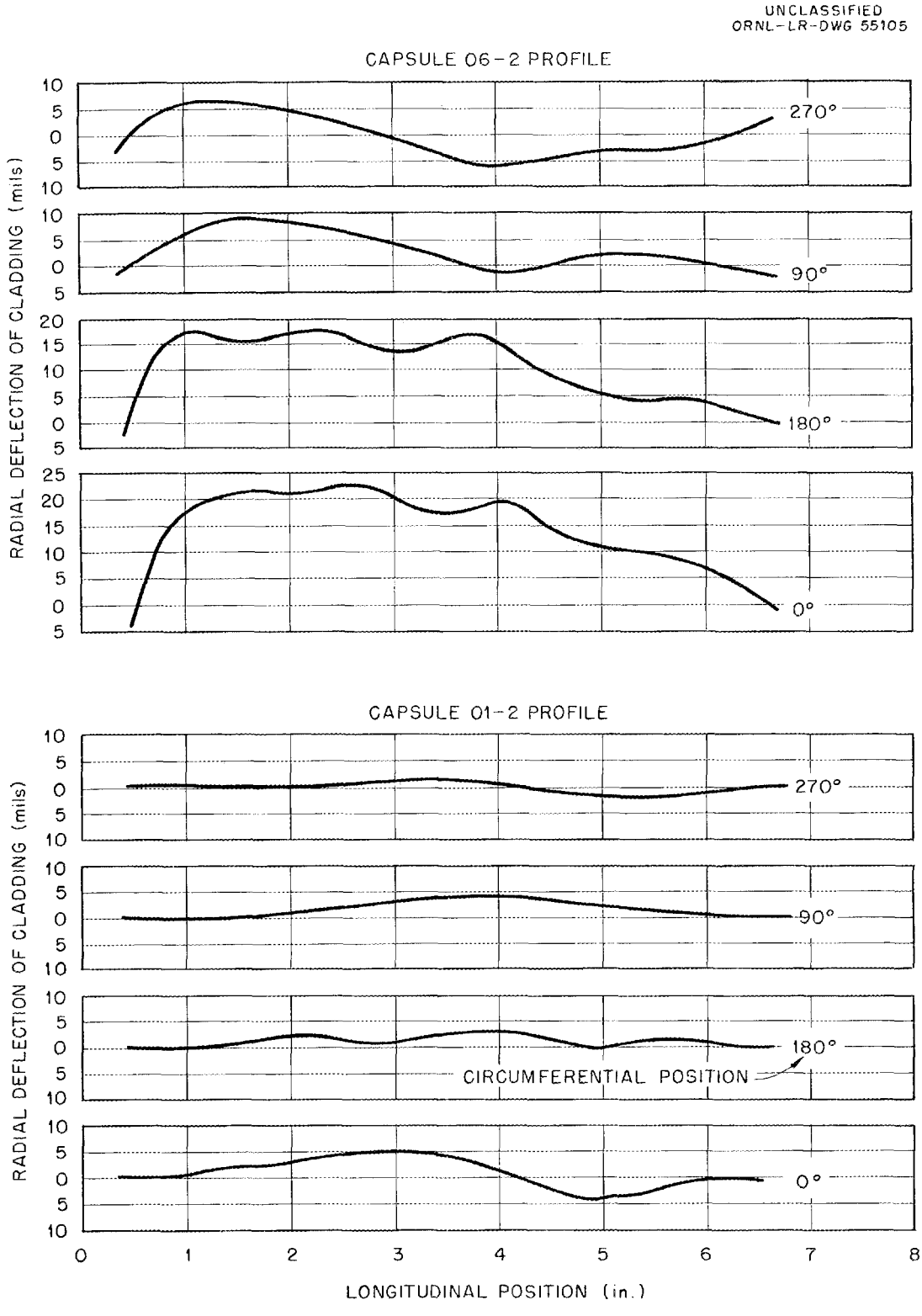


Fig. 6.11. Maximum and Minimum Profile Variations for Group II Capsules, Deflections Greatly Exaggerated.

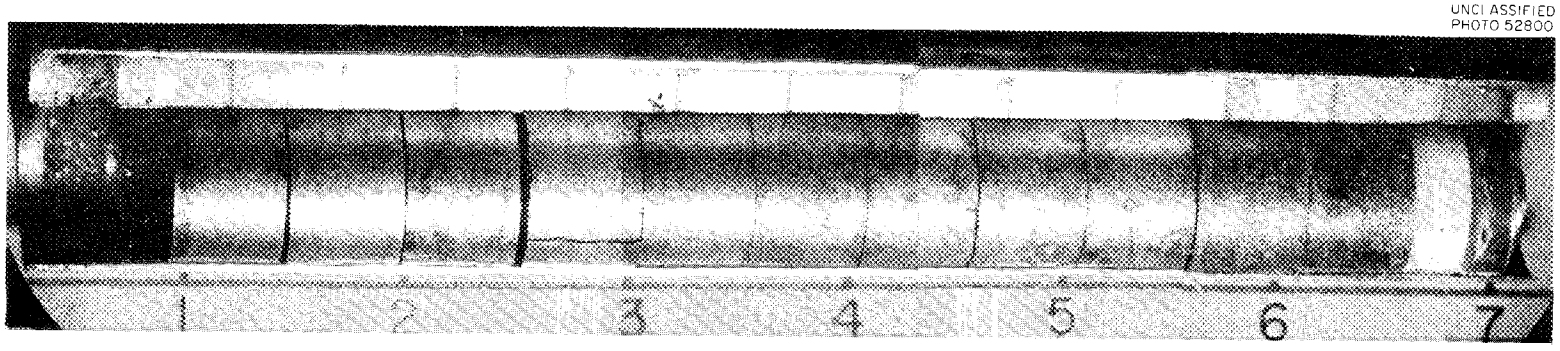
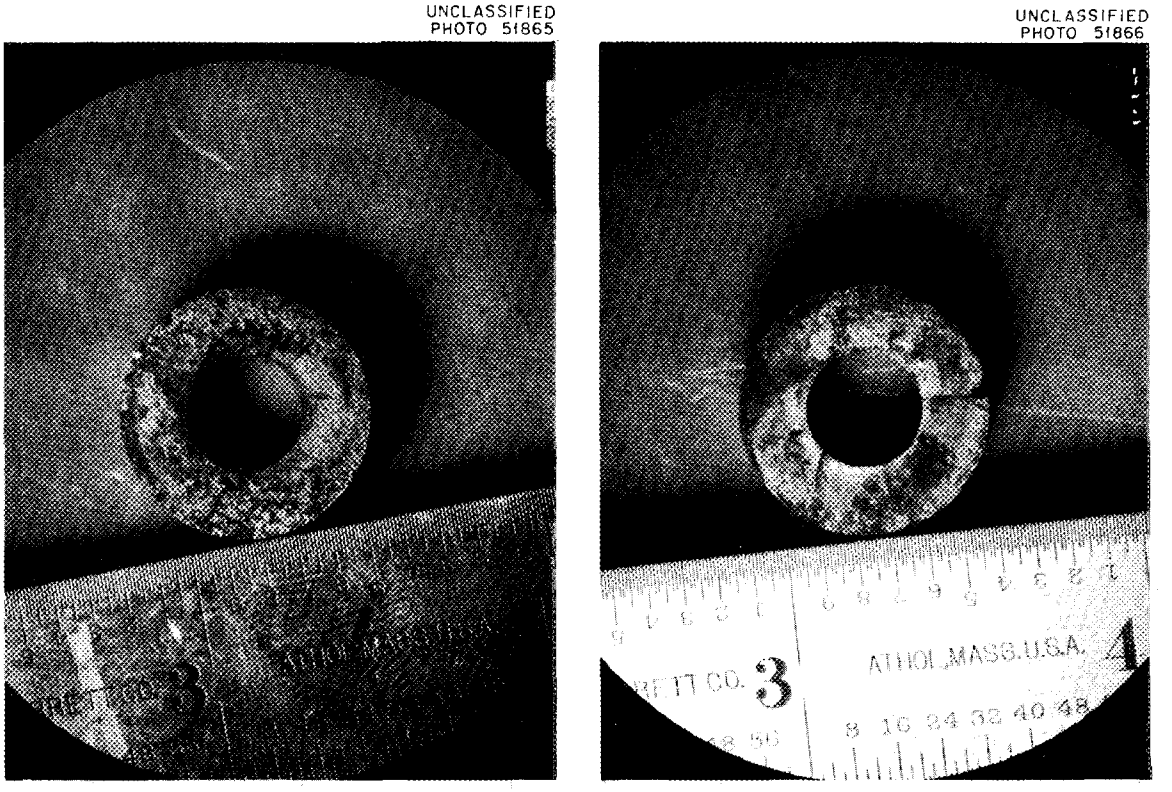


Fig. 6.12. ORR-Irradiated Capsule 02-1 with Cladding Removed to Show Fuel Pellets.

the can undamaged, as shown in Fig. 6.13. It is felt that the improved condition of the pellets is due to improved techniques and more careful handling in the hot cell. The conclusion is reached that the pellets were whole while in the reactor, but they were full of small cracks and perhaps microcracks. They were therefore fragile and easily broken during handling.

The BeO bushing from the center of capsule 06-1 is shown in Fig. 6.14. It was not badly damaged, but some reaction areas are evident. Deposits that were presumed to be BeO were found on some of the UO_2 pellets (see Fig. 6.15). It has been postulated that the deposits, which were too thin for sampling, were formed by the water vapor within the capsule causing the BeO to hydrolize at the high central temperatures. The Be(OH) thus formed migrated to cooler surfaces, where it disassociated into BeO and H_2O. The BeO remained on the cooler surface and the water vapor returned



TOP BOTTOM

Fig. 6.13. UO_2 Pellet 220-5 Which Was Removed Intact from Capsule 02-1. Fine cracks are visible.

to the central BeO plug to continue the reaction, migration, and deposition cycle.

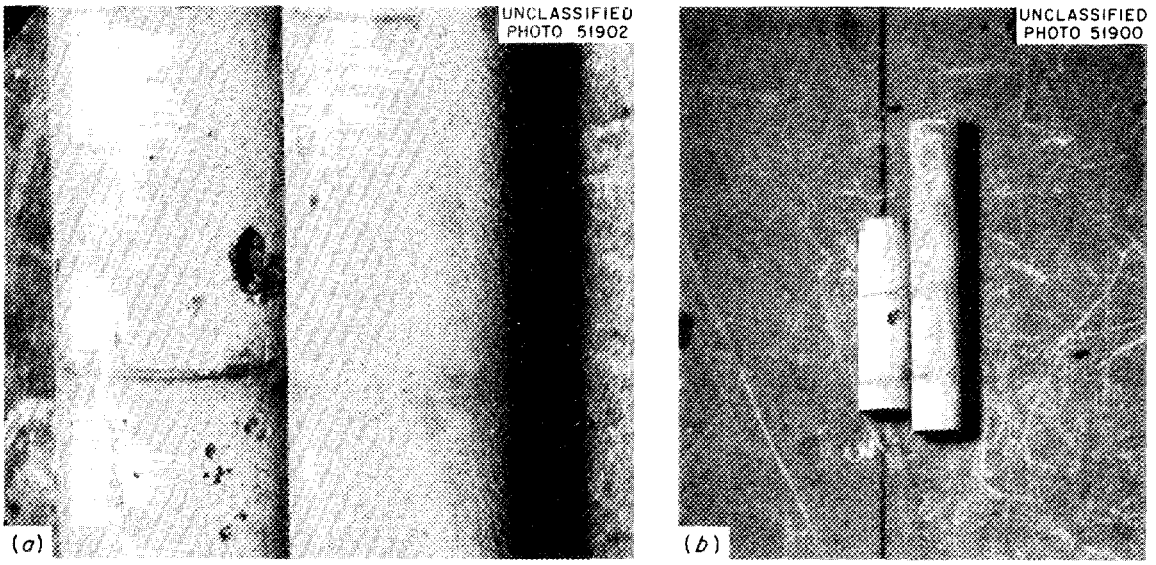


Fig. 6.14. BeO Bushing from Capsule 06-1 Showing Reaction Area. (a) Reaction area, 4.7X. (b) Entire bushing.

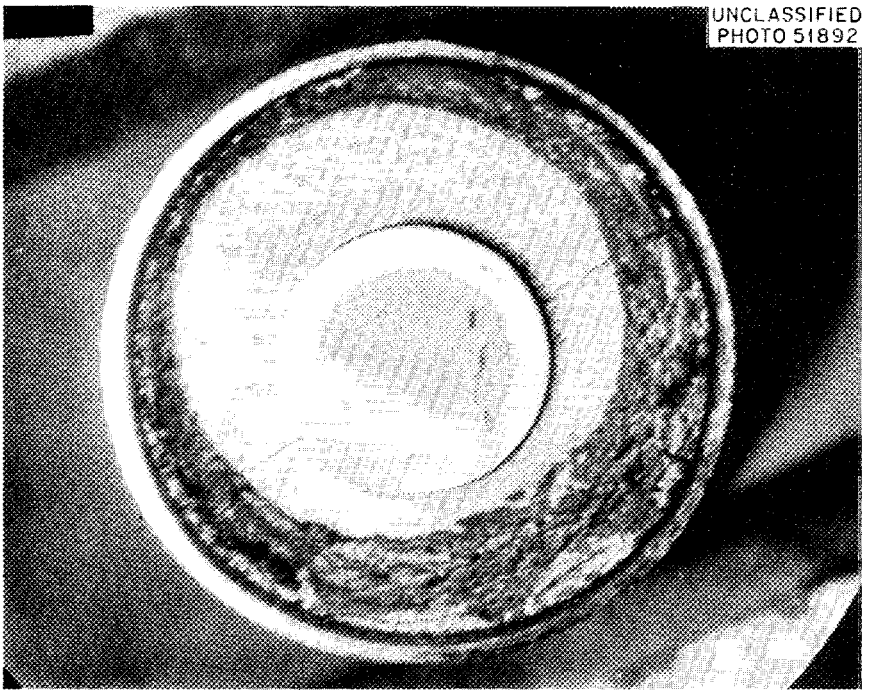


Fig. 6.15. Pellet 226-7 from Capsule 06-1 Showing BeO Bushing and Discoloration on UO_2 Pellet.

Instantaneous Fission-Gas-Release Experiment

(R. M. Carroll, M. D. Karkhanavala)

Examination of Thin-Plate UO_2 Sample

The fuel capsule that contained the thin-plate UO_2 sample that was the source for the instantaneous fission-gas-release experiments was examined in the GE-Vallecitos hot cells. The UO_2 fuel had been oxidized during irradiation by trace quantities of oxygen in the sweep gas, and hydrogen had been added to the sweep gas to reduce the fuel during irradiation. During the time the fuel was in the reducing atmosphere it became obvious, from temperature relations, that the thin-plate sample had broken and perhaps crumbled near the end of the run. When the capsule was opened, it was found that the UO_2 was in granules 0.050 in. in diameter or smaller. This extreme fragmentation is not characteristic of irradiated UO_2 and can probably be attributed to the reduction reaction.

Tests of a Graphite-Clad UO_2 Sample

A sample of high-density UO_2 (0.50 in. o.d., 0.50 in. long, with a 0.23-in. axial hole) clad in low-permeability graphite treated with a 0.001-in. coating of pyrolytic carbon was irradiated to evaluate the effectiveness of the graphite-carbon cladding in retaining fission gases. This sample leaked fission gas from the very beginning of the irradiation. The amount of fission gas emerging from the sample increased with temperature. There were thermocouples pressed against the graphite cladding, but the temperature of the UO_2 can only be estimated.

Bursts of activity were produced with very little temperature change when the sweep gas was changed from helium to argon. The activity increase was abrupt when the argon reached the sample, whereas a time lag would be expected for a low-permeability cladding. The bursts were analyzed, and the major part of the gamma activity was due to Xe^{135}, Xe^{133}, Kr^{85m}, and Kr^{88}. Other isotopes of xenon and krypton were present, but their contribution to the total activity was small. The flow rate of the sweep gas gave a 36-min decay time between the fuel and the spectrometer, so the very short-lived isotopes had decayed.

The steady-state release of Xe^{135} from the graphite-clad UO_2 was compared with release from unclad UO_2 (see Table 6.7), and no significant difference was found. The ratios of isotopes of xenon and krypton were compared for the three samples, since any holdup by the cladding would result in a relative increase of the longer-lived isotopes, but there was no significant variation in the proportions of Xe^{135}, Xe^{133}, Kr^{85m}, and Kr^{88} released from unclad and clad UO_2. These observations have led to the conclusion that the graphite cladding on the sample now being irradiated is broken (possibly because of differential thermal expansion between the UO_2 and graphite) to the extent that it allows rapid passage of gas toward or away from the UO_2, even when no pressure differential exists. The argon sweep gas penetrates the broken graphite, and, because of the poor thermal conductivity of argon (compared with that of helium), the temperature of the UO_2 increases and causes an increase in the fission-gas-release rate. The graphite barrier between the thermocouples and the UO_2 masks the high temperature increase of the UO_2.

A comparison of the relative percentages of the different isotopes of xenon and krypton as they emerge from the fuel may offer an important tool for evaluating the gas-retention properties. The isotopes Xe^{133},

Table 6.7. Comparison of Steady-State Release of Xenon from Various Types of Fuel Material

Fuel Material	Irradiation Temperature (°F)	Steady State Release of Xe^{135} (%)
Unclad ThO_2-UO_2 mixture	1660, gas	0.036
	1877, pellet surface	0.1
Unclad thin plates of UO_2	1942, maximum	0.023
Graphite-clad UO_2		
Sample 1	720, graphite cladding	0.019
	870, argon atmosphere	0.023
	1100, UO_2 pellet	0.09
Sample 2	640, graphite cladding	0.001
	1100, helium atmosphere	0.009
	1140, UO_2 pellet	0.018

Xe^{135}, Kr^{85m}, and Kr^{88} appeared to be retained by the UO_2 for the same average time, in the order of 5 hr, so a higher proportion of Xe^{133} (5-day half-life) was released than Kr^{88} (2.8 hr), and the other isotopes were released in proportion to retention time. The retention time varied with temperature. Because of the wide range of temperatures (which could not be measured) in the graphite-clad sample, no definitive study can be made of the variation of retention time with temperature. It is especially interesting to note that, although Xe^{133} is released after an apparent holdup time in the UO_2 of only a few hours at the temperatures employed, the amount of Xe^{133} released was only a very small proportion (less than 0.1%) of the total formed. This seems to indicate that all the gas formed in a particular part of the fuel escapes with the same average time of diffusion and the gas formed in another part either does not escape or escapes so slowly that radioactive decay is the dominant loss for these isotopes.

The graphite-clad sample has been removed from the LITR facility for these experiments, and thin-plate samples of high-density UO_2 have been inserted. Fission-gas-release studies and thermal- and electrical-conductivity measurements will be made with these samples.

Oxygen-to-Uranium Ratio Determinations (M. D. Karkhanavala)

The properties of UO_2 fuel elements are influenced to a large extent by the oxygen-to-uranium ratio. Consequently techniques for determining the oxygen-to-uranium ratio of irradiated UO_2 are being studied. The methods commonly used for determining excess oxygen in unirradiated UO_2 are (1) determination of total oxygen in a given weight of the sample, (2) determination of the concentration of U^{6+} ions (and U^{4+} ions) in a given weight of the sample by either reduction-oxidation titration or polarographic analysis, and (3) determination of the weight change upon complete oxidation to U_3O_8. The determination of the ratio in irradiated fuel is made uncertain, however, by (1) burnup of a certain percentage of the uranium, which cannot be determined with the degree of accuracy required for the over-all estimation, (2) the generation of fission products, which oxidize simultaneously with UO_2, (3) the varying and uncertain degrees

of oxidation of the fission products, and (4) the intense radiation, which disassociates the oxidizing chemicals used in normal analysis. Further, the method of analysis must be amenable to adaptation for use in a hot cell.

A review of the existing methods has indicated that the thermogravimetric and polarographic methods, with minor changes, would be best suited for analyzing irradiated fuels. In the thermogravimetric method, it is possible to reduce the uncertainty caused by oxidation of fission products to within the limits of experimental error and to make a determination with a normal accuracy of 0.01 in excess oxygen by using a very small sample, about 10 to 20 mg, and employing a quartz spring-suspension balance. Experiments on oxidation of simulated fission product mixtures have shown that this method could, at best, be used for fuels with burnups of less than 1000 Mwd/MT. Higher burnups yield sufficient fission products to require corrections for the oxidation of fission products. Since the uncertainties involved in making these corrections are large, the method is not recommended in the higher burnup ranges.

The polarographic method, with minor modifications, is the most promising for all ranges of fuel burnup, and greater attention is being given to developing and adapting this method for use in hot cells. It has the advantage that weighing in the hot cells is eliminated and, except in cases of very high burnups, only the dissolution part of the procedure needs to be carried out in the hot cells. The actual polarographic run can be made outside the hot cell by locating the reduction cell behind 4 in. of lead shielding.

The procedure being adapted for this determination consists of (1) dissolution in an inert atmosphere of a small amount of the UO_2 in about $4\underline{N}$ H_2SO_4, with small amounts of fluoride added if required to aid dissolution, (2) making up the solution to a known volume, (3) polarographic determination of the U^{6+} concentration in an aliquot of the solution, (4) total oxidation of an aliquot of the solution to convert all U^{4+} to U^{6+}, (5) polarographic determination of the total U^{6+} in the aliquot obtained in step 4 (this total U^{6+} determination could also be made coulometrically), (6) calculation of U^{4+} and U^{6+} ion concentrations from results obtained in steps 3 and 5, and (7) calculation of the oxygen-to-uranium ratio.

During this work, it was found necessary to have a standard with a known and reproducible oxygen-to-uranium ratio. The air oxidation of UO_{2+x} ($x < 0.33$) at 250°C gave a stable and reproducible compound of the composition U_3O_7 that has served as a convenient standard.

ORR Closed-Cycle-Loop Experiments

(R. E. Reagan, C. D. Baumann, J. G. Morgan)

Graphite-Canned UO_2

A capsule containing two siliconized silicon carbide-coated graphite-canned UO_2 cylinders that was irradiated to a dose of 2.2×10^{20} neutrons/cm^2 at a coating temperature of 1500°F has been removed from the ORR closed-cycle-loop facility for examination. There was evidence of fission-gas release during the final thermal cycle before removal from the reactor.

Two samples of UO_2 canned in uncoated low-permeability graphite have been irradiated for 1000 hr at 1800°F and have been withdrawn from the reactor flux zone. Fission-gas-release measurements will be made when the capsule is pierced during hot-cell examination.

Graphite-Canned UC_2 Dispersed in Graphite

Out-of-pile tests are being conducted on two types of 29.7% enriched UC_2 dispersed in graphite and canned in siliconized silicon carbide-coated graphite. In one type of sample, the fuel matrix is integrally bonded to the graphite container. The other type of sample is canned in the conventional manner. One of the bonded samples has been heated by radio-frequency induction from 200 to 1800°F more than 12 000 times without weight or density changes. Both bonded and canned samples have been heated in air to 1800°F for 200 hr without weight or density changes.

Facility Modifications

After sample failure during two successive capsule irradiations, the in-pile tube assembly of the closed-cycle loop had become contaminated to an activity level that prevented continued use. A new in-pile tube assembly has been built and is scheduled for installation. The loop is being

redesigned to consist of a single-pass, air-cooled system, with helium gas as the fission-gas-transport medium. The new loop will include a stainless-steel-gauze trap located directly above the reactor vessel to collect daughters of short-lived fission gases.

Radiation Effects on Structural Metals

Pressure Vessel Steels (R. G. Berggren, T. J. Humphreys)

Equipment for irradiation experiment ORR-8, in which tensile and impact specimens of a weld metal and several steels will be irradiated at 150 to 700°F, has been assembled and will be inserted in the ORR during the January shutdown. This equipment also includes a controlled temperature facility for study of aging phenomena in zirconium-niobium alloy crystals. This equipment will, in addition, be used for some preliminary measurements of fast-neutron spectra in the poolside facility.

Designs have been completed for improved irradiation-experiment assemblies for use in the ORR poolside facilities. A flux-monitoring assembly has been designed that duplicates the specimen loading of the experiment assemblies and permits improved fast-neutron dosimetry measurements. This assembly will be used in several poolside positions to map the neutron spectra and distribution.

A set of tensile and impact test specimens of ASTM A-212, grade B, steel were installed in GCR-ORR loop No. 1, and a similar set of E-7016 weld metal specimens are being prepared for subsequent exposure in the same facility.

The three long-term experiments for which the ORNL Graphite Reactor was to be used have been postponed indefinitely because of high cost and uncertainty of obtaining meaningful data. Other means for obtaining long-time, low-flux exposure data are being studied.

Beryllium (J. R. Weir, W. W. Davis)

Postirradiation examination of specimens from the first high-temperature beryllium irradiation experiment is under way. The specimen histories

and density-change data were given previously.[4] The results of simple room-temperature bend tests performed on the specimens indicate that the beryllium was not embrittled by the irradiation and that the strength at room temperature was only slightly impaired. These results are consistent with the hypothesis that the helium generated by the (n,2n) and (n,α) reactions exists as relatively large bubbles within the beryllium and therefore permits easy plastic deformation. If the helium existed as a fine array of minute bubbles, a strengthening effect and embrittlement would be predicted. Metallographic examination has confirmed that the gas collected as large bubbles, as shown in Fig. 6.16. The difference between the unirradiated and irradiated beryllium is evidenced by the larger and more numerous dark areas on the photomicrograph of the irradiated specimen. It is postulated that the gas agglomerated on the inclusions that may be seen in the unirradiated specimen. Close observation of the irradiated specimen reveals that some of the gas also precipitated in grain boundaries. Metallographic analysis of these specimens is continuing.

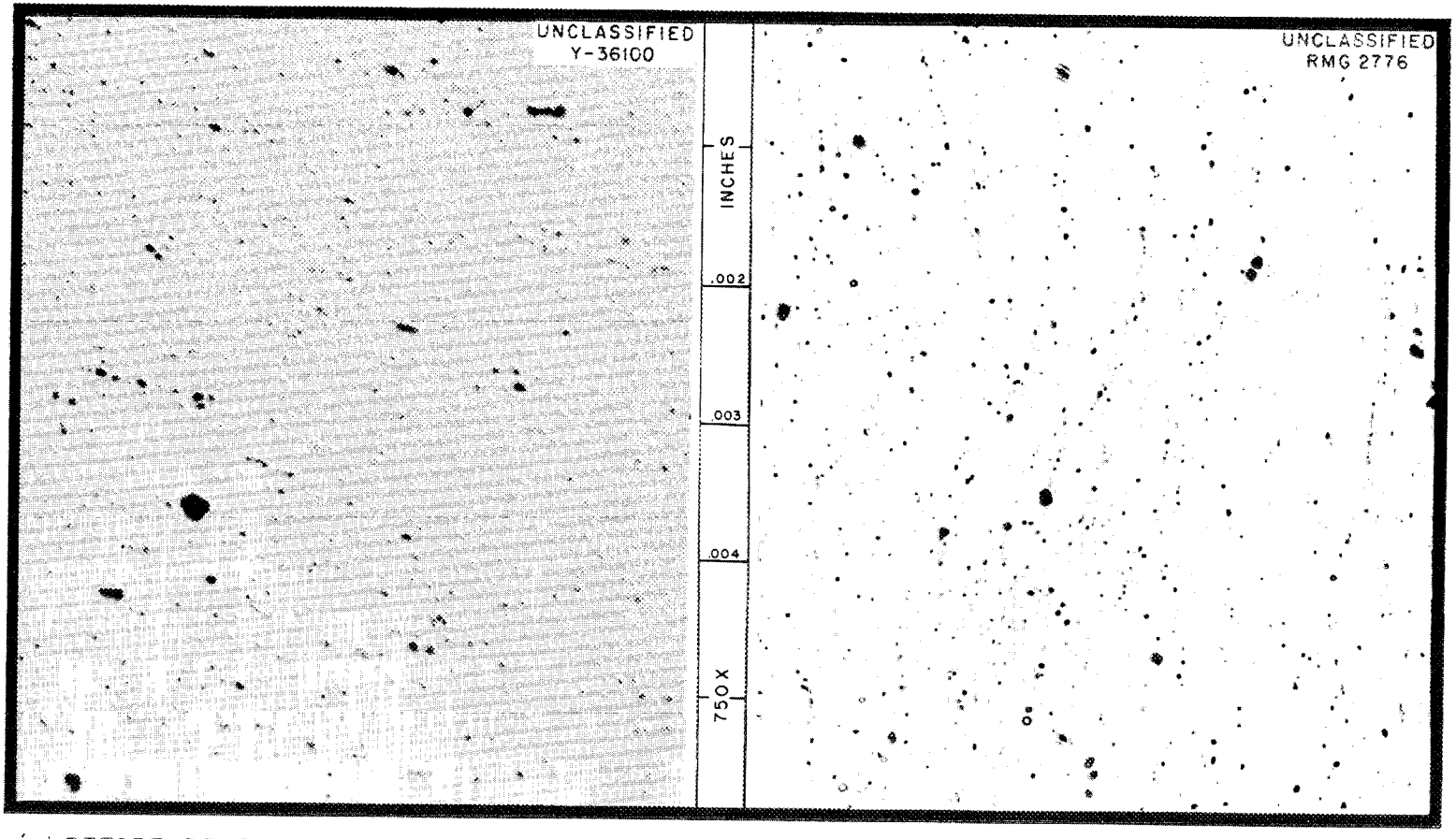
In the second high-temperature beryllium-swelling experiment, specimens were held at 500, 600, and 700°C and exposed to a dose of approximately 1.4×10^{20} neutrons/cm^2 (>1 Mev) during a one-month reactor cycle. The specimens used in this experiment were representative of the following fabrication schedules: (1) hot pressing (commercial and high purity), (2) hot extrusion (rod), (3) unidirectional hot rolling, and (4) hot cross rolling.

The density decreases observed for these specimens were in the range 0.2 to 0.5% ± 0.2%. Similar data obtained for beryllium held at 700°C for one month in the absence of irradiation indicate density decreases of 0.2 to 0.3% ± 0.2%. Thus the data indicate that the swelling of beryllium under the conditions in this experiment was smaller than the experimental error in density measurement.

Bend test results indicate that the mechanical properties (strength and ductility at room temperature) were not affected by the irradiation. Hardness measurements, metallographic examinations, and gas analyses will be performed on some of the specimens from this experiment.

---

[4]"GCR Quar. Prog. Rep. June 30, 1960," ORNL-2964, pp. 176–8.



(a) BEFORE IRRADIATION

(b) AFTER IRRADIATION AT APPROXIMATELY 600°C

Fig. 6.16. Cross-Rolled Beryllium Sheet Before and After Irradiation. 750X. As polished.

Specimens from the cold irradiation experiment, in which the exposure was 6×10^{20} neutrons/cm^2 (>1 Mev) at 120°F, have been bend tested in the as-irradiated condition. The results indicate that embrittlement occurred. In the case of specimens fabricated from hot-pressed block, unidirectionally rolled sheet, and cross rolled sheet, the deflection at fracture has been decreased to one-half to one-sixth the preirradiation deflection. Along with this loss in ductility, there were reductions in strength, as measured by the load at fracture in the bend tests. Results for specimens manufactured by hot extrusion indicate fracture deflections one-twelfth the preirradiation value. Comparison of these data with data for other types of fabrication may indicate an orientation-dependent effect. It may be possible to check this point by examining the preferred orientation in the specimens. Postirradiation-annealing experiments are under way to determine the time-temperature relationships for the annealing of the defects that cause the embrittlement of the specimens and to investigate the swelling.

The third high-temperature-swelling experiment is under way in position B-8 of the ORR. In this experiment, tubular specimens are being held at 600, 700, and 750°C and will be taken to an exposure of 4×10^{20} neutrons/cm^2 (>1 Mev). Tubes manufactured by machining from hot-pressed block, machining from warm-extruded rod, warm extrusion, hot-impact extrusion, and hot extrusion are included in this experiment.

Equipment was constructed for two in-pile tube-burst experiments, and the experiments are under way in an ORR poolside position and in core position B-8. In these experiments the stress-rupture strength of beryllium tubes will be investigated at 600°C as a function of neutron exposure up to 4×10^{20} neutrons/cm^2 (>1 Mev).

Type 304 Stainless Steel (N. E. Hinkle, J. W. Woods, J. C. Zukas)

The cladding material for the EGCR fuel elements, type 304 stainless steel, is being tested in in-pile tube-burst-type stress-rupture tests. The results of the first test are presented in Table 6.8. The data obtained in out-of-pile tests of similar specimens are not yet complete enough for conclusive comparison. In the second experiment, ten tube burst specimens of type 304 stainless steel (Superior Tube Company, heat

Table 6.8. Results of In-Pile Tube-Burst Tests of Type 304 Stainless Steel at 1300°F in Air

Flux: 10^{13} neutrons/cm^2·sec (>1 Mev)

Specimen No.	Stress (psi)	Time to Rupture (hr)
15-2	13 000	130
3	13 000	197[a]
6	13 000	144
8	13 000	122
4	11 000	512
7	11 000	480
10	11 000	462
1	9 000	1680
5	9 000	>1850[b]
9	9 000	>1850[b]

[a]Irradiated at 1300°F for approximately 8400 Mw-hr prior to application of stress.

[b]Test concluded before rupture.

No. 2399x) were tested at temperatures of 1500 and 1600°F in air. The stress levels were chosen to provide rupture within the duration of the experiment, but, as a result of excessive reactor downtime, three specimens did not rupture. Table 6.9 summarizes the results of this experiment, previous comparable experiments, and the available out-of-pile data on this heat of material.

It is apparent that at 1500°F, neutron bombardment reduces the rupture strength of this material by about 1500 psi in the stress range studied. Both the in-pile and out-of-pile data are fairly consistent and reproducible. The out-of-pile available data for this material from tests at 1600°F are insufficient at present for comparison.

Inconel (N. E. Hinkle, J. W. Woods, J. C. Zukas)

Specimens from six special heats of Inconel are being prepared for in-pile tube-burst tests. These heats, which were received from the International Nickel Company, have different boron contents, as follows: heat

Table 6.9. Results of Tube Burst Tests of Type 304 Stainless Steel in Air in the ORR

Flux: 2×10^{13} neutrons/cm^2·sec (>1 Mev)

Specimen No.	Stress (psi)	Temperature (°F)	Irradiation Dose at Rupture (Mw-hr)	Time to Rupture (hr)
(a)[b]	6300	1500	0	510[c]
(a)[b]	6300	1500	0	490
97	6300	1500	0	184
(a)[b]	5800	1500	0	690
(a)[b]	5250	1500	0	1330
(a)	5250	1500	0	1250
9-7	5000	1500	5 400	337
9-8	5000	1500	8 300	518
(a)[b]	4200	1500	0	2450
(a)	4200	1500	0	1650
7-3	4000	1500	12 300	895
9-6	4000	1500	8 900	672
17-3	4000	1500	36 900	851[d]
17-10	3500	1500	50 080	>1600[e]
17-1	3000	1500	50 080	>1600
17-9	3000	1500	50 080	>1600
17-8	5060	1600	3 750	49
(a)[b]	3700	1600	0	265
17-5	3000	1600	13 500	414
17-6	2600	1600	27 100	870
17-4	2200	1600	43 900	1430
17-7	2200	1600	47 400	>1505[f]

[a] Out-of-pile specimens.

[b] These specimens are 6 in. long. All other specimens are 2 1/2 in. long.

[c] All out-of-pile data were received from J. W. Woods and J. T. Venard of the ORNL Metallurgy Division. The stresses were recalculated to correspond with those used for the in-pile specimens.

[d] This specimen was stressed after 11 500 Mw-hr of irradiation at 1500°F.

[e] Three specimens held at 1500°F had not ruptured when the experiment was terminated.

[f] This test was terminated when the thermocouples failed and control was lost.

0B, <10 ppm; heat 2B, 20 ppm, natural B; heat 10B, 100 ppm, natural B; heat 4B 11, 40 ppm, enriched in B^{11}; heat 6B 11, 60 ppm, enriched in B^{11}; heat 6B 10, 60 ppm, enriched in B^{10}. Specimens are also being prepared from two heats of Inconel which were previously tested in the reactor. These heats, MTR Inconel and CX-900 Inconel, contain 30 and 40 ppm natural boron, respectively.

7. OUT-OF-PILE TESTING OF MATERIALS AND COMPONENTS

Compatibility Tests of Graphite, Structural Materials, and Helium

(J. H. DeVan, A. M. Smith)

Tests have been in progress for evaluating the behavior of stainless and low-alloy steels during extended exposures in helium contaminated with impurities desorbed from graphite. The planned experiments have been completed, except for those dealing with controlled CO_2-CO impurity additions.

The fourth controlled impurity experiment (TCL No. 13) was run to evaluate the oxidation resistance of wrought chromium steels in helium containing 500 ppm (by volume) CO_2 and 450 ppm (by volume) CO. The impure helium was circulated at a pressure of 30 psig by natural convection through a type 316 stainless steel section heated to a maximum temperature of 1100°F and a section cooled to 500°F. Specimens of the various steels listed in Table 7.1 were suspended in the heated section of the loop and were surrounded by a cylinder of AGOT graphite. In addition, an independently heated type 304 stainless steel tube was mounted above the

Table 7.1. Results of Thermal-Convection Loop Test No. 13 in Which Steel Specimens Were Exposed at 1100°F to Helium Containing 500 ppm CO_2 and 450 ppm CO

Composition of Steel Specimen (wt %)	Specimen Weight Gain (mg/cm^2)	Weight of Film Removed from Specimen (mg/cm^2)	Weight of Metal Reacting (mg/cm^2)
Mild steel (0.15 C)	3.5	12.8	9.3
2.25 Cr, 1 Mo, bal Fe	2.9	10.5	7.6
3 Cr, 0.9 Mo, bal Fe	2.1	7.9	5.8
5 Cr, 0.5 Mo, bal Fe	1.6	5.9	4.3
7 Cr, 0.5 Mo, bal Fe	0.24		
12 Cr, bal Fe	0.11		
18 Cr, 8 Ni, bal Fe[a]	0.17		

[a]Type 304 stainless steel.

specimens and was maintained at a temperature of 1500°F. All specimens were exposed to the loop atmosphere for a total period of 740 hr.

The extent of the oxidation that occurred during this test is indicated in Table 7.1. The steels that contained less than 7% chromium gained appreciable weight and had relatively heavy, poorly adherent oxide films. Evidence of the poor adherence of the films is presented in Fig. 7.1, which shows specimens exposed in test No. 13. The mild steel specimen and the specimen containing 5% Cr showed scaling or blistering of the oxide film. As may be seen, the extent of scaling was considerably less for the chromium-containing steel. In contrast, steel specimens containing 7% or more chromium had relatively thin, extremely adherent oxide films and showed minor increases in weight. The type 304 stainless steel specimen shown in Fig. 7.1 is typical of the steels containing 7% or more chromium. The type 304 stainless steel tube which was independently heated to 1500°F had a somewhat heavier but equally protective oxide film.

The amount of metal lost by the lower alloy steels due to oxidation was determined by completely stripping the oxide films and comparing the weights after stripping with weights before the test. Stripping was accomplished by applying adhesive tape to each side of the specimen. The oxide film adhered to the tape and was completely taken up as the tape was pulled from the specimen. The amounts of metal that reacted with the oxygen in the loop atmosphere are also listed in Table 7.1. The equivalent loss of wall thickness in the specimen that contained 5% chromium was calculated to be approximately 0.1 mil.

As reported previously,[1,2] two loop experiments that were similar to test No. 13, but for which the impurity levels in the helium were higher, also resulted in scaling of carbon and medium-alloy steels. The helium circulated in the first of these loops (TCL No. 10) contained 1320 ppm CO_2 and 1850 ppm CO, whereas the helium circulated in the second (TCL No. 12) contained 1500 ppm CO_2 and 1800 ppm CO. The weight gains of specimens

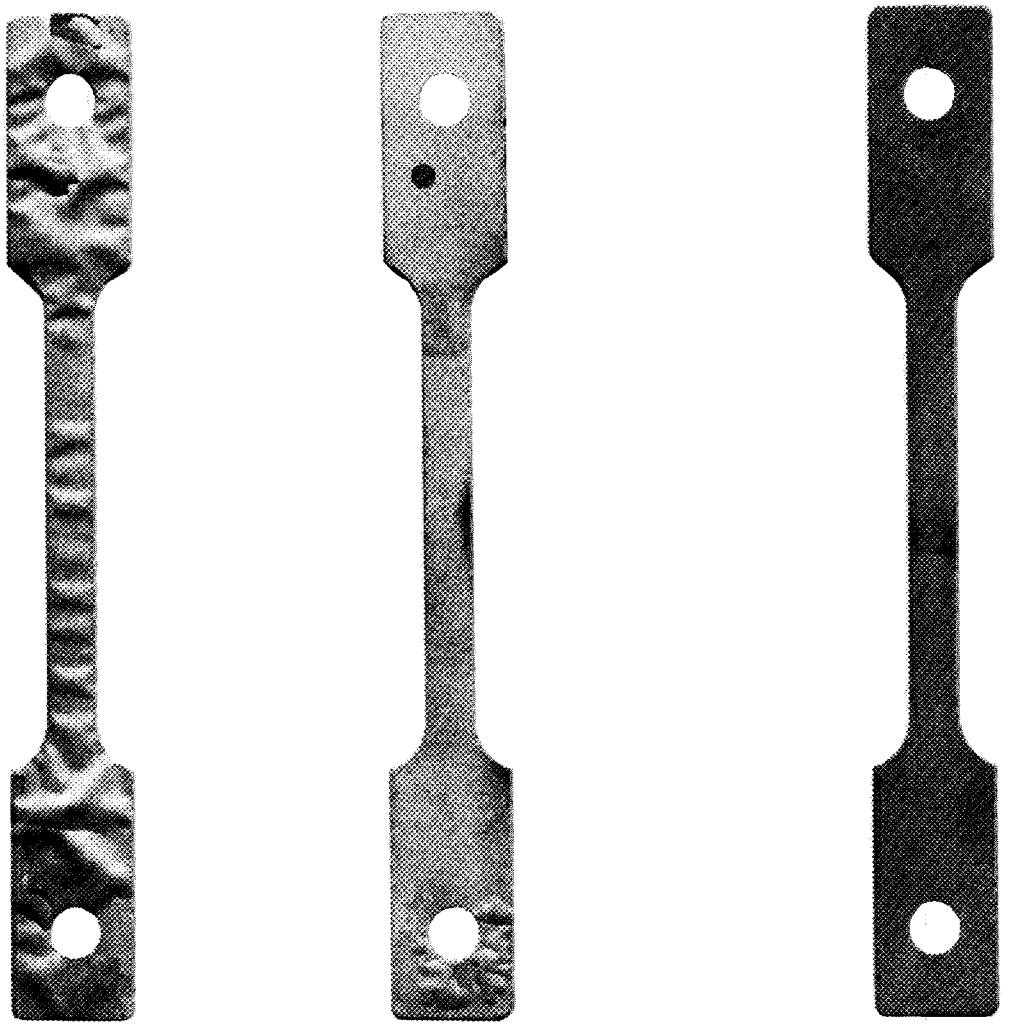
---

[1] "GCR Quar. Prog. Rep. June 30, 1960," ORNL-2964, pp. 186-8.

[2] "GCR Quar. Prog. Rep. Sept. 30, 1960," ORNL-3015, pp. 123-4.

exposed in these tests are compared in Fig. 7.2 with the weight gains of the corresponding specimens from test No. 13. It is apparent that differences in the ratios and amounts of CO and CO_2 among these tests had little effect on the rates of oxidation (based on weight changes). However, a

UNCLASSIFIED
PHOTO 52658



MILD STEEL

AISI 502 STEEL
5% Cr, 0.5% Mo, BAL. Fe

TYPE 304 STAINLESS STEEL
18% Cr, 10% Ni, BAL. Fe

Fig. 7.1. Steel Specimens After Exposure to Helium Containing 500 ppm CO_2 and 450 ppm CO for 740 hr at 1100°F.

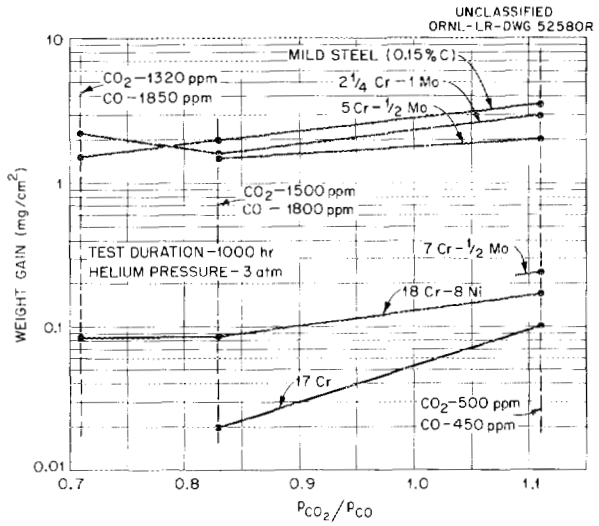


Fig. 7.2. Weight Gains of Mild and Wrought Chromium-Containing Steels Exposed to CO_2-CO Impurities in Helium at 1100°F.

slight but consistent increase in the rate of oxidation accompanies increases in the ratio of the partial pressure of CO_2 to that of CO.

A fifth controlled impurity experiment (TCL No. 14) was carried out to evaluate the effects of CO_2-CO concentrations lower than those of previous tests. The specimens used in this test were of the same general type as those described in Table 7.1, and test temperatures were identical to those of Test No. 13. Since the graphite used in this test had previously been degassed in test No. 13, it was anticipated that an impurity level of 500 ppm or less of CO and of CO_2 would be easily attained during test No. 14. However, even with a continuous low-volume purge from the system and periodic bleeding and repressurization, the concentration of CO_2 reached values of 900 to 1000 ppm for a short period of time after operating conditions were established. Hydrogen and water vapor concentrations during this period reached peaks of 0.98 and 0.06 vol %, respectively. Continued purging of the loop reduced the impurity levels of both CO and CO_2 to below 500 ppm, and the system was then allowed to attain equilibrium without further purging. A gradual reduction in CO and CO_2 was observed over the next 200 hr, and the quantities of both fell to approximately 100 ppm, where they remained during the rest of the 1000-hr test period. Disassembly of the test system has been completed, and preparations for test No. 15 are being made.

Tests of Prototype EGCR Purification System

(A. M. Smith, R. E. MacPherson)

A gas-purification system for treating the helium to be used as the coolant in the EGCR is required to limit the graphite burnup to 1% of the

reactor inventory during a 20-year period and to limit the graphite mass transfer resulting from the CO-CO_2 reaction to 500 lb during the same period. The impurities to be removed from the helium stream will be introduced by materials within the system or by inleakage from the surrounding environment. The allowable concentrations of impurities in the helium stream are given below:

Impurity	Allowable Concentration (ppm by vol)
CO_2	1600
H_2	2000
N_2	140
CO	140

Further, H_2O inleakage is to be limited to approximately 0.75 lb/day, and the moisture content of the helium recycled from the purification system is to be held to approximately 10 ppm by weight.

As presently designed (see Fig. 7.3), the purification system incorporates a platinum-catalyst-bed converter which, with O_2 additions, will oxidize the H_2 and CO. The purification system is fed by two continuous helium streams, one from the blower seal leak-off system and another from the low-pressure leak-off system. A third stream that is connected intermittently, with an estimated operating time of 300 hr per year, is introduced from the reactor coolant system through the catalytic converter when H_2 and CO levels in the coolant exceed the allowable limits. Another intermittent stream comes from the dryers during regeneration of these units.

These combined streams pass through the cooler, where water vapor is condensed, and then through a water separator. A compressor increases the gas pressure and forces the gas through a second water separator, through a dryer, and out through a filter to the vessel cooling system. Removal of CO_2 from the coolant stream will be accomplished by intermittent operation of the CO_2 adsorber when the level in the return stream to the vessel cooling system becomes excessive.

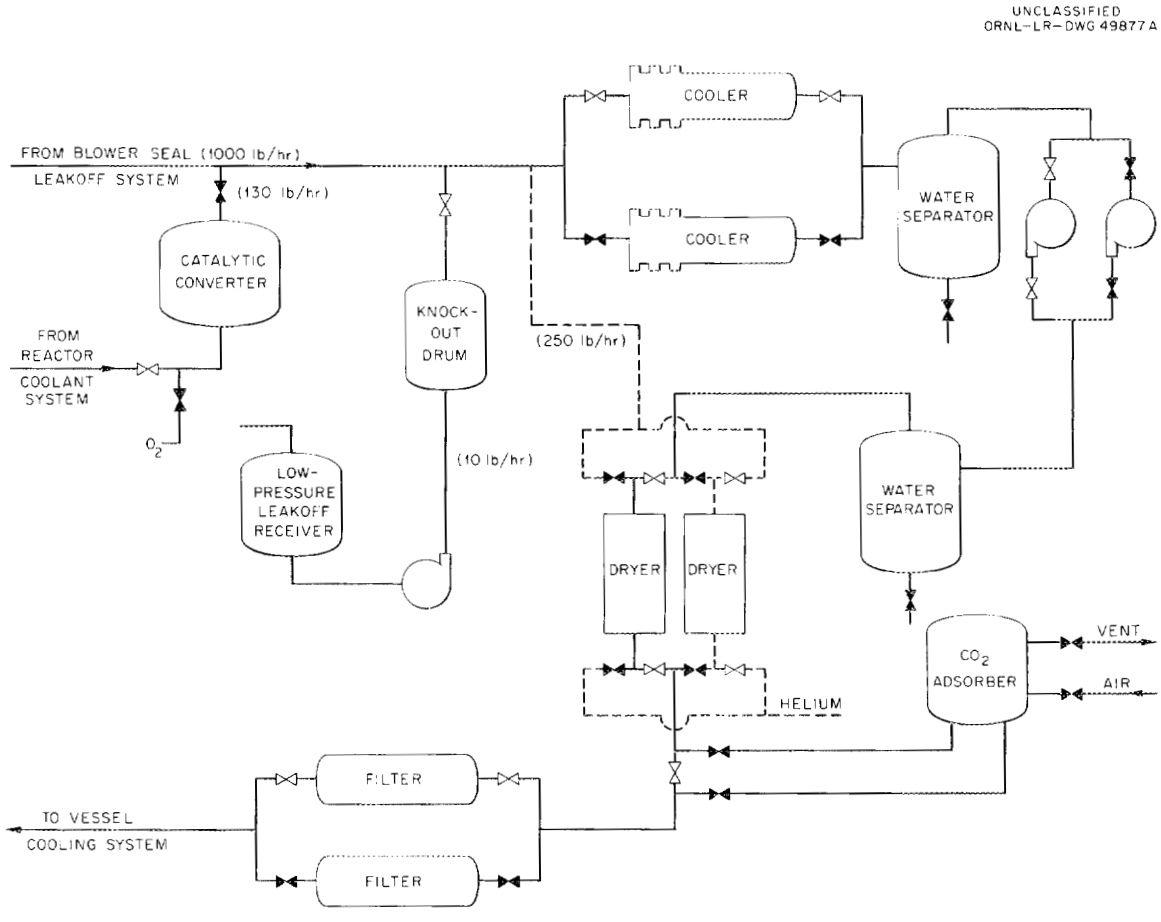


Fig. 7.3. EGCR Helium Purification System.

Tests are being carried out on a small-scale model of this purification system. The test system, shown in Fig. 7.4, is installed as a bypass loop on a forced-circulation loop that is being used for materials compatibility studies. The main loop consists of a compressor, a heater, a materials test section, and a steam cooler. Graphite sleeves that mock up a fuel element channel, a dummy fuel element assembly, and metal test specimens are located in the materials test section of the loop. The purification system is composed of a preheater on the inlet line, a catalytic converter with provisions for O_2 injection upstream, a water-cooled condenser, a water separator, a silica-gel bed for final moisture removal, and a molecular-sieve bed for CO_2 removal. Throttling valves in the inlet and exit lines and a flowmeter are used to control the flow of gas through the system.

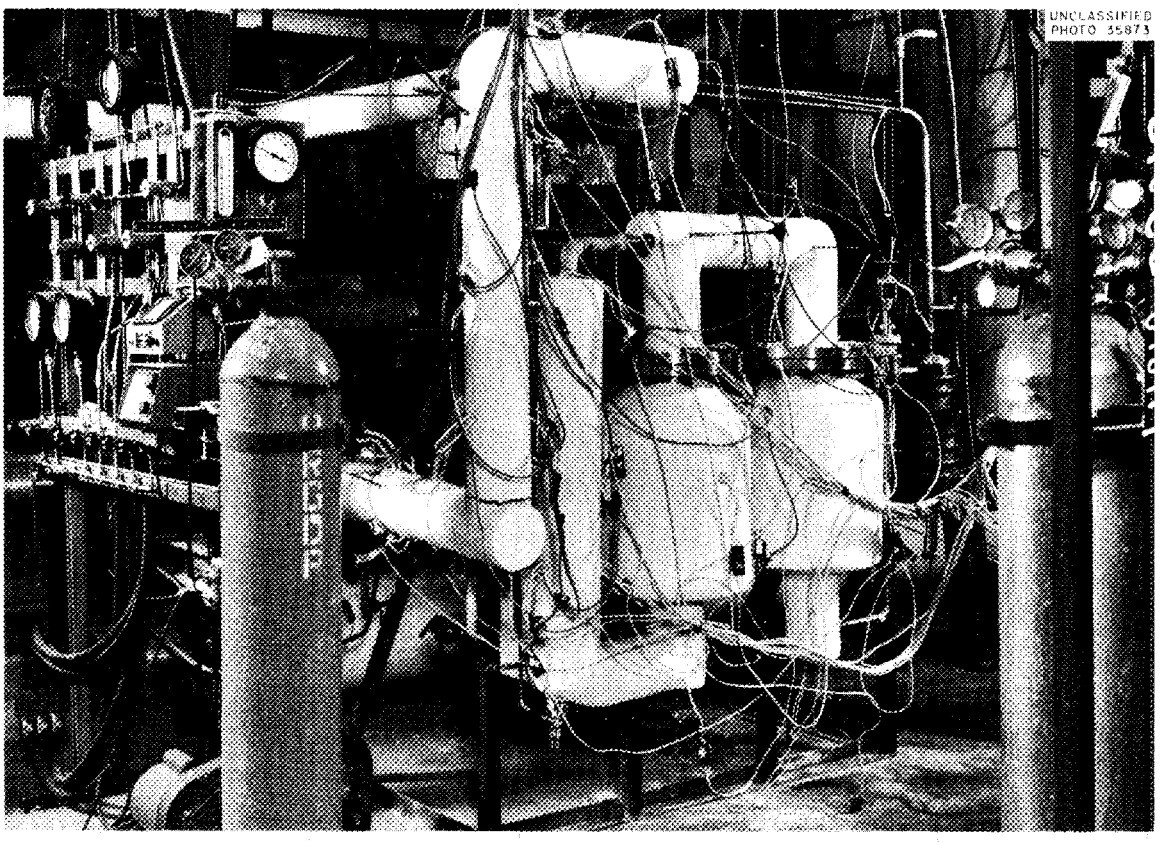


Fig. 7.4. Small-Scale Model of EGCR Helium Purification System.

A gas chromatograph, to which gas samples can be fed from various taps on the main test loop and the purification system, is used for impurity analyses. The instrument is capable of analyzing for H_2, CO_2, O_2, N_2, CH_4, and CO and produces a complete analysis every 20 min.

The gas is analyzed for water vapor with an electrolytic cell unit which continuously and quantitatively adsorbs and electrolyzes all water present in the gas sample. This unit is connected to the gas chromatograph header to provide for sampling at the same positions as the gas chromatograph.

The test program on the purification system was divided into three phases. The first phase involved the removal of H_2 and/or CO injected into the main loop while it was operating at a low temperature. This procedure permitted operation of the catalytic converter without the presence of extraneous impurities outgassed from the graphite and, at the

same time, prevented reaction of the injected impurities with hot metal surfaces in the main loop. In a typical test run the purification system preheater was used to heat the bypass stream to the catalytic converter to 1050°F at the desired flow rate. Hydrogen and/or CO was then injected into the main test loop until a desired impurity concentration was obtained. Oxygen was then injected in controlled amounts into the bypass stream immediately upstream of the catalytic converter to remove the H_2 and/or CO. Gas samples from either the main test loop or the converter outlet were then analyzed by the gas chromatograph in order to follow the impurity removal and to indicate the point during the O_2 injection period where excess O_2 was being added to the system.

The second phase of the test program involved the removal of the various gaseous impurities outgassed from the graphite contained in the main test loop when the loop was heated to operating temperature. This phase was initiated by heating the main loop to 1400°F for 3 hr and then reducing the temperature to 1050°F before opening the purification system and starting the removal of the degassed impurities. Cleanup of the degassed impurities was accomplished in two steps. First, the purification system was placed on stream and the CO_2 was removed with the molecular-sieve adsorber, and, second, the H_2, CO, and CH_4 were removed by oxidation in the catalytic converter.

The third phase of the test program consisted of operating the test loop at temperature and, by use of the purification system, maintaining acceptable impurity levels while making controlled injections of water into the main loop helium stream.

Ten tests were conducted during the first phase of the test program. During all tests, the main loop was operated at approximately 100°F, the purification system preheater was used to heat the bypass gas stream to 1050°F upstream from the catalytic converter, and the gas chromatograph was connected to the catalytic converter outlet to monitor the impurity levels during O_2 injection.

Results of the first seven tests, in which oxygen was injected at the rate of 5 cm^3 (STP)/min, are shown in Table 7.2. Representative plots of

Table 7.2. Results of First-Phase Oxidation Studies of Gas-Purification System

O_2 injection rate at catalytic converter: 5 cm^3/min

Purification System Flow Rate (lb/hr)	Duration of O_2 Addition (min)	Impurity Concentration at Start of Oxygen Injection (ppm)		Impurity Concentration at End of Oxygen Injection (ppm)		Material Balance (%)
		H_2	CO	H_2	CO	
0.37	52	1115		525		90.4
0.37	69	1145		360		90.6
0.818	72	1000		90		100.6
0.818	116	1440		95		92.3
0.818	112	1395		75		93.9
0.33	38	190	1085	130	760	80.8[a]
0.818	103	120	1170	45	310	72.3[a]

[a]Material balances for the tests with CO are low because the CO concentration readings are influenced by CO holdup in the molecular-sieve bed used to adsorb CO_2.

impurity concentration versus time are presented in Figs. 7.5 and 7.6. The curves show the theoretical concentrations of H_2 and CO at the converter inlet and outlet based on an initial system impurity level of 1500 ppm. The circles represent the actual converter outlet H_2 or CO analysis obtained with the gas chromatograph.

In the H_2 removal plot (Fig. 7.5), the points agree fairly well with the curve, and the final H_2 concentration is close to the predicted value. The water in the converter outlet stream rose during the O_2 injection period and then fell. The shift in the water curve is attributed to the length of line between the converter outlet sampling point and the water analyzer and to the inherent lag in the instrument when exposed to high concentrations of water vapor.

The measured initial concentration of O_2 given on the plot is questionable, since it indicates that H_2 and O_2 were coexisting in the loop. A check on the gas chromatograph with a standard sample revealed a slight upward shift in the zero point during the O_2 analysis, but the shift was

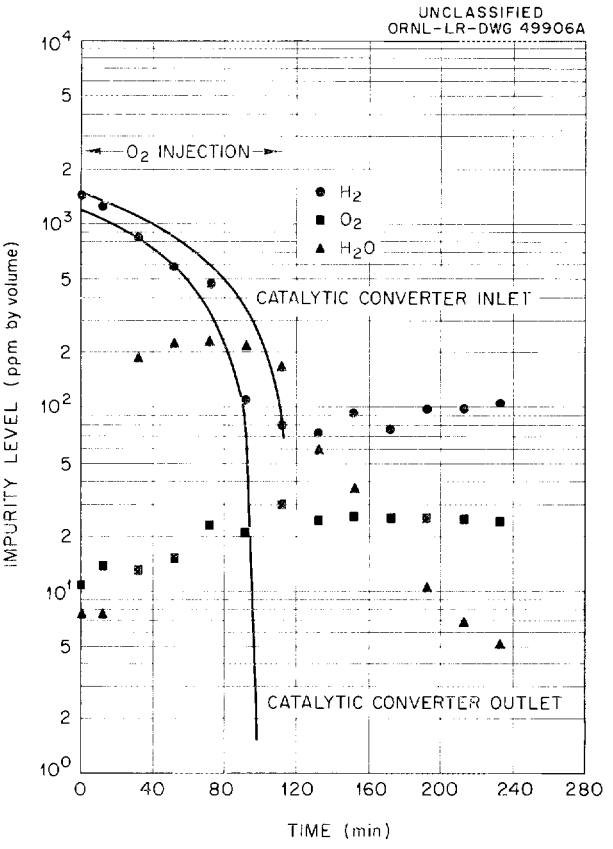


Fig. 7.5. Comparison of Predicted (Solid Lines) and Actual H_2 Removal from Helium Bypass Stream by Catalytic Converter.

not enough to account for the level indicated. Further checks on gas samples removed from the loop and submitted for mass spectrometer analysis showed argon to be present in the range of 5 ppm. Since the presence of argon has a direct effect on the oxygen level measured by chromatograph analysis, a combination of baseline shift and the argon would account for more than 90% of the discrepancy. On this basis, the indicated value for O_2 was assumed to be false, and an arbitrary zero for O_2 was taken at this point. Some O_2 undoubtedly passed through the catalyst bed during oxygen injection and was responsible for the increase shown. The actual O_2 level measured is, again, in doubt, since continued operation after oxygen injection was completed showed H_2 and O_2 coexisting in the loop. The efficiency of the catalyst bed in preventing O_2 carrythrough is undoubtedly lower in this test system than it would be in the reactor application because of more pronounced edge effects. The catalyst chamber is an 8-in. length of 1-in. pipe, and the catalyst pellets are 1/4 × 1/4-in. cylinders. The bed circumference-to-volume ratio is large, and bed packing is not as uniform as would be expected in a larger diameter vessel filled with the 1/4-in. pellets.

The results for CO removal (Fig. 7.6) are similar to those for H_2 removal. One difficulty encountered is the holdup of CO in the molecular-sieve bed that is used to adsorb the CO_2. This holdup interferes with the measurement of the CO in the loop and is partially responsible for

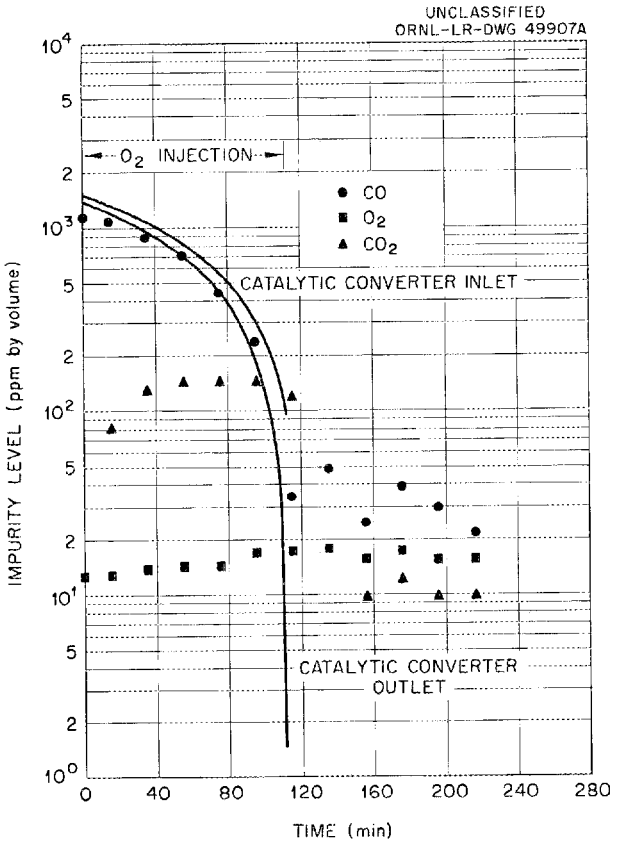


Fig. 7.6. Comparison of Predicted (Solid Lines) and Actual CO Removal from Helium Bypass Stream by Catalytic Converter.

the differences between the theoretical final concentration and the actual values represented by the circles on the plot.

Three other tests were carried out in which the quantity of O_2 injected was a fixed percentage of the amount required for 100% oxidation per pass. Results of these tests are presented in Table 7.3. Oxygen was added during these runs at a decreasing (stepwise) rate throughout the injection period to give an approximation of the theoretical curve for the indicated percentage of stoichiometric oxidation. In all runs, the chromatograph analysis obtained 20 min after the one which produced the oxygen concentrations tabulated in Table 7.3 showed a zero impurity level and a higher concentration of O_2 at the converter outlet. Such analyses obviously do not represent the actual situation, since they indicate that the system impurities had been removed before sufficient O_2 had been added to accomplish the removal stoichiometrically. Such analyses could result, however, from poor mixing of the bypass stream with the main loop stream, from poor O_2 flow control at the low flow rates required toward the end of the cleanup period, or from failure of the stepwise O_2 injection to duplicate the theoretical curve exactly. Continuous monitoring of the converter effluent for H_2, CO, and O_2 should effectively prevent the problem of excess O_2 in the EGCR application. However, if a concentration of 17 ppm O_2 in the effluent is assumed, a calculation based upon 300 hr per year operation

Table 7.3. Results of Oxygen Injection as a Fixed Percentage of the Amount Required for 100% Oxidation

	Step 1	Step 2	Step 3
O_2 addition rate, % of stoichiometric	50	80	62
Initial impurity level, ppm by volume			
H_2	1500	1740	1480
CO			~1500
O_2 level at catalytic converter outlet, ppm	17	10	17
Time after start of O_2 injection, min	7	2	2
Total O_2 injection period, min	33	27	39

of the converter shows that the maximum burnup over 20 years of operation would be only 2.3% of the design allowable burnup of 3500 lb.

The second phase of the test program consisted of degassing the graphite in the main test loop and the removal of the impurities by use of the purification system. The impurity levels of H_2, CO_2, and CO reached peaks higher than could be measured by the gas chromatograph during the degassing period at 1400°F, and consequently gas samples were removed from the main test loop for mass spectrometer analysis in order to evaluate the peak concentrations. These peak concentrations were:

	Concentration (vol %)
H_2	2.26
CO_2	0.19
N_2 + CO	1.03

The combined total of N_2 and CO is shown because both constituents have the same mass number, and accurate individual identification is not possible with the mass spectrometer. The maximum value for CH_4 was observed to be 0.79 vol % by the gas chromatograph and 0.56 vol % by the mass spectrometer analysis.

Following the establishment of a maximum impurity level and the reduction of main loop temperatures from 1400 to 1050°F, cleanup of the degassed impurities was accomplished in two steps. The first step consisted of placing the purification system on stream and reducing the CO_2 level with the molecular-sieve adsorber. The concentration of CO_2 was successfully reduced from 9100 to 40 ppm in less than 20 min (<2.5 system turnovers). The second step consisted of removing H_2, CO, and CH_4 by oxidation in the catalytic converter. This was accomplished during four individual O_2 injection periods; the results are described in Table 7.4.

In the third-phase of the program, five water-injection tests have been completed. Preliminary results indicate that although there is a slight increase in the H_2, CO, and H_2O levels, the addition of water vapor while the purification system is operating causes no serious problem in maintaining acceptable impurity levels in the loop.

Three tests were conducted with the dryer and CO_2 adsorber on stream while injecting water vapor for a period of approximately seven days. The remaining two tests consisted of injecting water vapor into the loop with the purification system shut off and then operating the water and CO_2 adsorbers to remove the impurities. In all tests, flow through the

Table 7.4. Results of Various Steps in Second Phase of Gas-Purification System Studies

	Step 1	Step 2	Step 3	Step 4
Initial impurity concentration, ppm				
H_2	20 200	2 600	240	100
CO	3 440	1 800	800	580
CH_4	6 300	5 500	116	40
O_2 injection rate, cm^3 (STP)/min	80	10	5	5
Total injection period, min	25	70	45.5	42
Final impurity concentration, ppm				
H_2	3 900	300	100	50
CO	1 300	310	420	190
CH_4	3 600	260	90	20

purification system was 0.37 lb/hr and, except in the final test, where approximately 0.2 cm^3 of water was injected directly into the loop, the water injection rate was 0.11 cm^3 (liquid)/hr.

Results of the three tests in which the adsorbers were operated continuously showed an initial increase of 300 to 700 ppm H_2, 40 to 80 ppm CO, and 200 to 300 ppm H_2O shortly after the water injection was started. However, after 24 hr of operation, the impurity levels appeared to reach an equilibrium, and they fell slowly over the remainder of the test period. The maximum values observed during these tests were of the order of 0.1 vol % H_2, 0.04 vol % H_2O, and 0.010 vol % CO. The CO_2 level was kept at 10 ppm or less over the entire test period as a result of constant removal by the CO_2 adsorber.

The final two tests were conducted to determine the rate of water and CO_2 buildup in the loop when the purification system was not in use. The first of these consisted of injecting water vapor at a rate of 0.11 cm^3/hr for approximately 5 hr and allowing the various impurity concentrations to build up and remain in the system for an additional 16 hr. When the purification system was put on stream there was a rapid reduction in CO_2 and water levels and a gradual reduction in the hydrogen level. As would be expected, the buildup of CO_2 in this test occurred much sooner and reached a higher concentration than in the previous tests.

The last test consisted of injecting approximately 0.2 cm^3 of water directly into the loop which had previously been contaminated by direct injections of H_2, CO, and CO_2. The water concentration was then allowed to reach its peak and start to fall off before operation with the purification system dryer and CO_2 adsorber on stream. Results of this test showed that the water concentration rose rapidly from 4 ppm to 190 ppm and, within 6 hr after the purification system was started, the concentration was reduced to 10 ppm. The hydrogen concentration during this period went from 960 to 1200 ppm and back to 1000 ppm. The CO_2 concentration remained unchanged, and, once the CO_2 adsorber was placed in operation, the observed values were readily reduced to the order of 1 to 5 ppm.

The results of this test program have led to the following conclusions: (1) The removal of CO_2 and H_2O is straightforward. (2) Removal of large quantities of H_2 and CO, as well as the impurities degassed from the graphite, has no adverse effect on the oxidizing catalyst. (3) Oxygen breakthrough in the catalytic converter is not a serious problem with injection rates of up to 80% of stoichiometric, and it is felt that even better results can be obtained in a larger purification system where control of the O_2 injection will be simplified, the edge effects of the catalyst pellets will be smaller, and continuous monitoring of the converter effluent for O_2 should be available. (4) Water injection rates higher than the allowable EGCR rate and system water concentrations higher than expected in the reactor coolant did not produce unacceptable H_2, CO, and CO_2 levels with the purification system on stream.

Evolution of Gas from Graphite

(L. G. Overholser, J. P. Blakely)

Experimental studies of the degassing behavior of selected grades of graphite have been continued with the use of the techniques described previously.[3] A series of graphite samples prepared from needle coke by the Speer Carbon Co. have been degassed to ascertain what effect variations in the particle size of the coke mix might have. High-temperature degassing studies have been made on needle coke graphites prepared by National Carbon Co. and Great Lakes Carbon Corp. that had been examined earlier at lower temperatures. Rate data have been obtained for several of these graphites at 600 and 1000°C along with data related to the volume and composition of gas evolved.

The graphite samples examined during this quarter included:

1. SP21B (grade 940), which is a Speer Carbon Co. 4 1/2 × 4 1/2-in. extrusion prepared from a No. 60 flour mix of Great Lakes Continental needle coke.

---

[3]"GCR Semiann. Prog. Rep. June 30, 1959," ORNL-2767, p. 190.

2. SP22B (grade 950), which is the same as sample SP21B except that a No. 50 flour mix was used.

3. SP26A, which is similar to sample SP21B, except that it received additional purification.

4. SP28A, which is the same as sample SP22B, except that it was given further purification.

5. SP29A (grade 964), which differs from samples SP26A and SP28A only in that a regular-particle-size coke mix was used. Results for the less pure counterpart, SP23B, were given previously,[4] along with a description of this graphite.

6. GLC, which was prepared by Great Lakes Carbon Co. from needle coke as described previously.[5]

7. AGOT-LS, which was prepared by National Carbon Co. from needle coke as described previously.[5]

Data obtained by degassing specimens of the various types of graphite at a maximum temperature of 1000°C (external resistance heating) are given in Table 7.5. The temperatures listed are the temperatures of gas collection. The corresponding gas volume represents the volume of gas evolved between that temperature and the next lower temperature, with a large fraction of the gas being collected at the recorded temperature. (The volume given for 300°C represents the gas collected between room temperature and 300°C.)

The data given in Table 7.5 show that the degassing behavior of these graphite samples is very similar. The total volume of gas evolved through 1000°C ranges from ~7 to 10 cm^3 per 100 cm^3 of graphite and the ratio of H_2 to $CO + CO_2$ is at least 2 in all cases. A large fraction of the total gas evolved was collected above 600°C in all instances. These results are in agreement with those reported earlier[4] for sample N964. These results indicate that variations in the particle-size distribution in the coke mix do not have a significant effect on the gas content of the graphite.

---

[4] "GCR Quar. Prog. Rep. June 30, 1960," ORNL-2964, p. 190.

[5] "GCR Quar. Prog. Rep. Sept. 30, 1960," ORNL-3015, p. 125.

Table 7.5. Volume and Composition of Gas Evolved by 1 1/2-in.-diam, 2-in.-Long Speer Carbon Co. Graphite Specimens at 300, 600, and 1000°C

Graphite Sample	Temperature (°C)	Time (hr)	Gas Volume (cm^3/100 cm^3 of graphite)	Gas Constituents											
				H_2		Hydrocarbons		H_2O		CO_2		N_2		CO	
				vol %	cm^3	vol %	cm^3	vol %	cm^3	vol %	cm^3	vol %	cm^3	vol %	cm^3
SP26A-1B	300	17	0.5	4		11		58	0.3	6		15	0.1	5	
	600	22	2.6	20	0.5	28	0.7	16	0.4	10	0.3	4	0.1	23	0.6
	1000	20	7.1	80	5.7	3	0.2	0.9	0.1	0.8	0.1	0.6		15	1.1
	Total		10.2		6.2		0.9		0.8		0.4		0.2		1.7
SP26A-2B	300	12	0.4	4		16	0.1	46	0.2	7		17	0.1	7	
	600	9	2.4	12	0.3	21	0.5	12	0.3	8	0.2	3	0.1	41	0.9
	1000	12	6.1	81	4.9	2	0.1	0.4		0.4		0.7		16	1.0
	Total		8.9		5.2		0.7		0.5		0.2		0.2		1.9
SP28A-1	300	16	0.4	4		16	0.1	55	0.2	5		12	0.1	6	
	600	23	1.5	18	0.3	24	0.4	16	0.2	13	0.2	3		26	0.4
	1000	95	8.6	82	7.1	2	0.1	0.5		0.3		0.6	0.1	15	1.3
	Total		10.5		7.4		0.6		0.4		0.2		0.2		1.7
SP28A-2	300	9	0.4	7		19	0.1	50	0.2	4		0.7		18	0.1
	600	23	1.6	18	0.3	24	0.4	21	0.3	10	0.2	3		24	0.4
	1000	65	6.7	74	5.0	3	0.2	0.6		0.4		0.7		21	1.4
	Total		8.7		5.3		0.7		0.5		0.2				1.9
SP29A-1A	300	16	0.4	6		24	0.1	36	0.1	7		13	0.1	13	0.1
	600	6	2.1	20	0.4	31	0.6	10	0.2	11	0.2	5	0.1	24	0.5
	1000	39	6.2	78	4.9	0.6		0.4		0.4		9	0.6	11	0.7
	Total		8.7		5.3		0.7		0.3		0.2		0.8		1.3
SP29A-3A	300	5	0.7	4		15	0.1	54	0.4	6		15	0.2	5	
	600	19	3.2	27	0.9	30	0.9	14	0.4	7	0.2	4	0.1	19	0.6
	1000	19	5.0	77	3.8	2	0.1	5	0.3	0.2		0.9		15	0.8
	Total		8.9		4.7		1.1		1.1		0.2		0.3		1.4

Table 7.5 (continued)

Graphite Sample	Temperature (°C)	Time (hr)	Gas Volume (cm^3/100 cm^3 of graphite)	Gas Constituents											
				H_2		Hydrocarbons		H_2O		CO_2		N_2		CO	
				vol %	cm^3	vol %	cm^3	vol %	cm^3	vol %	cm^3	vol %	cm^3	vol %	cm^3
SP29A-2A	300	16	0.6	5		20	0.2	33	0.2	7		16	0.1	11	0.1
	600	7	1.7	17	0.3	12	0.2	15	0.2	15	0.3	6	0.1	36	0.6
	1000	46	5.3	80	4.2	1	0.1	0.4	—	0.2	—	2	0.1	16	0.9
	Total		7.6		4.5		0.5		0.4		0.3		0.3		1.6
SP21B-1	300	16	0.5	3		9		55	0.3	5		19	0.1	9	
	600	23	1.8	24	0.4	30	0.6	18	0.3	7	0.1	4	0.1	17	0.3
	1000	21	4.6	73	3.4	3	0.1	0.6	—	0.6	—	0.8	—	22	1.1
	Total		6.9		3.8		0.7		0.6		0.1		0.2		1.4
SP21B-2	300	6	0.4	17	0.1	9		21	0.1	7		30	0.1	15	0.1
	600	16	1.4	20	0.3	34	0.4	10	0.1	9	0.1	5	0.1	23	0.3
	1000	21	4.5	73	3.3	3	0.1	0.3	—	0.4	—	1	—	23	1.1
	Total		6.3		3.7		0.5		0.2		0.1		0.2		1.5
SP22B-1	300	11	0.5	6		21	0.1	18	0.1	11	0.1	31	0.1	13	0.1
	600	22	2.4	20	0.5	32	0.7	14	0.3	9	0.2	3	0.1	22	0.5
	1000	26	7.4	74	5.4	2	0.2	1	0.1	0.2	—	0.8	0.1	22	1.6
	Total		10.3		5.9		1.0		0.5		0.3		0.3		2.2
SP22B-2	300	16	0.5	6		21	0.1	18	0.1	11	0.1	31	0.1	13	0.1
	600	26	2.4	25	0.6	26	0.6	13	0.3	10	0.2	4	0.1	24	0.5
	1000	50	7.0	75	5.3	2	0.1	0.4	—	0.2	—	0.7	0.1	22	1.5
	Total		9.9		5.9		0.8		0.4		0.3		0.3		2.1

Other variables in the manufacturing process are probably more important. The similarity of the results given for the A and B series graphite samples is unexpected. The A series samples, as noted, had received additional purification and, as a consequence, had higher DIH purity than the comparable samples in the B series. The fact that there is no significant difference in the degassing behavior of these specimens suggests that the higher purity graphite may have been subjected to exposure conditions different from those of the B series of samples prior to outgassing.

Data obtained by degassing the different graphite samples to a maximum temperature of 1800°C by induction heating are presented in Table 7.6. Where data are given only at 1800°C, the specimen was heated to 1700°C for 30 to 60 min in contact with the evolved gas; the temperature was lowered; the gas was pumped off; the temperature was brought up to 1800°C, while pumping; and the temperature was then held at 1800°C until the evolution of gas was essentially complete. In the other runs, the specimen was heated to 1000°C without pumping, held at 1000°C for 1 hr, and cooled; and the evolved gas was pumped off. The temperature was then returned to 1000°C, while pumping, and held at 1000°C until the gas evolution was essentially complete. The gas collected at 1400°C includes the gas pumped off while raising the temperature from 1000 to 1400°C plus that evolved during the holding period at 1400°C. Similarly, the 1800°C fraction was collected while raising the temperature to 1800°C, as well as while heating at 1800°C.

A comparison of the data for the Speer Carbon Co. samples in Table 7.6 reveals no marked differences in the outgassing behavior. The B series of samples evolved somewhat less gas than the A series despite the fact that the A series received additional purification. No gross differences are evident, however, that might be attributed to variations in the particle size of the coke mix employed for the various samples. It may be noted that, except in one instance, the ratio of H_2 to $CO + CO_2$ in the evolved gas is greater than one. Also, these samples evolved an appreciable fraction of their gas at temperatures above 1400°C.

Preliminary data reported previously[5] for the Great Lakes Carbon Co. needle coke graphite suggested a rather low gas content. Subsequent data,

Table 7.6. Volume and Composition of Gas Evolved by 1 1/4-in.-diam, 1-in.-Long Graphite Specimens at 1000, 1400, and 1800°C

Graphite Sample	Temperature (°C)	Time (hr)	Gas Volume (cm^3/100 cm^3 of graphite)	Gas Constituents											
				H_2		Hydrocarbons		H_2O		CO_2		N_2		CO	
				vol %	cm^3	vol %	cm^3	vol %	cm^3	vol %	cm^3	vol %	cm^3	vol %	cm^3
National Carbon AGOT-LS-5	1000	6	37.2	45	16.9	0.5	0.2	0.2	0.1	0.2	0.1	0.4	0.4	53	19.6
	1400	5	8.9	34	3.1	0.7	0.1	0.2		0.2		61	5.4	3	0.3
	1800	4	5.7	64	3.6	0.8				0.1		9	0.5	25	1.5
	Total		51.8		23.6		0.3		0.1		0.1		6.3		21.4
AGOT-LS-4	1800	9	69	26	18	0.4	0.3	0.6	0.4	1.4	1.0	9	6.0	63	43
AGOT-LS-8	1800	8	51	60	30	0.7	0.4	0.8	0.4	0.4	0.2	4.1	2.1	35	18
AGOT-LS-7	1000	5	39.8	44	17.5	0.5	0.2	0.4	0.2	0.3	0.1	1	0.5	54	21.3
	1400	5	6.8	14	1.0	0.3		2	0.1	0.3		20	1.4	63	4.3
	1800	3	2.1	7	0.2	0.2				0.4		33	0.7	58	1.2
	Total		48.7		18.7		0.2		0.3		0.1		2.6		26.8
Great Lakes GLC-3B	1000	7	14.1	56	7.9	2	0.3	0.4	0.1	1.4	0.2	0.4	0.1	40	5.6
	1400	11	14.9	48	7.2	0.6	0.1	0.1		0.2		3	0.4	48	7.2
	1800	9	10.0	69	6.9	1	0.1			0.1		10	1.0	20	2.0
	Total		39.0		22.0		0.5		0.1		0.2		1.5		14.8
GLC-1A	1800	11	46	67	31	0.6	0.3			0.1		3	1.4	29	13.6
GLC-1B	1800	10	47	66	31	0.7	0.3	0.1		0.2	0.1	2.6	1.2	31	14.5
GLC-3C	1800	8	40	47	19	0.4	0.2	0.2	0.1	0.2	0.1	4	1.6	46	18.4
GLC-3D	1000	6	17.2	62	10.7	2	0.3	0.2		1.4	0.2	0.5	0.1	34	5.8
	1400	5	15.1	61	9.3	0.7	0.1	0.3		0.2		2	0.3	35	5.3
	1800	7	8.8	72	6.3	0.8	0.1					9	0.8	18	1.6
	Total		41.1		26.3		0.5				0.2		1.2		12.7

Table 7.6 (Continued)

Graphite Sample	Temperature (°C)	Time (hr)	Gas Volume (cm^3/100 cm^3 of graphite)	Gas Constituents											
				H_2		Hydrocarbons		H_2O		CO_2		N_2		CO	
				vol %	cm^3	vol %	cm^3	vol %	cm^3	vol %	cm^3	vol %	cm^3	vol %	cm^3
Speer	1000	7	13.4	56	7.5	0.9	0.1	0.3		0.5	0.1	14	1.9	28	3.7
SP26A-2A	1400	12	13.3	75	10	0.9	0.1	0.4	0.1	0.1		3	0.4	21	2.8
	1800	14	9.4	45	4.3	0.3				0.2		7	0.6	46	4.3
	Total		36.1		21.8		0.2		0.1		0.1		2.9		10.8
SP26A-1A	1800	12	41	78	32	0.5	0.2	0.4	0.2	0.2	0.1	1.4	0.6	20	8.2
SP28A-5	1000	6	16.6	71	11.8	2	0.3	1	0.2	0.8	0.1	0.2		25	4.1
	1400	8	13.4	65	8.7	0.5	0.1	0.5	0.1	0.2	0.3	2	0.3	31	4.2
	1800	7	10.6	39	4.1	1	0.1			3	0.3	4	0.4	52	5.5
	Total		40.6		24.6		0.5		0.3		0.7		0.7		13.8
SP28A-4	1800	7	39	72	28	0.7	0.3	0.6	0.2	0.2	0.1	0.7	0.3	26	10
SP28A-6	1800	8	36	68	24	0.7	0.2	0.5	0.2	0.3	0.1	0.8	0.3	30	11
SP29A-2B	1000	8	19.7	84	16.5	1	0.2	0.5	0.1	0.4	0.1	0.2		14	2.8
	1400	7	12.8	70	9.0	0.7	0.1	0.1		0.2		2	0.3	27	3.5
	1800	14	13.4	54	7.2	0.5	0.1			0.1		4	0.5	41	5.5
	Total		45.9		32.7		0.4		0.1		0.1		0.8		11.8
SP29A-1A	1800	9	51	71	36	0.5	0.3	0.5	0.3	0.1	0.1	3	2	24	12
SP29A-4B	1800	8	43	77	33	0.6	0.3	0.2	0.1	0.2	0.1	0.8	0.3	21	9

Table 7.6 (Continued)

Graphite Sample	Temperature (°C)	Time (hr)	Gas Volume (cm^3/100 cm^3 of graphite)	Gas Constituents											
				H_2		Hydrocarbons		H_2O		CO_2		N_2		CO	
				vol %	cm^3	vol %	cm^3	vol %	cm^3	vol %	cm^3	vol %	cm^3	vol %	cm^3
SP21B-5	1000	7	16.2	73	11.8	2	0.3	0.6	0.1	0.8	0.1	0.5	0.1	24	3.9
	1400	23	15.0	67	10.1	0.8	0.1	0.5	0.1	0.2		2	0.3	29	4.4
	1800	7	7.5	43	3.2	0.4				0.2		7	0.5	49	3.7
	Total		38.7		25.1		0.4		0.2		0.1		0.9		12.0
SP21B-3	1800	8	40	63	25	0.4	0.2	0.4	0.2	0.1		4	1.6	32	13
SP21B-4	1800	7	36	72	26	0.5	0.2	0.2	0.1	0.1		2	0.7	26	9
SP22B-5	1000	7	10.1	78	7.9	1	0.1	0.4		0.4				20	2.0
	1400	7	7.2	66	4.7	0.4		2	0.1			4	0.3	28	2.0
	1800	16	8.3	17	1.4	0.1				0.3		6	0.5	76	6.3
	Total		25.6		14.0		0.1		0.1				0.8		10.3
SP22B-3	1800	8	30	44	13	0.6	0.2	0.3	0.1	0.4	0.1	1	0.3	53	16
SP22B-4	1800	10	22	53	12	0.8	0.2	0.1		0.5	0.1	1	0.2	46	10
SP22B-6	1800	7	32	75	24	0.7	0.2	0.8	0.3	0.2	0.1	1	0.3	22	7

given in Table 7.6, fail to agree with the earlier data, and it is now believed that the higher values are more representative of the gas content of this graphite. The total gas content, relative composition of the evolved gas, and the volumes evolved at the various collection temperatures for the GLC graphite appear to be quite similar to those given for the SP graphite. The other needle coke graphite, namely AGOT-LS, which was prepared under specifications similar to those for the GLC graphite, evolved slightly more gas than did the GLC graphite. Differences in the compositions of the evolved gas are also evident. AGOT-LS graphite evolved a large fraction of the total gas at 1000°C, and only small amounts were collected above 1400°C. The GLC and AGOT-LS graphite specimens were manufactured by different vendors and the differences noted in their degassing behavior are undoubtedly due to unknown variations in the manufacturing processes.

Rate data obtained for several of the SP graphite samples are given in Figs. 7.7, 7.8, and 7.9. Data reported for 600°C were collected from

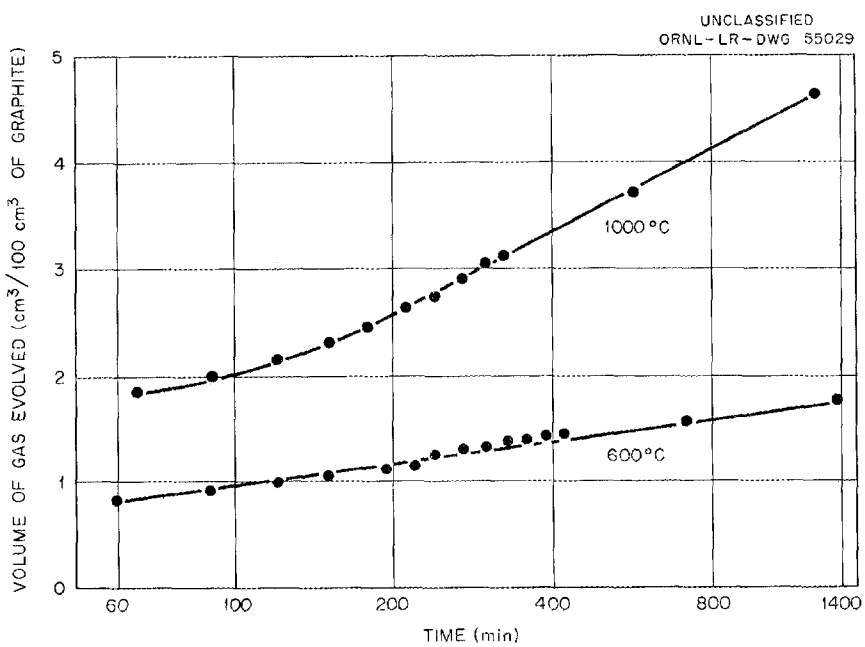


Fig. 7.7. Volume of Gas Evolved by SP21B Graphite Plotted Against Log of Time.

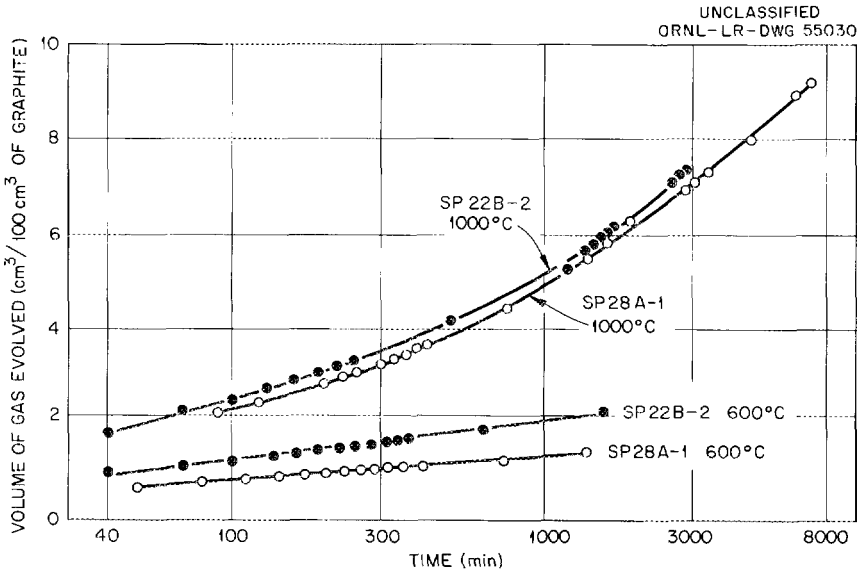


Fig. 7.8. Volume of Gas Evolved by SP22B and SP28A Graphite Plotted Against Log of Time.

specimens previously degassed at 300°C, and, similarly, the 1000°C data were obtained from specimens previously degassed at 600°C. Data collected during the first hour after attainment of the test temperature may not be reliable, because gas is evolved while the specimen is coming up to temperature and the rate of evolution may exceed the capacity of the pump.

The rate data given in Figs. 7.7 and 7.8 show that at 600°C a plot of the volume of gas evolved versus the log of time gives a linear relationship. Similar results have been found for SP26A and SP29A specimens, although these are not presented. This behavior is in agreement with that found previously[4,5] for specimens prepared from needle coke by the Speer Carbon Co. and the Great Lakes Carbon Corp. In contrast, the rate data obtained at 1000°C, also presented in Figs. 7.7 and 7.8, indicate that the relationship between the volume of gas evolved and time is not linear at the higher temperature. The data for all three samples (SP21B, SP22B, and SP28A) give curves which show upward curvature; however, there is also some indication that essentially linear relationships exist over certain intervals of the time recorded. The data for the SP22B and SP28A specimens are also given in Fig. 7.9, where the volume of gas evolved is plotted against the square root of time. Treated in this manner, the data for SP28A

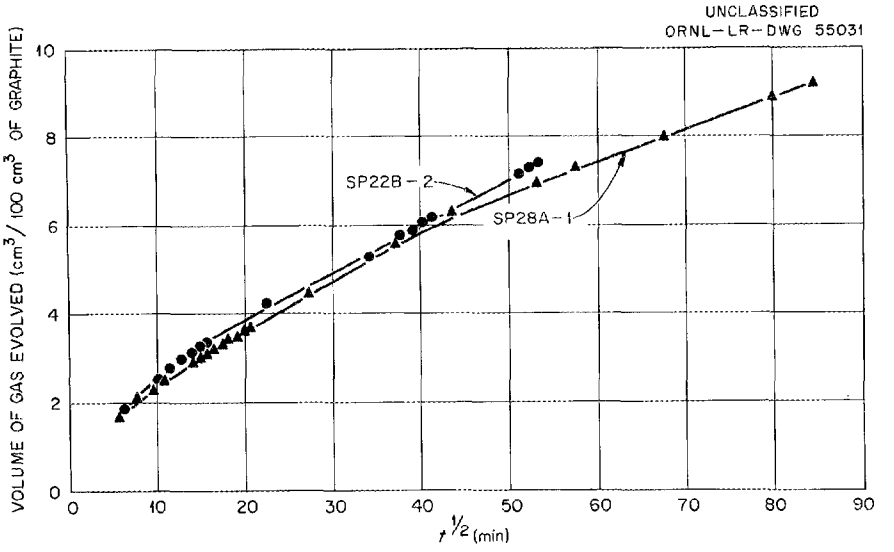


Fig. 7.9. Volume of Gas Evolved by SP22B and SP28A Graphite at 1000°C Plotted Against the Square Root of Time.

graphite show two regions where essentially linear relationships exit, but the slopes of the two sections of the curves differ. This behavior suggests that different processes of gas evolution exist during the early and latter parts of the degassing period. It is known that the composition of the evolved gas changes with time when a specimen is brought up to 1000°C from 600°C and held at 1000°C. The relative concentration of hydrogen increases at the expense of the CO + CO_2 concentration, and it appears likely that the change in slope noted may be associated with these changes in relative concentrations as the degassing proceeds.

Transport of Gases Through Graphite

(W. T. Ward, N. V. Smith)

A series of room-temperature permeability determinations were made on a typical EGCR-moderator graphite block. Of the 12 specimens cut from the same block of AGOT needle coke graphite, eight gave permeabilities to helium of between 25 and 70 millidarcys, in good agreement with the values

reported perviously[6,7] for AGOT. On the other hand, permeability values for the other four specimens ranged from 100 to 200 millidarcys. The data are indicative of the considerable variation which may be encountered even in the same block of graphite.

It is anticipated that graphite of considerably lower permeability will be required for certain reactor applications. Therefore studies are being made of the permeability and related characteristics of low-permeability materials. An apparatus has been built and is now in use for obtaining permeability data in the range of $K = 10^{-4}$ to 10^{-6} cm^2/sec, where

$$Q_a P_a = K \frac{A}{L} \Delta P = \frac{k}{\mu} \frac{A}{L} P_m \Delta P \quad .$$

In this expression Q_a is the volumetric flow rate of gas (measured at pressure P_a) which passes through a graphite specimen of cross sectional area A and thickness L under a pressure drop ΔP. Permeability may also be expressed in terms of viscosity of the gas according to the relation

$$k = K \frac{\mu}{P_m} \quad ,$$

where μ is the viscosity of the gas. When μ is expressed in centipoises and P_m in atmospheres, k is in darcys.[7] For permeable materials, k is a true constant that is independent of P_m and μ.

The apparatus provides for measuring the rate of pressure rise on one side of a previously evacuated specimen while applying a constant gas pressure to the other side. It is designed to accommodate graphite pipe or tube specimens up to 2 1/4 in. in outside diameter and 7 in. in length. The ends of the specimen are sealed off with brass plates and neoprene gaskets under pressure. This assembly is enclosed in a container consisting of an 8-in. section of standard 4-in. pyrex pipe with flanged ends and metal end plates. This container serves as the pressure chamber

---

[6] "GCR Quar. Prog. Rep. Sept. 30, 1960," ORNL-3015, pp. 137-41.

[7] N. V. Smith and Jack Truitt, "EGCR Graphite Permeability Tests: Results of Forced Flow Experiments on EGCR Fuel Element Sleeves and Sleeve Material," ORNL CF-60-7-101 (July 29, 1960).

in which up to five atmospheres of pressure can be applied to the outside of the specimen. A tubing connection through the end plate connects the interior of the specimen to a series of calibrated metal containers in which the pressure rise is measured with a specially designed McLeod gage. The linear scale of the gage has a range of 0 to 15 mm Hg that can be read accurately to 0.02 mm Hg. A flow diagram of the system is shown in Fig. 7.10. The gasometer and other equipment used in calibrating the volume of the system are also indicated.

It is thought that this apparatus can be adapted to lower permeability measurements by substituting electronic vacuum gages for the McLeod gage. However, no graphite with a permeability less than 10^{-5} cm^2/sec has been obtained thus far.

Two types of graphite have been investigated with the new apparatus: type CEY (National Carbon Co.) pipe, 1 1/4 in. o.d., 7/8 in. i.d., and a

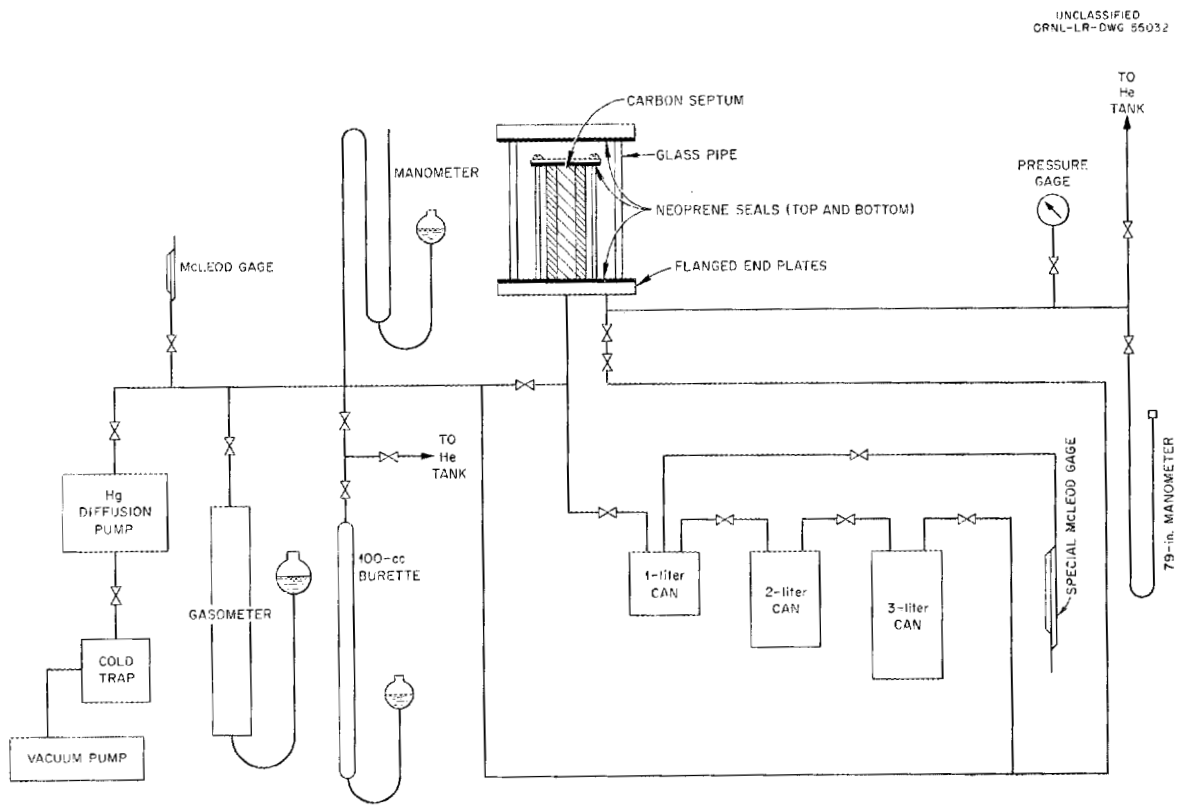


Fig. 7.10. Flow Diagram of Apparatus for Low-Permeability Measurements.

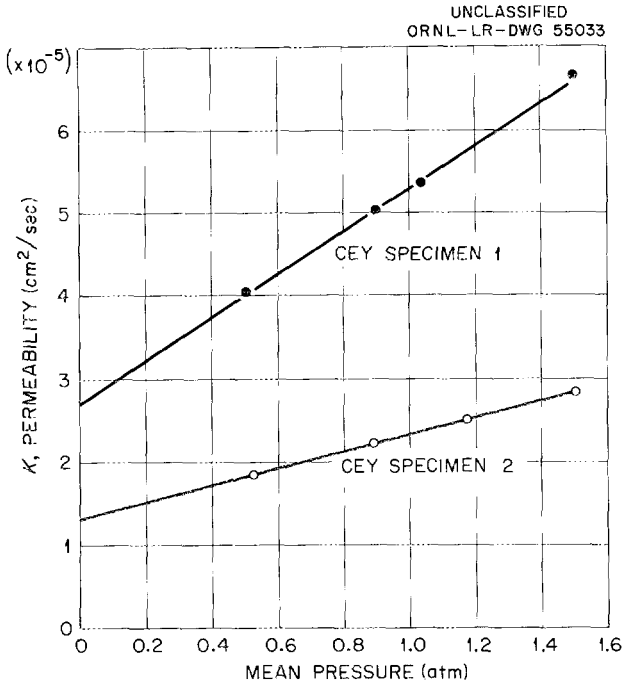


Fig. 7.11. Permeability to Argon of Two Adjacent Cuts of Type CEY Graphite Pipe.

piece of duPont's "explosively compacted high-density graphite." Two specimens of the CEY graphite (adjacent cuts from the same piece of pipe) were tested with argon and found to differ in permeability by more than a factor of 2, as shown in Fig. 7.11.

The permeability coefficients were determined by utilizing one of these CEY specimens and three different gases. These data are plotted as a function of mean pressure in Fig. 7.12. The fact that the coefficients are higher for CO_2 than for argon is due to the lower viscosity of CO_2. When the permeability constant, k, is plotted versus the reciprocal of the mean pressure, as in Fig. 7.13, it can be seen that the constant tends to vary inversely with the square root of the molecular weight of the gas. When these curves are extrapolated to infinite mean pressure ($1/P_{mean} = 0$), they tend to converge at a single point that may be considered as characteristic of the particular graphite and is not dependent on gas properties.

Treatments given to graphite for the purpose of reducing its permeability frequently result in a permeability gradient through the graphite, with the surface layers being more impermeable than the material in the interior of the specimen. As a rough measure of the extent of this phenomenon in CEY graphite, a specimen of CEY pipe for which argon permeability data had previously been obtained was put into a lathe and cuts approximately 0.009 in. deep were taken from both the outside and inside surfaces. This reduced the thickness of the specimen by approximately 10%. The permeability to argon at 25°C and a mean pressure of one atmosphere rose from $K = 5.5 \times 10^{-5}$ cm²/sec to $K = 19.4 \times 10^{-5}$ cm²/sec.

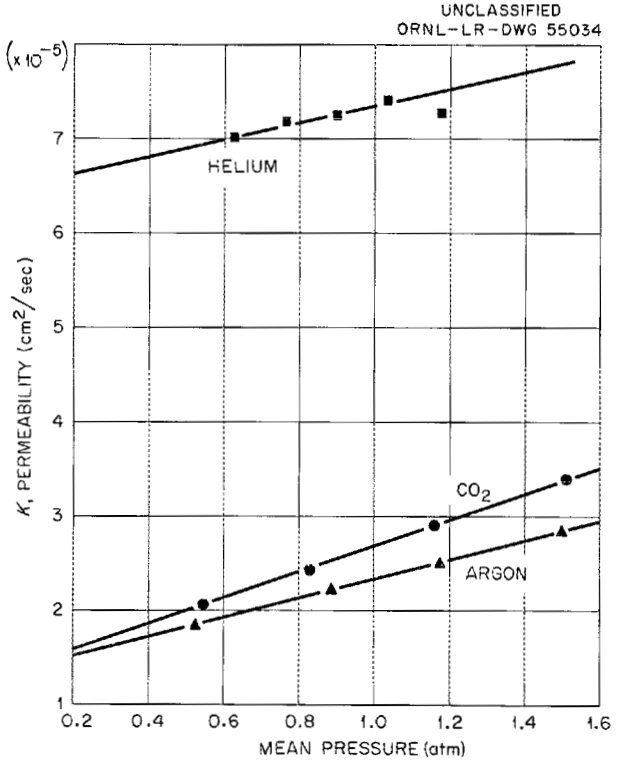


Fig. 7.12. Permeability of Type CEY Graphite to Helium, CO_2, and Argon.

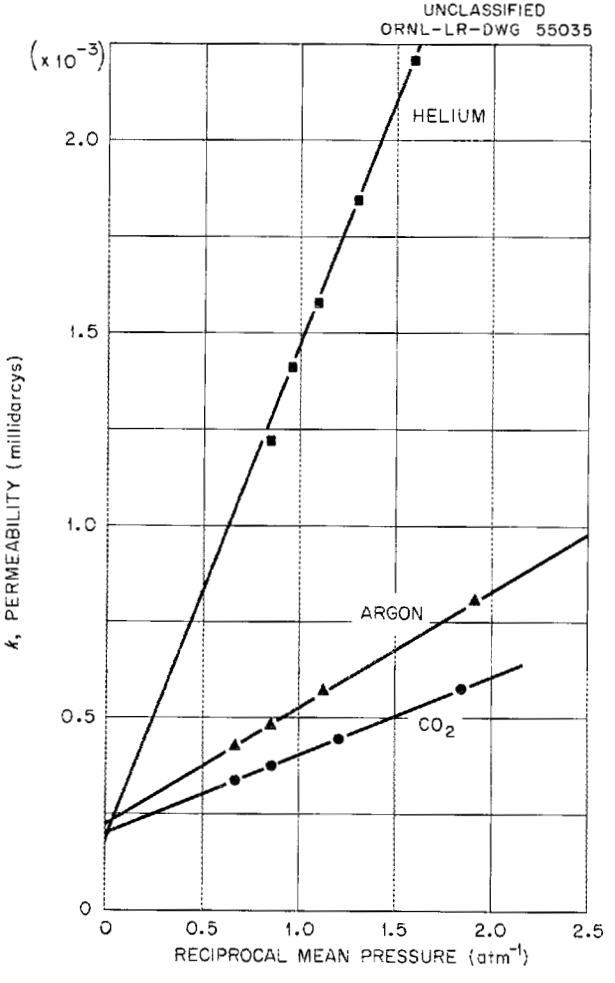


Fig. 7.13. Permeability Data of Fig. 7.12 Plotted Versus the Reciprocal Mean Pressure.

The permeability to helium of the duPont "explosively compacted high-density graphite" at 25°C was found to be 2.5×10^{-4} cm^2/sec, and it did not vary with mean pressure. Following this determination, the specimen was baked at 1000°C in a helium atmosphere for 1 1/2 hr. After cooling to room temperature, the permeability was redetermined and was found to have increased by approximately a factor of 9.

Investigation of Adsorbers for Removing Fission-Product Gases from Coolants

(W. E. Browning, R. D. Ackley, R. E. Adams)

Investigations are under way of means for removing radioactive volatile fission products from coolants in gas-cooled reactors and loops in order to prevent contamination of equipment and to reduce the hazard that would result from release of the coolant to the atmosphere. Iodine, krypton, and xenon are the principal contaminants to be removed from coolants and other carrier gases.

Tests conducted in the study of the removal of radioactive iodine vapor from high-temperature helium streams have indicated that activated charcoal removes iodine vapor with high efficiency at temperatures as high as 430°C. A test bed of activated charcoal (Pittsburgh BPL, 8/14 mesh) 3 in. in depth, operating at either 300 or 430°C, removed 99.9% of the iodine vapor from a helium stream moving at a velocity of 25 ft/min. In these experiments the adsorbed iodine was not removed from the charcoal by continued helium flow for periods of up to 3 hr. Other experimenters have indicated, however, that continued helium flow will slowly remove the iodine contained in a charcoal bed.[8] Therefore radioactive iodine vapor was adsorbed from a helium stream onto a 0.375-in.-deep charcoal bed (Pittsburgh BPL) operating at 320°C, and the elution characteristics were studied. After 144 hr of operation at temperature, it was found that only 16% of the iodine initially present on the bed had been retained.

---

[8]J. T. Sox and D. J. Burkhart, "Iodine Sorption in Charcoal Filters at High Temperatures," KT-540 (October 3, 1960).

In order to obtain comparative data, two experiments have been run with silver-plated copper ribbon (10 wt % Ag) as the iodine-removal material. Iodine vapor, tagged with I^{131}, was injected into a 6-in.-deep bed of the ribbon at a temperature of 320°C for 20 min in helium at a linear velocity of 13.6 ft/min. The helium flow was continued for 166.5 hr after injection of the iodine vapor. In order to measure gas velocity effects, the linear velocity of the helium sweep gas was varied intermittently from 2.7 to 42.6 ft/min over the duration of the test. At the end of the test it was determined that 99.3% of the injected iodine had remained on the Ag-Cu bed. The major fraction of the eluted iodine passed from the bed during the first several hours of operation. Over the remainder of the run the rate of release of iodine was barely detectable.

A second bed of Ag-Cu mesh, 0.33 in. in depth, was then studied to obtain data on the characteristics of iodine release from silver surfaces. The manner of construction and mode of operation were very similar to those used for the tests with the 0.375-in.-thick bed of BPL charcoal. After operation at 320°C for 193 hr, this Ag-Cu bed was found to have retained 95.7% of the iodine initially present. The manner and rate in which the iodine was eluted from the silver surface was significantly different from the iodine elution from charcoal. The data obtained thus far are insufficient to define quantitatively the mechanism of release of iodine from charcoal or silver surfaces, and experimental work and theoretical analyses are in progress. It may be observed, however, that silver appears to be a more promising iodine-removal material than charcoal for application at high temperatures under EGCR conditions.

A re-evaluation of the previously reported[9] design of the charcoal trap in the nitrogen leak-detection system for GCR-ORR loop No. 1 is in progress. Changes in operating conditions and additional laboratory data on adsorption of krypton from slowly moving gas streams necessitated the re-evaluation. Experimental krypton elution curves were obtained under

---

[9]R. E. Adams and W. E. Browning, "Evaluation of Activated Charcoal Fission Gas Adsorbers Designed for the GCR-ORR Loop Experiment No. 1," ORNL CF-60-1-24 (March 16, 1960).

the new conditions, and these data are being used to revise the calculated radiation doses that could be produced by release of fission gases from this charcoal trap.

In adsorbers operating at low carrier gas velocities, the transport of krypton or xenon by longitudinal diffusion assumes importance. Consequently, a study of this mechanism was undertaken, as mentioned previously,[10] in order to provide information useful for predicting adsorber performance under low-velocity conditions. Natural krypton with Kr^{85} tracer is injected in one end of a charcoal column, and the relative krypton concentration as a function of time is measured at the other end by a G-M counter tube. The data are analyzed in accordance with the following equation:[11]

$$\frac{C}{C_0} = \frac{h}{H} + \frac{2}{\pi} \sum_{1}^{\infty} \frac{1}{n} \sin \frac{n\pi h}{H} \cos n\pi \, e^{-(n^2\pi^2 Dt/H^2)} \quad ,$$

where C_0 is initial krypton concentration in that portion of charcoal of length h into which krypton is injected, C is concentration at other end of column of over-all length H, D is the effective diffusion coefficient, and t is time. The actual value of h is not important for the present purposes when $h \ll H$. By comparison of experimental data with quantities calculated from the above equation with the aid of an Oracle program and, also, by use of the equation in an approximate straight-line form, which is applicable at sufficiently high Dt/H^2, effective diffusion coefficients may be evaluated. This was done for recently obtained measurements for krypton diffusion through Pittsburgh PCB 12/30 activated carbon. The results for 0, 25, and 60°C, respectively, with static helium at 1 atm as the predominant component of the gas phase, were 0.0021, 0.0057, and 0.0141 cm^2/sec. These coefficients are approximately inversely proportional to the corresponding slopes of the adsorption isotherms of krypton on PCB

[10] "GCR Quar. Prog. Rep. Sept. 30, 1960," ORNL-3015, p. 149.

[11] For derivation see, for example, Richard M. Barrer, "Diffusion in and Through Solids," p. 14, Cambridge University Press, 1941.

charcoal, which is a consequence of the relative quantity of krypton available for gaseous diffusion being determined by the extent of adsorption.

A few measurements were made at 24°C to briefly investigate the effect of krypton concentration on its transport through charcoal by diffusion. No appreciable effect was observed at this temperature for a variation in krypton concentration over a factor of 7. Further work will include analyses of other available data and an effort to relate quantitatively the effective diffusion coefficient with various gas and adsorbent properties.

Static or equilibrium krypton and xenon adsorption isotherms have been determined for some adsorbent samples of interest. Such data are useful as a check of dynamic adsorption measurements and, also, for providing information on xenon adsorption, because the Xe^{133} tracer for dynamic measurements is not as readily available as Kr^{85}. When the isotherms are linear, the slopes or V/P (ratio of volume adsorbed to pressure) may be identified theoretically with the dynamic k-value. When the isotherms are non-linear, the V/P ratios and k-values are a function of pressure, which must be recognized in the calculation of holdup times. The isotherm results, which were obtained at the Oak Ridge Gaseous Diffusion Plant, are summarized in Table 7.7, along with a few k-values for comparison. The k-values are those obtained with helium as the carrier gas, since helium is not appreciably adsorbed at these temperatures and so does not interfere with krypton or xenon adsorption, except as it might hinder the attainment of equilibrium. The agreement between k-values and V/P ratios is satisfactory, which is indicative of the usefulness of the static data.

Retention of fission-product gases by Linde molecular sieves partially saturated with water and/or carbon dioxide is of importance because the sieve beds are being considered for removing traces of water vapor and carbon dioxide from various coolant streams associated with reactors. Possible applications are the EGCR helium experimental loops and pebble-bed reactor coolant side streams. Since the molecular sieve beds may be vented to the atmosphere on regeneration, the quantity of retained radioactive gases must be low. An investigation for determining the extent of such retention was made by members of the M.I.T. Practice School. Details

Table 7.7. Adsorption of Krypton and Xenon from Helium Carrier Gas

Adsorbent	Gas Absorbed	Isotherm Temperature (°C)	Pressure Range (mm)	Average or Range[a] of V/P ($cm^3/g \cdot atm$)	Dynamic Adsorption Coefficient, k ($cm^3 \cdot atm/g \cdot atm$)
Columbia G, 8/14	Kr	0	0.07–1.98	139	
		25	0.05–2.39	61	61
		60	0.02–2.49	24	23
	Xe	0	0.16–2.00	4000–2200	
		25	0.09–2.00	1240–940	
		60	0.07–2.22	460–290	
Columbia ACC, 6/14X	Kr	0	0.08–2.16	114	119
		25	0.30–2.33	49	57
		60	0.17–1.97	22	
	Xe	0	0.16–1.85	3100–1700	
		25	0.11–1.88	950–760	
		60	0.33–1.94	270–230	
Columbia HCC, 12/28X	Kr	0	0.13–1.94	114	112
		25	0.34–2.21	51	57
		60	0.27–2.04	14	
	Xe	0	0.17–2.34	2800–1800	
		25	0.16–2.14	1070–810	
		60	0.60–1.94	280–250	
Pittsburgh PCB, 12/30	Kr	0	0.10–2.05	133	122
		25	0.32–2.61	56	52
		60	0.18–2.28	21	
	Xe	0	0.06–2.27	2900–1900	
		25	0.17–2.34	1130–810	
		60	0.29–2.28	270–190	
5A Linde molecular sieves, 1/16-in. pellets	Kr	0	0.17–1.95	19	
		25	0.32–2.18	10	12
		60	0.51–2.07	5	
	Xe	0	0.07–1.81	159	
		25	0.15–2.00	72	73
		60	0.43–1.91	25	

[a]The krypton isotherms were essentially linear; but the xenon isotherms were not, except for the Linde sieves.

of this study appear elsewhere.[12] Molecular sieve type 5A, 1/16-in. pellets, was used, and it was observed that the holdup of krypton at 25°C, as indicated by the dynamic adsorption coefficient k, with helium as the carrier gas, decreased with increasing degree of saturation and became less than 1 cm^3/g at 12 g of H_2O per 100 g of dry adsorbent or at 17 g of CO_2 per 100 g

[12]E. E. Wright, Jr. and A. R. McLain, "Krypton Holdup in Molecular Sieves," KT-548 (November 8, 1960).

of dry adsorbent. Information will be needed on the holdup of xenon and the occlusion of the krypton and xenon present during sorption of water and CO_2.

An effect of some interest, as previously discussed, is the temperature rise of an adsorber upon sudden pressurization.[13] An expression for the temperature rise due to heat of compression was derived as follows: for one mole of gas, at PV = RT, the associated varying mass of charcoal is given by $m = V\rho/\epsilon$, where ρ is charcoal bulk density and ϵ is its void fraction. Then, for adiabatic compression,

$$-PdV = C_v dT + c\,\frac{V\rho}{\epsilon}\,dT \quad ,$$

where C_v is molar heat capacity of gas at constant volume and c is specific heat capacity of the charcoal. Use of the ideal gas law and a rearrangement then give

$$\frac{dT}{dP} = \frac{1}{\frac{\rho c}{\epsilon} + \frac{P}{T} + \frac{C_v P}{RT}} \quad .$$

Integration then gives

$$\left(\frac{T_2}{T_1}\right)^{\gamma} = \left(\frac{C_v P_2 + \beta R T_2}{C_v P_1 + \beta R T_1}\right)^{\gamma - 1} \quad ,$$

where γ is the usual C_p/C_v ratio and β is $\rho c/\epsilon$. For present purposes, the differential form is the more convenient. Using $\rho = 0.5$ g/cm^3, $\epsilon = 0.75$, $c = 0.165$ cal/g·°C, $C_v = 3$ cal/deg·mole for helium and 5 for nitrogen, it is found that dT/dP for helium varies from 0.015 to 0.012°C/psi as the pressure varies from 0 to 2000 psia, and that dT/dP for N_2 (same units and pressure ranges) varies from 0.015 to 0.011. The initial adsorber temperatures under consideration here are in the vicinity of room temperature. In

[13] "GCR Quar. Prog. Rep. Sept. 30, 1960," ORNL-3015, p. 150.

the case of nitrogen, there are important heat effects due to adsorption, and calculations of the resulting temperature increases were made on the basis of available information. Omitting details, temperature increases as high as approximately 90°C were estimated (for N_2 on coconut charcoal at 25°C). At very high pressures, ~1000 psia, increases in adsorption with pressure become very small, so additional heat effects due to adsorption are probably negligible once a fairly high pressure has been exceeded. Some $\Delta T/\Delta P$ measurements were made for helium and nitrogen using a small-scale trap filled with charcoal in which a thermocouple was located. Various ranges for ΔP were employed, the highest pressures involved being about 1800 psig. For helium, the observed temperature increases averaged approximately 60% those calculated. For nitrogen, the analogous figure was 80%, even though the basis for the calculations was more uncertain. Since the experimental conditions deviated considerably from being adiabatic, it was concluded that observed and calculated results were in fairly good agreement.

Measurement of High Temperatures

(W. T. Rainey, R. L. Bennett, W. M. McClain)

Thermocouples in Stagnant Helium

Studies have been continued of the negative emf drifts of Chromel-P–Alumel thermocouples in stagnant helium at 1000°C. When dull oxidized Chromel-P wires were introduced into a furnace at 1000°C a sudden evolution of gas was noted. Pressure measurements indicated that there was an initial burst of gas during the first minute that was followed by slower evolution during the next 10 to 15 min. Wires which had been carefully cleaned with an organic solvent showed much less initial gas evolution but showed approximately the same slower evolution. Bright-annealed Chromel-P wires which had been solvent cleaned gave indications of only traces of gas.

When dull Chromel-P wires were heated in quartz tubes that were being evacuated with a mechanical pump, the wires developed a metallic surface

appearance during the first 30 min of treatment. If the quartz tube was sealed off while being evacuated, the metallic appearance remained indefinitely, and no changes were noted which might cause emf drift. Previous experiments had indicated that the thermocouples showed no negative emf drift while in a continuously pumped vacuum.

When dull Chromel-P wires were sealed under vacuum into quartz tubes before insertion into the furnace, the results were quite different. At first the wires became metallic in appearance, but they gradually regained the dull black surface, except in the sharp thermal-gradient region. In this region the wire retained the metallic film and in places showed evidence of a black powdery coating.

Mass spectrographic analysis of the gas obtained after the initial burst from the dull Chromel-P wire indicated the presence of CO_2, (N_2 + CO), H_2, and a trace of H_2O. When the gas was left in contact with the hot Chromel-P wire for 40 hr, analysis showed the remaining gas to be predominately H_2, with a small amount of (N_2 + CO). No CO_2 or water was found in the latter experiment.

Analyses of sections of Chromel-P wire after various periods of heating at 1000°C in stagnant helium showed a progressive loss of oxygen and carbon from the wires in the 1000°C region. There was a corresponding increase in oxygen and carbon content in the thermal-gradient region. The changes in surface appearance of the wires during the various heating periods followed a definite pattern. The wire immediately became shiny at the end deepest in the furnace. With time the nickel film appeared further down the wire until all wire at temperatures greater than 600 to 800°C was shiny. With longer time the nickel film disappeared except in the sharp thermal-gradient region, leaving the wire black. The remaining nickel film was relatively heavy and became loose, exposing a black surface under the film. A section of wire exposed under these conditions is shown in Fig. 7.14. The loose nickel film and black underlayer are apparent.

Metallographic examination of the wires gave results which were in general agreement with the above observations. Wires from the time experiments described above were sectioned at the thermal-gradient region and

at the end deepest in the furnace. A longitudinal section, as-polished, from the end of a wire exposed at 1000°C for 2 min is shown in Fig. 7.15. The upper, heavy, white, nickel layer and the spongy, gray, copper layer were applied to the wires to protect the surfaces during polishing. The thin, intermittent, white film mentioned above appears under the copper layer. It is interesting to note that there was also a layer of oxide on the wire under the nickel film.

An as-polished section from the thermal-gradient region of a wire heated for 120 hr is shown in Fig. 7.16. The loose nickel film is not so apparent in this section. Of most importance is the rather heavy intergranular oxidation of the chromium. With increased time at temperature, the depth of oxidation increased. Intergranular oxidation was not visible

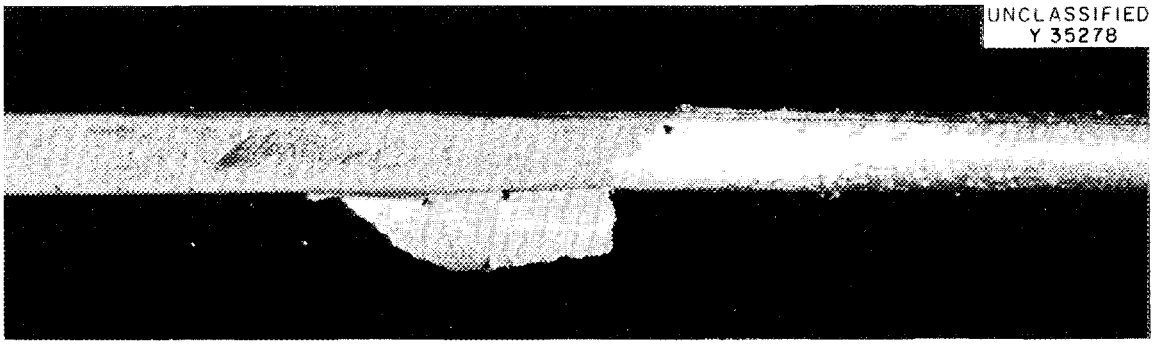


Fig. 7.14. Surface Appearance of Chromel-P Wire Exposed to Static Helium in Thermal-Gradient Region of Furnace.



Fig. 7.15. Longitudinal Section of Chromel-P Wire Taken from Isothermal Region of Furnace at 1000°C After Heating for 2 min.

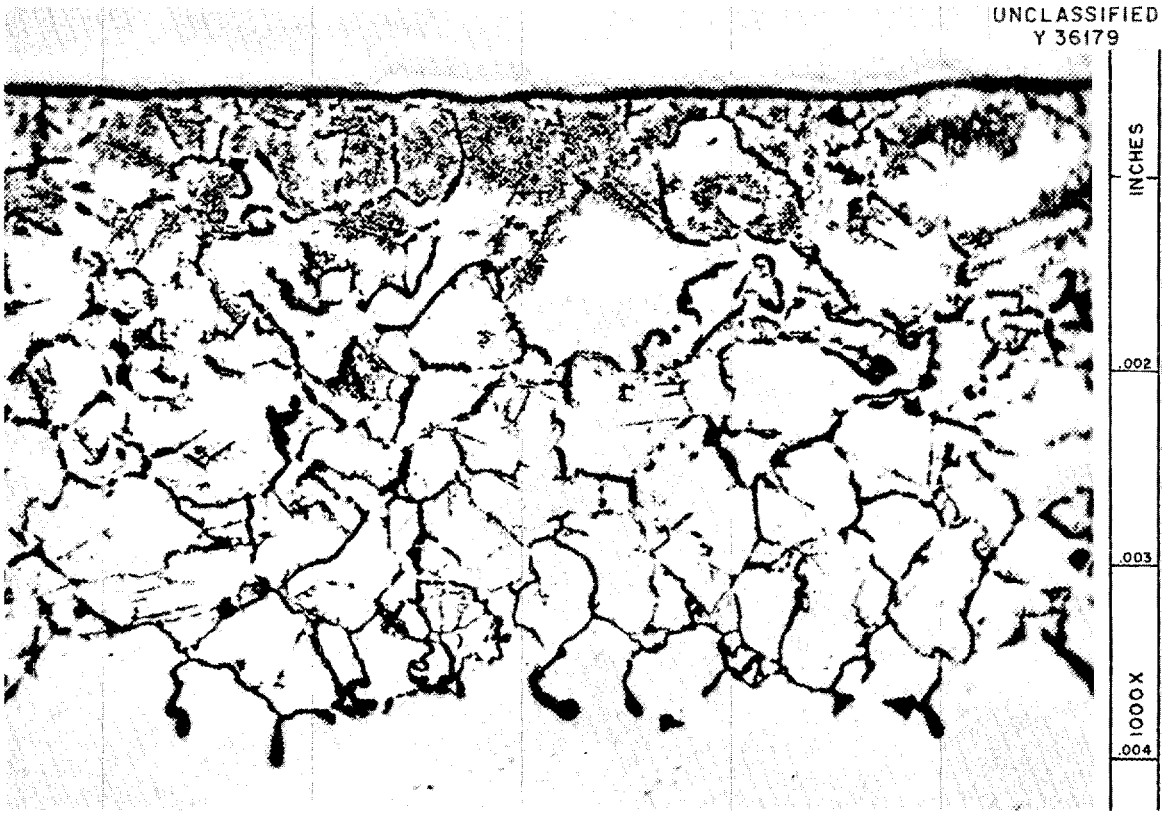


Fig. 7.16. Longitudinal Section of Chromel-P Wire Taken from Thermal-Gradient Region of Furnace at 1000°C After 120 hr of Heating.

in sections other than those from the 800 to 900°C region. Oxidation in other portions of the wire appeared to be surface oxidation.

These results indicate that the principal mechanism involved in the negative emf drift phenomenon is the selective oxidation of chromium in the 800 to 900°C region of the Chromel-P wire. It may also be possible that reactions with carbon monoxide and dioxide are in part responsible for the emf drift. Previous work has shown this to be possible. The results also indicate that the selective intergranular oxidation of chromium occurs only in a limited temperature range and in rather critical limits of atmospheric oxidizing potential. The oxidation of Chromel-P at temperatures other than 800 to 900°C and in atmospheres containing appreciable oxygen appears to be a nonselective surface effect. The apparent lower limits of temperature and oxygen concentration may have been influenced by low reaction rates.

Thermocouples Inserted in Graphite in a Helium Atmosphere

Experience has shown that Chromel-P is very susceptible to carburization, which results in large negative emf errors in thermocouple applications using bare wires. Since Chromel-P–Alumel thermocouples sheathed in stainless steel have been specified for the EGCR, it was thought advisable to study the emf drift of sheathed thermocouples in graphite in a helium atmosphere. Normal drift rates should be experienced until diffusion of carbon through the sheath occurs.

Long term emf drift experiments have been under way for seven weeks with periodic emf measurements and withdrawal of specimens for metallographic examination. Grounded-junction thermocouples sheathed in types 304 and 310 stainless steel were used in the first series of tests. The type 304 stainless steel sheath was 0.070 in. in diameter and was a special-order item. The type 310 stainless steel sheath was 0.062 in. in diameter and was standard material. One-half of each group of thermocouples was given a 0.002-in. copper plate before testing. The test was designed so that the thermocouples were inserted 13.5 in. into an AGOT graphite block and held at 1600°F in a stagnant helium atmosphere. Controls were protected from the test atmospheres by heavy stainless steel protection tubes, but they were exposed to the same thermal effects.

The experimental results obtained thus far indicate that the material sheathed in type 304 stainless steel developed an inhomogeneity in the Chromel-P wire in the temperature region of 1380°F within one week. All the type 304 stainless steel-sheathed thermocouples have drifted −0.75 mv (−19°C) during the seven weeks of testing. The thermocouples sheathed with type 310 stainless steel and the controls of both types have shown either slight positive or negligible emf drifts. These results are significant, but further work will be necessary before the cause of the emf drifts is known. It seems probable that the atmosphere is responsible for the drift, since controls exposed to the same thermal effects but open to air showed only slight positive drifts. Metallographic studies of samples are under way. These drift experiments will be continued with material from other sources as well as the currently available material.

8. DEVELOPMENT OF TEST LOOPS AND COMPONENTS

EGCR In-Pile Loops

(F. H. Neill)

The AEC has notified ORNL that completion of loop installation is to be deferred until at least July 1, 1965. Minimum provisions are to be made now in the EGCR construction for necessary permanent portions of the eight loop assemblies to permit future installation of up to four selected loops.

Present plans are to proceed with Title II design of the upper and lower nozzle tee sections, the upper and lower horizontal chase piping, and the necessary chase cooling duct work. All other loop design work will be carried through Title I design only. A preliminary hazards report will be prepared.

A summary of the work in progress at the time the program was deferred is presented here. Title I drawings of the top and bottom nozzle tee sections had been completed for loop TL-4. These drawings had been circulated for comments. Materials specifications for all bottom nozzle tee sections had been completed. Criteria for fabrication of the tee sections had been written. Detail drawings of the bottom nozzle tee section are being made.

Final design criteria for the sniffer gas system and for the helium supply system had been established. Preliminary criteria for the loop cooling water system had been prepared. A design history had been compiled for the mainstream gas cooler. This information was to be included with the cooler specifications to be submitted to various heat exchanger manufacturers. Criteria had been prepared for the cell washdown system for Title I approval. This decontamination system employs a high-pressure, hot-water jet to remotely clean the experimental cell. One such unit would have served all the experimental cells.

The Title I design of the filter vessel, the prefilter, the postfilter, the filter shield, and the support structure had been completed. A test program for the absolute filter element is being prepared. The final design

criteria for part of the purification system had been prepared. Title I design of the heat exchanger and charcoal bed is proceeding.

The flow sheet for the gas transfer and storage system and the purification system had been prepared. The safety surge system had been eliminated from the loop. The function of the safety surge system, which was to maintain full mass flow following loss of one Bristol Siddeley compressor, was to be fulfilled by placing a 4-in. bypass line, including a check valve, around each compressor. Criteria for the EGCR experimental loops mainstream piping (out-of-cell) and for the in-cell mainstream piping, including the design conditions and the materials of construction, had been prepared.

Title I design of the lower chase mainstream (inlet) piping had been approved. Title I design of the in-cell mainstream piping had been completed, and a Title I design analysis had been written. The calculated stresses are below code allowances. The Title II design of the lower chase (inlet) and in-cell mainstream piping is to be completed. Title I design of the in-cell mainstream piping had been completed; however, the design analysis had not been prepared.

Data preparations have begun for an analog study of the loss of all electric power to the loop equipment. The shutdown heat removal following loop depressurization from a helium-cooled, attemperated experiment has been analyzed. The conclusion is that melting of the steel cladding is probable.

A study of the capabilities of the EGCR service machine has indicated that the latest designs for the loops and for the service machine do not permit cooling of the experimental assembly during removal. Various methods for eliminating this problem are being considered.

The design work carried out during the period covered by this report is described in the following sections.

Through-Tube Design (R. E. Helms, L. W. Noggle)

There are eight through-tube assemblies for in-pile experiments in the EGCR. Four are 5 1/2 in. in outside diameter and are designated TS-1, -2, -3, and -4. The other four are 9 1/2 in. in outside diameter and are designated TL-1, -2, -3, and -4. The four loops with 5 1/2-in. through-tubes

and two of the loops with 9 1/2-in. through-tubes (TL-1 and -3) are designed for operation with helium and CO_2. Loop TL-4 is designed for operation with hydrogen, and loop TL-2 is for operation with steam. The through-tube assembly consists of the tube and the top and bottom nozzle tee sections, as shown in Fig. 8.1. Design layouts have been completed for the through-tube assemblies for loops TS-1, -2, -3, and -4 and for loops TL-1, -2, and -3. Preliminary design layouts for loop TL-4 have been made. Title I drawings have been approved for the through-tube assemblies for loops TS-1, -2, -3, and -4 and for TL-1 and -3. Detail drawings are being made for the through-tube assemblies for loops TS-1, -2, -3, and -4 and for TL-1, -2, and -3.

Experimental data for the thermal conductivity of reflective insulation were used for heat transfer calculations for sections of the through-tube assembly in order to determine temperature drops across the tube wall and the heat loss and temperatures of the nozzle coolant at several points along the tube axis. These calculations were made for 1/4- and 1/2-in.-thick reflective insulation inside the tube. The gross thermal conductivity of this insulation in helium at a pressure of 1000 psia is plotted versus temperature in Fig. 8.2. The effectiveness of the insulation at various positions is indicated in Figs. 8.3 through 8.8 for a 5 1/2-in. through-tube. Data for the bottom nozzle section with 1/4 in. of insulation inside the tube are plotted in Fig. 8.3. Similar data for 1/2 in. of insulation inside the tube are plotted in Fig. 8.4. Data for the plenum region of the reactor with 1/4 in. of insulation inside the tube are plotted in Fig. 8.5 as a function of the reactor plenum gas film coefficient. Similar data for 1/2 in. of insulation inside the tube are plotted in Fig. 8.6. Data for the top nozzle section with 1/4 in. of insulation inside the tube are plotted in Fig. 8.7, and similar data for 1/2 in. of insulation inside the tube are plotted in Fig. 8.8.

A transient heat transfer analysis of the bottom tee section of a 5 1/2-in. through-tube is under way for which the TIGER I code is being used. Analyses of the radial and axial temperature profiles of a 5 1/2-in. through-tube containing a fuel assembly have been completed for both attemperated and unattemperated assemblies.

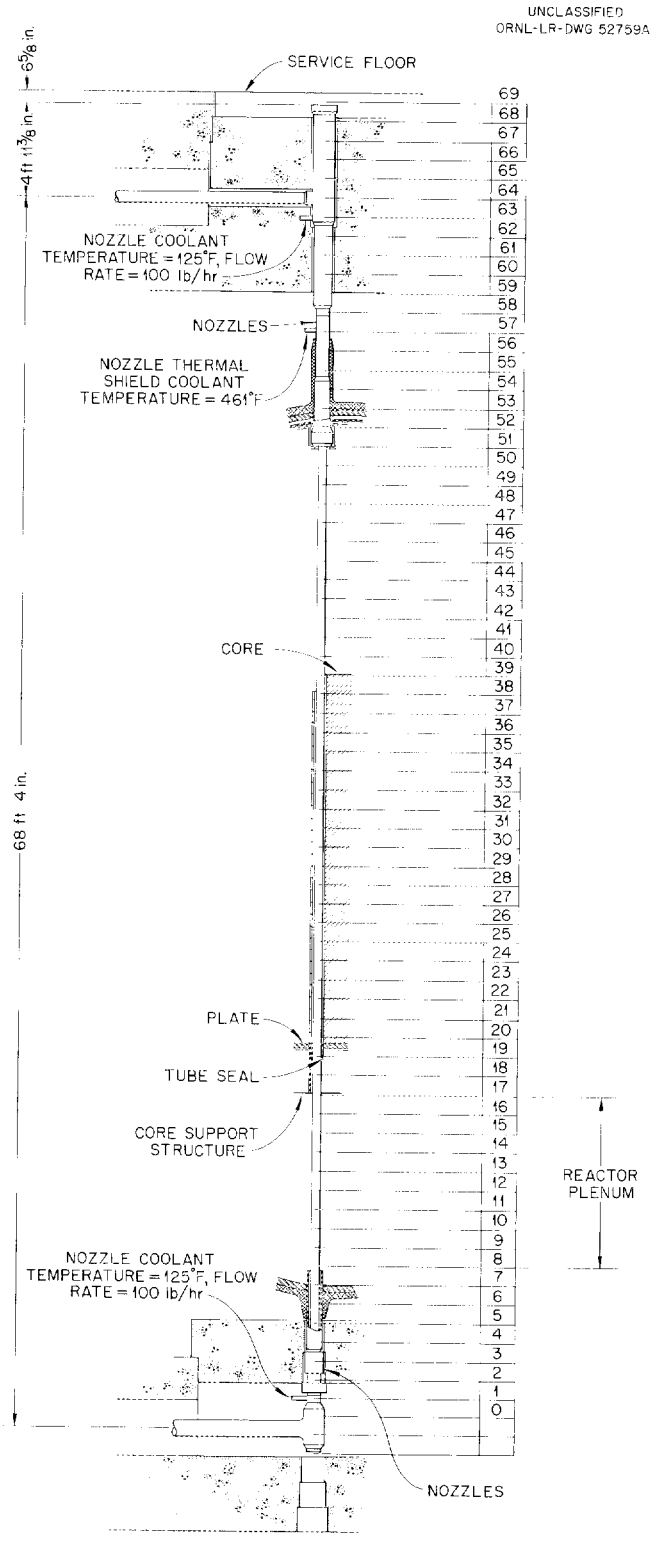


Fig. 8.1. EGCR Through-Tube Assembly.

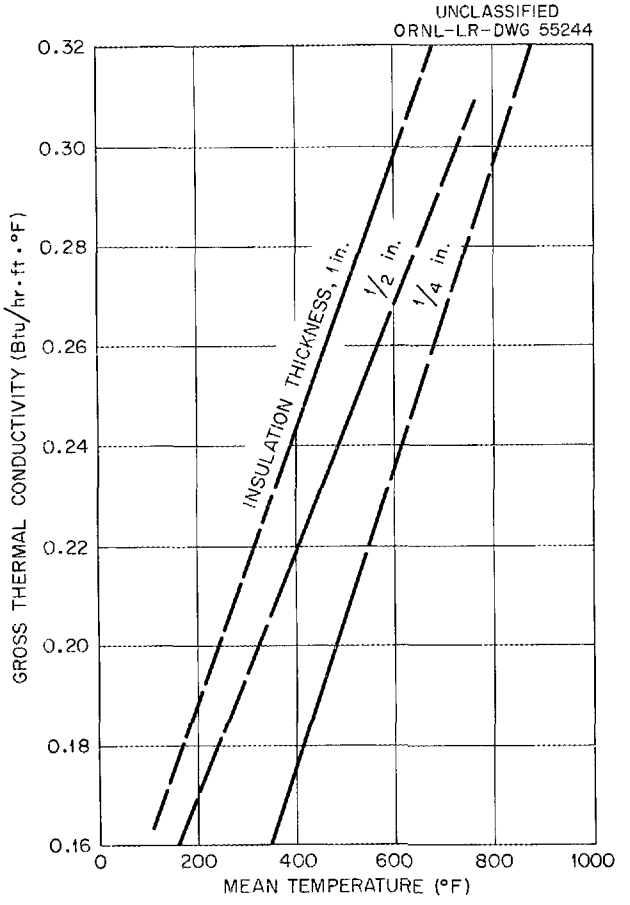


Fig. 8.2. Thermal Conductivity of Reflective Insulation in Helium at a Pressure of 1000 psia.

Loop Component Designs

Cooler. (W. S. Chmielewski) Preliminary stress calculations on various cooler designs have been made to clarify problem areas and determine feasibility of construction. The re-entrant tube evaporator design has been studied in detail with respect to materials, vibrational, and fabrication problems. The membrane and pressure discontinuity stresses have been determined for the gas shell and the tube sheet. Heat transfer calculations for the evaporator are complete and are nearing completion for the steam condenser.

Auxiliary Gas Systems. (W. S. Delicate, L. C. Fuller) Final design criteria for the gas distribution system were prepared. The system basically consists of two high-pressure headers (one for helium and one for carbon dioxide) extending throughout the length of the utility tunnel and four pressure-reducing stations per cell. Each reducing station is designed to handle either helium or carbon dioxide. The reducing stations provide gas for the buffer gas system, gas storage tank filling, safety surge tank filling, loop filling, through-tube pressurizing, and gas sampling-station purging.

Preliminary design criteria were established for the helium supply system, the CO_2 supply system, the through-tube pressurizer and loop fill system, the loop off-gas system, the loop gas purification system, and the decontamination system. The helium supply system basically consists of a bottle trailer, a cooler, and two silica-gel beds. U. S. Bureau of Mines grade A helium rated at 99.995% by volume is specified. The CO_2 supply

system is designed to receive liquid CO_2; cool, compress, and dry it in an adsorption column; vaporize it at constant pressure; and store it at an elevated temperature to prevent throttling to partial liquid or solid states. The through-tube pressurizer and loop fill system is designed

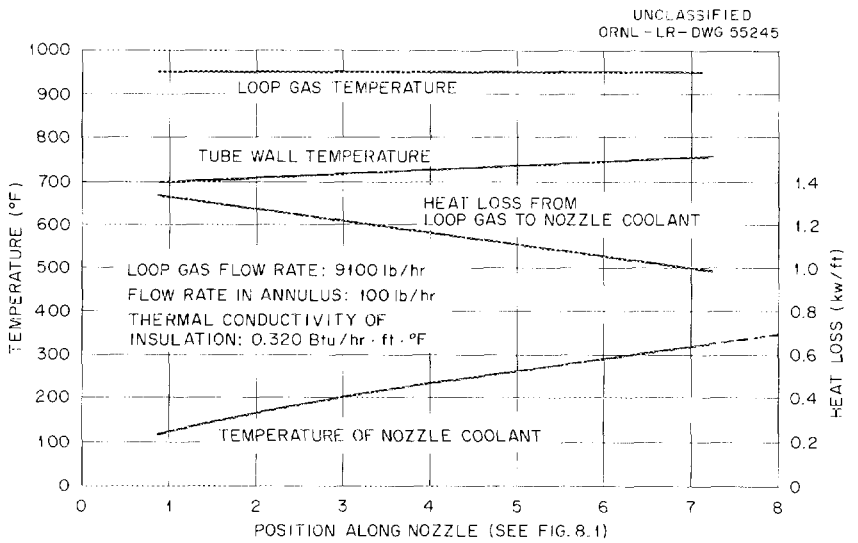


Fig. 8.3. Effect of 1/4-in.-Thick Reflective Insulation in Bottom Nozzle Section.

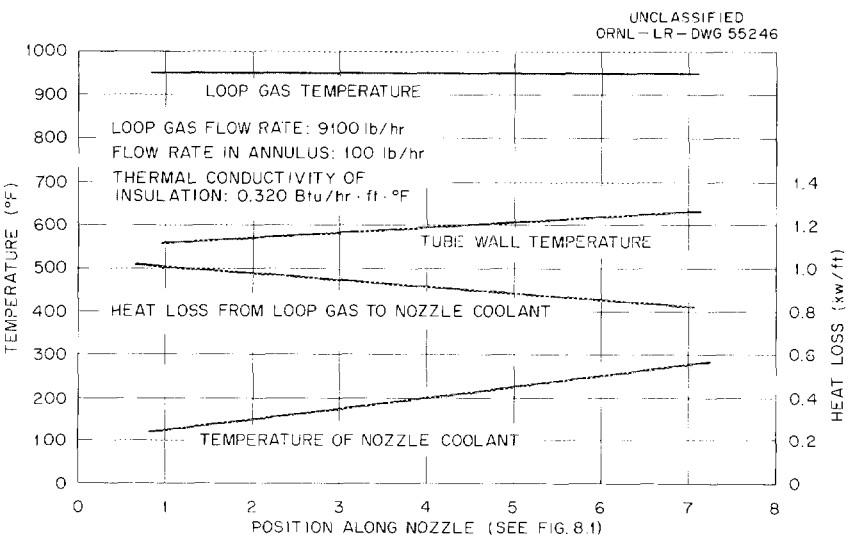


Fig. 8.4. Effect of 1/2-in.-Thick Reflective Insulation in Bottom Nozzle Section.

to maintain pressure in the through-tube and thus permit reactor operation when an experimental loop is shut down, fill an experimental loop, and pressurize in-cell loop piping during leak hunting.

The loop off-gas system is designed to permit safe discharge of contaminated gas from the loop to the plant stack. The system consists of

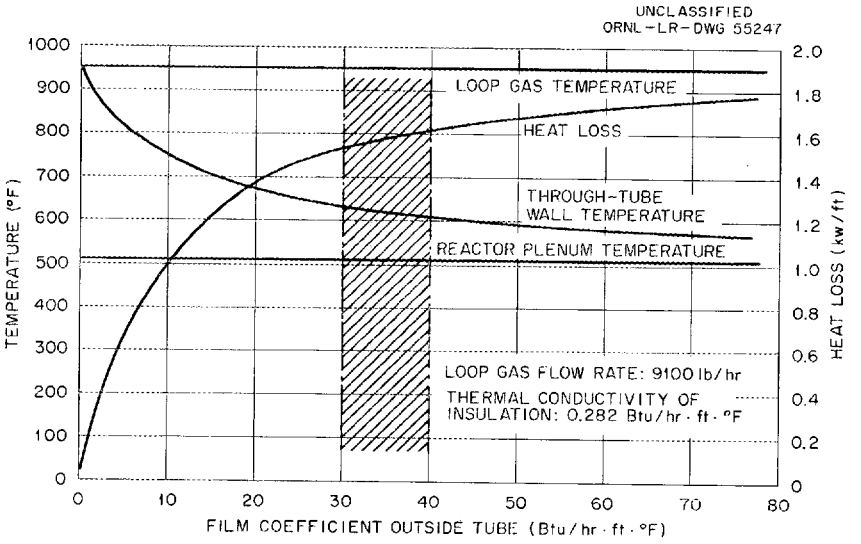


Fig. 8.5. Effect of 1/4-in.-Thick Reflective Insulation in Reactor Plenum Section.

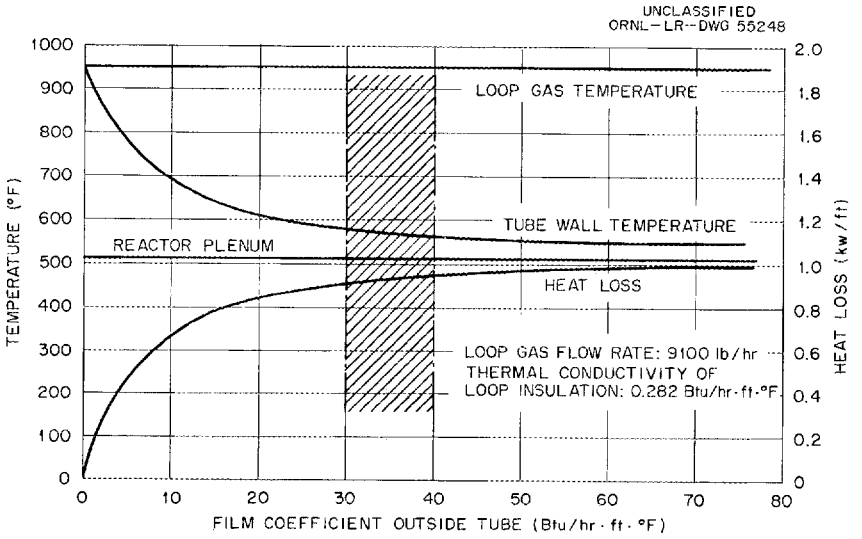


Fig. 8.6. Effect of 1/2-in.-Thick Reflective Insulation in Reactor Plenum Section.

a moisture separator for condensing water vapor generated during decontamination operations, a vacuum pump, a charcoal bed, and an absolute type of filter. The loop purification system has been separated into two parts, physical cleanup and chemical cleanup. The system consists of a gas cooler and a charcoal bed. The cooler controls the temperature

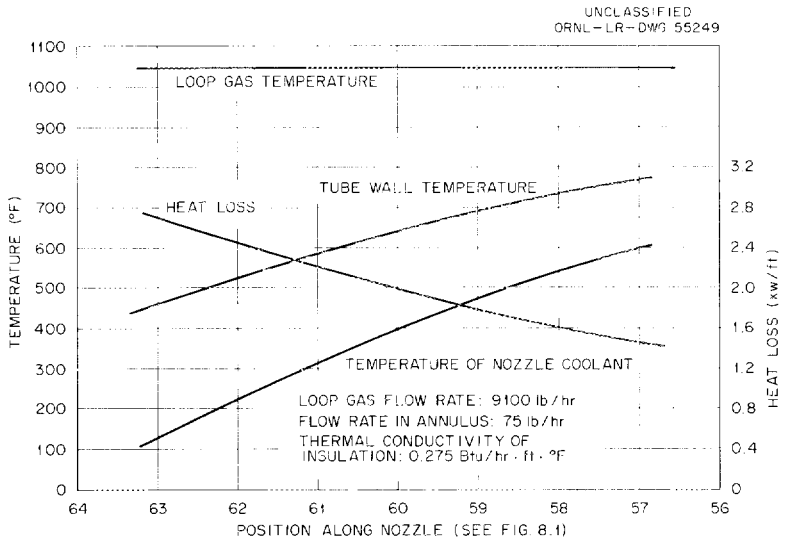


Fig. 8.7. Effect of 1/4-in.-Thick Reflective Insulation in Top Nozzle Section.

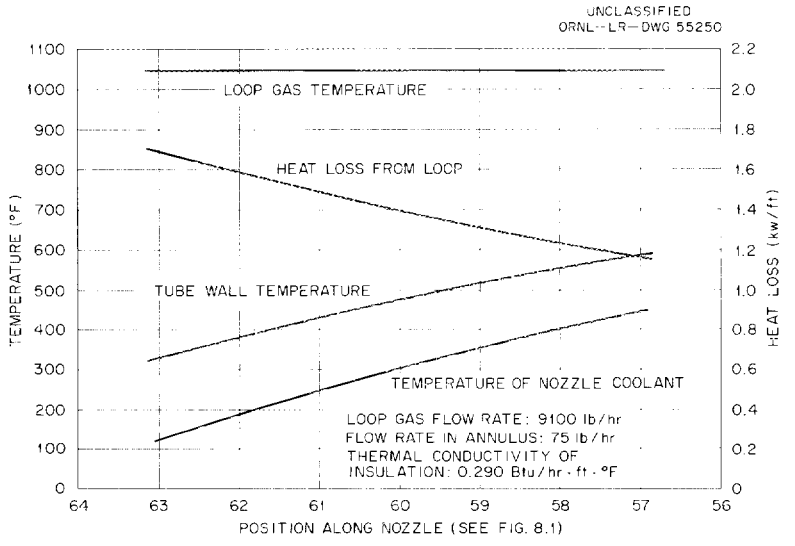


Fig. 8.8. Effect of 1/2-in.-Thick Reflective Insulation in Top Nozzle Section.

of the gas entering the charcoal bed. The charcoal bed contains about 1/4 lb of silver wire followed by about 30 lb of BPL charcoal and a high-temperature, absolute type of after-filter. Title I design of the equipment is under way.

The decontamination system consists of reagent mixing tanks, feed pumps, and associated piping. Present experimental evidence indicates that the decontaminating reagent will be 4% sodium oxalate, 3% hydrogen peroxide solution, with the pH adjusted to 4 to 5 by additions of oxalic acid.

Loop Cooling Water System. (A. W. Culp) The cooling water system designs have been completely revamped to accommodate an evaporative cooler. Demineralized water is now specified for cooling in-cell components, providing makeup to the steam system and for emergency cooling. The river water is used directly in the steam condensers as process water. Two large pumps, formerly used on the demineralized water system, are employed as booster pumps on the river-water system. The condensing units are tentatively located on the sixth floor.

Cell Ventilation System. (A. W. Culp) The cell ventilation system will not be used when the loop gas contains a large amount of fission products. A small bypass line containing a remotely operated valve will be used around the main outlet valve to provide pressure relief for the system as long as the radiation level of the vent gas is low. Should the radiation level in the cell increase rapidly because of a rupture in the loop piping, the cell will be sealed.

The cell cooling system design provides for two 50-kw coolers to remove the energy dissipated in the cell. These units transfer the heat directly to river water. These "coolers" also contain heating elements. For CO_2 operation, the cell temperature is maintained at or above 90°F by throttling coolant flow and using the heater. This prevents condensation of CO_2 in the in-cell piping. No regulation of the cell temperature is anticipated for the helium loops.

Hazards Evaluations (R. G. Mallon)

The loop conditions capable of causing a reactor scram and the required safety actions were outlined. The conditions are excessive gas

temperature at experiment outlet, insufficient loop gas pressure, and insufficient volume flow of loop gas. Cooling of the EGCR in-pile loops by convection was re-evaluated using data obtained recently on pressure drop through the inoperative main loop compressors. The analysis shows that convection is adequate for decay heat removal if the loop pressure is near the normal operating pressure. A preliminary statement of requirements for auxiliary blowers for the EGCR loops that could be activated in the case of a loss-of-pressure accident has been prepared.

Stress Analyses (W. S. Chmielewski)

Stress criteria for the loops were developed with the "Navy Code" (Tentative Structural Design Basis for Reactor Pressure Vessels and Directly Associated Components) as a basis. In this design philosophy, the combined stresses may exceed the proportional limit of the material, but justification entails calculation of the fatigue life from the strain cycling that occurs. Allowable stress intensities for type 347 stainless steel, INOR-8, Inconel, and SA-212, grade B, steel have been determined. Five hundred cycles of "cold" startup and emergency operation are specified for the EGCR loops; this allows, on an average, two complete shutdowns of the loops per month for 20 years.

Revised Pressure Drop Estimate for Small Loops (C. Michelson)

The pressure drop estimate for the 5 1/2-in. loops has been revised to take into account the present loop piping layout and conceptual component designs that should closely approximate the final loop design. Each small loop was assumed to consist of an in-pile test section, pipe and fittings, six isolating valves, one loop cooler, one main-line filter, and one electric heater. Total pressure drops were computed for helium and carbon dioxide cooling at 500 and 1000 psia pressure. The in-pile test section was assumed to be generating 1500 kw of combined fission and gamma heat, with a gas inlet temperature of 600°F and an outlet temperature of 1050°F. The case of reduced power operation (335 kw) for a gas inlet temperature of 950°F was also calculated based on a constant mass

flow rate. In all cases it was assumed that the exit gas from the in-pile test section was attemperated to 1050°F.

The calculated system pressure drops and the values reported previously are given in Table 8.1. The considerable increase in pipe pressure drop is due to the addition of insulation to the inside of the through-tube (not considered in the first estimate), the use of 4-in. pipe for certain sections of the through-tube entrance and exit piping, and a large increase in the equivalent length of pipe and fittings (from 650 ft to approximately 1000 ft) resulting from the many additional expansion loops. The isolation-valve pressure drop was reduced a factor of 10 by assuming full-clearance gate valves. The heater pressure drop reduction resulted from simplifying the heater to a section of resistance-heated pipe. The cooler pressure drop increase resulted from changing a single water-jacketed pipe to a multitube straight-through evaporator. The diverter valve was eliminated. The filter design remained essentially unchanged. These substantial changes in piping and components increased the total pressure drop for the loop by up to 4% for CO_2 cooling and 16% for helium cooling.

A comparison of the revised pressure drop calculations with the original compressor specifications is given in Table 8.2. The two points of concern are the pressure drops for operation with helium at 500 psia at 600 and 950°F, which increased 6 and 28%, respectively. These operating points had already been amended in the compressor specification to permit continued operation with two compressors running by increasing the system pressure (due to a maximum speed limitation), and the situation is now further aggravated by the revised pressure drop estimate.

GCR-ORR Loop No. 2

(J. Zasler, P. C. Bertelson, C. J. Claffey,
W. R. Huntley, T. S. Kress, J. LaGraff)

Construction of the 4-ft-thick barytes concrete cell walls and roof was initiated in October. The roof and walls have been completed and the concrete forms removed. Work has now begun on installation of the 1/8-in. stainless steel cell liner. Also some 150 tons of lead shielding have been

Table 8.1. Comparison of Previous and Revised Pressure Drop Calculations for Operation of EGCR Small Loops with Loop Heater Off

Component	Pressure Drop (psi)							
	For Operation at 1000 psia and 600°F		For Operation at 1000 psia and 950°F		For Operation at 500 psia and 600°F		For Operation at 500 psia and 950°F	
	Previous Estimate[a]	Revised Estimate	Previous Estimate[a]	Revised Estimate	Previous Estimate[a]	Revised Estimate	Previous Estimate[a]	Revised Estimate
				Operation with CO_2 Cooling				
In-pile section	53.6	53.0	8.9	8.9	26.2	26.2	4.4	4.4
Piping and equipment								
Pipe	3.25	6.103	4.17	7.754	6.40	12.114	8.30	15.474
Diverter valve	1.97		1.97		3.93		3.93	
Cooler	0.80	1.350	0.79	1.730	1.35	2.700	1.40	3.460
Isolation valves	1.17	0.116	1.54	0.166	2.33	0.233	3.10	0.332
Filter	0.15	0.152	0.21	0.217	0.340	0.304	0.410	0.430
Heater	0.86	0.200	1.12	0.276	1.65	0.397	2.26	0.553
Total piping and equipment	8.2	7.9	9.8	10.1	16.0	15.8	19.4	20.3
Total system	61.8	60.9	18.7	19.0	42.2	42.0	23.8	24.7
				Operation with Helium Cooling				
In-pile section	21.2	21.2	3.5	3.5	10.6	10.6	1.7	1.8
Piping and equipment								
Pipe	1.80	3.716	2.25	4.681	3.60	7.399	4.49	9.254
Diverter valve	1.06		1.06		2.13		2.13	
Cooler	0.42	9.955	0.43	1.190	0.72	1.910	0.83	2.380
Isolation valves	0.63	0.064	0.83	0.091	1.24	0.127	1.65	0.181
Filter	0.13	0.141	0.17	0.206	0.24	0.282	0.34	0.408
Heater	0.46	0.124	0.61	0.168	0.92	0.246	1.22	0.332
Total piping and equipment	4.5	5.0	5.4	6.3	8.9	10.0	10.7	12.6
Total system	25.7	26.2	8.9	9.8	19.5	20.6	12.4	14.4

[a]See GCR Quar. Prog. Rep. June 30, 1960, ORNL-2964, pp. 230–4.

Table 8.2. Comparison of Compressor Specifications[a] and Revised Pressure Drop Estimates for Operation of EGCR Small Loops with Loop Heater On

Loop Operating Conditions			Total System Pressure Drop (psi)	
Coolant	Pressure (psia)	Temperature (°F)	Specified	Revised Estimate
CO_2	1000	600	59.1	60.7
		950	20.1	18.8
	500	600	37.5	41.6
		950	19.0	24.2
Helium	1000	600	25.5	26.1
		950	9.4	9.7
	500	600	19.2	20.3
		950	11.0	14.1

[a]As of February 1, 1960.

installed adjacent to the south facility plug and under the floor of the cryostat room.

The remotely operated crane and single-arm manipulator have been delivered and have been installed in a test facility, where operations requiring their use are being studied. The fabricated parts of a tool for remote manipulation of flanged joints have been received and are being assembled.

Design and detailing have been completed on the component shields (lead filled) and the movable rack on which the loop components are mounted. Procurement of these items is now in progress.

The following primary loop components have been fabricated and received: heater, evaporator, condenser, and side stream cooler. The activated charcoal for the fission-product traps was received, sampled, and analyzed. The fission-gas holdup characteristics of the charcoal were found to be approximately those used for designing the traps.

In order to maintain double containment, the side-stream carbon-trap cooling system was revised. The "brine," trichloromonofluoroethylene, will be circulated through 72 ft of 1/2-in. copper tubing coiled around the trap in a vented annulus containing ethylene glycol water solution.

A design of a test section for handling horizontal fuel elements has been established. This constitutes a change in concept from previous designs to permit removal of test fuel elements between tests without removing the pressure piping from the facility plug. Provision has also been made to prevent neutron activation of stainless steel components outside the plug.

An analysis was made to determine whether the main loop piping would be left in the in-pile section with the fuel element removed, without flow of loop gas, and with the reactor at power. It was determined that this could be done if the pipe were withdrawn about 1 ft out of the high gamma flux region and if an annulus were provided around the pipe through which cooling water could pass. A "cooling-finger" in the interior of the piping arrangement would also be desirable.

Investigations are being made to determine the temperature distributions in the concrete shield plug in the in-pile section. Some analyses have been completed, and electrical analogues will be made to study the more complex geometries.

An analytical estimate was made of the amount of flow to expect through slip joints which might be used in the loop. The flow was correlated with the joint clearance and length as a function of the pressure differential across the joint.

Where internal insulation is desired in the loop piping or components, it has been decided to use a reflective type exclusively. The available experimental data on reflective insulation is being studied to determine how it may be applied to loop 2 configurations.

Some of the heat-transfer components have been subjected to performance tests. The evaporator, condenser, and heater were tested in a loop in Bldg. 9201-3. The evaporator and condenser performed quite satisfactorily, but the heater suffered electrical failures that stopped the tests. Investigations are now under way to determine remedies for the heater failure. It is believed that increasing the gas velocity through the heater will help considerably in preventing failures. Preliminary tests of the regenerator were conducted at the manufacturer's plant.

Criteria were prepared for a sampling station for the EGCR loops and ORR loop 2. The gas pressure will be reduced and the flow will be restricted so that the sampling can be done manually in a dry-box type of containment vessel located outside the loop cell. The number of sampling points is being studied. Consideration is being given to using the sampling system at only two points: the main loop after the compressors and the bypass cleanup system after the carbon trap. The differences between specific isotope concentrations in the gas before and after the main loop components may be too small to measure in samples taken from such locations. The sample lines will be permitted to cool to ambient temperature before reaching the first block valve. This will permit the use of low-temperature valves containing plastics and elastomers.

The potential hazard of a water-line rupture inside the cell has been studied. It now appears that a large cell drain adequate in size to handle the largest possible water leak within the cell is the best solution. A water seal will be provided in this drain to maintain the secondary containment. The problem of where to direct this drain is now under investigation.

Component Tests

Heater and Microswitch Electrical Breakdown Tests (A. S. Olson)

EGCR Loop Heaters. Electric breakdown testing was begun on a section of Chromalox tubular heater in a helium atmosphere using the test apparatus previously described.[1] The test stand and pressure vessel are shown in Fig. 8.9. For these tests, a 2-in.-long specimen was cut from the terminal end of the heater. On the cut end, the MgO insulation was removed and the heater wire was cut well back inside the sheath. This open space was repacked with MgO, and a cap was welded over the end. At the open end of the specimen, the spacing between the terminal pin and sheath varied from 0.100 to 0.113 in. The terminal pin was 0.142 in. in diameter and the outside sheath was 0.440 in. in diameter, with a wall thickness of 0.040 in.

[1] "GCR Quar. Prog. Rep. Sept. 30, 1960," ORNL-3015, pp. 170–1.

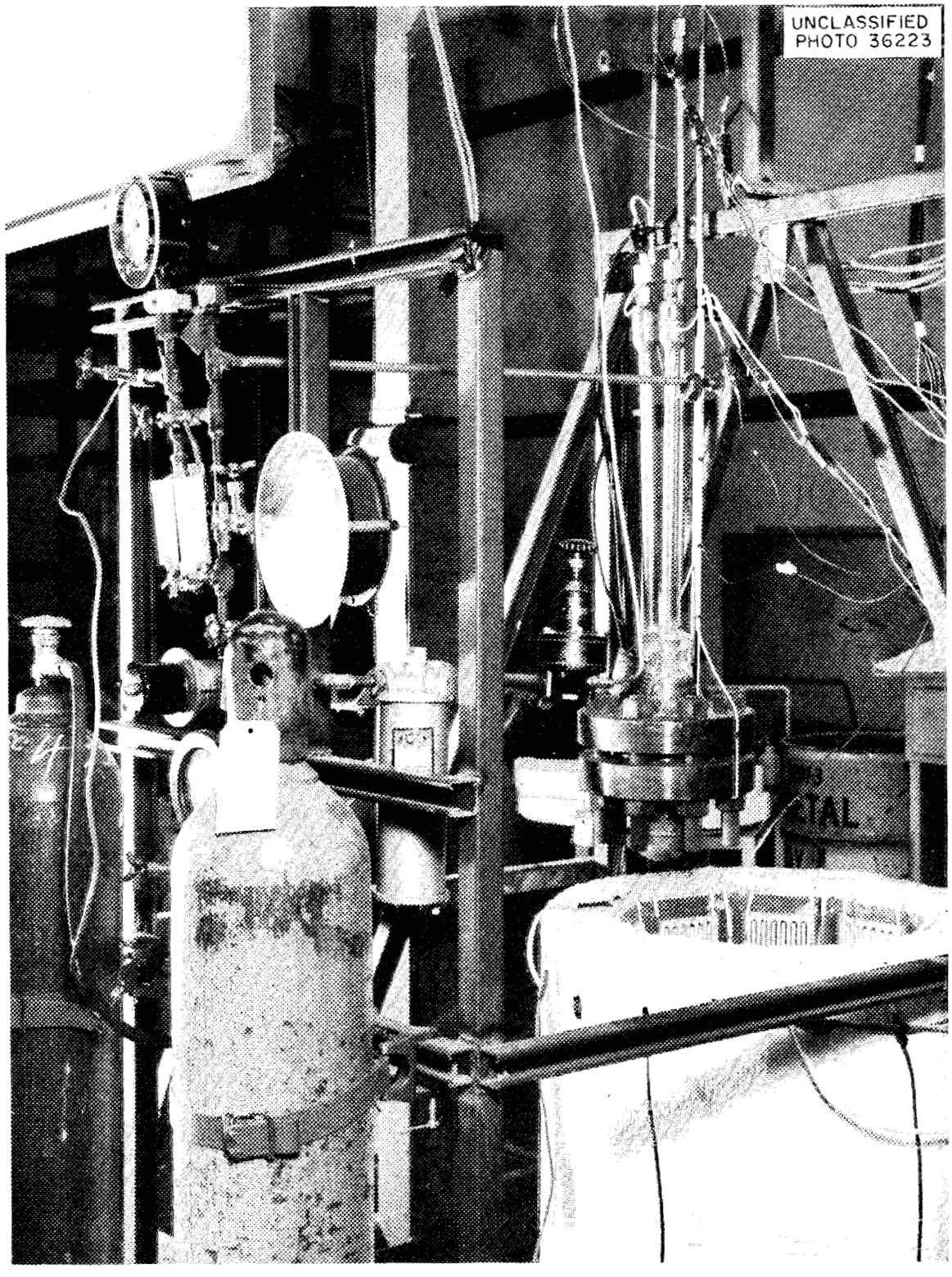


Fig. 8.9. Test Stand and Pressure Vessel for Electrical Breakdown Testing of a Chromolox Tubular Heater and Microswitch.

The resistance of the heater section before electrical testing and after baking at 300°F for several days was 60 megohms. The specimen was placed inside the pressure vessel, with electrical leads, one each from the heater sheath and heater terminal pin, extending through two Conax seals. Sixty-cycle alternating-current voltage was applied to the section in a range from 0 to 1000 v. The range of helium test pressures was 0 to 1000 psig. Tests were made at four temperatures: room temperature (~75°F), 300, 600, and 900°F.

At the specified operating conditions of the terminal end of the Chromalox heaters (900°F and 1000 psig), no electrical breakdown was experienced at potentials up to 1000 v. This potential did result in breakdown when the pressure was lowered to 70 psig while maintaining the same temperature level. At 1 psig, a potential of 325 v caused electrical arcing. At the operating potential of the heaters (480 v) with the terminal held at 900°F, a pressure of 20 psig was sufficient to suppress voltage breakdown. The breakdown voltages are plotted versus pressure at various test temperatures in Fig. 8.10.

The heater section was also tested for electrical breakdown in air at room temperature and with pressures ranging from 0 to 100 psig. No electrical breakdown was indicated. Instrument air with a dew point of +30°F, i.e., approximately 5500 ppm of water vapor, was used.

An enlarged view of the open end of the heater section after testing is shown in Fig. 8.11. No damage is visible.

ORR Loop No. 2 Heaters. Testing of the voltage-breakdown characteristics of a modified tubular heater for use in ORR loop No. 2 has been completed. A 2-in.-long section of tubular heater was filled at the terminal end with insulation material (Sauereisen No. 29). After air drying and baking at 250°F for several days, the heater section was placed in the voltage-breakdown-test pressure vessel shown in Fig. 8.9.

Initial testing was done in a nitrogen atmosphere with the heater section at 500°F. No electrical breakdown occurred at any pressure with potentials in the range of 0 to 1000 v ac between the heater sheath and terminal pin. Subsequently, the voltage was increased until electrical breakdown occurred at 1380 v ac.

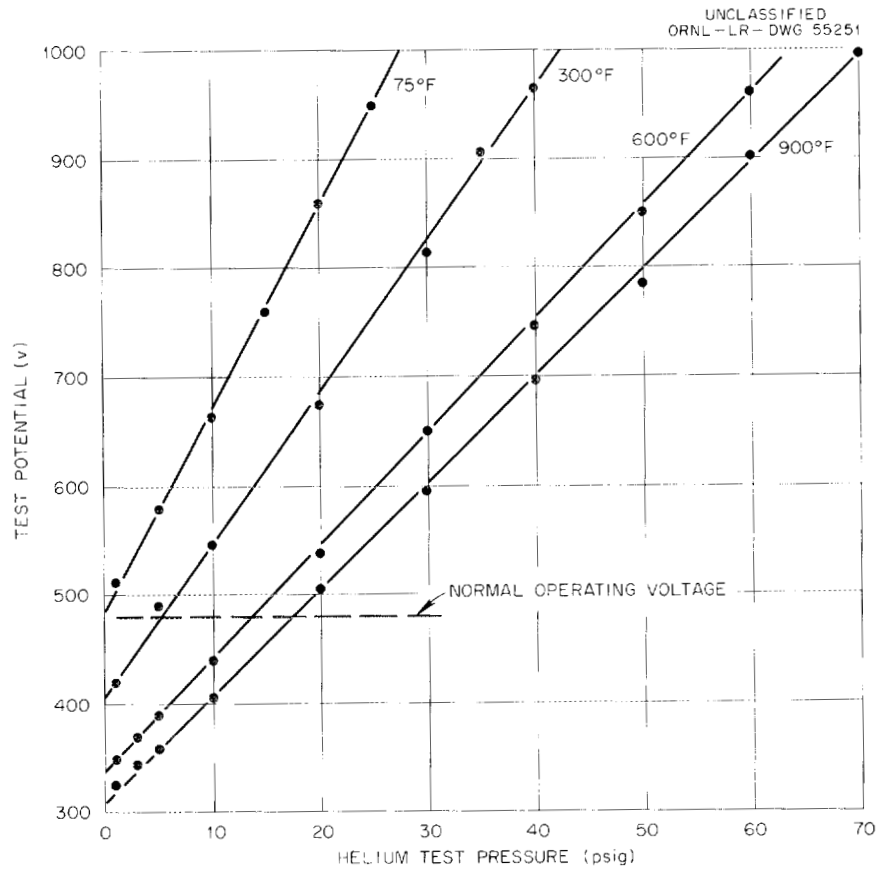


Fig. 8.10. Electrical Breakdown Voltages Versus Test Pressure at Various Temperatures.

With the temperature of the heater section at 900°F, electrical breakdown occurred at approximately 700 v ac and, subsequently, at 280 v ac in the nitrogen atmosphere, regardless of the test pressure. After lowering the test temperature to 500°F, electrical breakdown occurred at voltages ranging from 600 to 990 v ac and was independent of pressure.

After removal of the heater section from the pressure vessel, it was observed that some of the Sauereisen insulation had a dark gray color instead of the normal white appearance, as shown in Fig. 8.12. The minimum spacing between the terminal pin and sheath of the Chromalox heater section used for this test was 0.100 in., which is greater than the spacing between the heater leads of the heaters proposed for use. Because of the erratic

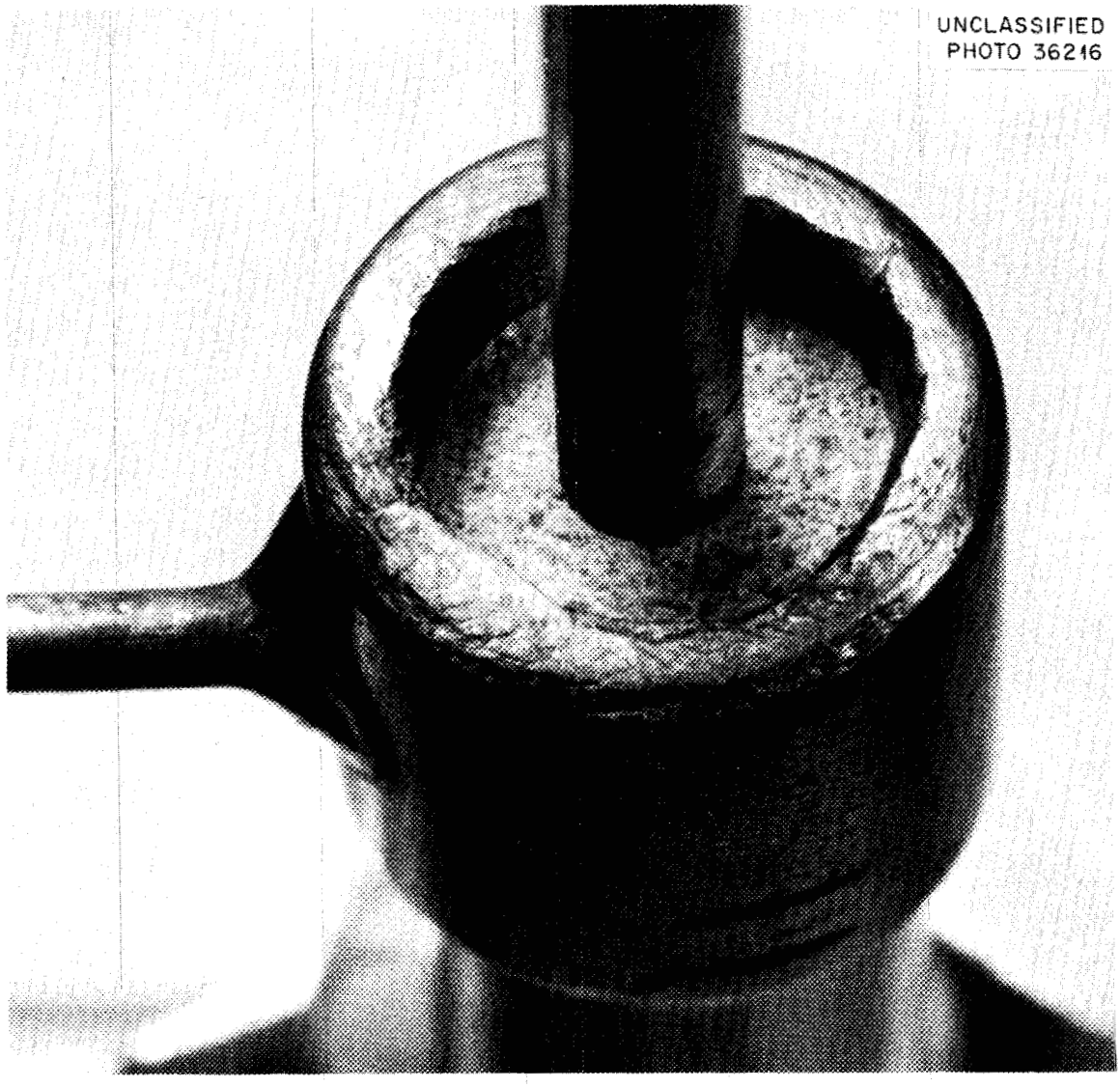


Fig. 8.11. Enlarged Photograph of Open End of Chromalox Heater Section After Testing. No damage is visible.

results obtained with the Sauereisen insulation, it is not recommended for use at elevated temperatures as a high-voltage insulation.

EGCR Microswitch. Preliminary tests have been made of a type V3-1301 switch, manufactured by the Micro-Switch Company. This switch is being proposed for use in the EGCR charge and service machines, under the following service conditions: temperature, 70 to 510°F; pressure, atmospheric to 300 psig; atmosphere, helium; electrical loading, 115 ac, type



Fig. 8.12. Enlarged Photograph of Heater Section Showing Damage to Sauereisen Insulation During Testing.

SG auxiliary relay (Westinghouse), with an impedance of 1320 ohms and an operating current of ~0.1 amp.

An initial test on one microswitch in air at atmospheric pressure and temperature indicated no electrical breakdown at 1000 v ac between open contacts. The resistance between open contacts under the same conditions, as measured with a megohm meter, indicated greater than 1000 megohms.

Subsequent tests on the same switch in helium at pressures from 1 to 300 psig and at temperatures from ambient to 515°F indicated no electrical breakdown at 120 v ac. These tests were made between the "normally open" and "common" contacts of the switch.

Tests in progress in a helium atmosphere are yielding values of electrical breakdown voltages, for the purpose of making comparisons with data reported by Tracerlab, Inc.,[2] on the same type of switch. The voltage range for testing is being extended to breakdown values or 500 v ac, whichever is greater. The breakdown voltage is defined here as that potential which causes a sudden increase in leakage current across the open contacts of the switch. The breakdown voltages between the "normally open" and "common" contacts of the switch, as obtained in these tests, are listed in Table 8.3. Similar tests will be made between the "normally closed" and "common" contacts of the switch. Proposed tests include operating the switch 3500 times under the service

[2]Harlan C. Shaw, "The Effects of Intense Gamma Irradiation on Electrical Breakdown in Helium," Report No. TLW-1060, Tracerlab, Inc., Reactor Monitoring Center, Richmond, California.

Table 8.3. Voltage Breakdown in Helium of V3-1301 Microswitch in Tests with Potential Applied Across Normally Open and Common Contacts

Helium Pressure (psig)	Test Temperature (°F)	Breakdown Potential (v, ac)
1	70	302
300	70	>500[a]
300	530	>500[a]
1	530	230
10	530	270
20	530	310

[a]Highest potential applied; no breakdown evident.

conditions described, with periodic checks for excessive leakage current between open contacts.

EGCR Valve Tests (A. S. Olson)

One of the three types of valves to be tested for use in the EGCR loops has been received. It is a ball valve with a Limitorque operator designed as shown in Fig. 8.13. It was manufactured by the General Kinetics Corporation.

No difficulty was encountered in welding stainless steel pipe caps to the inlet and outlet ports of the stainless steel valve casting. Dye check and radiographic examinations indicated excellent welds. The valve was closed by means of the hand wheel, and preliminary leak checks with helium at room temperature were satisfactory, as indicated below:

Pressure Drop Across Valve Seat (psig)	Helium Leakage [cm^3 (STP)/hr]
50	2.1
100	5.6
200	14.1
300	21.9
400	33.9

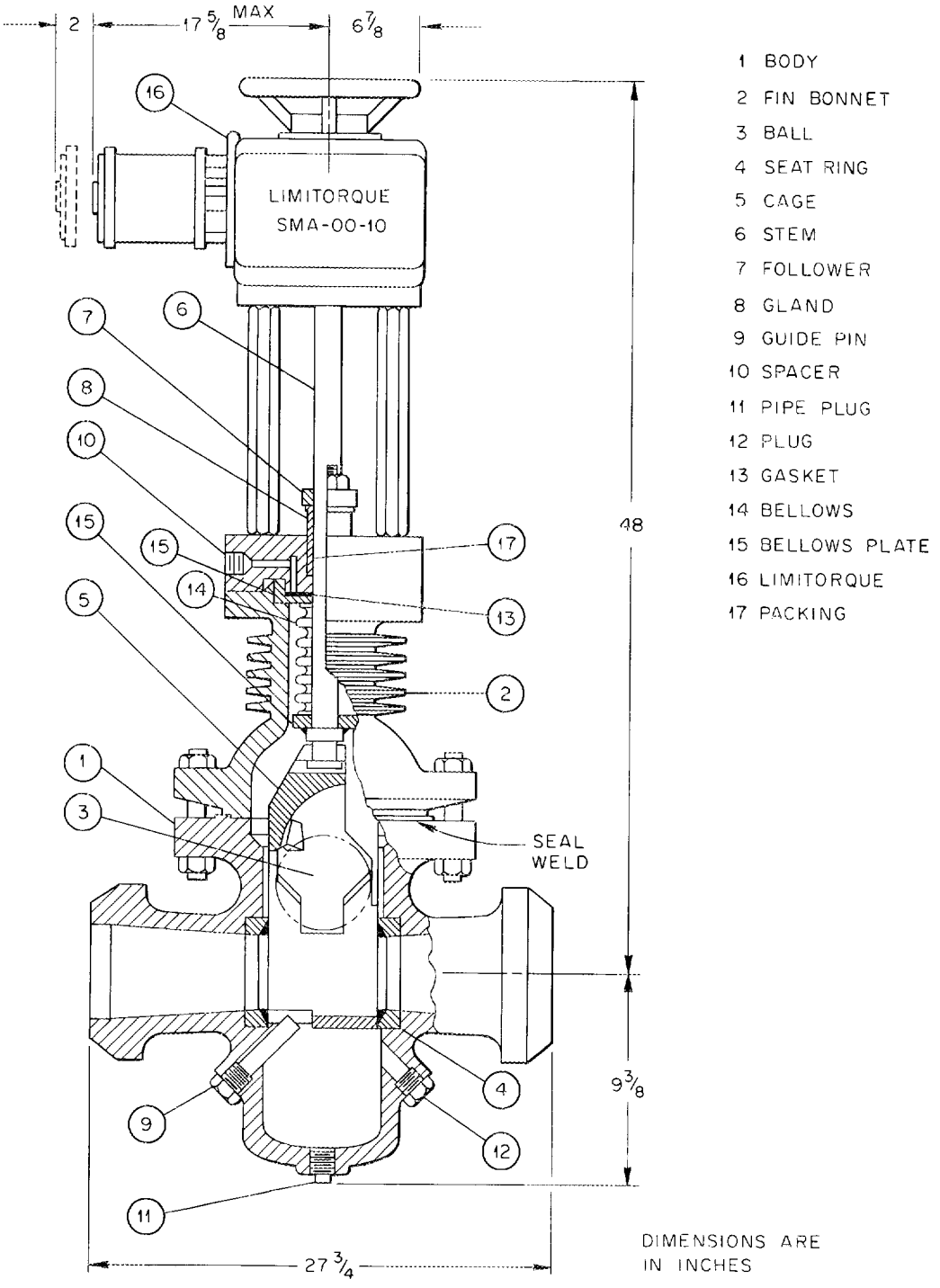


Fig. 8.13. Ball Valve with Limitorque Operator.

The bellows seal was checked with a helium leak detector, and no leakage was indicated.

After installation of the valve in the test furnace, as shown in Fig. 8.14, the valve was closed by means of the Limitorque drive. A leak check of the valve seat with a pressure differential of 300 psig of helium indicated 72 cm^3 (STP)/hr.

With the valve in the open position, it was heated to approximately 1000°F in 3 hr. Upon closing the valve, it was not possible to maintain a pressure difference across the valve seat. The bellows seal was rechecked, and there was no indication of leakge; after cooling the unit, however, gross leakage was still evident across the valve seat. During these tests, the volume between the valve stem packing and bellows seal was at the same pressure as that in the valve.

Communication with the valve manufacturer revealed that the valve had been designed to operate with 1000-psig internal pressure and no bellows backup pressure. Since the bellows effective area is 8 $in.^2$, the stem drive unit was arranged to deliver 8300 lb of thrust, 8000 lb of which was necessary to overcome the thrust from the internal pressure. With bellows backup pressure applied, the seating thrust was greatly increased and the valve would not seat properly.

The valve was returned to the manufacturer for examination and repair. When opened, evidence of damage from the high stem loading was found and, in addition, some warpage of the seat ring was noted. This warpage has been attributed to the uneven temperature distribution in the massive valve body as a result of heat losses through the bonnet section. The valve is currently being repaired and will be returned for further testing.

GCR-ORR Loop No. 2 Components (F. A. Flint)

Assembly of the out-of-pile loop for testing ORR loop No. 2 components was completed, and, following pressure tests and shakedown, performance tests were begun. With the complete loop on stream, primary attention was given first to the performance of the heater unit, composed of three individual heater groups, when operating at various gas flow rates and

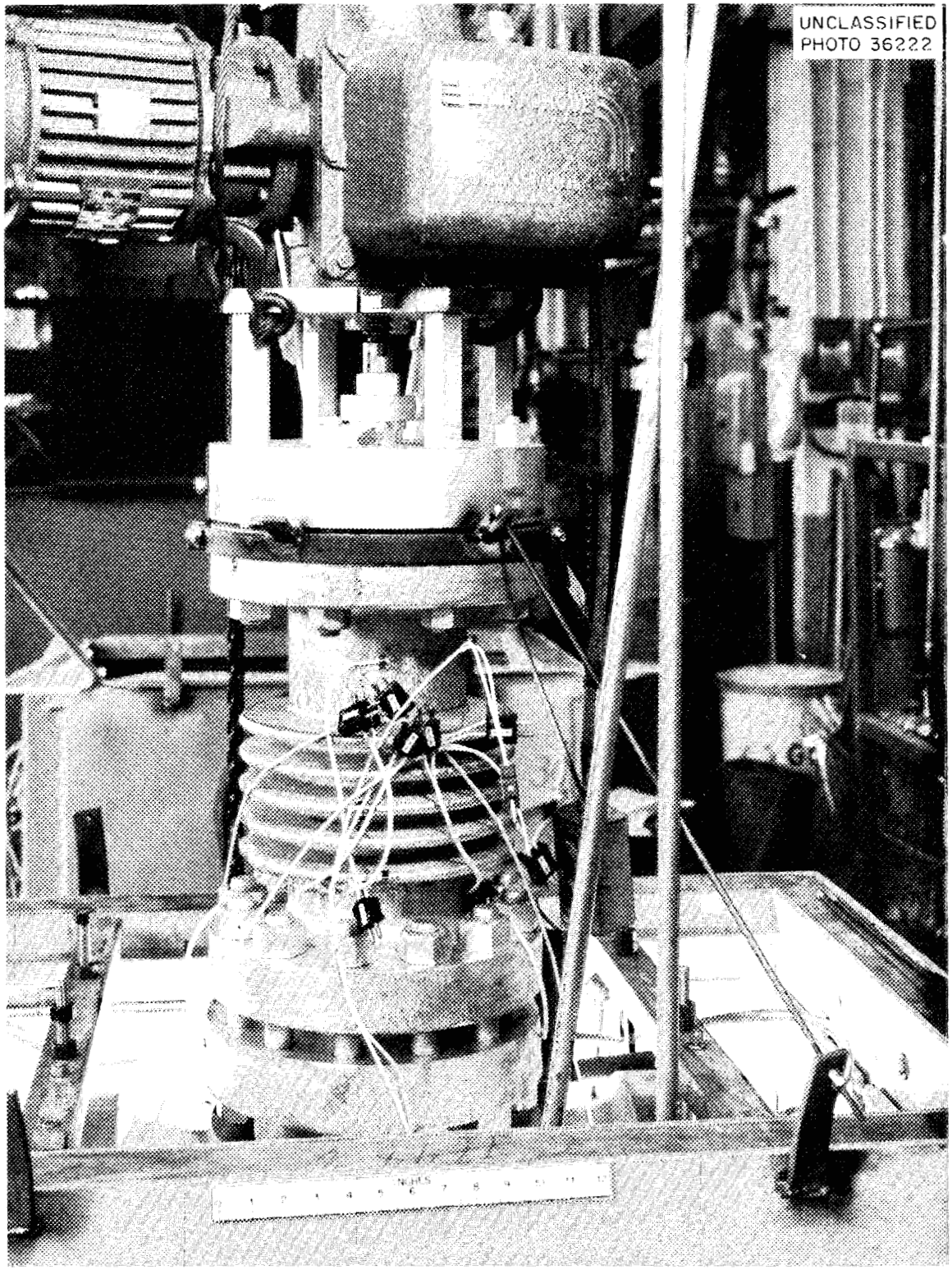


Fig. 8.14. General Kinetics Corporation Ball Valve with Limitorque Operator Installed in Test Furnace.

power settings. Heater group 1 partially failed at a gas flow rate of 165 lb/hr and a power setting of 33 kw, approximately 59% of the nominal heater group rating. The failure was manifested by an upscale reading of the voltmeter and a downscale reading of the ammeter, indicating an increase in resistance in one or more of the twelve heater cartridges in group 1. At the time of the failure, the maximum indicated cartridge cladding temperature was 1500°F. In testing heater group 2 at a gas flow rate of 265 lb/hr, it was impossible to apply more than 23 kw of power without causing the heater-cartridge-cladding high-temperature alarm to sound (alarm sounds at approximately 1640°F). This indicated either poor gas flow distribution or that the thermocouples on heater group 1 were sensing relatively cool spots. In order to improve the heater performance and reliability, the loop pressure was increased from 300 to 400 psig, thereby extending the range of attainable mass flow rates. However, the heaters failed shortly thereafter while operating at a flow rate of 720 lb/hr and a total power output of 112 kw. The first symptoms of failure were downscale readings on both ammeter and voltmeter on heater group 1 (groups 2 and 3 had been normal when last checked). Moments later, loop pressure was lost through the power terminal end of the heater.

Subsequent dismantling of the heater revealed major damage. All the terminals to the 36 heater cartridges had been melted away. Five of the cartridges had large holes melted through their skins, one of them being practically melted in two. The remaining 31 cartridges were undamaged of themselves and would have been operable had the terminals not melted away.

It is hypothesized that the melt holes in the five cartridges were caused by hot spots (hottest recorded temperature was 1620°F) not sensed by the thermocouples and that helium leaked through the melt holes, along the MgO insulation, and into the terminal compartment where it ionized and caused arcing across the terminals. The heater is currently being redesigned, and testing will be resumed when a replacement unit is available.

Mechanical Joint Service Testing (J. C. Amos)

Mechanical joint testing during this report period has been devoted to evaluating 5-in.-IPS, double-seal, gas-buffered Conoseal joints and

6-in.-IPS, double-seal, gas-buffered Grayloc joints. Sixteen closures were made with three 5-in.-IPS Conoseal joints. While eleven of these closures resulted in inner seal helium leakage of less than 1×10^{-5} cm^3 (STP)/sec when tested at room temperature with 15-psia internal helium pressure, only five closures met the specified maximum allowable inner seal leakage of less than 1×10^{-6} cm^3 (STP)/sec with 300-psig internal helium pressure. One unit was subjected to 50 bending-moment cycles from 0 to 72 000 in.-lb with an internal gas temperature of 700°F and a pressure of 300 psig, with no adverse effect on the seal. However, both inner and outer seal leakage increased substantially after two thermal cycles between room temperature and 700°F. Since previous tests of 2 1/2-in.-IPS, double-seal Conoseal joints of similar design indicated that these units would remain leaktight under repeated bending-moment and thermal cycling at operating temperatures up to 1300°F, it was felt that the performance of the 5-in.-IPS units could be improved. One unit was returned to the vendor for modification. The vendor remachined the clamp and increased the width of the gaskets. The inner and outer seal leakage rates were then less than 1×10^{-10} cm^3 (STP)/sec at room temperature and atmospheric pressure. Wider gaskets are being furnished for the 5-in.-IPS test unit currently installed in the bending-moment test stand to allow further evaluation of this unit at elevated temperatures.

Eight closures were made with two 6-in.-IPS, double-seal, gas-buffered Grayloc joints, and the specified maximum inner seal leakage of less than 1×10^{-6} cm^3 (STP)/sec was exceeded in all but one instance. One of these units has been returned to the vendor for modification. The vendor is currently experimenting with silver-plated seal rings that have a slightly different angle between the sealing surface of the ring and the flange.

Special Compressors

Regenerative Compressors (I. K. Namba)

The two regenerative compressors that were installed in the twin-turbine vessel of GCR-ORR loop No. 1 have continued to operate satisfactorily for approximately 1000 hr. During this period the compressors have

operated as single units and as two units in series over a range of speeds, 6000 to 12 000 rpm, and temperatures, up to 600°F, with the suction pressure limited to 45 psig.

The defective compressor housings mentioned previously have been repaired by chemically plating the coolant channels, and the assembled compressor units have been prooftested and are available for service. The compressor housing being repaired by the mechanical-chemical technique will require further repairs before prooftesting.

Compressors with Gas-Lubricated Bearings (D. L. Gray)

The Bristol Siddeley compressor was operated at 400 psia at the manufacturer's plant with the original 2.25-in.-diam, 6-in.-long bearing. Rubbing was detected at approximately 11 800 rpm. The pressure was then reduced to 200 psia and the rubbing reoccurred upon increasing the speed to 11 500 rpm. The mode of whirl was suspected to be conical, so each bearing was mounted in two diaphragms to provide added stiffness; subsequent testing indicated no improvement in the whirl-speed threshold. Next, an unsuccessful attempt was made to improve performance by reducing the bearing length to 4 1/2 in. from 6 in. The following program for eliminating the bearing whirl difficulties was then undertaken:

1. The existing monel bearings were shortened to 3 in. from the previous 4 1/2 in. length.

2. A standard-length bearing was modified to incorporate the 150-deg antiwhirl grooves used successfully in another compressor.

3. A Stellite-surfaced shaft and chrome-plated bearings were provided to eliminate differential thermal expansion.

4. The bearing thickness was reduced to reduce the transverse moment of inertia.

Subsequent tests with the 150-deg antiwhirl bearing also indicated rubbing at 11 800 rpm.

The application of hydrodynamic bearing theory to these problems has been studied further at ORNL. Curves showing the effect on threshold speed of the conical mode of bearing whirl were prepared for various ambient pressures and ratios of journal radius to bearing radial clearance. Curves of

the threshold speed for shaft cylindrical whirl for the compressor as a function of bearing clearance and for ambient pressures of 100, 250, and 400 psia were prepared. Analysis revealed that the threshold speed for whirl is lowest for cylindrical whirl of the shaft, next highest for conical whirl of the shaft, and highest for conical whirl of the bearing. Bearing cylindrical whirl should not occur because of radial stiffness of the bearing mount.

High-Temperature Gas Bearing Compressor Test System (D. L. Gray)

The GABE I compressor was accepted from the vendor on the basis of inspection results. After assembly it was determined experimentally that a 5-psig differential pressure would lift the rotary assembly off the thrust plate.

The test loop was pneumostatically tested at 715 psig and certified for operation at 1000°F and 410 psig. The installation of thermocouples and gas feed lines was completed. Controls and control cabinets are being installed.

Study of Back Diffusion Through Labyrinth Seals

(E. R. Taylor)

The study of back diffusion of water vapor against the flow of helium through labyrinth-type seals has been completed. This study was initiated, in collaboration with the Mechanical Development Department at the Oak Ridge Gaseous Diffusion Project, to determine the degree to which this phenomenon might be present in water-buffered seals used in rotating machinery for gas-cooled reactor application. The final test was conducted with a cold radial clearance of the labyrinth of 0.0028 in. The results of this test are presented in Table 8.4.

Table 8.4. Results of Tests of a Water-Buffered Labyrinth-Type Seal with Helium as the Cell Gas

Test No.	Shaft Speed (rpm)	Buffer Water Pressure (psi)	Cell Gas Pressure (psi)	Cell Gas Temperature (°F)	Pressure Drop Across Labyrinth (psi)	Labyrinth Flow (scfh)	Duration of Test (hr)
1	3600	250	253	500	1.0	1387	1 1/2
2	3600	250	253	500	0.5	931	3/4
3	0	250	253	500	0.5	931	1/2

The elevated-temperature radial clearance of the labyrinth was approximately 2 mils. The exact clearance could not be measured directly and was therefore calculated from the conditions of flow and the flow parameters. The numerous tests performed failed to show any evidence of water-vapor back diffusion into the gas chamber.

Previous reports in this series are:

ORNL-2500	Parts 1-4, issued April 1, 1958
ORNL-2505	Issued June 19, 1958
ORNL-2510	Issued September 18, 1958
ORNL-2676	Period Ending December 31, 1958
ORNL-2767	Period Ending June 30, 1959
ORNL-2835	Period Ending September 30, 1959
ORNL-2888	Period Ending December 31, 1959
ORNL-2929	Period Ending March 31, 1960
ORNL-2964	Period Ending June 30, 1960
ORNL-3015	Period Ending September 30, 1960

ORNL-3049

Reactor Technology
TID-4500 (16th ed.)

INTERNAL DISTRIBUTION

1. G. M. Adamson
2. S. A. Beall
3. R. J. Beaver
4. M. Bender
5. D. S. Billington
6. E. P. Blizard
7. A. L. Boch
8. C. J. Borkowski
9. W. F. Boudreau
10. G. E. Boyd
11. E. J. Breeding
12. J. C. Bresee
13. R. B. Briggs
14. W. E. Browning
15. C. E. Center (K-25)
16. R. A. Charpie
17. R. S. Cockreham
18. T. E. Cole
19. J. H. Coobs
20. J. A. Conlin
21. W. B. Cottrell
22. J. A. Cox
23. F. L. Culler
24. H. N. Culver
25. J. H. DeVan
26. D. A. Douglas
27. E. P. Epler
28. R. B. Evans
29. D. E. Ferguson
30. J. Foster
31. J. L. Fowler
32. A. P. Fraas
33. J. H. Frye, Jr.
34. A. E. Goldman
35. B. L. Greenstreet
36. W. R. Grimes
37. E. Guth
38. J. P. Hammond
39. W. O. Harms
40. T. Hikido
41. M. R. Hill
42. H. W. Hoffman
43. A. Hollaender
44. A. S. Householder
45. H. Inouye
46. W. H. Jordan
47. P. R. Kasten
48. G. W. Keilholtz
49. C. P. Keim
50. M. T. Kelley
51. J. J. Keyes
52. R. B. Korsmeyer
53. P. Lafyatis
54. J. A. Lane
55. R. S. Livingston
56. H. G. MacPherson
57. W. D. Manly
58. E. R. Mann
59. R. W. McClung
60. H. E. McCoy
61. H. C. McCurdy
62. H. F. McDuffie
63. C. J. McHargue
64. F. R. McQuilkin
65. H. J. Metz
66. A. J. Miller
67. R. S. Miller
68. J. G. Morgan
69. K. Z. Morgan
70. F. H. Neill
71. M. L. Nelson
72. L. G. Overholser
73. N. Ozisik
74. P. Patriarca
75. A. M. Perry
76. D. Phillips
77. C. A. Preskitt
78. M. E. Ramsey
79-80. P. M. Reyling
81. T. K. Roche
82. M. W. Rosenthal
83. A. F. Rupp
84. G. Samuels
85. H. W. Savage

86. A. W. Savolainen
87. J. L. Scott
88. O. Sisman
89. E. D. Shipley
90. M. J. Skinner
91. G. M. Slaughter
92. A. H. Snell
93. I. Spiewak
94. E. Storto
95. R. D. Stulting
96. J. C. Suddath
97. C. D. Susano
98. J. A. Swartout
99. E. H. Taylor
100. D. F. Toner
101. W. C. Thurber
102. D. B. Trauger
103. C. S. Walker
104. J. L. Wantland
105. G. M. Watson
106. A. M. Weinberg
107. M. E. Whatley
108. J. R. Weir
109. J. C. White
110. E. A. Wick
111. G. C. Williams
112. C. E. Winters
113. J. Zasler
114-117. ORNL — Y-12 Technical Library Document Reference Section
118-187. Laboratory Records Department
188. Laboratory Records Department, ORNL R. C.
189-191. Central Research Library

EXTERNAL DISTRIBUTION

192-194. W. F. Banks, Allis-Chalmers Mfg. Co.
195-197. P. D. Bush, Kaiser Engineers
198. E. Creutz, General Atomic
199-201. R. B. Duffield, General Atomic
202. D. H. Fax, Westinghouse Atomic Power Division
203. T. Jarvis, Ford Instrument Co.
204. Richard Kirkpatrick, AEC, Washington
205-206. H. Lichtenburger, General Nuclear Engineering Corp.
207. J. P. McGee, Bureau of Mines, Appalachian Experiment Station
208. S. G. Nordlinger, AEC, Washington
209. H. B. Rahner, Savannah River Operations Office
210. Corwin Rickard, General Atomic
211. S. T. Robinson, Sanderson & Porter
212. M. T. Simnad, General Atomic
213. Donald Stewart, AEC, Washington
214. G. W. Tompkin, Mallinckrodt Nuclear Corporation
215. Philip L. Walker, Pennsylvania State University
216. R. E. Watt, Los Alamos Scientific Laboratory
217-218. W. L. Webb, East Central Nuclear Group, Inc.
219. Division of Research and Development, AEC, ORO
220-821. Given distribution as shown in TID-4500 (16th ed.) under Reactor Technology category (75 copies — OTS)